Effects Of Faults And Stress On Open Stope Design

by

Fidelis Tawiah Suorineni

A thesis

presented to the University of Waterloo

in the fulfillment of the

thesis requirement for the degree of

Doctor of Philosophy

in

Earth Sciences

Waterloo, Ontario, Canada, 1998

© Fidelis Tawiah Suorineni 1998

National Library of Canada
Acquisitions and Bibliographic Services
395 Wellington Street
Ottawa ON K1A 0N4
Canada

Bibliothèque nationale du Canada
Acquisitions et services bibliographiques
395, rue Wellington
Ottawa ON K1A 0N4
Canada

Your file Votre référence

Our file Notre référence

The author has granted a non-exclusive licence allowing the National Library of Canada to reproduce, loan, distribute or sell copies of this thesis in microform, paper or electronic formats.

L'auteur a accordé une licence non exclusive permettant à la Bibliothèque nationale du Canada de reproduire, prêter, distribuer ou vendre des copies de cette thèse sous la forme de microfiche/film, de reproduction sur papier ou sur format électronique.

The author retains ownership of the copyright in this thesis. Neither the thesis nor substantial extracts from it may be printed or otherwise reproduced without the author's permission.

L'auteur conserve la propriété du droit d'auteur qui protège cette thèse. Ni la thèse ni des extraits substantiels de celle-ci ne doivent être imprimés ou autrement reproduits sans son autorisation.

0-612-32861-9

Canada

The University of Waterloo requires the signatures of all persons using or photocopying this thesis. Please sign below, and give address and date.

ABSTRACT

The thesis is focused on evaluating the effects of faults on the stability of open stopes. Faults are often the source for open stope overbreak and dilution. How faults affect stope stability is still not well understood. This thesis identifies and evaluates the fault characteristics that adversely affect stope stability. The modified stability graph method (Mathews et al. 1980, Potvin 1988) is an empirical design tool that is popular for open stope design. However, this design method does not include a factor to account for the presence of faults or soft zones on excavation stability. Substantial effort was devoted in this thesis to improve the applicability of the stability graph method.

The two main goals of the thesis are to:

- Determine how faults affect the stability of stopes and to provide a method for estimating overbreak due to faults, and
- Develop a fault factor for incorporation into the stability graph to improve the method.

The secondary objectives are to:

- Verify the applicability of the stability graph method in a geological environment outside Canada, with poorer rockmass qualities
- Present statistical tools for optimally defining the boundaries between stability zones in the stability graph, and determine the reliability of a stability graph, and
- Provide alternative likelihood-based stability graphs, and stability graphs based on a modified definition of span.

Characteristics of faults that adversely affect the stability of stopes are given. These characteristics are considered in numerical models to examine their influence on the effect of faults on stope stability. A procedure for estimating overbreak in open stopes due to faults, using numerical models, is presented and applied to case histories from Kidd Mine, Ontario, Canada.

To overcome the weakness in the stability graph method resulting from faults, a methodology for determining a fault factor for incorporation into an empirical design procedure for open stopes, using the stability graph method is developed. The method is applied to case histories from Kidd Mine in Canada. For large faults and shear zones intersecting stope surfaces, the rockmass quality of the soft zone is important for the stability of a stope. A procedure for accounting for soft zones in the stability number N' is given. The approach is applied to case histories from Ashanti Goldfields Mine in Ghana, Africa. The Kidd database contains 112 case histories, and the Ashanti database has 130 case histories.

Ashanti Goldfields is in a different geological setting from which the stability graph was developed, and is characterized by much weaker rocks. The stability graph method is used at Ashanti Goldfields Mine to verify its applicability.

Statistical tools are presented based on the likelihood ratio statistic to optimally define the boundaries between stability zones in the stability graph, and to determine the reliability of a stability graph. Alternative likelihood-based, stability graphs and a stability graph based on a modified definition of span are introduced. Procedures are given for determination of the possible errors in design when the stability graph is used, and methods are presented for defining and optimizing the boundaries between zones in the stability graph.

A stability graph method based on the use of a modified span rather than hydraulic radius is presented as an alternative tool to the conventional stability graph.

The main conclusions of the thesis are as follows:

- For stopes with nearby faults, the faults affect the stability of the stopes by their tendency to increase the zone of low stress or relaxation near the stopes.
- For a stope with a nearby fault, the angle between the fault and the stope surface and the relative position of the fault are the most important factors controlling the severity of fault-related overbreak.
- The effects of faults on open stope stability are influenced by stope geometry, distance of fault from stope surface and in situ stress.
- Numerical models can be used to estimate the extent of overbreak due to a fault near a stope surface, and the parameter for measuring fault-related overbreak is defined as the increase in overbreak for a stope with a fault compared to one without a fault. The method can be used in estimating active support lengths and capacity requirements.
- A fault factor can be determined based on overbreak due to the fault, that can be used to revise the stability number N' to account for the presence of faults near a stope surface. The effect of soft fault gouge can be accounted for in the stability number by relating the width of the soft zone to that of the surface it intersects.
- The stability graph method is applicable to weaker orebodies, than those from which it was originally developed are; however the stope backs require support to prevent progressive caving of the backs in such cases.
- The likelihood ratio is a suitable statistical tool for use in interpreting the stability graph because it can be used to:
  - Optimally define the boundaries between zones in the stability graph based on misclassification cost and inequality of data subgroups,
  - Prove overlap of the stability graph zones and that the zones defined as stable, unstable and cave are not absolute,

  - Determine the magnitude of errors that can be made in predicting stope performance when the stability graph is used, and
  - Develop likelihood-based stability graphs that are useful for new mines and on-the-spot design.
- A stability index graph that includes rockmass parameters omitted in the conventional stability graph, and based on modified span, is presented as an alternative open stope design method.

The application of the results of this thesis in the mining industry should lead to improved understanding of fault effects on open stope stability and increased confidence in the use of the stability graph as a robust empirical design tool.

ACKNOWLEDGEMENTS

I would like to thank my supervisors, Professors P.K. Kaiser, M.B. Dusseault, and Dr. D.D. Tannant for their continued encouragement and guidance to the completion of the thesis.

I would like to also thank Professor Dusseault for his effort in making my studies in University of Waterloo and the Geomechanics Research Centre, Laurentian University, possible. It has been a wonderful and exciting experience of learning in the joint program between these two institutions. Special thanks also go to Professor Kaiser and Dr. Tannant for their academic guidance. It has been a pleasure working with Dr. Tannant.

The following have given financial support for this research, and I am grateful to them:

- Government of Ghana,
- Geomechanics Research Centre,
- University of Waterloo, and
- Ashanti Goldfields Company, (Gh) Ltd.

I acknowledge the co-operation given me by Shawn Seldon and Falconbridge Kidd Mine during the data collection period in Kidd Mine, Timmins, Ontario, Canada.

Mr. J. Amanor played an important role in asking management of Ashanti Goldfields Mine in Obuasi for permission on my behalf to use the mine as one of the research sites. I am grateful to Mr. Amanor, and Management for their assistance and co-operation.

Appreciation is extended to all staff of GRC, and my colleagues who have given me support in the course of my work, especially, Jeanette Fooks, and Parsa Pezeshkpour, both graduate students of the Geomechanics Group in University of Waterloo. I also, wish to express my appreciation to Dr. John Franklin for his encouragement, company and the academic material that he provided for the research.

Finally, I thank my wife and children for their support and encouragement throughout the research.

DEDICATION

This thesis is dedicated to my late brother,

John Bosco Naah Suorineni.

May his soul rest in peace.

TABLE OF CONTENTS

ABSTRACT iv

ACKNOWLEDGEMENTS vii

DEDICATION viii

1 INTRODUCTION 1

1.1 Problem Definition 1

1.2 Objectives of Research 6

1.3 Scope and Organization of the Thesis 7

1.3.1 Scope of the thesis 7

1.3.2 Organization of the thesis 7

2 REVIEW OF ROCKMASS CLASSIFICATIONS AND UNDERGROUND EXCAVATION DESIGN METHODS 10

2.1 Introduction 10

2.2 Analytical Methods 10

2.3 Numerical simulation Methods 11

2.4 Rockmass Classifications and Empirical Underground Excavation Design Methods 11

2.4.1 Rockmass classification systems 12

2.4.1.1 Terzaghi's rockmass classification system 12

2.4.1.2 Rock quality designation *RQD* 13

2.4.1.3 Lauffer's rockmass classification system 14

2.4.1.4 Geomechanics rockmass rating system *RMR* 14

2.4.1.5 Mining rockmass classification system 15

2.4.1.6 NGI Q classification system 19
2.4.2 Comparison of Q and *RMR* 22
2.4.3 Application of classification systems for underground excavations design 24
2.4.3.1 Terzaghi rock load classification system 24
2.4.3.2 Application of *RQD* classification system to underground excavation design 24
2.4.3.3 Lauffer's stand-up time - span design method 25
2.4.3.4 *RMR* span - stand-up time method 26
2.4.3.5 Laubscher's *MRMR* - hydraulic radius *HR* design method 28
2.4.3.6 The shape factor 29
2.4.3.7 Mathews open stope design method 30
2.4.3.8 Potvin's Modifications to the stability graph 36
2.4.3.9 NGI's Q - equivalent dimension D_e design approach 37
2.4.3.10 Dilution design method 40
2.4.3.11 Rockmass index *RMi* design approach 41
2.5 Observations and inferences from the Q - D_e system and the modified Mathews method 41
2.5.1 Stress factor A and stress reduction factor *SRF* 44
2.5.2 Excavation support ratio *ESR* 46
2.6 Summary 48
3 APPLICATION OF STATISTICS TO INTERPRETATION OF STABILITY GRAPH 50
3.1 Introduction 50
3.2 Distant Methods and Discriminant Analysis 52
3.3 The Calibration Database 53
3.4 Previous Use of Statistics and the Stability Graph 53
3.5 Defining the Transition Zones 55
3.5.1 The multivariate likelihood statistic 58
3.5.2 Method 1: Approximation method 62
3.5.2.1 Theory of equiprobability contours 62
3.5.2.2 Application to the stability graph 66
3.5.3 Method 2: Using likelihood statistic 69
3.5.4 Method 3: Multiple design curve stability graph 73
3.5.5 Theoretical Implications of the Stability Graph Regions 74
3.6 Accounting for Misclassification Errors and Risk Cost 75
3.6.1 Performance prediction errors in the stability graph 75
3.6.2 Misclassification Risk Cost 77
3.7 Summary 79

4 RELAXATION SLOUGHAGE 83
4.1 Introduction 83
4.2 Definition and Causes of Relaxation 83
4.3 Limit Equilibrium Wedge Analysis 87
4.3.1.1 Rhombohedral prism 88
4.3.2 Triangular prism - equilateral or isosceles 94
4.4 Discussion of Wedge analysis 97
4.5 Summary 99
5 DETERMINATION OF STOPE OVERBREAK AND FAULT FACTORS: IMPLICATION FOR OPEN STOPE DESIGN 100
5.1 Introduction 100
5.2 Observational Assessment 104
5.3 Effect of Fault Shear Strength and Orientation - Analytical Models 106
5.3.1 Fault slip - Method 1 106
5.3.2 Fault slip – method 2 108
5.4 Numerical Modelling 115
5.4.1 PHASE^2 117
5.4.2 EXAMINE^{2D} 120
5.4.3 Model and hypothesis 121
5.4.4 Procedure for determining overbreak 123
5.4.4.1 Comparison of 2-D elastic and plastic models 125
5.4.4.2 Effect of fault position 126
5.4.4.3 Fault intersecting stope at toe 127
5.4.4.4 Fault intersecting stope at middle 128
5.4.4.5 Fault intersecting stope at back or crown 128
5.4.4.6 Effect of angle between fault and stope surface 129
5.4.4.7 Effect of fault shear strength 129
5.4.4.8 Effect of in situ stress state (K-ratio) on influence of faults on stope stability 131
5.4.4.9 Effect of stope aspect ratio A_r 135
5.4.4.10 Effect of stope dip on fault effect 136
5.4.4.11 Effect of distance of fault from stope surface - included angle $\xi = 0$ 137
5.4.5 Development of generic $ELOS_f$ chart 138
5.4.6 Development of fault factor F_w 143
5.4.6.1 Effect of fault position and included angle 145
5.4.6.2 Effect of fault shear friction angle 146

5.4.6.3 Effect of stress ratio 147
5.4.6.4 Effect of stope aspect ratio 148
5.4.6.5 Effect of stope dip 148
5.4.6.6 Effect of fault distance 149
5.4.7 Generic fault factor 150
5.5 Discussion of results and implications 154
5.5.1 Observational and analytical generic fault factors 154
5.5.2 Summary of individual parameter effects 155
5.5.3 Implications for overbreak estimation and support design 158
5.6 Summary 158
6 KIDD MINE CASE HISTORIES 160
6.1 Introduction 160
6.2 Mining Methods 162
6.3 Mine Geology 166
6.3.1 Massive sulphides 166
6.3.2 Rhyolites 167
6.3.3 Andesite-diorite 168
6.3.4 Main faults and shear zones 168
6.4 Rock Properties 170
6.4.1 Introduction 170
6.4.2 Rock properties 171
6.4.3 Discontinuity survey 178
6.4.4 Classification of Kidd Mine main rock units 181
6.4.5 In Situ Stresses at Kidd Mine 182
6.5 Stope Performance 183
6.6 Kidd Mine Stability Graph 186
6.6.1 Stope wall hydraulic radii 187
6.6.2 Selecting a stability graph data analysis procedure 188
6.7 Application of Fault Factor 192
6.8 Optimization of Stability Graph Boundaries and Risk Cost 204
6.9 Summary 206
7 EVALUATION OF ASHANTI OPEN STOPE PERFORMANCE 208
7.1 Introduction 208
7.2 Objectives 210

7.3 Geology 210
7.3.1 General geology 210
7.3.2 Geology of Blocks 2 and 7 - Kwesi Mensah Shaft (KMS) 212
7.3.3 ETS shaft pillar geology 213
7.4 Implications of Geologic Structure to Open Stope Mining 214
7.5 Mining Methods 214
7.6 Rock Properties 218
7.6.1 Rock material and rockmass properties 218
7.6.2 Geotechnical discontinuity mapping 219
7.6.2.1 Block 2 220
7.6.2.2 Block 7 223
7.6.2.3 Block 8 224
7.6.3 Implications of discontinuity patterns 225
7.6.4 Rock quality designation *RQD* 226
7.6.5 Modified rockmass quality *Q'* 228
7.7 Shape Factors 228
7.8 In situ Stresses 229
7.9 Stope Performance 233
7.10 Fault Gouge Rockmass Quality Correction 237
7.10.1 Fault gouge rockmass correction factor Q'_m 237
7.10.2 Estimation of fault gouge (graphite) thickness 239
7.11 Ashanti Stability Graph 242
7.12 Evaluation of Mining Methods in Ashanti 247
7.12.1 Accounting for bifurcations in design 247
7.12.2 Alternative mining methods for Ashanti 248
7.13 Summary 253
8 CONCLUSIONS AND RECOMMENDATIONS 254
8.1 Conclusions 254
8.1.1 Fault effects 255
8.1.2 Case histories 257
8.1.3 Stability graph and applications of statistics 258
8.1.4 Alternative stability graphs 259
8.2 Recommendations For Future Research 259

A STATISTICAL MODELS FOR EMPIRICAL DATA INTERPRETATION 261
A.1 Bayes' theorem and the likelihood statistic 261
A.2 Mahalanobis Distance Method 265
A.3 Calibration database 267
A.4 Verification of the bivariate normality assumption 278
B OVERBREAK AND FAULT FACTOR 282
B.1 Influence of Fault Shear Strength on Fault Effect on Stope Stability 282
B.1.1 Fault friction angle is 15° - Shear strength (i) 282
B.1.2 Fault friction is 20° - Shear strength (ii) 283
B.1.3 Fault friction is 30° - Shear strength (iii) 283
B.2 Influence of stope aspect ratio on fault effect on stope stability 285
B.2.1 Effect of $A_r = 0.4$ 285
B.2.2 Effect of $A_r = 0.8$ 285
B.2.3 Effect of $A_r = 1.5$ 286
B.2.4 Effect of Ar=0.2 288
B.3 Analytical procedures for Fault and Stope Geometry Determination 289
B.3.1 Method 1: Using three coordinates on the plane 289
B.3.2 Method 2: When dip and dip direction of the plane are known 290
B.3.3 Method 3: Cross product of two vectors in the plane 292
B.3.4 Included Angle Between Fault or Joint Set and a Stope Surface 293
B.3.5 Distance Between a Fault and a Point on a Stope Surface 293
C DETAILS OF STOPES AND FAULTS IN KIDD DATABASE 295
D ASHANTI GOLDFIELDS CORPORATION (GHANA) LTD. 328
REFERENCES 335

LIST OF TABLES

Table 2.1 Terzaghi's (1946) rockmass classification system 13

Table 2.2 Deere's (1964) rockmass classification system 13

Table 2.3 Lauffer's (1958) rockmass classification system 14

Table 2.4 Summary of revised parameter ratings for *RMR* classifaction system (after Laubscher and Taylor 1976) 17

Table 2.5 Assessment of joint condition - adjustments as cumulative percentages of total possible rating of 40 (from Brady and Brown, 1993) 18

Table 2.6 Gravity adjustment factors based on number of joint sets (after Laubscher, 1990) 19

Table 2.7 Adjustments for faults and shear zones relative orientations (from Potvin, 1988 19

Table 2.8 Summary of the possible total adjustment factors (from Potvin, 1988) 19

Table 2.9 Updated *SRF* values (after Barton, 1994) 21

Table 2.10 Correlation matrix showing levels of significance of rockmass classification parameters on rockmass quality 23

Table 2.11 Excavation support ratios *ESR* for underground excavations (after Barton, 1988) 39

Table 2.12 *Q* values for walls 39

Table 3.1 Calibration database composition 53

Table 3.2 Chronology of number of transition zones - Author dependent 55

Table 3.3 Confusion matrix for determination of classification rule performance 75

Table 3.4 Misclassification cost matrix 78

Table 4.1 Summary of critical clamping stress analysis 99

Table 5.1 Qualitative assessment of effects of faults on stability of underground excavations 105

Table 5.2 Characteristics of stopes 121

Table 5.3 Rockmass and fault properties 122

Table 5.4 Stress states used in the models 122

Table 5.5 Groups of ELOS curves based on fault effects 139

Table 5.6 Summary of fault factor curves according to similarity in behaviour as per Figure 5.41 150

Table 5.7 Summary of fault effect on stope stability with reference to parameter groups 154

Table 5.8 Evaluation of factors influencing the effects of faults on open stope stability 156

Table 5.9 Assessment of effect of distance of fault to stope surface on surface stability 156

Table 5.10 Classification of fault effects on stability based on position and included angle ξ 156

Table 6.1 Summary of the mechanical properties of main rock units at Kidd Mine 171

Table 6.2 General rockmass ratings (after Yu and Quesnel, 1984) 172

Table 6.3 *RMR* rockmass classification of Kidd rock types (after Yu and Vongpaisal, 1996) 172

Table 6.4 Properties of main structural discontinuities (after Henning et al., 1992) 173

Table 6.5 Geotechnical properties of main rock types at Kidd Mine 173

Table 6.6 Anisotropic strength factors for strength correction 173
Table 6.7 Summary of *RQD* analysis based on rock type 175
Table 6.8 Summary of joint analysis results 180
Table 6.9 Summary of schistosity analysis results. (Tannant et al., 1997) 181
Table 6.10 Resultant joint sets in main rock units after accounting for schistosity 181
Table 6.11 Classification of main rock types at Kidd Mine 182
Table 6.12 Classification of *ELOS* into stability graph terminology 186
Table 6.13 Data discriminability indices as a measure of data overlap 191
Table 6.14 Comparison of measured average overbreak with predicted $ELOS_f$ 197
Table 6.15 Comparison of performances of stope performance classification criteria 200
Table 6.16 Cost matrix for misclassification risk cost determination 205
Table 6.17 Confusion matrix for Kidd Mine database 205
Table 7.1 Summary of mining methods at Ashanti Goldfields Company underground mines (after Mireku-Gyimah and Suglo, (1993) 215
Table 7.2 Summary of rock material and rockmass properties 219
Table 7.3 Summary of KMS Block 2 rockmasses discontinuity characteristics 222
Table 7.4 Summary of discontinuity characteristics of KMS Block 7 rock units 224
Table 7.5 Summary of discontinuity characteristics of GCS Block 8 rock units 225
Table 7.6 Estimated *RQD*s from fracture frequencies 227
Table 7.7 Modified rockmass qualities Q' at Ashanti Goldfields mine 228
Table 7.8 Geometric information on stopes as obtained from the mine 229
Table 7.9 Summary of in situ stress measurement results 230
Table 7.10 Bifurcation in stopes and association with crown stability 236
Table 7.11 Estimated effective graphite thicknesses (m) in stope surfaces 242
Table 7.12 Classification of dips of orebodies and discontinuities for mining method selection and stability considerations - stress factor $A = 1$ 249
Table A.1 Summary of the unsupported calibration database 267
Table A.2 Summary of supported case histories database 273
Table C.1 Stope surface dimensions and orientations 295
Table C.2 Summary of fault database relating fault to stope surface 308
Table C.3 Kidd Mine stability graph database 323
Table D.1 Rock Mass Rating 328
Table D.2 Rock Mass Rating Adjustments 328
Table D.3 Mining Rock Mass Rating 328
Table D.4 Summary of stope geometry and performance data collected from Ashanti 329
Table D.5 Ashanti Goldfields Company open stope database 330

LIST OF FIGURES

Figure 1.1 Footwall fault failure (from Dune and Pakalnis, 1996) - Canada....2
Figure 1.2 Vertical sections showing locations of orebodies, faults and details of progressive failure in ROB5 (from Mikula, 1993) - Australia....2
Figure 1.3 Large open stope with faults associated with orebody at Mount Isa Mines, Australia (from Potvin, 1998)....3
Figure 1.4 Fault related overbreak in hangingwall of an open stope causing approximately 30% dilution....3
Figure 1.5 Typical sliding caused by unfavourable directions of a fault and joints in relation to a power plant hall (from Brekke and Selmer-Olsen, 1966)....4
Figure 1.6 Graphite (soft zone) related caving in an open stope at Ashanti Goldfields in Ghana....5
Figure 2.1 Assessment of joint -space rating (Laubscher, 1990)....16
Figure 2.2 Updated *SRF* values for competent, squeezing and swelling rocks (Re-plotted after Barton, 1994) showing number of cases for which various *SRF* values are defined including the uspper limit of *SRF*....22
Figure 2.3 Proposed relationship between *RQD* and rock support (from Hoek and Brown, 1980)....25
Figure 2.4 Definition of active span and span (from Hoek and Brown, 1980)....25
Figure 2.5 Lauffer's span – stand-up time chart (after Hoek and Brown, 1980)....26
Figure 2.6 Graph relating stand-up time, unsupported span, and rockmass quality *RMR* (from Hutchinson and Diederichs, 1996; original data from Bieniawski, 1989)....27
Figure 2.7 Modified span - stand-time diagram. Bieniawski's straight-line contours (extrapolated) are compared with curvilinear *RMR* contours proposed by Franklin and Palasi (after Franklin and Palasi, 1993)....28
Figure 2.8 Laubscher's stability index graph (after Laubscher, 1990)....29
Figure 2.9 Stability graph factors (after Mathews et al., 1980)....32
Figure 2.10 Chart for determining joint orientation factor *B* (Re-plotted from Hutchinson and Diederichs, 1996)....33
Figure 2.11 Mathews stability graph (from Mathews et al., 1980)....35
Figure 2.12 Proposed graph for the determination of the gravity factor *C* for footwalls and sliding (after Hadjigeorgiou et al., 1995)....36
Figure 2.13 Potvin's re-calibrated stability graph factors (from Nickson, 1992): Dashed lines in *B* factor graph represent strike differences increasing from 0° to 90° at top at 15° increments except from 0° to 30° in first two lower curves....37
Figure 2.14 Potvin's modified Mathews stability graph (from Nickson, 1992)....37
Figure 2.15 Updated Q-D_e design chart (from Grimstad and Barton, 1993)....40
Figure 2.16 Dilution based empirical design (after Pakalnis and Vongpaisal, 1993)....41

Figure 2.17 Comparison of *Q - De* and *N'-HR* empirical design charts: *ESR* =3 42
Figure 2.18 Stability graph using hydraulic radius and modified span 43
Figure 2.19 Re-plotted stress factor graph 44
Figure 2.20 Comparison of stress factor *A* and stress reduction factor *SRF* 45
Figure 2.21 Chart for determining *C* based on excavation type 47
Figure 2.22 Relationship between excavation type as described in and Excavation Support Ratio *ESR* (Table 2.11) 48
Figure 3.1 Nickson's (1992) statistically derived boundaries 54
Figure 3.2 Stability graph showing statistically derived boundaries by Hadjigeorgiou et al. and Potvin (1988) hand drawn zone (after Hadjigeorgiou et al., 1995) 55
Figure 3.3 *ELOS* stability graph showing *ELOS* values superimposed on dilution contours proposed by Scobble and Moss (1994) by Pakalnis and Vongpaisal (after Pakalnis and Vongpaisal, 1998) 56
Figure 3.4 Stability graph zones proposed by Stewart and Forsyth (1995) 57
Figure 3.5 Definition of the transition zone in the stability graph using the Potvin-Nickson (1992) stability graph 58
Figure 3.6 Scatter plots showing shapes and association of bivariate normal distributions $\rho_{HRN'}$ is the covariance coefficient 61
Figure 3.7 Equiprobability contours showing spread and association of variables *N'* and *HR* for a bivariate single data group where $\mu_{N'}$ and μ_{HR} are the means of the stability numbers and hydraulic radii for the given stability state 63
Figure 3.8 Intersection of equiprobability contours and estimation of transition zone 64
Figure 3.9 Various types of transition surfaces 65
Figure 3.10 Overlapping data and discrimination efficiency: υ decreases for example from 20 t0 5 to 0.1 in the bottom diagram 66
Figure 3.11 Equiprobability contours and estimated the transition zones with *N'* and *HR* plotted on log axes 67
Figure 3.12 Overlapping of equiprobability contours showing that the stability zones in the stability graph are not independent (*N'* and *HR* on log axes) 69
Figure 3.13 Stability graph boundaries using unsupported cases and defining the transition zone 72
Figure 3.14 Re-defined stability graph boundaries and transition zone using only unsupported case records 72
Figure 3.15 Likelihood-based stability graph 74
Figure 4.1 Generic examples of stress paths that a) lead to stope wall failure and b) cause no major stability problems (after Tannant et al., 1997) 84

Figure 4.2 Excavation geometries and stress ratios that enhance relaxation: (a) & (b) Unfavourable stress ratio; (c) & (d) Changes in mining geometry - excavation step 2 creates stress shadow around excavation 1; (e) Abutment yield; (f) Intersection - relaxed roof; (g) Undercut; and (h) Concave structure (after Diederichs and Kaiser, 1998) 85
Figure 4.3 Stress distribution around stope with no obvious undercut. Solid black pattern indicates tension in the model 86
Figure 4.4 Effect of undercutting on stress distributions due to vertical orebody thickness variation. Solid black pattern indicates tension in the model 87
Figure 4.5 Possible failure modes in a blocky rockmass, related to mining activities 88
Figure 4.6 Rhombohedral prism in a stope back 89
Figure 4.7 Plot of factor of safety versus dip of joint for Rhombohedral prism: Joint friction is 15° 90
Figure 4.8 Plot of factor of safety versus dip of joint 70°, for Rhombohedral prism: Joint friction is 30° 91
Figure 4.9 The Book analogy for determination of critical clamping stress for a parallelepiped shaped block 92
Figure 4.10 Factor of safety versus clamping stress for various block sizes (Book analogy - α=90° for rhombohedral case) and joint friction angles of 15° and 30° 93
Figure 4.11 Representation of triangular prism in back of excavation 94
Figure 4.12 Triangular prism critical stress for a joint friction angle of 15° 96
Figure 4.13 Triangular prism critical stress for joint friction angle of 30° 97
Figure 4.14 Illustrating the importance of stress in preventing slip along weak planes such as faults 98
Figure 5.1 Conceptual model of the effects of faults for (a) stope surface equivalent linear overbreak slough due to fault $ELOS_f$ and (b) for fault factor development 101
Figure 5.2 Definition of included angle ξ between stope and fault 105
Figure 5.3 Model for effect of fault shear strength and fault orientation on stope surface stability: (a) Rock specimen with fault under triaxial compression and (b) Equivalent stope sidewall with fault (biaxial stress state) 106
Figure 5.4 Effect of fault total friction angle ϕ^* and included angle on stope wall stability 108
Figure 5.5 Kirsch solution for stresses around a circular opening - definition of parameters 109
Figure 5.6 (a) Plot of shear stress/normal stress ratio versus distance along a plane of weakness (b) close to but not intersecting, a circular excavation (Re-plotted (a) and redrawn (b) after Brady and Brown, 1993) 110
Figure 5.7 General representation of fault-excavation geometrical relations 111
Figure 5.8 Effect of fault dip on amount of slip: K=2.1, excavation radius =7.5 m, fault friction ϕ^* = 20° 113
Figure 5.9 Effect of fault distance to excavation surface on fault slip: K=2.1, excavation radius a=7.5 m, fault friction ϕ^*=20°, α=90°, b=0 114

Figure 5.10 Effect of fault dip on excavation fault slip: K = 2.1, excavation radius a = 7.5 m, fault friction ϕ^* = 20°, α .=.90° 115
Figure 5.11 Typical PHASE^2 finite element mesh for the rockmass and fault for included angle of 30°, 3-noded triangular elements, number of elements = 4460, excavation nodes are 150, maximum iterations = 500, tolerance = 0.001, solvertype is Gaussian elimination 119
Figure 5.12 Model for analyzing fault effects on stope stability 122
Figure 5.13 Comparison of tension zones from elastic (a) and non-elastic (b) models for a stress ratio K = 2.1, c = 100, ϕ = 37° 125
Figure 5.14 Comparison of results from elastic and plastic models in terms of $ELOS_f$ 126
Figure 5.15 Model results for fault intersecting stope at bottom at stated included angles: Stress ratio K = 2.1, stope aspect ratio A_r = 0.4, fault friction angle ϕ^* = 20°, stope dip α = 72°, F = fault and ξ = included angles 127
Figure 5.16 Effect of fault intersecting stope at middle at various included angles: Stress ratio K = 2.1, stope aspect ratio A_r = 0.4, fault friction angle ϕ^* = 20°, stope dip α = 72°, F = fault and ξ = included angles 128
Figure 5.17 Effect of fault intersecting stope at middle at various included angles: Stress ratio K = 2.1, stope aspect ratio A_r = 0.4, fault friction angle ϕ^* = 20°, stope dip α = 72°, F = fault, ξ = included angle 128
Figure 5.18 Effect of fault shear strength on stope stability using $ELOS_f$: Stress ratio K = 2.1, stope aspect ratio A_r = 0.4, fault friction angle ϕ^* = 8°, 15°, 20° and 30°, stope dip α = 72°, Fault at bottom of stope 130
Figure 5.19 Plots of normal stress versus distance along faults, measured from point fault intersects stope, showing zero normal stresses on faults dependent on fault orientation relative to stope surface, for included angles of 5°, 10°, 20° and 30 131
Figure 5.20 Effect of in situ stress state on overbreak in terms $ELOS_f$ due to faults: Stress ratio K = 1.2, 2.1, 3.2, stope aspect ratio A_r = 0.4, fault friction angle ϕ^* = 20°, stope dip α = 72° 132
Figure 5.21 Effect of K- ratio = 1.2 on the influence of faults on stope stability, stope aspect ratio A_r = 0.4, fault friction angle ϕ^* = 20°; stope dip α = 72°, Fault intersecting stope at bottom, F = fault, ξ = included angle 133
Figure 5.22 Effect of K-ratio = 3.2 on the influence of faults on stope stability: Stress ratio = 3.2, stope aspect ratio = 0.4, fault friction ϕ^* = 20°; stope dip = 72° 134
Figure 5.23 Effect of stope aspect ratio A_r on the influence of faults on hangingwall $ELOS_f$: stress ratio K = 2.1, stope aspect ratio A_r = 0.2, 0.3 (for α = 55°), 0.4, 0.8, and 1.5, fault friction angle ϕ^* = 20°; stope dip α = 72° 135
Figure 5.24 Effect of stope dip on the influence of a fault on stope stability: Stress ratio K = 2.1, stope aspect ratio A_r = 0.4, 0.3 fault friction angle ϕ^* = 20°; stope dip α = 55°, 72° 136

Figure 5.25 Effect of varying included angle on the influence of a fault on the stability of a stope dipping at 55°: Stress ratio $K = 2.1$, stope aspect ratio $A_r = 0.3$, fault friction angle $\phi^* = 20°$; stope dip $\alpha = 55°$, F = fault, ξ = included angle 137
Figure 5.26 Effect of distance of fault from stope surface on the influence of the fault on $ELOS_f$: Stress ratio $K = 2.1$, stope aspect ratio $A_r = 0.4$, fault friction angle $\phi^* = 20°$; stope dip $\alpha = 72°$ 138
Figure 5.27 Plot of all parameters $ELOS_f$ versus included angle ξ 139
Figure 5.28 Curve-fitting to groups (F1 to F7) of data in $ELOS_f$ graph (Figure 5.27), Group 8 and Group 9 140
Figure 5.29 $ELOS_f$ curves for estimating depths of overbreak due to faults intersecting stope under various ground conditions and stope geometries 141
Figure 5.30 $ELOS_f$ curve for very weak faults: $\phi^* = 8°$ 141
Figure 5.31 $ELOS_f$ curve for non-intersecting faults $\xi \approx 0°$ 142
Figure 5.32 Illustration of the calculation of $ELOS_f$ when fault passes through stope intersecting both hangingwall and footwall (a). 143
Figure 5.33 *ELOS* stability graph (from Clark and Pakalnis, 1997) 144
Figure 5.34 Determination of fault factor F_w 145
Figure 5.35 Fault factor graph based on fault position: Stress ratio $K = 2.1$, stope aspect ratio $A_r = 0.4$, fault friction angle $\phi^* = 20°$, stope dip $\alpha = 72°$ 146
Figure 5.36 Fault factor based as a function of fault shear strength: Stress ratio $K = 2.1$, stope aspect ratio $A_r = 0.4$, fault friction $\phi^* = 8°$, 15°, 20°, 30°; stope dip $\alpha = 72°$ 147
Figure 5.37 Fault factor as a function of stress ratio K: Stress ratio $K = 1.2$, 2.1, 3.2; stope aspect ratio $A_r = 0.4$, fault friction angle $\phi^* = 20°$; stope dip $\alpha = 72°$ 147
Figure 5.38 Effect of stope aspect ratio A_r on fault factor: Stress ratio $K = 2.1$, stope aspect ratio A_r = 0.4, 0.8, 1.5, fault friction angle $\phi^* = 20°$; stope dip $\alpha = 72°$ 148
Figure 5.39 Fault factor showing effect of stope dip: Stress ratio $K = 2.1$, stope aspect ratio $A_r = 0.4$, 0.3, fault friction angle $\phi = 20°$, stope dip $\alpha = 55°$, 72° 149
Figure 5.40 Effect of fault distance on fault factor: Stress ratio $K = 2.1$, stope aspect ratio $A_r = 0.4$, fault friction angle $\phi^* = 20°$; stope dip $\alpha = 72°$ 149
Figure 5.41 Plot of all parameters fault factor graphs, showing parameter groupings 150
Figure 5.42 Curves fitted to groups (G1 to G7) of data in fault factor graph (Figure 5.41), and smoothened graph for non-intersecting faults (Group 8) (cont. next page) 151
Figure 5.43 Fault factor curves for faults intersecting stopes 152
Figure 5.44 Fault factor curve for very weak faults intersecting stope at bottom 152
Figure 5.45 Fault factor curve for non-intersecting faults with $\xi \approx 0$ 153
Figure 5.46 Generic fault factor graphs based on observational and analytical models (a) effect of included angle (b) effect of fault friction angle (c) & (d) effect of distance 155
Figure 6.1 Kidd mine showing the position of #3 Mine 161

Figure 6.2 Infrastructure of #3 Mine 161
Figure 6.3 Typical stope sequence in #3 Mine 162
Figure 6.4 Plan view of 5400 level showing a typical panel sequence in #3 Mine 163
Figure 6.5 Stope sequence when orebody is wide 163
Figure 6.6 Copper stringer and massive sulphide orebodies showing stope sizes and sequencing: Stopes are 40 m high (some 70 m), 15 to 20 m lengths and, 15 to 40 m footwall to hangingwall widths 164
Figure 6.7 Plan and longitudinal section of 56-695 stope showing stope development in #3 Mine 165
Figure 6.8 Details of blast rings and slot for 56-695 stope as is typical for #3 Mine 165
Figure 6.9 Exposure times of stopes (after Tannant and Diederichs, 1997) 167
Figure 6.10 Simplified geology of #3 Mine as seen on 5100 level showing main faults and minor faults, and their relationships to stope walls in the copper stringer and massive sulphide orebodies. Dip direction of orebodies is NE. 169
Figure 6.11 Definition of stope wall volume for determination of stope wall *RQD* in *RQD* data file 174
Figure 6.12 Contours of *RQD* values taken on 5200 level, showing relationship of *RQD* with faults and stope surfaces (after Tannant and Diederichs, 1997) 175
Figure 6.13 Contours of *RQD* values taken along a cross-section centred on 735 panel (after Tannant and Diederichs, 1997) 176
Figure 6.14 Distances between stope walls and faults 177
Figure 6.15 Equal area contours plots of poles of joints in andesite/diorite 178
Figure 6.16 Equal area contour plots of poles of joints in volcaniclastic rhyolite 178
Figure 6.17 Equal area contour plots of poles of joints in cherty breccia (massive rhyolite 179
Figure 6.18 Equal are contour plots of poles of joints in massive sulphide 179
Figure 6.19 Equal area contour plots of poles of schistosity in (a) cherty breccia and (b) rhyolite volcaniclastic 179
Figure 6.20 Equal area stereonet of faults on 52 Level 180
Figure 6.21 Measured in situ principal stresses at various levels (solid squares) at Kidd Mine, and predicted stresses (open squares) at depth - Broken line ($\sigma_1 = \sigma_3$) represents hydrostatic stress case (Re-plotted from Tannant et al., 1997) 182
Figure 6.22 Section through the centre of 56-705 stope looking NW - Well performed stope with no overbreak 184
Figure 6.23 Section through the centre of 53-695 stope looking NW - Poorly performed tall stope hangingwall with 7.5 m overbreak 184
Figure 6.24 Overbreak distribution throughout #3 Mine 185
Figure 6.25 Distribution of stope surfaces in the database 186
Figure 6.26 *EIOS* stability graph with transition zones as defined by Potvin (1988) and Nickson (1992) (after Clark and Pakalnis, 1997) 187

Figure 6.27 Illustrations of problems in statistical discrimination with respect to individual mine data.....188
Figure 6.28 Conventional Kidd Mine modified stability graph with Potvin (1988) "unsupported transition zone" and Nickson (1992) "supported transition zone" (a) Semi-log scale (b) Log-log scale. 189
Figure 6.29 Data in Figure 6.28 re-plotted with boundaries as redefined in the thesis, on a log-log scale..190
Figure 6.30 Modified stability graph showing three case histories of back failure where soft inclusions of weak material were present (after Potvin and Milne, 1992).....192
Figure 6.31 Sections of stopes with faults close to or intersecting hangingwalls and or footwalls (cont. next page) 193
Figure 6.32 Conventional stability graphs without fault factor corrections for the nine stope surfaces 195
Figure 6.33 Re-plotted stability graph for the nine stope surfaces corrected for fault effects 196
Figure 6.34 Stope section showing fault intersecting stope surface but lying entirely in ore that is mined, and therefore does not affect stability of stope surface - F_w=1 198
Figure 6.35 Modified stability graph for (a) uncorrected stability numbers for fault effects (b) corrected stability numbers for fault effects, with boundaries as defined by Potvin (1988) and Nickson (1992).....199
Figure 6.36 Modified stability graph for corrected stability numbers for fault effects, with boundaries as defined in Chapter 3 of thesis.....200
Figure 6.37 Mine excavation stability index graph for Kidd Mine, (ESR = 3).....201
Figure 6.38 Plot of likelihood ratio against average depth of failure 202
Figure 6.39 Likelihood-based multiple design curves stability graph using hydraulic radius.....203
Figure 6.40 Likelihood-based multiple design curves stability graph using modified span.....203
Figure 6.41 Optimized boundary between stable and unstable stopes.....206
Figure 7.1 Longitudinal section of part of Ashanti Goldfields mine at Obuasi showing the blocks studied 209
Figure 7.2 Map of Ghana showing geology and location of Obuasi - Ashanti Goldfields mine.....211
Figure 7.3 Main fissures and shears at Ashanti as observed near Adansi shaft (after Amanor and Gyapong, 1988).....212
Figure 7.4 Open stope design at Ashanti for GCS Block 8, showing a plan view of blast rings.....216
Figure 7.5 Longitudinal section showing open stope design in Block 8 of GCS 216
Figure 7.6 3D-wire frame of ETS shaft pillar orebody viewed along strike, with ramp and main levels....217
Figure 7.7 Longitudinal section showing stope sequence at ETS shaft pillar. 217
Figure 7.8 Plan view of the ETS shaft pillar orebody as seen on 35 level.....218
Figure 7.9 Contour plot of discontinuity poles and major planes showing discontinuity structure in KMS Block 2 orebody as obtained from verification survey 220
Figure 7.10 Contour plots of discontinuity poles and major planes showing discontinuity structure in KMS Block 2 orebody (after Udo, 1996) as obtained from mine.....221

Figure 7.11 Contour plots of discontinuity poles showing discontinuity structure in KMS Block 2 hangingwall 221
Figure 7.12 Contour plot of discontinuity poles showing discontinuity structure in KMS Block 2 footwall 222
Figure 7.13 Contour plot of discontinuity poles showing discontinuity structure in KMS Block 7 orebody 223
Figure 7.14 Contour plot of discontinuity poles in KMS Block 7 hangingwall 223
Figure 7.15 Contour plot of discontinuity poles showing discontinuity structure in KMS Block 7 footwall 223
Figure 7.16 Contour plot of discontinuity poles in GCS Block 8 hangingwall 224
Figure 7.17 Contour plot of discontinuity poles showing discontinuity structure in GCS Block 8 footwall 225
Figure 7.18 Comparison of GCS (South) and ETS (North) *RQD* values 226
Figure 7.19 *RQD* and fracture frequency relationship for Ashanti data 227
Figure 7.20 Plot of vertical stresses against depth below surface (after Hoek and Brown, 1980) with Ashanti data superimposed 231
Figure 7.21 Plot of variation of ratio of average horizontal stress to vertical stress with depth below surface (after Hoek and Brown, 1980), with Ashanti data superimposed 232
Figure 7.22 Graph for estimating in situ stresses at upper levels in Ashanti 232
Figure 7.23 Section showing progressive stope failure in pillar 7 of Block 2 Kwesi Mensah Shaft 233
Figure 7.24 Vertical projection, showing sidewall failure in Pillar 7 - 158 pillar breached 234
Figure 7.25 ETS shaft pillar stope 1 failure 235
Figure 7.26 Tension fractures as observed in stope 1 position hangingwall 235
Figure 7.27 Cablebolted back of stope 2 in Block 8, and part of stop1 hangingwall (left) - GCS 236
Figure 7.28 Illustration of soft zones (black band) in faults, in various stope surfaces and the calculation of ω 238
Figure 7.29 Effect of weakness zone gouge quality on adjacent rockmass quality 239
Figure 7.30 Graphite (dark) in crown with quartz (light) 239
Figure 7.31 Gravity related failure due to graphite 240
Figure 7.32 Longitudinal section of pillar 8 showing graphite in hangingwall 240
Figure 7.33 Longitudinal section of stope 1 at ETS shaft pillar showing graphite in hangingwall and footwall, and the failure that occurred 241
Figure 7.34 Conventional stability graph for Ashanti (with transition zone statistically defined using the unsupported calibration database) on a log-log scale - no correction for graphite 243
Figure 7.35 Stability graph showing examples of movement of points after correcting for graphitic zones in stope surfaces 244
Figure 7.36 Ashanti stability graph after correcting for graphite zones 245

Figure 7.37 Recommended stability graph for Ashanti 246
Figure 7.38 Plot of modified span versus mine excavation stability index *MESI*. 247
Figure 7.39 Bifurcation of orebody and mining practice 248
Figure 7.40 Relationship between orebody dips and mining methods 250
Figure 7.41 Relationship between rockmass quality and mining methods 251
Figure 8.1 Effect of included angle and location of fault (bottom, middle and top) on $ELOS_f$: $K = 2.1$, $\phi* = 20°$, $\alpha = 72°$, $Ar = 0.4$ 256
Figure 8.2 Example fault factor graph for conditions corresponding to those in Figure 8.1 257
Figure A.1 Quantile-quantile plot for the stable class in the calibration database 279
Figure A.2 Quantile-quantile plot for the unstable class in the calibration database 279
Figure A.3 Quantile-quantile plot for the caving class in the calibration database 280
Figure A.4 Chi-square plot for the stable class of data 280
Figure A.5 Chi-square plot for the unstable class of data 281
Figure A.6 Chi-square plot for the caving class of data 281
Figure B.1 Effect of fault with friction angle 15° on stope stability: Stress ratio K=2.1, Stope aspect ratio A_r=0.4, fault friction angle ϕ=15°, stope dip α=72° 283
Figure B.2 Effect of fault with friction angle 30° on stope stability: Stress ratio K=1.8, Stope aspect ratio A_r=0.4, fault friction angle ϕ=30°, stope dip α=72° 284
Figure B.3 Effect of stope aspect ratio Ar =0.8 on the influence of faults on stope stability: Stress ratio K=2.1, stope aspect ratio A_r=0.8, fault friction angle ϕ=20°; stope dip α=72° 285
Figure B.4 Effect of stope aspect ratio Ar =1.5 on the influence of faults on stope stability: Stress ratio K=2.1, stope aspect ratio A_r=1.5, fault friction ϕ=20°; stope dip α=72° 286
Figure B.5 Effect of fault distance to stope on the influence of the fault on stope stability: Stress ratio K=2.1, stope aspect ratio A_r=0.4, fault friction angle ϕ=20°; stope dip α=72° 287
Figure B.6 Influence of stope aspect ratio Ar on fault effect on stope stability: K=2.1, fault friction angle ϕ=20°, stope dip α=72° 288
Figure B.7 Plane representing stope face showing geometry (left) and three points (right) for determination of stope plane equation 289
Figure B.8 Normal vector to plane showing direction cosines (left) and dip and dip direction of a plane (right) 290
Figure B.9 Two vectors on a stope plane for defining normal vector to plane 292
Figure B.10 Determination of distance of fault to a point on a stope surface 294

CHAPTER 1

INTRODUCTION

1.1 Problem Definition

Faults are a problem because they lead to instability of nearby excavations. This is often the case for metalliferous mines, where faults are commonly present due to orebody genesis. The stability graph is used to dimension open stopes, but does not consider the important influence of faults.

The thesis is focused on evaluating the effects of faults on the stability of open stopes. Open stope mining is a low cost, high tonnage mining method that is practiced around the world.

Faults have been cited as responsible for the instability of both mining and civil underground excavations. Several publications (Deere, 1974; Cording and Mahar, 1978; Brekke and Selmer-Olsen, 1966; Hoek and Brown, 1980; Quesnel and Gordon, 1991; Potvin and Milne, 1992; Reschke and Romanowski, 1993; Mikula, 1993; Dune and Pakalnis, 1996; Potvin, 1998) have cited faults as causes of underground excavation instability.

Figure 1.1 shows a fault in the footwall of an open stope that caused caving of the footwall with the release of 5500 tonnes of waste rock.

Mikula (1993) cited many fault-related problems in the Mt Charlotte Mine, Australia. The relationship between the faults, orebody and stopes is shown in Figure 1.2. The mining method is open stoping. A special case of caving in ROB5 occurred up to the Flanagan fault. Figure 1.2b shows the details of the progressive failure of ROB5.

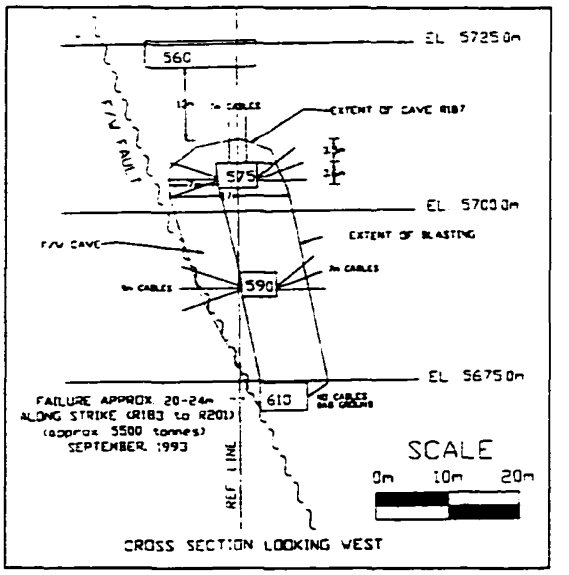


Figure 1.1 Footwall fault failure (from Dune and Pakalnis, 1996) - Canada

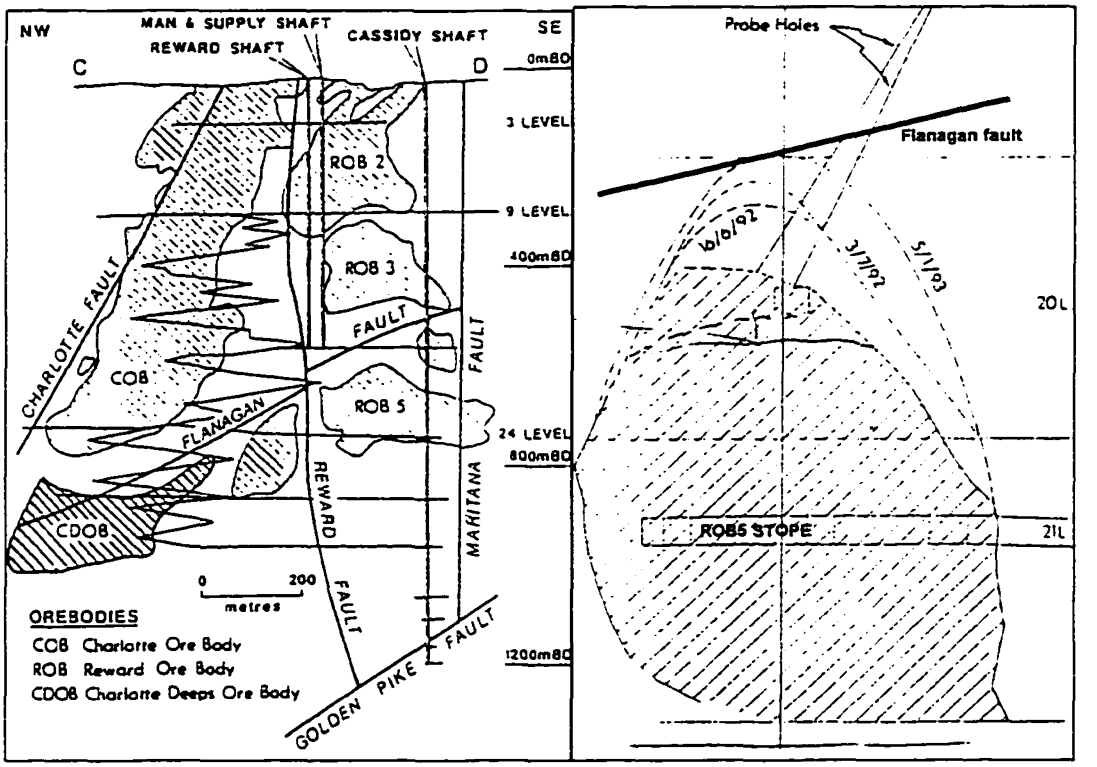


Figure 1.2 Vertical sections showing locations of orebodies, faults and details of progressive failure in ROB5 (from Mikula, 1993) – Australia

Fault related problems, are also reported by Potvin (1998) at Mount Isa Mines in Australia where open stope sizes of 40 m by 40 m in plan view are mined. Figure 1.3 shows a relationship of faults to a stope at this mine.

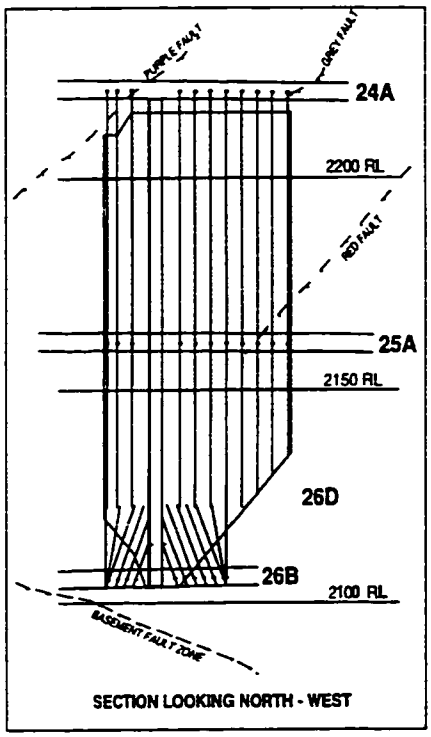


Figure 1.3 Large open stope with faults associated with orebody at Mount Isa Mines, Australia (from Potvin, 1998)

At Kidd Mine, a fault related failure in the 54-735 stope of the #3 mine resulted in approximately 30% dilution. Figure 1.4 shows the fault in relation to the stope. This stope is discussed further in Chapter 6 of this thesis.

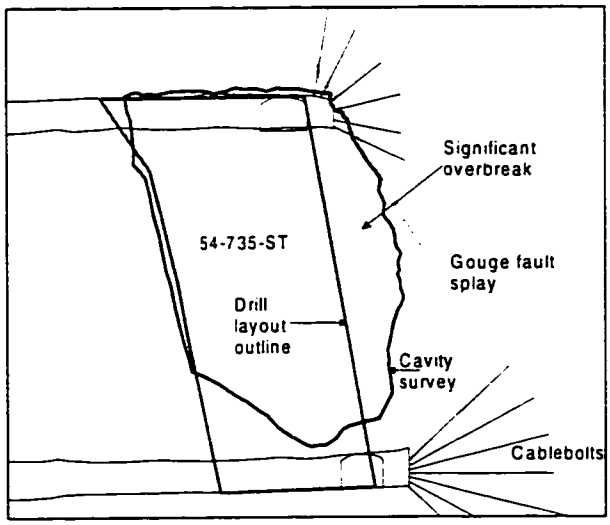


Figure 1.4 Fault related overbreak in hangingwall of an open stope causing approximately 30% dilution

Brekke and Selmer-Olsen (1966) conducted a survey of factors influencing the stability of underground constructions in Norway. They concluded that ground falls in underground constructions seem to be caused by one or more of the following factors:

- Unfavourable orientations and combinations of faults, joints and fissures in relation to the construction site,
- The especially poor cohesion and friction in faults, joints and fissures carrying chlorite, talc, graphite, etc.
- The solubility of calcite, especially when the calcite is porous or flaky.
- Washing out or ground fall of low consolidated inactive clay material from joints and fault fillings,
- Rock pressure, and
- The swelling capacity of the montmorillonite clay minerals.

Figure 1.5 shows typical sliding caused by unfavourable directions of a fault and joints in a power plant hall.

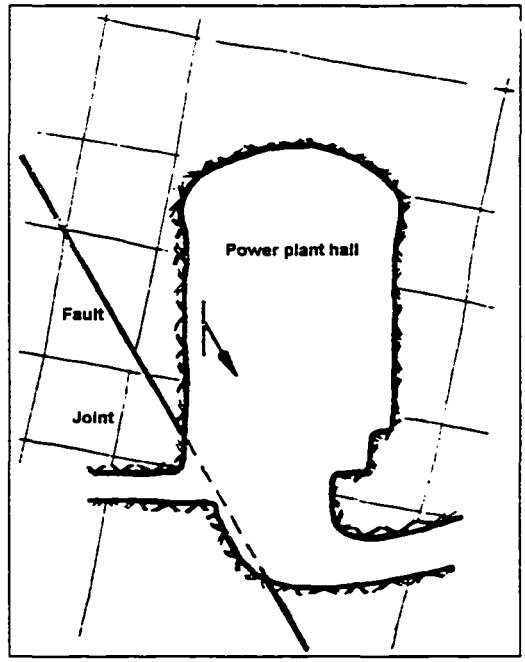


Figure 1.5 Typical sliding caused by unfavourable directions of a fault and joints in relation to a power plant hall (from Brekke and Selmer-Olsen, 1966)

Soft zones due to faults or shear zones that are significantly wide in relation to the excavation surface they intersect are another important source of ground falls in underground excavations as indicated by Brekke and Olsen (1966).

Figure 1.6 shows a graphite-related ground fall in Ashanti Goldfields. This mechanism has resulted in progressive back failures at this mine.

The characteristics of faults that adversely affect the stability of underground excavations are not well defined. How the various fault characteristics influence the effects of the faults on the stability of an excavation are not understood.

Empirical methods of underground excavation design make use of rockmass classification systems. The most popular rockmass classification systems in use are the rockmass rating *RMR* system (Bieniawski, 1973), and the tunnelling quality index *Q* system (Barton et al., 1974).

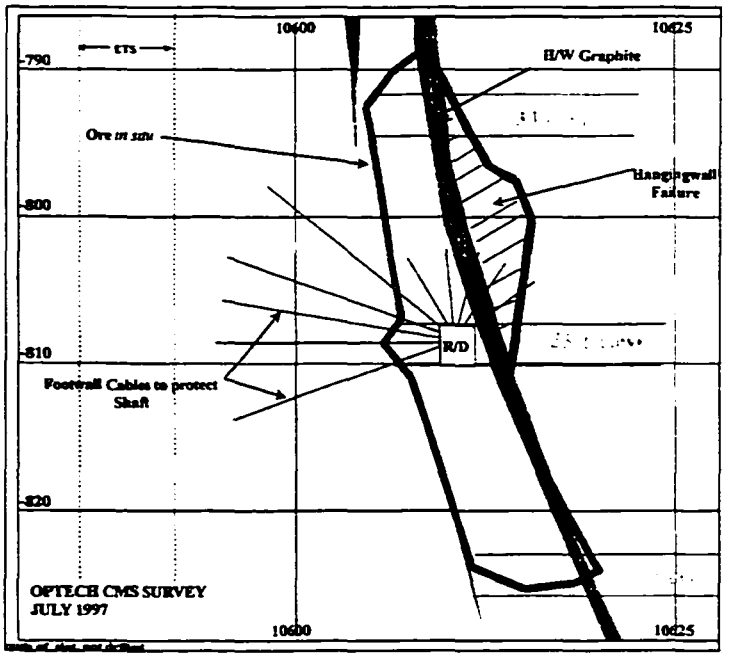


Figure 1.6 Graphite (soft zone) related caving in an open stope at Ashanti Goldfields in Ghana

The stability graph method (Mathews et al., 1980; Potvin, 1988) uses the *Q* system of rockmass classification. The design of open stopes is largely based on empirical methods, with numerical modelling sometimes used to estimate the amount of stress likely to be encountered. The stability graph method was based on a database collected mainly from Canadian underground mines (Mathews et al., 1980, Potvin, 1988) with relatively competent rocks.

The stability graph method of open stope design uses a stability number N' defined as:

$$N' = Q' \bullet A \bullet B \bullet C \qquad 1.1$$

Where, Q' is a modified tunnelling quality index Q, A = stress factor, B = rock defect orientation factor and C = gravity factor. The stability number N' is plotted against the stope surface shape factor called hydraulic radius *HR*, defined as stope surface area divided by stope surface perimeter.

In Chapter 2 of the thesis, rockmass classifications and use of the rockmass classifications for underground excavation design are reviewed, including the stability graph method. The stability graph method contains a rock defect orientation factor to account for unfavourable orientation of joints. Most rockmass classification systems do not specifically include factors that account for presence and relative location of faults in a rockmass. In the empirical methods that use the rockmass classification systems for underground excavation design, again the effects of faults, when present near the excavation, on the excavation stability are not considered in the stability index. The stability graph method is often criticized (Quesnel and Gordon, 1991; Hutchinson and Diederichs, 1996; Potvin and Milne, 1992; Reschke and Romanowski, 1993) for not including a fault factor to account for the effects of faults near stopes. Hence, a crucial factor ignored in Equation 1.1 is a factor that accounts for the presence of faults. Most metalliferous orebodies are associated with faults by the mode of their formation. The occurrences of faults result in unfavourable stress zones in the immediate vicinity (Hafner, 1951; Anderson, 1942; Ryder, 1988), and generally adversely affect the stability of excavations near them.

The stability graph has three zones, defined as stable, unstable and cave. Mathews et al. (1980) and Potvin (1988) drew in the boundaries between the zones of the stability graph by hand. Nickson, (1992) and Hadjigeorgiou et al. (1995) statistically defined the boundaries with single curves. However, the boundaries between the zones of the stability graph are too broad to be represented with single curves. Some users of the stability graph also have the impression that when a point plots in the stable zone, absolute stability is guaranteed. The inherent error in the calibration stability graph is not quantified. More rigorous application of statistics can be used to determine whether addition of a parameter or modification of a parameter improves the stability graph method.

This thesis is focused on the design of open stopes near faults, and aims at providing statistical tools that will assist in improving the reliability of the stability graph.

1.2 Objectives of Research

The overall goals of this research are to determine the effects of faults and stress on open stope stability and to improve the reliability of the stability graph as a design tool.

The main objectives of this research are to:

- Identify characteristics of faults that influence the stability of open stopes,
- Develop a procedure for estimating fault-related overbreak in open stopes,
- Develop a fault factor for incorporation into the stability graph method,
- Examine the role of stress in the context of slough in the stability graph.
- Determine the applicability of the stability graph method in a different geologic environment, from which it was developed,

- Provide statistical tools for interpretation of the stability graph, and
- Develop alternative stability graphs based on a likelihood statistic, and a graph that uses improved modified N' and a modified definition of span.

1.3 Scope and Organization of the Thesis

1.3.1 Scope of the thesis

The thesis is focused on assessing the effects of faults and stress on stope stability. Procedures for estimating overbreak due to faults, and for determining a fault factor for incorporation into the stability number N' are researched. In the context of the thesis, all discrete weak geological structures such as shear zones can be treated as faults. Undercutting of stope walls, and exposure times of stope walls are not addressed in detail in this thesis.

1.3.2 Organization of the thesis

Chapter 2 is a review of underground excavation design methods. Design of underground mining excavations is largely empirical, based on rockmass classification systems, which are reviewed here. The rockmass rating *RMR* system (Bieniawski, 1973) and the tunnelling quality index Q system (Barton et al, 1974) are the main rockmass classification systems in use. These classification systems do not include factors that account for faults in the rockmass. For open stope design, the modified Mathews stability graph method is the most popular empirical design method. The factors considered in the stability graph method are reviewed. The method does not incorporate factors to account for faults and soft zones near stopes.

Chapter 3 is a stand-alone chapter that presents statistical tools for use in the interpretation of empirical data such as that used in the stability graph. Three methods for defining the boundaries between the stable, unstable and cave zone of the stability graph are given, and applied to the calibration database. Equiprobability contours are used to show that the zones of the stability graph are not absolute but overlap, and interpretation of the stability graph should take this into account. Overlap of zones of the stability graph implies certain misclassification errors. Misclassification errors have associated risk cost to the mine. Methods are presented for calculating misclassification or prediction errors and the associated risk costs. Procedures for optimizing the stability graph zones, to minimize misclassification errors, are given. Because the distribution of data in the stability graph is largely probabilistic, a likelihood-based stability graph is presented as an alternative plot. The statistical tools presented in this chapter are applied to case studies in Chapters 6 and 7 that deal with the stability graph method.

Chapter 4 looks at stress, and the concept of stope wall relaxation. It is found that relaxation is important in open stope instability. 70% of the cases in the calibration database are in relaxed stress states. The concept of relaxation is defined in this chapter, and the various causes of relaxation identified. Faults, undercutting, mining of parallel veins, mining of adjacent stopes, and crushing of weak rocks are the major causes of relaxation. Limit equilibrium analyses, using different wedge shapes, is applied to determine a critical clamping stress below which rock wedges of the type typically encountered in underground mine failures will slough under gravity. This chapter and Chapter 2 conclude that the stress factor in the stability graph method is inadequate.

Chapter 5 examines the effects of faults on the performance of open stopes. The characteristics of faults that influence the stability of underground excavations are identified. Empirical or observational, analytical and numerical models are applied to examine the effects of faults on the stability of underground openings, with an emphasis on open stopes. A theory is presented on how faults near open stopes affect the stability of such stopes. It is found that, the geometry of the stope surface, the angle between the stope surface and a fault, and the distance of a fault from a stope surface are important factors influencing stope stability. Mathematical equations are introduced in the chapter for defining stope surface geometries, determining included angles between stope surfaces and faults, and for finding the distance of faults from stope surfaces. Numerical modelling of open stopes with faults is the main theme of this chapter. A parametric study is conducted using stresses and fault and stope geometries. A parameter for assessing the effect of a fault on stope stability is defined in this chapter. The chapter concludes with two sets of charts for predicting fault-related overbreak in open stopes, and for determining fault factors for incorporation into the stability graph method.

Chapter 6 is application of the results of work in Chapters 3 and 5 to a case study at Kidd Mine in Timmins, Ontario, Canada. Data from the #3 Mine of Kidd Mine was used to validate the overbreak charts and the fault factor chart developed in Chapter 5. The boundaries between the zones of the stability graph that were statistically defined with the statistical tools and calibration database are applied to the Kidd Mine database, which consists of 112 case histories. The mathematical formulae developed in Chapter 5 were used to determine stope geometrical properties such as stope surface dimensions and orientation of stope surfaces. The formulae were also used to determine included angles between stope surfaces and faults, and distances of faults to stope surfaces. The data separability index introduced in Chapter 3 is an important parameter in determining levels of improvement to the stability graph that might be due to the addition of a new parameter or modification of an existing parameter. A likelihood based stability graph is plotted as an alternative to the conventional stability graph. Optimization of the stability graph boundaries is shown and can be used to minimize misclassification cost.

In Chapter 7, the issue of soft zones is presented. A method of adjusting the stope surface rockmass quality when soft zones are present is given, and applied to case histories from the Ashanti Goldfields Mine in

Ghana. This database consists of 130 case histories. Ashanti Mine is characterized by many graphitic shears, which make it ideal for this investigation. Again, the statistical tools in Chapter 3 are applied in the interpretation of the data. In this chapter it is shown that the stability graph method can be applied to stopes in this environment, but with supported backs. The effect of orebody bifurcation on open stope stability is discussed in this chapter. The chapter also examines alternative mining methods for Ashanti in view of the poor quality rockmasses at the mine. Two charts based on orebody geometry and rockmass quality are presented for the selection of appropriate mining methods based purely on geomechanics requirements.

It is frequently argued that span is not a useful parameter for 3-dimensional excavations, such as open stopes, when assessing performance. In this thesis, it is shown that there is no significant difference between the use of span and hydraulic radius in the stability graph. Considering this fact, and the fault adjustment factors presented in Chapters 6 and 7, a new stability index graph called the mine excavation stability index graph *MESIG* is presented. *MESIG* is a plot of the revised stability number versus a modified span defined as span divided by excavation support ratio *ESR*. The method is applied separately to the calibration database, to the database from Kidd Mine, and to the database from Ashanti Goldfields Mine.

Chapter 8 is a summary of the major conclusions of the research, and contains suggestions for future work.

CHAPTER 2

REVIEW OF ROCKMASS CLASSIFICATIONS AND UNDERGROUND EXCAVATION DESIGN METHODS

2.1 Introduction

The following methods are used in the design of underground excavations:

- Analytical method
- Numerical modelling,
- Empirical methods, and
- Observational methods.

Each of these methods has advantages and disadvantages. It is observed that best results are obtained when all methods are applied in the design and construction process. The first two methods are only briefly discussed, and the last two are discussed in detail for reasons given in Section 2.4.

2.2 Analytical Methods

Analytical methods are generally based on the use of closed form solutions, such as Kirsch's equations, and statics. Only simple excavation geometries such as circular openings, and wedges in two-dimensions can be considered using analytical design methods. For more complex excavation geometries and failure modes, and three-dimensional cases, numerical models are the best tools.

2.3 Numerical simulation Methods

Advances in numerical modelling and computer technology have added insight into the design of underground openings. Most underground mining excavations are irregular in shape and are often grouped near to other excavations. Also, because orebodies are often associated with geological features such as faults and intrusions the rock properties are seldom uniform in the rock volume of interest. Thus, closed form solutions and analytical methods become of limited value for calculating stresses, displacements and failure of the rockmass surrounding mining excavations. Numerical methods provide the means for approximate solutions to these problems (Hoek et al., 1995).

Unlike engineered materials such as steel, rock material properties vary widely. Consequently, it is often a problem defining the correct input parameters in modelling underground excavations in rockmasses.

Numerical codes still depend on empirical failure criteria as a basis for judging the performance of the structure in the assumed conditions. The Mohr-Coulomb and Hoek and Brown failure criteria are the two failure criteria often used. Details of the Hoek and Brown failure criterion are available in Hoek and Brown (1980, 1983, 1988, and 1997), and Hoek (1983, 1990, 1994).

Although advances in computer modelling have added insight into the design of underground openings, the design of underground excavations is still largely empirical, and based on the judgement of experienced experts in underground excavation construction. Empirical and observational designs are often considered simultaneously in design and construction.

2.4 Rockmass Classifications and Empirical Underground Excavation Design Methods

Rockmass classification systems are empirical. Franklin (1993) defined empirical design as quantified judgment based on experience. He observed that being based on real data, empirical predictions are often closer to the truth and form the standard against which theoretical predictions are judged.

The development of rockmass classifications was the first step to collect accumulated experience for empirical design of underground openings. Rockmass classifications have become the basis for most underground excavation design methods. Rockmass classification systems were developed originally from experience in civil engineering construction and have been modified in various forms for mining purposes.

A distinction is drawn between rockmass classification systems that use the inherent rockmass properties to assess the rockmass quality, and that of empirical underground excavation design that combines the geometry of an excavation and the rockmass quality to predict stability.

Rockmass classifications use a set of the rockmass properties to rate the quality of the rockmass in situ. Rockmass classifications can be used for various purposes. One use is in the prediction or assessment of the performance of excavations made in the rockmass. Empirical underground excavation design couples the geometry of the excavation to the rockmass quality to give a stability index that can be used to estimate support requirements. Rockmass classification systems are discussed first and their application to underground excavation design second.

2.4.1 Rockmass classification systems

Several rockmass classification systems exist in the literature and only the common systems used in engineering practice are discussed in the following sections. These classification systems range from single parameter classification systems to multivariate classification systems. The greater the number of relevant rockmass characteristics included in a classification system, the better it should be able to capture the actual rockmass behaviour. There is however a practical limit to the number of parameters that can be included in a given classification system since the classification must be simple, and also must be representative of the critical parameters useful in understanding the rockmass behaviour.

2.4.1.1 Terzaghi's rockmass classification system

This is the first rockmass classification system ever introduced, and is always discussed for its historic role in Rock Mechanics Engineering. This classification system is a quantification of Terzaghi's experience in tunneling and steel arch support in various ground conditions. It is not directly related to any specific properties of the rockmass. Terzaghi's rockmass classification system is well discussed by Kirkaldie (1988), and is summarized in Table 2.1.

Terzaghi's rockmass classification system conveys to the reader that the various rockmass classes are distinct and independent. In practice, there are no defined boundaries between the various rockmass classes in Table 2.1. The Terzaghi classification system is subjective, and is based on a qualitative assessment of the rockmass.

The Terzaghi's rockmass classification system gives explicit definitions to the various rockmass classes. From these definitions, an engineer can predict the nature of the problems to be encountered at a given construction site knowing the qualitative description of the rockmass.

Table 2.1 Terzaghi's (1946) rockmass classification system

Rockmass class	Description
Intact rock	Contains neither joints nor hair cracks. Hence if it breaks it breaks across sound rock. On account of the injury due to blasting, spalls may drop off the roof several hours or days after blasting. This is known as spalling condition. Hard intact rocks may also be encountered in the popping condition involving the spontaneous and violent detachment of rock slabs from sides or roof.
Stratified rock	Consists of individual strata with little or no resistance against separation along the boundaries between strata. The strata may or may not be weakened by transverse joints. In such rock, the spalling condition is quite common.
Moderately jointed rock	Contains joints and hair cracks but the blocks between joints are locally grown together or so intimately interlocked that vertical walls do not require lateral support. In rocks of this type, both the spalling and the popping condition may be encountered.
Blocky and seamy rock	Consists of chemically intact or almost intact rock fragments that are entirely separated from each other and imperfectly interlocked. In such rock vertical walls may require support.
Crushed but chemically intact rock	Has the character of a crusher run. If most or all of the fragments are as small as fine sand grains and no re-cementation has taken place, crushed rock below the water table exhibits the properties of a water-bearing sand.
Squeezing rock	Slowly advances into the tunnel without perceptible volume increase. A prerequisite for squeezing is a high percentage of microcosmic and sub-microscopic particles of micaceous minerals or of clay minerals with a low swelling capacity.
Swelling rock	Advances into the tunnel chiefly on account of expansion. The capacity to swell seems to be limited to those rocks that contain clay minerals such as montmorillonite, with a high swelling capacity.

2.4.1.2 Rock quality designation *RQD*

Deere (1964) was the first to quantitatively relate the quality of the rockmass to its structure by the term *RQD*. *RQD* is based on core recovery using NQ core (54mm diameter core) as recommended by ISRM (1980), and is defined as the percentage of core recovered in intact pieces greater than or equal to 100 mm to the total length of the core run. Table 2.2 gives the details of this classification system.

Table 2.2 Deere's (1964) rockmass classification system

RQD (%)	Rock mass quality
< 25	Very poor
25 - 50	Poor
50 - 75	Fair
75 - 90	Good
90 - 100	Very good

The *RQD* classification system is a single parameter system. It does not account for the characteristics of the joints or faults. Joint condition affects the stability of rock wedges and is detailed by Brekke and Howard (1972).

RQD is only affected by open joints (Deere and Miller, 1966). In foliated rockmasses *RQD* may be high but such rocks behave poorly in service underground, particularly when the foliations are parallel to a wall

of the excavation. *RQD* varies with direction and is therefore a vector rather than a scalar. *RQD* values should be used with caution if they are not determined from oriented core.

Despite the problems associated with *RQD* it is a major parameter in most of the rockmass classification systems used today. Determining *RQD* should be an integral part of any exploration core-logging program. Support design is discussed using these methods in Section 2.4.3.1.

2.4.1.3 Lauffer's rockmass classification system

Following Terzaghi (1946) and Stini (1950), Lauffer (1958) also qualitatively defined rockmass classes that he related to tunnel supports. Table 2.3 presents the classification system.

Table 2.3 Lauffer's (1958) rockmass classification system

Rockmass class	Description	Remarks: Terzaghi's rock load equivalent
A	Stable rock	Intact rock
B	Rock unstable after a long time	Massive moderately jointed rock and to stratified or schistose rock.
C	Unstable rock after a short time	Moderately blocky and seamy rock
D	Broken rock	Very blocky and seamy rock
E	Very broken rock	Completely crushed rock
F	Squeezing rock	Squeezing rock
G	Heavy squeezing rock	Heavy squeezing rock

Lauffer's classification system is less explicit compared to the detailed description of rockmass classes given by Terzaghi (1946).

The significance of Lauffer's classification system is its linkage to excavation stand-up time and active span. Support design based on Lauffer's classification system is discussed in Section 2.4.3.3.

2.4.1.4 Geomechanics rockmass rating system *RMR*

Bieniawski (1973) introduced a multivariate rockmass classification index popularly known as Rock Mass Rating index *RMR*. The system is referred to as the Geomechanics Rockmass Classification system, sometimes controversially called the Council for Scientific and Industrial Research, *CSIR*, system.

The five parameters used in the *RMR*-system are:

- Rock Quality Designation *RQD*,
- Uniaxial compressive strength of intact rock,
- Spacing of joints and bedding,
- Condition of joints, and
- Groundwater inflow.

These parameters are rated, and depending on the quantitative value or qualitative description of a parameter, a rating is assigned to each parameter from a range of values. The ratings are then summed up to give the total rockmass rating. Range of values for the rockmass is from 0 to 100 on an arithmetic scale. The total rockmass rating obtained is adjusted according to whether the tunnel is favourably or unfavourably oriented with respect to the critical geologic structure.

Details of tables for the rating of the parameters, and procedure for application of the method are widely published (Bieniawski, 1973, 1974, 1976, 1979, 1983, 1984, 1988, 1989, 1993; Hoek and Brown, 1980; Hutchinson and Diederichs, 1996), and therefore are not repeated.

RMR places a lot of emphasis on block size by incorporating both joint spacing and *RQD* in the rating of the rockmass. The two parameters alone have a total rating of 50 (Bieniawski, 1976) and now 40 (Bieniawski, 1989, 1993) out of the total of 100 for all the five parameters added together.

Uniaxial compressive strength is divided into classes in the *RMR* system, and each class given a rating. The classes are so broad that they are not sensitive to changes in uniaxial compressive strength. For example, given that all other parameters are equal for two different rockmasses except the uniaxial compressive strengths of their intact rock materials, the two rockmasses with uniaxial compressive strengths of 51 MPa and 99 MPa, will have the same rockmass quality. Laubscher and Taylor (1976) have rectified this problem in the modified *RMR* system discussed in Section 2.4.1.5.

RMR has had a lot of successes in its application in civil and mining site investigations. It has been empirically related to the constants, m and s (Priest and Brown 1983) in the Hoek and Brown (1980, 1988, 1997) failure criterion.

$$\sigma_1' = \sigma_3' + \sqrt{\left(m\sigma_c\sigma_3' + s\sigma_c\right)} \qquad 2.1$$

It is also related to the rockmass modulus (Bieniawski, 1978) and to the tunneling quality index (Bieniawski, 1976) of Barton et al. (1974).

$$E = 2RMR - 100 \qquad 2.2$$

$$RMR = 9\ln Q + 44 \qquad 2.3$$

In Section 2.4.3.4, support design based on *RMR* is presented.

2.4.1.5 Mining rockmass classification system

Laubscher and Taylor (1976) modified *RMR* for mining purposes. The joint spacing factor in *RMR* was completely changed and replaced with Figure 2.1 to more appropriately represent some measure of block size in the rockmass matrix. The joint condition parameter was described in more detail to account for joint

roughness, alteration and filling. The importance rating of joint condition was increased from 25% to 30% of the total scale while intact rock strength was reduced from 15% of the scale to 10%. *RQD* and joint water factors were unaltered. The resultant total rating was referred to as the in situ rockmass rating. These changes were necessary to improve on the applicability of *RMR* to mining at depth. Table 2.4 is a summary of the revised parameter ratings for *MRMR*.

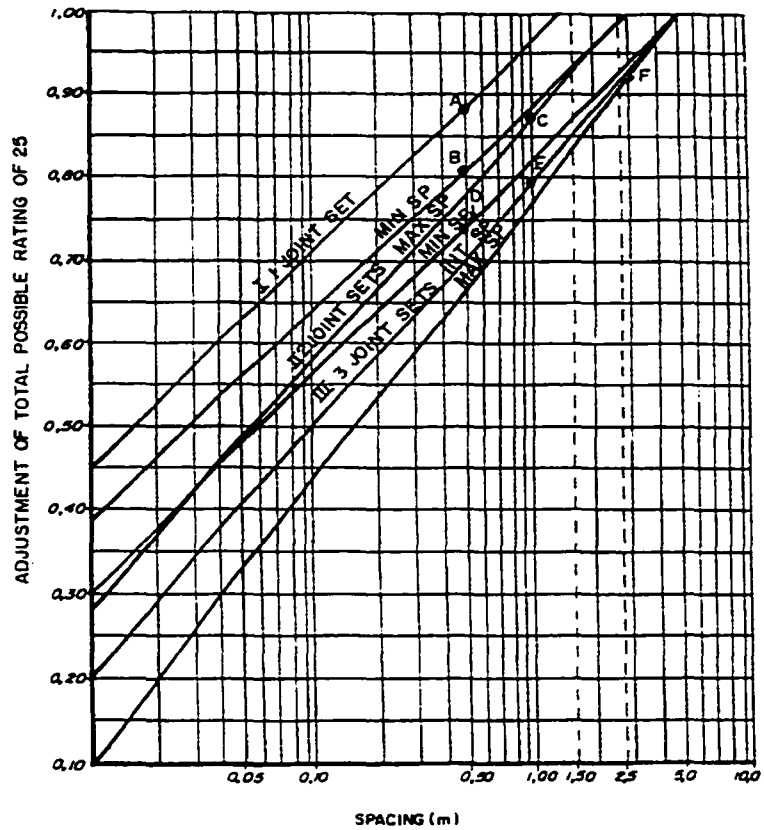


Figure 2.1 Assessment of joint -space rating (Laubscher, 1990)

NB x = spacingx100

A 1-Joint set R = 25x ((26,4 x $\log_{10}$x) + 45)/100

B 2-Joint set R = 25 x ((25,9 x $\log_{10}x_{min}$) + 38)/100 x ((30.0 x $\log_{10}x_{max}$) + 28)/100

C 3-Joint set R = 25 x ((25.9 x $\log_{10}x_{min}$) +30))/100x((29.6 x $\log_{10}x_{int}$) + 20)/100 x ((33.3 x $\log_{10}x_{max}$) + 10)/100

EXAMPLE:

One set spacing at 0.5 m = A, rating = 0.88 x 25 = 22

Two sets, spacing at 0.5 m, and 1.0 m=B+C, rating=0.81 x 0.86 x 25 = 17

Three sets, spacing at 0.5 m, 1 0 m, and 3.0 m = D,E,+F, rating = 0.74 x 0.80 x 0.93 x 25 = 14

The sources of instability in mining that were observed by Laubscher and Taylor (1976) to be weathering, induced stresses, stress changes, effect of strike and dip, blasting effects, and gravity.

Various guidelines are given by Laubscher and Taylor (1976) to degrade the classification parameters to reflect the influence of the above factors. The ratings for joint condition are given in Table 2.5. Gravity effect is accounted for in.Table 2.6.

Table 2.4 Summary of revised parameter ratings for *RMR* classifaction system (after Laubscher and Taylor 1976)

Class	1		2		3		4		5		
Rating	100-81		80-1		60-41		40-21		20-0		
Description	very good		good		fair		poor		very poor		
Subclasses	A	B	A	B	A	B	A	B	A	B	
Item											
RQD	100-97		96-84	83-71	70-56	55-44	43-31	30-17	16-4	3-0	
Rating (*RQD**0.15)	15		14	12	10	8	6	4	2	0	
UCS, MPa	>185	184-165	164-145	144-125	125-104	104-85	84-65	64-45	44-25	24-5	4-0
Rating (0.1**IRS*)	20	18	16	14	12	10	8	6	4	2	0
Joint spacing					refer to Figure 2.1						
Rating	20										0
Joint condition including groundwater					refer to Table 2.5						
Rating	40										0
(40*A*B*C*D/10^{8})											

Table 2.5 Assessment of joint condition - adjustments as cumulative percentages of total possible rating of 40 (from Brady and Brown, 1993)

Parameter	Description		Dry conditions	Moist conditions	Wet conditions: Moderate pressure 25-125l/min	Wet conditions: Severe pressure >125l/min
A. Joint expression (large scale Irregularities)	wavy multi-directional		100	100	95	90
	uni-directional		95-90	95-90	90-85	80-75
	curved		89-90	85-75	80-70	70-60
	straight		79-70	74-65	60	40
B. Joint expression (small-scale Irregularities or roughness)	very rough		100	100	95	90
	striated or rough		99-85	99-85	80	70
	smooth		84-60	80-55	60	50
	polished		59-50	50-40	30	20
C. Joint wall Alteration Zone)	stronger than wall rock		100	100	100	100
	no alteration		100	100	100	100
	weaker than wall rock		75	70	65	60
D. Joint filling	no fill - surface staining only		100	100	100	100
	non-softening and sheared material(clay or talc free)	coarse sheared	95	90	70	50
		medium sheared	90	85	65	45
	soft sheared material (e.g., talc)	fine sheared	85	80	60	40
		coarse sheared	70	65	40	20
		medium sheared	65	60	35	15
		fine sheared	60	50	30	10
	gouge thickness < amplitude of irregularities		40	30	10	
	gouge thickness > amplitude of irregularities		20	10	flowing material 5	

Table 2.6 is based on number of joint sets and their inclination from the vertical. Laubscher and Taylor (1976), and Potvin (1988), give a complete description of the guidelines for application Table 2.6.

Special adjustments are made to the total in situ rockmass rating for the backs of undercuts based on the orientation of shear zones when these features are present (Table 2.7). It is assumed that for dips of walls

in the range 75° - 90°, no adjustment is required. A summary of the possible adjustment factors is given Table 2.8.

Table 2.6 Gravity adjustment factors based on number of joint sets (after Laubscher, 1990)

No of defining joints	No of faces inclined away from vertical and adjustment percentage				
	70%	75%	80%	85%	90%
3	3		2		
4	4	3		2	
5	5	4	3	2	1
6	6	5	4	3	2,1

Table 2.7 Adjustments for faults and shear zones relative orientations (from Potvin, 1988

Relative difference in orientation	Adjustment (%)
0 – 15°	76
15 – 45°	84
45 – 75°	92

Table 2.8 Summary of the possible total adjustment factors (from Potvin, 1988)

Parameter	*RQD*	*UCS*	Joint spacing	Condition of joints	Total
Weathering	95%	96%		82%	75%
Field and induced stresses				120% to 76%	120% to 76%
Changes in stress				120% to 60%	120% to 60%
Strike and dip orientation			70%		70%
Blasting	93%			86%	80%

The modified *RMR* system was a great improvement on *RMR*. *MRMR* however requires a lot of field experience before one can apply it adequately in the field. *MRMR* was plotted against hydraulic radius *HR* for empirical cave mining design. Diering and Laubscher (1987) modified the cave mining design chart for open stope mining (Figure 2.8).

2.4.1.6 NGI *Q* classification system

Barton et al. (1974) developed the *Q*-system. The *Q*-system is a multivariate system consisting of six parameters. The value of *Q* varies from 0.001 to 1000 on a logarithmic scale. The system covers a wide range of rock conditions, from heavy squeezing ground to sound rock. The six-parameters used in this classification system are:

- Rock Quality Designation *RQD*,
- Joint set number J_n,
- Joint roughness number J_r,
- Joint alteration number J_a,
- Joint water reduction factor J_w, and
- Stress Reduction Factor *SRF*.

The numerical value of Q, is given by a product of quotients in the following form:

$$Q = \left(\frac{RQD}{J_n}\right)\left(\frac{J_r}{J_a}\right)\left(\frac{J_w}{SRF}\right) \qquad 2.4$$

The first quotient is interpreted as a crude measure of block size, the second represents the roughness and frictional characteristics of the joint walls or infilling, and gives a measure of the inter-block shear strength. The third quotient is a rather ambiguous term defined as active stress. Values of the parameters are given in various tables and widely published (Barton et al., 1974, 1976; Barton, 1977, 1983, 1988, 1994; and Butler 1990), and are therefore not included in this thesis. Depending on the qualitative description of a parameter some numerical value is assigned from the tables, and the final rockmass quality index obtained from Equation 2.4.

The only revised parameter in the Q-system is the stress reduction factor *SRF*. The frequent revision of *SRF* indicates the difficulties related to its determination. Barton (1994) gives the most recent values of *SRF* for competent, squeezing and swelling rocks (Table 2.9). The rest of the tables remain unchanged. It appears that the volume of data available control the limit of *SRF*. Figure 2.2 shows that the current upper limit of SRF of 400 is based on 14 cases. It is likely that an upper limit of this parameter will be in the range 800-1000 if sufficient case histories become available compared to the current number of 5 cases.

Løset (1992) observed that *SRF* is time dependent and some time lapse is required for stress redistribution in the excavation to occur before its determination. The controversy this brings is that Q is required before excavation starts, so that an effective ground control strategy can be put in place. Experience with a particular ground could however make time-dependent *SRF* prediction possible.

The inclusion of a stress factor in Q is inappropriate and unfortunate. Stress becomes important only when an excavation is made in the rockmass. Stress is therefore an external factor. External factors and inherent rockmass properties affecting underground excavation stability are discussed in Chapter 4.

Table 2.9 Updated *SRF* values (after Barton, 1994)

b) Competent rocks, rock stress problems		σ_c/σ_1	σ_θ/σ_c	*SRF*
H	Low stress, near surface, open joints	>200	<0.01	2.5
J	Medium stress, favourable stress condition	200-10	0.01-0.3	1
K	High stress, very tight structure. Usually favourable to stability, may be unfavourable for wall stability.	10-5	0.3-0.4	0.5-2
L	Moderate slabbing after > 1 hour in massive rock	5-3	0.5-0.65	5-50
M	Slabbing and rock burst after a few minutes in Massive rock	3-2	0.65-1	50-200
N	Heavy rock burst (strain burst) and immediate Dynamic deformation in massive rock	<2	>1	200-400
Note ii)	For strongly anisotropic virgin stress field (if measured): when $5 \le \sigma_1/\sigma_3 \le 10$, reduce σ_c to $0.75\sigma_c$. When $\sigma_1/\sigma_3 > 10$, reduce σ_c to $0.5\sigma_c$, where σ_c = unconfined compression strength , σ_1 and σ_3 are the major and, minor principal stresses, and σ_θ = maximum tangential stress (estimated from elastic theory)			
iii)	Few case records available where depth of crown below surface is less than span width. Suggest *SRF* increase from 2.5 to 5 for such cases (see H).			
c) Squeezing rock: plastic flow of incompetent rock under the influence of high rock pressure			σ_θ/σ_c	SRF
O	Mild squeezing rock pressure		1-5	5-10
P	Heavy squeezing rock pressure		>5	10-20
Note iv)	Cases of squeezing rock may occur for depth $H>350Q^{1/3}$ (Singh et al., 1992). Rock mass compression strength can be estimated from $q = 7\,\gamma\,Q^{1/3}$ (MPa) where γ = rock density in gm/cc (Singh, 1993).			
d) Swelling rock: chemical swelling activity depending on presence of water				
R	Mild swelling rock pressure			5-10
S	Heavy rock swelling pressure			10-15

Another modification to the *Q* system is the suggestion by Løset (1990), and recommended by Grimstad et al. (1993) to adjust *Q* if a soft or weakness zone is present. This is achieved by considering the weakness zone quality Q_z, and the adjacent rockmass quality Q_a using the equation:

$$log_{10}\,Q_m = \frac{b^{*}\,log_{10}\,Q_z + log_{10}\,Q_a}{b^{*}+1} \qquad 2.5$$

where

Q_m = mean *Q*-value for zone and side rock,

Q_z = *Q*-value of weakness zone,

Q_a = *Q*-value of adjacent rock, and

b^{*} = Corrected width (metres) of weakness zone, using the following factors:

$b^{*} = 1b$ for zone/tunnel axis intersection angles 90°-45°

$b^{*} = 2b$ for zone/tunnel axis intersection angles 45°-20°

$b^{*} = 3b$ for zone/tunnel axis intersection angles 20°-10°,

$b^{*} = 4b$ for zone/tunnel axis intersection angles <10°, and

b = actual width of the weakness zone.

The orientation adjustment seems to account for the effect of gravity on the weak zone in the given tunnel wall. It is significant to note that despite accounting for the presence of weakness zones in Q using higher SRF, it is still found necessary to account for the quality of such a zone. Stability number N' has no adjustment for the presence of faults, fissures and shear zones. These structures are often associated with orebodies and must be taken into account in designing extraction methods.

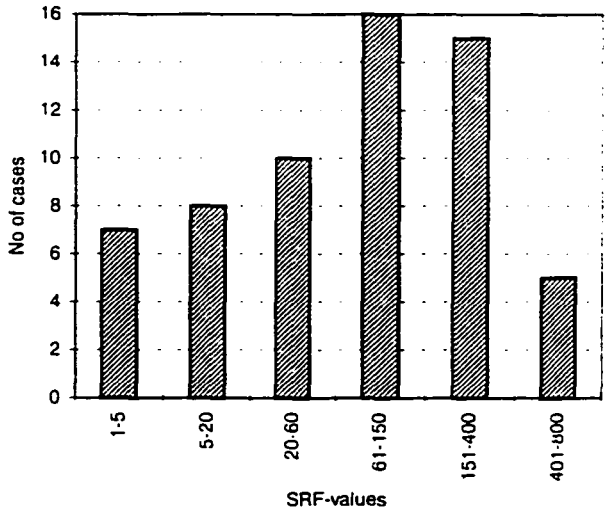


Figure 2.2 Updated SRF values for competent, squeezing and swelling rocks (Re-plotted after Barton, 1994) showing number of cases for which various SRF values are defined including the uspper limit of SRF

The Q system has gained recognition in the civil and mining world, and is the basis of many empirical mine design methods.

2.4.2 Comparison of Q and RMR

The Q system uses six parameters to assess the rockmass quality by means of the product of three quotients, while RMR applies five parameters and is additive. RMR ranges between 0 and 100 on an arithmetic scale. Q goes from 0.001 to 1000 on a logarithmic scale. The uniaxial compressive strength of intact rock is considered in RMR while Q places more emphasis on inter-block shear strength.

In order to identify the influence of each of the rockmass classification parameters on rockmass quality, statistical tools can be used. Results on rockmass classifications published in the literature was collected, and a statistical analysis of the common rockmass classification parameters using Pearson correlation coefficients (Table 2.10), shows that intact rock strength has the least effect on the rockmass quality. The results confirm a critique of the RMR by Kirsten (1988), and an observation by Udd and Wang (1985) that uniaxial compressive strength is less important in rockmass quality assessment. Table 2.10 also shows that most of the parameters in the classification systems are inter-correlated.

Table 2.10 Correlation matrix showing levels of significance of rockmass classification parameters on rockmass quality

Parameter	*UCS*	*RQD*	*Js*	*Jc*	*Gw*	*Jo*	*RMR*
UCS	1.00000 0.0	0.32287 0.0126	-0.09558 0.4715	-0.11543 0.3840	0.00205 0.9877	0.01183 0.9292	0.23278 0.070
RQD		1.00000 0.0	0.34307 0.0078	0.25840 0.0482	0.30370 0.0194	0.51295 0.0001	0.75342 0.0001
Js			1.00000 0.0	0.20858 0.1129	0.35563 0.0057	0.33776 0.0089	0.8031 0.0001
Jc				1.00000 0.0	0.4065 0.0002	0.30502 0.0188	0.63972 0.0001
Gw					1.00000	0.21861 0.092	0.58089 0.0001
Jo					0.0	1.00000 0.0	0.63870 0.0001
RMR							1.0000 0.0

where

J_s = Joint spacing,

J_c = Joint condition,

J_o = Relative orientation of excavation to critical discontinuity, and

G_w = Groundwater condition.

All other parameters have their usual meaning.

RMR recognizes the effect of discontinuity orientation on the stability of an excavation and adjusts the total rockmass index to account for it. The *Q*-system does not account for discontinuity orientation.

The *Q*-system accounts for stress while the *RMR* system does not.

Both *RMR* and *Q* do not account for the presence and influence of major discrete structures such as faults and fissures. The *Q*-system only accounts for joints. Minor structures such as foliation and schistosity are inadequately accounted for even though these features are recognized as being responsible for most failures underground.

RMR double counts the effect of block size by considering both joint spacing and *RQD* in its rating system. Because *RMR* deals with discontinuity frequency and *RQD*, the presence of foliation and schistosity can be accommodated.

RMR was developed in a hard rock environment, and is not sensitive to weak rocks. The *Q*-system is most appropriate in weak rockmasses because this class of rocks was included in its development.

Despite the limitations of the two classification systems, they have revolutionized site investigation procedures in the civil and mining sectors that hitherto had no guidelines. The two classification systems

have been successfully applied in various ground conditions, and it is advisable to use the most appropriate one, in each project.

2.4.3 Application of classification systems for underground excavations design

The most useful classification systems relevant to mining are discussed above. Empirical underground excavation design methods based on these classification systems are discussed in the following sections.

2.4.3.1 Terzaghi rock load classification system

Terzaghi (1946) related his rockmass classification system to steel arch support determination in tunnels based on his experience in tunneling.

The supportable rock load is determined from some linear relationship (Milne, 1997) between the tunnel width and ultimate height. The supportable rock load is dependent on the qualitative description of the rockmass. The Terzaghi rock load classification system was the first system to relate tunnel stability to its geometry and support.

This empirical design method assesses the stability of the tunnel as a whole, and not the individual walls or roof. In civil engineering, failure of any part of the structure is a failure of the whole structure with respect to safety.

Terzaghi's rock load design method has little application in hard rock mining at depth except in cases when shear zones and fissures are intersected in drives, and steel archs are used as support.

2.4.3.2 Application of *RQD* classification system to underground excavation design

Merrit (1972) related Deere's rockmass classification system to tunnel width and support requirements. This empirical system of underground excavation support design is important as the first quantitative rockmass classification system to be related to underground excavation design.

Figure 2.3 is used to predict the support demand on a tunnel based on the *RQD* value of the rockmass. Because of the various deficiencies in the *RQD* value discussed in Section 2.4.1.2, this method of design is inadequate. Also, the design approach is related to tunnels at shallow depths and has not been adapted for mining at depth.

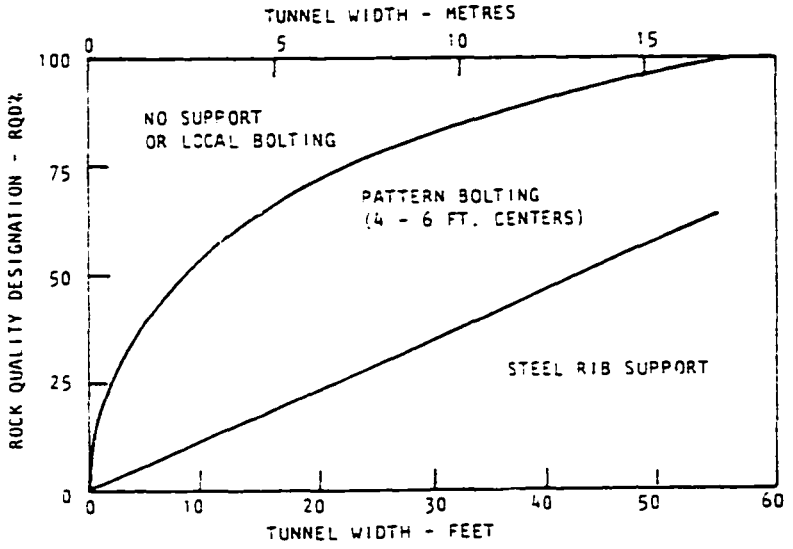


Figure 2.3 Proposed relationship between *RQD* and rock support (from Hoek and Brown, 1980)

2.4.3.3 Lauffer's stand-up time - span design method

This empirical design method introduced two important parameters, active span and stand-up time of the active span. The stand-up time is the length of time that an underground opening will stand unsupported after excavation and barring down. Active span is defined as, the largest unsupported span, in a tunnel section between the face and supports (Figure 2.5).

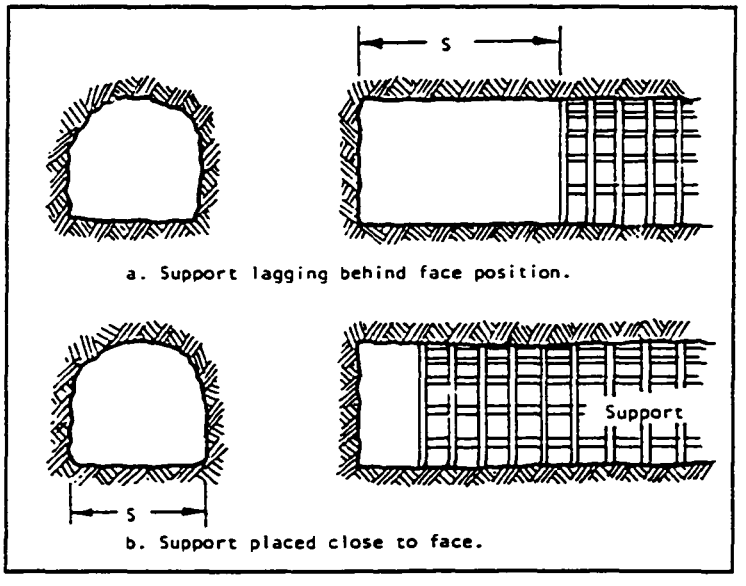


Figure 2.4 Definition of active span and span (from Hoek and Brown, 1980)

Span is therefore not always the width of the tunnel but could be the strike length to available supports if this is larger.

Figure 2.5 is Lauffer's underground excavation design chart that relates stand-up time, active span, and rockmass description, as given in Table 2.3.

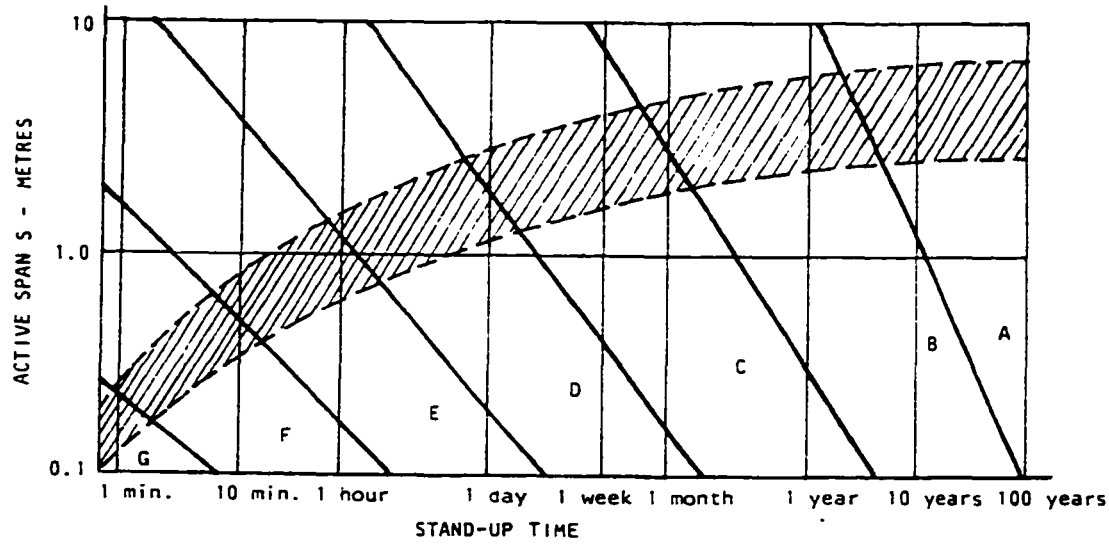


Figure 2.5 Lauffer's span – stand-up time chart (after Hoek and Brown, 1980)

By definition, if stand-up time is predicted to be longer than the expected usage time of the excavation, no support is required. Within the stand-up time window, the rockmass is self-supporting. In open stope mining, if the stand-up time of the rockmasses (ore and host rocks) are known for some designed stope geometry, extraction and possibly backfill could be planned such that it is completed before the onset of pervasive overbreak. This approach could result in low production cost. The incorporation of stand-up time in an empirical stope design procedure should be a major step forward.

The disadvantages of Lauffer's empirical underground excavation design method are its qualitative and subjective nature. Bieniawski (1973) improved on Lauffer's classification system by introducing a five-parameter quantitative rockmass quality index *RMR* to replace the qualitative rockmass descriptions in Lauffer's design chart (Table 2.3).

2.4.3.4 *RMR* span - stand-up time method

Bieniawski (1973) related *RMR* to excavation span and stand-up time (Figure 2.6) as a guide to predicting excavation stability and support requirements.

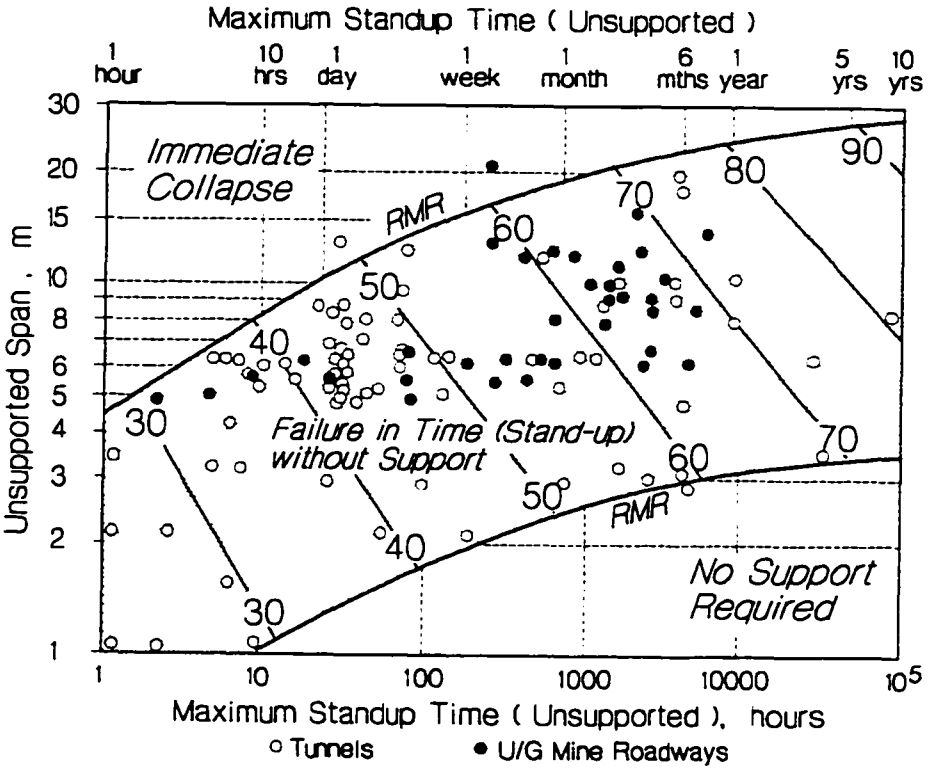


Figure 2.6 Graph relating stand-up time, unsupported span, and rockmass quality *RMR* (from Hutchinson and Diederichs, 1996; original data from Bieniawski, 1989)

The span - stand-up time design chart should be of enormous value to mining engineers in their design strategy. If advantage is taken of the self-support capacity of the rockmass, production costs could be lowered significantly.

One disadvantage of the *RMR* span - stand-up time method is that it uses the tunnel span to assess the stability of the whole excavation (back, end walls and sidewalls). This is in inadequate since the span will not control the stability of the sidewalls, even in tunnels.

The stability of the individual stope sides must be considered in mining since sloughage can have major consequences. Failure of hangingwalls and footwalls cause dilution, while failure of end walls in ore result in ore enhancement, but could lead to ore sterilization. Loss of ore could result when adjacent pillars are partly lost to opened stopes, and become impossible to mine.

Franklin and Palasi (1993) argue that Bieniawski's upper and lower bound curves are only limitations of the data, and have nothing to do with the annotations "immediate collapse" and "no support required" that are associated with them. Figure 2.7 was proposed to show that for a given rockmass quality, the stand-up time decreases with increasing span to immediate collapse, but requires more data to prove the hypothesis.

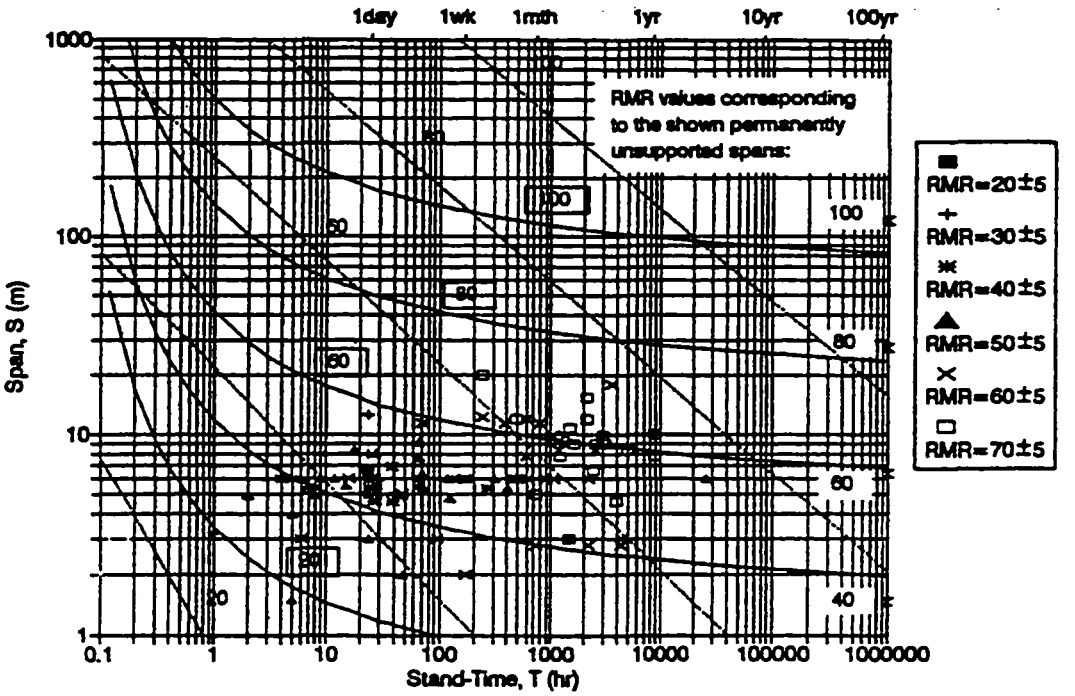


Figure 2.7 Modified span - stand-time diagram. Bieniawski's straight-line contours (extrapolated) are compared with curvilinear *RMR* contours proposed by Franklin and Palasi (after Franklin and Palasi, 1993)

RMR has been modified by Laubscher and Taylor (1976) and applied to cave mining and open stope design.

2.4.3.5 Laubscher's *MRMR* - hydraulic radius *HR* design method

By integrating *MRMR* with stope geometry, Laubscher and Taylor (1976) introduced a design method for cavability, and Laubscher (1990) extended the procedure to open stope stability, using hydraulic radius. Milne and Pakalnis (1997) argued that hydraulic radius *HR* is the most relevant stope surface geometrical parameter for stability assessment in a given rockmass quality compared to span, because stopes are three-dimensional. The term span is mostly associated with one-way span excavations such as tunnels.

Hydraulic radius *HR* is defined as area of the surface investigated divided by its perimeter. The stability of the individual surfaces of a stope can be investigated when the surface hydraulic radius *HR* is related to the quality of the rockmass.

Laubscher and Taylor (1976) originally proposed *MRMR* - *HR* method for cave mining. In this method, *MRMR* is plotted against *HR* for various case histories of known stability states. The empirical graph is then zoned into stable, unstable and caving (Figure 2.8).

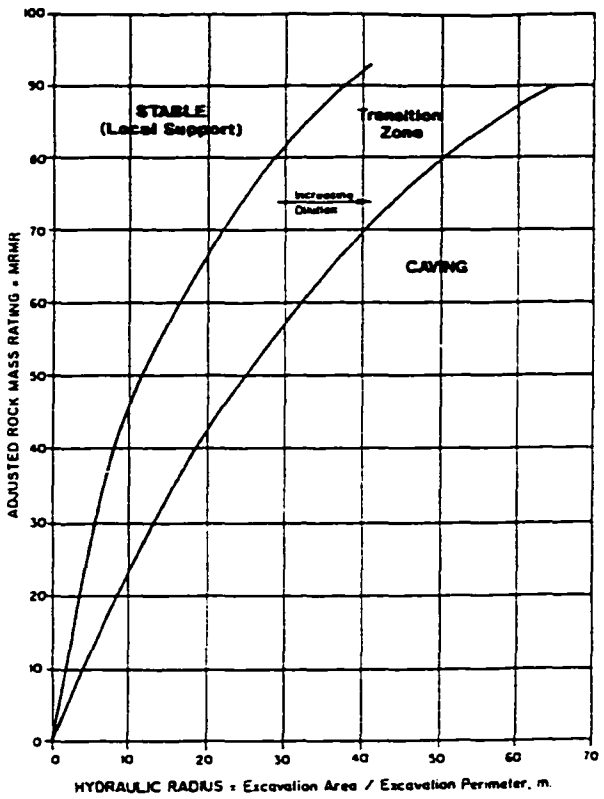


Figure 2.8 Laubscher's stability index graph (after Laubscher, 1990)

Laubscher (1994) defined two types of caving; stress caving and subsidence caving. Stress caving occurs in virgin cave blocks when the stresses in the cave back exceed the rockmass strength, so that caving progresses by sloughing from the back, and stops when a stable arch develops. Subsidence caving occurs when adjacent mining has removed the lateral restraint, and the failed zone is undercut, resulting in a rapid propagation of the cave, often with limited bulking. Subsidence caving can also occur when the rate of undercutting exceeds the rate of stress caving of the back, leading to failure en masse with the possibility of an air blast. Laubscher (1981) stated that Figure 2.8 is for stress induced caving. For subsidence caving or caving due to relaxation, the suitability of Figure 2.8 requires further investigation. Laubscher's stability index graph is inadequate in dealing with open stope stability (Potvin, 1988; Milne, 1997).

2.4.3.6 The shape factor

The shape of a stope surface affects its stability. The hydraulic radius, span (including modified span) and radius factor are the shape factors in use for open stope design.

Laubscher and Taylor (1976) used the hydraulic radius concept for stope design. Mathews et al. (1980) used hydraulic radius *HR* to develop an empirical open stope design graph.

Germain et al. (1996) recognized that the actual profiles of stope surfaces differ geometrically from those used in computing shape factors. Planar stope geometries are often assumed in computing hydraulic radii.

After blasting, stope surface geometries are often irregular or complex. Irregular and complex shape factors give different shape factors from those calculated by assuming planar surfaces.

Irregular and complex surfaces also lead to different stress distributions from planar ones. Because of these effects, an actual stope surface stability state may be different from that predicted. A volumetric index was proposed by Germain et al. (1996) to correct for stope surface complexity.

The stability graph is meant to guide the initial determination of stope sizes. At these initial stages, the complexities of stope geometries are unknown. The use of volumetric index in correcting for stope performance, makes it difficult to assign overbreak to a particular surface. This is because it attributes the sloughage to all stope walls, a case that is of interest in open stope mining because sloughage from a hangingwall or footwall will cause dilution while sloughage from a sidewall in ore causes ore enhancement.

Milne and Pakalnis (1997) showed that while the hydraulic radius term was a major improvement from the single span term, it was only adequate for simple planar surfaces. When complex stope surfaces are involved, the hydraulic radius term is inadequate. They introduced the radius factor *RF* (Milne et al., 1996) term to eliminate the limitation of *HR* when complex stope surface geometries are involved.

The radius factor (Milne and Pakalnis, 1997) is linked with the deformation of hangingwalls for stability prediction. In this case *RF* is redefined in terms of an effective radius factor *ERF* (Milne et al., 1997) that deals with deformation of points in the stope surface.

$$RF = \frac{0.5}{\frac{1}{n}\sum_{\theta=1}^{n}\frac{1}{r_\theta}} \qquad 2.6$$

where r_θ = Distance from surface center to the abutments at angle θ, and n = Number of rays measured to the surface edge.

The radius factor *RF* can be calculated anywhere on a given surface. However, if the calculation is not done at the centre of the surface, the term is called effective radius factor *ERF* (Milne and Pakalnis, 1997). The *ERF* value is zero at a surface abutments and it is a maximum at the centre of the surface. The *ERF* value is a measure of the relative stability of points on a surface. *ERF* is shown to be related to surface deformation and degree of slough in hangingwalls by Milne and Pakalnis (1997), and can be projected to estimate the effect of continuous mining.

2.4.3.7 Mathews open stope design method

Mathews et al. (1980) developed the open stope stability graph method commonly referred to as the Mathews method. It uses a modified Q referred to as Q'. Q' is obtained by setting the stress reduction

factor *SRF* to 1 in Q (Equation 2.7). Q' is a measure of the rockmass strength, structure, and water pressure.

$$Q' = \left(\frac{RQD}{J_n}\right)\left(\frac{J_r}{J_a}\right)(J_w) \qquad 2.7$$

J_w is set to 1 in the Canadian hard rock underground mines where dry conditions prevail. Q' for dry conditions is then given by:

$$Q' = \left(\frac{RQD}{J_n}\right)\left(\frac{J_r}{J_a}\right) \qquad 2.8$$

Q' is the rockmass quality as mapped underground before stoping.

Three types of failures were recognized to be associated with open stope stability (Mathews et al., 1980):

- Structurally controlled failures caused by opening and movement along unfavourably oriented structure (usually zones of low stress).
- Stress-controlled failure through intact rock.
- A combination of structural and stress-controlled failure caused by movement along joints combined with failure of the bridge of intact rock between structures.

Mathews et al. (1980) introduced a stress factor A, a joint defect factor B and a gravity factor C shown in Figure 2.9 to account for these three types of failure. They made the following assumptions in developing the stress factor A graph:

- Bridging type failure between fractures should not occur when the ratio of intact rock strength to induced stress exceeds 10. Failures in this case are structurally controlled and $A = 1$.
- Failure is stress controlled when the ratio of intact rock strength to induced stress approaches 1 in which case A approaches zero (Figure 2.9).
- Combined stress and structurally controlled failure can occur between the first two extremes. A straight-line relationship is assumed between the two extremes.

Tensile stresses can be induced in the walls of tall openings with increasing values of horizontal to vertical in situ stress ratios K. When these conditions are encountered, the induced stress is set to zero (Mathews et al., 1980; Brummer, 1990). The stress factor A then goes to zero. This implies an N' of zero under tensile stress conditions. This is a problem in the use of the stability graph since N' is plotted on a log scale, and log scales can not handle zeros. Therefore, the stress factor A in the stability graph does not adequately account for relaxation. This is discussed further in Section 2.5.

Failure due to a combination of structure and stress is by movement along joints combined with failure of the bridge of intact rock between structures. This failure process is dominated by the failure of the intact

rock strength and is similar to stress-controlled failure through intact rock. This is because failure of the rockmass must be initiated by first fracturing the intact rock that serves as a bridge between discontinuities. Therefore, the two types of failure are not different.

It could be concluded from Mathews et al. (1980) discussion, and from the above analysis that the stress factor *A* for both high compression and tension, approaches zero (see Kaiser et al., 1997). In relaxed discontinuous rockmasses, stability is controlled by gravity rather than by stress. The gravity factor *C* is a supplement to *A* to account for stability in relaxed stope surfaces with moderate to high jointing.

Additional factors were introduced to reflect the consequences of mining on open stope stability. During mining, joints with unfavourable orientations may be exposed on the stope surfaces, which will reduce face stability through gravitational action. Also, blasting may induce fractures that intersect pre-existing fractures to liberate unstable wedges. To compensate for rock structure and gravity, a joint orientation factor *B* and a gravity factor *C* were introduced. The basis of *B* is briefly discussed in this section, and the *C* factor is explained in Section 2.5.2.

Figure 2.9 contains charts for determining *B* and *C*.

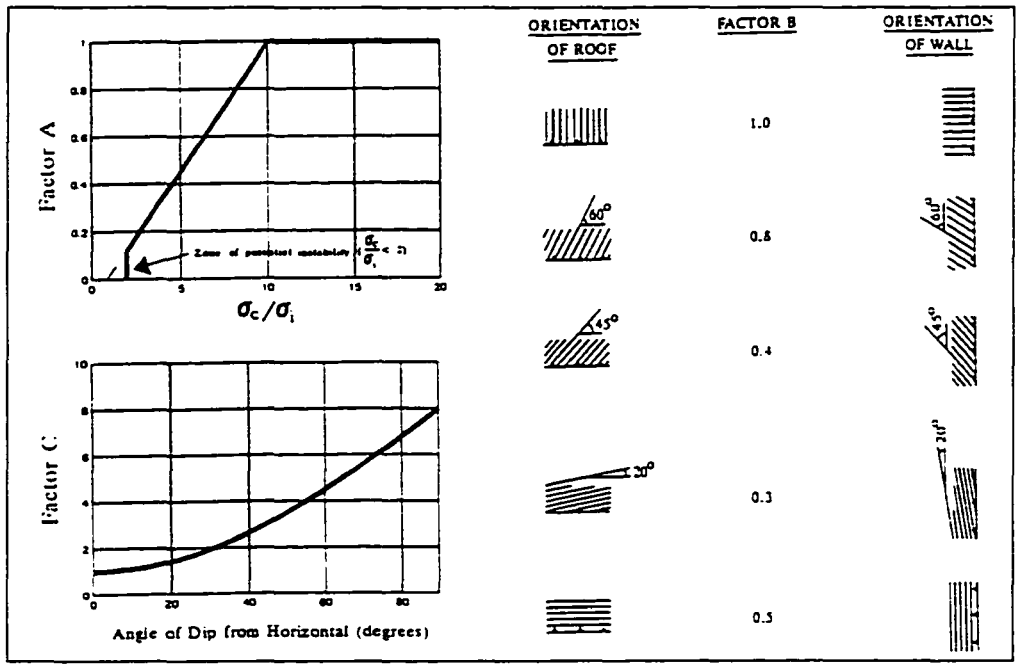


Figure 2.9 Stability graph factors (after Mathews et al., 1980)

The inclusion of factor *B* was necessary in the stability graph method since it is important but absent in the *Q*-system. Factor *B* is based on the premise that as the angle between a surface and a joint decreases, the probability of fracturing the intact rock bridge between the surface and joint by blasting increases. The *B*

factor therefore accounts for the possibility of breaking intact rock bridges due to blasting and indirectly accounts for blasting effects. It also accounts for likely shear fracturing of rock bridges.

For two-way span excavations, the inclusion of dip direction by Potvin (1988) is unnecessary. Also, the included angle ξ accounts for dip and dip direction effects if any. Figure 2.10 is sufficient for determining *B*. *B* can also be determined from the following equation:

$$B = \begin{vmatrix} -0.01\xi + 0.3 \\ 0.2 \\ 0.02\xi - 0.4 \\ 0.0067 + 0.4 \end{vmatrix} \text{ for } \begin{vmatrix} \xi < 10^\circ \\ 10^\circ \le \xi \le 30^\circ \\ 30^\circ < \xi < 60^\circ \\ 60 < \xi \le 90^\circ \end{vmatrix} \qquad 2.9$$

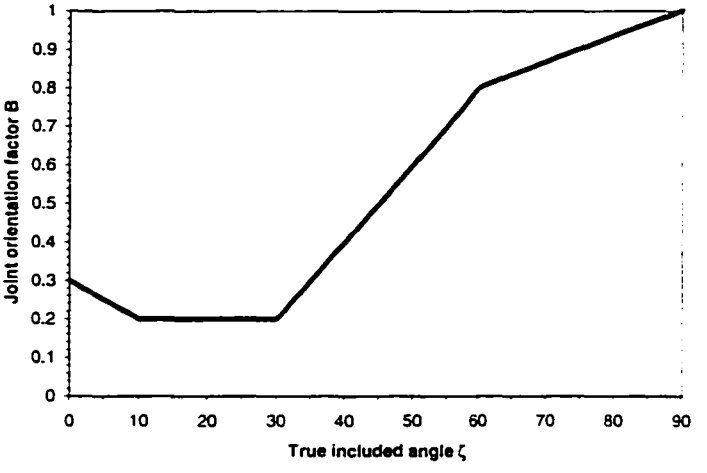


Figure 2.10 Chart for determining joint orientation factor *B* (Re-plotted from Hutchinson and Diederichs, 1996)

Figure 2.10 differs from the *B* factor diagram in Figure 2.13 in that it does not account for difference in strike between joint and excavation surface. Hutchinson and Diederichs (1996) state that Figure 2.13 is only appropriate for horizontal backs or joints.

In Chapter 5 and Appendix B, a procedure for calculating the included ξ is presented, and further details are given in Suorineni et al. (1997).

The stress factor *A* does not account for failure in tension. It is switched off in these circumstances by setting it to unity. The gravity factor plays a more important role in assessing the stability of excavations in relaxed grounds. In relaxation, failure is by sliding or free fall. Figure 2.13 includes graphs for the determination of *C*. The two graphs are translated into Equations 2.10 and 2.11 for free fall and sliding respectively.

For free fall and buckling:

$$C = 8 - 6Cos\theta_s \qquad 2.10$$

where θ_s is the stope surface dip.

For sliding:

$$C = \begin{matrix} 8 & \text{for} & \theta_j < 30° \\ 11 - 0.1\theta_j & \text{for} & 30° \le \theta_j > 90° \end{matrix} \qquad 2.11$$

where θ_j is the joint dip.

The rockmass quality Q' is combined with factors A, B and C to give a stability number N:

$$N = Q' \bullet A \bullet B \bullet C \qquad 2.12$$

The stability number is then empirically plotted against a shape factor called hydraulic radius HR. Figure 2.11 is the Mathews stability graph. It is divided into a stable zone, potentially unstable zone, and potentially caving zone with two transition zones.

The main limitations of the Mathews method are:

- It was based on a limited number of points,
- It does not account for faults, shear zones and fissures,
- Undercutting of stopes is not considered,
- HR is inadequate for partly filled stopes or stope surfaces with complex geometry,
- Time of exposure of stope surfaces is not accounted for but should be considered since long exposure times lead to significant stress changes and possibly weathering, and
- Blasting effects are not specifically included in the factors.

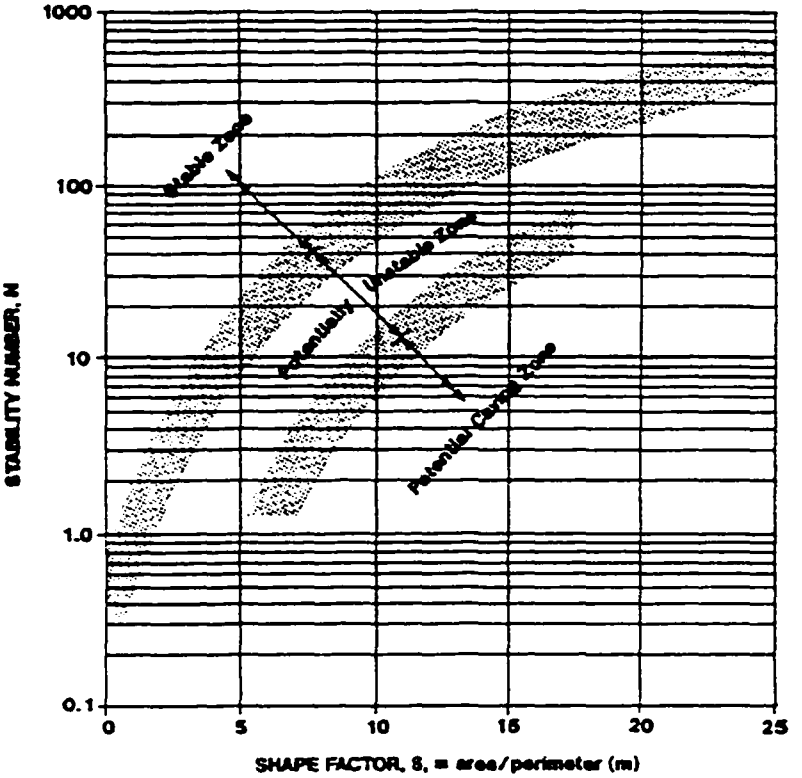


Figure 2.11 Mathews stability graph (from Mathews et al., 1980)

Time effects from environmental agents may not have serious consequences on the stability of stopes in hard rock mines because of short stope life. However, in rocks with unstable minerals, such as the clay minerals, time effects become important. On excavation of a rockmass, stress redistribution occurs with stresses migrating back into more competent rock. Stress redistribution is not instantaneous, but time dependent. It is this time-dependent stress distribution that makes it difficult to assign stress factors to excavation surfaces for calculation of excavation stability indices. Løset (1992) observed this problem.

Blast damage to rockmasses occurs when bad blasting practices are used at a mine. Damage due to blasting is not explicitly accounted for in the stability graph, and is one of the major criticisms against the stability graph method of open stope design.

In addition to the limitations listed above, the definitions of the stress and gravity factors are ambiguous. Difficulties are encountered in defining *C* for low dipping footwalls (Pakalnis et al., 1996; Clark and Pakalnis, 1997). Hadjigeorgiou et al. (1995) proposed a modification to the determination of *C* (Figure 2.12) when recent work showed that the Potvin (1988) nomogram for sliding was inappropriate. Included in Figure 2.12 is a curve for determining C for footwalls when the dip of the footwall is less than the critical joint dip.

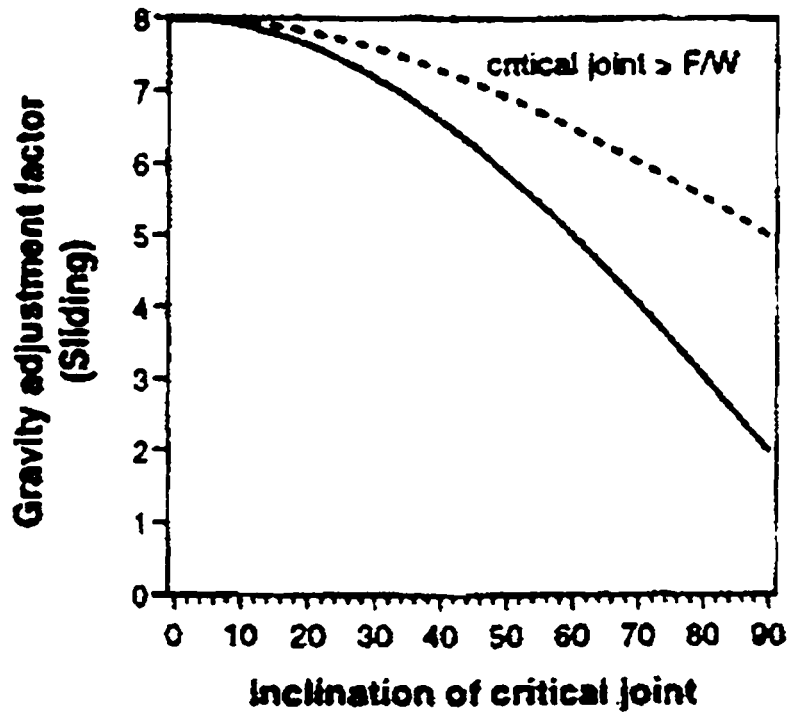


Figure 2.12 Proposed graph for the determination of the gravity factor *C* for footwalls and sliding (after Hadjigeorgiou et al., 1995)

2.4.3.8 Potvin's Modifications to the stability graph

Potvin (1988) increased the Mathews database from 50 to 175 unsupported case histories and 66 cases of cablebolted stopes, thus improving the size of the empirical database. Factors *A*, *B* and *C* were re-calibrated (Figure 2.14), and the transition zones re-defined and changed from two to one (Figure 2.14).

Potvin's work resulted in increased confidence in the application of the stability graph method. It is now widely used in Canadian underground mines.

Potvin's re-calibration of the stability graph factors, including stress factor *A* has not fully resolved the problems of the stress factor.

The stability graph still requires further improvement by elimination of the limitations discussed above as well as the list of limitations given on pages 34 and 35.

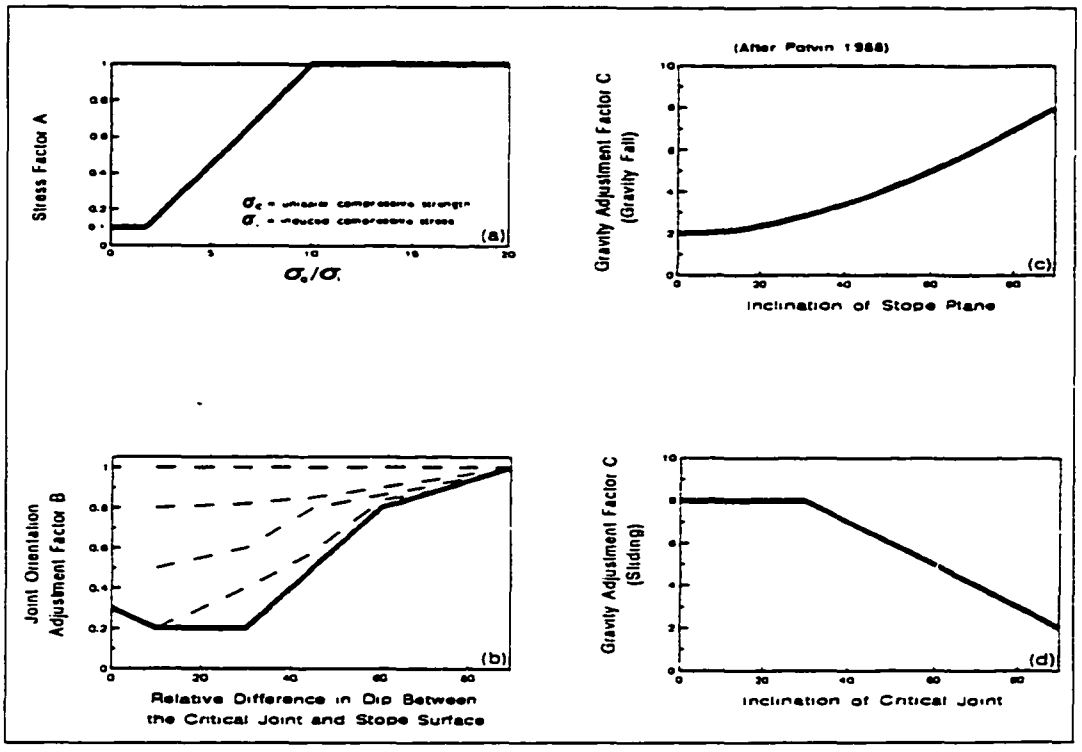


Figure 2.13 Potvin's re-calibrated stability graph factors (from Nickson, 1992): Dashed lines in *B* factor graph represent strike differences increasing from 0° to 90° at top at 15° increments except from 0° to 30° in first two lower curves.

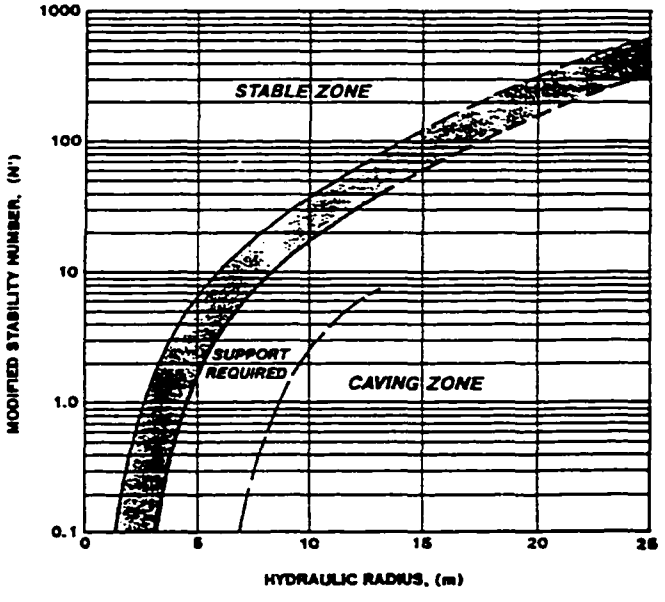


Figure 2.14 Potvin's modified Mathews stability graph (from Nickson, 1992)

2.4.3.9 NGI's Q - equivalent dimension D_e design approach

The NGI rockmass classification system was discussed in Section 2.4.1.6. By plotting values of Q against some geometrical factors of observed performance of excavations, an empirical design chart for

underground excavations was introduced by Barton et al. (1974). The chart includes the various support types that were used in the excavations. The geometrical factor of the excavation used is referred to as equivalent dimension D_e or modified span (Stacey and Page, 1986). The Q - D_e system is a forward predicting method of design, allowing updating of the support system as the ground is observed during preliminary design, excavation and monitoring.

Equivalent dimension D_e is a function of excavation size (span, diameter or height) and purpose (Equation 2.13). The function of the excavation is integrated into the design procedure by the parameter called "excavation support ratio *ESR*", that is an indirect inverse of factor of safety (Hoek and Brown, 1980). *ESR* is also related to the expected life span of the excavation. Table 2.11 gives the range of applicable values of *ESR*, for different types of excavations. Question marks in column 2 of Table 2.11 imply uncertainty in the *ESR* value because of the limited number of cases (number of cases is given in column 3 of Table 2.11) on which it was based.

$$D_e = \frac{\textit{Excavation span, diameter, or height}}{\textit{Excavation Support Ratio ESR}} \qquad 2.13$$

Span and diameter are used when dealing with the back of a tunnel while diameter or height is considered when dealing with wall support. The use of tunnel span for back stability assessment, and wall height for wall stability assessment is an improvement on the use of only span for support and stability prediction. *RMR* and Lauffer's stand-time methods, and Terzaghi rock load system, all use only tunnel span for the prediction of stability of the excavation back and walls.

The back of a tunnel is confined or restrained by the sidewalls except for excessive back relaxation. The distance between the sidewalls, determine the amount of confinement and consequently, the stability of the back. On the other hand, confinement for the sidewalls is, provided by the back and floor of the tunnel. The distance between the tunnel back and floor (i.e., the wall height) should control wall stability in tunnels.

The Q - D_e empirical design approach recognizes that tunnel walls and backs have different support demands depending on the rockmass quality. The poorer the rockmass, the more the influence of gravity will be on the stability of the back. Gravity has maximum influence on back stability.

Table 2.12 presents the adjustments to the overall rockmass quality as mapped, as recommended by Barton et al., (1974) for tunnel walls to reduce the equivalent wall support demand.

Table 2.11 Excavation support ratios *ESR* for underground excavations (after Barton, 1988)

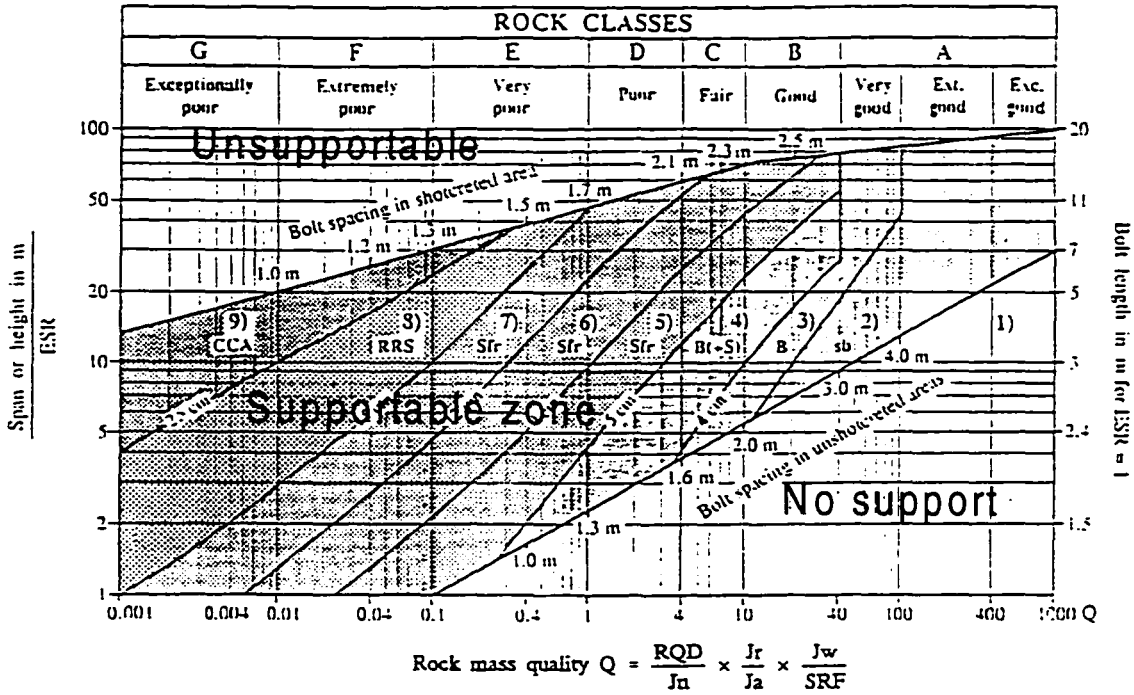
Type of excavation	*ESR*	No. of cases
A. Temporary mine openings	3 - 5?	2
B. Permanent mine openings, water tunnels for hydropower (exclude high-pressure penstocks), pilot tunnels, drifts and headings for large excavations, etc.	1.6	83
C. Storage rooms, water treatment plants, minor road and railway tunnels, surge chambers, access tunnels, etc. (hemispherical caverns?)	1.3	25
D. Power stations, major and railway tunnels, civil defense chambers, portals, intersections, etc.	1.0	79
E. Underground nuclear power stations, railway stations, sports and public facilities, factories, etc.	0.8?	2

Table 2.12 Q values for walls

Q range	Q_{wall}
$Q>10$	$5.0Q$
$Q<10$	$2.5Q$
$Q<0.1$	$1.0Q$

The NGI empirical method of Q-D_e underground excavation design (Figure 2.15) has been successfully used in tunneling, and has shown promise in mining. However, for the method to work adequately in mining at depth, the following factors affecting stability must be incorporated in the method:

- Joint orientation with respect to the excavation elements,
- Blasting effects,
- Effects of faults, shear zones and fissures,
- Influence of gravity,
- Schistosity and foliation, and
- Re-definition of stress factor because of the ambiguity of *SRF*.



1) Unsupported
2) Spot bolting, sb
3) Systematic bolting, B
4) Systematic bolting, (and unreinforced shotcrete and 4-10cm, B(+S)
5) Fibre reinforced shotcrete and bolting, 5-9cm, Sfr+B
6) Fibre reinforced shotcrete and bolting, 9-12cm, Sfr+B
7) Fibre reinforced shotcrete and bolting, 12-15cm, Sfr+B
8) Fibre reinforced shotcrete >15cm, reinforced ribs of bolting, Sfr, RRS+B
9) Cast concrete lining, CCA

Figure 2.15 Updated Q-D_e design chart (from Grimstad and Barton, 1993)

2.4.3.10 Dilution design method

Pakalnis (1986) related *RMR* to slough or dilution to develop a dilution-based open stope empirical design method. Exposure rate and hydraulic radius are major factors in this design approach. They account for rockmass quality deterioration with time, and stope surface geometrical effects on stability. Figure 2.16 illustrates the method.

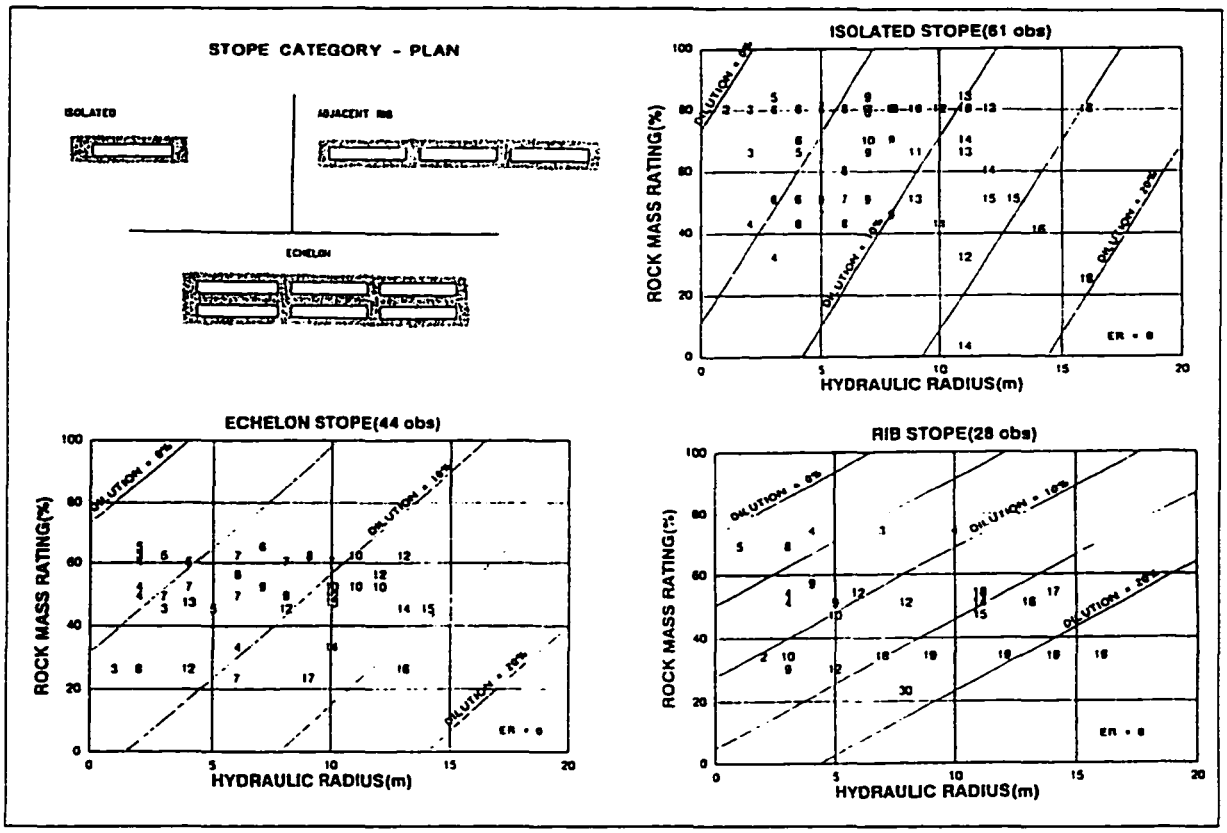


Figure 2.16 Dilution based empirical design (after Pakalnis and Vongpaisal, 1993)

2.4.3.11 Rockmass index *RMi* design approach

Palmström (1995) discussed a different method of rockmass classification for support purposes. This method is referred to as Rockmass index *RMi* method. The procedure is used for civil engineering tunneling and has yet to be tested for use in mining at depth.

2.5 Observations and inferences from the Q - D_e system and the modified Mathews method

The modified Mathews stability graph evolved from the Q- system. The stress factor A was substituted for *SRF*, and additional factors B and C were introduced to correct for joint orientation and gravity effects.

The Q-D_e system integrates the span for backs, the diameter for tunnels or the height or width for walls of the excavation to predict support. The graph, even though biased towards civil engineering tunnels includes some mining data (Barton, 1988), and is able to decipher between stable and unstable surfaces as shown by Barton et al. (1974) and Barton (1988). There is a "no support" zone as well as a "supportable" zone and an unsupportable zone. The use of different spans for excavation backs and walls is a major factor in the successful application of the method for support design.

The stability number N' in the modified stability graph is an improvement of Q in the $Q - D_e$ design method as original Q does not account for joint orientation, stress at depth, and gravity. The equivalent span term D_e is replaced with hydraulic radius HR to differentiate between two-way span excavations and one-way spans in tunnels. The use of back span and wall height for tunnels in effect accounted for a two-way span situation in the $Q - D_e$, system, however.

In principle, the design graphs of the two systems should be similar (Kaiser et al., 1997) if not identical when plotted in the same space because N' is equivalent to Q and HR is equivalent to equivalent dimension D_e. The Q - D_e graph of Barton et al. (1974) is plotted showing the upper and lower support limits in Figure 2.17. Hydraulic radii HR in the calibration database were converted into spans s according assumptions for square to rectangular stope faces with maximum span $s_{max} \leq 2s_{min}$, HR is between 0.25 and 0.33 times the shortest span s_{min} (Kaiser et al., 1997). The stability graph showing the supportable zones as statistically re-defined in Chapter 3 of this thesis are superimposed in the same log-log space with the Q - D_e graph, with the vertical axis representing hydraulic radius HR and modified span, and the horizontal axis representing N' and Q (Figure 2.17). The lower "no support" line of the Q - D_e-system almost coincides with the lower "no support" line of the unsupported transition zone. The only difference discernible is the large spectrum of spans that can be supported in the case of Q - D_e-system.

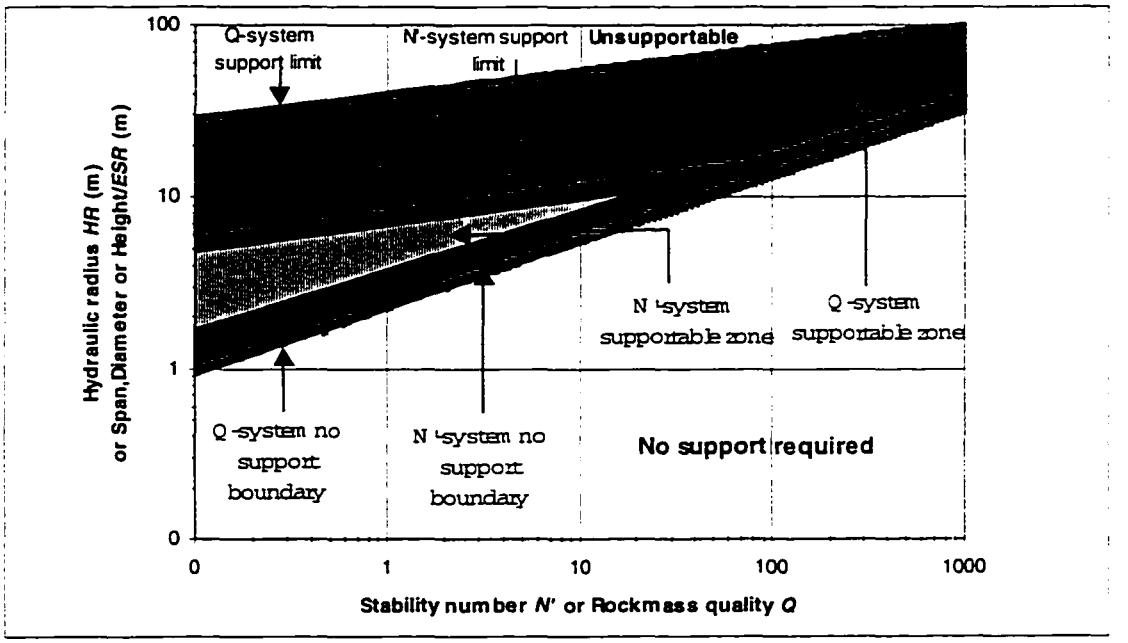
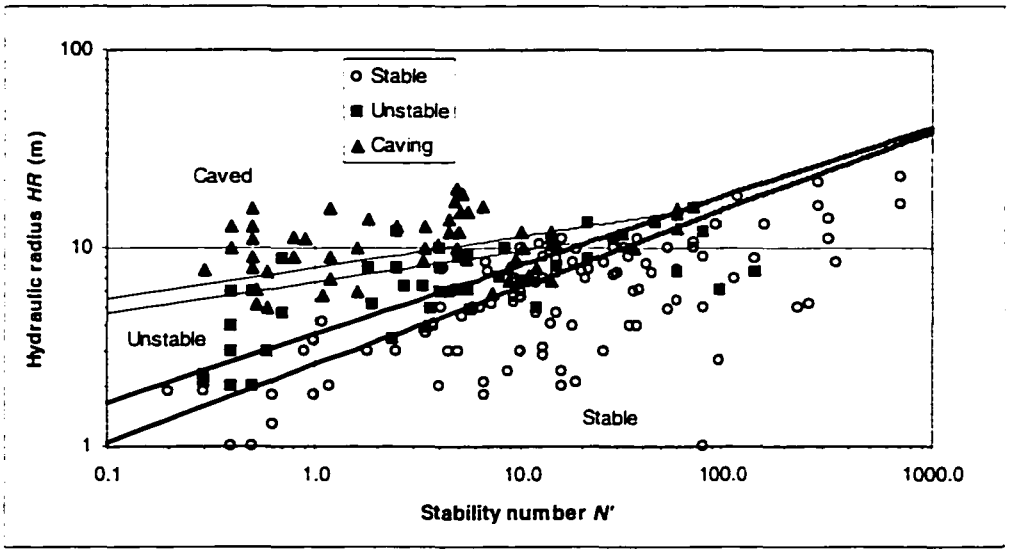


Figure 2.17 Comparison of Q - De and N'-HR empirical design charts: ESR =3

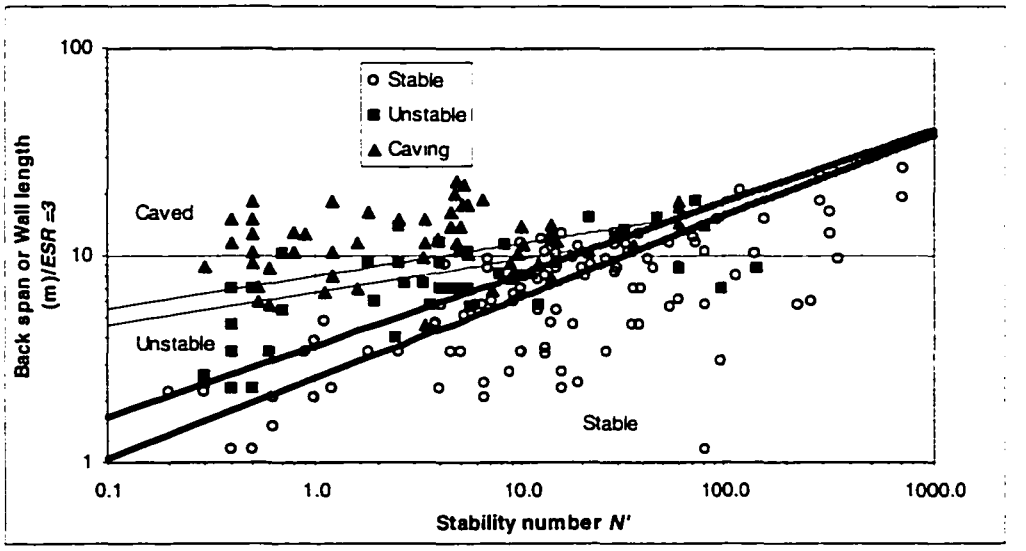
Kaiser et al. (1997) gives mining induced relaxation as the primary reason for the large differences in supportable spans in the Q-D_e and the stability graph. In mining, the support's effectiveness is limited due to rockmass relaxation. Another reason for difference in supportable spans is that in civil engineering we

can use all support necessary where as in mining we tend to alter the stope dimensions to achieve stability. Hence, a narrower range of supportable spans is observed.

The significance of Figure 2.17 is that, spans are effective even in 3-dimensional or two-way span situations, provided span is well defined for each stope surface. Figure 2.18 shows plots of the stability graph using equivalent dimension or modified span based on the assumptions cited, and hydraulic radius; and the calibration database consisting of the Potvin (1988) data, Nickson (1992) data and Mathews et al. (1980) data. An *ESR* value of 3 is used to determine equivalent dimension or modified span because open stopes are temporary mine openings (see Barton et al., 1974). The calibration database used is further discussed in Chapter 3.



(a) Stability graph re-plotted with hydraulic radius as vertical axis



(b) Stability graph re-plotted with modified span (*ESR* = 3) as vertical axis

Figure 2.18 Stability graph using hydraulic radius and modified span

Figure 2.18a and b are very similar. Figure 2.18b suggests that the modified span can be equally used for the design of open stopes, and can give the specific linear dimensions of the stope in plan view. When hydraulic radius is used further work is often required to determine the specific stope dimensions.

2.5.1 Stress factor *A* and stress reduction factor *SRF*

The stress factor *A* in the stability number *N'* is a function of the intact rock strength and induced stress. The following equation expresses the original stress factor graph as a step function of the ratio of intact rock strength to induced stress.

$$A = \begin{cases} 0.1 & \text{for } \frac{\sigma_c}{\sigma_t} < 2 \\ 0.1125\frac{\sigma_c}{\sigma_t} - 0.125 & \text{for } \frac{\sigma_c}{\sigma_t} < 10 \\ 1 & \text{for } \frac{\sigma_c}{\sigma_t} \geq 10 \end{cases} \qquad 2.14$$

Figure 2.9 contains the Mathews et al. (1980) stress factor graph. In applying factor *A*, the anticipated stresses in the stope life should be used.

The stress factor *A* is re-plotted in Figure 2.19 to show increasing induced stresses from left to right as against the conventional plot in which induced stresses increase from right to left.

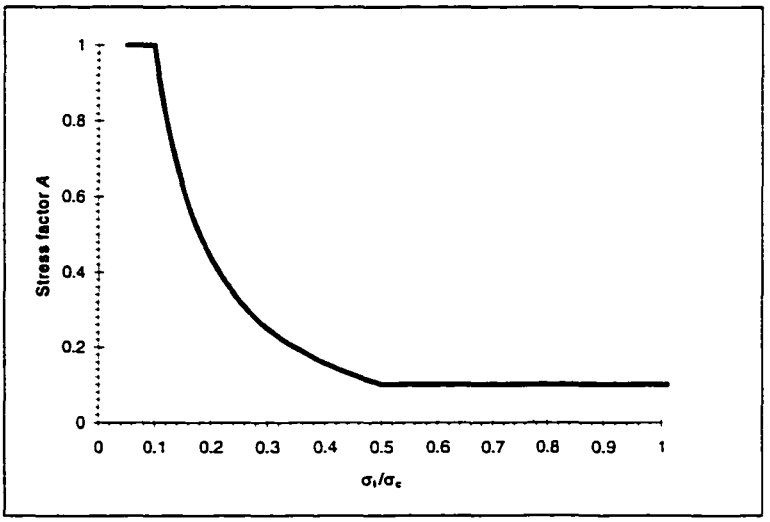


Figure 2.19 Re-plotted stress factor graph

SRF in the *Q*-system was replaced with the stress factor *A* in the Mathews method. *SRF* and stress factor *A* are compared. *SRF* is high for both relaxed ground and in highly stressed situations (Table 2.9). As *SRF* increases, *Q* decreases, and vice-versa. High *SRF* in both relaxed and high compression therefore imply small span openings to avoid ground fall in relaxed cases, and crushing failure in high compression

situations. In the life of a mine opening, the rockmass surrounding the opening goes through relaxation and high compression stresses at some stages in the mining cycle (Wagner and Godfrey, 1976).

The stress factor A is approximately an inverse of SRF (Kaiser et al., 1997):

$$A = \frac{1}{SRF} \qquad 2.15$$

A and $1/SRF$ are compared in Figure 2.20 for competent rocks for which A is appropriate.

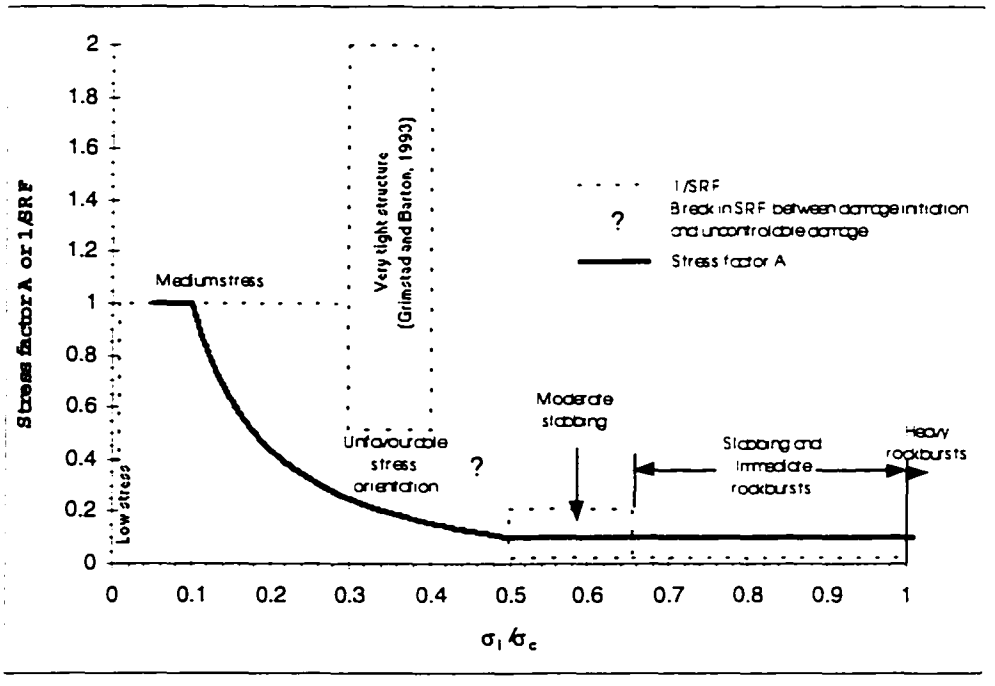


Figure 2.20 Comparison of stress factor A and stress reduction factor SRF

The stress factor A using $1/SRF$ gives a wider range of moderate stresses favorable to stability for stress ratios between 0 and 0.3. Medium stresses often favour stability of excavations. Martin and Chandler (1994) showed failure initiation starts at the induced stress to uniaxial compressive stress ratio of 0.3. Consequently, for stress ratios below 0.3 failure of intact rock may not occur.

There is a discontinuity in the scale of SRF values where induced stress to compressive strength ratio is between 0.4 and 0.5. This region is known (Hudson, 1993; Budavari, 1983; Wagner and Godfrey, 1976) to be the onset of uncontrollable failure of the rockmass in underground mines. Mathews et al. (1980) observed that a stress ratio greater than or equal to 0.5 is a sign of potential danger.

Figure 2.20 shows the horizontal axis goes to infinity. When induced stress is tensile, Mathews et al. (1980) and Brummer (1990) state that the induced stress should be set to zero. When this happens, the ratio of induced stress to strength is zero (the reciprocal is infinity) and the stress factor A is zero. A zero stress

factor gives an N' of zero in Equation 2.12. A zero N' cannot be plotted on the conventional stability graph since the N' scale is logarithmic. The modified stability graph then becomes inapplicable to completely relaxed rockmasses.

1/SRF ranges from less than 0.01 to a maximum of 2 on Figure 2.20. At a maximum *1/SRF* value of 2, for $0.3 \leq \sigma_t/\sigma_c \leq 0.4$, a jointed rockmass is tight if the stress orientation is favourable. However, if stresses are unfavourably oriented, instability of the structure may occur.

Some similarities exist between the stress factor *A* and *1/SRF*. It is therefore not surprising that the stability graph, and the Q - D_e graph compare favourably. In the N'-system, relaxation is at least theoretically accounted for in the gravity factor *C*. In relaxed stress environments, stress factor *A* is set to unity, implying that no intact rock failure can occur. Any failures occurring are presumed structurally controlled. In massive rockmasses in tension, tension fractures are induced normal to excavation walls and do not lead to instability in a manner detrimental to mining (Potvin 1988). In the Q - *De*-system relaxation, as well as high compression, is to some extent accounted for by *SRF*. Modelling of several mining stages during which a stope will be open could be used to determine the stress factor. The uniaxial compressive strength will remain constant but the induced stresses will change with the mining sequence.

Substituting stress factor *A* for *SRF* was an important contribution to the improvement of empirical underground excavation design. The problem with the stress factor is its inability to deal with extreme relaxation that may occur in various forms such as mining of adjacent stopes, undercutting of stope walls, delamination due to deformation, and faults. A major problem in the application of both *A* and *SRF* is that the stress state following an underground excavation is not constant but varies with mining sequence and geometry due to stress redistribution. The problem then is when to determine the stress factor for input into the design in order to find the stability before support and the appropriate support type.

2.5.2 Excavation support ratio *ESR*

Mathews et al. (1980) used an *ESR* of 1.6 for permanent openings in developing *C*. An *ESR* of 3 is recommended for temporary mine openings by Barton et al. (1974), and 1.6 for permanent mine openings (Table 2.11). The use of an *ESR* of 1.6 for non-entry stopes is therefore highly conservative. Mathews et al. (1980) stated that *ESR* could be used in accounting for the effect of blasting in the stability number N'. The choice of an *ESR* of 1.6 was probably made with this in mind.

The general form of Equation 2.10 is:

$$C = 5ESR - (5ESR - 2)Cos\theta \qquad 2.16$$

The constant 5 in Equation 2.16 originates from Barton et al. (1974) when they observed that walls are five times more stable than backs.

Blasting effects in N' are partly accounted for by the *ESR* value of 1.6, because of the level of conservatism implied by its use for temporary mine openings. Blasting effects can be effectively accounted for at individual mines by lowering *ESR* to an appropriate value in Equation 2.16. This equation should then be used to determine C in the stability number computation for the stability graph. To facilitate this, the *ESR* values in Table 2.11 are plotted in Figure 2.22.

Hutchinson and Diederichs (1996) observed that though the stability graph method is meant for open stope design, it could be applied to the design of other mine excavations with appropriate calibrations for those openings. There are different *ESRs* for different types of excavations, depending on function and expected life (Table 2.11). The following gravity chart is applicable for the design of other mine excavations if used together with the other factors in N' and re-calibrated for the intended openings.

It should be noted that when dealing with footwalls, the C factor applies only to steeply dipping (75°) footwalls, and in the case of other orientations the maximum value of 8 is recommended (Clark and Pakalnis, 1997; 1998).

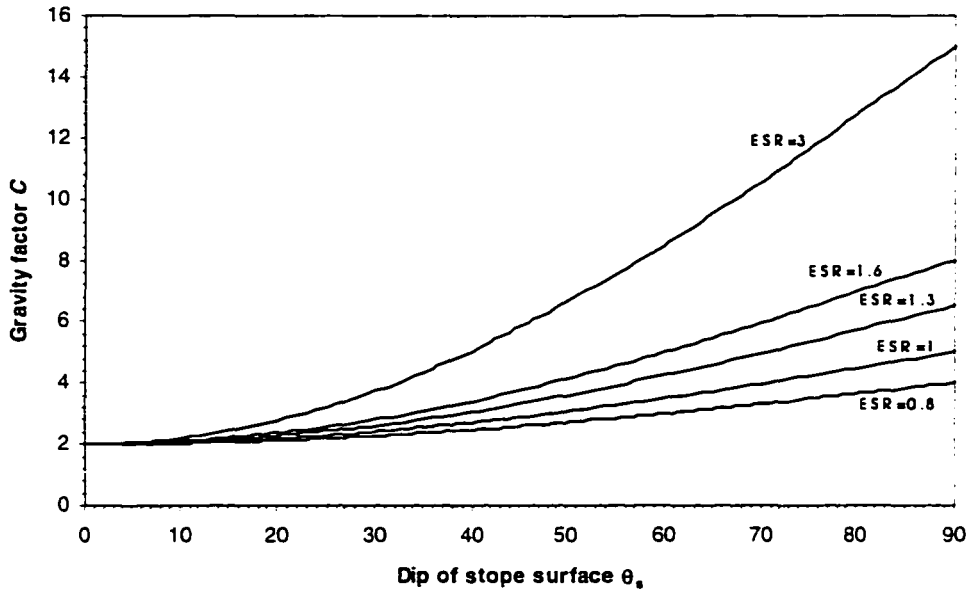


Figure 2.21 Chart for determining C based on excavation type

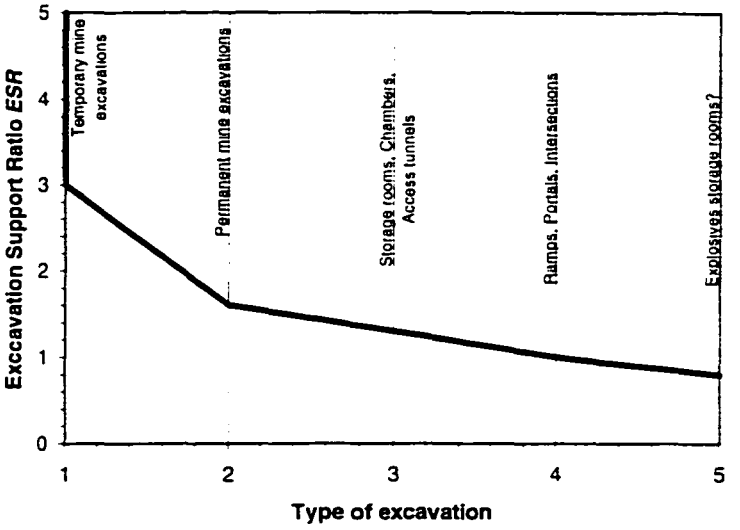


Figure 2.22 Relationship between excavation type as described in and Excavation Support Ratio *ESR* (Table 2.11)

Numbers in the horizontal axis in Figure 2.22 have the following equivalents in Table 2.11: A = 1, B = 2, C = 3, D = 4, and E = 5.

In massive rockmasses, *B* will be dominant in controlling blasting effects while *C* will be more important in controlling blasting effects in poor quality rockmasses.

2.6 Summary

Empirical methods of rockmass classification have distinct from empirical underground excavation design methods. The latter combines the geometry of the excavation with the rockmass quality to predict stability and support demand, while the former is dependent on only the inherent rockmass characteristics. Rockmass classification systems should treat stress separately not as a rockmass quality but as an excavation stability factor.

Limitations of the rockmass classification systems together with the advantages associated with each are given in the review. It is recommended that for optimum results the most appropriate rockmass classification system should be used in each investigation.

Empirical methods of underground excavation design have been discussed, with the view of identifying key rockmass properties and excavation surface shape factors that are best for open stope design. Existing empirical open stope design methods are examined to define limitations and advantages to determine areas

requiring further improvement. Empirical tunnel design methods are included in the discussion for comparison, and how such methods could be adapted for mining at depth.

The stability graph and the Q - D_e graph are essentially equivalent. The stress factor A and SRF are similar and N' is an improved Q in the $Q - D_e$ method of underground excavation design. In the stability number N' gravity and joint orientation relative to the excavation are taken into account, but are not considered in the $Q - D_e$ method. Both A and SRF are time dependent and still ambiguously defined.

Hydraulic radius was often found to be inadequate for complex stope geometries, and radius factor RF was introduced to account for complex stope surface geometries (Milne and Pakalnis, 1997). Alternatively, the principle of span for one-way span excavations can be extended to two-way span excavations if modified span as defined for D_e in the Q - D_e-system is used for the individual excavation surfaces. Modified span for ESR=3 can equally be applied in the stability graph without loss of excavation performance predictive power.

The main limitations of the stability graph that require further study are its linkage to stand-up time, micro structures such as schistosity and foliation, and accounting for faults, shear zones and fissures. The focus of this thesis, among others, is the development of a fault factor for implementation in a stability index graph.

CHAPTER 3

APPLICATION OF STATISTICS TO INTERPRETATION OF STABILITY GRAPH

3.1 Introduction

There are three data groups that make up the stability graph database, and define the three zones in the stability graph:

- Stable,
- Unstable, and
- Caving.

Stable stope surfaces are defined as stope surfaces exhibiting little or no deterioration during their service life (Hutchinson and Diederichs, 1996) and with the advent of cavity monitoring survey *CMS* stable stope surfaces are defined in this thesis as stope surfaces with equivalent linear overbreak sloughage *ELOS* (Clark and Pakalnis, 1996) less than or equal to 0.5 m. Unstable stope surfaces are defined as those surfaces exhibiting little wall failure or block fallout involving less than 30% of the face area (Hutchinson and Diederichs, 1996) and these stope surfaces are classified as stope surfaces with *ELOS* values between 1 m to 5 m. Caved stope surfaces suffer unacceptable dilution with block fallout involving more than 30% of the stope surface. Caved stope surfaces have *ELOS* values greater than 5 m.

Reliability on the stability graph depends on several factors, such as the accuracy of the input parameters Q', A, B, and C, among others. When the input parameters are accurate, reliability on the stability graph depends on how well the transition zones are defined. Therefore, the definition of the transition zones

should be unambiguous. This thesis provides statistical tools to assist in describing the implications of points plotting anywhere on the stability graph, when the stability graph is used as a design tool.

There are uncertainties implicit in empirical methods of design. There are also errors associated with the use of empirical methods. Most empirical designs in Rock Engineering require a demarcation between two or more groups of data such as observed failed cases and observed cases of non-failure. The demarcation may be done visually by "eye-balling" or by analytical statistics.

Subjective statistics refer to cases where events with known characteristics are plotted and clusters of events of similar characteristics identified, and curves drawn by hand to separate clusters of cases of similar performance into groups. This type of data analysis is different from the three known classes of statistics defined by Statisticians, namely: descriptive statistics, inferential statistics, and correlation or predictive statistics. When data is limited, the use of subjective statistics is advantageous. However, when subjective statistics is used, a human factor is inherently included in the results. Results obtained from subjective statistics are often difficult to reproduce exactly.

When sufficient numerical data is available, the use of descriptive, inferential and predictive statistics (mathematical statistics) are recommended to eliminate the human factor and to optimize the demarcation zone between the data groupings. Krige (1994) observed that the science of statistics has expanded rapidly during the last two decades and research workers as well as the commercial and industrial world now recognize its value as a powerful and indispensable tool. However, in the field of mining engineering full advantage has not been taken of statistics as an analytical tool.

In analytical statistics, criteria are established that govern the admission or rejection of given events into a particular cluster. Correlated variables are examined by established and proven statistical methods for analytical correlation factors. Results obtained from analytical statistics are reproducible. Statistical methods are capable of quantifying experience. The use of analytical statistics should however be governed by engineering judgement since for example a statistical function that separates two data groups well may not have any physical meaning.

Years of observation and experience on the performance of underground openings have resulted in various databases. These databases are the basis for empirical design in civil tunneling and mining, as has been discussed in Chapter 2.

In Appendix A and in this chapter, statistical procedures are presented for interpretation of empirical data, and for application to the stability graph method of open stope design. The procedures are tailored to:

- Account for possible errors associated with unequal costs of misclassification of events,
- Account for unequal number of data in data groups (unequal a priori probabilities of occurrence, for example we may have 25 failed cases against 100 stable cases in the database),

- Optimize the boundaries often used as design lines between data groups by incorporating misclassification risk cost in such analysis, and
- To show implications of data overlap in empirical design, such as in the stability graph method.

Barton et al. (1974) demonstrate the importance of statistics, in the analysis of empirical data, in the following statement:

> "It seems unlikely that conventional safety factors can ever be specified for structures as complex as lined underground excavations in jointed rock. There are too many uncertainties concerning the interacting modes of failure between the support and the surrounding rockmass.
>
> A statistical analysis might at first sight appear to provide a promising approach. Ideally, the analysis should incorporate the uncertainties in the input parameters and the uncertainties in the mathematical models of the failure modes. The theoretically optimum design could be determined based on the probabilities of failure in the different modes and on the cost of construction and failure."

Barton et al. (1974) concluded that if this could be achieved, results obtained from the statistical analysis would be superior to design based on conventional safety factors. They however lamented that statistical design of the form discussed was probably a very long way off, as we knew nothing about the modes and mathematics of failure.

Diederichs and Kaiser (1996) accounted for variability in the input parameters to the stability graph using the calibration database. The approach used was a probabilistic one. The probabilistic approach in statistics is widely used in rock engineering (see Pine, 1992; Pine et al., 1992; Tyler, 1991; Tyler et al., 1991; Tyler and Trueman, 1993; Whitman, 1984; Kirsten, 1983; Priest and Brown, 1983; Suorineni et al., 1995; Brummer and Kaiser, 1995; etc.).

The emphasis in this chapter is on classification of empirical data and the implications in design. The issue of classification arises when an investigator makes a number of measurements on an individual parameter and wishes to classify the results into one of several groups on the basis of these measurements.

3.2 Distant Methods and Discriminant Analysis

There are several methods of data classification grouped under distance methods and discriminant functions. Distance methods consist of the Euclidean distance method, Mahalanobis distance method, and the Fisher classification method. The Euclidean distance method becomes ineffective when the variables in the data are correlated. The Mahalanobis distance and the Fisher methods are similar. The Mahalanobis distance method corrects for correlation of the variables by standardization of the variables. Standardization is achieved by rotation of coordinates to coincide with the two axes of symmetry of the ellipse formed as a result of the correlation of the variables. The standardized variables are then used in

classification. The classification procedure involves computation of distances of given observations from each of the subgroup centroids.

Geer (1971) defines discriminant analysis as that statistical procedure which enables one to find out whether there is a compound score of variables that differentiates optimally between subgroups, to specify this compound score, and to find out how far it can be used to decide to which subgroup an individual probably belongs. There are two forms of discriminant analysis. They are the correlation-based and Bayesian rule-based discriminant methods.

Correlation-based discriminant analysis is similar to the distance methods when the correlation matrix is standardized.

The discriminant score is the difference between functions or likelihoods of two data subgroups. Several statistical packages exist for multivariate discriminant analysis. The most popular are SAS and SPSS. However, these are general and have not been tailored to specific needs. This chapter presents statistical tools for interpretation of the stability graph, with emphasis on determination of associated errors in prediction, determination of risk cost associated with prediction errors, and optimization of the boundaries between the zones in the stability graph with the objective of minimizing prediction errors. The methods are verified with the calibration database and applied to new databases from Kidd Mine in Canada and Ashanti Goldfields in Ghana. Additional details regarding these methods are provided in Appendix A.

3.3 The Calibration Database

The Potvin's expanded database, increased confidence in the use of the stability graph, following its original development on a limited database by Mathews et al. (1980), and is referred to as the calibration database. This database has been augmented during the cause of this study with 26 well-documented case histories in the literature, totaling 201 case records. The database is included in Appendix A. A summary of the calibration database composition is given in Table 3.1:

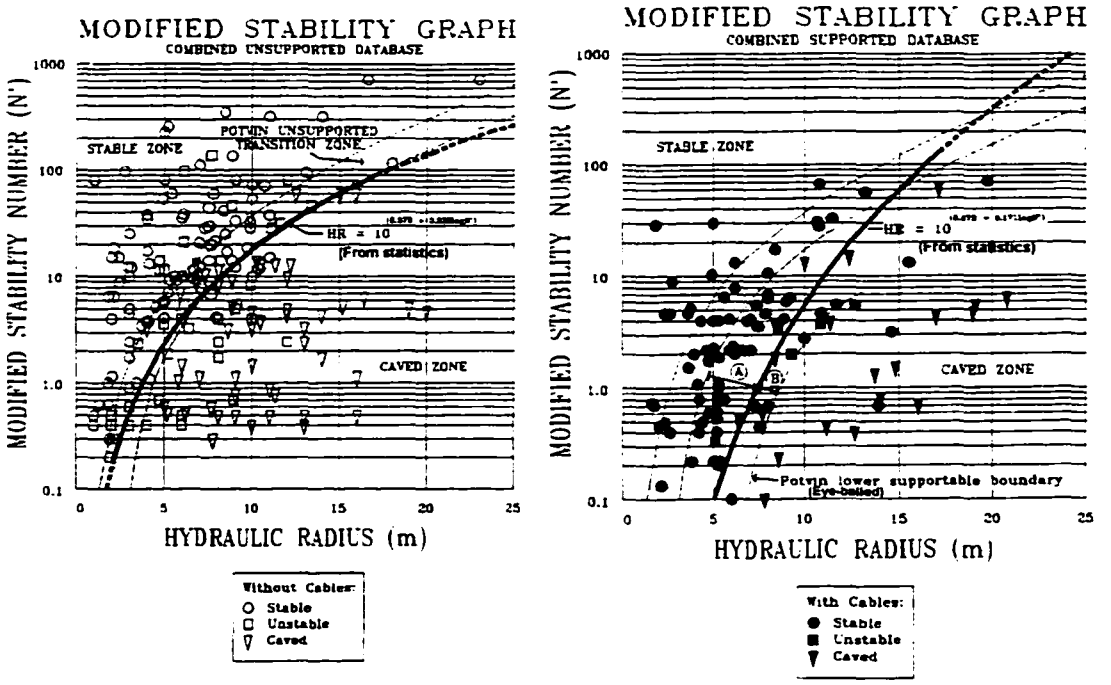
Table 3.1 Calibration database composition

Source	Hangingwalls	Footwalls	Backs	Walls	Total
Nickson (1992)	8	-	4	-	12
Potvin (1988)	102	4	56	13	175
Mathews (1980)	-	1	11	2	14
Total	110	5	71	15	201

3.4 Previous Use of Statistics and the Stability Graph

Mathews et al. (1980) (Figure 2.11) and Potvin (1988) (Figure 2.14) drew in the boundaries of the stability graph by hand. In 1988, Potvin suggested a possible application of statistics to define the boundaries in the

stability graph instead of the "eye balling" method used. Nickson (1992) applied statistics to the revised unsupported open stope stability graph database to separate between stable and failed unsupported open stopes (Figure 3.1a), and to define the supportable limit, using supported stope data (Figure 3.1b).



(a) Statistical boundary for unsupported stopes (b) Statistical boundary for supported stopes

Figure 3.1 Nickson's (1992) statistically derived boundaries

Hadjigeorgiou et al. (1995) also used statistics to redefine the unsupported and the supported transition zones (Figure 3.2). Both Nickson's and Hadjigeorgiou's used the Mahalanobis distance method of discriminant statistics to define the boundaries. Nickson and Hadjigeorgious' boundaries for the stable and failed unsupported stopes are single curves. Hadjigeorgiou's support limit is also a single curve. Nickson's support limit boundary has an upper and lower limit (2 curves).

The boundaries between the zones in the stability graph are too broad to be represented with single curves. Bands defined by upper and lower limits best represent the boundaries between the zones of the stability graph. The boundaries between the zones in the stability graph are each represented by two curves (see Mathews et al., 1980; Potvin, 1988). The two boundaries, between unsupported stable and failed stopes, and supported stable and caved stopes, are often referred to as transition zones.

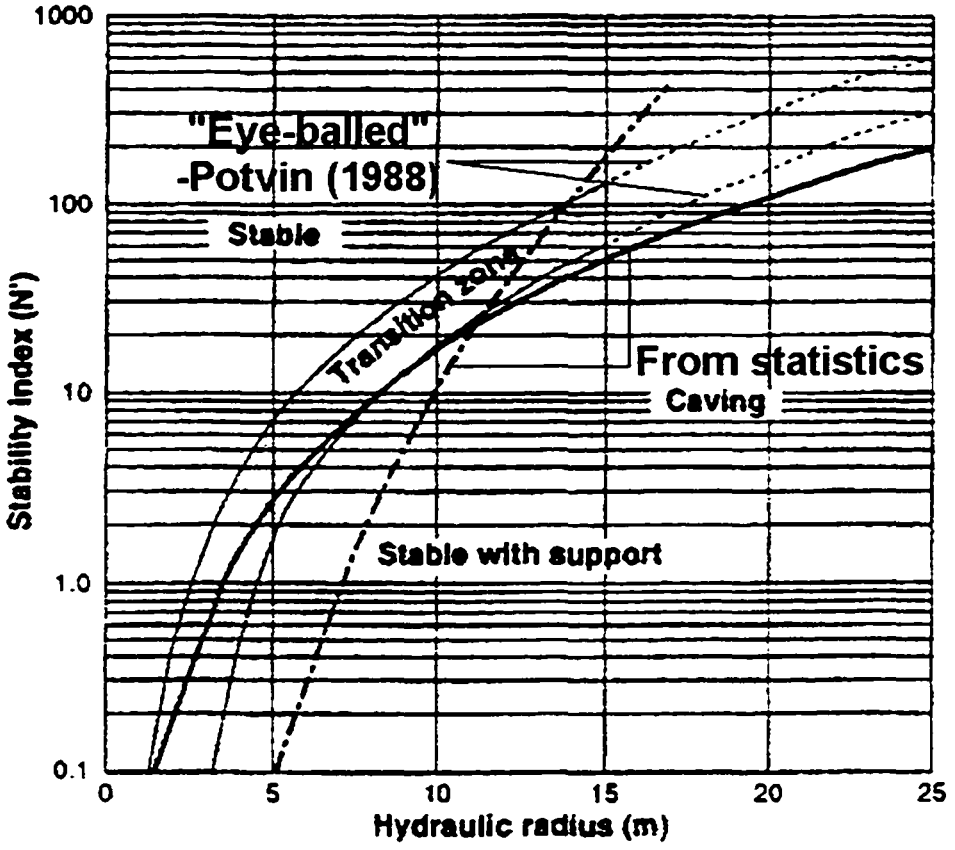


Figure 3.2 Stability graph showing statistically derived boundaries by Hadjigeorgiou et al. and Potvin (1988) hand drawn zone (after Hadjigeorgiou et al., 1995)

3.5 Defining the Transition Zones

The historical development and calibration of the stability graph transition zones show that the number of transition zones to use is still unclear. Table 3.2 shows the transition zones or boundaries defined by various researchers.

Table 3.2 Chronology of number of transition zones - Author dependent

Reference	Number of transition zones	Remarks
Mathews et al. (1980) - Figure 2.11	2	Limited data (empirical) – wide (2 bands)
Potvin (1988) – Figure 2.14	1	Sufficient data (empirical) - (1 band)
Nickson (1992)	1	Potvin's increased database (statistical - single line)
Scobble and Moss (1994) - Figure 3.3	4	Dilution based (conceptual) - single lines
Stewart and Forsyth (1995) - Figure 3.4	3	Mathews et. al., (1980) increased database (empirical) -wide (band)
Pakalnis et al., (1996) - Figure 3.3	4	Based on dilution levels (adopted from Scobble and Moss, 1994). Actual data used (empirical) - single boundary

Figure 3.3 suggests that in terms of dilution, multiple design curves each representing an amount of average overbreak defined as equivalent linear overbreak sloughage *ELOS* (Clark and Pakalnis 1996) is required. Even though the data show some scatter, the *ELOS* stability graph is useful for open stope design. Addition of more data is required to fine tune the ELOS contours and to define contours for *ELOS* values greater than 2 m.

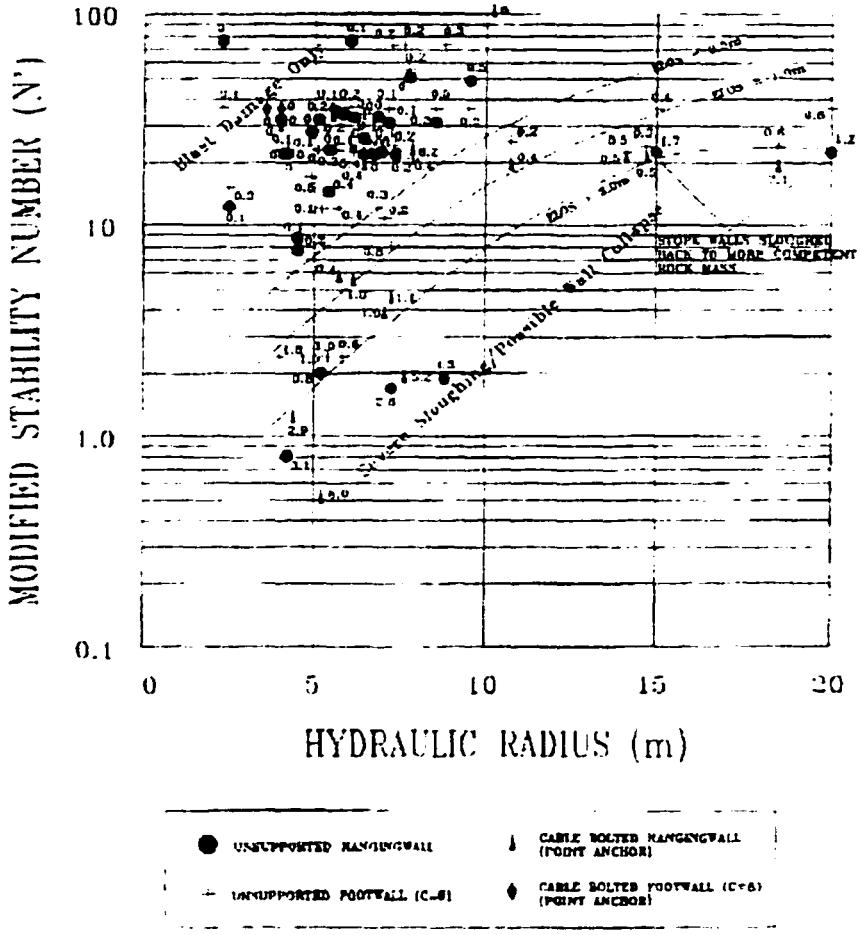


Figure 3.3 *ELOS* stability graph showing *ELOS* values superimposed on dilution contours proposed by Scobble and Moss (1994) by Pakalnis and Vongpaisal (after Pakalnis and Vongpaisal, 1998)

Stewart and Forsyth (1995) reviewed the stability graph method and proposed three transition zones as shown in Figure 3.4. They contended that because the stability graph method is non-rigorous, the use of a single boundary between stable and failed stopes by Potvin (1988) was inappropriate because it gave the user the feeling that stopes are either stable or failed.

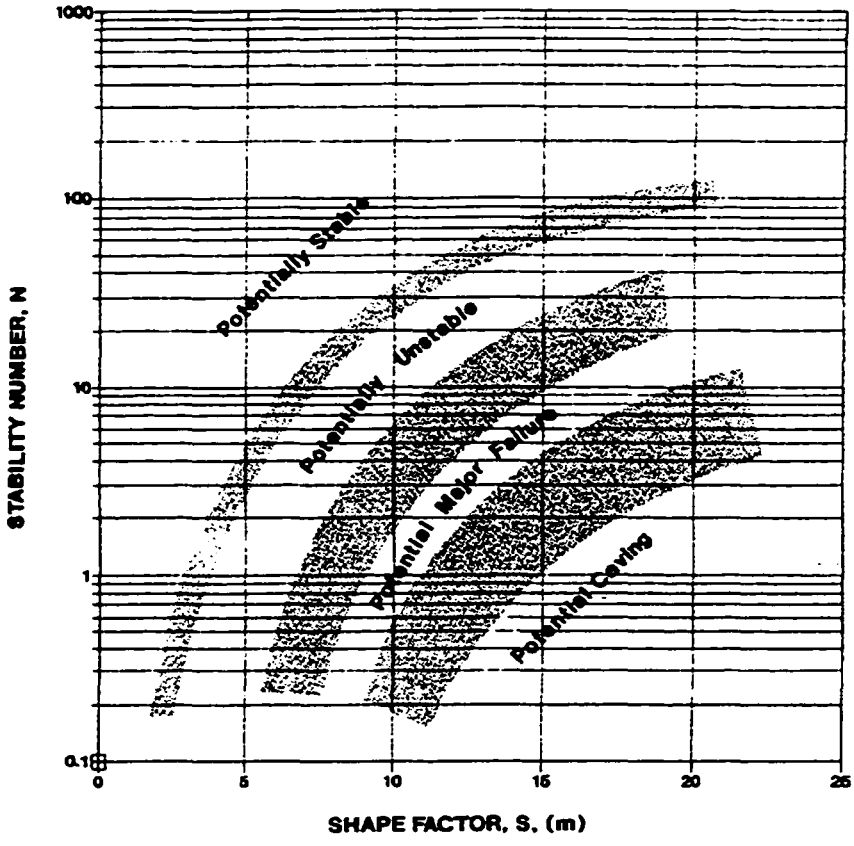


Figure 3.4 Stability graph zones proposed by Stewart and Forsyth (1995)

It seems that the use of multiple curves to explain that stability state of stopes plotting on the stability graph is a more practical approach to explaining the use of the stability graph as a non rigorous design tool.

There should be a boundary between stable and unstable (upper boundary of transition zone), and unstable and caving stopes (lower boundary of transition zone in the unsupported stability graph database (Figure 3.5). This gives two boundaries defining a transition zone. The zone of unstable stopes is the transition between stable and caving stopes (stopes are caved or stable).

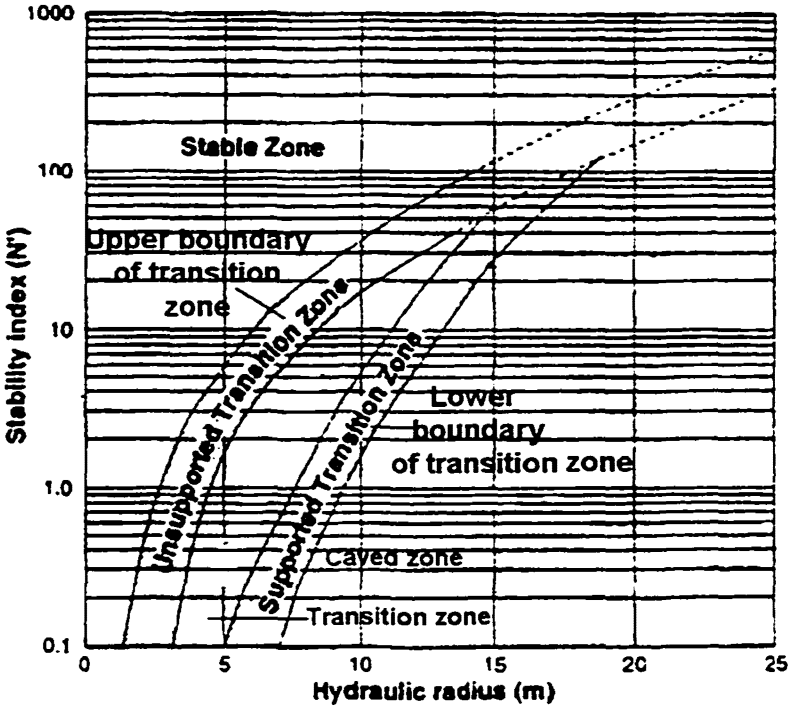


Figure 3.5 Definition of the transition zone in the stability graph using the Potvin-Nickson (1992) stability graph

In the following sections, the statistical procedures presented in Appendix A and in this chapter are used to derive boundaries between the stable and unstable classes, and the unstable and caving classes. An upper and a lower limit, represented by curves define each boundary. The two boundaries then define the limits of the transition zone.

Examination of Table 3.2 shows an inclination towards multiple transition zones, particularly, in the use of dilution data for design. For the purposes of a multiple curve stability graph, a boundary between stable and failed stopes (unstable plus cave) is also determined. In Section 3.5.4, a multiple design curve stability graph is introduced.

3.5.1 The multivariate likelihood statistic

Bayes' rule as discussed in Appendix A, is difficult to apply directly to this database because of the problem of determining **a posteriori** probabilities, defined as empirical probability measured by relative frequency of occurrence of an event. However, Bayes' theorem links **a posteriori** probabilities to conditional probabilities that can be defined in a given sample space. Determining conditional probabilities require large volumes of data. Difficulties associated with direct use of Bayes' classification are removed when the data approximates a normal distribution. The assumption of normal distribution is often met in practice (James, 1985; Johnson and Wichern, 1992).

Univariate normal distribution describes the probability of occurrence of a single variable x_i, which is specified by its mean and standard deviation. The equivalents of the mean and standard deviation in a univariate normal distribution are respectively the mean vector and variance-covariance matrix in a multivariate normal distribution.

The joint probability distribution of the independent variables in each data subgroup is referred to as a likelihood function, discriminant function or discriminant score. The likelihood function is often expressed as a multivariate normal distribution function. The ratio of two likelihood functions is called the likelihood ratio. The likelihood ratio is equal to the ratio of conditional probabilities in Bayes' theorem.

The likelihood principle is an immediate consequence of the Bayesian approach to statistical inference that enables formation of posterior distributions from prior distributions. The method is more appropriate where data is collected that describe the characteristics of event clusters.

Statistical methods of classification are compared on the basis of power. Power measures the ability of a test to reject when a hypothesis is not true. The likelihood ratio has the highest power among all tests at the same significance level (Johnson and Wichern, 1992). Therefore, conclusions or inferences drawn from a classification method with the likelihood statistic as a basis are more reliable. Likelihood statistic-based classification methods are also optimal (James, 1985), compared to any other classification method. Bayes' rule of classification is discussed in detail in Appendix A as the preferred classification procedure compared to the distance methods.

Barnard et al. (1962) exhaustively discussed the advantages of the likelihood principle, over the use of probability. They concluded that when, on the evidence of given data, the plausibilities of various hypotheses are to be compared, then the primary inference is provided by the likelihood function, and it should be given more attention. In the stability graph we compare the stability states of the stopes based on given mining conditions.

Bayes' rule can be used to introduce misclassification risk cost in the stability graph. Misclassification of an unstable stope as a stable stope and vice versa, is a real possibility when using the stability graph as a design tool, because the zones of the stability graph are not absolute but overlap as shown in Section 3.5.2.2. Bayes' rule also allows corrections for unequal numbers of data in the data groups. Consequently, the boundaries of the transition zone in the stability graph can be optimized to minimize risk of misclassification by accounting for unequal misclassification costs and unequal **a priori** probabilities (Defined as factual outcomes of an experiment. **A priori** probability is related to the system) of the data groups.

Two quantitative variables, the stability number N' and hydraulic radius HR, are used in the stability graph. The variables in each class are therefore considered bivariate normal (Appendix A) with mean vectors and variance-covariance matrices as follows:

- $\bar{\mathbf{S}}_S$ = Mean vector of stable stopes
- $\overline{HR}$ = Mean hydraulic radius of stable stopes,
- $\overline{N'}$ = Mean stability number of stable stopes

The parameters for the unstable and caved stopes are similarly defined.

Stable class

$$\bar{\mathbf{S}}_s = \left(\overline{HR} \quad \overline{N'}\right)_s \tag{3.1}$$

$$\mathbf{S}_s = \begin{pmatrix} \sigma_{HR} & \sigma_{HRN'} \\ \sigma_{N'HR} & \sigma_{N'} \end{pmatrix}_s \tag{3.2}$$

Unstable class

$$\bar{\mathbf{U}} = \left(\overline{HR} \quad \overline{N'}\right)_u \tag{3.3}$$

$$\mathbf{U} = \begin{pmatrix} \sigma_{HR} & \sigma_{HRN'} \\ \sigma_{N'HR} & \sigma_{N'} \end{pmatrix}_u \tag{3.4}$$

Caved class

$$\bar{\mathbf{C}} = \left(\overline{HR} \quad \overline{N'}\right)_c \tag{3.5}$$

$$\mathbf{C} = \begin{pmatrix} \sigma_{HR} & \sigma_{HRN'} \\ \sigma_{N'HR} & \sigma_{N'} \end{pmatrix}_c \tag{3.6}$$

The shapes of the scatter plots of the distributions determine the appropriateness of discriminating between given data groups, and the accuracy of the predictions made from the results. The variance-covariance matrix determines the shape of the distribution (Figure 3.6).

The diagonal terms in Equations 3.2, 3.4, and 3.6 measure the data spread, while the off-diagonal terms determine correlation of the variables. The diagonal terms determine the degree of overlap or diffusion of the data groups.

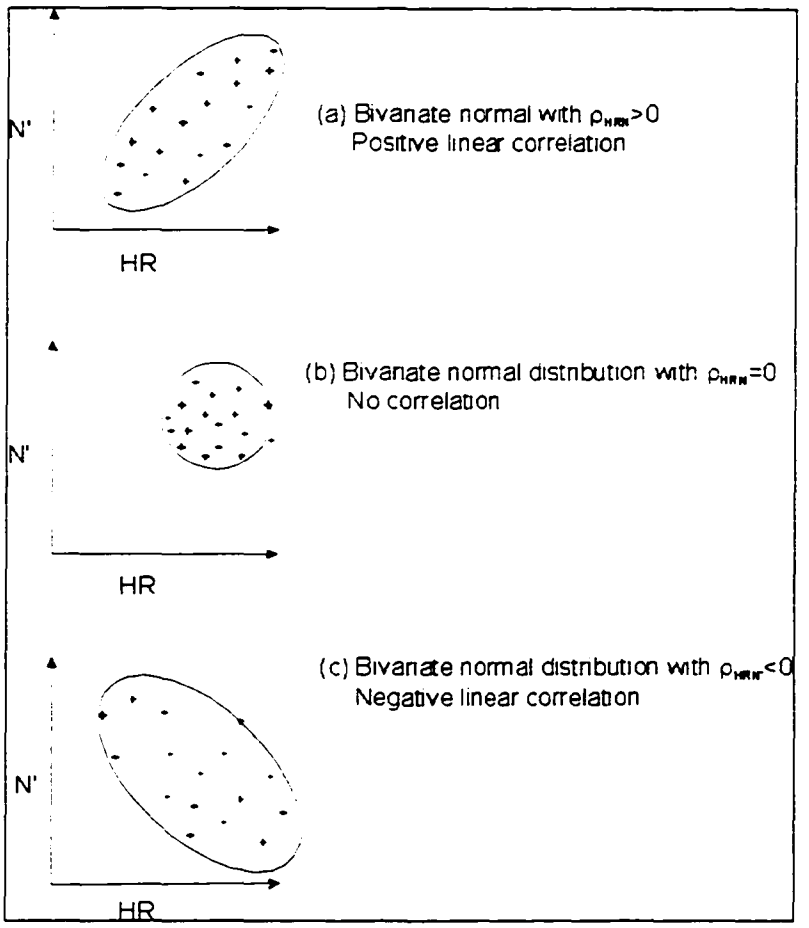


Figure 3.6 Scatter plots showing shapes and association of bivariate normal distributions $\rho_{HRN'}$ is the covariance coefficient

The likelihood ratio approach will be used to:

- Define limits of the boundaries between unsupported stable and unstable stopes, and unsupported unstable and caved stopes,
- Optimize the boundaries between the data groups by correcting for unequal numbers of data in data groups, and correcting for unequal cost of misclassifications (Is it more costly to predict a stable stope as unstable or to predict an unstable stope as stable?),
- Determine degree of overlap or diffusion of the zones in the stability graph (to what degree are stable and failed stope data mixed up? see Figure 3.5),
- Determine possible design or stope performance prediction errors in the stability graph, and
- Develop multiple design curve stability graph, based on, likelihood of failure - Dynamic design stability graph.

Three methods are presented for defining the boundaries of the transition zone. Each of these methods conveys a different emphasis that is of importance in the interpretation of the stability graph. The following are the methods:

- Equiprobability contours - approximation method,
- Special case of the likelihood ratio (likelihood ratio = 1) method - exact method, and
- General likelihood method (likelihood ratio ≠ 1) - multiple design curves.

3.5.2 Method 1: Approximation method

3.5.2.1 Theory of equiprobability contours

From Appendix A, it can be shown that:

$$f_u(\mathbf{X}) = \frac{1}{2\pi\sigma_{HR}\sigma_{N'}\sqrt{1-\rho_{HRN'}}} exp\left[-\frac{1}{2}\left(\mathbf{X}-\overline{\mathbf{X}}\right)^{\mathrm{T}}\mathbf{S}_u^{-1}\left(\mathbf{X}-\overline{\mathbf{X}}\right)\right] \quad 3.7$$

$$f_s(\mathbf{X}) = \frac{1}{2\pi\sigma_{HR}\sigma_{N'}\sqrt{1-\rho_{HRN'}}} exp\left[-\frac{1}{2}\left(\mathbf{X}-\overline{\mathbf{X}}\right)^{\mathrm{T}}\mathbf{S}_s^{-1}\left(\mathbf{X}-\overline{\mathbf{X}}\right)\right] \quad 3.8$$

where $\mathbf{X}$ is the matrix of the corresponding stability state hydraulic radii and stability numbers, $\mathbf{S}^{-1}_u$ is inverse of the variance of the unstable cases. Parameters for the stable case are similarly defined as for the unstable case.

For some set of points $(\mathbf{HR\ N'})_u$ and $(\mathbf{HR\ N'})_s$, the functions $f_u(\mathbf{X})$ and $f_s(\mathbf{X})$ are constant. For this to be true, the terms in the square bracket in each equation must be constant:

$$\left(\mathbf{X}-\overline{\mathbf{X}}\right)^{\mathrm{T}}\mathbf{S}_u^{-1}\left(\mathbf{X}-\overline{\mathbf{X}}\right) = \mathbf{k} \quad 3.9$$

$$\left(\mathbf{X}-\overline{\mathbf{X}}\right)^{\mathrm{T}}\mathbf{S}_s^{-1}\left(\mathbf{X}-\overline{\mathbf{X}}\right) = \mathbf{c} \quad 3.10$$

The sets of points for which each of $f_u(\mathbf{X})$ and $f_s(\mathbf{X})$ is constant define an equiprobability contour.

The constants in Equations 3.9 and 3.10 are defined as chi-square $\chi^2_p(\alpha)$ distributions (Johnson and Wichern 1992), because they represent sums of independently derived squares of scores (Bernstein et al., 1987). Equations 3.9 and 3.10 represent second degree polynomials, and are ellipses. Figure 3.7 is an example equiprobability contour plot for a single data group, and shows spread and correlation.

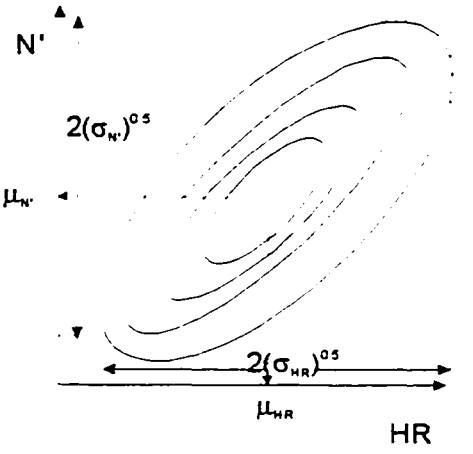


Figure 3.7 Equiprobability contours showing spread and association of variables N' and HR for a bivariate single data group where $\mu_{N'}$ and μ_{HR} are the means of the stability numbers and hydraulic radii for the given stability state

$\chi^2_p(\alpha)$ is the upper $(100\alpha)^{th}$ percentile of a chi-square distribution with p-degrees of freedom. Equation 3.11 leads to contours that contain $(1-\alpha)100\%$ of the probability of an observation occurring for giving alphas.

$$\left(\mathbf{X}-\overline{\mathbf{X}}\right)^{T}\mathbf{S}^{-1}\left(\mathbf{X}-\overline{\mathbf{X}}\right)\leq\lambda_p^2(\alpha) \qquad 3.11$$

These contours can take various shapes (spread) determined by the variance-covariance matrix. The spread is measured by the variance.

The ratio between $f_u(\mathbf{X})$ and $f_s(\mathbf{X})$ is the likelihood ratio. For the special case when the likelihood ratio is equal to 1, we have:

$$f_u(\mathbf{X}) = f_s(\mathbf{X}) = c = k \qquad 3.12$$

This development gives us two intersecting equiprobability contours. The likelihood curve for $\ln(\Lambda) = 0$ (Λ = likelihood ratio – see Appendix A) passes through the intersections of corresponding equiprobability contours. A curve, defined by joining the intersections of corresponding equiprobability contours optimally partitions the two data groups into two in space. Such a curve is called the likelihood curve. Along the likelihood curve, all points have equal likelihood of belonging to either set of the data groups, but above or below it, an object has a higher or lower likelihood of belonging to one data group. Figure 3.8 illustrates the use of equiprobability contours to define a boundary between two data groups.

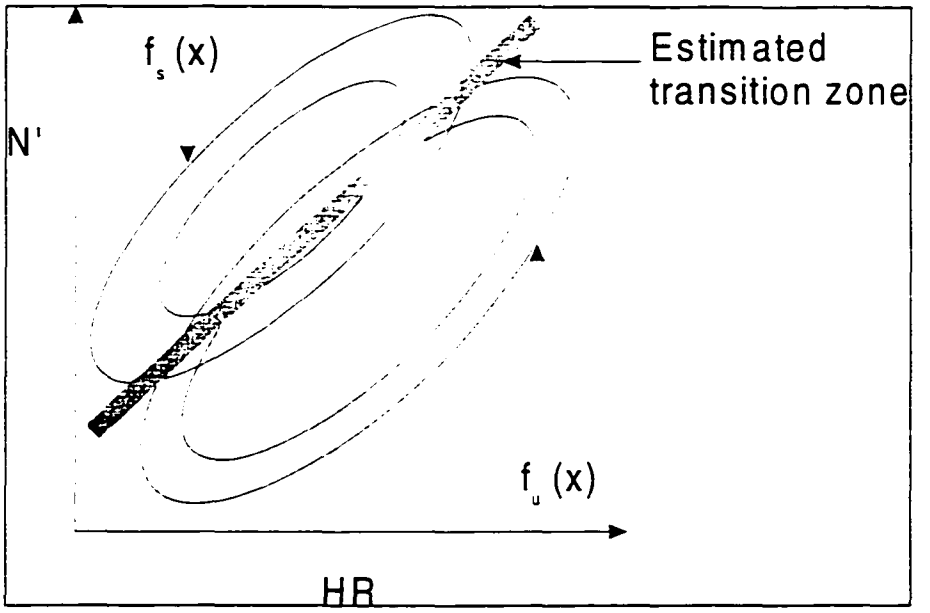


Figure 3.8 Intersection of equiprobability contours and estimation of transition zone

The shape of the likelihood curve or discriminating surface (linear, quadratic or elliptical) depends on the nature of the variances and covariances of the data groups (Cooley and Lohnes, 1985). For example, if either the variances of *N'* and *HR* or the *N'-HR* covariance are different for the stable and failed data groups, the equiprobability contours for the two data groups will not have the same shape and orientation. Therefore, the partitioning curve would not be a straight line. Various shapes of partitioning curves are illustrated in Figure 3.9.

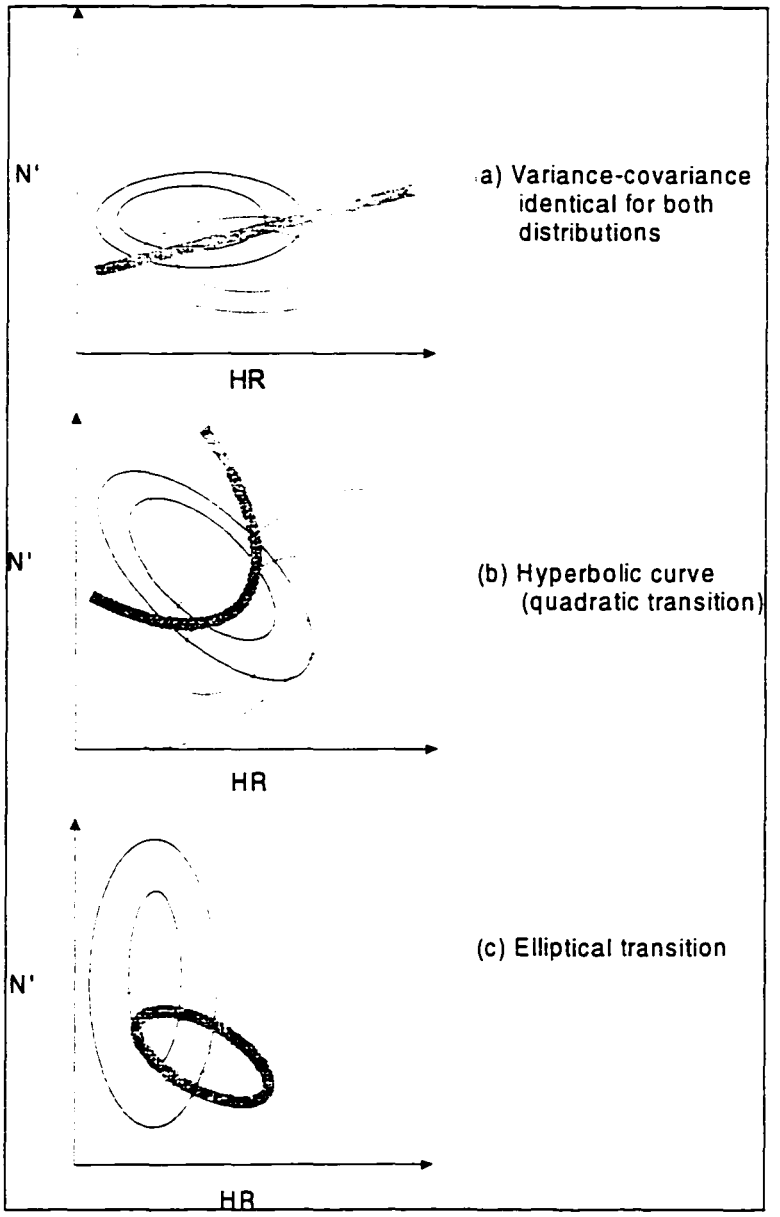


Figure 3.9 Various types of transition surfaces

In discriminant analysis, the success of the discriminating rule depends on the amount of overlap of the data groups (Figure 3.10). If the overlap is large, many wrong decisions will be made. On the other hand, if the overlap is small, only a few decisions will be in error.

A measure of the amount of overlap, ϑ, is the ratio of the distance between the mean vectors to the spread within the distributions (variance-covariance), assuming both distributions have equal spread (pooled variance-covariance):

$$\vartheta = \frac{|\overline{\mathbf{X}}_u - \overline{\mathbf{X}}_s|}{\mathbf{S}} = \frac{|\mathbf{d}|}{\mathbf{S}} \qquad 3.13$$

The larger the value of ϑ, the better the two groups can be discriminated and vice versa. Equation 3.13 is also a measure of data separability, and can be used as a means of comparing the effects of parameters on data zoning.

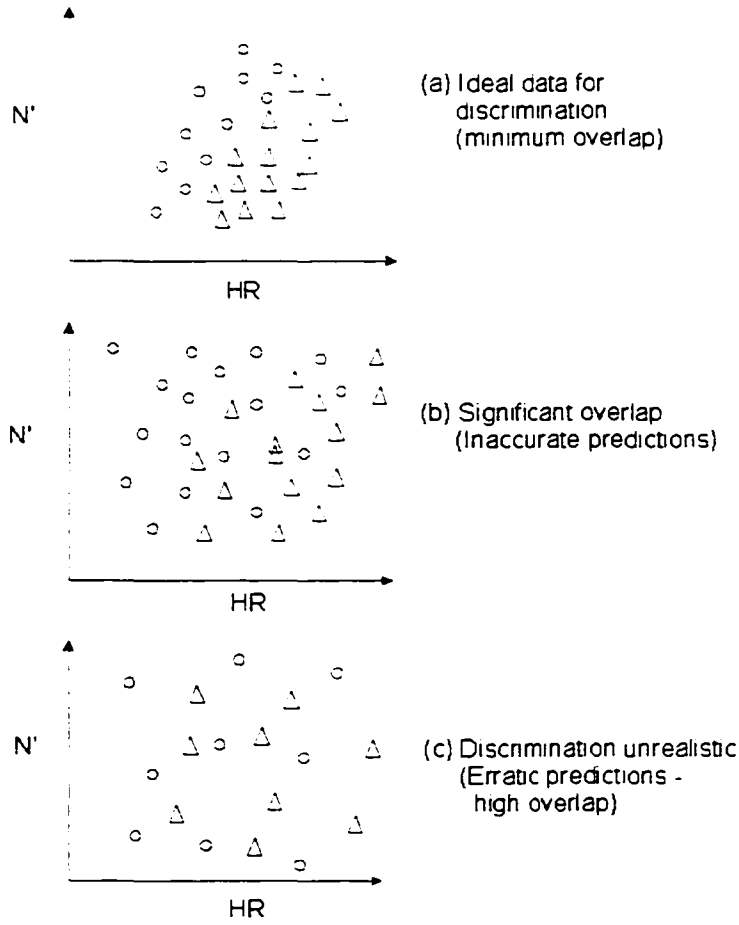


Figure 3.10 Overlapping data and discrimination efficiency: υ decreases for example from 20 t0 5 to 0.1 in the bottom diagram

3.5.2.2 Application to the stability graph

The transition zones are first estimated from the calibration database by applying equiprobability contours using the SYSTAT statistics package. The transition zone boundary between the unsupported stable and unstable classes is given by the intersections of corresponding equiprobability contours of stable and unstable, and stable and caving classes. The intersections of corresponding contours of stable and unstable classes give the upper limit of the upper boundary of the transition zone. The lower limit of the upper boundary of the transition zone is given by the intersections of corresponding contours of stable and caving classes. Similarly the intersections of corresponding probability contours of the unstable and caving data groups define the lower limit of the boundary between the two classes. Ideally, unstable stopes should fall in the zone between the two boundaries defined.

Equiprobability contours are generated with for α = 90%, 80%, 60%, 40%, and 20% corresponding to equiprobability contours of 10%, 20%, 40%, 60%, and 80% respectively (increasing outwards in Figure 3.11).

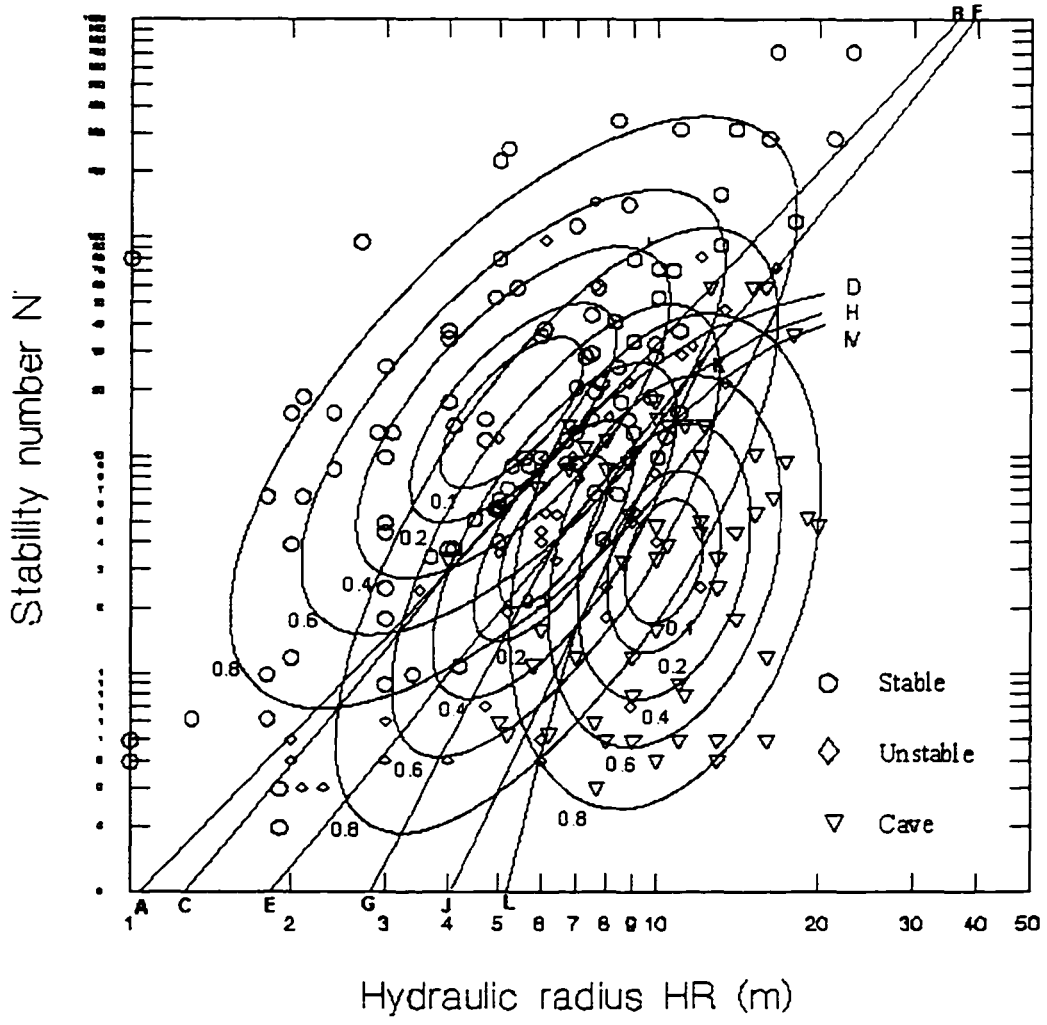


Figure 3.11 Equiprobability contours and estimated the transition zones with *N'* and *HR* plotted on log axes

Figure 3.11 shows the transition zone boundaries as AB or CD, EF or GH, and JK or LM as explained below. Examination of the zone defined by AB and JK shows that it contains the unstable stopes.

AB = Upper limit of upper boundary of transition zone as a linear extrapolation of straight portion of actual path CD of corresponding equiprobability contours for stable and unstable classes within data region of high density and confidence.

CD = Actual path of the intersection of corresponding equiprobability contours for stable and unstable classes (curvilinear).

EF = Lower limit of upper boundary of transition zone as linear extrapolation of straight portion of actual path GH of corresponding equiprobability contours for stable and caved classes within data region of high density and confidence.

GH = Actual path of the intersections of corresponding equiprobability contours for stable and caving classes (curvilinear)

JK = Lower limit of lower boundary of transition zone as a linear extrapolation of straight portion of actual path LM of intersection of corresponding equiprobability contours for unstable and caved classes within data region of high density and confidence, and

LM = Actual path of the intersections of corresponding equiprobability contours for unstable and caving classes (curvilinear).

Figure 3.11 illustrates and explains the confusion behind the definition of the transition zones in the stability graph, and is explained as follows:

The transition zone is the zone between stable and caved stopes. The transition zone should contain unstable stopes that are supportable. Using the straight-line estimations, this zone is bounded by ABEF and JK (i.e., EJK). Potvin's "transition zone" is simply the boundary ABEF between stable and failed (unstable plus caved) stopes, and is strictly not a transition zone. He has no lower boundary for the transition zone. In Mathews et al. (1980) original graph, two bands bound the transition zone between stable and unstable and unstable and caved stopes. The line JK in Figure 3.11 defines the boundary between unstable and caved stopes and approximately coincides with the boundary between supportable and unsupportable cases indicated by Potvin (1988) and Nickson 1992).

The use of bands, rather than single lines to define boundaries, is important as they show that there are no sharp boundaries among the three classes of stopes. It appears that the addition by Stewart and Forsyth (1995) of a third boundary after the lower boundary of the supportable cases is unnecessary.

The equiprobability contours of the three classes of stopes overlap indicating that one can expect any of the stability states in any region within some limits. In Figure 3.12, the location of the letters J, K, L, and M illustrate the problem. J is contained within the 80% probability contour of the stable zone. K is contained in the 10% probability contour of the stable zone but in the 80% probability contour of the unstable zone. Similarly, L is contained in the 60% probability contour of the stable zone, but in the 10% probability contour of the unstable zone, and in the 60% probability contour of the cave zone (equal chances of being stable and caving). Also, M is contained in 10% probability contour of the caving zone but in 80% equiprobability contour of unstable zone. These interpretations mean that the stability regions defined in the stability graph are not absolute. Each region has some probability of having a stope in the stability state of any of the other stability regions.

The overlapping of equiprobability contours implies the increasing tendency towards one stability state. This behaviour signals the need for a multiple design-curve stability graph in which curves will show increasing likelihood of stability as the engineer moves from right to left in the graph.

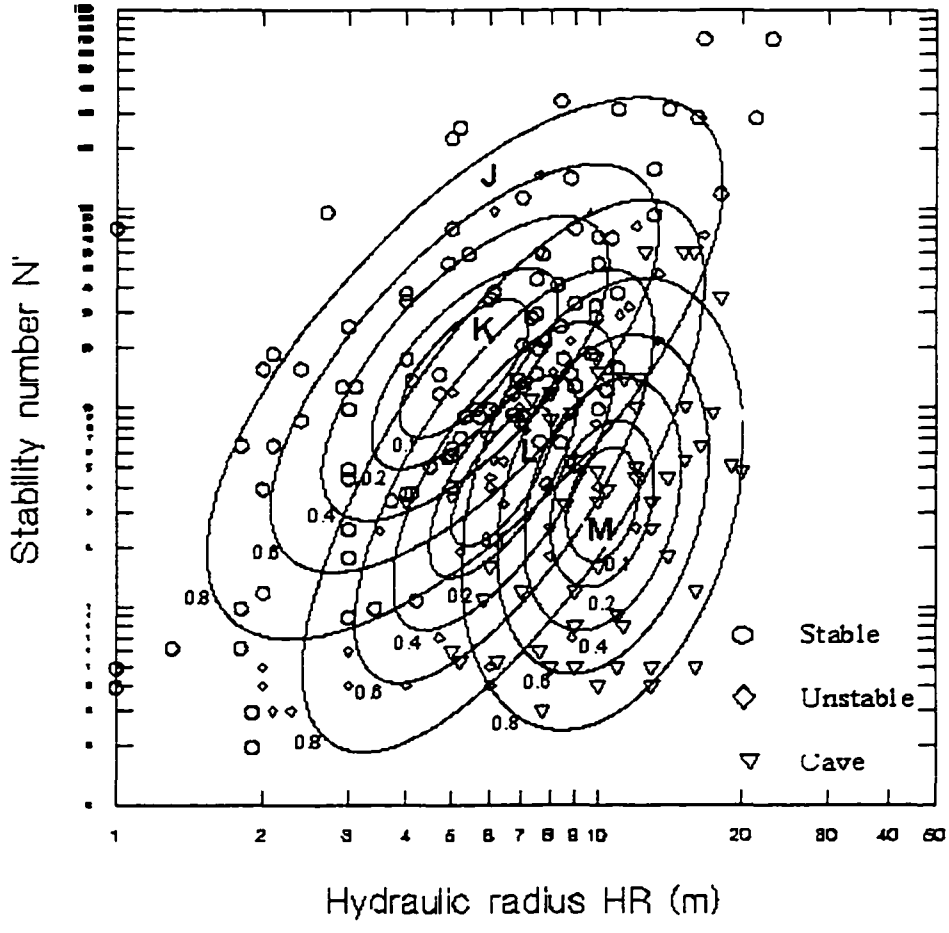


Figure 3.12 Overlapping of equiprobability contours showing that the stability zones in the stability graph are not independent (*N'* and *HR* on log axes)

3.5.3 Method 2: Using likelihood statistic

From Appendix A, it can be shown that:

$$2\mathbf{X}_i^T\mathbf{S}^{-1}\left(\overline{\mathbf{S}_s}-\overline{\mathbf{U}}\right)+\mathbf{K}=0 \qquad 3.14$$

where

$$\mathbf{K}=\left(\overline{\mathbf{U}}^T\mathbf{S}^{-1}\mathbf{U}-\overline{\mathbf{S}}_s^T\mathbf{S}^{-1}\mathbf{S}_s\right) \qquad 3.15$$

Equation 3.15 is a scalar, and therefore Equation 3.16 is the equation of a straight line of the form:

$$m_1 HR + m_2 N' + k = 0 \qquad 3.16$$

where

$$M = \begin{bmatrix} m_1 \\ m_2 \end{bmatrix} = 2\mathbf{S}^{-1}\left(\bar{\mathbf{S}} - \bar{\mathbf{U}}\right) \qquad 3.17$$

For the upper limit of the upper boundary of the transition zone:

and

$$k = \left[\log\left(\overline{\mathbf{HR_S}}\right) \quad \log\left(\bar{\mathbf{N}}_{\mathbf{S}}'\right)\right] \bullet \frac{1}{|\mathbf{S}|} \bullet \left[\mathbf{C_0}(\mathbf{S})^{\mathbf{T}}\right] \bullet \begin{bmatrix} \log\left(\overline{\mathbf{HR_S}}\right) \\ \log\left(\bar{\mathbf{N}}_{\mathbf{S}}'\right) \end{bmatrix} - \left[\log\left(\overline{\mathbf{HR_u}}\right) \quad \log\left(\bar{\mathbf{N}}_{\mathbf{S}}'\right)\right] \bullet \frac{1}{|\mathbf{S}|} \bullet \left[\mathbf{C_0}(\mathbf{S})^{\mathbf{T}}\right] \bullet \begin{bmatrix} \log\left(\overline{\mathbf{HR_u}}\right) \\ \log\left(\bar{\mathbf{N}}_{\mathbf{S}}'\right) \end{bmatrix} \qquad 3.18$$

The curves defining the limits of the boundaries of the transition zone have equations of the form:

$$HR = 10^{(\beta_0 + \beta_1 \log(N'))} \qquad 3.19$$

Where

$$\beta_0 = \frac{-k}{m_1} \qquad 3.20$$

And

$$\beta_1 = \frac{-m_2}{m_1} \qquad 3.21$$

Similarly, the equation of the lower boundary curve is derived using the stable and caving classes. The two curves together give the boundary, separating stable from the failed classes (unstable plus caved). This band is equivalent to the Potvin "transition zone" that is actually the upper boundary of the transition zone.

The following equations define the limits of the upper boundary of the transition zone:

Upper boundary upper limit:

$$HR = 10^{(0.5666 + 0.3471 \log(N'))} \qquad 3.22$$

Upper boundary, lower limit:

$$HR = 10^{\left(0.4105+0.3915\log\left(N'\right)\right)} \quad 3.23$$

A third limit is determined by considering the stable class and the combined classes of unstable and caved stopes. Equation 3.24 is the result, and is approximately the center of the upper boundary of the transition zone.

$$HR = 10^{(0.4905+0.3738\log(N'))} \quad 3.24$$

The lower boundary of the transition zone is also defined from the unsupported case histories. The upper limit of the lower boundary is defined by considering the unstable and caving classes. The lower limit of the lower boundary of the transition zone is determined assuming that it has the same gradient as the upper boundary. The equation of the straight-line (because of the log-log scale) parallel to the statistically derived line is then determined. The following equations define the limits of this boundary:

Upper limit of lower boundary:

$$HR = 10^{(0.7941+0.1854\log(N'))} \quad 3.25$$

Lower limit of lower boundary:

$$HR = 10^{(0.8704+0.1854\log(N'))} \quad 3.26$$

From the supported data, the lower and upper limits are given by the following equations:

$$HR = 10^{\left(0.8278+0.1578\log\left(N'\right)\right)} \quad 3.27$$

$$HR = 10^{\left(0.9016+0.1578\log\left(N'\right)\right)} \quad 3.28$$

Figure 3.13 shows the stability graph with the boundaries superimposed as determined from the unsupported case records. The lower boundary of the transition is compared with the Nickson (1992) support transition zone defined from the supported case records. Practically, there is no difference between the lower limit of the transition zone as determined from the unsupported case records, and that determined from the supported case histories.

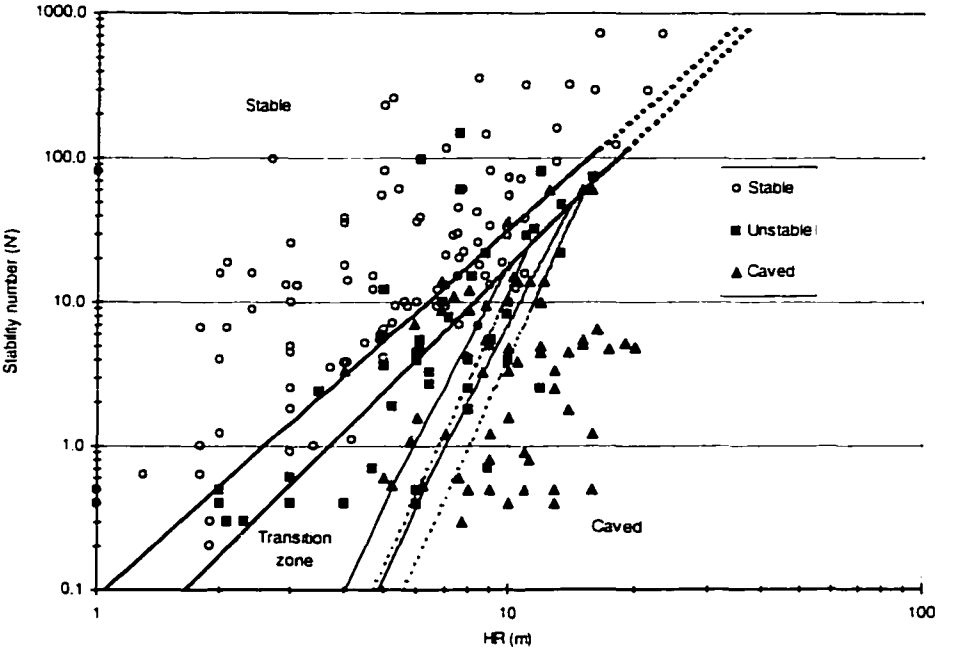


Figure 3.13 Stability graph boundaries using unsupported cases and defining the transition zone

The lower limit of the transition zone is the boundary between unstable and caved stopes. Because there is no difference between the boundaries for supportable stopes defined from supported stopes data, and that defined from unsupported case records, it implies that potentially caving stopes are assumed to be unsupportable.

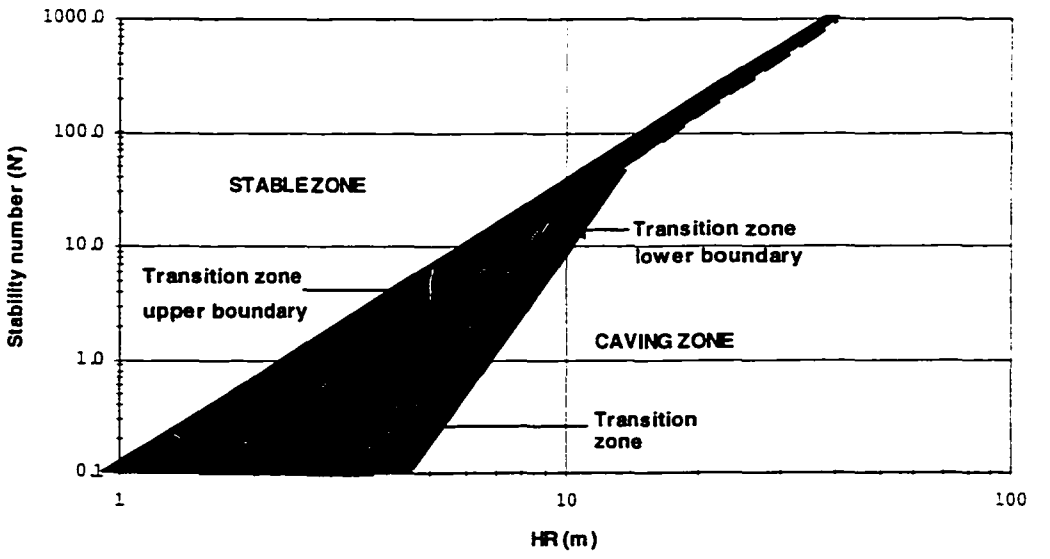


Figure 3.14 Re-defined stability graph boundaries and transition zone using only unsupported case records

Figure 3.14 shows the transition zone boundaries established using this technique, which are reproducible from the above equations.

There is only one transition zone containing unstable stopes defined by upper and lower boundaries between the stope performance classes. The boundaries are bands, stressing that there are no sharp borders between the stability states. The stability state of a stope that falls in the transition zone can not be determined, since it could be stable, unstable or caving. Stopes within the transition zone tend to be unstable, and stability is improved only when a stope is well supported. Therefore, it can be concluded that all stopes falling in this zone must be supported to improve stability. Supported stopes that fall in the transition zone and are unstable or cave during extraction are an indication of support ineffectiveness. Division of the database into supported and unsupported cases for the purpose of determining support limits is irrelevant.

The definition of the stability graph transition zone as determined above is unambiguous and recommended for assessment of the performance of open stopes.

3.5.4 Method 3: Multiple design curve stability graph

In Figure 3.11 and Figure 3.12 it is observed that as one moves from the caving zone through the transition zone to the stable zone, stability improves. It is also observed that the three zones are diffused. Designing a stope then means choosing an acceptable level of risk based on likelihood of failure. A stability graph with multiple design curves representing various levels of risk is an ideal alternative.

Equation 3.24 was derived by considering stable and failed (unstable plus caved) stopes and approximately represents the center of the upper boundary of the transition zone. This equation is convenient to use in developing the multiple design curve stability graph because it represents a 50% likelihood of failure and a 50% likelihood of stability. A stope falling on this line has a probability of failure of 50%. The equation is rewritten in the form:

$$2\,log\left(\frac{f_s(\mathbf{S})}{f_u(\mathbf{U})}\right) = 0.3738\,log(N') - log(HR) + 0.4905 \qquad 3.29$$

By re-arranging Equation 3.29, we have:

$$HR = 10^{(0.4905 - 2\,log(A) + 0.3738\,log(N'))} \qquad 3.30$$

For various values of the likelihood ratio, different levels of stability are defined in the stability graph. Such a graph is presented in Figure 3.15 for various likelihood ratios. The likelihood ratio increases from the caving zone to the stable zone indicating increasing likelihood of stability. The graph is a dynamic

design graph, in that the mining engineer can choose any stability level preferred according to the on-the-spot ground conditions.

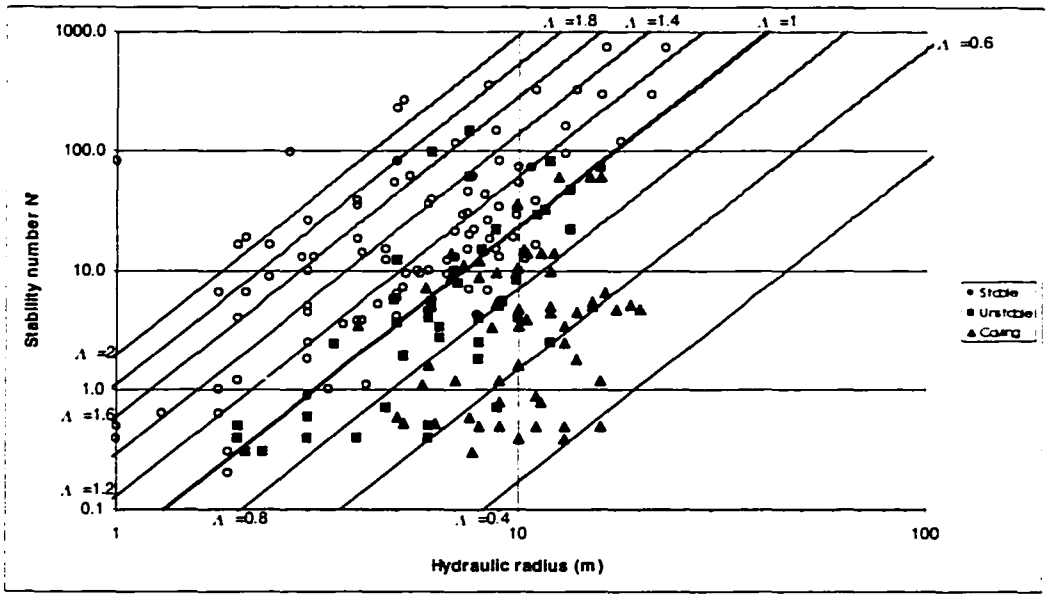


Figure 3.15 Likelihood-based stability graph

The graph assumes that **a priori** probabilities and misclassification cost are equal. The assumptions of equal misclassification cost and equal **a priori** probabilities are discussed in Section 3.6.

3.5.5 Theoretical Implications of the Stability Graph Regions

The stability graph regions were discussed in detail in this section with a re-definition of the transition zone to eliminate ambiguity. Equiprobability contours presented in Figure 3.11 and Figure 3.12, show overlap of the three stability states. Consequently, errors can be made in predicting the stability state of an open stope. Such an error carries with it a risk that could be costly.

A second source of error apart from overlapping is inequality in **a priori** probabilities of the various stability states. This means that there may be more cases of stability in the database compared with instability. In such a case the classification rule is biased towards the most frequently occurring event, and can result in wrong predictions. Inequality of **a priori** probabilities of the data groups should be corrected to prevent bias towards the most frequently occurring stability condition observed in the database. The next section discusses the reliability of the transition zone boundaries for accurate predictions, as defined by the classification rule used.

3.6 Accounting for Misclassification Errors and Risk Cost

3.6.1 Performance prediction errors in the stability graph

The equiprobability contours in Section 3.5.2 show that there are overlaps of the three regions defined in the stability graph. Consequently, there is a tendency to err in decision making or design. This section discusses methods of minimizing misclassification errors by optimizing the dividing boundaries between stability states.

How frequently can a mining engineer wrongly predict the stability of an open stope by using a stability graph as a design tool? The answer to this question is important to the user of the stability graph.

Users of the stability graph should be aware that it is not fool proof because the failed and stable cases are not independent since the data groups overlap. Unequal costs in events associated with errors from misclassifications should be accounted for in the classification procedures, as well as for the unequal numbers of case records in the data sub-groups.

The confusion matrix given in Table 3.3 is used to determine the error frequency in the stability graph based on the calibration database and the classification rule used in Figure 3.15 as an example for a likelihood ratio Λ=1. In this case, the stability graph is divided into stable and failed stopes only using Equation 3. 30.

Table 3.3 Confusion matrix for determination of classification rule performance

		Predicted membership		
		Stable	Unstable	Total number of cases
Actual Membership	Stable	n_{sc} = 88	n_{sm} = 12	n_s = 100
	Unstable	n_{um} = 19	n_{uc} = 82	n_u = 101

where

n_{sc} = Number within stable zone items correctly classified as stable,

n_{sm} = Number within stable zone items misclassified as unstable,

n_{uc} = Number within unstable zone items correctly classified as unstable,

n_{um} = Number within unstable zone items misclassified as stable,

n_s = Number of stable cases,

n_u = Number of unstable cases, and

$n_t = n_s + n_u$

Numbers in the confusion matrix correspond to numbers from the stability graph using the calibration database, and Equation 3. 30 as the classification criterion.

The **a priori** probabilities for stable *P(S)* and unstable *P(U)* states are determined from the confusion matrix as:

$$P(S) = \frac{n_S}{n_t} \qquad 3.31$$

$$P(U) = \frac{n_U}{n_t}$$

P(stable) = 0.498 (i.e., 100/201)

P(unstable) = 0.502 (i.e., 101/201)

The conditional probabilities are determined from the confusion matrix as follows:

P(Stable|unstable) = 12% (i.e., 12/100)

P(Unstable|stable) = 19% (i.e., 19/101)

By coincidence, the prior probabilities of stable and unstable stopes are approximately equal. Because of overlap or group diffusion, the error rate in using Figure 3.15 is given by the apparent error rate *APER* as:

APER = 15% (i.e. (19 +12)/201)

There is an error rate of 15% associated with Figure 3.15 if the classification rule defined by Equation 3.24 is used as classification criterion. This implies that 15% of stopes designed using this classification rule are likely to be incorrect predictions.

The transition zone boundaries should be optimized to the advantage of a given mine based on its local experience. Optimization accounts for two factors:

- Inequality in costs of misclassifying a stable stope as unstable or an unstable stable stope as stable, and
- Inequality in the frequency of occurrence of the events in the database.

Each factor can be accounted for separately to optimize the design curve. Complete optimization is achieved when both effects are accounted for in the design curve.

The efficiency of classification rules can be assessed or compared on the basis of their error rates. A good classification system should result in few misclassification errors. Sources of error in a classification include unequal numbers of data in the data groups, and unequal costs in erring on one either data group. These errors should be corrected in the classification rule. These corrections require knowledge of the misclassification probabilities.

True misclassification probabilities require the normal density functions of the population that are difficult to define. A more pragmatic approach is to use a confusion matrix (Johnson and Wichern, 1992) based on the applied classification criterion.

For misclassifying an unstable stope as stable, we have:

$$P(Stable|unstable) = \frac{n_{um}}{n_u} \tag{3.32}$$

Similarly, the probability of misclassifying a stable stope as unstable is given by:

$$P(Unstable|stable) = \frac{n_{sm}}{n_s} \tag{3.33}$$

These probabilities can be estimated from a confusion matrix (Table 3.3).

The efficiency of the classification rule is defined as the apparent error rate *APER*:

$$APER = \left(\frac{n_{sm} + n_{um}}{n_s + n_u}\right)100\% \tag{3.34}$$

The smaller the apparent errors rate *APER*, the better the classification system. Therefore, the strength of the stability graph depends on how well the dividing boundaries are defined.

Misclassifying the stability state of a stope could be costly to a mine. As a result of the misclassification, support, dilution, and available ore, will all be miss-judged. Accounting for misclassification cost in the stability graph is discussed in Section 3.6.2.

3.6.2 Misclassification Risk Cost

Inherent in most empirical and analytical statistical methods of classification is the assumption that the seriousness of erring on either side of the dividing boundary between the data groups is the same. Are the consequences of predicting an unstable stope as stable and that of predicting a stable stope as unstable the same? The answer to this question may be mine dependent because of the cost difference in mining practices. However, engineering principles require that we err on the side of stability rather than failure. An adjustment to the dividing boundary is suggested to account for misclassification risk cost or relative seriousness in erring. Cost in this sense can be in any units and absolute cost is unnecessary. It is the ratio of the two costs that is important. This simplifies the situation in a mining environment since absolute cost is often difficult to determine.

The cost of misclassification is defined by a misclassification cost matrix as follows:

Table 3.4 Misclassification cost matrix

True population	Classify as stable zone	Classify as unstable zone
Stable	0	c*(unstable|stable)
Unstable	c*(stable|unstable)	0

* cost

The expected cost of misclassification *ECM* (Equation 3.35) is given by the product of the off-diagonal entries of the cost matrix (Table 3.4) and their respective probabilities of occurrence in Equations 3.32 and 3.33.

$$ECM = c(unstable|stable)P(unstable|stable)P(S) + c(stable|unstable)P(stable|unstable)P(U) \qquad 3.35$$

This is the total cost for misclassification. Each term on the right represents the specific cost for unstable and stable stopes when they are misclassified.

The discussion up to this point shows that there is risk in using any classification system, particularly in cases where the data groups overlap.

A procedure for optimizing the transition zone to account for cumulative misclassification risk cost (unequal **a priori** probabilities and unequal cost in misclassification) is discussed in Section 3.6.2.

Risk is defined as the product of the probability of occurrence of an unwanted event and the consequences or cost due to the event occurring. This is expressed as:

$$Risk = (probability\ of\ failure)(consequence) \qquad 3.36$$

In the context of this study probability of failure is the probability of misclassification in the sense of the stability graph data. Misclassification is the undesirable event and the cost associated with misclassification is the consequence. Risk in this sense is defined as:

$$Risk = (misclassification\ probability)(misclassification\ cost) \qquad 3.37$$

A relative risk cost ratio is introduced and defined as ξ:

$$\xi = \frac{Risk\ of\ misclassifying\ stable\ stopes\ as\ unstable}{Risk\ of\ misclassifying\ unstable\ stope\ as\ stable} \qquad 3.38$$

Equation 3.38 translates into Equation 3.39 as follows:

$$\xi = \frac{c(unstable|stable)P(unstable|stable)P(stable)}{c(stable|unstable)P(stable|unstable)P(unstable)} \qquad 3.39$$

The cost ratio term ξ_r (Equation 3.40) is:

$$\xi_r = \frac{C(unstable|stable)}{C(stable|unstable)} \tag{3.40}$$

Equation 3.40 is more mine specific. A rough idea of the ratio of the relative costs is sufficient to compute ξ_r.

The optimized discrimination function accounting for unequal **a priori** probabilities and unequal misclassification cost is obtained from Equation 3.41.

$$ln(\Lambda) + ln(\xi) = \mathbf{X}^T\mathbf{S}^{-1}\mathbf{d} - \frac{1}{2}\left(\overline{\mathbf{X}}_\mathbf{u}^T\mathbf{S}^{-1}\overline{\mathbf{X}}_\mathbf{u} - \overline{\mathbf{X}}_\mathbf{s}^T\mathbf{S}^{-1}\overline{\mathbf{X}}_\mathbf{s}\right) \tag{3.41}$$

Introduction of the risk factor will shift the transition zone above or below its original position depending on the risk factor acceptable to the mine. Application of this concept is given in Chapter 6 Figure 6.41.

3.7 Summary

The interpretation of empirical data based purely on experience and engineering judgment introduces human bias, and does not allow reproduction of results. Application of statistical tools minimizes the human factor.

Statistical tools were presented and tested with the expanded Potvin's (1988) database. The likelihood ratio method is found to be an excellent tool for use in interpreting the stability graph. Results of the application of the statistical tools are presented in graphs (Figure 3.13, Figure 3.14, and Figure 3.15) defining the transition zone, and as an alternative plot to the stability graph, based on acceptable risk.

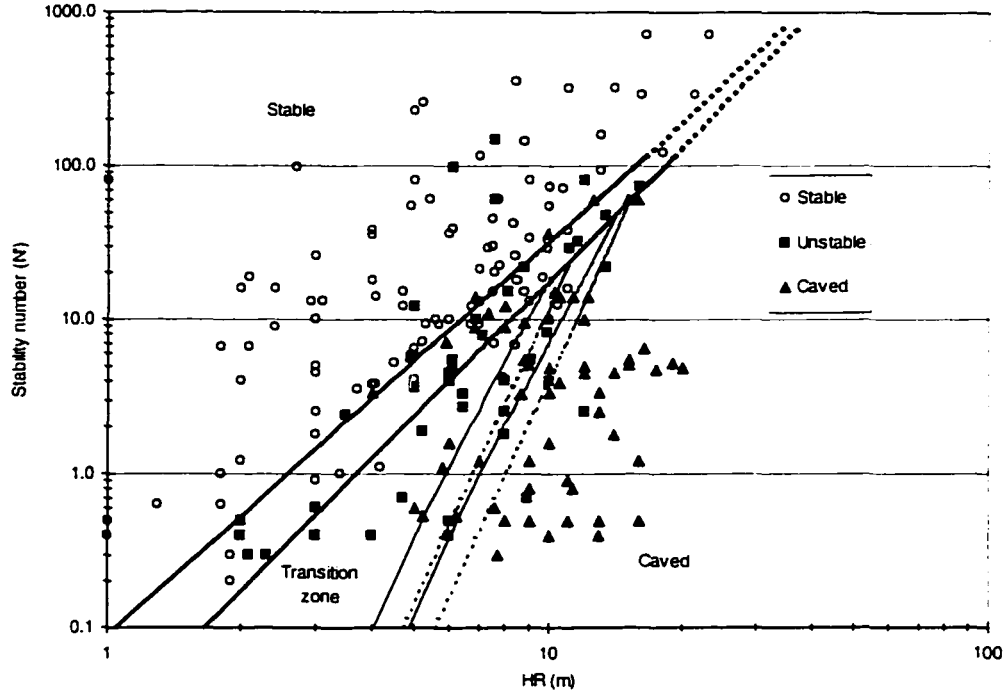


Figure 3.13 Stability graph boundaries using unsupported cases

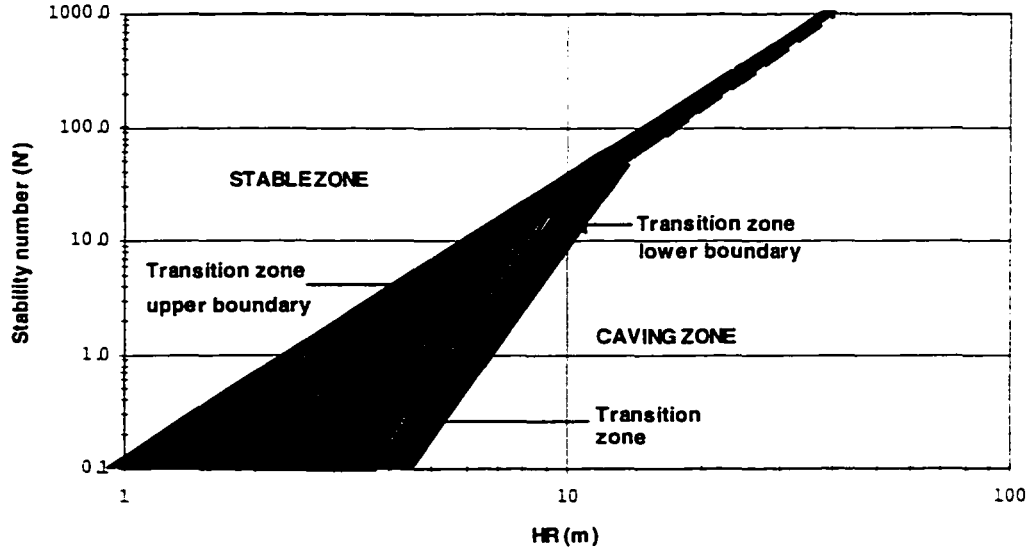


Figure 3.14 Re-defined stability graph boundaries and transition zone using only unsupported case records

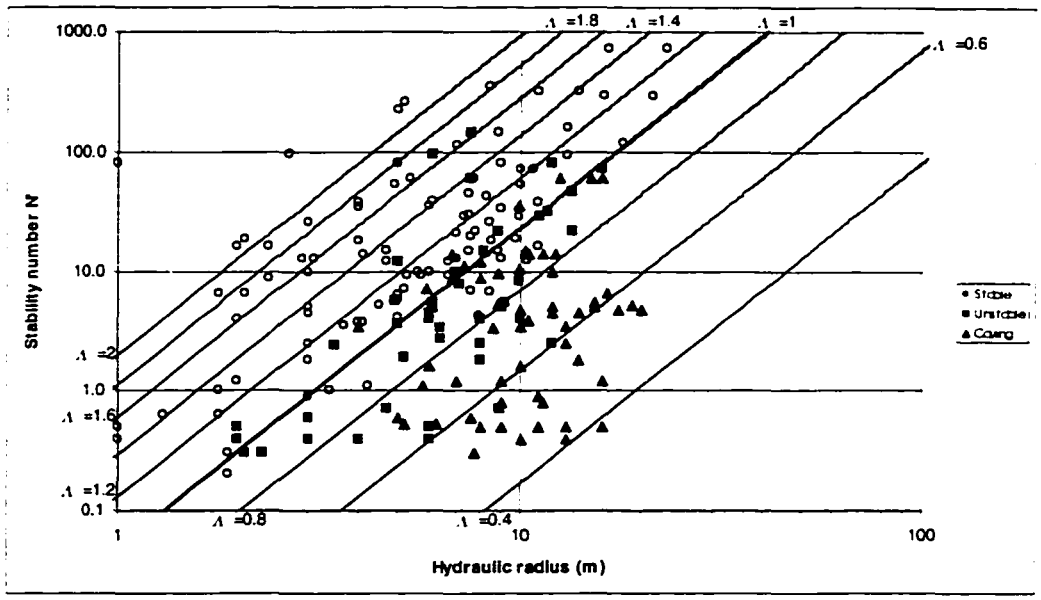


Figure 3.15 Likelihood-based stability graph

The transition zone of the stability graph is defined using equiprobability contours and the likelihood method of multivariate discriminant analysis. There is only one transition zone that is characterized by unstable stopes, even though stopes of the stable and caving classes are also present. The transition zone is defined by upper and lower boundaries, which are bands emphasizing that there are no clear borders between the stability classes. An upper and a lower limit that is statistically fitted to the data define each band, of the transition zone boundaries.

The lower boundary of the transition zone is the limit of the supportable stope surfaces, and is definable from the unsupported case records using the statistical procedures presented within the zone. A failed or unstable supported stope in the transition zone is a measure of support ineffectiveness or practice.

Because the zones of the stability graph are not absolute, users of the stability graph must be informed of the inherent error a stability graph can give. Statistical tools are provided for calculating possible misclassification errors in the stability graph. Methods are also provided for assessing the misclassification costs that are likely to be incurred as a result of misclassification or wrong prediction of stope performance.

The stability graph can be specifically optimized to account for risk cost arising from misclassification of stope performance due to inequality of misclassification cost of events and inequality of **a priori** probabilities.

A dynamic design stability graph is introduced with multiple design curves for various levels of risk. This graph has an advantage over the current stability graph in that it allows the mining engineer to select a curve that fits local decisions. On-the-spot design can be made with the graph. The multiple design curve stability graph implicitly allows optimization by moving below or above the 1:1 likelihood of failure curve

according to expected mining conditions. The graph is also advantageous where mines have not yet built their own databases (e.g., new mines).

The stability graph boundaries established with the calibration database would be applied and verified by the case histories from Kidd Mine in Canada, and Ashanti Goldfields in Ghana. The statistical tools for estimating misclassification errors support efficiency and data separability will all be employed in interpreting the stability graphs for Kidd and Ashanti. In particular, the data separability index will be used as a means of assessing the amount of improvement on data zoning in the stability graphs for the two mines by introduction of the fault factor and soft zone corrections.

CHAPTER 4

RELAXATION SLOUGHAGE

4.1 Introduction

Stress is recognized as one of the principal factors responsible for the instability of underground excavations in rock. Two aspects of stress that are detrimental to the stability of underground excavations are high compression stresses and low or tensile stresses. Between the two extremes, stress may be beneficial to the stability of underground excavations.

Review of the databases developed for the calibration of the empirical design methods show that instability of most underground excavations is due to lack of stress rather than too much of it. About 70% of the stope surfaces in the calibration database existed in conditions of stress relaxation. Therefore, this chapter focuses on relaxation as a cause of stope wall sloughage.

The chapter gives a definition of relaxation, identifies the causes of relaxation, and uses limit equilibrium analysis to determine critical relaxation stresses below which stope wall sloughage may possibly occur.

4.2 Definition and Causes of Relaxation

The following definition of relaxation is taken from Kaiser et al. (1997). The definition supports the notion that relaxation should deal with stresses tangential to excavation walls rather than those normal or radial to excavation walls. Mathews et al. (1980) noted that it is stresses parallel to open stope walls that control their stability.

Rockmass relaxation is defined as that stress state where the stresses in the tangential direction to the excavation wall are reduced in the rockmass, often to values far below those predicted by linear elastic models, because the rockmass has been allowed to deform some degree. Rockmass relaxation therefore refers mostly to stress reduction parallel to the excavation wall and not to stress reductions in the radial direction or a reduction in confinement.

In the principal stress space, relaxation is therefore reflected in a stress path that points downwards or toward the origin (Figure 4.1). In each graph of Figure 4.1, we have three branches of stress paths from a common virgin stress state. The two lowest curve in each 3-branch stress path shows relaxation, while the other two indicates steady or increasing compression in the tangential direction. In all cases, instability sets in when the stress path crosses the failure criterion determined for the rockmass. Instability occurs when the rockmass has reached a critical relaxation threshold at which gravity-driven failure modes or slip along weakness planes is encountered. Consequently full relaxation, causing zero or even tensile stress conditions, is not required to cause relaxation induced failure.

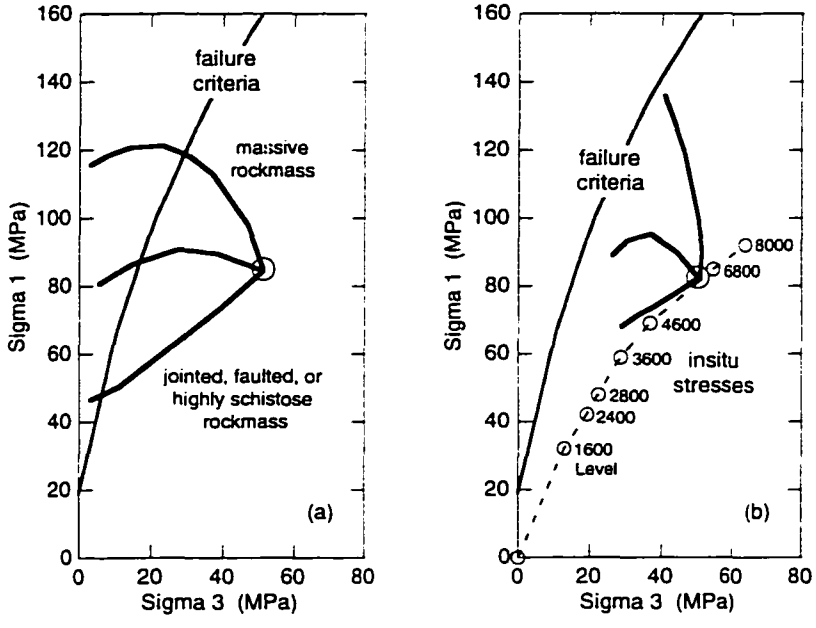


Figure 4.1 Generic examples of stress paths that a) lead to stope wall failure and b) cause no major stability problems (after Tannant et al., 1997)

In practice conditions that lead to relaxation are encountered in the following situations:

- Undercutting of hangingwalls (e.g., intentionally or caving),
- Mining of adjacent stopes (secondary and tertiary stopes fall in this category),
- Crushing of weak rock formations, and
- Slippage along faults, and relaxation of stope backs when mining parallel veins.

When single openings are advanced as is the case in civil engineering practice, stress arching normally occurs in the direction of the shortest span (Terzaghi, 1946) and if the arch is stable, the excavation can remain unsupported. However, if the abutments of the arch are allowed to move away from the excavation by deformation, the stresses relax and instability may occur. At intersections, due to the geometry of the excavation, lateral deformations are permitted to occur in the direction of preferred arch formation and this leads to rockmass relaxation rather than arching in the back of intersections. It is for this reason that intersections are less stable than single openings of similar size (Kaiser et al., 1997). In the case of stope design, relaxation may also result from disturbance of the stress field by adjacent mining activities.

The influences of the items listed above are to increase the zone of relaxation compared to the excavation without the influence of these effects. Various excavation geometries that often lead to relaxation are shown in Figure 4.2.

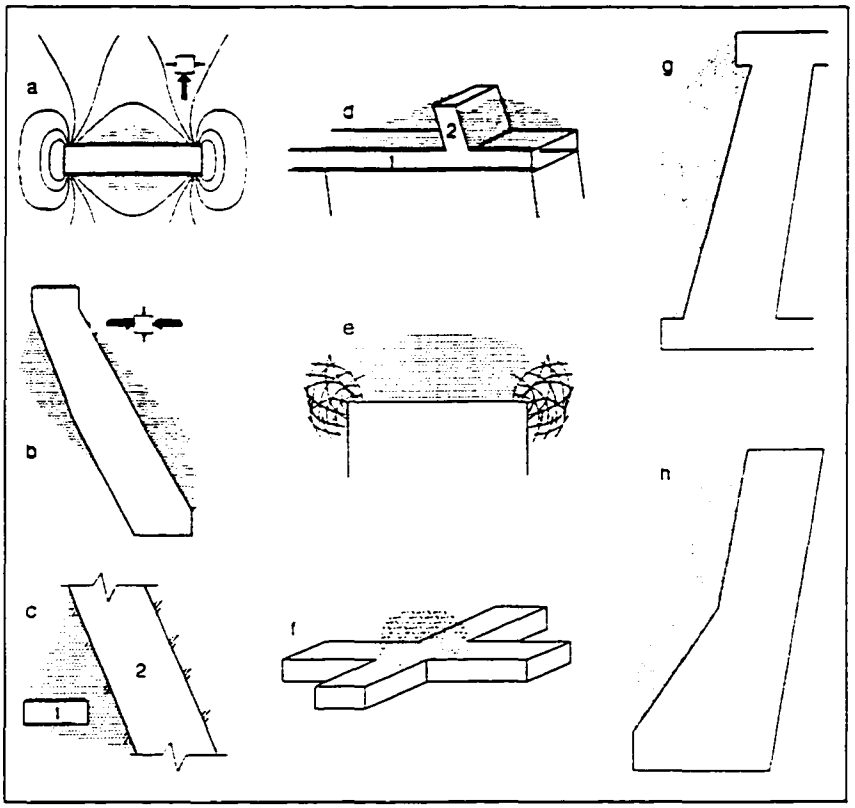


Figure 4.2 Excavation geometries and stress ratios that enhance relaxation: (a) & (b) Unfavourable stress ratio; (c) & (d) Changes in mining geometry - excavation step 2 creates stress shadow around excavation 1; (e) Abutment yield; (f) Intersection - relaxed roof; (g) Undercut; and (h) Concave structure (after Diederichs and Kaiser, 1998)

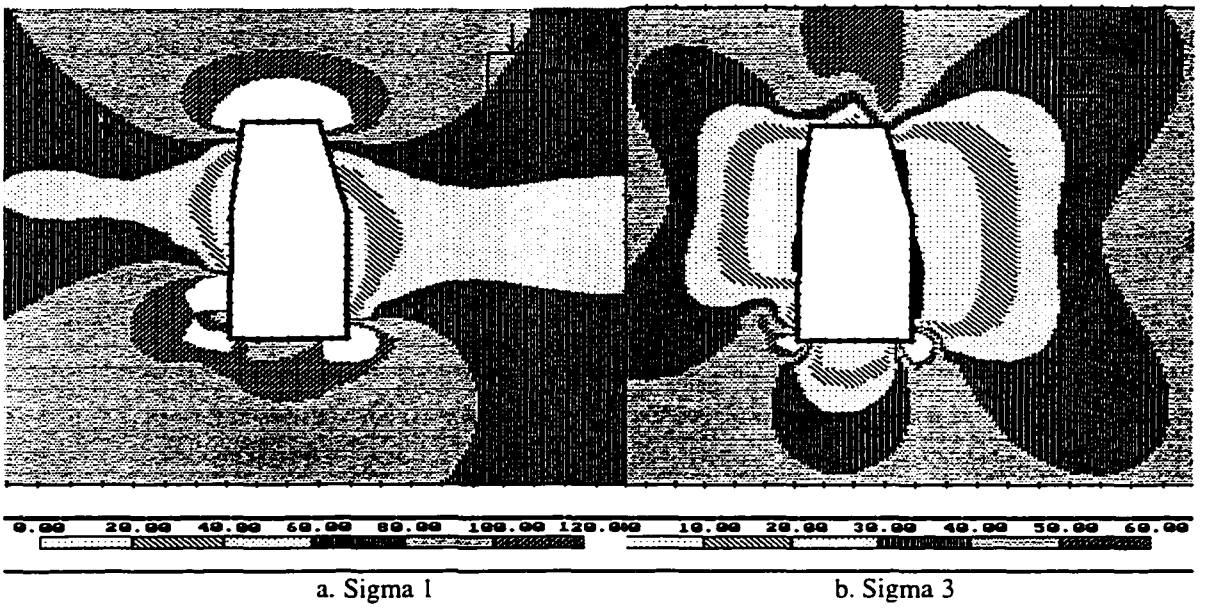
In open stope mining, undercutting is unavoidable but should be minimized to avoid overhanging rock. Apart from some cases of primary stopes, almost all stopes are undercut to some extent because of the bottom-up mining sequence often adopted in open stope mining. Hangingwalls are also undercut when vertical variations in orebody dip or thickness or both occur. In order to define orebody boundaries,

geologist often request drifting into the host rock to some extent to determine the pay zone. Consequently, hangingwalls are often undercut by stope development crosscuts. Also, cablebolt support requirements often result in undercutting of hangingwalls. The effect of undercutting is to increase the de-stressed zone and therefore increase the probability of slough into the excavation.

The influence of undercutting depends on the size and orientation of the excavation. An undercut generated across a full stope width by an underlying stope is worse than a crosscut driven parallel to the stope hangingwall which is worst than a drift that punches through vertically into a hangingwall.

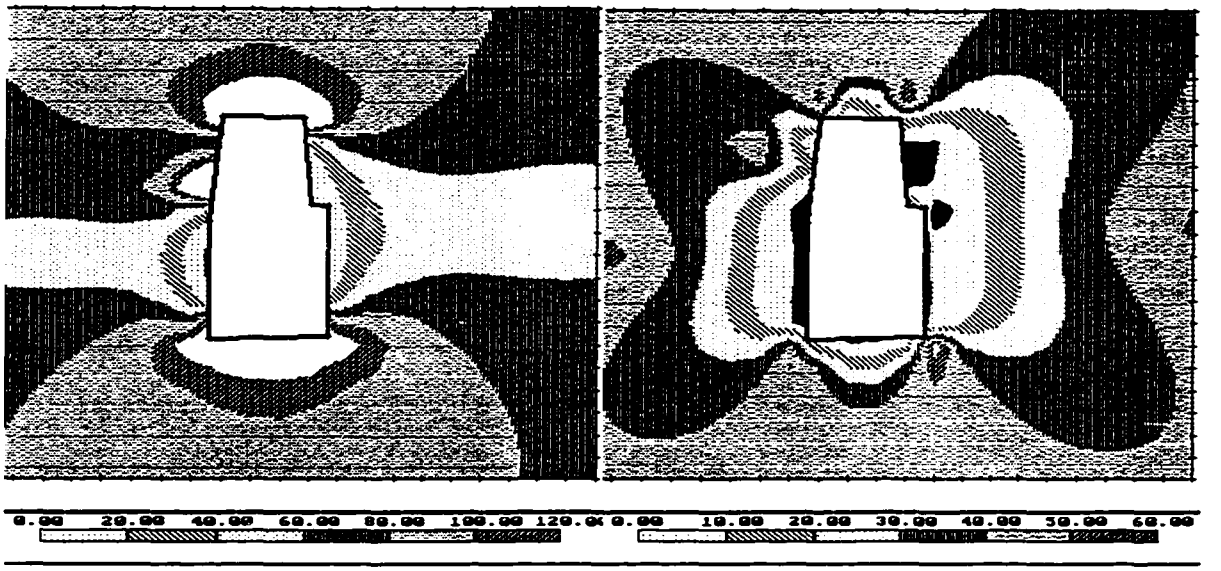
Numerical modelling indicates the difference between cases where a stope hangingwall is not undercut (Figure 4.3) but undercut in the other (Figure 4.4). Comparison of the stress distributions in the two figures shows an increase in the de-stressed zone in Figure 4.4, and consequently gives it a higher potential for sloughage.

Undercutting results in failures that otherwise would generally be preventable. Undercutting causes stress relief by deformation of the rockmass, often used to induce caving of competent rockmasses.



a. Sigma 1 b. Sigma 3

Figure 4.3 Stress distribution around stope with no obvious undercut. Solid black pattern indicates tension in the model



a. Sigma 1 b. Sigma 3

Figure 4.4 Effect of undercutting on stress distributions due to vertical orebody thickness variation. Solid black pattern indicates tension in the model

Faults and shear zones near stopes also affect stresses near such stopes. Faults often result in low stress zones (Hafner, 1951; Anderson, 1942) near stopes, and therefore have a tendency to increase the zone of low stresses when they are close to or intersect excavations. Faults and shear zones have three effects on stability of mine openings. They lead to larger volumes of failure than would otherwise occur due to joints alone. Also, their presence may result in changes in stress direction, with stresses tending to align parallel to the geologic structure. They also increase the number of degrees of freedom for wedge movement.

The effects of faults and shear zones on underground opening stability are the primary focus of this thesis and are further discussed in Chapter 5.

4.3 Limit Equilibrium Wedge Analysis

Gravity is an important factor in unravelling due to relaxation. This section demonstrates the dependency of wedge stability on clamping stress and uses limit equilibrium wedge analysis to determine a critical relaxation stress below which gravity may cause sloughage.

Even though the discussion in the following sections are limited to single blocks, it is assumed that a single block that is a keyblock (Goodman and Shi, 1985), when removed, could trigger more extensive stope surface sloughage. Falls of large volumes of single wedges are by themselves also important. Figure 4.5 shows a link between various failure situations in blocky rockmasses.

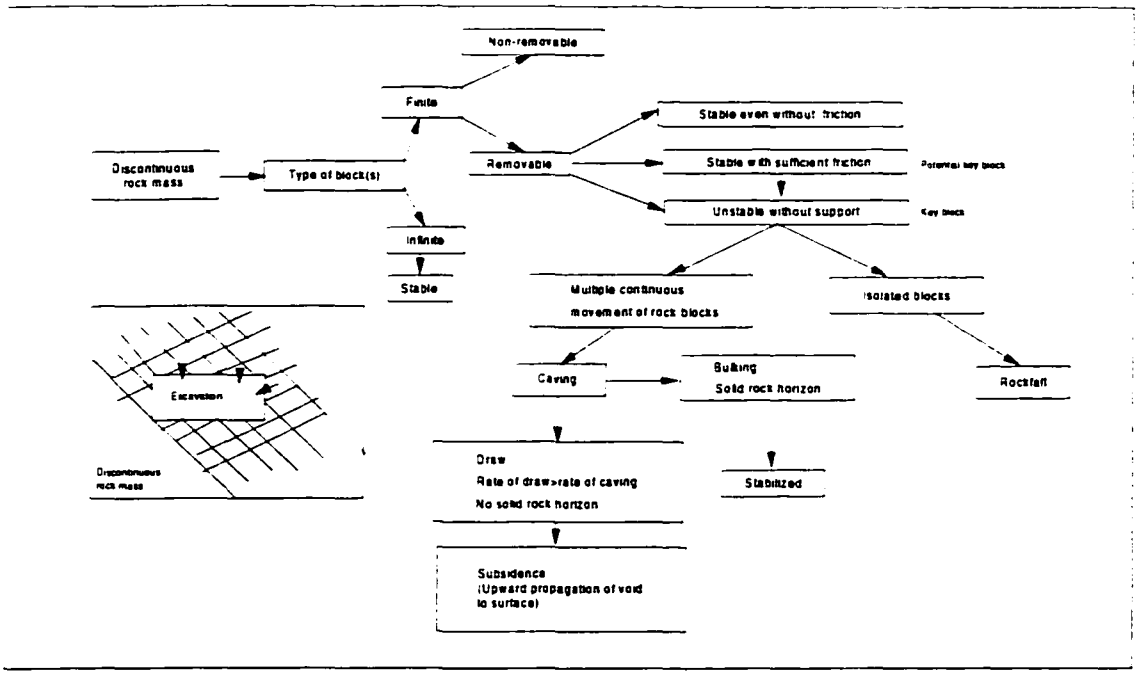


Figure 4.5 Possible failure modes in a blocky rockmass, related to mining activities

Limit equilibrium analysis was conducted using three wedge types:

- Rhombohedral,
- Rectangular, and
- Triangular (symmetrical about the vertical).

A critical clamping stress is defined as the stress for which the factor of safety is unity. The critical stresses are determined for each block using this criterion.

Joint spacing and joint dips are used in the analysis because these are the parameters usually measured in the field. The joint spacing also determines the block size (Laubscher, 1990).

Friction angles for the discontinuities in the models are taken between 15° and 30° to represent situations particularly prone to relaxation-related ground falls. The Mohr-Coulomb failure criterion is used as a slip criterion with cohesion assumed to be zero in all cases.

4.3.1.1 Rhombohedral prism

Figure 4.2 presents the geometry of a rhombohedral prism and the stresses acting on it to maintain equilibrium.

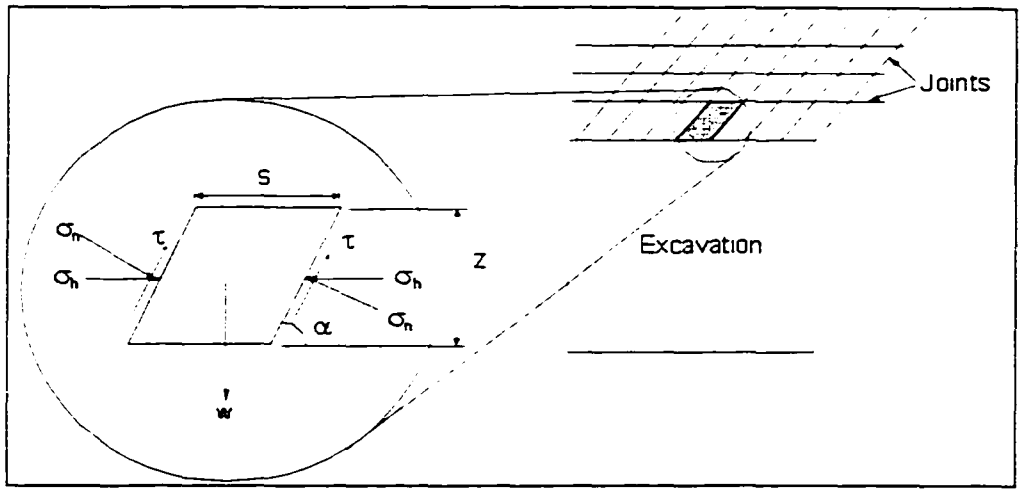


Figure 4.6 Rhombohedral prism in a stope back

The factor of safety of the prism in the given stress state is given by:

$$FS = \frac{(2\sigma_h - s\rho\cos\alpha)\tan\phi}{s\gamma\sin\alpha} \qquad 4.1$$

The rock density is ρ. Equation 4.1 shows that the stability of the wedge is largely controlled by the clamping stress σ_h. Therefore, any mining practices that would result in reduction of the clamping stress would lower the factor of safety and result in ground falls. The wedge falls when σ_h diminishes to some critical value. Assuming a rock unit weight of 0.027MN/m^3, and typical joint friction angles of 15° and 30°, critical clamping stresses for the wedge at 20° and 70° joint dip angles are plotted in Figure 4.7 and Figure 4.8.

Figure 4.7 and Figure 4.8 show that the wedge at a given clamping stress is more stable at low dip angles compared to high dip angles. At low dip angles there is increased normal stress and therefore increased resistance to shear failure compared to dips at high angles. At a dip of 90° Equation 4.1 simplifies to Equation 4.2. This results in a simplified model of the rhombohedral wedge called the "book analogy" (Figure 4.9). Stability also improves with increasing joint friction. By this model, the bigger the wedge the more clamping stress is required to retain stability. A normal stress in the order of $\sigma_n \geq 0.05$ MPa is sufficient to cause instability for the conditions described.

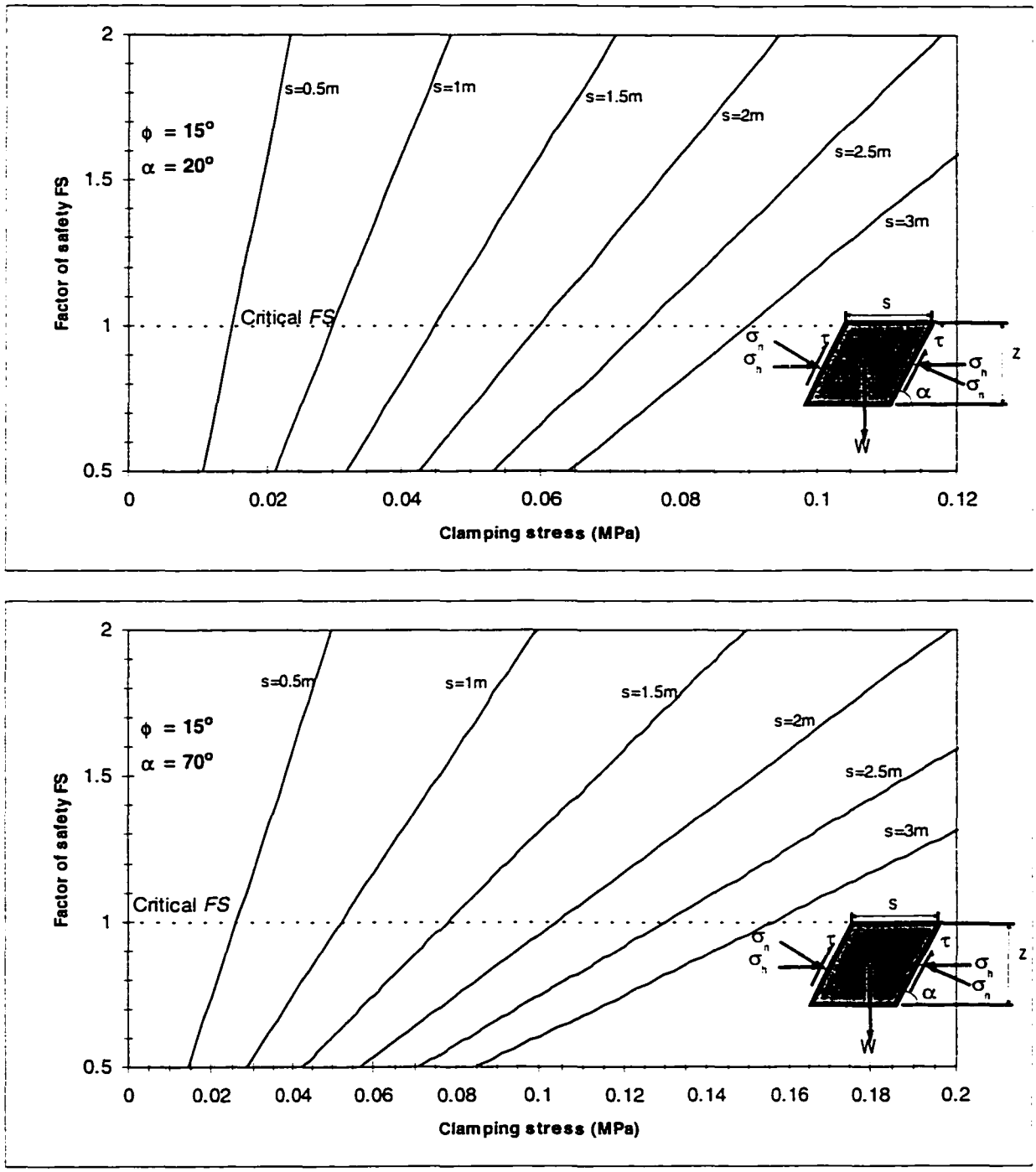
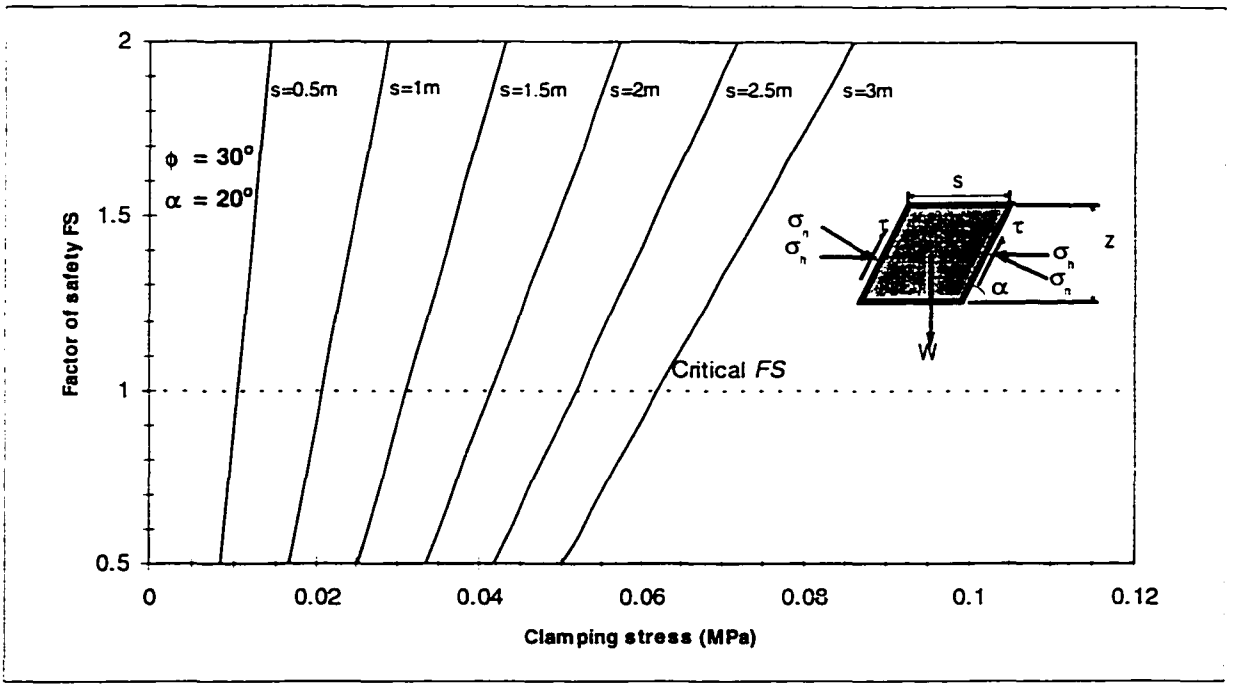


Figure 4.7 Plot of factor of safety versus dip of joint for Rhombohedral prism: Joint friction is 15°



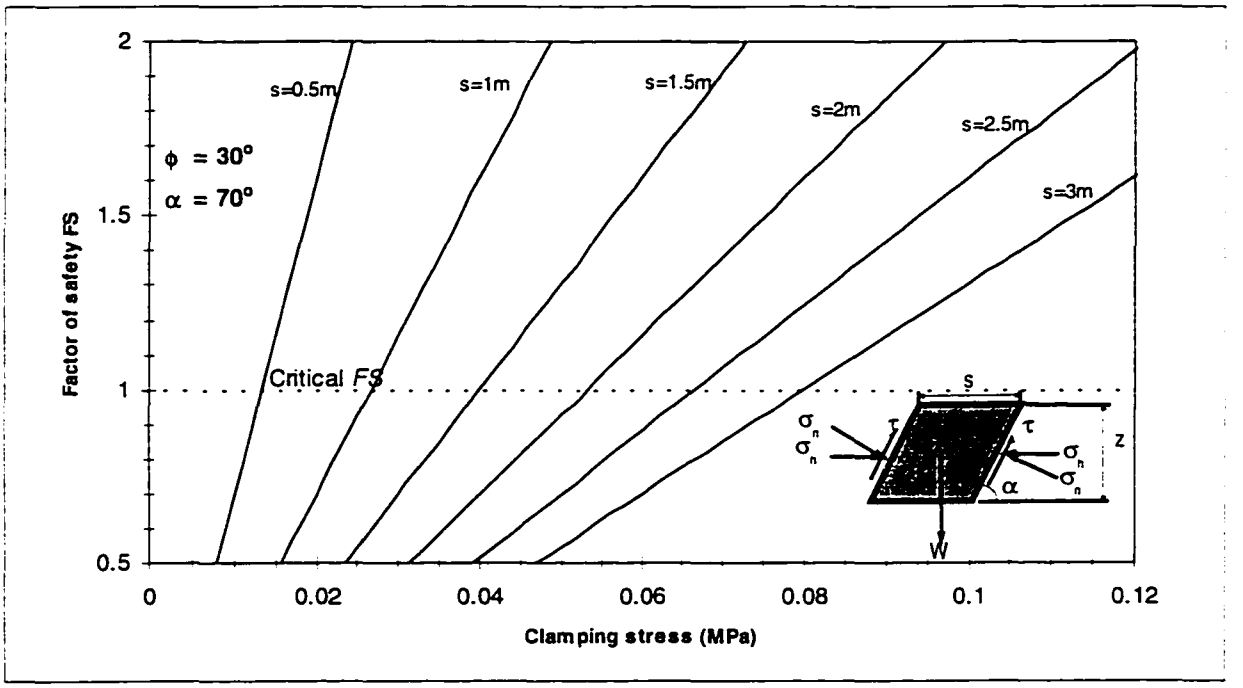


Figure 4.8 Plot of factor of safety versus dip of joint 70°, for Rhombohedral prism: Joint friction is 30°

Figure 4.9 is a rectangular parallelepiped in a relaxed excavation back. The following assumptions are made in the analysis:

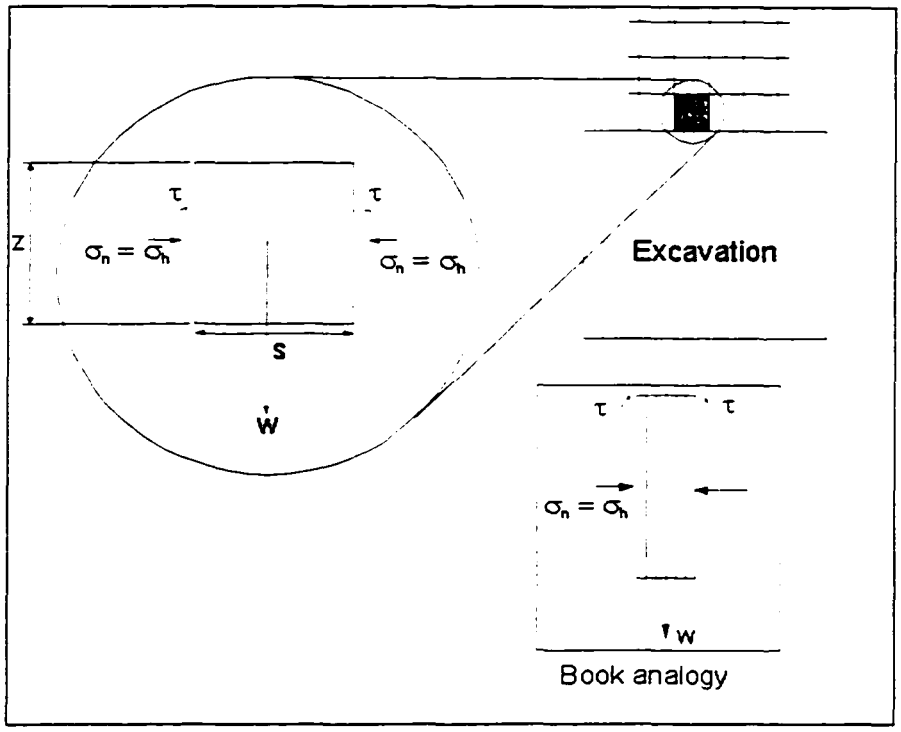


Figure 4.9 The Book analogy for determination of critical clamping stress for a parallelepiped shaped block

- Two joint sets are assumed which together with the excavation surface form the block
- Unit weight of the rock is $\gamma = 0.027$ MN/m^3
- Unit thickness of the block is considered
- An angle of internal friction ϕ of 15° and 30° is assumed for joints,
- No cohesion on joint surfaces

z and s are the height and width of block in metres, respectively.

The factor of safety is given by Equation 4.2 for z = s.

$$FS = \frac{2\sigma_h \tan\phi}{\gamma s} \qquad 4.2$$

Again, Equation 4.2 implies that at least some stress is required to maintain stability of the books or vertical rectangular parallelepiped. Also, as with the rhombohedral prism, the model shows that larger wedges are less stable than smaller ones.

For a given angle of friction and range of clamping stress, the critical clamping stresses for a given block size is determined. Figure 4.10 shows a plot of factor of safety against clamping stress, for various block sizes for assumed friction angles.

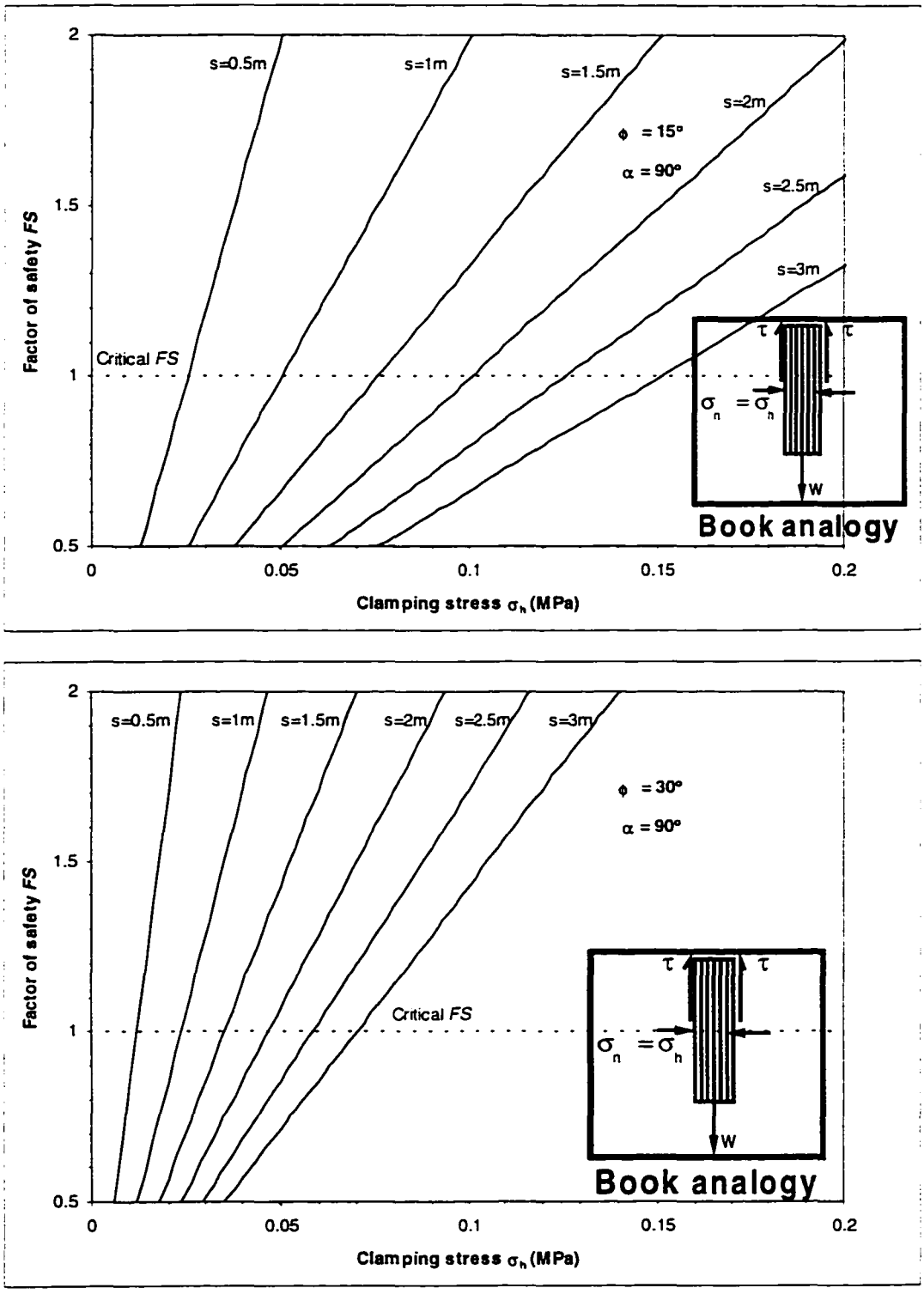


Figure 4.10 Factor of safety versus clamping stress for various block sizes (Book analogy - α=90° for rhombohedral case) and joint friction angles of 15° and 30°

For this model, clamping stresses on the order of $\sigma_n \geq 0.1$ MPa lead to stable conditions for the assumed parameters.

4.3.2 Triangular prism - equilateral or isosceles

Brady and Brown (1993) have discussed the stability of triangular prisms in underground excavations with respect to support.

In this analysis the objective is to determine the critical stresses at which the wedges become unstable. Figure 4.11 is a representation of a long triangular prism in the back of an excavation for which the bounding planes dip at equal and opposite angles, creating a symmetric wedge apex.

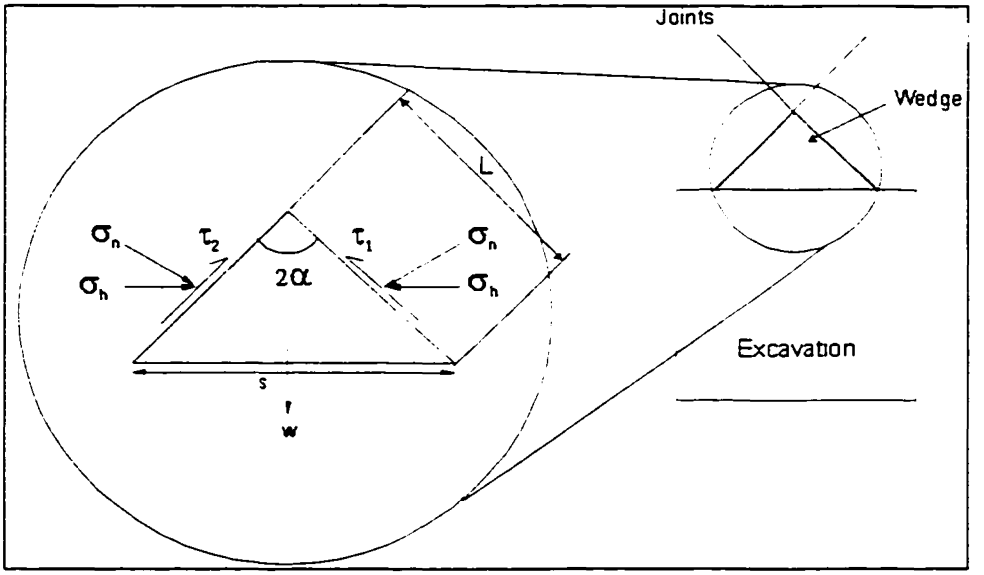


Figure 4.11 Representation of triangular prism in back of excavation

where

α = Semi apex angle,

σ_n= Normal stress on joint surface,

$\tau_1 = \tau_2 = \tau$= Shear stresses on joint surfaces,

σ_h = Horizontal clamping stress at relaxation,

W = Weight of prism,

l = Side length of prism, and

s = Joint spacing as observed on excavation boundary.

The following equation is given by Brady and Brown (1993) for the wedge to be in static equilibrium in the vertical direction:

$$R = 2l\sigma_n \tan(\phi - \alpha) \qquad 4.3$$

Where R is the resisting force to gravity induced ground fall. The factor of safety of the prism is given by:

$$FS = \frac{4\sigma_h \tan(\phi - \alpha)}{\rho s \cos(90 - \alpha)\tan(90 - \alpha)} \qquad 4.4$$

$$FS = \frac{4\sigma_h \tan(\phi - \alpha)}{\rho s \sin(90 - \alpha)}$$

Once again, the stability of the triangular prism depends on the clamping stress. A clamping stress $\sigma_h \leq 0$ implies instability of the wedge independent of any other factor except when the wedge is supported. For various apex angles 20° and 28°, joint spacing as a measure of block size, factors of safety are determined at various stages of relaxation for assumed joint friction angles of 15° and 30°. Figure 4.12 and Figure 4.13 are graphs of factors of safety against clamping stress for the assumed joint friction angles of 15° and 30°.

When critical clamping stresses are approached during mining, support should installed to prevent wall sloughage or the resulting dilution should be considered acceptable.

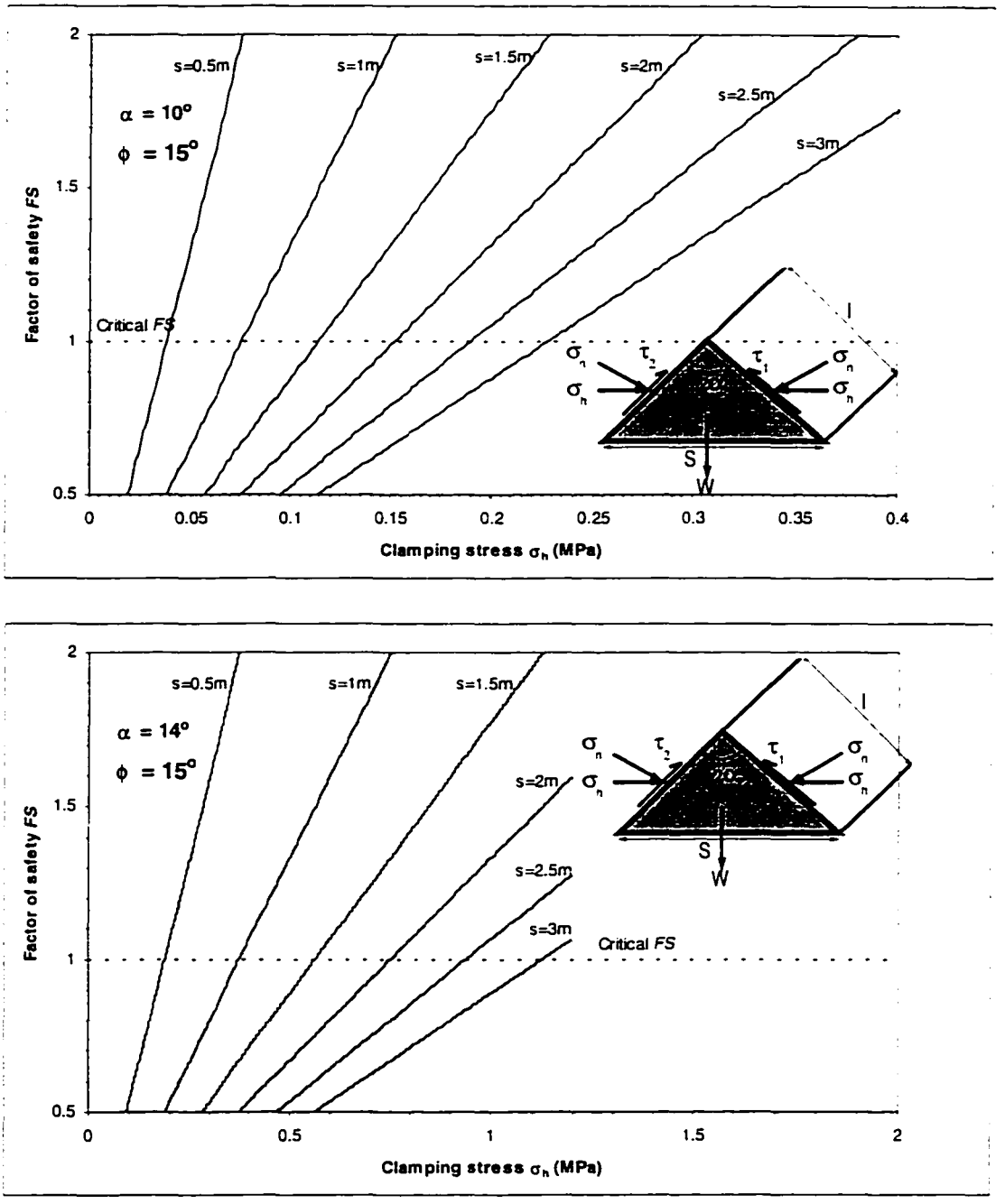


Figure 4.12 Triangular prism critical stress for a joint friction angle of 15°

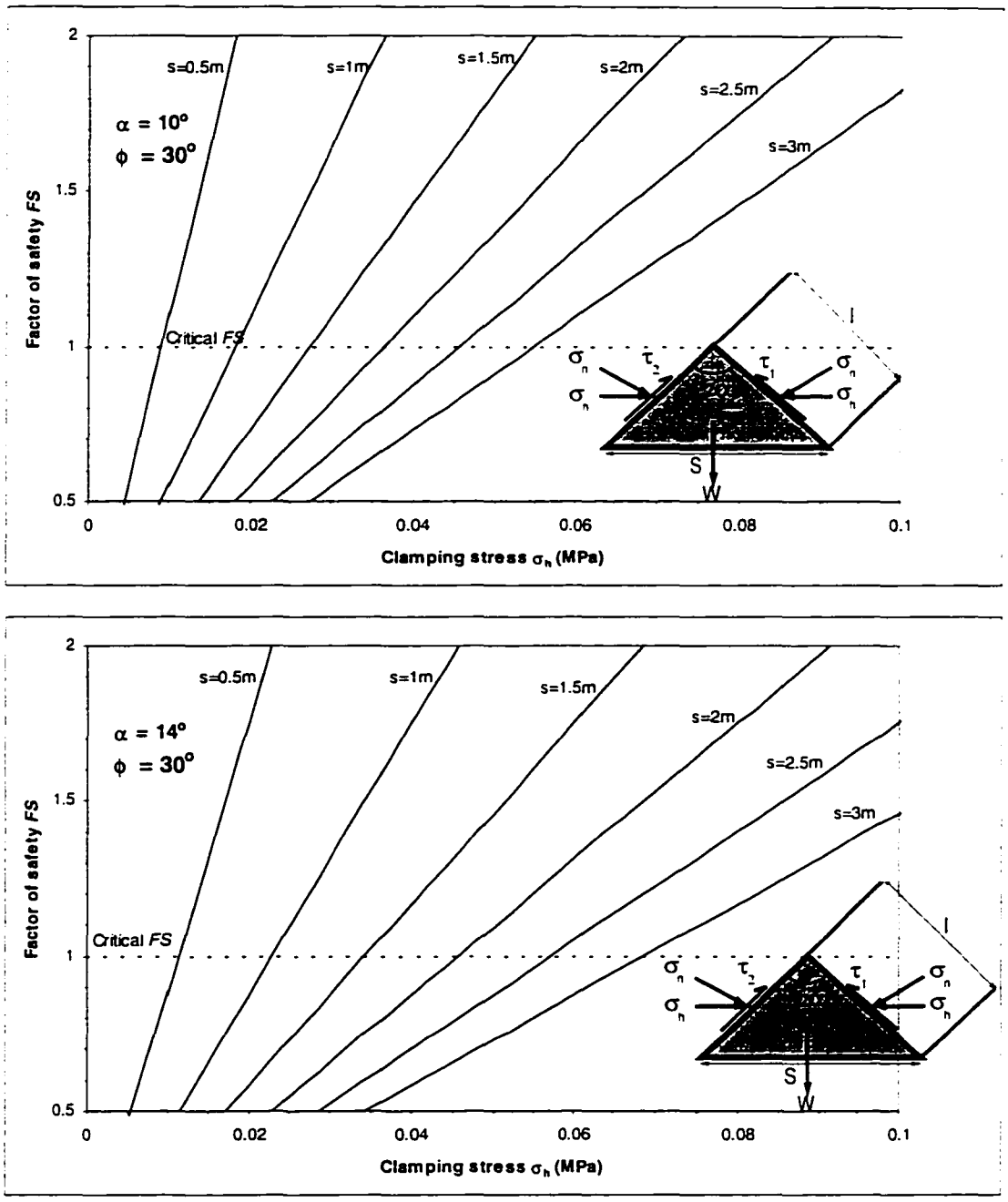


Figure 4.13 Triangular prism critical stress for joint friction angle of 30°

Again, typically a normal stress of $\sigma_n \geq 0.1$ MPa is the critical stress for stability for the assumed parameters.

4.4 Discussion of Wedge analysis

All the models used for determining the critical clamping stress under relaxation show that wedge stability is dependent on the horizontal clamping stress σ_h. This observation is in line with the conclusions of Brady

and Brown (1993) that the horizontal force components acting on triangular prism surfaces are important in maintaining their stability; and that any mining activity that reduces these surface forces increase the tendency of instability of the prism.

Brady and Brown (1993) in a more general form, defined the limiting stress conditions for slip along any plane defined by a dip angle β (Figure 4.14)as:

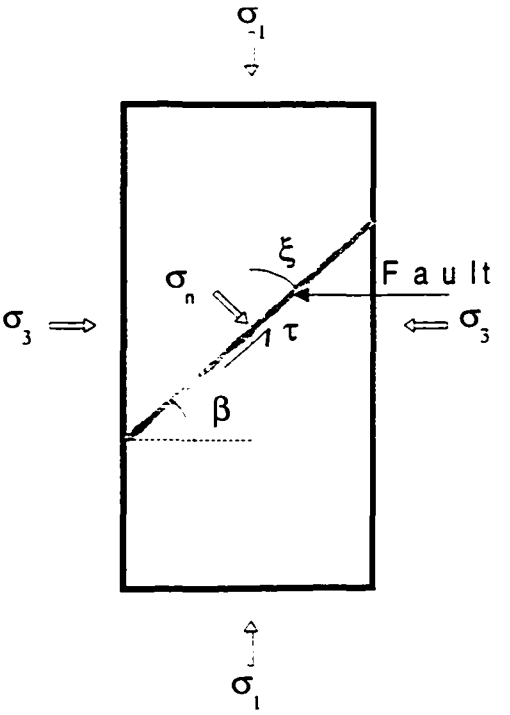


Figure 4.14 Illustrating the importance of stress in preventing slip along weak planes such as faults

The slip criterion is the Mohr-Coulomb failure criterion.

$$\sigma_1 = \frac{2c+\sigma_3\left[\sin 2\beta+\tan\phi\left(1-\cos 2\beta\right)\right]}{\sin 2\beta-\tan\phi\left(1+\cos 2\beta\right)} \qquad 4.5$$

Where σ_3 is the minimum principal stress acting on the plane, c is cohesion, ϕ is friction angle along the plane and β is the angle the weakness plane makes with the σ_3 direction. Equation 4.5 shows that for discontinuities with no cohesion, the stability of the plane is strongly dependent on the clamping stress. Table 4.1 summarizes the range of critical stresses below which typical wedges encountered in mining will fall due to relaxation.

Table 4.1 Summary of critical clamping stress analysis

Wedge type	Dip α(°)	Discontinuity friction angle ϕ (°)	Critical stress (MPa) for wedge size =0.5m-3m
Rhombohedral	20	15	0.01-0.09
	20	30	0.01-0.06
	70	15	0.03-0.16
	70	30	0.01-0.08
Book analogy	90	15	0.02-0.15
	90	30	0.01-0.07
Triangular prism (symmetrical)	80	15*	0.04-0.2
	76	15*	0.2-1.14
	80*	30	0.01-0.05
	76*	30	0.01-0.07

*Non-typical cases – very slender triangular prisms not commonly encountered

The range of critical clamping stresses for the cases in Table 4.1 is 0.01-0.2 MPa. For practical purposes it can be concluded that clamping stresses of less than or equal to 0.1 MPa or 100 kPa, will create situations susceptible to relaxation related failures in a blocky rockmass.

4.5 Summary

Lack of stress due to relaxation is a predominant cause of open stope wall sloughage. A definition of relaxation relevant to mining is given. The causes of relaxation are unfavourable excavation geometry and sequence, major discrete discontinuities such as faults and shears, and undercutting of excavation walls.

Three types of blocks are analyzed using the limit equilibrium method. The models show that the stability of all block types is stress dependent. This implies that any mining activity that reduces stresses to below a threshold value should be preceded with support or avoided if possible.

The factor of safety concept is used to define a range of critical clamping stresses below which wedge instability will be eminent. The critical range of clamping stresses is about 0.01 – 0.2 MPa for wedges of sizes ranging from 0.5 m to 3 m. For practical purposes, a threshold value of 100 kPa or 0.1 MPa, is suggested as a general guideline value.

CHAPTER 5

DETERMINATION OF STOPE OVERBREAK AND FAULT FACTORS: IMPLICATION FOR OPEN STOPE DESIGN

5.1 Introduction

Open stope overbreak is of concern at mines, and faults are a frequent cause of overbreak. Overbreak due to faults have been reported by Brekke and Selmer-Olsen (1966), Quesnel and Ley (1991), Speight (1992), Mikula (1992), Dune and Pakalnis (1996), and Potvin (1998), among others. The frequently poor performance of the stability graph as an open stope design tool is suspected to be largely due to the lack of a correction factor for faults. Evidence of this limitation is sighted in Quesnel and Gordon (1991), Reschke and Romanowski (1993), Stewart and Forsyth (1995), and Hutchinson and Diederichs (1996). Potvin and Milne (1992) stated as follows:

> "The design technique (referring to the stability graph method) cannot account for discrete geological features such as faults, shear zones, dykes or waste inclusions which may act to cause instability."

The objectives of this chapter are:

- To present a method for estimating overbreak due to faults, and
- To develop a fault factor based on overbreak due to faults for incorporation into the stability graph method.

To achieve the first objective, numerical simulations (Section 5.4) are used to estimate overbreak for various stope and fault geometries, and stress states.

In the development of the fault factor, various approaches are employed. First, observational experiences of the effects of faults on underground opening performance are examined. Second, two simple analytical

models are used to examine conditions under which slip occurs along a fault. Finally, the results of overbreak from PHASE^2 are used together with the equivalent linear overbreak sloughage *ELOS* stability graph by Clark and Pakalnis (1997) to determine a fault factor.

It is hypothesized that the most important parameter governing stope overbreak due to faults is the angle between the stope surface and the fault, $\xi°$. Overbreak increases as the angle between the stope surface and the fault changes from, 0° towards some critical angle, and then decreases again between the critical angle and 90°. To account for this effect the fault factor must correspondingly change between $0°<\xi°<90°$. The following figure illustrates the concept.

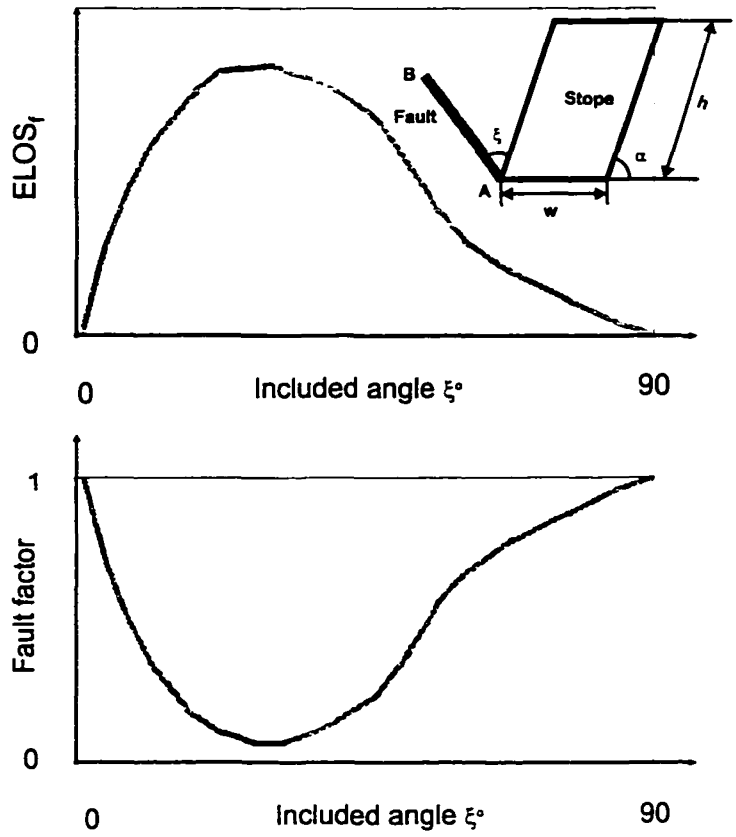


Figure 5.1 Conceptual model of the effects of faults for (a) stope surface equivalent linear overbreak slough due to fault $ELOS_f$ and (b) for fault factor development

This chapter, presents procedures for estimating stope overbreak due to faults and for determining the fault factors. The procedures are based on the stope geometry, fault geometry and in situ stress. These factors are considered to be key factors controlling stope surface performance.

When a fault has a large thickness with weak gouge such as graphite and intersects the stope surface, sloughage of the gouge becomes important. A different correction factor for this case based on an equation by Løset (1990) is introduced in Chapter 7 and applied to case histories from Ashanti Goldfields mine.

The results of the observational and analytical approaches are compared with the results from numerical modelling. The numerical analyses are synthesized into charts for predicting overbreak, and the fault factors. The fault factors are applied to the stability graph in Chapters 6 and 7 for the analysis of case histories from Kidd Mine in Canada and Ashanti Goldfields mine in Ghana.

Faults affect the stability of underground openings in three ways:

- They cause non-uniform redistribution of stresses in the excavation vicinity, and result in stress rotation that could be detrimental to an otherwise stable excavation. High stresses may result in the adjacent ground, while relaxation occurs within and around the fault that may increase the relaxed zone near the excavation surface. Increased stress may cause rock fracturing when the induced stress exceeds approximately one-third of the unconfined strength of the intact rock Martin and Chandler (1994). Gravity-induced structural failures will also occur in relaxed regions, where the critical clamping stress is less than about 100 kPa (see Chapter 4).
- The difference in rockmass quality between the fault gouge and the adjacent rockmass, is another factor that determines the degree of instability in an underground opening. For a wide fault with thickness less than the width or diameter of the underground opening it intersects, but greater than about 0.5 m, the adjacent competent rockmass causes the silo or arching effect (Palmström, 1995), which may lead to improved stability of the wall than if the adjacent rockmass quality were the same as the fault gouge rockmass quality. The silo or arching effect may enhance confinement to the loose fault gouge provided by the competent adjacent rockmass.
- Faults also provide free surfaces for movement of rock wedges. By their presence, they increase the degrees of freedom of movement of a rock wedge. It can be concluded from this statement that whether faults intersect, or are at a distance from the excavation will govern the extent of their influence on the stability of the excavation.

In accounting for the influence of faults on the stability of an underground excavation, the effects of the following factors on the magnitude of the influence of the faults must be investigated:

- Stress level, and orientation
- The position at which the fault daylights in the excavation surface, if al all
- Shear strength and width of fault or weakness zone,
- Fault gouge rockmass quality,
- Distance of fault from excavation surface, if it does not daylight
- Frequency or number of faults,
- Orientation of fault relative to excavation surface - amount of included angle,
- Excavation Geometry,
  - excavation aspect ratio particularly 3-dimensional excavations
  - excavation dip

- Arching effect and sloughing, and
- Water.

The effect of number of faults near or intersecting a given stope surface is beyond the scope of this thesis. However, it is suspected that the effect of this factor is probabilistic. The more the number of faults near a stope surface, the higher the probability that one of the faults will intersect the stope at critical included angle to cause caving. Also the more the number of faults, the higher the degrees of freedom for wedge movement. In Sections 5.3 and 5.4 the effects of the other factors are investigated, with effects of arching and slough examined in Chapter 7 in accounting for soft zones intersecting stope surfaces.

There are three general approaches to design. They are the observational or empirical, analytical and numerical methods. Each approach has its advantages and limitations, as was discussed in Chapter 2. The ideal design situation is to consider all three methods. These three approaches are used in examining the influence of the above factors on the effects of faults on open stope stability.

Empirical or observational methods of design have the advantage of dealing with complex materials like rockmasses. They involve bringing together the experience and expert knowledge of various specialists on the behaviour of excavations in different geological environments. Performance of excavations takes into account the complex interplay of the various factors such as the rockmass structure, stress and time that may affect stability. The ability of empirical methods in dealing with cases involving multiple parameters, and time, give them an advantage over analytical and numerical methods.

The disadvantages of empirical methods are that:

- They are subjective,
- The precise degree of inherent conservatism is unknown, and
- Particular geological peculiarities and local practices influence them.

Empirical methods rely on availability of data. When data are limited, analytical and numerical models are the best options.

Analytical procedures have the limitation that they are incapable of accounting for complex rockmass characteristics, and time. Analytical methods are only useful in dealing with simple two-dimensional cases and geometrical shapes such as circular openings for which close form solutions are applicable. When three-dimensional shapes and complex failure modes are involved, numerical simulations is the best alternative.

In mining, most excavations such as stopes are irregular in shape and are often grouped close to other excavations. Also, because most orebodies are often associated with geological features such as faults and

shear zones the rock properties are seldom uniform within the rock volume of interest (Hoek et al., 1995). In cases of this nature closed form solutions are not applicable and numerical simulations are useful.

The results of an analytical procedure or numerical model are only reliable when the input parameters are correct and when all factors affecting the structure are accounted for in the method. Knowing the correct rockmass properties is often a challenge, and accounting for all factors influencing the structure is not possible.

5.2 Observational Assessment

The varieties of factors that may separately or in combination determine the magnitude of the influence of a fault on excavation stability are listed in Section 5.1. The interplay of these factors makes it difficult to accurately determine stresses that exist around the opening, and to evaluate the in situ strength along the plane of weakness. Failures of openings in these conditions are better examined empirically when sufficient data is available.

Observational assessments of the performance of underground excavations consist of documentation of the performance of these excavations, and the prevailing ground conditions, as observed. Fortunately, civil engineering tunnelling has been in existence for sometime, and the experiences gained on the behaviour of tunnels when constructed close to or are intersected by faults or shear zones have been documented. The information from recorded performance of underground openings, and the set of conditions in which such excavations were made, assist in future excavation design in similar ground conditions.

Obert and Duvall (1967) presented a qualitative assessment, based on field observations, of the effects of planes of weakness on the stability of tunnels. Dip of the plane of weakness, and its strike relative to the tunnel axis, were recognized as important factors. For two-way span excavations such as stopes, it was observed in Chapter 2 that dip direction of the fault is irrelevant, and the included angle ξ between the fault and excavation surface is the important factor. Figure 5.2 gives the definition of included angle ξ between the stope surface and a fault CD. An example of a fault with a zero included angle is fault AB at a distance d from the stope surface.

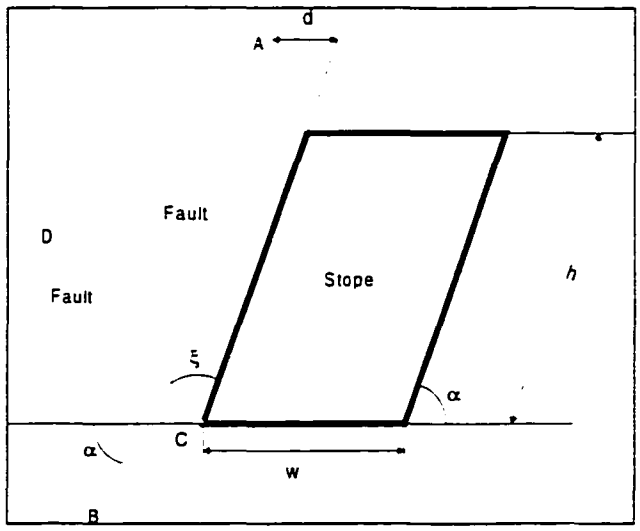


Figure 5.2 Definition of included angle ξ between stope and fault

Table 5.1 is a summary of the effects of planes of weakness on open stope stability using included angles. Table 5.1 is based on the observations of Obert and Duvall (1967) on the performance of tunnels intersected by planes of weakness (e.g. faults).

The fault can intersect the stope surface at any point. The worst condition for stability is when a fault intersects the stope surface at an unfavourable angle, say at included angles ξ less than 40°. The distance of the fault from the stope surface at any orientation is important for that surface stability.

Table 5.1 shows that the stability of a stope surface is highest at included angles of zero degrees, and 90 degrees. Between zero and ninety degrees, stability is largely dependent on the shear strength of the fault and the in situ state of stress. The next section examines a simplified model for the influence of fault orientation and shear strength on the stability of underground excavations.

Table 5.1 Qualitative assessment of effects of faults on stability of underground excavations

Range of included angle ξ° (Figure 5.2)	Qualitative assessment of underground excavation stability
0	Plane of weakness will form a plate in roof and columns in sidewalls. Fracture is through intact rock and depends on thickness and strength of beam or column
0 - 20	Failure eminent along plane of weakness
20 - 70	Failure may occur by shear along weakness plane
70 - 90	Failure occurs through intact rock rather or by shear along plane of weakness. Failure depends on stress concentration and rock strength
90	Stable

5.3 Effect of Fault Shear Strength and Orientation - Analytical Models

The factors governing unstable slip along faults are the prevailing level of shear stresses and the frictional properties along the fault plane. Slip occurs along the fault when the shear stress in the fault plane exceeds the shear strength of the fault. The consequence of a fault slip is immediate relief of excess shear stresses, and stress redistribution elsewhere (Ryder 1988, Hafner, 1951). This process of excess shear stress shedding is a cyclic process that may result in a stick-slip mechanism related to earthquakes and rockbursts. It may also trigger groundfall.

5.3.1 Fault slip - Method 1

The intersection of a stope surface by a fault is analogous to the single plane of weakness theory of rock anisotropy discussed by Jaeger (1960), Hoek and Brown (1980), and Brady and Brown (1993). Figure 5.3 presents a model of a single discontinuity plane to examine the effects of fault shear strength and orientation on stope stability.

Using the Mohr-Coulomb failure criterion, the shear strength along the fault τ is given by:

$$\tau = c + \sigma_n \tan\phi^* \qquad 5.1$$

where, σ_n = normal stress on fault; c = cohesion on fault; and ϕ^* = fault basic friction angle plus its roughness angle i.

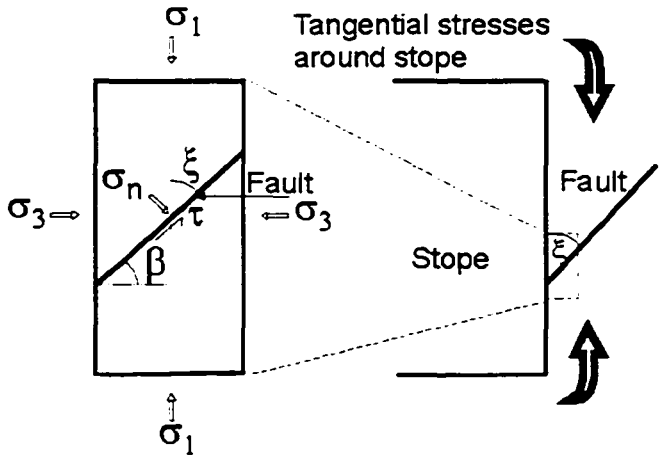


Figure 5.3 Model for effect of fault shear strength and fault orientation on stope surface stability: (a) Rock specimen with fault under triaxial compression and (b) Equivalent stope sidewall with fault (biaxial stress state)

The shear stress on the fault s is given by:

$$s = \frac{1}{2}(\sigma 1 - \sigma 3)\sin 2\beta \qquad 5.2$$

where, σ_1 = major principal stress; and σ_3 = minor principal stress at the fault location; and β = dip of plane of weakness.

The normal stress σ_n in Equation 5.1, on the plane of weakness is given by:

$$\sigma_n = \frac{1}{2}(\sigma 1 + \sigma 3) + \frac{1}{2}(\sigma 1 - \sigma 3)\cos 2\beta \qquad 5.3$$

From Equations 5.1 and 5.2, the factor of safety against slip of the stope surface is given by:

$$F = \frac{c + \sigma_n \tan\phi^*}{\frac{1}{2}(\sigma 1 - \sigma 3)\sin 2\beta} \qquad 5.4$$

Substituting for σ_n in Equation 5.4 and we have:

$$F = \frac{c + \left[\frac{1}{2}(\sigma_1 - \sigma_3) + \frac{1}{2}(\sigma_1 - \sigma_3)cos2\beta\right]tan\phi}{\frac{1}{2}(\sigma_1 - \sigma_3)sin2\beta} \qquad 5.5$$

A fault gouge cohesion of zero is assumed in the analysis. According to Deere (1973, 1979), Brekke and Selmer-Olsen (1966), and Brady and Brown (1993), most fault gouge materials are cohesionless. At the stope surface σ_3 is zero. Applying these assumptions to Equation 5.5 and simplifying gives a factor of safety of the stope surface against shear failure as:

$$F = \frac{(1 + \cos 2\beta)\tan\phi^*}{\sin 2\beta} \qquad 5.6$$

From Figure 5.3a, the included angle ξ is given by:

$$\xi = 90 - \beta \qquad 5.7$$

The factor of safety is then given in terms of the included angle as:

$$F = \frac{[1 + \cos 2(90 - \xi)]\tan\phi^*}{\sin 2(90 - \xi)} \qquad 5.8$$

Equation 5.8 suggests that the stability of the stope surfaces is independent of the stress tangential to the stope wall. The fault friction and included angles control slip along the fault.

Figure 5.4 is a graph of factor of safety against fault slip as a function of the included angle ξ for fault total friction angles ϕ * of 15°, 20°, 30° and 45.

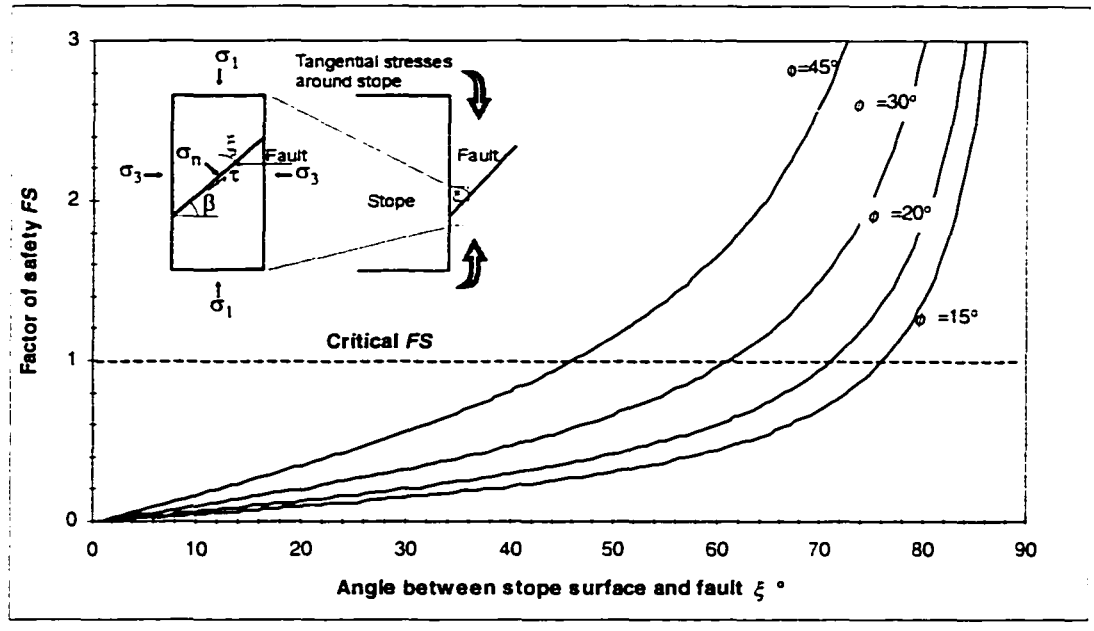


Figure 5.4 Effect of fault total friction angle ϕ*and included angle on stope wall stability

Figure 5.4 shows that above included angles between 45° to 75°, depending upon the fault friction angle ϕ*, the critical factor of safety against slip along the fault is equal to one. The factor of safety is greater one above the critical included angles corresponding to the various fault friction angles. As the included angle approaches 80°, the factor of safety becomes large. Figure 5.4 shows that slip occurs at included angles less than 45° for *ϕ = 45°, 60° for ϕ* = 30°, less than 70° for ϕ * = 20° and 75° for ϕ* = 15°.

At an included angle of 0° (fault parallel to stope surface) failure may occur by buckling of columns between the fault and the stope surface and will depend on the thickness of pillar between fault and stope surface. Column and beam failures are not accounted for in the model (Figure 5.3). Euler's stress-induced column buckling theory becomes applicable when columns of rock are involved. In the next section elastic stress analysis is used to investigate the effect of fault distance to stope surface on fault slip.

5.3.2 Fault slip – method 2

Kirsch (1898) provides equations (Equations 5.9 to 5.10) for elastic stresses around circular openings in a homogeneous, isotropic, elastic continuum medium. The equations allow determination of the normal and shear stresses on an inclined discontinuity plane. Figure 5.5 defines the parameters in Kirsch's equations.

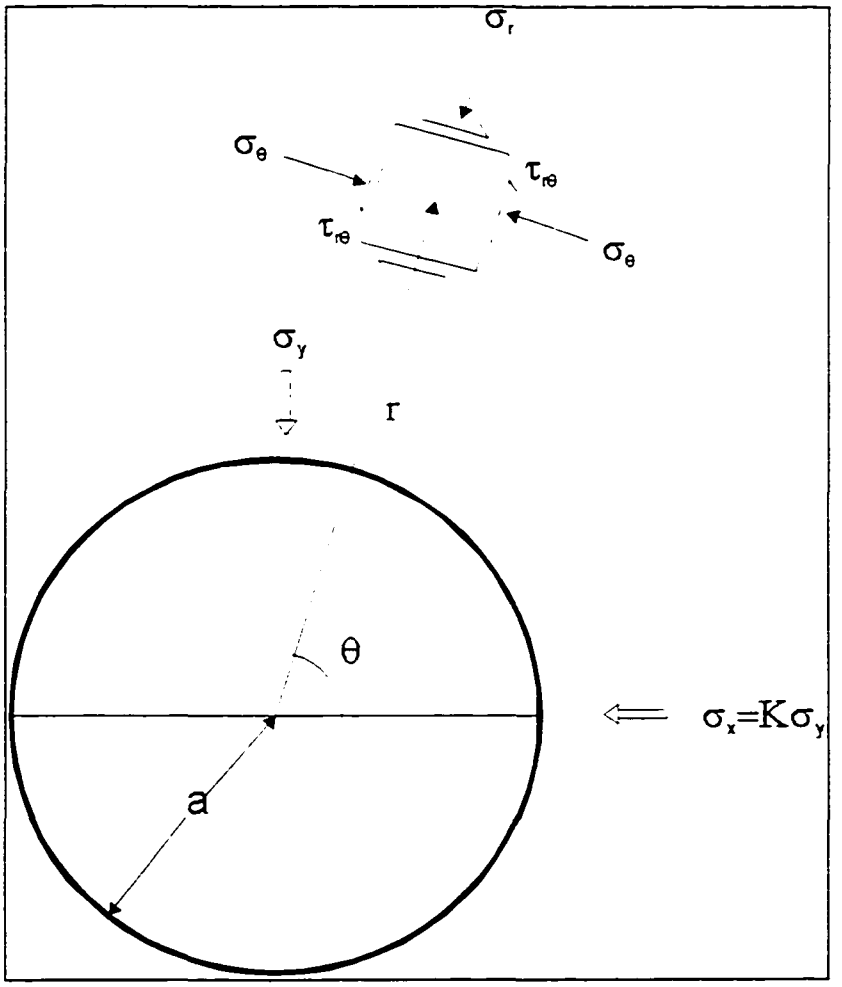


Figure 5.5 Kirsch solution for stresses around a circular opening - definition of parameters

$$\sigma_r = \frac{\sigma_v}{2}\left[(1+K)\left(1-\frac{a^2}{r^2}\right)-(1-K)\left(1-\frac{4a^2}{r^2}+\frac{3a^4}{r^4}\right)cos2\theta\right] \qquad 5.9$$

$$\sigma_\theta = \frac{\sigma_v}{2}\left[(1+K)\left(1+\frac{a^2}{r^2}\right)+(1-K)\left(1+\frac{3a^4}{r^4}\right)cos2\theta\right] \qquad 5.10$$

$$\sigma_{r\theta} = \frac{\sigma_v}{2}\left[(1-K)\left(1+\frac{2a^2}{r^2}-\frac{3a^4}{r^4}\right)sin2\theta\right] \qquad 5.11$$

where, K = horizontal to vertical in situ stress ratio.

By comparing the strength along the discontinuity to the state of stress in the adjacent rockmass, it is possible to determine portions of the discontinuity that are not capable of supporting the predicted continuum stresses in the adjacent rockmass.

Brady and Brown (1993) have examined major discontinuities such as faults with two objectives. The first, was to determine the conditions under which elastic stress analysis is still valid for use in analyzing a discontinuous rockmass. The second objective was to assess the potential effect of a discontinuity, such as a fault, on the stability of the excavation periphery (Figure 5.6b). Special cases of $\theta = 0°$, 45° and 90° were used for a hydrostatic in situ state of stress. Brady and Brown, using the Mohr-Coulomb failure criterion (Equation 5.1), determined ratios of shear stress to shear strengths at points along the plane of weakness, assuming no cohesion along fault (c=0). They plotted the ratios of τ/σ_n against the distances along the fault (Figure 5.6a).

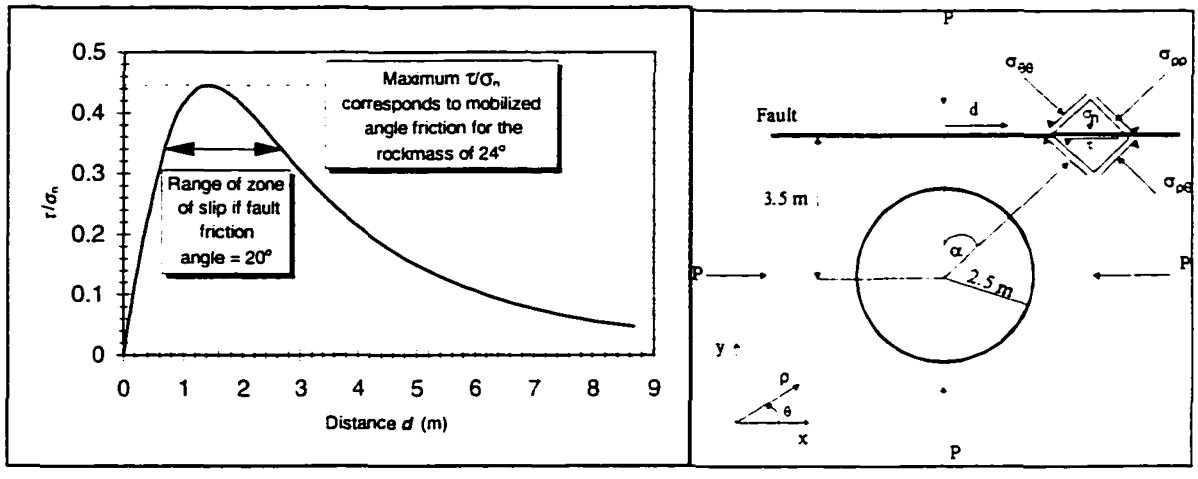


Figure 5.6 (a) Plot of shear stress/normal stress ratio versus distance along a plane of weakness (b) close to but not intersecting, a circular excavation (Re-plotted (a) and redrawn (b) after Brady and Brown, 1993)

The maximum point in Figure 5.6a, corresponds to a maximum mobilized angle of friction, of about 24°. If the angle of friction for the fault exceeds 24°, no slip is predicted on the plane, and the elastic stress distributions can be maintained. For a fault with an angle of friction of 20°, the extent of the predicted zone of slip is shown in Figure 5.6a, by comparing the mobilized angle of friction along the fault with the fault friction angle.

Brady and Brown (1993) concluded that in some cases elastic analysis still presents a perfectly valid basis for design in a discontinuous rockmass. They also concluded that in some cases elastic stress analysis involving discontinuous rockmasses provides a basis for judgment of the engineering significance of a discontinuity. Priest (1993) used a similar approach to Brady and Brown for a more general method of determining effects of faults on excavations.

Daemen (1983), based on Kirsch's equations and the Mohr-Coulomb failure criterion, presented analytical solutions for calculating slip zone boundaries for parallel sets of weakness planes around circular tunnels or shafts. He defined slip zones as the areas where the strength is exceeded point wise along the weakness

planes with a given dip and strength and location. The analysis showed that the orientation of the slip zone is determined by the dip of the weakness plane and its shear strength. It was also shown that zones within which tensile stresses develop across weakness planes strongly depend on the orientation of the weakness systems. The effects of other factors on slip zones, such as fault strength, virgin stress field and internal pressure, were also demonstrated. Kumar (1997) undertook a similar analysis to Daemen, but with the Hoek-Brown failure criterion rather than Mohr-Coulomb criterion. Identical results were obtained with the material considered as a Hoek-Brown medium rather than as a Mohr-Coulomb material.

The objective of this analysis is to examine the effects of fault-excavation geometrical relations on the stability of an excavation surface, with emphasis on distance and orientation. The concept of factor of safety is used to determine the effect of varying distances between fault and excavation surface and, along the fault, for given fault shear strength, and in situ stress state.

Figure 5.7 is a circular excavation with a fault at a distance *d* from its surface, and *b* is any distance along the fault. The geometrical relationship between the excavation and fault are defined in the diagram.

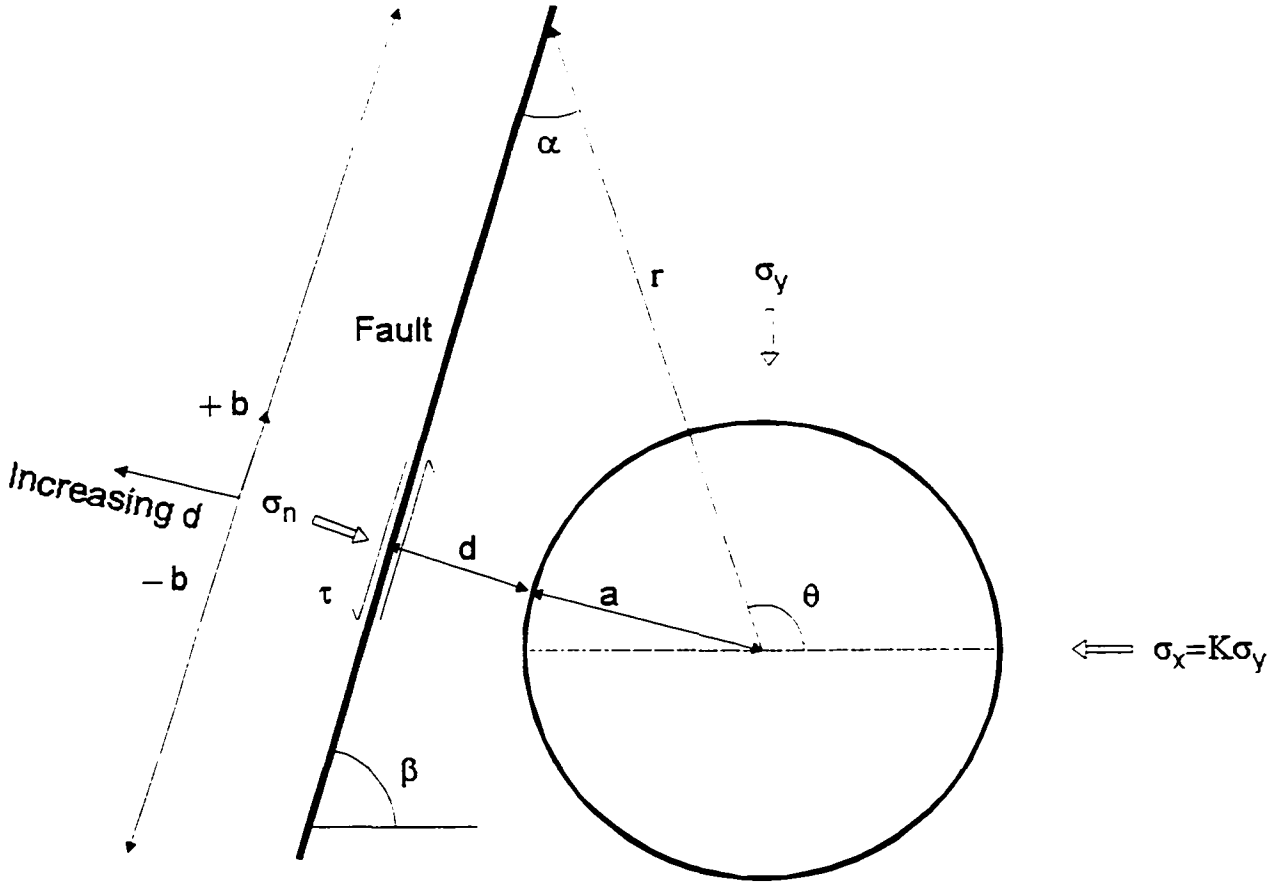


Figure 5.7 General representation of fault-excavation geometrical relations

At the point of interest, b=0, and as the distance along the fault increases ($+b$) zero, ($+b$ and $-b$) slip along the fault can be determined.

The normal and shear stresses σ_n and σ_{mn}, at the point of interest at a radial distance $r = d$ from the centre of the excavation, are obtained from stress transformations as:

$$\sigma_n = \sigma_r \sin^2\alpha + \sigma_\theta \cos^2\alpha + 2\sigma_{r\theta} \sin\alpha\cos\alpha \qquad 5.12$$

$$\sigma_{mn} = \sigma_r \cos\alpha \sin\alpha - \sigma_\theta \sin\alpha\cos\alpha + \sigma_{r\theta}\left(\cos^2\alpha - \sin^2\alpha\right) \qquad 5.13$$

The following geometrical relationships can be established from Figure 5.7

$$r = \sqrt{(d+a)^2 + b^2} \qquad 5.14$$

$$\alpha = \tan^{-1}\left[\frac{(d+a)}{b}\right] \qquad 5.15$$

$$\theta = \beta + \alpha \qquad 5.16$$

Substituting Equation 5.12 in Equation 5.1 gives shear strength along the fault, ignoring cohesion as:

$$\tau = \left(\sigma_r \sin^2\alpha + \sigma\theta \cos^2\alpha + 2\sigma_{r\theta} \sin\alpha\cos\alpha\right)\tan\phi^* \qquad 5.17$$

The shear stress along the fault is given by Equation 5.13. Therefore, the factor of safety against slip along the fault, for a given stress state is defined as:

$$F = \frac{\left(\sigma_r \sin^2\alpha + \sigma\theta \cos^2\alpha + 2\sigma_{r\theta} \sin\alpha\cos\alpha\right)\tan\phi^*}{\sigma_r \cos\alpha\sin\alpha - \sigma\theta \sin\alpha\cos\alpha + \sigma_{r\theta}\left(\cos^2\alpha - \sin^2\alpha\right)} \qquad 5.18$$

Slip occurs when the factor of safety is less than unity. Figure 5.8 is a plot of Equation 5.18 for faults at a 12.5-m distance from the centre of a circular excavation, and dipping at 20°, 40°, 60° and 80°. The K-ratio used is 2.1 with the major principal stress horizontal. The extent of slip along the fault can be obtained from Figure 5.8 by reading off the distance corresponding to the point where the factor of safety is unity.

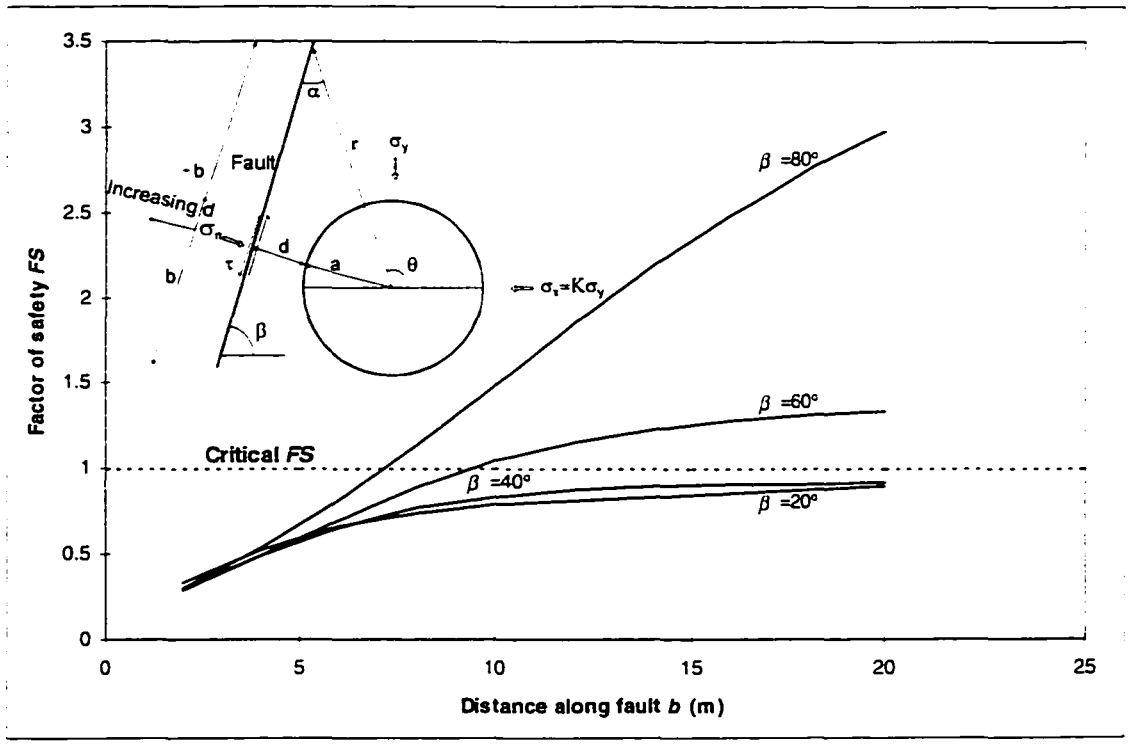


Figure 5.8 Effect of fault dip on amount of slip: K=2.1, excavation radius =7.5 m, fault friction $\phi^* = 20°$

Large areal extents of slippage are observed for dips of 20° and 40°, while slip for 60° and 80° dipping faults are relatively small. It is concluded that low dipping faults will slip more readily than steeply dipping faults under the given conditions.

The extent over which slip occurs away from the excavation is a measure of the extent of the slip zone from the excavation periphery. Extent of slip is considered for the special case of $b = 0$ in Figure 5.9. The point with most unfavourable stress condition due to the interaction of the fault and excavation will be at the closest point to the excavation surface where $b = 0$. For this condition $r = d+a$, $\alpha = 90°$ and $\theta = 90+\beta$. Equation 5.18 simplifies to:

$$F = \frac{\sigma_r \tan\phi^*}{-\sigma_r\theta} \qquad 5.19$$

By substituting Equations 5.9 and 5.11 in Equation 5.19 we have:

$$F = \frac{\left[(1+K)\left(1-\frac{a^2}{(d+a)^2}\right)-(1-K)\left(1-\frac{4a^2}{(d+a)^2}+\frac{3a^4}{(d+a)^4}\right)\cos 2\theta\right]\tan\phi}{-\left[(1-K)\left(1+\frac{2a^2}{(d+a)^2}-\frac{3a^4}{(d+a)^4}\right)\sin 2\theta\right]} \qquad 5.20$$

The factor of safety F, can be determined at given fault orientations, fault friction angles and distances from the excavation surface d, for a given horizontal to vertical stress ratio K, and radius of excavation a. Figure 5.9 and Figure 5.10 are example plots for K = 2.1, fault friction angle ϕ*=20° and excavation diameter = 15m showing effects of fault dip, and fault distance to excavation.

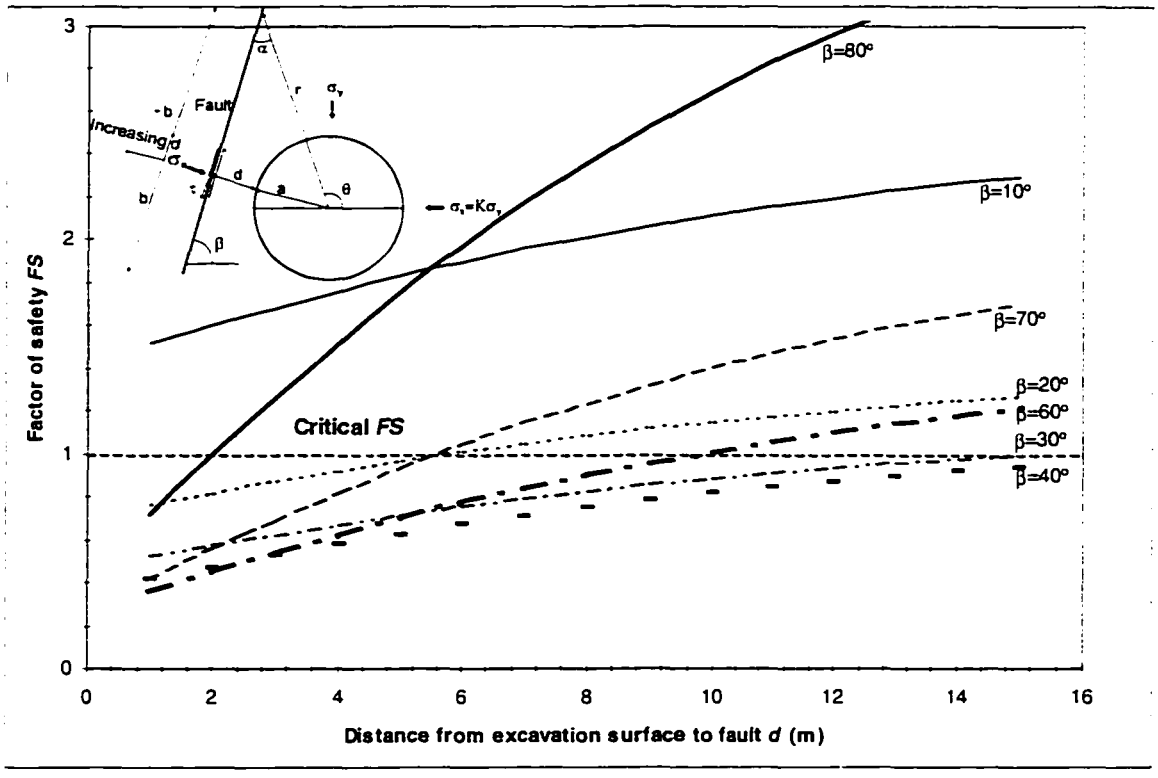


Figure 5.9 Effect of fault distance to excavation surface on fault slip: K=2.1, excavation radius a=7.5 m, fault friction ϕ*=20°, α=90°, b=0

In Figure 5.9, the points at which the critical factor of safety (FS = 1) line intersects the respective curves, approximates the depths of slip from the excavation surface due to the fault. Amount of slip from the excavation surface into the rockmass decreases with the distance of the fault from the excavation surface. The extent of the slip zone also depends on the dip of the fault. For steeply dipping and shallow dipping faults, the extent of slip is less. Critical dips are in the range 20° to 60° for the assumed rockmass properties, fault properties, and in situ stress ratio.

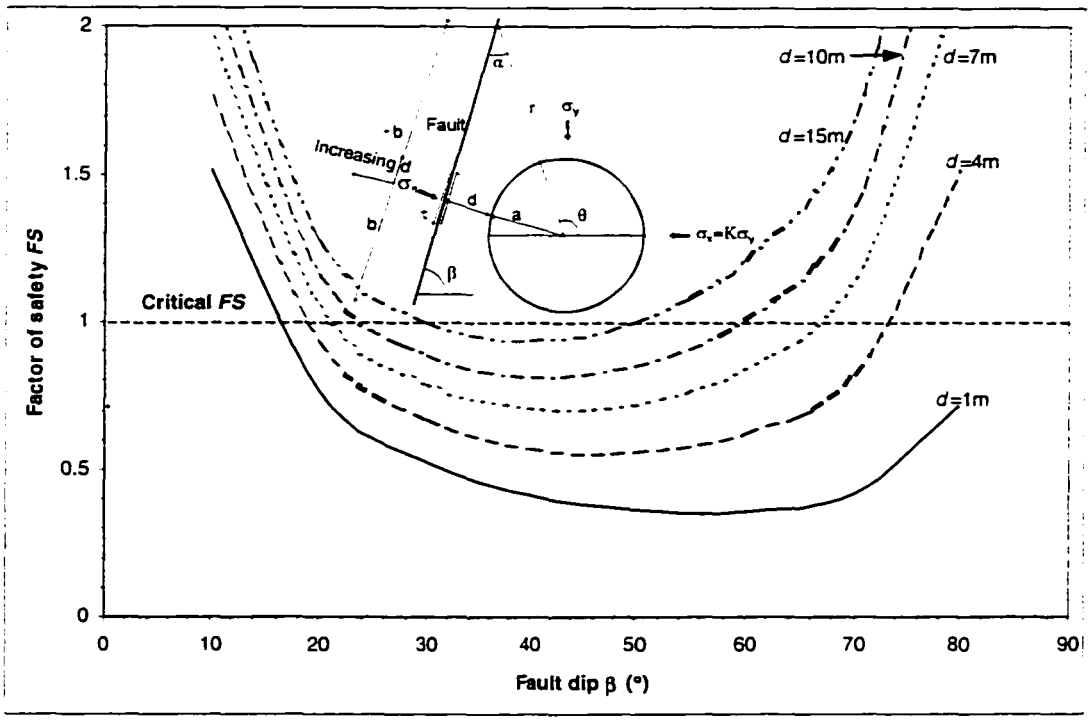


Figure 5.10 Effect of fault dip on excavation fault slip: K = 2.1, excavation radius a = 7.5 m, fault friction ϕ^* = 20°, α .=.90°

Figure 5.10 shows that for a given fault distance from the excavation surface, slip is unlikely for low ($\beta \leq$ 15°) and steeply ($\beta \geq 70°$) dipping faults. Further more, the closer the fault is to the stope surface the more prone it is to slipping.

In the next section, numerical models are used to determine effects of faults on excavation stability. These models will also demonstrate the relationship between fault slip and excavation surface sloughage.

5.4 Numerical Modelling

Numerical stress models are used in this thesis to identify the key factors governing the effects of faults on the stability of stopes. The numerical models are used to perform parametric analyses to assess the extent of influence of each factor on the effect of the fault on stope stability.

Non-circular stope geometries are modelled using PHASE^2. Emphasis in interpretation is placed on the size of the zone of elements that yield in tension, as this dictates the influence of the fault on stresses in the stope surface, and therefore the potential for wall sloughage. It has been hypothesized that the effect of faults near stopes is to increase the low stress or relaxation zone.

The factors governing slip along faults are the prevailing level of shear stresses and the frictional properties along the fault plane. Slip occurs along the fault when the shear stress in the fault plane exceeds the shear

strength of the fault. The consequence of a fault slip is immediate relief of excess shear stresses, and stress redistribution elsewhere (Ryder 1988, Hafner, 1951). This process of excess shear stress shedding is a cyclic process that may result in a stick-slip mechanism related to earthquakes and rockbursts.

Slip zones along a fault are not necessarily related to tension zones in the rockmass around an excavation near the fault. However, in many situations the presence of a fault can influence the shape and size of a tensile zone in the rockmass near the excavation. The main hypothesis of this thesis is that the tension zone that occurs near the stope wall affects the stability of an open stope and hence, understanding how a fault influences the size and shape of the tensile zone is important. Overbreak problems in open stope hangingwalls are due to lack of stress (Hoek and Brown, 1980; Fuller et al., 1985) and dominate concerns in regular mining environments because of dilution.

Little numerical and quantitative work on the effects of faults on non-circular openings has been done, particularly on open stopes. It is well known (Hoek and Brown, 1980; Brady and Brown, 1993; Potvin, 1988) that stress distributions around underground excavations are strongly influenced by the excavation geometry. Most publications (Deere, 1973, 1979; Obert and Duvall, 1967; Mahtab and Dixon, 1976; Brekke and Selmer-Olsen, 1966; Laubscher, 1990; Hoek and Brown, 1980; Barton et al., 1974, 1993; Løset, 1990) on fault effects on stability of excavations are qualitative. Others such as those by Kastner (1979), Daemen (1983), Priest (1993), Brady and Brown (1993) and Kumar (1997) are analytical and based on circular openings with emphasis on slip zones.

Goodman (1966) published one of the earlier works on numerical modelling of weakness planes using finite element method. He used the contact between two rock types as the weakness plane. Circular openings were modelled, and the effects of different contact orientations and varying rock stress conditions were examined. The analysis showed that when a circular tunnel is excavated along a vertical contact between two rock types with different elastic moduli, the stresses are found to increase in the harder material while the softer rock is relatively de-stressed. It was also shown that greater departures of stress distributions from the homogeneous unlayered case arise when the contact between layers is parallel or at a small angle to the direction of uniaxial stress than when contact is perpendicular to the load. Shen and Barton (1997) published effects of ubiquitous joints on tunnel stability based on a two-dimensional distinct element code, UDEC. They reported that the region where rock blocks fall is found in the immediate vicinity of the tunnel (failure zone), and that the location of loose blocks is decided by the orientation of the joints. Shen and Barton also described an open zone where joints open, surrounding the failure zone. The open zone enlarges with reducing joint spacing and reducing in situ stress ratio. Wiles and Nicholls (1993) used MAP3D to simulate rockmass response to various fault orientations. The purpose of the simulations was to demonstrate the capability of MAP3D in handling faults for given underground situations. The scope and extent of their work were limited to a few examples from a mine.

There are relatively few good three-dimensional numerical codes suitable for routine stress analysis work in a typical mining environment (Hoek et al., 1995). These numerical codes are often expensive and results from these analysis require interpretations by a specialist. In many cases it is possible to simplify the problem to two dimensions by considering stresses on critical sections in a three-dimensional model. In a mining environment results are often needed on time, and model results should not require specialist interpretations.

A two-dimensional plastic finite element program, PHASE^2 (Curran and Corkum, 1997), and an elastic two-dimensional boundary element package , EXAMINE^{2D} (Curran and Corkum, 1995), were used in the analysis. The two packages are fast, and relatively cheap compared to three-dimensional packages. Furthermore, they do not require specialist interpretations and provide reliable information on the performance of underground excavations. The results from the two models were compared and found to be similar. PHASE^2 was selected for the study because it suites the needs of the mining industry and takes into account stress redistribution due to yielding. EXAMINE^{2D} does not account for tension cutoff stress redistribution.

5.4.1 PHASE^2

PHASE^2 is a two-dimensional finite element program for calculating stresses and estimating support around underground excavation developed by the Rock Engineering Group of the University of Toronto (Curran and Corkum, 1997). PHASE^2 can be used to solve a wide variety of mining and civil engineering problems, including:

- Plane strain or axisymmetric problems,
- Elastic or plastic materials,
- Staged excavations,
- Multiple materials,
- Support (bolts / shotcrete), and
- Constant or gravity field stress.

In PHASE^2, the strength factor is calculated by dividing the rock strength based on the failure criterion used, by the induced stress at every point in the mesh. Joint or discontinuity (faults) elements, discontinuities can be incorporated into the finite element analysis. The user has a choice of quadrilateral or triangular finite elements. PHASE^2 allows for graded meshing, uniform meshing, and radial meshing. All of which are automatically generated.

The external boundary in PHASE^2 can be modelled with springs which allows the far field rockmass to have a stiffness, as well as using fixed/pinned displacement conditions. More generalized nodal conditions

are available, which allows the user to specify force or displacement boundary conditions on individual nodes of the mesh. Tractions can also be staged for multi-stage models.

PHASE^2 contains DXF file creation features for use with AutoCAD™ allowing printing using AutoCAD's comprehensive set of printer drivers.

The procedure for modelling was as follows:

The limits of the x-y coordinates were first set to give a space of about 400 m by 350 m. The model analysis and initial parameters were then set to up: A one stage plane strain analysis was used with a maximum iterations of 500 for a tolerance of 0.001 using the Gaussian Elimination solver. No disk swapping was allowed.

The geometry of the stope was then input by entering the coordinates of the four corners of the stope. Stopes of various sizes and dips were used (see Table 5.2). The fault was added at specified included angles with the hangingwall and intersected the stope, at the bottom, middle, or top. The external boundary defining the limits of the finite elements was box type (rectangle) with an expansion factor of 3. The external boundary was automatically generated when selected. Nodal boundary conditions were fixed XY (Figure 5.11). A model with infinite elements was run and the results compared with one with fixed external boundaries for the given conditions, and the two models gave very similar results. The results from the two models were compared and found to be similar. Fixed boundary conditions were used because it gives faster solutions. The fault shown in the Figure 5.11 was discretized to 100 elements using the custom discretization tool. The fault does not pass through the stope in the models and a case illustrating how to apply the procedure when a fault passes through the stope is explained in Section 5.4.5.

The mesh setup consisted of 150 excavation nodes with a gradation factor of 0.1. The mesh type was set to graded with the element type as three-nodded triangle. A typical mesh used in the analysis is shown in Figure 5.11.

The in situ field stress condition was set to constant. Various field stresses were used as shown in Table 5.4.

One material type was used to represent the rockmass in each model. The rockmass was considered isotropic with an elastic modulus of 30,000 MPa, and a Poisson ratio of 0.25. The strength parameters of the rockmass are detailed in Table 5.3. The rockmass was considered as an isotropic plastic material. The Mohr-Coulomb failure criterion (Equation 5.1) was used for the rockmass, and as a slip criterion for the fault. The fault aperture was taken as 0.3 m, with normal and shear stiffnesses of 100,000 MPa/m and 40,000 MPa/m respectively. Fault shear strength was assumed to be controlled by friction only, with cohesion being zero. Initial fault deformation was not allowed, fault slip was allowed.

Typical computation time for the model in Figure 5.11 takes 4 hours for a 486 DX50 and about 10 minutes in Pentium II 350 MHz machine.

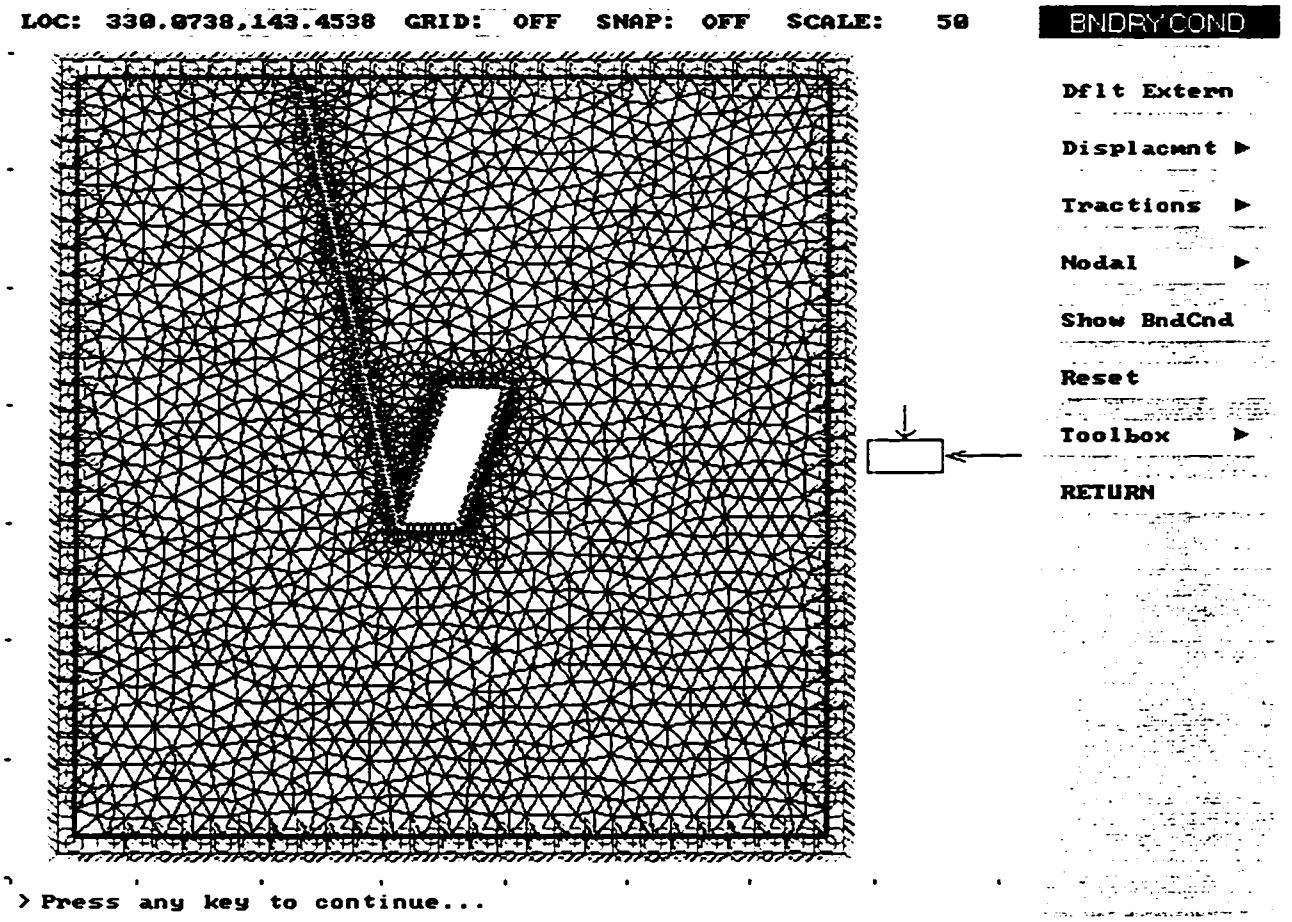


Figure 5.11 Typical PHASE^2 finite element mesh for the rockmass and fault for included angle of 30°, 3-noded triangular elements, number of elements = 4460, excavation nodes are 150, maximum iterations = 500, tolerance = 0.001, solvertype is Gaussian elimination

Using INTERPRET, the strength factor contours are displayed and the yield points in the rockmass and fault superimposed. In the DOS version of PHASE^2 the yield point can be superimposed in the strength factor contour option. The DOS version was used in the analysis, which allows for DXF output.

The strength factor output file with the yielded points superimposed is sent to AutoCAD as a DXF file, where the perimeter of the zone of the elements that yielded in tension is digitized and the area of the entity of yielded elements determined. The method of obtaining the equivalent linear overbreak sloughage $ELOS_f$ due to the fault is detailed in Section 5.4.4.

5.4.2 EXAMINE^{2D}

EXAMINE^{2D} is a very fast two-dimensional indirect boundary element and displacement discontinuity program for calculating stresses and displacements around underground and surface excavations in rock. Unlike the Finite Element and Finite Difference methods, the boundary element method only requires meshing around the excavation boundaries, eliminating the need for complex volume mesh generation.

EXAMINE^{2D} provides an integrated graphical environment for data entry and visualization. A CAD based modeler allows for point and click geometry input and editing. Popup windows allow for easy entry and modification of model parameters.

The simple editing tools provide a convenient method for performing parametric studies. The graphical data interpreter offers a rich set of tools for the convenient display of model results. With EXAMINE^{2D} you can quickly create and mesh a model, perform a stress analysis, and interpret the results.

Element types to choose from are constant, linear, quadratic formulation displacement continuities, virtual number of elements is user defined, with a default value of 50. Modelling consists of graphical data entry, with editing capabilities. far field stresses are either constant, gravitational or user defined. The possible material types are isotropic and transversely isotropic materials. There is automatic meshing of excavations and joints. Plane strain and complete plane strain options are available. Strength criteria to choose from are Hoek-Brown, Modified Hoek-Brown, and Mohr-Coulomb.

Joints can be included as either ubiquitous or discrete, in the model. Hoek-Brown Joint deformation due to excavation stresses and/or far field stresses, elastic joints, seam elements, nonlinear joints - Mohr-Coulomb/Barton-Bandis/No tension criteria are choices to choose from.

Other capabilities in EXAMINE^{2D} are: AutoCAD DXF import/export, import 2D sections from EXAMINE^{2D}, and full screen/cropped image capture direct to PCX file or printer. The interface for EXAMNE^{2D} is based on the FEINT user interface (ver. 3).

The modeling procedure in EXAMINE^{2D} is similar to that of PHASE^2. The procedure for analyzing the output files from EXAMINE^{2D} is briefly described in Section 5.4.4. Even though PHASE^2 and EXAMINE^{2D} gave similar results PHASE^2 was preferred in the analysis and was the sole modelling tool in the research for reasons cited in Section 5.4.4.

The properties and in situ stress states are the same for those used in PHASE^2. The failure criterion used in EXAMINE^{2D} was minor principal stress less than zero.

5.4.3 Model and hypothesis

Figure 5.12 is a representation of the model stope used for the investigation. Table 5.2 shows details of the stope geometries used in the study. It is recognized that stope geometries differ and the results may not be generally applicable for stopes that have dimensions that are significantly different form those studied here. However, the approach presented here can be used to apply the method to other situations. Four cases were analyzed as shown in Figure 5.12, taking each case at a time.

Table 5.2 Characteristics of stopes

Stope vertical height (m)	Stope slant height, h (m)	Stope width, w (m)	Stope aspect ratio, A_r	Stope dips	Remarks
60	73.2	24	0.3	55°	Flat stope for open stope mining
60	63.1	12	0.2	72°	Slender/thin stope
60	63.1	24	0.4	72°	Base study stope
30	31.5	24	0.8	72°	squat stope
15	15.8	24	1.5	72°	squat stop

The rockmass properties used in the numerical models are given in Table 5.3, with the various in situ stress states considered listed in Table 5.4. The major principal in situ stress is horizontal σ_1, and the minor stress σ_3 is vertical. Rockmass properties (except cohesion) were selected such that they are typical of most rockmasses encountered in open stope mining, at least in the Canadian Shield, with Kidd Mine as an example. Rockmass cohesion c was selected such that yielding in shear is prevented because sloughage in stope walls is due low stresses or relaxation. The stress range used in the modelling was also selected to cover depth ranges commonly encountered in the Canadian Shield underground mines, again with Kidd Mine as an example. The procedure used here can be adapted to other rockmass characteristics, stope geometries, and in situ stress states. It is easy to use, and can be applied at any mine site for its specific situation.

The Mohr-Coulomb failure criterion was used in both the elastic and plastic models. This failure criterion was applied to both the faults and rockmass, and was also used in the analytical models in Section 5.3. The rockmass friction and cohesion values were selected to represent a moderately jointed rockmass. Furthermore, the rockmass cohesion of 35 MPa was used to minimize the amount of yield that occurred in shear while the rockmass tensile strength of 0.6 MPa allowed for yield at near-tensile stresses. The parameters selected for the Mohr-Coulomb failure criterion enabled the stress modelling to focus on assessing the influence of low stresses on the extent of yielding in PHASE^2 while preventing the modelling from being dominated by yield in shear and stress redistribution caused by zones of high stress near the stope corners.

Table 5.3 Rockmass and fault properties

Material property	Fault	Rockmass
Cohesion c (MPa)	0	35 except for Figure 5.16 where c = 100
Friction ϕ (°)	8, 15, 20, 30, 45	37
Tensile strength σ_t (MPa)	0	0.6
Young's modulus E (MPa)		30,000
Poisson ratio v		0.25
Normal stiffness (MPa/m)	100000	
Shear stiffness MPa/m	40000	
Thickness (m)	0.3	

Table 5.4 Stress states used in the models

Case	Stresses (MPa)			Stress ratio				Out of plane stress (MPa)
	σ_1	σ_2	σ_3	$\sigma_1+\sigma_2/2\sigma_3$	σ_1/σ_3	σ_2/σ_3	σ_1/σ_2	
1	37	35	30	1.2	1.2	1.1	1.1	35
2	75	52	35	1.8	2.1	1.3	1.3	52
3	80	45	25	2.5	3.2	1.8	1.8	45

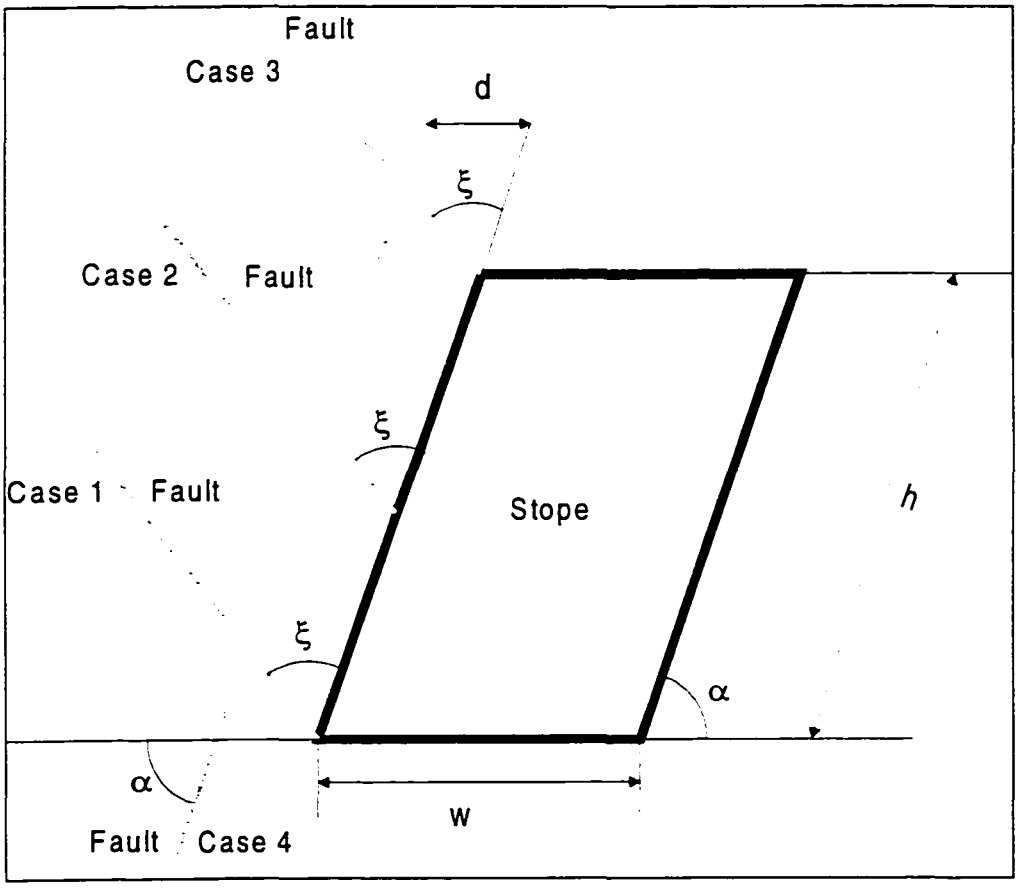


Figure 5.12 Model for analyzing fault effects on stope stability

It is hypothesized that faults affect stope stability due to their tendency to increase the zone of relaxation, resulting in increased sloughage into the stope. Faults also provide an additional free surface for rock block movement and fallout. They thus increase the degrees of freedom for block movement.

The following factors are modelled to investigate the influence of faults on the size of the tension zone:

- In situ stress state: K-ratio,
- Shear strength and width of fault,
- Position of fault on stope surface,
- Distance of fault to stope surface d,
- Orientation of fault relative to stope surface - included angle ξ
- Stope geometry, i.e., stope aspect ratio A_r defined as:

$$A_r = \frac{w}{h} \qquad 5.21$$

where, w = width of stope in two dimensions, or, longest lateral dimension in three dimensions; h = height of stope; and stope dip α.

5.4.4 Procedure for determining overbreak

Two criteria have been used to define fault effects on underground excavation stability:

- Criterion for slip along a fault,
- Criterion for sloughage.

The Mohr-Coulomb criterion for slip along a fault is well known. It is hypothesized in this study, based on limit equilibrium analysis in Chapter 4 that the criterion for structurally governed failure by sloughage under gravity is approximately 0.1 MPa. In other words, it is assumed that a confinement loss to near zero is a valid criterion for defining the extent of sloughage. The tensile strength of the rockmass used in the PHASE2 analyses was 0.6 MPa. This value, for all practical purposes, is equivalent to near-zero.

This assumption should be valid for a jointed rockmass in which the tensile strength is very small (near zero), implying that the rockmass has no self-supporting capacity. Recent works by Diederichs and Kaiser (1998) support this view. For a rockmass of excellent quality (e.g., Q' = 1000), the method will not apply, and a different approach must be used.

For describing the severity of overbreak due to a fault, a parameter that quantifies the extent of overbreak is useful. Pakalnis et al. (1996) introduced the term Equivalent Linear Overbreak/Slough *ELOS* defined as:

$$ELOS = \frac{Volume\ of\ slough}{Stope\ surface\ area} \qquad 5.22$$

ELOS is expressed in metres, and is the equivalent average depth of overbreak from the stope surface.

A parameter for quantifying the severity of overbreak due to a fault is defined in this thesis as:

$$ELOS_f = ELOS_t - ELOS_n \qquad 5.23$$

Where $ELOS_f$ = Depth of incremental sloughage due to a fault; $ELOS_t$ = Total depth of sloughage considering a fault near the stope; and $ELOS_n$ = Depth of sloughage that would have occurred without a fault.

In two-dimensional elastic and plastic numerical modelling, the fault effect is defined as:

$$ELOS_f = \frac{Area\ in\ tension\ when\ stope\ is\ modelled\ with\ fault - Area\ in\ tension\ without\ fault}{Stope\ height} \qquad 5.24$$

The area, within the zero principal stress contours gives the cross-sectional area in tension in elastic models. In plastic models, the cross-sectional area in tension is given by the area obtained by digitizing around the yield points in tension. In PHASE^2, the yield points in tension are obtained in the Strength Factor option of INTERPRET.

The fault has no adverse effect on stope sloughage if $ELOS_f \leq 0$. Equation 5.24 is used throughout the analysis to determine the effect of faults on hangingwall stability (stope stability) under various combinations of ground conditions, and fault and stope geometries. The $ELOS_f$ obtained in Equation 5.24 is also used to define a fault factor F_W in Section 5.4.6. The fault factor is used to determine a revised N' by correcting the rockmass quality Q' for the effects of faults near a stope surface.

Defining the area of the tension zone in elastic models is straightforward. The tension zones in elastic models correspond to colour coded principal stress contours. The model output can be exported into AutoCAD, the area within the zero contour digitized, and the area of the entity determined. Elastic models do not redistribute tensile stresses. This is a limitation in elastic models since stress redistribution is a true field phenomenon.

In an isotropic plastic finite element model, such as PHASE^2, the tension zone is estimated from the contour enveloping the elements that yielded in tension. The yield points in PHASE^2 are historic and cumulative and can be used to assess the size of the tension zone under given ground conditions. The yield points in PHASE^2 are coded differently for yielding in tension (red dots), and yielding in shear (shear bands) as can be seen in the Strength Factor contour plots (e.g., Figure 5.15). The Strength Factor plots can then be exported into AutoCAD, and the area containing the yielded points in tension contoured by digitizing the perimeter. The area of the entity containing the yielded points in tension can then be

determined. This procedure has been adopted for determining the areas of tension zones in the plastic models.

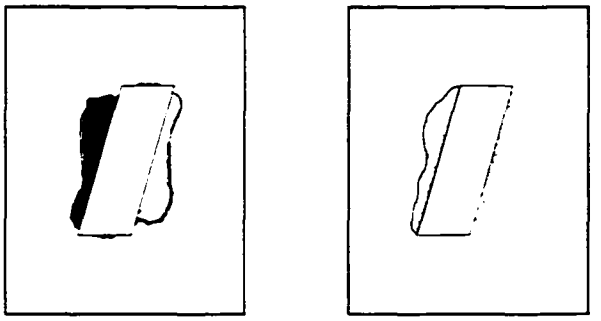
The first part of Section 5.4 examines $ELOS_f$ as a parameter for quantifying fault effects due to the influence of the various factors identified and presented at the beginning of this chapter. The final result is, a $ELOS_f$ chart for predicting overbreak in open stopes due to faults. Other uses of the $ELOS_f$ chart are discussed later.

The second part of the model analysis focuses on the development of a fault factor for incorporation into empirical open stope design methods such as the stability graph method. The final result is a series of curves for various combinations of factors such as stope geometries, in situ stress ratios, and fault geometry and strength given in a single chart.

The modelling procedure is discussed in the next section. Two-dimensional boundary element elastic models and finite element plastic models are used, and their limits of applicability assessed for this investigation.

5.4.4.1 Comparison of 2-D elastic and plastic models

Two-dimensional boundary element elastic models and two-dimensional finite element plastic models are compared for assessing the area of the tension or relaxation (Figure 5.13).



(a) Hangingwall tension zone from elastic model (Area = 404m^2) (b) Zone of elements that yielded in tension in plastic model (Area = 383m^2)

Figure 5.13 Comparison of tension zones from elastic (a) and non-elastic (b) models for a stress ratio K = 2.1, c = 100, $\phi = 37°$

It can be observed from the two models that the tension zones are practically identical for this stope geometry and the assumed parameters in Section 5.4.3.

5.4.4.2 Effect of fault position

Further to the comparison in Figure 5.13, faults were introduced at the bottom, middle, and top of the stope; and both elastic and plastic models were used to assess the fault effect on the stope. The results are presented in Figure 5.14, and Figure 5.15 for conditions where stope back is stable or does not yield in compression or tension. If the rockmass is assumed to be weaker, and yield occurs in the back of stope (Figure 5.15c) the tension zone is affected.

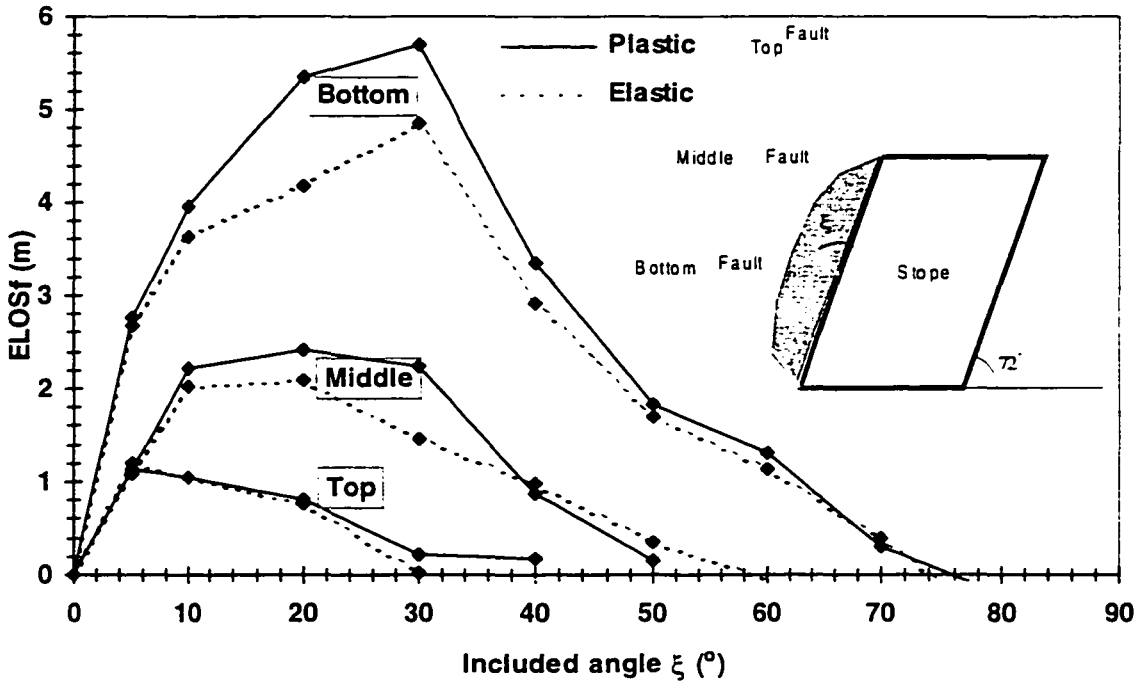


Figure 5.14 Comparison of results from elastic and plastic models in terms of $ELOS_f$

Figure 5.14 shows that even though the plastic models (full symbols) give slightly higher $ELOS_f$, practically, there is no difference between the two models in the overall trend. EXAMINE^{2D} (Curran and Corkum, 1995) and PHASE^2 were both used in the elastic modelling for comparison. An elastic or plastic model could therefore be used in the investigation, as long as the stope back remains stable. Plastic modelling using PHASE^2 (Curran and Corkum, 1997) was adopted in the analysis because it takes into account the effect of tension related stress redistribution. Results used in assessing the tension zones in Figure 5.14 for the plastic analysis are given in Figure 5.15a - h, Figure 5.16a - d, and Figure 5.17a - e for fault intersecting the stope surface at toe, middle and top respectively.

5.4.4.3 Fault intersecting stope at toe

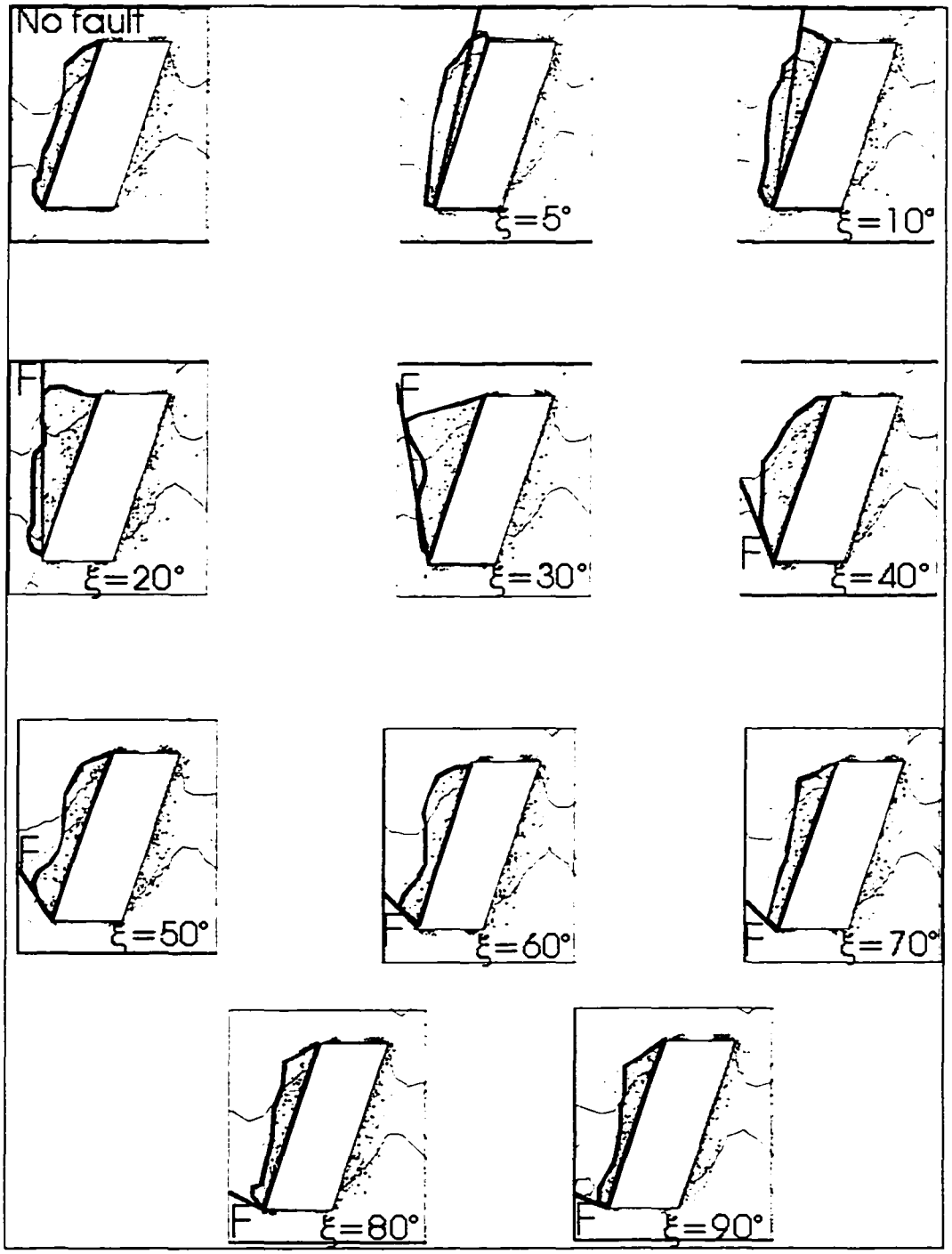


Figure 5.15 Model results for fault intersecting stope at bottom at stated included angles: Stress ratio K = 2.1, stope aspect ratio A_r = 0.4, fault friction angle ϕ^* = 20°, stope dip α = 72°, F = fault and ξ = included angles

5.4.4.4 Fault intersecting stope at middle

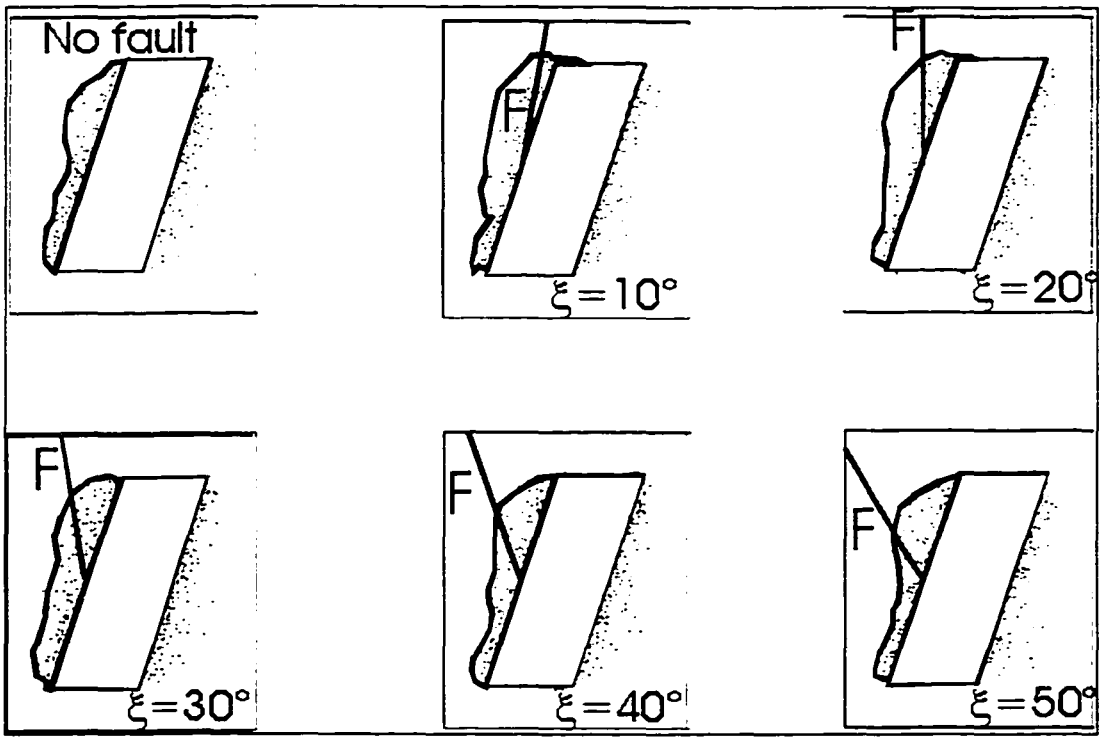


Figure 5.16 Effect of fault intersecting stope at middle at various included angles: Stress ratio K = 2.1, stope aspect ratio A_r = 0.4, fault friction angle ϕ^* = 20°, stope dip α = 72°, F = fault and ξ = included angles

5.4.4.5 Fault intersecting stope at back or crown

Typical example run results for this case are shown in Figure 5.17

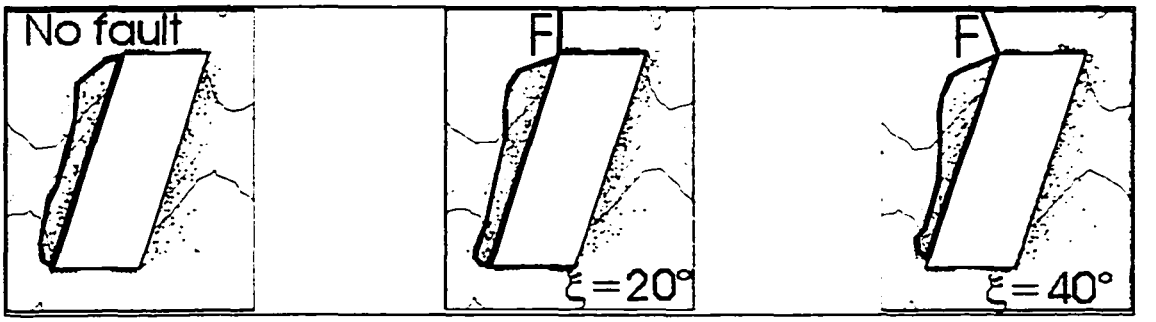


Figure 5.17 Effect of fault intersecting stope at middle at various included angles: Stress ratio K = 2.1, stope aspect ratio A_r = 0.4, fault friction angle ϕ^* = 20°, stope dip α = 72°, F = fault, ξ = included angle

It is concluded that the fault position on the stope surface has a strong influence on the amount of overbreak it causes. A fault at the stope bottom or toe causes the most serious damage followed by a fault at the stope centre. Little overbreak is observed when the fault intersects the stope at the back. These results are for a non-yielding stope back, for the assumed rockmass properties, K-ratio, and stope geometry.

5.4.4.6 Effect of angle between fault and stope surface

For all fault positions in the stope surface, the tension zone increases as the included angle increases up to a critical included angle where the effect of the fault diminishes. An included angle ξ between 0° and 60° affect the face stability with $\xi = 0°$ to 30° having the most effect.

5.4.4.7 Effect of fault shear strength

The effect of fault shear strength on the stope surface stability is investigated by considering a fault intersecting the stope at the bottom or toe. The fault shear strength is assumed to be governed primarily by fault friction with cohesion being zero. The effect of water on fault shear strength will be to reduce fault friction and normal stress in the Mohr-Coulomb equation (Equation 5.1).

Fault surfaces and gouges often contain high contents of silt, clay, mica, chlorite, montmorillonite, talc, calcite, serpentine, and graphite. These soil types and minerals often result in low fault shear strengths. Cohesion in most faults is negligible, and shear strength is controlled by friction only. Friction angles are low in fault gouges because of the platy nature of the characteristic minerals found in them. Deere (1973) states that frictional resistance offered by gouge materials is expected not to be more than 15° to 25°. Hoek and Brown (1980) give residual friction angles ϕ_r of joints and faults ranging from 6° to 35°. Fault total friction angles $\phi^* = \phi_r + i$ (residual friction ϕ_r angle plus roughness angle i) of 8°, 15°, 20°, 30°, and 45° are used in the analysis, where i is the basic friction angle. The results are presented in Figure 5.18. The model outputs used in determining $ELOS_f$ for ϕ^* = 8°, 15° and 30° are given in Appendix B. Model outputs for ϕ^* = 20° are presented in Figure 5.15.

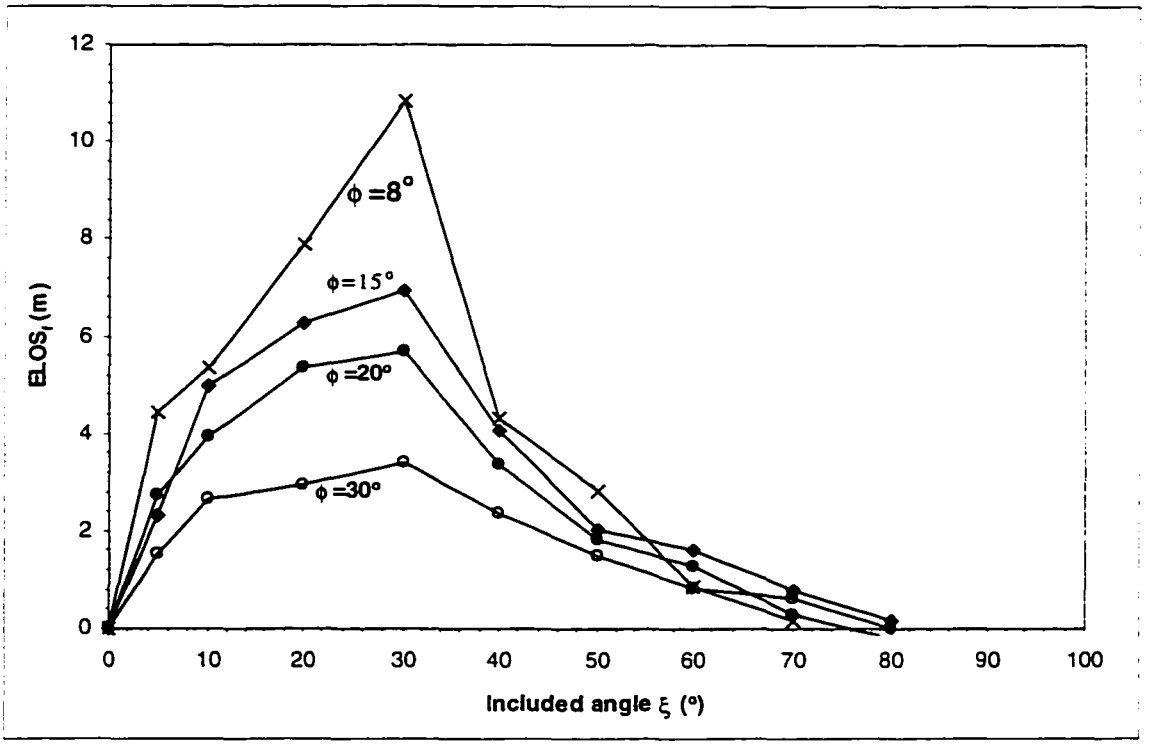
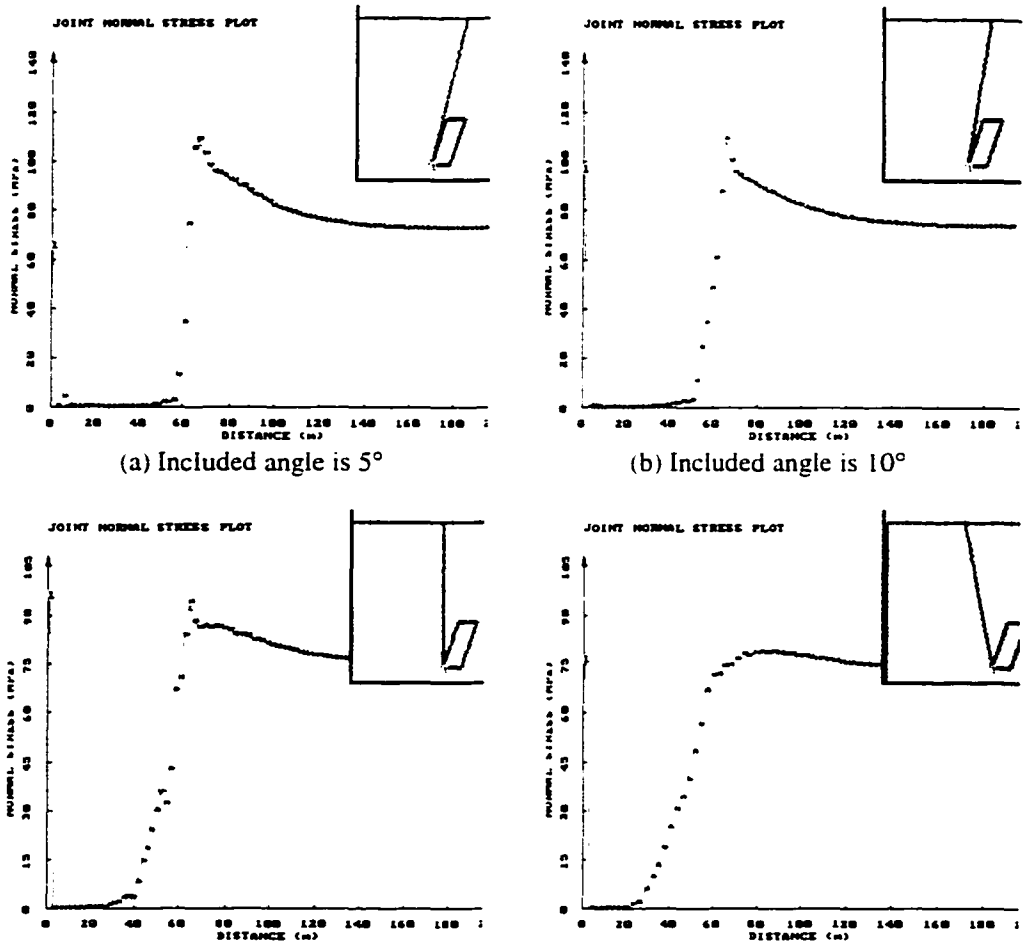


Figure 5.18 Effect of fault shear strength on stope stability using $ELOS_f$: Stress ratio $K = 2.1$, stope aspect ratio $A_r = 0.4$, fault friction angle $\phi^* = 8°$, 15°, 20° and 30°, stope dip $\alpha = 72°$, Fault at bottom of stope

Figure 5.18 shows that for fault friction angles in the range between 8° and 30° $ELOS_f$ changes by a factor of about 3. At friction angle of 45° (not shown) the fault had little to no effect on stope sloughage.

Figure 5.19 shows decreasing loss of normal stress along the fault, with increasing included angle. Complete loss in normal stress results in increasing size and depth of tension zones along the fault. Under conditions of no compressive normal stress across the fault the Mohr-Coulomb criterion for slip is invalid (Daemen, 1983). Note that, for the same included angle ranges tension zones in the stope hangingwall rather increase in size and depth.



(a) Included angle is 5° (b) Included angle is 10°

(c) Included angle is 10° (d) Included angle is 30°

Figure 5.19 Plots of normal stress versus distance along faults, measured from point fault intersects stope, showing zero normal stresses on faults dependent on fault orientation relative to stope surface, for included angles of 5°, 10°, 20° and 30

5.4.4.8 Effect of in situ stress state (*K*-ratio) on influence of faults on stope stability

Figure 5.20 is plot of the amount of overbreak against included angles for each stress ratio. The conventional definition of stress ratio as major principal stress to minor principal stress gives *K* values as 1.2, 2.1, and 3.2 (Table 5.4) and are shown in Figure 5.20.

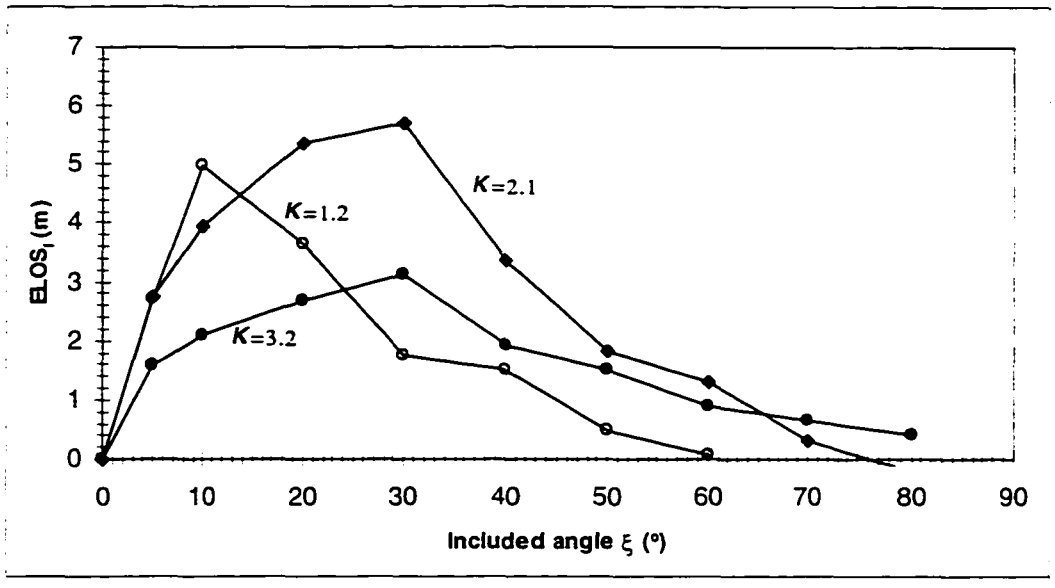


Figure 5.20 Effect of in situ stress state on overbreak in terms $ELOS_f$ due to faults: Stress ratio K = 1.2, 2.1, 3.2, stope aspect ratio A_r = 0.4, fault friction angle ϕ^* = 20°, stope dip α = 72°

Figure 5.21 shows the effect of a K-ratio of 1.2 on the effect of a fault on the stability of a stope at various included angles. Figure 5.21a shows no yield in tension for stope without fault. Introduction of a fault intersecting the stope at the toe resulted in limited tension zones in the stope hangingwall. Observations of Figure 5.21b, c, and possibly d illustrate an interesting type of failure mechanism in which the pillar between the fault and stope surface is cut-off at the toe and top. Thus, while the total area of the tension zones by itself is not significant at near hydrostatic stress conditions, the tension zones can result in massive wedge failures by this wedge cut-off mechanism. Figure 5.21b and c, show the cut-off wedges, and these are the likely volumes that will slough into the stope. In calculating the area of sloughage in Figure 5.21b and c, the cut-off wedge areas are included.

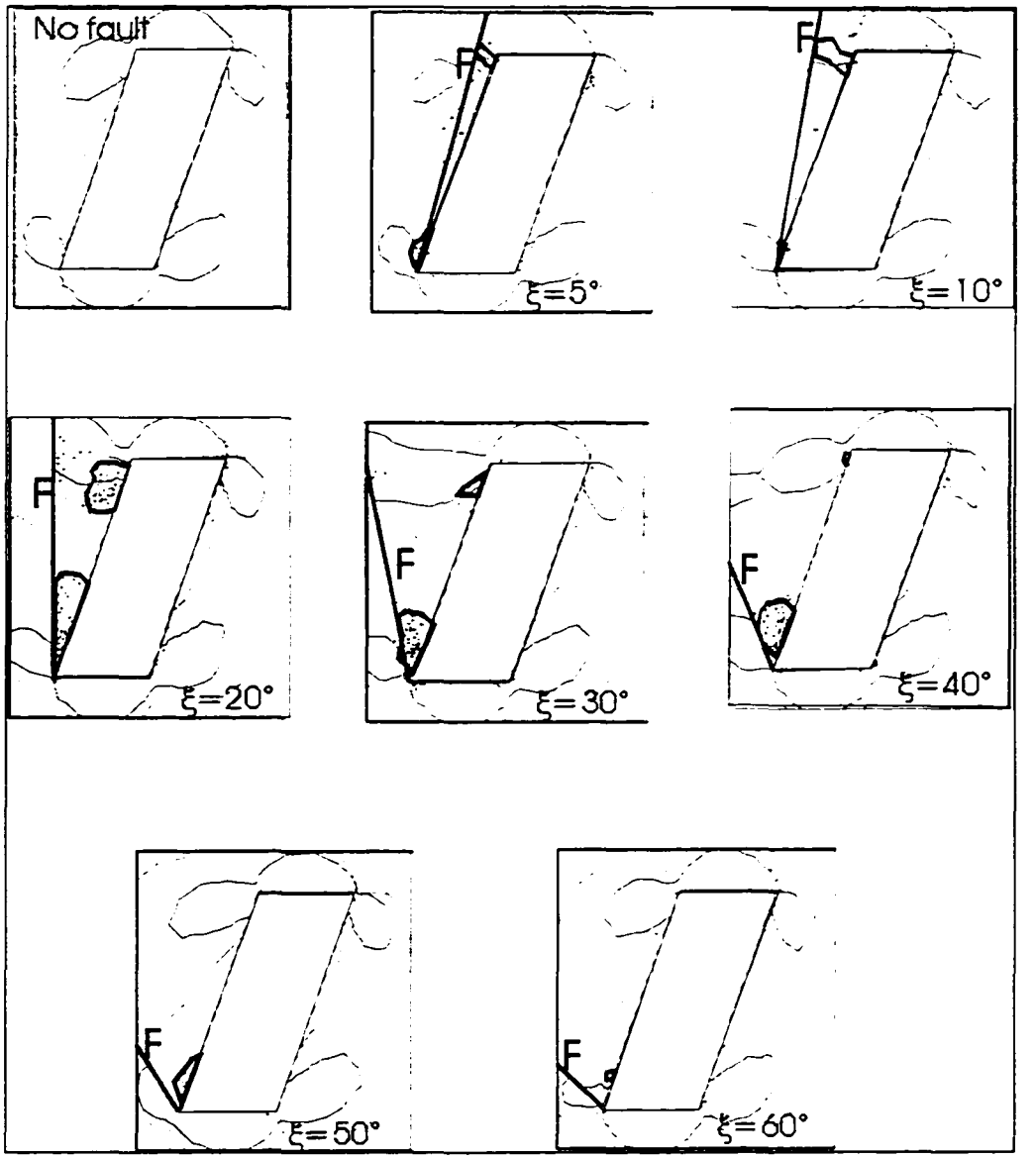


Figure 5.21 Effect of K- ratio = 1.2 on the influence of faults on stope stability, stope aspect ratio A_r = 0.4, fault friction angle ϕ^* = 20°; stope dip α = 72°, Fault intersecting stope at bottom, F = fault, ξ = included angle

The outputs for models with K = 2.1 are presented in Figure 5.15. At a stress ratio of 3.2, and for the assumed strength properties there is now sufficient stress to cause yield at the stope back (Figure 5.22), and deep "pre-fault" tension yield zones occur in the stope hangingwall, at the assumed rockmass properties.

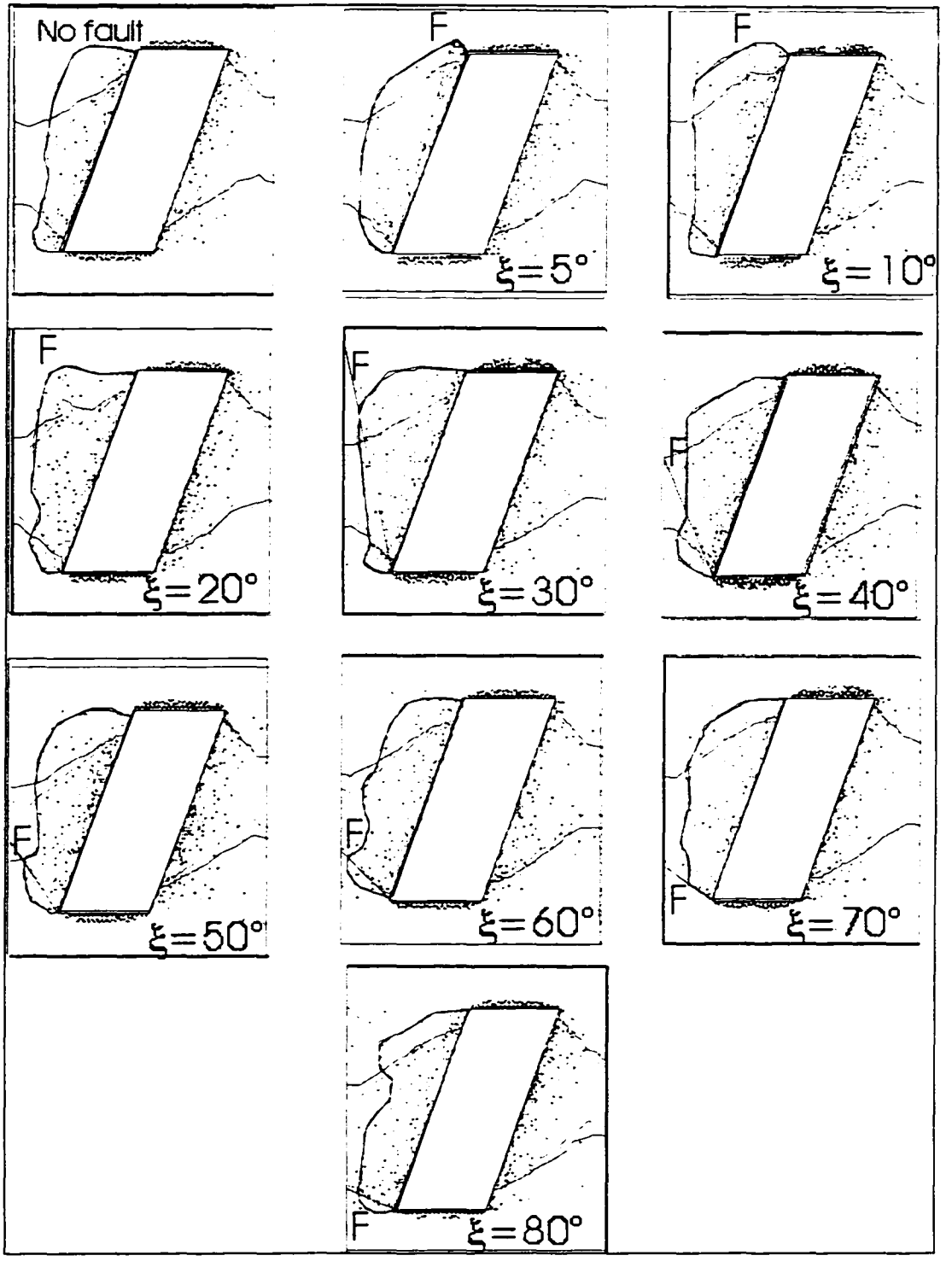


Figure 5.22 Effect of K-ratio = 3.2 on the influence of faults on stope stability: Stress ratio = 3.2, stope aspect ratio = 0.4, fault friction $\phi^* = 20°$; stope dip = 72°

A fault intersecting the hangingwall at the toe leads to a further increase in the area of the tension zone into the rockmass. The deepening of the tension zone at $K = 3.2$ is not obvious in Figure 5.20. This is because

even without a fault there is already an extensive yield zone, so that introduction of the fault has relatively less impact in extending the yield zone.

5.4.4.9 Effect of stope aspect ratio A_r

The stope aspect ratio A_r is defined as the largest lateral dimension of the stope w divided by stope height h. If the stope is not vertical the slant height should be used in the calculation of A_r. Stope heights are selected to cover the range of sub-levels normally used in sub-level open stope mining.

The results for this analysis are given in Figure 5.23 for $K = 2.1$. The model outputs are given in Appendix B. Figure 5.23 shows a clear separation of the curves for the different A_r values. This implies that there is a strong effect of stope aspect ratio A_r on the influence of a fault on stope stability, for K ratio of 2.1, but may not be case for a K ratio less than 1.

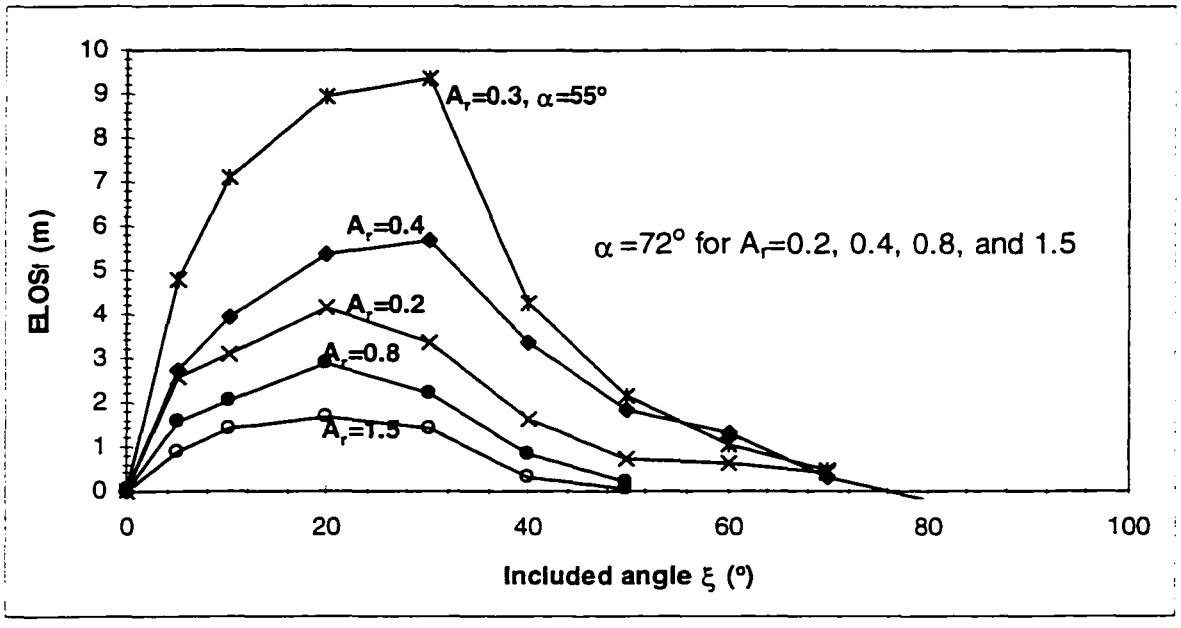


Figure 5.23 Effect of stope aspect ratio A_r on the influence of faults on hangingwall $ELOS_f$: stress ratio K = 2.1, stope aspect ratio A_r = 0.2, 0.3 (for $\alpha = 55°$), 0.4, 0.8, and 1.5, fault friction angle $\phi^* = 20°$; stope dip α = 72°

The worst overbreak occurs when the stope surface dip is 55° with an aspect ratio A_r of 0.3. The least overbreak occurs when the stope surface dip is 72° with an aspect ratio of 1.5 for the same stress ratio of 2.1. The fault has less influence on shorter stopes compared to taller ones. Stopes with smaller dips are more affected by the fault than stopes with higher dips for the same stress states and rockmass properties.

5.4.4.10 Effect of stope dip on fault effect

Two different stope dips of 72° and 55° were used in the models in order to evaluate the effect of stope dip on stope stability due to a fault, at a *K*-ratio of 2.1. The dip range used is selected to cover range of dips normally encountered in open stope mining. The results are shown in Figure 5.24 and Figure 5.25.

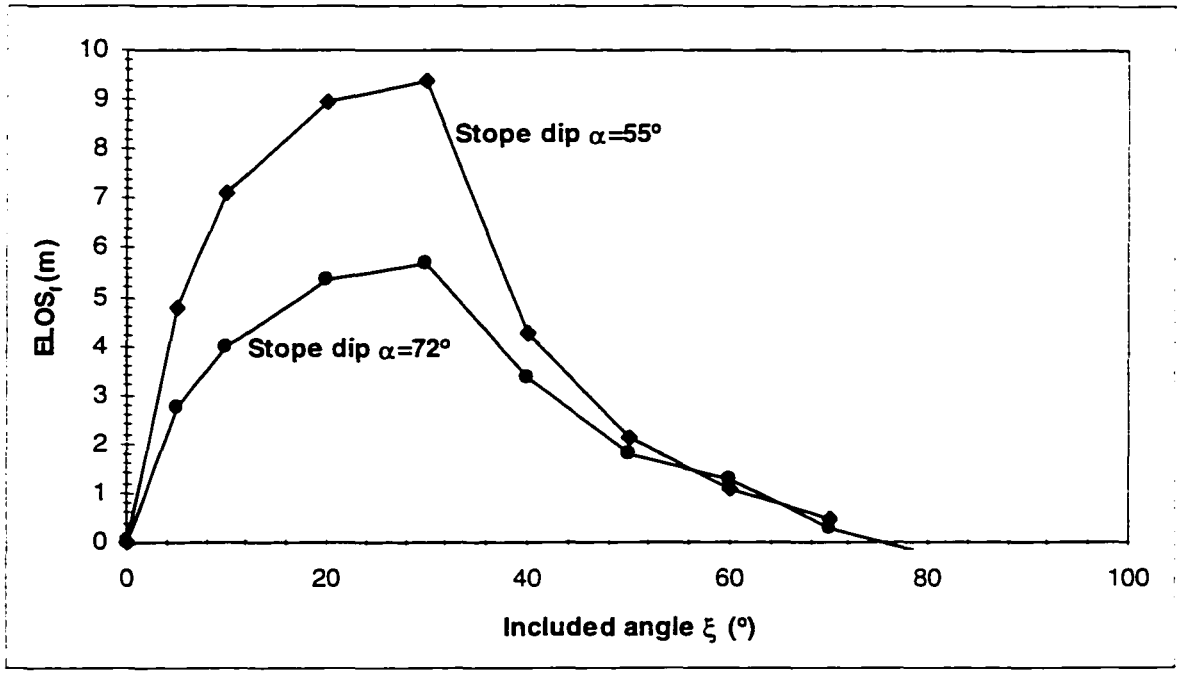


Figure 5.24 Effect of stope dip on the influence of a fault on stope stability: Stress ratio K = 2.1, stope aspect ratio A_r = 0.4, 0.3 fault friction angle ϕ^* = 20°; stope dip α = 55°, 72°

Figure 5.24 shows a very strong dependence on stope dip α, of fault effect on stope stability. Flat stopes are more affected by the fault compared to stopes with high dips for the same in situ stress state and rockmass properties. Figure 5.25 illustrates the effect of the fault at various included angles for a given stope dip α of 55° (flat stope). The tension zone, at included angles ξ of 5°, 10°, and 20° affects the stope backs for flat stopes at the assumed rockmass properties.

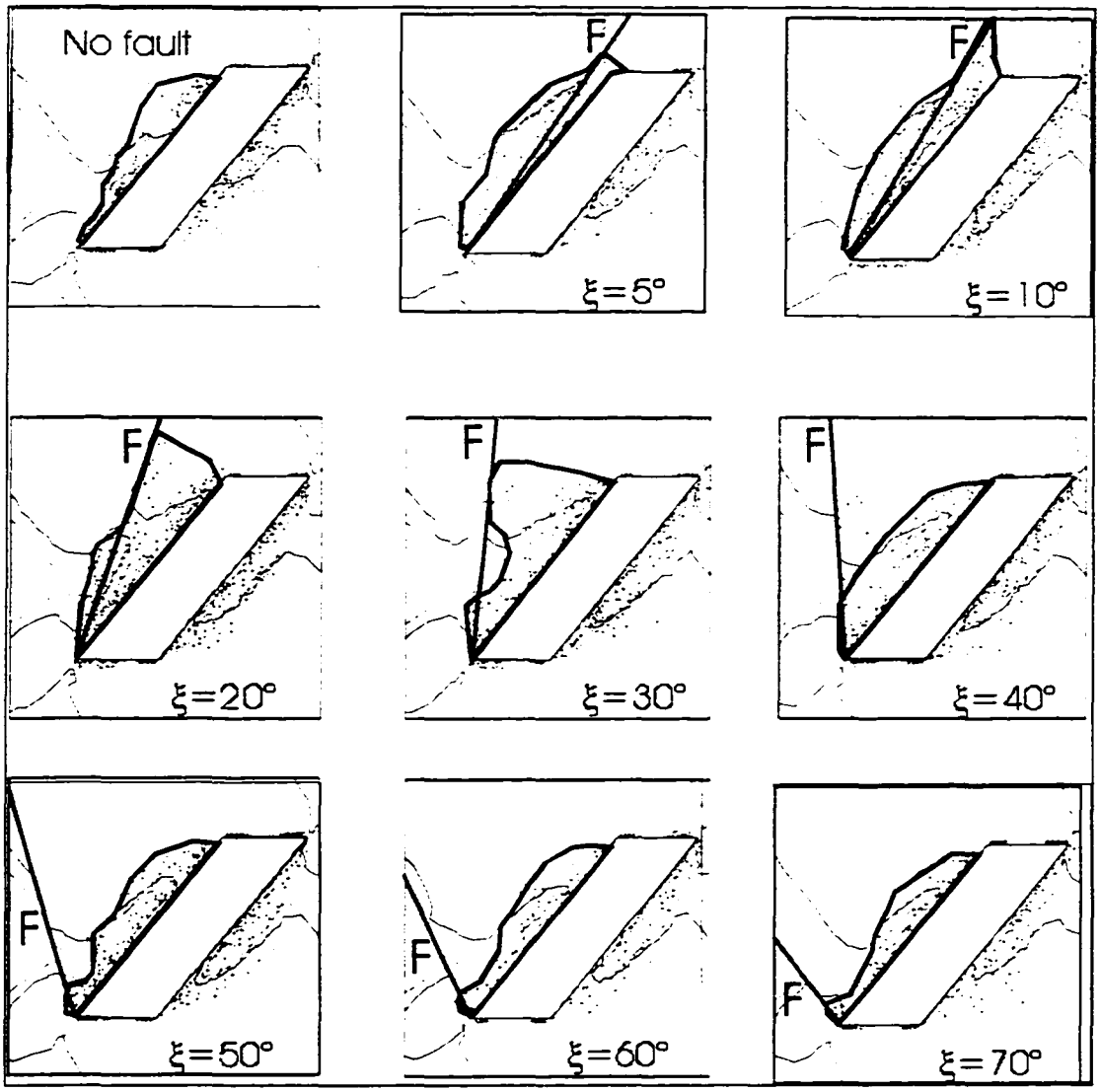


Figure 5.25 Effect of varying included angle on the influence of a fault on the stability of a stope dipping at 55°: Stress ratio $K = 2.1$, stope aspect ratio $A_r = 0.3$, fault friction angle $\phi^* = 20°$; stope dip $\alpha = 55°$, F = fault, ξ = included angle

5.4.4.11 Effect of distance of fault from stope surface - included angle $\xi = 0$

In the models for analyzing the effect of fault distance from stope surface on stope stability, the faults are introduced parallel to the stope surface at each selected distance of 1, 3, 6, 10, 15, 20 and 25 metres; or at normalized distances from 0.0-0.4.

The results are presented in Figure 5.26 for $K = 2.1$ and the assumed rockmass properties. The model outputs are presented in Appendix B. The fault distances are normalized by the stope height.

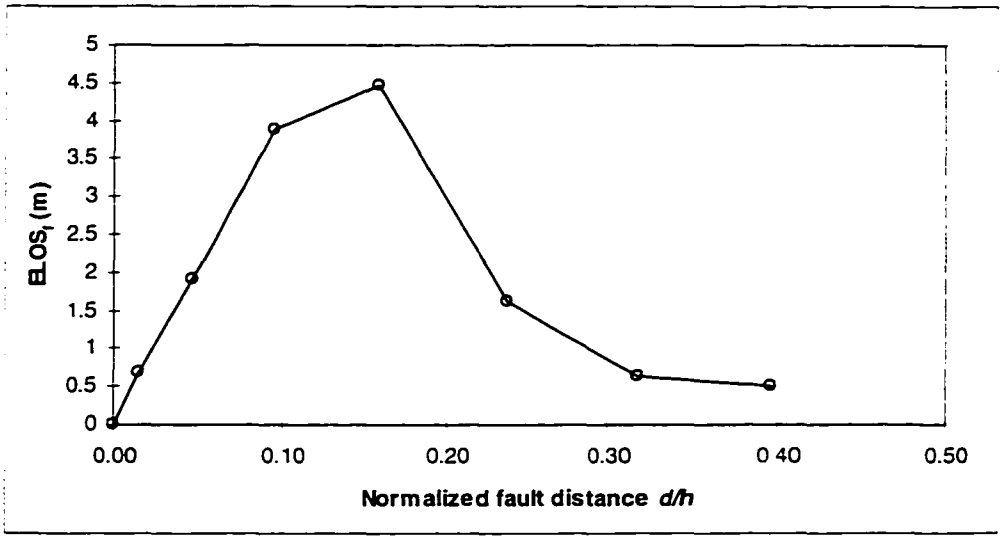


Figure 5.26 Effect of distance of fault from stope surface on the influence of the fault on $ELOS_f$: Stress ratio $K = 2.1$, stope aspect ratio $A_r = 0.4$, fault friction angle $\phi^* = 20°$; stope dip $\alpha = 72°$

Figure 5.26 shows that the distance of fault from the stope affects stope stability up to a critical distance, after which the effect diminishes. The fault distances are normalized by the slant heights of the stope surfaces. The range of normalized distance at which the fault has the most severe influence on the stope stability is 0.08 to 0.2. At normalized distances less than 0.08, the fault is, in most cases, in the tension zone of the stope without the fault. At normalized distances greater than 0.2, the effect of the fault is moderate to weak.

5.4.5 Development of generic $ELOS_f$ chart

A key guideline in developing empirical methods in rock engineering applications is that they must be simple and straightforward. They must also be strongly practically oriented so that they can form part of normal geological and rock engineering investigations for planning and design. The analysis presented above indicates several factors that have significant impact on overbreak due to faults. A parameter grouping procedure is adopted to integrate the effects of parameters that have similar effects into one.

Grouping of parameter effects is real not only for simplification purposes but because stability problems in the field are caused by a combination of factors. For example, Brekke and Selmer-Olsen (1966), state that the most relevant combinations of factors leading to difficult stability problems are montmorillonite and chlorite, in combination with very high or very low rock in situ stresses, and unfavourable directions of faults and fissures.

Figure 5.27 is plots of all parameters used in the analysis and plotted as $ELOS_f$ curves on a single $ELOS_f$ chart.

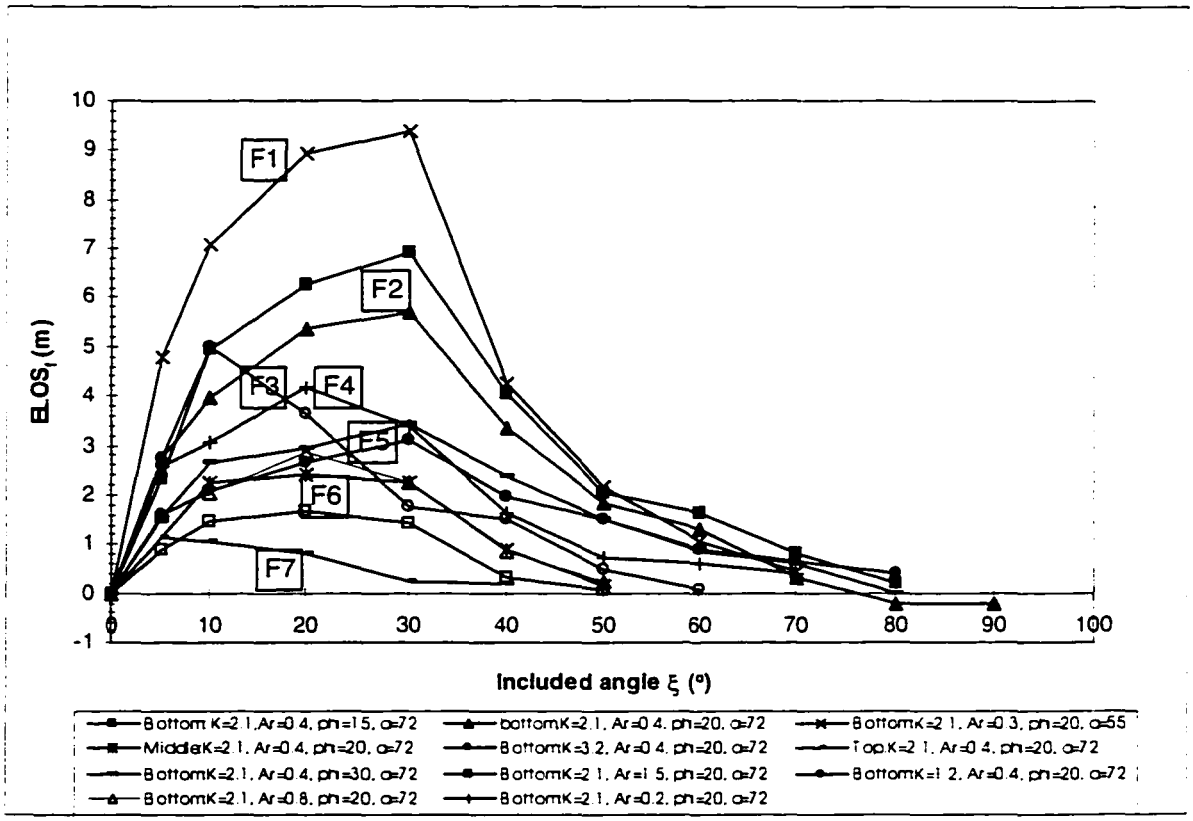
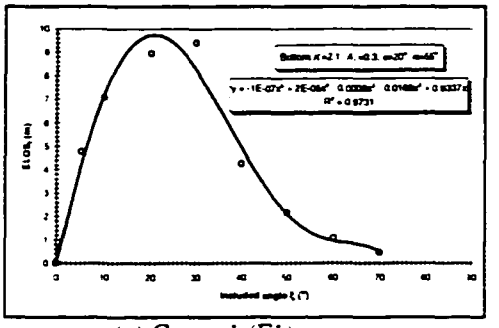


Figure 5.27 Plot of all parameters $ELOS_f$ versus included angle ξ

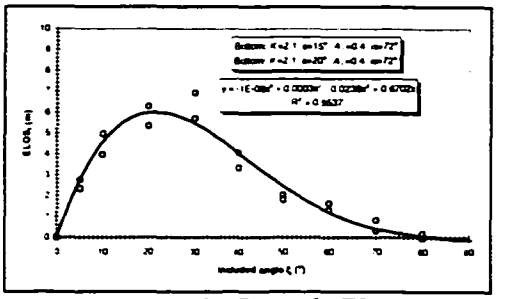
Figure 5.27 shows groups of curves (Table 5.5) with similar fault effect on overbreak of a stope surface. Seven groups of curves (F1, F2, F3, F4, F5, F6, and F7) can be identified in Figure 5.27. For each group of curves a single curve determined by curve fitting to the data can be used to represent their effects. The results of such curve-fittings, for curves of groups F1 to F7 are shown in Figure 5.28. Group 8 is for non-intersecting faults, and Group 9 for very weak faults ($\phi^* = 8°$ - residual friction angle ϕ_r plus roughness angle i).

Table 5.5 Groups of ELOS curves based on fault effects

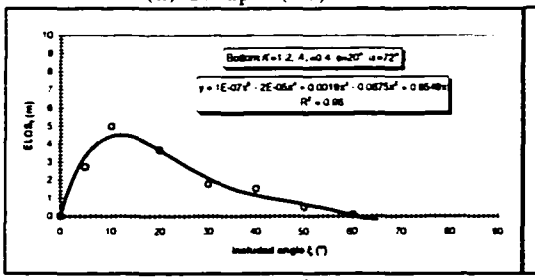
Group	Description
F1	Bottom: $K = 2.1$, $A_r = 0.3$, $\phi^* = 20°$, $\alpha = 55°$
F2	Bottom: $K = 2.1$, $A_r = 0.4$, $\phi^* = 15°$, $\alpha = 72°$
	Bottom: $K = 2.1$, $A_r = 0.4$, $\phi^* = 20°$, $\alpha = 72°$
F3	Bottom: $K = 1.2$, $A_r = 0.4$, $\phi^* = 20°$, $\alpha = 72°$
F4	Bottom: $K = 2.1$, $A_r = 0.2$, $\phi^* = 20°$, $\alpha = 72°$
F5	Bottom: $K = 2.1$, $A_r = 0.4$, $\phi^* = 30°$, $\alpha = 72°$
	Bottom: $K = 3.2$, $A_r = 0.4$, $\phi^* = 20°$, $\alpha = 72°$
F6	Middle: $K = 2.1$, $A_r = 0.4$, $\phi^* = 20°$, $\alpha = 72°$
	Bottom: $K = 2.1$, $A_r = 1.5$, $\phi^* = 20°$, $\alpha = 72°$
F7	Top: $K = 2.1$, $A_r = 0.4$, $\phi^* = 20°$, $\alpha = 72°$



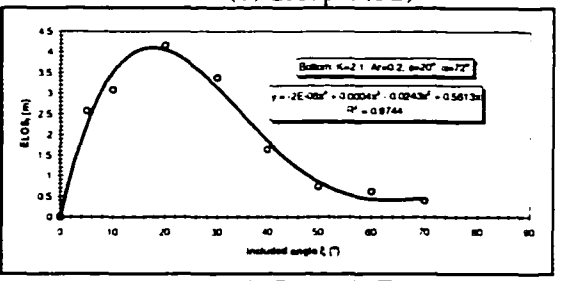
(a) Group 1 (F1)



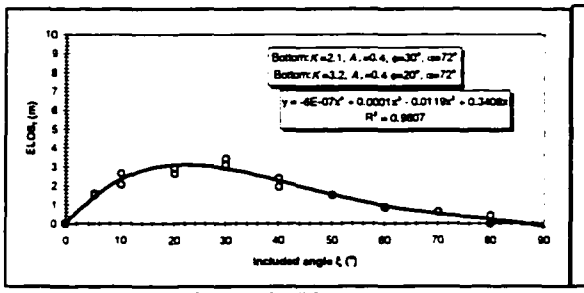
(b) Group 2 (F2)



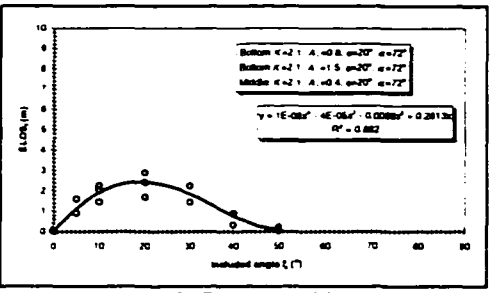
(c) Group 3 (F3)



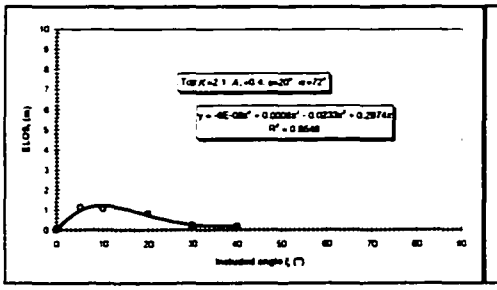
(d) Group 4 (F4)



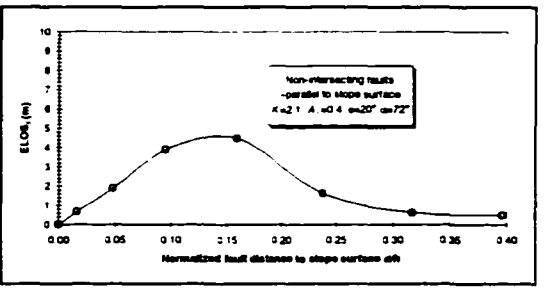
(e) Group 5 (F5)



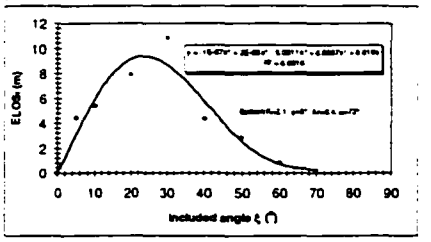
(f) Group 6 (F6)



(g) Group 7 (F7)



Group 8 (F8)



Group 9 (F9)

Figure 5.28 Curve-fitting to groups (F1 to F7) of data in $ELOS_f$ graph (Figure 5.27), Group 8 and Group 9

The generic $ELOS_f$ chart is presented in Figure 5.29.

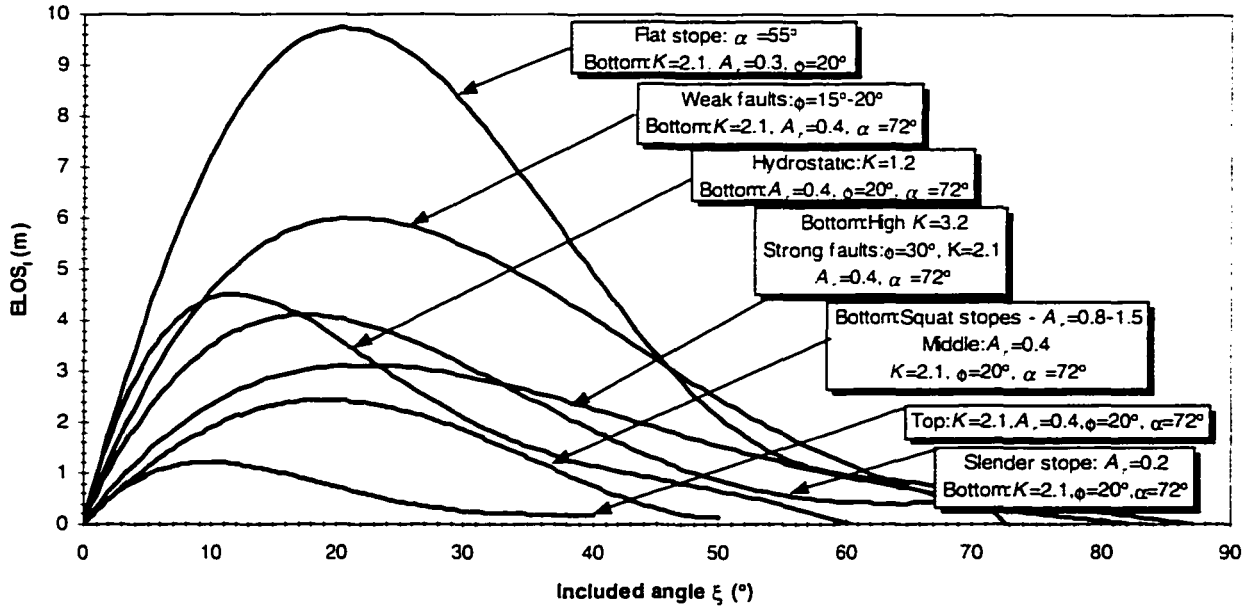


Figure 5.29 $ELOS_f$ curves for estimating depths of overbreak due to faults intersecting stope under various ground conditions and stope geometries

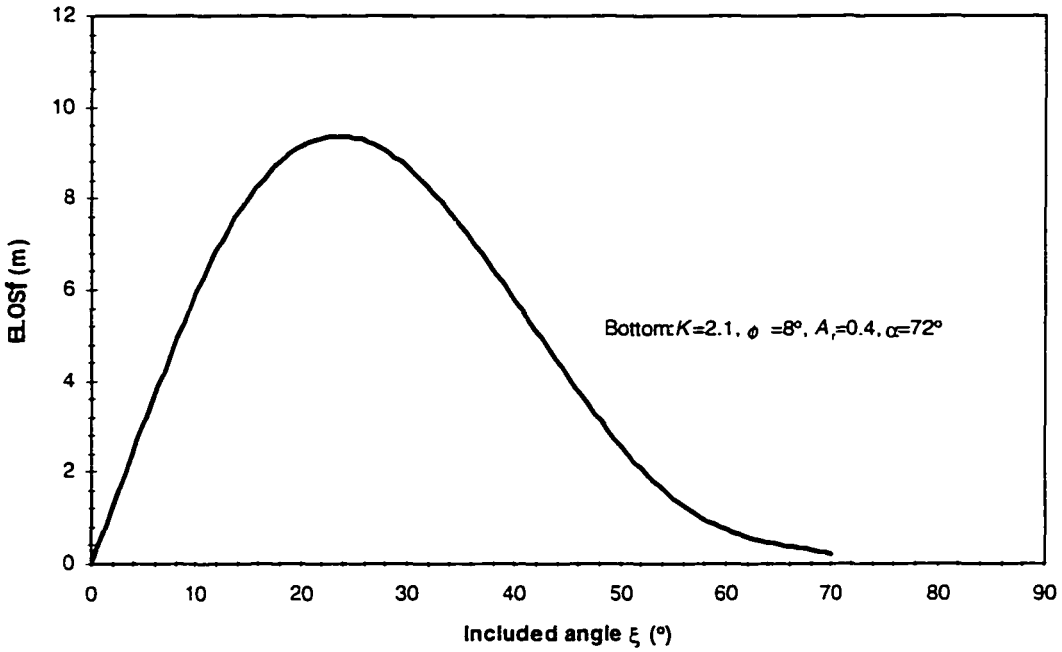


Figure 5.30 $ELOS_f$ curve for very weak faults: $\phi^* = 8°$

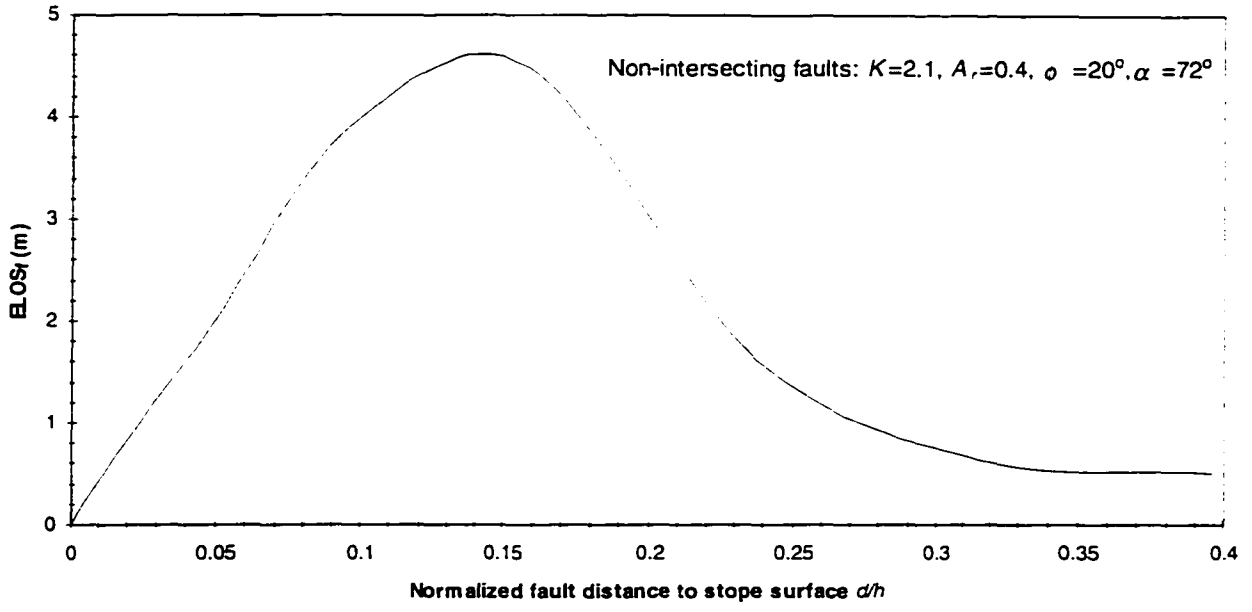


Figure 5.31 $ELOS_f$ curve for non-intersecting faults $\xi \approx 0°$

The stope surface is most affected by the fault when the fault intersects the stope surface at the bottom and the stope has a dip of 55°, or when the fault shear strength is very small, say with a friction angle of 8° and no cohesion. For the conditions investigated, the fault has little effect on the stope surface when it intersects that surface at the top. Shorter stopes are less affected by the fault compared to taller ones. For non-intersecting faults nearly parallel to the stope, the worst condition is observed when the normalized fault distance is between 0.1 and 0.2.

The procedures as presented have not accounted for a case where the fault passes through the stope intersecting both hangingwall and footwall (Figure 5.32). There is no gravity in the model, and therefore Figure 5.32 should be used in the determination of $ELOS_f$ when a fault passes through the stope. For this case, the footwall and hangingwall should be considered as separate cases and the procedure as presented applied to each case as shown.

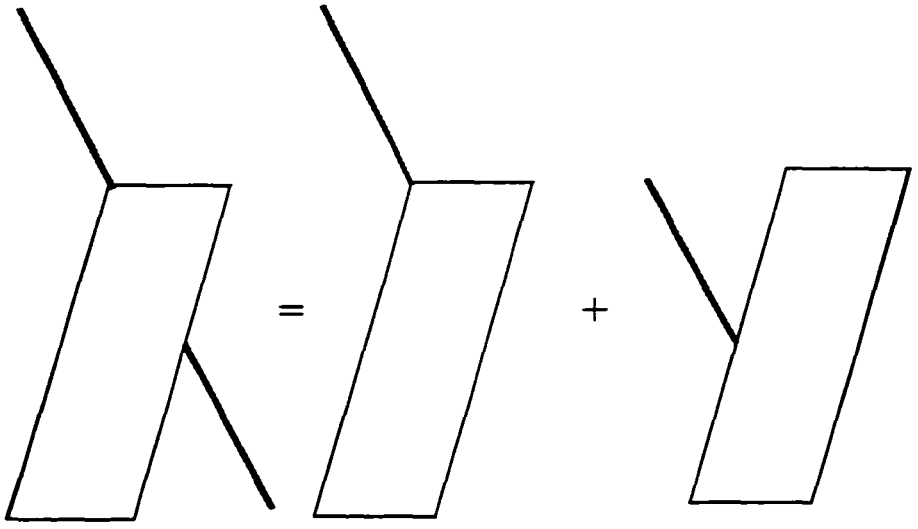


Figure 5.32 Illustration of the calculation of $ELOS_f$ when fault passes through stope intersecting both hangingwall and footwall (a).

5.4.6 Development of fault factor F_w

The principal aim of the analysis is to develop a fault factor F_w for incorporation into an empirical underground excavation design method such as the stability graph method. Thus, the fault factor to be developed should be related to existing practices of open stope design and overbreak assessment. Pakalnis and Clark (1997), following the concept of Scobble and Moss (1994), superimposed *ELOS*s on the stability graph (Figure 5.33). The *ELOS* stability graph can be used to calibrate the effects of faults on the stability number N', at various included angles ξ for different combinations of ground conditions, fault characteristics, and stope geometries.

In the *ELOS* stability graph, stope surfaces with $ELOS \leq 0.5$ m are considered stable and a 0.5 m-*ELOS* contour is used as a boundary between stable stopes and unstable stopes (stope surfaces with $ELOS > 0.5$ m).

The procedure adopted in defining the fault factor from the *ELOS* stability graph is as follows:

- Determine $ELOS_f$ due to fault in stope surface, using the included angle between the stope surface and the fault as discussed.
- Determine a hydraulic radius for the hangingwall of the modelled stope by assuming a design stope length - a length of 15 m is used throughout the analysis.
- The minimum $ELOS_f$ is always zero ($ELOS_f$ is incremental), and falls on the *ELOS* contour for stable stope surfaces, $ELOS \leq 0.5$ m.
- Trace the hydraulic radius vertically up to meet the $ELOS = 0.5$ m curve. By moving horizontally from the point of intersection of *HR* and $ELOS = 0.5$ m curve to the N'- axis, the corresponding stability number N'_o for no sloughage is determined for the rockmass (Figure 5.34).

- Use the same procedure to determine the stability numbers for all other $ELOS_f$ values N'_ξ from the *ELOS* stability graph (Figure 5.33). Extrapolation between contours on the *ELOS* stability graph is sometimes necessary.
- The ratio of N'_ξ at given included angles to the stability number for no sloughage N'_0, is defined as the fault factor F_w. (Equation 7.27).

$$F_w = \frac{N'_\xi}{N'_0} \qquad 5.25$$

F_w will have a maximum value of 1 where the fault has no adverse effect on stope sloughage and a minimum value close to zero. The minimum value is determined from the analysis.

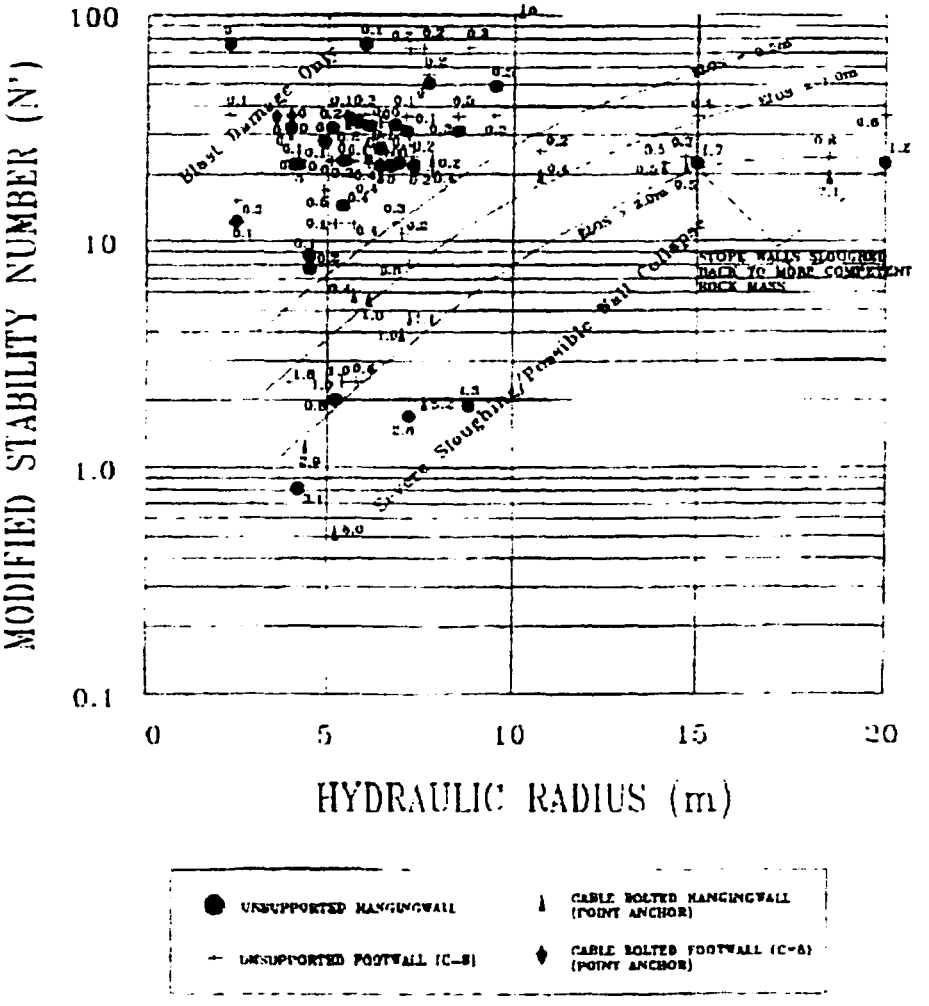


Figure 5.33 *ELOS* stability graph (from Clark and Pakalnis, 1997)

Figure 5.33 presents results of equivalent linear overbreak sloughage *ELOS* values superimposed on the stability graph by Clark and Pakalnis (1996), according to dilution contours proposed by Scobble and Moss

(1994). The graph is still in the stage of being fine-tuned, as more data become available. There is some scatter in the data, but the graph is sufficiently accurate for use in predicting dilution and the fault factor. The addition of data will help define contours below ELOS values of 2 but will not significantly affect current contours. Figure 5.33 is used in defining the fault factor as shown in Figure 5.34.

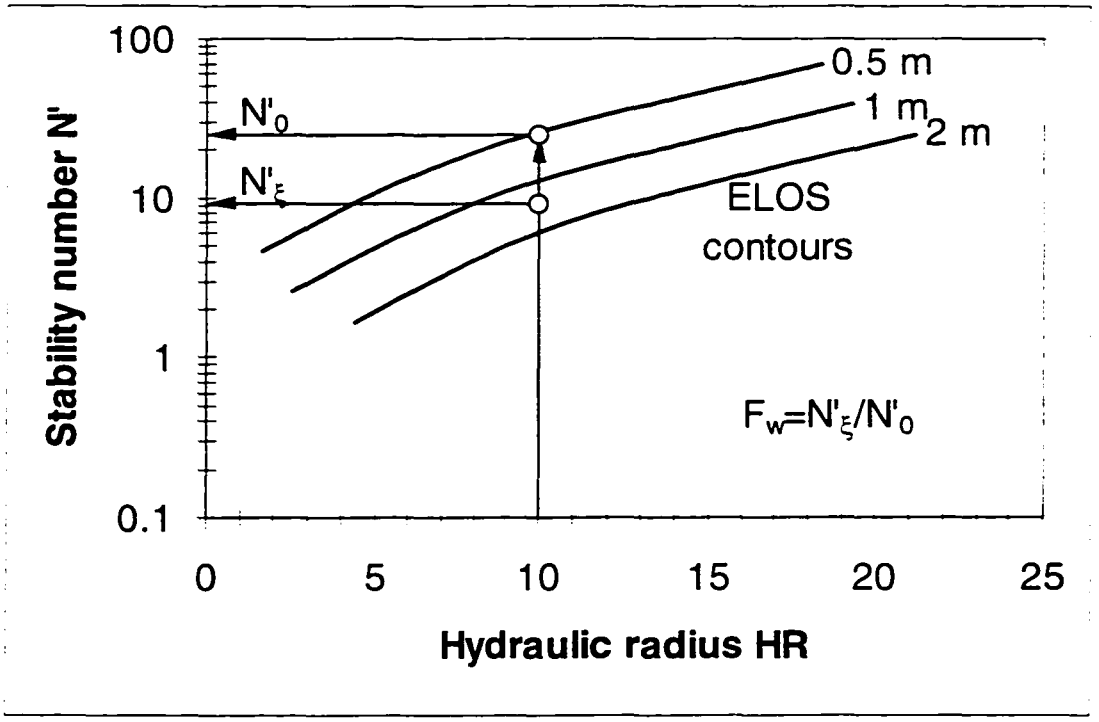


Figure 5.34 Determination of fault factor F_w

The procedure presented above was used to determine fault factors for the various factors that are identified to influence the effects of faults on open stope stability. It was stated in Section 5.1 that the fault factor curves are the inverse of the overbreak curves, as shown in the sections that follow, by using the procedure presented in this section.

5.4.6.1 Effect of fault position and included angle

A fault factor graph based on fault position is presented in Figure 5.35. A stability index such as the modified stability number N' can be adjusted to cater for the intersection of the stope surface by a fault, if the position of the intersection and the included angle are known.

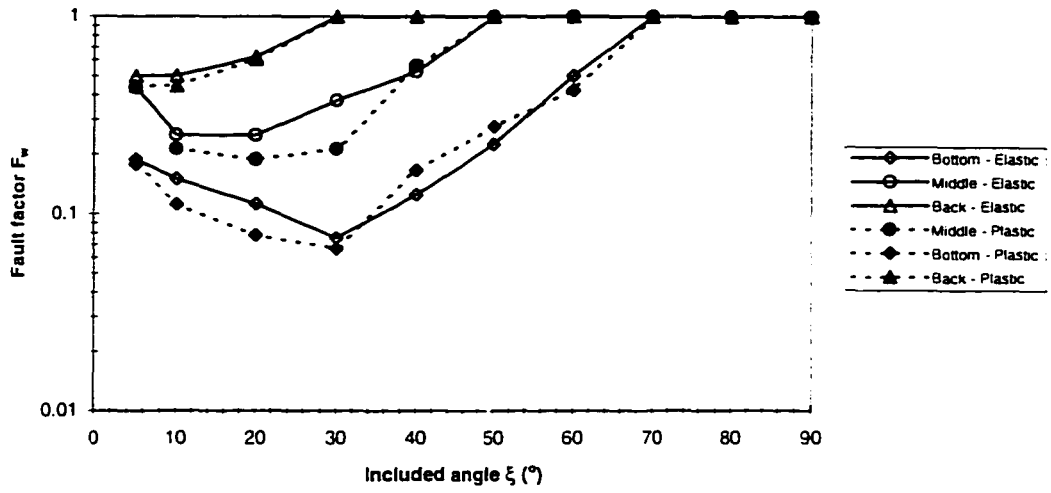


Figure 5.35 Fault factor graph based on fault position: Stress ratio $K = 2.1$, stope aspect ratio $A_r = 0.4$, fault friction angle $\phi^* = 20°$, stope dip $\alpha = 72°$.

The graph also shows that for each fault position the fault factor depends on the angle between the fault and the stope surface. The value of a given N' could be reduced by about one order of magnitude depending on the position of the fault on the stope surface.

5.4.6.2 Effect of fault shear friction angle

The fault factors for the three fault friction angles used are presented in Figure 5.36. It shows that for fault friction angles greater than 30°, fault friction angle has relatively little influence on the fault factor for the assumed stress state and rockmass strength parameters. For weak faults with shear strengths of $\phi^* = 8°$, the fault factor could reduce N' by about three orders of magnitude.

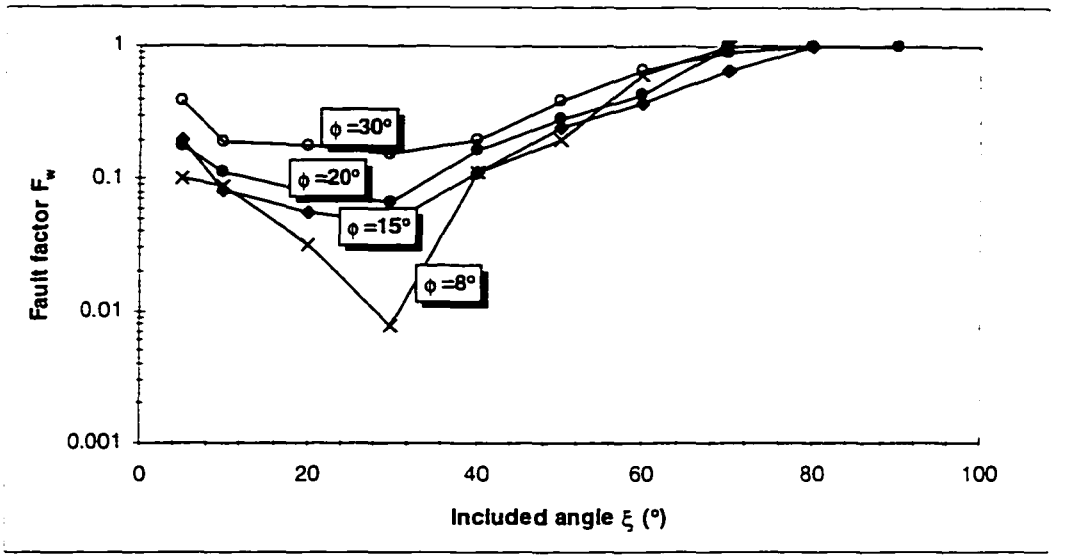


Figure 5.36 Fault factor based as a function of fault shear strength: Stress ratio K = 2.1, stope aspect ratio A_r = 0.4, fault friction ϕ^* = 8°, 15°, 20°, 30°; stope dip α = 72°

5.4.6.3 Effect of stress ratio

Figure 5.37 is a fault factor graph for stress ratios of 1.2, 2.1, and 3.2. There is a moderate influence of K-ratio on the fault factor. The wedge cut-off mechanism results in strong fault effect on stope stability as conditions approach the hydrostatic state, for the assumed rockmass properties. If the ξ between the stope and fault surface is between 40° and 45°, the fault effect is much less, and negligible for included angles ξ equal to or greater than 45°.

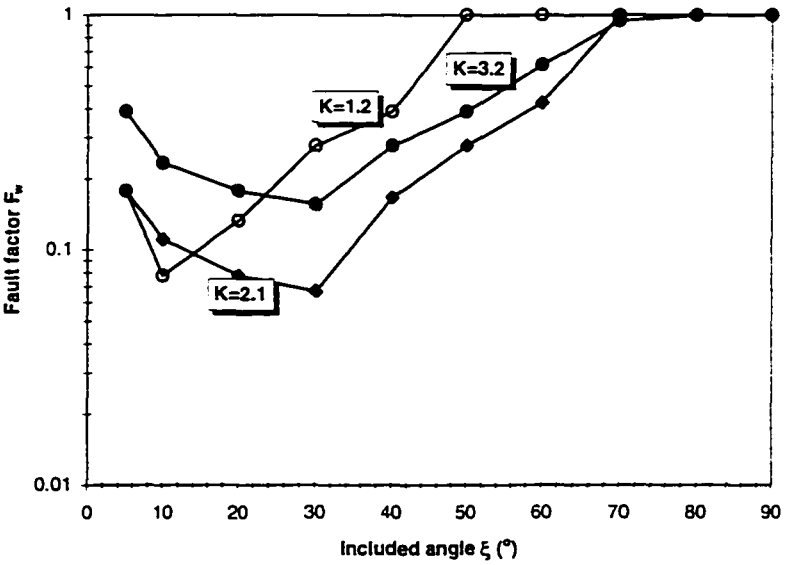


Figure 5.37 Fault factor as a function of stress ratio K: Stress ratio K = 1.2, 2.1, 3.2; stope aspect ratio A_r = 0.4, fault friction angle ϕ^* = 20°; stope dip α = 72°

Effect of K ratio could result in a reduction in N' by about as much as one order of magnitude.

5.4.6.4 Effect of stope aspect ratio

A fault factor graph based on stope aspect ratio is given in Figure 5.38

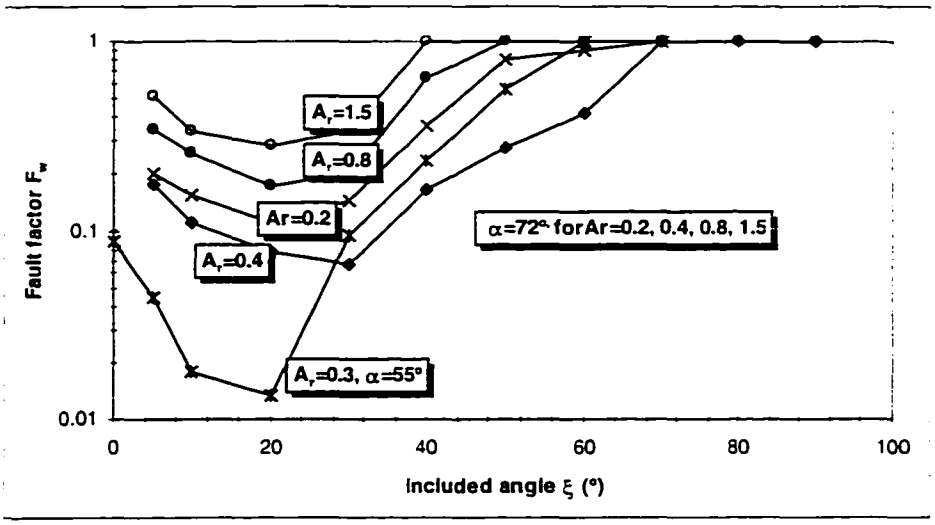


Figure 5.38 Effect of stope aspect ratio A_r on fault factor: Stress ratio $K = 2.1$, stope aspect ratio $A_r = 0.4$, 0.8, 1.5, fault friction angle $\phi^* = 20°$; stope dip $\alpha = 72°$

Figure 5.38 shows stope aspect ratio could reduce N' by about one order of magnitude, for given rockmass parameters and stope geometry and K-ratio.

5.4.6.5 Effect of stope dip

The effect of a stope dip α on the fault factor is presented in Figure 5.39 for stope dips of 55° and 72°, at the assumed rockmass properties and $K = 2.1$.

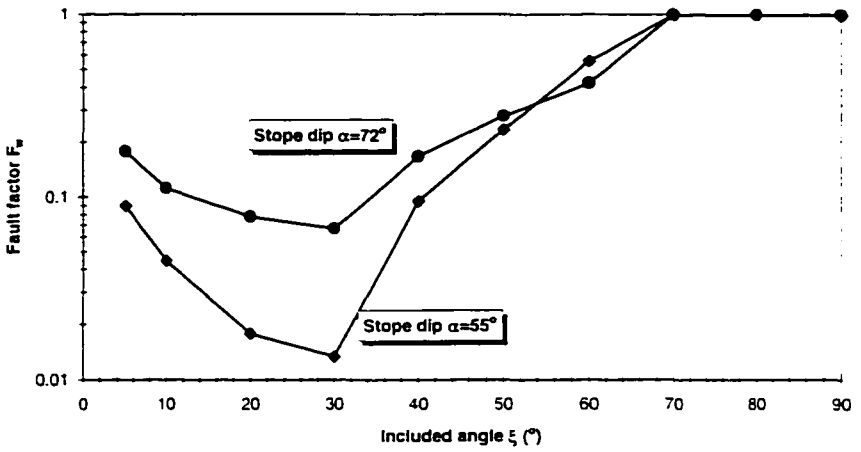


Figure 5.39 Fault factor showing effect of stope dip: Stress ratio $K = 2.1$, stope aspect ratio $A_r = 0.4, 0.3$, fault friction angle $\phi = 20°$, stope dip $\alpha = 55°, 72°$

Figure 5.39 shows that the influence of stope dip on the fault factor, is very strong. Faults will affect flat stopes more than vertical stopes by reducing N' by about two orders of magnitude.

5.4.6.6 Effect of fault distance

Figure 5.40 is the fault factor graph for non-intersecting faults approximately parallel to a stope surface. Figure 5.40 shows that the most critical normalized distance is between 0.08 and 0.2.

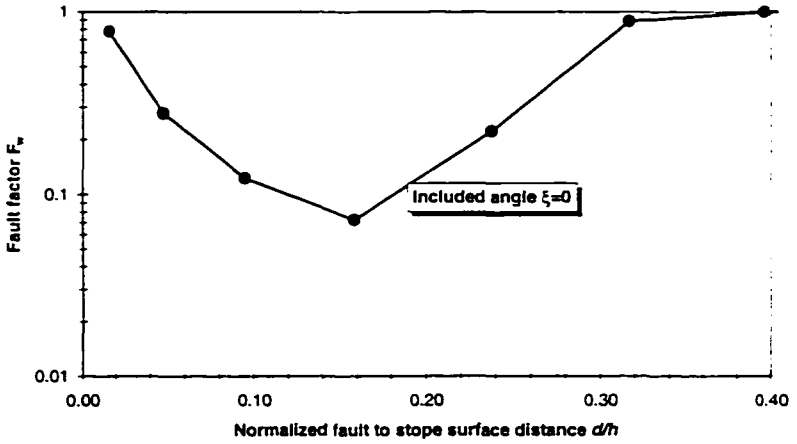


Figure 5.40 Effect of fault distance on fault factor: Stress ratio $K = 2.1$, stope aspect ratio $A_r = 0.4$, fault friction angle $\phi^* = 20°$; stope dip $\alpha = 72°$

The fault factor could reduce N' by about one order of magnitude.

5.4.7 Generic fault factor

Similar analysis used in Section 5.4.5 to arrive at general $ELOS_f$ curves is used to develop a generic fault factor graph. Figure 5.42 presents the curve fitting results for groups G1, G2, G3, G4, G5, G6 and G7 in Figure 5.41. Table 5.6 is a summary of the group descriptions. A smoothened curve for non-intersecting faults (Group 8) is presented. Group 9 is for very weak faults with ϕ^*=8°. Groups 6, 7 and 9 will reduce N' by about 2 to 3 orders of magnitude. Groups 1to 5 will generally reduce N' by about 1 to 2 orders of magnitue.

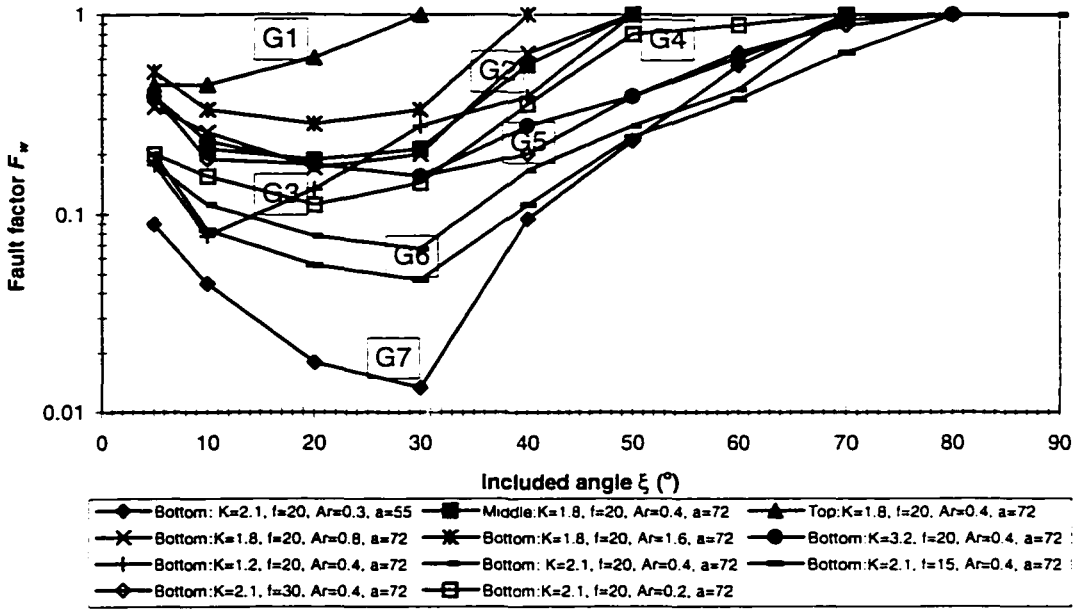
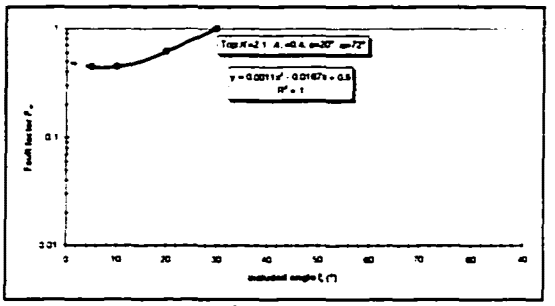


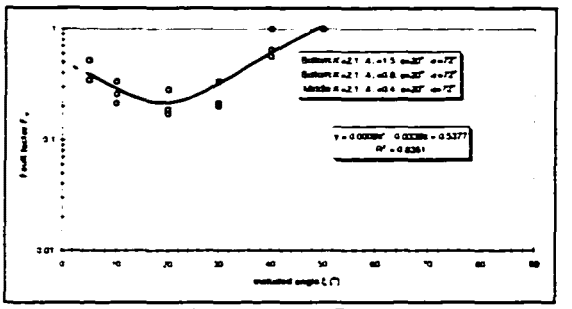
Figure 5.41 Plot of all parameters fault factor graphs, showing parameter groupings

Table 5.6 Summary of fault factor curves according to similarity in behaviour as per Figure 5.41

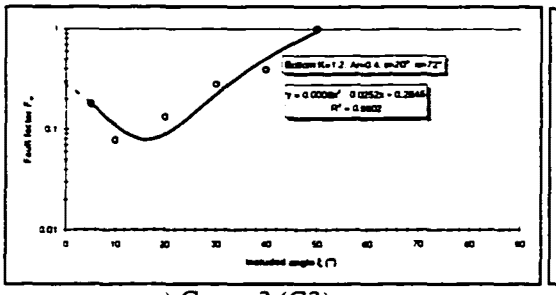
Group	Description
G1	Bottom: K = 2.1, A_r=0.3, ϕ^* = 20°, α = 55°
G2	Bottom: K = 2.1, A_r = 0.4, ϕ^* = 15°, α = 72°
	Bottom: K = 2.1, A_r = 0.4, ϕ^* = 20°, α = 72°
F3	Bottom: K = 1.2, A_r = 0.4, ϕ^* = 20°, α = 72°
G4	Bottom: K = 2.1, A_r = 0.2, ϕ^* = 20°, α = 72°
G5	Bottom: K = 2.1, A_r = 0.4, ϕ^* = 30°, α = 72°
	Bottom: K = 3.2, A_r = 0.4, ϕ^* = 20°, α = 72°
G6	Middle: K = 2.1, A_r = 0.4, ϕ^* = 20°, α = 72°
	Bottom: K = 2.1, A_r = 1.5, ϕ^* = 20°, α = 72°
G7	Top: K = 2.1, A_r = 0.4, ϕ^* = 20°, α = 72°



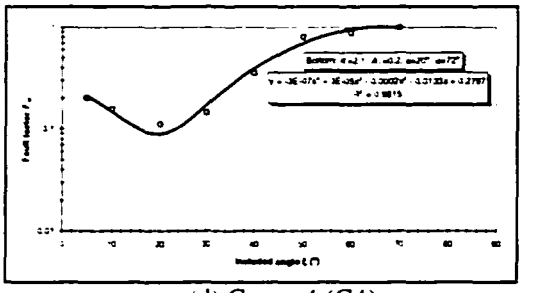
(a) Group 1 (G1)



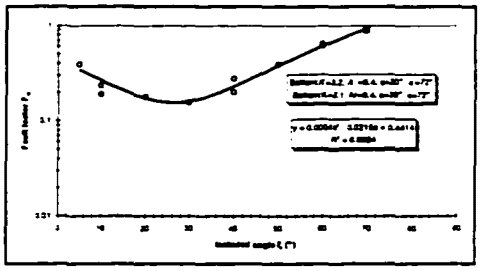
(b) Group 2 (G2)



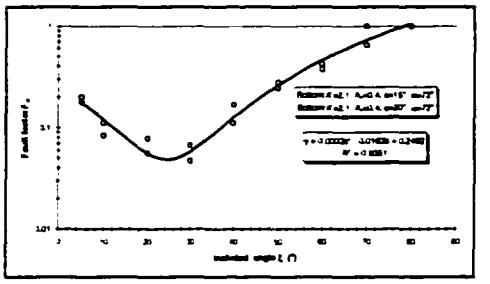
(c) Group 3 (G3)



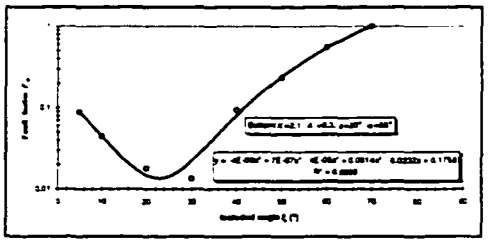
(d) Group 4 (G4)



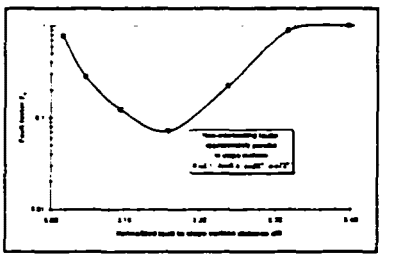
(e) Group 5 (G5)



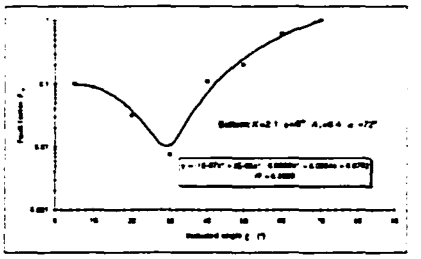
(f) Group 6 (G6)



(g) Group 7 (G7)



Group 8 (G8)



Group 9 (G9)

Figure 5.42 Curves fitted to groups (G1 to G7) of data in fault factor graph (Figure 5.41), and smoothened graph for non-intersecting faults (Group 8) (cont. next page)

Figure 5.43 is the simplified generic fault factor graph for all data groups in Figure 5.41 for faults intersecting stopes. The fault factor curves very weak faults (Group 9) and non-intersecting faults (Group 8) are presented separately in Figure 5.44 and Figure 5.45.

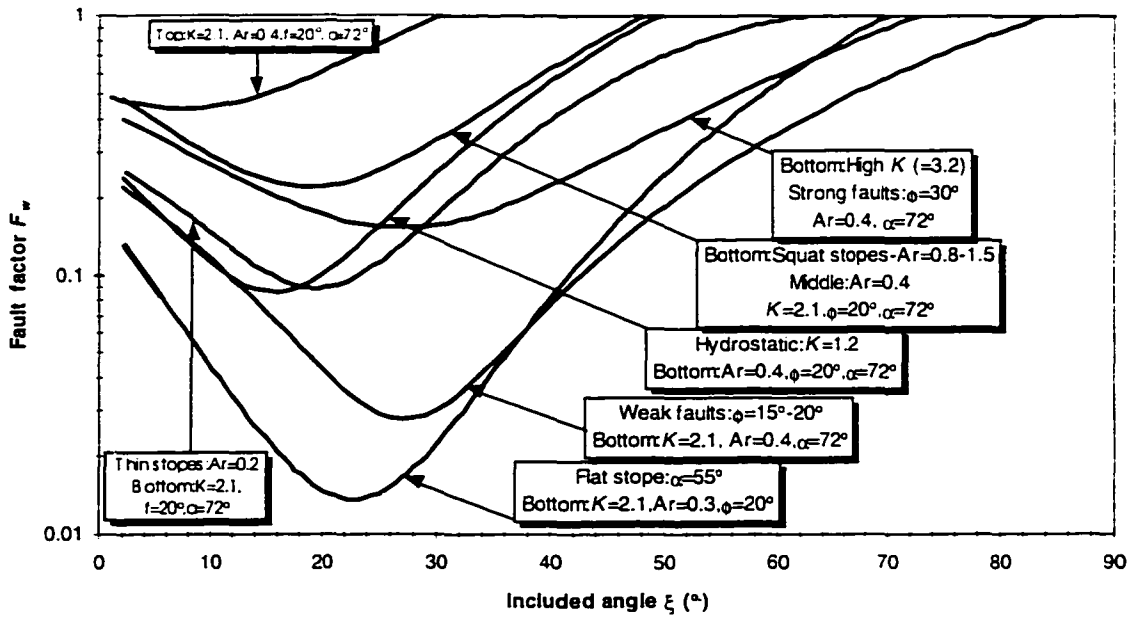


Figure 5.43 Fault factor curves for faults intersecting stopes

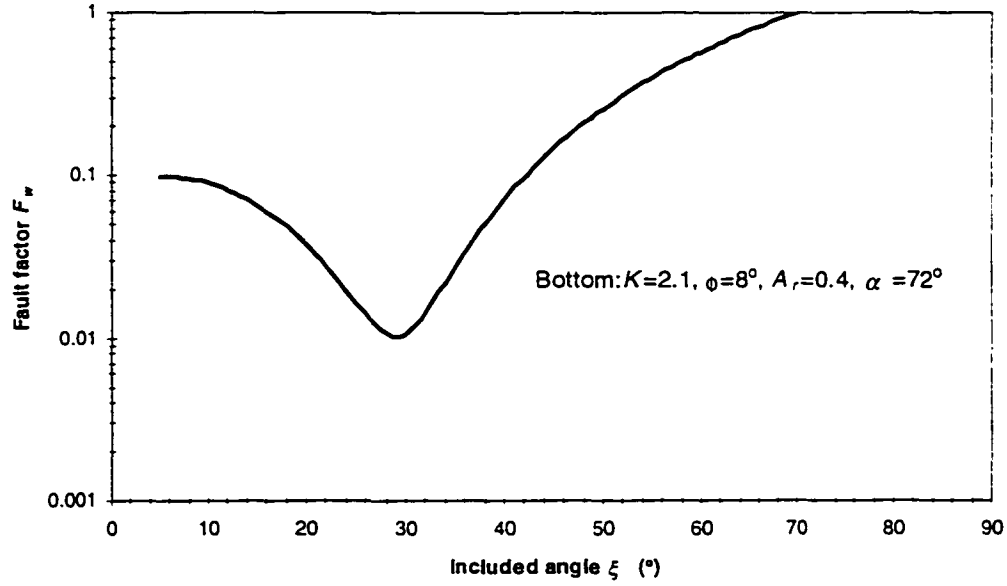


Figure 5.44 Fault factor curve for very weak faults intersecting stope at bottom

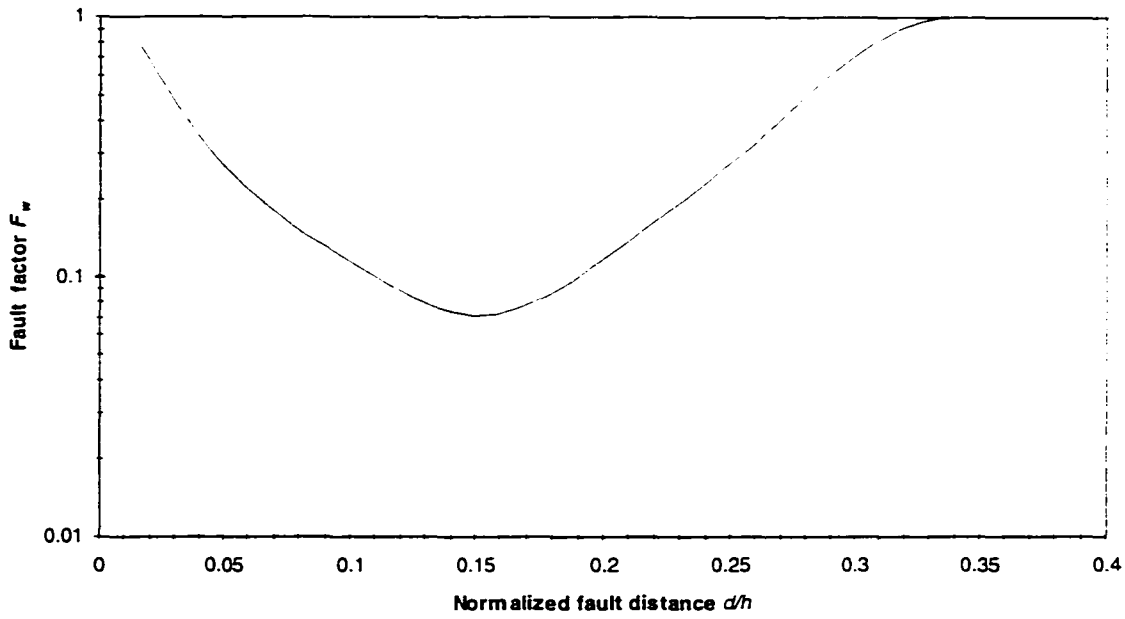


Figure 5.45 Fault factor curve for non-intersecting faults with $\xi = 0$

The fault factor curves are recommended for assessing fault effects on open stope stability, but should be further calibrated for flat stopes. It can be incorporated into the stability graph method and is applied to a case study in Chapter 6.

The fault factor F_w ranges between 0.008 to 1 and can reduce the value of N' by up to 3 orders of magnitude. The joint defect factor B reduces N' by only one order of magnitude, and the gravity factor C, affects N' by only 0.4 orders of magnitude. Consequently, the fault factor is more important in assessing stope stability than B and C when faults are near a stope.

A total of seven identical groups of parameters have been identified in Figure 5.27 and Figure 5.41. The seven groups have practical implications in stope design, and are summarized in Table 5.7.

The parameter combinations are, generally, not additive, but depends on how similar a given combination affects the stope compared to other combinations of factors. However, in field situations, combinations of sensitive parameters such as poor fault friction angle, low dipping hangingwalls, unfavourable stope aspect ratio A_r and unfavourable K-ratio could result in a fault factor F_w that can reduce N', by more than three orders of magnitude.

Table 5.7 Summary of fault effect on stope stability with reference to parameter groups

Parameter group	Impact on stope performance	Remarks
Fault intersecting stope at top	N' reduced by about 2 times	High compressive stresses at back clamp fault
Slender/thin stopes	N' could be reduced by about 10 times	Relatively tall and slender stopes
Flat stopes	N' could be reduced by about 80 times	Exposed hangingwall surface is increased, and gravity has maximum effect on wedges
Squat stopes and faults intersecting stope at middle	N' could be reduced by about 5 times	Short stopes and when fault intersects stope at middle
Very weak faults ($\phi^* = 8°$)	N' could be reduced by about 100 times	Faults strengths encountered in the field ($\phi^* = 6°$-$36°$)
Near hydrostatic stress state	N' reduced by about 2 times	Wedge cut-off mechanism may occur
High K-ratio and strong faults	N' reduced by 5 times	$K = 3.2$ and faults with $\phi^* = 30$
Non-intersecting faults $\xi \leq 0°$	N' could be reduced by about 15 times	Faults approximately parallel to stope surface.

5.5 Discussion of results and implications

5.5.1 Observational and analytical generic fault factors

Schematic fault factor graphs deduced from the observational data in Table 5.1 and from the analytical methods are presented in Figure 5.46. The fault factor graphs from these methods show similar characteristics to those obtained from the numerical models (Figure 5.46).

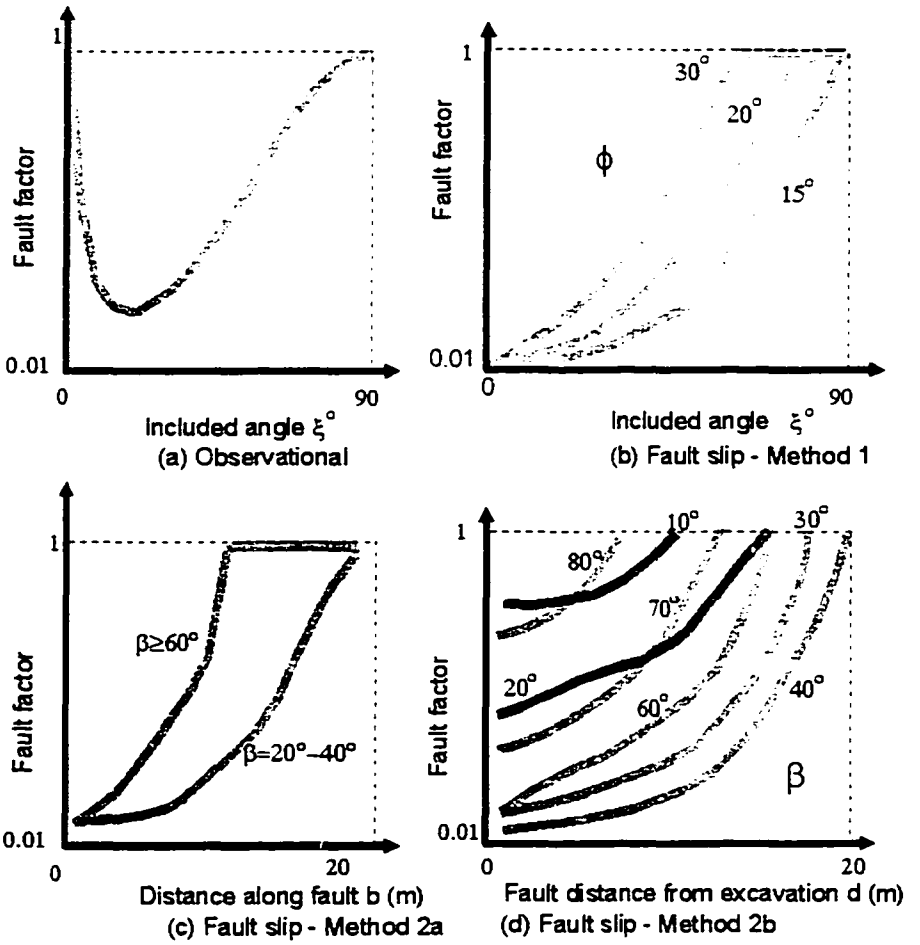


Figure 5.46 Generic fault factor graphs based on observational and analytical models (a) effect of included angle (b) effect of fault friction angle (c) & (d) effect of distance

The similarity between effect of fault friction angle on the fault factor from the analytical and numerical models is significant at large included angles. However, at low included angles, the fault factor from analytical models, approaches zero, for all friction angles. This is a defect of the analytical model. Figure 5.46d indicates that the effect of fault distance on the fault factor, for non-intersecting faults, strongly depends on the orientation of the fault. This aspect has not been considered in the numerical models, but is essential and could be accounted for using the established procedures.

5.5.2 Summary of individual parameter effects

Table 5.8, Table 5.9 and Table 5.10 summarize the influence of individual parameters on fault effect on stope stability.

Table 5.8 Evaluation of factors influencing the effects of faults on open stope stability

Factor	Estimation of fault effect F_w on N'	Remarks
Fault position	N' reduced by about 1 order of magnitude	
Included angle between fault and stope surface $\xi°$	N' could be reduced by about 1 orders of magnitude	This is dependent on other the factors
Stress ratio K	N' could be reduced by as much as 2 orders of magnitude	At high stress ratio such as K = 3.2, stopes without faults by themselves suffer deep relaxation. Introduction of a fault makes little influence
Stope aspect ratio A_r	N' could be reduced by 2 (Ar = 0.3 α = 55°) orders of magnitude	Strong for fault factor when
Fault shear strength τ_{fs}	N' could be reduced by as much as 3 orders (ϕ = 8°) of magnitude	Weak at shear strengths of gouge materials normally encountered (i.e. ϕ * = 6° - 36°)
Fault distance from stope surface	N' reduced by about 1 orders of magnitude	See table below
Stope dip $\alpha°$	N' reduced by about 2 orders of magnitude	

Table 5.9 Assessment of effect of distance of fault to stope surface on surface stability

Distance (m)	Classification	Remarks
<0.08	F_w> = 0.15	Faults in relaxed zone of excavation without the fault
0.08 - 0.2	F_w between 0.07 – 0.15	Faults outside relaxed zone of stope without fault
0.2 - 0.3	F_w between 0.15 – 0.9	Fault significantly distant from stope
>0.3	F_w>0.9	Fault too far to affect stope significantly

Table 5.10 Classification of fault effects on stability based on position and included angle ξ

Fault intersecting position	Included angle $\xi(°)$	Severity of effect
Bottom	<10	Moderate
	10 – 40	Very strong
	40 – 80	Moderate to weak
	>80	Weak
Middle	<10	Moderate
	10 – 30	Very strong
	30 – 45	Moderate to weak
	>45	Weak
Back/top	<15	Moderate
	15 – 30	Moderate to weak
	>30	Weak

The tables show that where a fault is near a stope, or intersects the stope, N' could be reduced by as much as two orders of magnitude. The worst effect occurs when the included angle between the stope surface

and fault is between 10° and 40°, with the fault intersecting the stope surface at the bottom. When the fault is favourably oriented (i.e. at angles near 90°) the value of N' is unaffected.

The position at which a fault intersects the stope wall has a very strong influence on the size of the tension zone. For the same ground conditions at the same included angles, the tension zone is greatest when the fault intersects the stope surface at the toe. Tension zones for faults intersecting stope surfaces at the middle are larger compared to the fault intersecting the stope at the top.

The model results show that the angle between the fault and stope surface has a very strong impact on the size of the tension zone. This agrees with observations made by Daemen (1983) from elastic analysis results on the effect of weakness planes, on stresses around circular openings. For included angles less than or equal 20°, the tension zones have the tendency to extend above the back of the stope even at low K-ratios.

Stope backs are usually highly stressed, particularly in regions of relatively high horizontal stresses. Instability by fracture of intact rock may occur when induced stresses approximate 0.3 of uniaxial compressive strength UCS of intact rock. In these circumstances, faults at included angles less than or equal 20° become advantageous as de-stressing agents, provided the de-stressing does not lead to loss in confinement to below 100 kPa.

A K-ratio near hydrostatic condition gave the minimum tension areas for corresponding included angles, compared to K values of 2.1 and 3.2. However, K-ratios close to one have the tendency to induce isolated tension zones at the toe and top of the hangingwall (Figure 5.21b and c) thereby detaching the wedge between the fault and stope surface. This wedge cut-off phenomenon can lead to a massive failure in the hangingwall even though the tension zones by themselves are negligible. A K-ratio of 3.2 resulted in deep tension zones in the hangingwall.

Faults intersecting the stope at the back at included angles less than 25° with the hangingwall are clamped, by the large induced back stresses and have little adverse effect on hangingwall stability.

Excavation geometry affects the stress distribution in the excavation walls. Stope dip and stope aspect ratios were varied to evaluate their effect on the influence of a fault, on the size of the tension zone. A definition of stope aspect ratio for both longitudinal and transverse stopes is given as ratio of stope largest horizontal dimension to stope height. The stope aspect ratio is found to have very strong influence on the average depth of overbreak, with an aspect ratio A_r of 1.5 not critical. The example case of a slender stope with Ar = 0.2 is equivalent to a high vertical stress relative to horizontal stress regime. The stope dip also has a very strong influence on the size of the tension zone. It could be concluded that for open stopes in an orebody that will have dips less than or equal to 55°, open stope mining may not be a suitable mining method, where faults are present.

The distance of a non-intersecting fault on the stope surface is an important factor that affects stope performance. These types of faults are more dangerous than faults that daylight in the stope surface. Non-intersecting near parallel faults can cause unexpected massive failures. Deere (1979) describes invisible geologic structures as treacherous. Boyd (1988) observed that the most dangerous type of kinematic failure is that caused by a fracture that is invisible because it does not intersect the excavation surface.

5.5.3 Implications for overbreak estimation and support design

Kastner (1979) and Widerhofer (1970) provided a method for estimating plastic zones around circular tunnels in biaxial stress fields. Bieniawski and Bauer (1982) used the method to estimate potential failure zones around circular tunnels in deep coal mines that suggests that the results of the modelling could be of enormous assistance in controlling hangingwall overbreak.

The results of the analysis presented give an indication of the size of tension zones in open stope hangingwalls with or without faults under various combinations of influence factors. The tension zones are a measure of the deadweight that installed support is expected to carry. The tension zones have also been used to estimate the depth of overbreak in the hangingwall. Knowledge of depth of overbreak, and the extent of tension zones are important for the design of support for an excavation surface. Depth of overbreak and extent of tension zones provide estimates for lengths, spacing and capacity of active support, required to stabilize the surface. Figure 5.22 provides a means for estimating lengths of cable or rock bolt. The pictorial model outputs such as presented in Figure 5.22 and Figure 5.25, even though 2-dimensional, can be used in estimating support grid density and orientations. Similar figures for other geometries can be quickly generated from elastic models at mine sites with the proper input data.

5.6 Summary

Effects of faults on the stability of underground excavations have been analyzed using knowledge of observed field data, analytical methods and numerical models.

Faults tend to affect the stability of open stopes by their tendency to increase the zone of low stress near the stopes. The area of the tension zone around excavations in two-dimensions, or the volume in three-dimensional cases, is dependent on the angle between the stope surface and fault ξ, stope surface dip α, in situ stress ratio K, the stope aspect ratio A_r, the distance of the fault from the stope surface d, if non-intersecting, and the fault shear strength.

The effects of these factors in changing the size of the tension zones have been assessed. The tension zones provide an estimate of the amount of possible overbreak in the hangingwall due to the fault for a given rockmass properties and stress ratio. Hoek and Brown (1980) discuss the conditions for structurally controlled failure in excavation walls, and the mechanisms by which the failure occur.

A parameter for comparing the extent of overbreak, due to a fault, as a result of the influence of various factors is identified as $ELOS_f$. Figure 5.29 to Figure 5.31 are presented for estimating overbreak in open stope hangingwalls with faults. The procedure can also be applied to predict overbreak in stopes without faults.

A major criticism against the modified Mathews method of open stope design is the fact that it does not incorporate a factor for accounting for fault effects. Most metalliferous mines are associated with faults because of the mode of origin of these ore deposits. It is therefore imperative that design procedures for safe mining of these deposits, take into account, not only ubiquitous joints but more importantly discrete geologic structures such as faults as well.

A fault factor graph is developed to account for the effects of faults on open stope stability can be accounted for in the stability graph method. The fault factor is to be incorporated in the stability number N'. The fault factor can reduce N' by about 3 orders of magnitude compared to B and C that can only affect N' by about 0.4 and one order of magnitude respectively.

Figure 5.43 to Figure 5.45 are fault factor F_w curves for use in revising N' in the stability graph when faults are present. The most important parameters required for application of the fault factor curves are the included angle between the fault and stop surface, and the position at which the fault intersects the stope surface. Procedures for determining included angles between faults and stope surfaces, and distances of faults to stope surfaces, are given in Appendix B.

The $ELOS_f$ curves and the fault factor F_w curves are based on assumed rockmass properties, stope geometries and stress ratios, but the procedures developed can be used for more specific applications.

Further work is required on effects of faults on slender stopes, and on the effect of fault orientation on the fault factor for non-intersecting non-parallel faults.

In Chapters 6 and 7, the results of the analysis are applied to case histories from Kidd Mine in Canada and Ashanti Goldfields Company in Ghana. A validation of the fault factor graph and overbreak chart with field data is presented in Chapter 6.

CHAPTER 6

KIDD MINE CASE HISTORIES

6.1 Introduction

Kidd Mine is a property of Falconbridge Limited. It is located 27 km north of Timmins, Ontario, Canada. The Kidd copper-zinc-silver orebody was discovered in 1963, and active mining began in 1966. The mine is blocked out into #1, #2 and #3 Mines (Figure 6.1) for planning and administrative purposes (Kelly, 1991). #1 Mine extends from 244 m to 792 m. #2 mine extends from 792 m to 1,400 m. #3 Mine, is the most active mine at this time, and is expected to extend from the 1,400-m horizon to the 2,120-m horizon (Kelly, 1991; Whiteway, 1996).

In February 1996, under commission from Falconbridge Limited, Kidd Mine Division, a collaborative project was undertaken between Mark Board of Itasca Consulting Group Limited, Richard Brummer Associates and Peter Kaiser and Dwayne Tannant of the Geomechanics Research Centre at Laurentian University. This thesis was integrated into the project, and some of the work presented in this chapter is extracted from various reports presented to Kidd Mine. The work undertaken in the project concentrated largely on #3 Mine, and below. #3 Mine is therefore one of the research sites of this thesis. #3 Mine is accessed from #2 Mine on the 4600 Level. Figure 6.2 shows the infrastructure in #3 Mine.

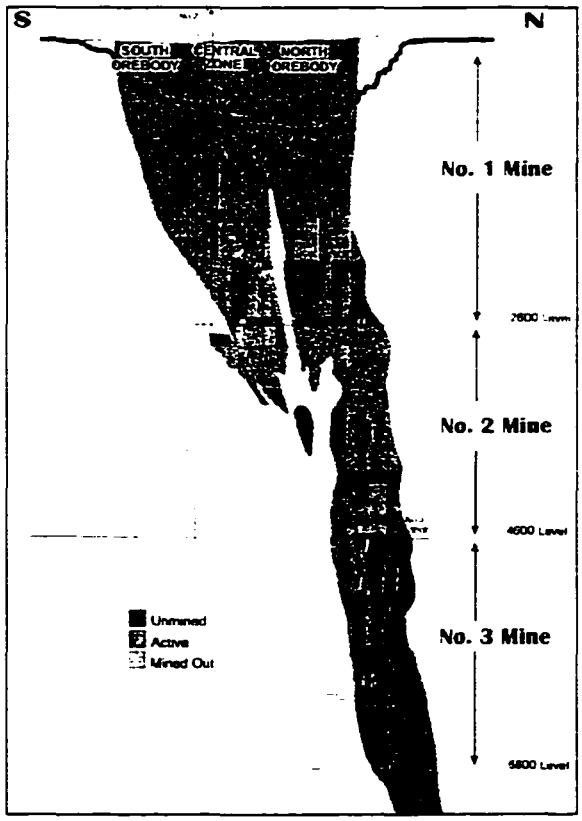


Figure 6.1 Kidd mine showing the position of #3 Mine

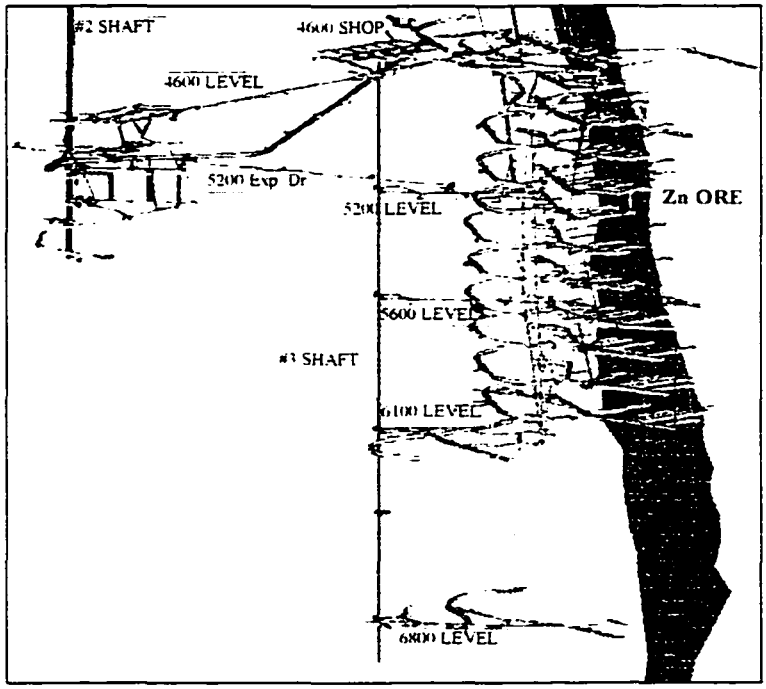


Figure 6.2 Infrastructure of #3 Mine

6.2 Mining Methods

The mining method in #3 Mine involves the use of an overhand primary/secondary sequence. Primary panels are mined in a 1, 4, 7 sequence with a width of 15 m. Secondary panels are also 15 m wide, and are mined from 2 and 5 positions. Finally, the tertiary panels, which are also 15 m wide, are extracted from the 3 and 6 positions (Figure 6.3), Figure 6.4 and Figure 6.5).

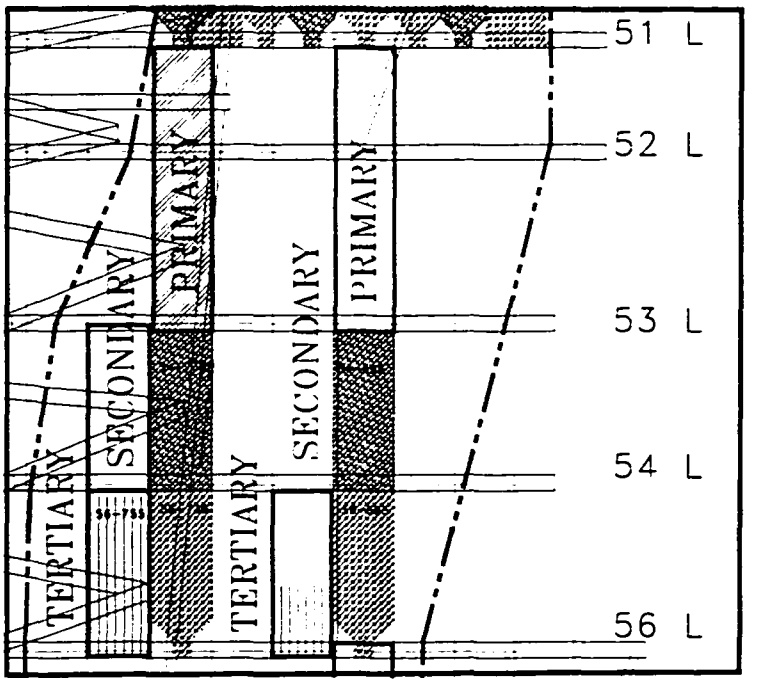


Figure 6.3 Typical stope sequence in #3 Mine

Stopes in #3 Mine are generally set at heights of 40 m, with a minimum height of 30 m between 5100 and 5200 Levels. Stope lengths are on average 20 m with a 30-m maximum. Figure 6.4 shows a plan view of stope layout, stope sizes and sequencing in #3 Mine.

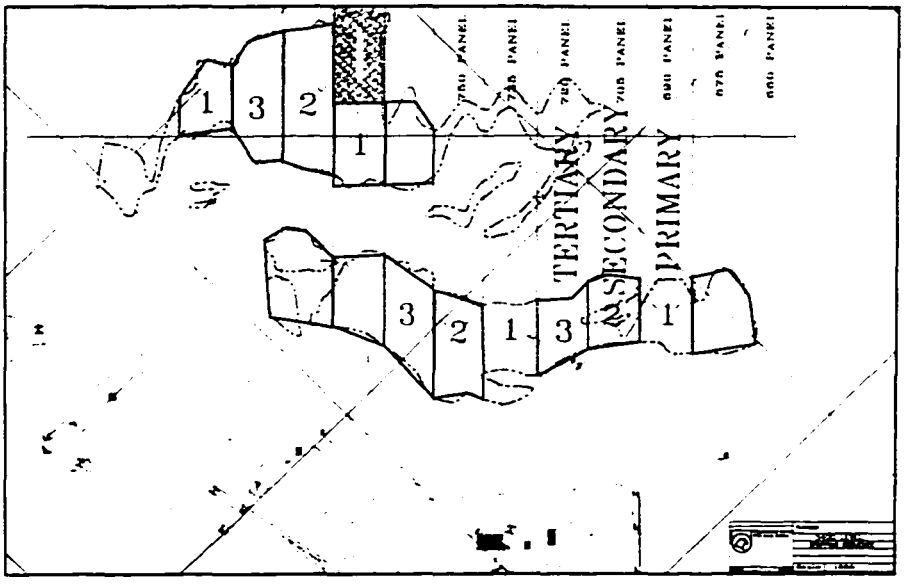


Figure 6.4 Plan view of 5400 level showing a typical panel sequence in #3 Mine

In the relatively narrow massive sulphide orebody as in Figure 6.4, single stopes are taken from hangingwall to footwall using footwall access crosscuts. In the copper and the lower zinc orebodies, that are relatively wide, multiple stopes are mined sequentially from hangingwall to footwall (Figure 6.5).

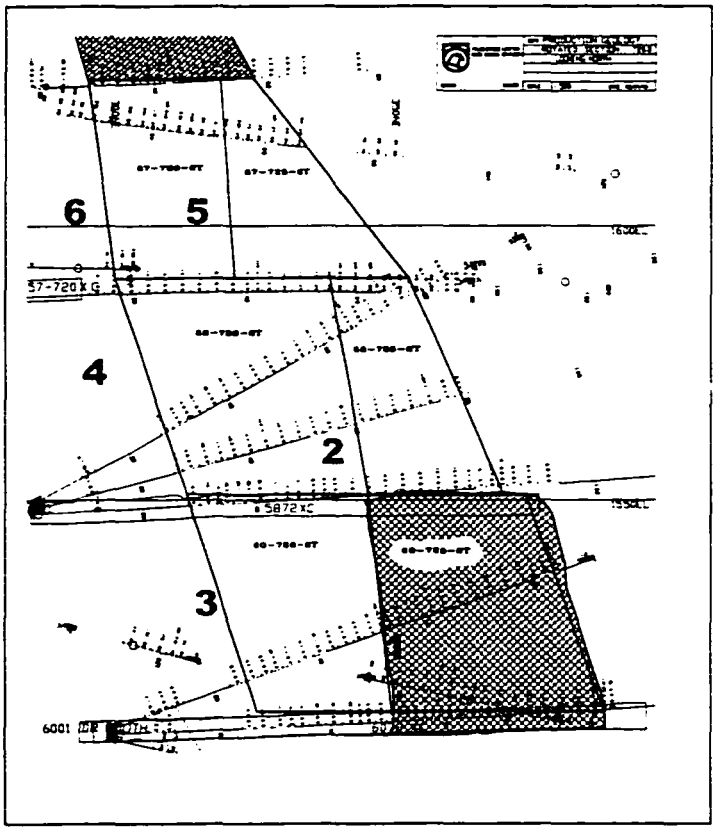
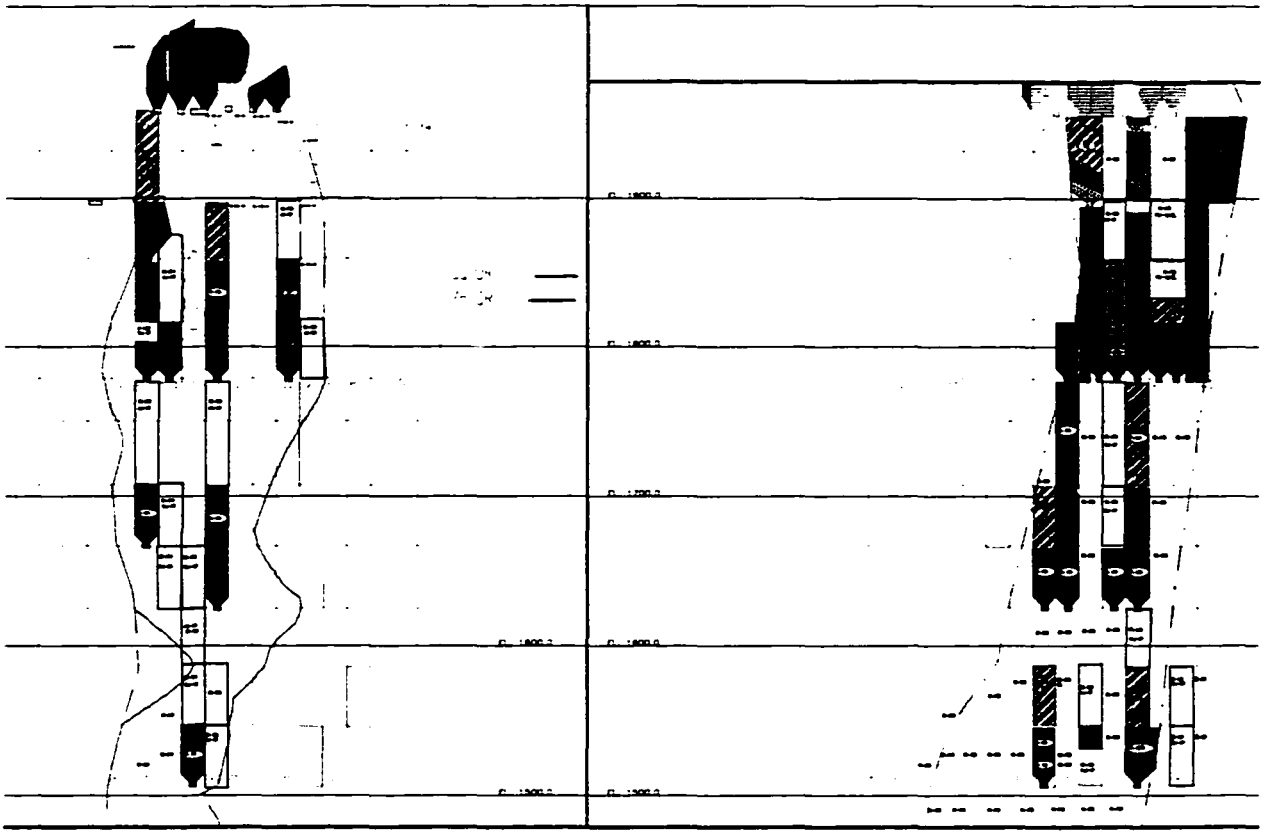


Figure 6.5 Stope sequence when orebody is wide

Figure 6.6 shows the longitudinal section of the copper stringer and massive sulphide orebodies. The figure shows the stope heights and widths that are normally used in #3 Mine. Some stopes are mined to heights of 70 m, and are observed to be more prone to wall instability as will be shown in Section 6.5.



Copper stringer **Massive sulphide**

Figure 6.6 Copper stringer and massive sulphide orebodies showing stope sizes and sequencing: Stopes are 40 m high (some 70 m), 15 to 20 m lengths and, 15 to 40 m footwall to hangingwall widths

Stope development consists of driving 4.5m by 3.8 m, crosscuts with 2-boom electric hydraulic jumbos. A slot drift location is determined when the crosscut is driven past the ore/waste contact. The slot drifts are at 90° to the crosscuts, and are 5 m by 3.8 m in size. Stope development is driven with a 20% arch supported with resin rebar and mesh. The slot is either 28" (0.7 m) or 4' (1.7 m) diameter. Figure 6.7 is a plan and longitudinal section of a typical stope development.

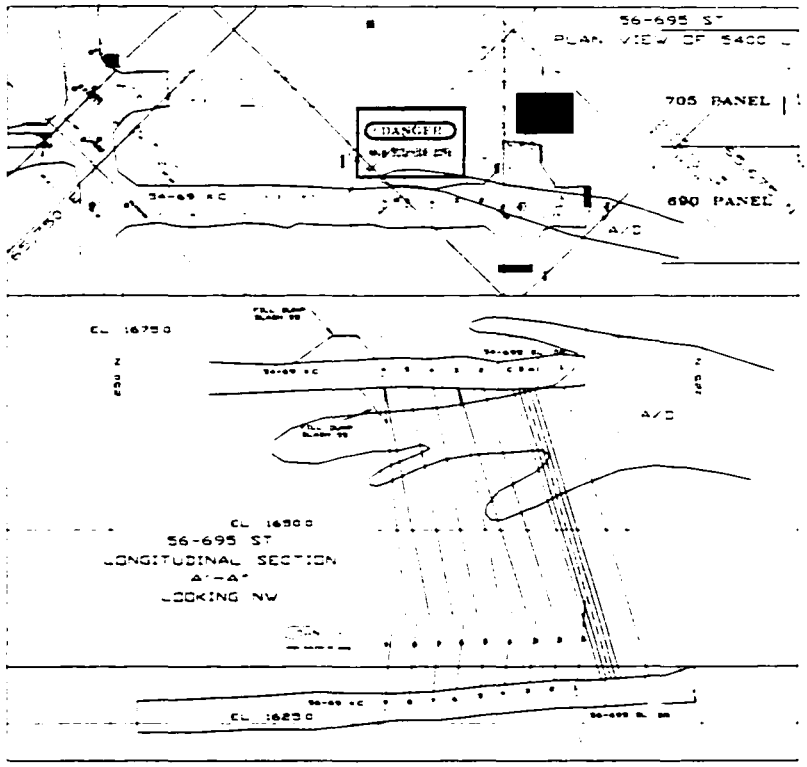


Figure 6.7 Plan and longitudinal section of 56-695 stope showing stope development in #3 Mine

Figure 6.8 shows the details of blast ring layout, and slot for 56-695 stope. Predominantly sub-vertical rings and slots are drilled with 4.5" (114 mm) or 5.5" (140 mm) ITH drill. Ring burden is 3 m to 4 m depending on ore type. Drill patterns range from 4 m to 5 m toe spacing. Down hole lengths vary from 5 m to 45 m. Upholes are limited to 30 m. The drill factor is about 24t/m in the rings.

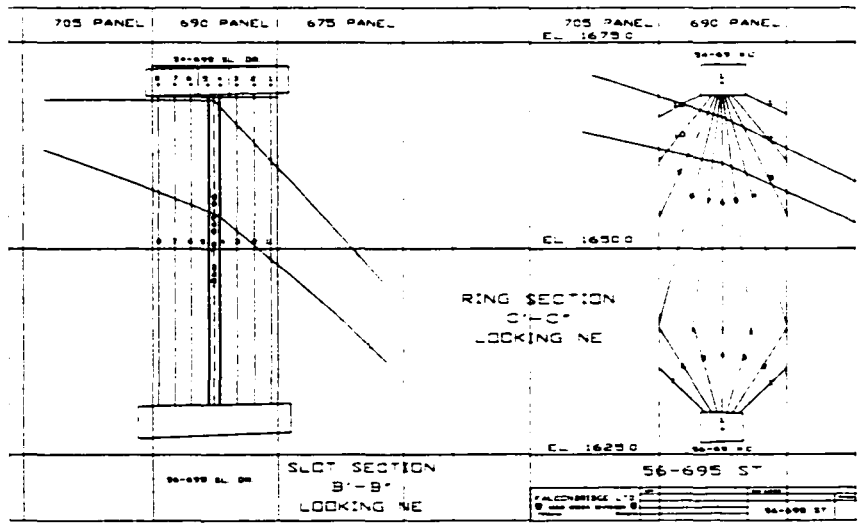


Figure 6.8 Details of blast rings and slot for 56-695 stope as is typical for #3 Mine

Consolidated rockfill is used as fill material in #3 Mine. Aggregate is sized to less than 150 mm with fines less than 10 mm removed. The aggregates arrive via a backfill raise system connected to surface. Cement slurry consisting of 40% cement and 60% flyash is added to the aggregate at about 4.5% by weight. The backfill is placed with 16 t and 26 t haul trucks loaded via backfill chutes located in the footwall. Backfill is dumped into the stope over the edge with the remaining void at the top of the stope being filled by remote controlled LHD.

The explosive used at Kidd is ANFO, under dry conditions. Emulsion is used for down-hole loading, and when pre-loading is required where hole crushing occurs. Water gel products are used for wet down-hole applications, and slots.

Blast initiation is through a central blasting system using a magnadet cap connected to trunk line firing long lead Nonel caps using a 0.20 kg cast primer.

On average stopes are designed for 3 months, after which they are supposed to be depleted and filled. However, delays often occur, and some stopes stay active or unfilled for over 5 months. Long exposure times may lead to increased instability and dilution. Figure 6.9 shows the exposure times of stopes, in #3 Mine.

6.3 Mine Geology

Ground control problems in underground mining are frequently related to the geologic structure of the mine, and the competence of the ore and host rocks. The major rock units at Kidd Mine #3 are briefly discussed in the following sections.

The ore in Kidd Mine occurs in three main deposits referred to as the north, south and central orebodies (Figure 6.1). Each orebody consists of a lens of massive sulphide underlain by a zone of stockwork mineralization. The north and south orebodies are separated by a major, near-vertical, east-striking fault with a major downward displacement on the north side. Post ore deformation resulted in brittle and ductile faults, folds, and cleavage and lineation fabrics. Figure 6.10 is a plan view of a simplified geology of Kidd Mine as seen on 5100 level. The ore bodies and the rocks immediately surrounding them strike north-northeast in marked contrast to the regional easterly strike.

6.3.1 Massive sulphides

The massive sulphides consist dominantly of pyrite, pyrrhotite and sphalerite, while the stockwork is made up, almost entirely, of chalcopyrite stringers. The massive sulphide unit occurs near the top of the rhyolites and is characterized by one strong sub-horizontal joint set. It is brittle and competent.

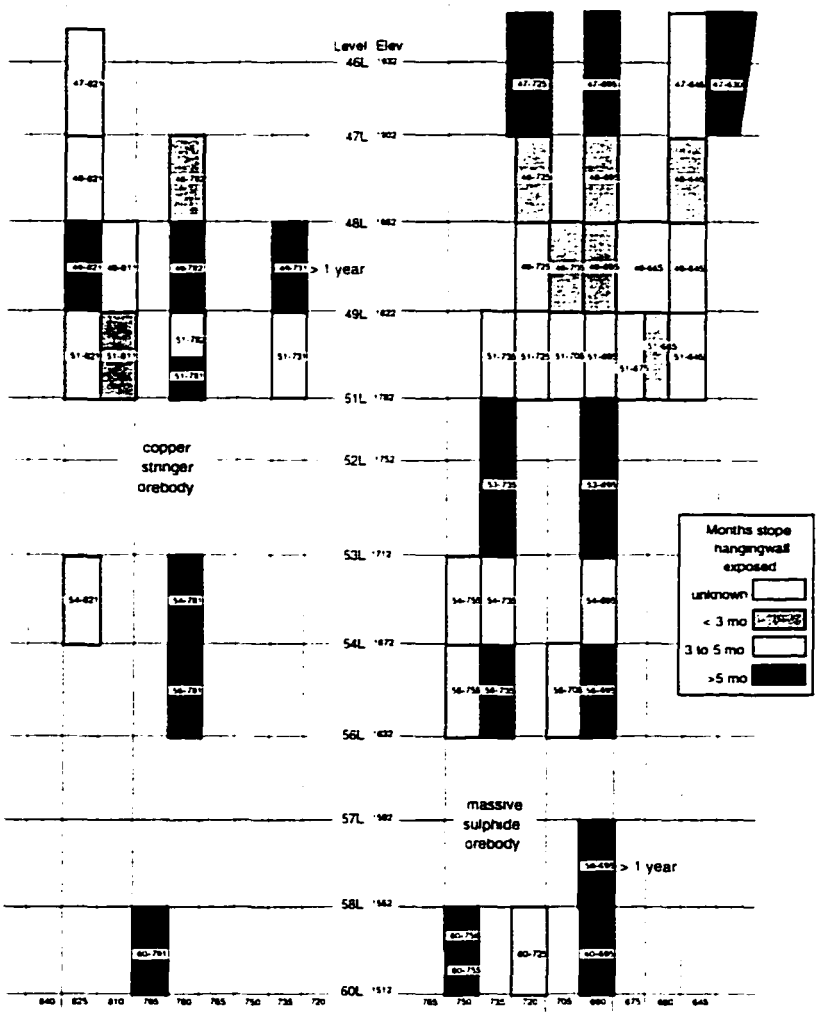


Figure 6.9 Exposure times of stopes (after Tannant and Diederichs, 1997)

6.3.2 Rhyolites

The rhyolites exhibit strong pervasive silification and fracture-controlled chloritization and sericitization of variable intensity (Kelly, 1991). In the proximity of mineralization the rhyolites are rich with iron and magnesium oxides, and depleted in sodium, calcium and aluminium oxides.

The rhyolites are felsic volcanics, and are the main hosts to the ore. The rhyolites include cherty breccia and mixed fragmentals. In the normal state, rhyolites are competent, hard, and brittle rocks. However, because of the schistose nature of the unit at Kidd Mine, the rhyolites are characterized by plastic creep behaviour when heavily loaded (Haapamaki, 1996). Displacements occur along the schistose planes. The schistosity is in two directions sub-parallel to the hangingwall rhyolite. S1 schistosity is at an azimuth of 276° to 282°, and dip of between 74° and 79°. The S2 schistosity is oriented at 012°/83°. Due to the sub-parallel nature of the schistosity planes in the rhyolites that form the stope hangingwalls, these

hangingwalls can fail at low stress levels. The hangingwalls are known to be a major source of dilution on the mine.

6.3.3 Andesite-diorite

The andesite is blocky in nature, and has an average block size of 0.6 m by 0.9 m by 1.2 m. At depth, there is increased intensity of quartz-carbonate filled tension joints. These features are extremely brittle, and are known to spit when exposed. This rock is far into the footwall from the stope surface, and contains main developments.

6.3.4 Main faults and shear zones

Brisbin et al. (1990) state that all lithologies in Kidd Mine including the ore have been subjected to complex folding and faulting. Two major fault systems affect stability of the mine in a large scale. The two fault systems are the Gouge Fault and Gouge Fault Splays, and the South dipping competent echelon faults. The Gouge Fault Splays have similar characteristics with the Gouge Fault.

The Gouge Fault strikes north-northwest, and dips 55° to 65° NE. It is contained in the diorite and rhyolite. Henning et al. (1992) report that the Gouge Fault contains a significant thickness of clay and silt, up to 30 cm locally. Sub-horizontal joints, commonly filled with quartz-calcite veins occur in the wall rock adjacent to the fault. The Gouge Fault commonly occurs as two anastomosing faults. In #3 Mine, the Gouge Fault is in the hangingwall, and is known to be a major source of dilution or wall sloughage. Figure 6.10 is a simplified geology of #3 Mine, as seen on 5100 level, showing the Gouge Fault and Gouge Fault Splays.

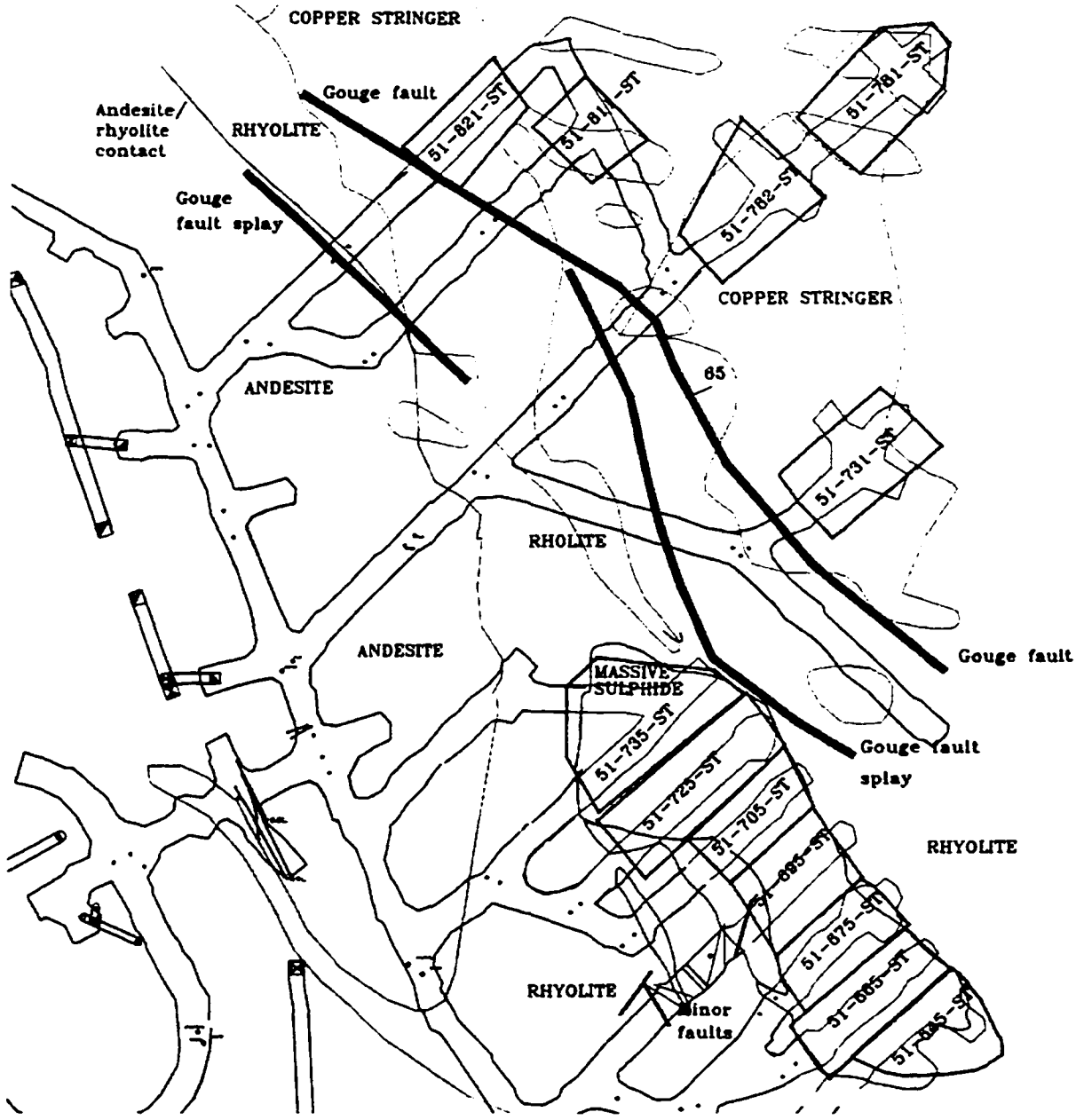


Figure 6.10 Simplified geology of #3 Mine as seen on 5100 level showing main faults and minor faults, and their relationships to stope walls in the copper stringer and massive sulphide orebodies. Dip direction of orebodies is NE.

Figure 6.10 also shows a typical stope layout and the relationships between the stope surfaces and the faults. The stope hangingwalls in the massive sulphide orebody are usually close to the faults, while for the copper stringer orebody the stope footwalls are closer to the faults. Consequently, the hangingwalls in the massive sulphide will be more affected by ground weakening due to the faults, and in the copper stringer orebody the footwall of the stopes will be more affected.

On the 5100 level, panels 735 and 750 will suffer from instabilities in the hangingwalls of the stopes in the massive sulphide orebody.

Smaller faults are often encountered in the footwall rhyolite which are often quartz or carbonate filled. These minor faults usually occur in a group but are relatively stronger than the Gouge Faults. Shear test results (Yu and Quesnel 1988) show that the friction angles for the Gouge Faults is 15° while for the smaller faults it is 30°. However, in some instances, the minor faults are weak and become a threat to stope wall stability. The additional problem the minor fault systems present is that they increase the potential degrees of freedom for wedge instability.

The south dipping faults strike east – southeast and dip 75° to 85° south. They are filled with gouge and or quartz calcite veins. They are predominantly found in the footwall. Slickensides in the fault surfaces plunge 75° Northeast.

Other minor faults and shear zones have been locally mapped and cannot be ignored in assessing stability. The North-South Shear Zone is a zone of strong cleavage, up to 18 m wide located predominantly in seriticized quartz porphyry. This shear zone has a northerly strike, and dips 75° east. The Middle Shear is a zone of intense cleavage and faulting up to 30 m wide. It has West to Northwest strike and dips 80° to 85° north. The East-West shear runs between the massive sulphide deposit and the North copper stringers.

The dominant cleavage present in the mine strikes Southeast, and dips 80° north. The intensity of cleavage is locally variable, and appears to be a function of both lithology and alteration intensity and type. Sericite-rich and talc-rich rocks commonly exhibit moderate to strong cleavage.

The next section presents the geomechanical properties of the major rock units at Kidd Mine.

6.4 Rock Properties

6.4.1 Introduction

In the empirical methods of underground excavation design, rockmass quality, intact rock strength, and stress are input parameters. This section presents the rock properties and stress conditions at Kidd Mine.

Data collection is the basis of any empirical design method. The following data were gathered from the mine:

- *RQD*,
- Rock cores,
- Discontinuity survey results,
- Cavity survey profiles,

- Wire frame model coordinates,
- Stope profiles from DATAMINE wire frame models,
- Blast design layouts,
- Drilling profiles and records of problems,
- Stope life records,
- Stoping sequence, and
- Cablebolt support records.

These records are used in characterization of the major rock units encountered in mining, and in the assessment of stope surface performances. The information is also used for the determination of stope surface and fault and shear zone geometries.

6.4.2 Rock properties

The following tables present data on intact rock, and rockmass properties for Kidd Mine rocks:

Table 6.1 Summary of the mechanical properties of main rock units at Kidd Mine

Rock type	UCS (MPa)	Tensile strength (MPa)	Unit weight (KN/m^3)	Friction (°)	Cohesion (MPa)	RMR	Source
Andesite	160	13.7				78	Yu & Vongpaisal (1996)
/diorite	120-200		29.6				Yu & Quesnel (1984)
	70-180	1.2		44*	6.5*	79	Haapamaki (1996)
	160		29.6*				Tinucci (1995)
Rhyolite	82-150	27					Yu & Quesnel (1984)
	65-130	0.6*	27*	37*	2.5*	69	Tinucci (1995)
	120						
Rhyolite tuff	140					64	Yu & Vongpaisal (1996)
Rhyolite lapilli tuff	133		26.4				Yu & Vongpaisal (1996)
Rhyolite (stringer)	120-140					75	Yu & Vongpaisal (1996)
Massive		8				82	Yu & Vongpaisal (1996)
sulphide	132-160		33.3				Yu & Quesnel (1984)
	140	0.9*	33.3*	38*	5*	77	Haapamaki (1996)
	140						Tinucci (1995)
Cherty breccia	133						Yu & Vongpaisal (1996)

*Rockmass properties

Schistosity and foliation control the rock strengths. In particular, the rhyolite unit has its strength strongly influenced by the degree of schistosity. Strength variation with schistosity in the rocks is observed even at the laboratory scale.

Yu and Quesnel (1984) gave rockmass strength and condition ratings, including global *RQD* values for each rock unit. Their results are summarized in Table 6.2.

Table 6.2 General rockmass ratings (after Yu and Quesnel, 1984)

Rock type	*RQD*	Strength rating	Rockmass condition
Rhyolite	72	Medium	Fair
Rhyolite (FW shear)	6.5	Low	Very poor
Ore	83	High to very high	Good
Dykes	50	High	Fair to poor
Andesite/diorite	82	High	Fair to good

Table 6.3 gives results from Yu and Vongpaisal (1996) of the classification of the important rock units at Kidd Mine, using *RMR*-system. The rhyolite varies in quality depending on location, and has been sub-divided for accurate classification.

Table 6.3 *RMR* rockmass classification of Kidd rock types (after Yu and Vongpaisal, 1996)

Rock type	*UCS* rating	*RQD* rating	Joint spacing rating	Joint condition rating	Ground water rating	Joint orientation factor	Availability of support	*RMR*
Andesite/diorite	12	17	25	20	8	-4	Nil	78
Altered rhyolite	12	15	25	21	8	-2	Nil	79
Rhyolite in 2030 P slot	12	15	20	12	7	-2	4	68
Rhyolite in shear zone	11	11	15	16	7	-8	5	57
Rhyolitic tuff – schistose	11	13	18	18	6	-2	Nil	64
Tuffless rhyolite – schistose	11	17	20	20	10	-3	Nil	75
Rhyolite/stringer ore	12	18	22	20	10	-2	2	82
Sulphide ore	12	18	23	24	7	-2	Nil	82
Chalcopyrite zone	12	17	22	20	7	-5	Nil	73
Cherty breccia	12	15	20	15	8	-2	4	72
Argillaceous graphite	10	13	15	20	6	-5	Nil	59
Talc – carbonaceous	10	17	25	18	10	-4	Nil	76

The joint condition rating in Table 6.3 ranges between 12 and 24. This translates to slightly rough to rough joints in the *Q*-system. Many joints are quartz-carbonate filled, and often contain chlorite and sericite. Shear test results (Yu and Quesnel, 1984) give joint friction angles between 26° and 31°. These considerations give J_r and J_a values in the *Q*-system (Barton et al., 1974) for Kidd Mine rocks as 1.5 and 2 respectively.

In assessing the performance of excavations in the rocks, the major structural weakness planes must be accounted for in the analysis. Major structural features at Kidd Mine include faults and shear zones. Henning et al. (1992) give shear test results (Table 6.4) on the main structural features.

Table 6.4 Properties of main structural discontinuities (after Henning et al., 1992)

Structural feature	Friction angle (°)	Cohesion (MPa)
Gouge fault	15	0
South dipping faults	30	1
N-S and E-W shear zones	20	0.5
North B fault	30	1
Rock joints	40	2

It was important to validate rock property data from the literature as the rock property data gave a large scatter. It was also important to examine strength variation due to schistosity and foliation as these features control hangingwall stability underground. Representative cores of major rock units were collected from the Kidd Mine for determination of *UCS*, and Young's modulus *E*. Table 6.5 summarizes results from the tests.

Table 6.5 Geotechnical properties of main rock types at Kidd Mine

Description	Uniaxial compressive strength test results					Hoek-Brown strength param.(Tannant et al, 1998)		Elastic parameters.	
Rock type	mean (MPa)	Min. (MPa)	Max. (MPa)	Std. (MPa)	No.	*m*	*s*	*E* (GPa)	*v*
Andesite/diorite	128	70	213	58	6	5.6	0.03	40	0.20
Greywacke	167	164	170	4	2	5.5	0.03	35	0.3
Talc-carbonate	65	44	90	23	3	2.7	0.02	20	0.4
Rhyolite	116	31	246	66	15	4.1	0.02	30	0.25
Massive sulphide	154	71	250	77	4	6.5	0.05	45	0.2

Effect of anisotropy on intact rock strength was examined by point load testing of rock samples approximately perpendicular (axial tests) and parallel (diametrical tests) to foliation/schistosity. Table 6.6 presents the anisotropic strength factors defined as the ratio of strength parallel to foliation to strength perpendicular to foliation.

Table 6.6 Anisotropic strength factors for strength correction

Rock type	Anisotropic strength factor from point load tests	*UCS* values for modeling (MPa)
Andesite/diorite	1	128
Greywacke	0.4	67
Talc-carbonate	0.8	52
Rhyolite	0.7	81
massive sulphide	1	154

Considering Table 6.6, the anisotropic strength factors and underground failure modes at Kidd Mine, the uniaxial compressive strengths in Table 6.6 are recommended as inputs for stability analysis.

RQD is probably the most important single, rockmass quality assessment parameter. *RQD* was determined for each individual stope surface in #3 Mine.

Records of *RQD* measurements from 4600L to 6000L were obtained from the geology department of the mine. The *RQD* data file contained 78,305 *RQD* values from diamond drill core logs in all directions. A file of stope wall coordinates and orientations was created from DATAMINE stope wire-frame models. The techniques used to create these data are given in Suorineni et al. (1997), and briefly discussed in Appendix B. A computer program was written to search through the *RQD* data file to find values that were located within volumes of rock defined by the stope walls (Figure 6.11).

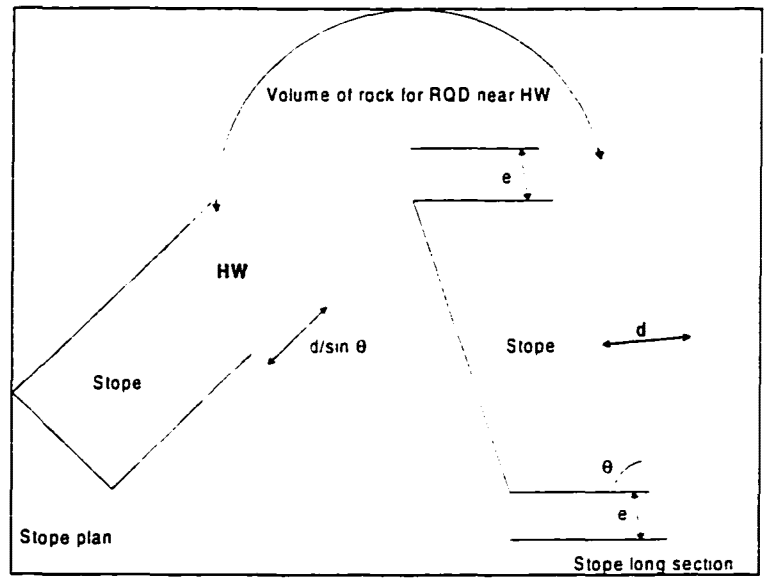


Figure 6.11 Definition of stope wall volume for determination of stope wall *RQD* in *RQD* data file

For each wall of a stope, a volume of rock was defined to be d = 15 m thick, measured perpendicular to the wall, and extending e = 3 m above and below the stope top and bottom respectively. The volume of rock was used to filter every *RQD* measurement within the stope wall volume. If an *RQD* value was located within the defined wall volume of rock, that *RQD* value was assigned to that wall, otherwise it was ignored and reconsidered for other walls.

Distributions of the *RQD* values for the stope walls generally showed strong skewness. For data distributions of this type, the median is the best representative value representing the centroid rather than a mean. Therefore, the median for the *RQD* values for each wall was used in subsequent analysis. In cases where the number of *RQD* values for a wall was less than 10, it was felt that the values will not be representative of the wall *RQD*. For such cases, an *RQD* value was assumed on the basis of rock type, rather than on the basis of the small sample size. The resultant *RQD* values used for each stope wall are included in the summary spreadsheet in Appendix C. Global *RQD* values for the main rock types are given in Table 6.7.

Table 6.7 Summary of *RQD* analysis based on rock type

Rock type	Median	Mean	Min.	Max.	Recommended value	Std.	No. of values
Andesite/diorite	95	94	20	100	95	12	822
Greywacke	70	57	10	85	70	25	27
Talc-carbonate	90	86	10	100	86	13	111
Rhyolite	90	85	10	100	85	18	791
massive sulphide	90	84	10	100	90	17	162

Figure 6.12 and Figure 6.13 show *RQD* contours of 5200 level and 735 panel respectively. The *RQD* values were contoured using SURFER (Golden Software, Inc., 1997).

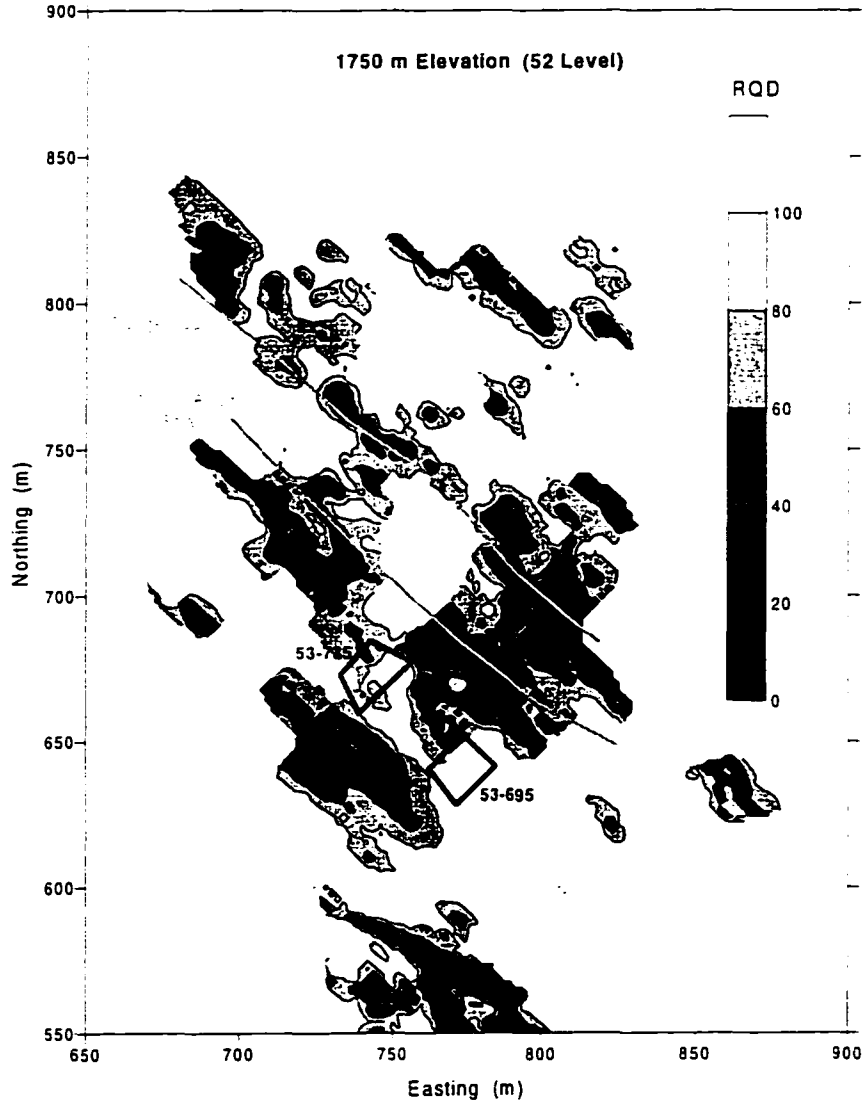


Figure 6.12 Contours of *RQD* values taken on 5200 level, showing relationship of *RQD* with faults and stope surfaces (after Tannant and Diederichs, 1997)

It is observed from Figure 6.12 that *RQD*s are lowest around the faults. The two major faults are the Gouge Faults and Gouge Fault Splay, and are located in hangingwall of the massive sulphide orebody.

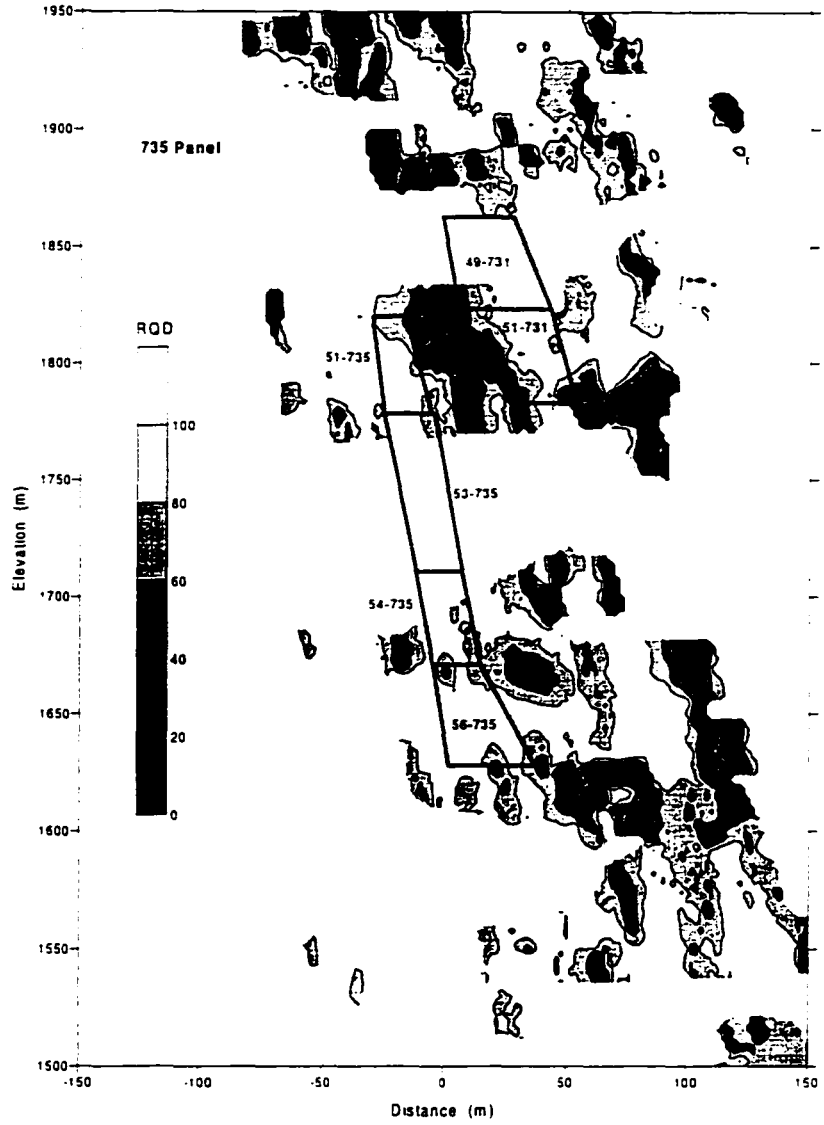


Figure 6.13 Contours of *RQD* values taken along a cross-section centred on 735 panel (after Tannant and Diederichs, 1997)

RQD measurements are often expected to capture the influence of the presence of faults. Some *RQD* contours show a good correlation between zones of low *RQD* and fault locations. In other cases, faults seem to have little influence on *RQD*, at least on a scale that shows on the contour plots, implying that *RQD* is inadequate in accounting for fault effects in these areas.

Figure 6.14 shows the distances between faults and the stope surfaces. The distances were determined using mathematical procedures developed, as presented in Suorineni et al. (1997).

The stopes on the upper part of the NW side of the massive sulphide orebody are most strongly affected by the faults. The faults near these stopes are shown in Figure 6.10. For many of these stopes faults were

located near and sub-parallel to the hangingwalls. These faults almost certainly contributed to hangingwall overbreak and caving at these locations.

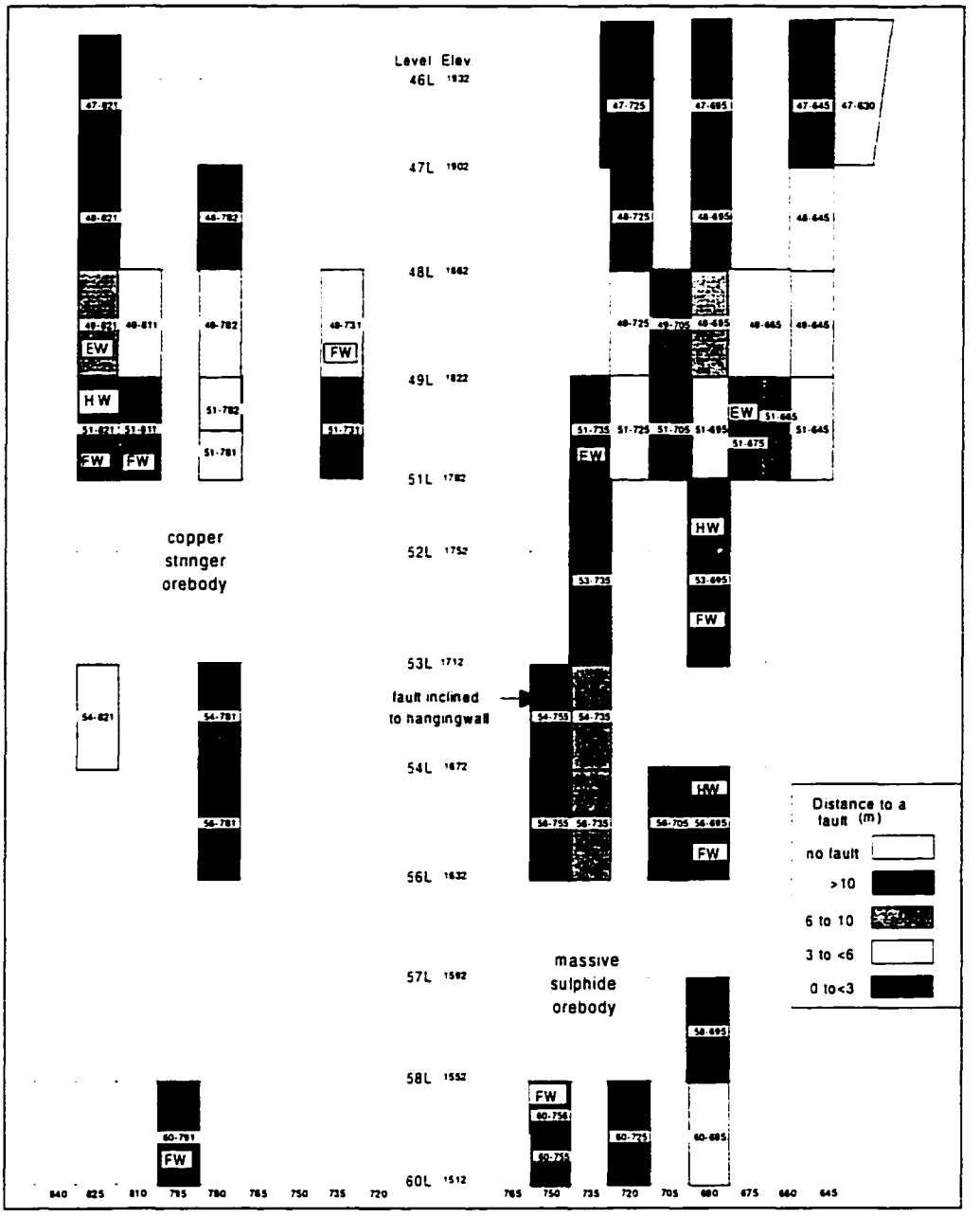


Figure 6.14 Distances between stope walls and faults

In the copper stringer orebody, there are few faults located near stope hangingwalls. In contrast, faults are more common near stope footwalls, and they have influenced footwall stability.

6.4.3 Discontinuity survey

Joint sets and condition of joints are primary requirements in the rockmass classification systems. Attitudes of joints, schistosity, and faults were taken directly from 1:500 AutoCAD plots generated by Kidd Mine geologists. The measurements were in dip and strike formats taken with reference to the Mine Grid coordinate system. An AutoLisp program was used (Tannant et al., 1997) for extracting the strikes and dips of the various discontinuities from the 1:500 level plans. The results were input into DIPS (Diederichs and Hoek, 1995) for analyzing the discontinuities.

Figure 6.15 shows the joint sets in the Andesite/diorite. The Andesite-diorite contains one dominant sub-horizontal joint set, and two less prominent sub-vertical joint sets. Figure 6.16 shows joint sets in the volcaniclastic rhyolite. The dominant joint set is sub-horizontal with random sub-vertical joints.

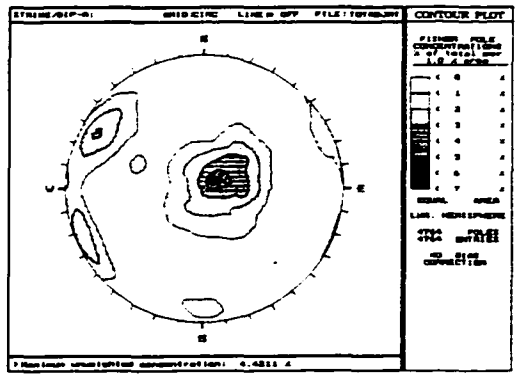


Figure 6.15 Equal area contours plots of poles of joints in andesite/diorite

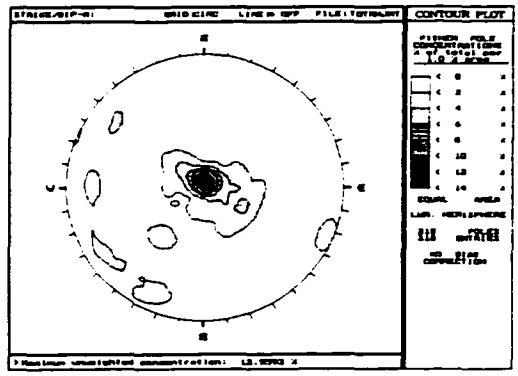


Figure 6.16 Equal area contour plots of poles of joints in volcaniclastic rhyolite

The cherty breccia hosts the copper stringer orebody, and therefore jointing in it corresponds to jointing in the copper stringer orebody. The massive rhyolite (cherty-breccia), (Figure 6.17) typically forms the footwall, and sometimes forms the hangingwall of the massive sulphide orebody. There are cases when the cherty breccia forms the hangingwall of the massive sulphide orebody. The main joint sets in Figure 6.17 are sub-horizontal.

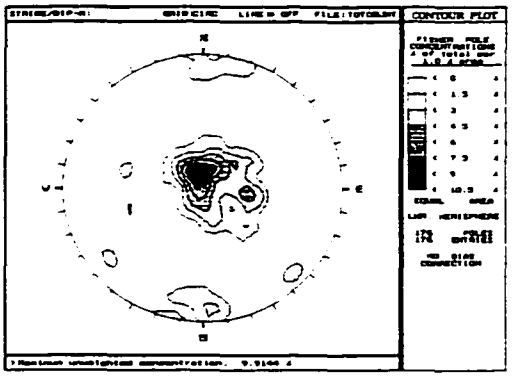


Figure 6.17 Equal area contour plots of poles of joints in cherty breccia (massive rhyolite

Figure 6.18 gives the joint sets in the massive sulphide orebody. There are two dominant joint sets. One joint set is near vertical, and the other is near horizontal. Some random joints are present.

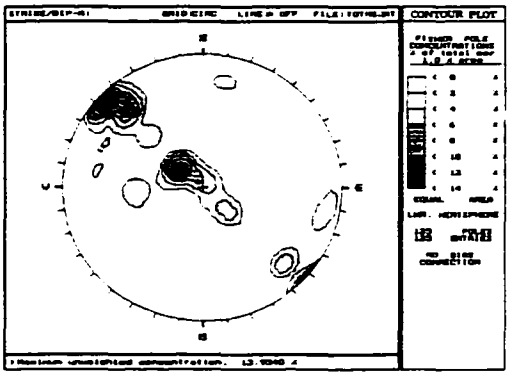
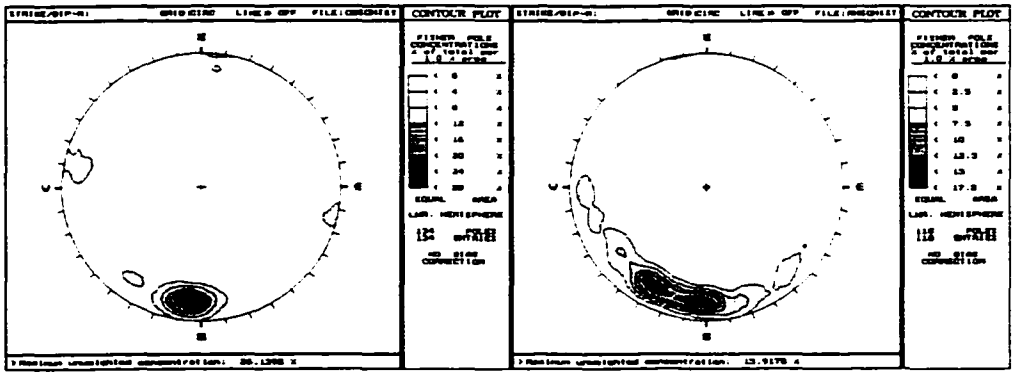


Figure 6.18 Equal are contour plots of poles of joints in massive sulphide

Schistosity plays a major role in the stability of the rhyolite hangingwall in Kidd Mine. Schistosity measurements in the rhyolite volcaniclastics and the cherty-breccia are plotted in Figure 6.19.



(a) Cherty breccia schistosity (b) Rhyolite volcaniclastic schistosity

Figure 6.19 Equal area contour plots of poles of schistosity in (a) cherty breccia and (b) rhyolite volcaniclastic

In the cherty breccia, the S1 schistosity is well defined at an azimuth of 276° to 282° and a dip of between 74° and 79°. The S2 schistosity is oriented at 012°/83° in the cherty breccia. The S1 schistosity is also well defined in the volcaniclastic rhyolite, with a similar orientation to that in the cherty breccia. The trend of the S2 schistosity in the volcaniclastic rhyolite varies between 220° and 000°.

Figure 6.20 shows a stereonet of all faults detected on 52L of Kidd Mine.

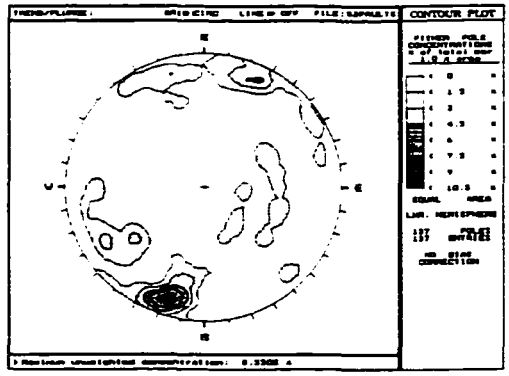


Figure 6.20 Equal area stereonet of faults on 52 Level

Some trends are identified with the gouge fault and the low angle faults (Bleeker, 1994). The most prominent cluster aligns with S1 schistosity. Table 6.8 (joints) and Table 6.9 (schistosity), present summaries of the discontinuity analysis.

Table 6.10 gives the number of joint sets in each rock type at Kidd, taking schistosity into account.

Table 6.8 Summary of joint analysis results

Rock type	No. of joint sets	Dip (±5°)	Dip direction (±5°)	Joint infilling
Andesite/diorite	3 plus random	17	255	regular and
		83	065	quartz
		78	120	regular
Cherty breccia	2 plus random	09	170	regular and
		87	355	quartz
Rhyolite	1 plus random	07	180	quartz and regular
Massive sulphide	2 plus random	08	130	regular
		85	135	regular

Table 6.9 Summary of schistosity analysis results. (Tannant et al., 1997)

Rock type	Type of schistosity	Dip (°)	Dip direction (°)	Infilling
Cherty breccia	S1	79	005	Chlorite
	S2	83	102	Chlorite
Rhyolite	S1	75	000 to 030	Chlorite
	S2	85	080	Chlorite

Table 6.10 Resultant joint sets in main rock units after accounting for schistosity

Rock type	No. of joint sets	Dip (±5°)	Dip direction (±5°)	Joint Infilling
Andesite/diorite	3 plus random	17	255	regular and
		83	065	quartz
		78	120	regular
				regular
Cherty breccia	3 plus random	09	170	regular and
		87	355	quartz
		79	005	regular and
				quartz
				chlorite
Rhyolite	3 plus random	07	180	quartz and
		75	000	regular
		75	030	Chlorite
				Chlorite
Massive sulphide	2 plus random	08	130	regular
		85	135	regular

Intrinsic rockmass properties and stress dictate the performance of underground openings. The inherent rockmass and rock material properties established above form the basis for ground characterization, and application of the empirical methods of underground opening design at Kidd Mine.

6.4.4 Classification of Kidd Mine main rock units

The stability graph method uses a modified Q' obtained by setting J_w and SRF to 1 in Barton et al. (1974) rockmass classification system. Table 6.11 is a summary of rockmass qualities at Kidd Mine, in terms of Q'.

Table 6.11 Classification of main rock types at Kidd Mine

Rock type	*RQD*	Number of joint sets	Joint set number J_n	Joint roughness number J_r	Joint alteration number J_a	Rockmass quality Q'
Andesite/diorite	95	3 plus random	12	1.5	2	6
Talc-carbonate	86	3 plus random	12	1.5	2	5
Cherty breccia	85	3 plus random	12	1.5	2	5
Rhyolite	85	3 plus random	12	1.5	2	5
Massive sulphide	90	2 plus random	6	1	1	15

6.4.5 In Situ Stresses at Kidd Mine

The overcoring method for determining in situ stress measurements has been used at various horizons at Kidd Mine to determine the pre-mining state of stress. Due to the complexity of the rock structure, a relatively high scattering of results has been reported. Figure 6.21 gives a summary of results of in situ stress measurements at Kidd Mine, as reported by (Tannant et al., 1997). Figure 6.21 shows a tendency for equalization of principal stresses at depth.

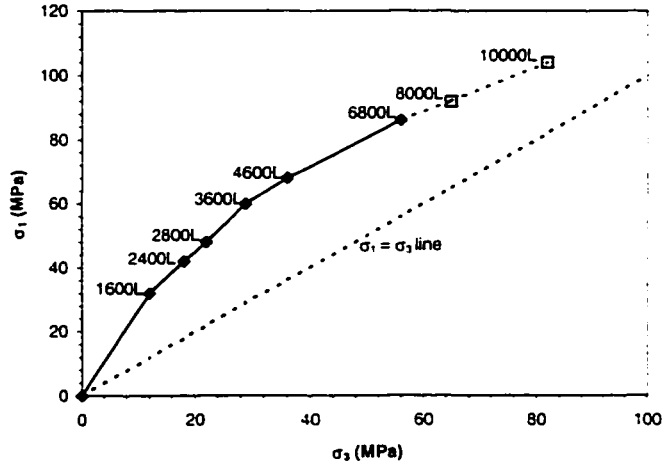


Figure 6.21 Measured in situ principal stresses at various levels (solid squares) at Kidd Mine, and predicted stresses (open squares) at depth - Broken line ($\sigma_1 = \sigma_3$) represents hydrostatic stress case (Re-plotted from Tannant et al., 1997)

6.5 Stope Performance

In assessing the performance of open stopes, use of Cavity Monitoring Systems *CMS* (Miller et al., 1992) has led to improved data collection in recent years. Cavity survey data at Kidd Mine was used to assess the performance of stopes that have been surveyed. Performance of some primary stopes not surveyed was based on drilling results of secondary stopes next to them.

The objective of the performance assessments was to determine the location and extent of overbreak. Overbreak is here defined as average distance from the planned stope wall defined by blast layouts, to the resulting cavity wall as picked by the cavity monitoring system after complete or near complete mucking of the stope. Overbreak may be enhancement or dilution, depending on whether failure occurred in ore or waste rock. Clark and Pakalnis (1996) have used the term "equivalent linear overbreak sloughage *ELOS*" to describe average depth of failure.

Profiles of cavity surveys, blasthole layouts, and sections from DATAMINE wire-frame models were superimposed by digitizing in AutoCAD. Such profiles sometimes included nearby faults and the cablebolt support layouts. Figure 6.22 shows an example of a stope with no overbreak problems in either hangingwall or footwall (overbreak = 0 m for both walls). Figure 6.23 shows a case of hangingwall failure in a tall stope (double height stope). In both figures, actual blasthole layouts differ significantly from the wire-frame model profiles, with blasthole layouts more approximating actual stope profile.

In assessing stope performance, blasthole layouts were therefore compared with cavity survey profiles rather than wire frame models.

To obtain overbreak for a given stope surface, a number of measurements are taken along the stope height where overbreak occurred. The mean of the measurements is overbreak for that surface. Where cavity surveys were not present, overbreak in primary stopes were assessed from drill hole records from the adjacent secondary stopes.

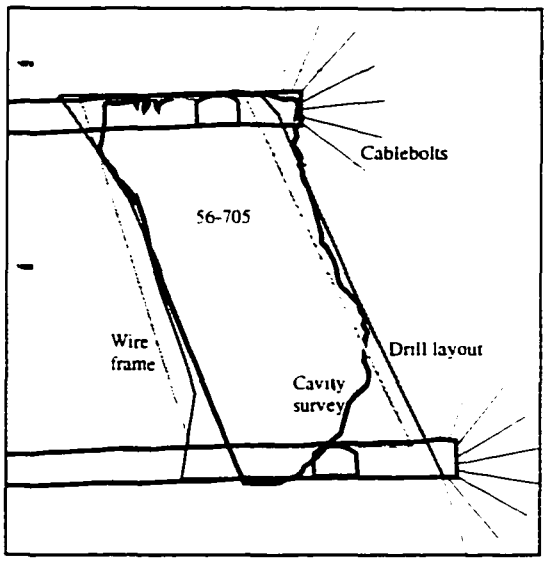


Figure 6.22 Section through the centre of 56-705 stope looking NW - Well performed stope with no overbreak

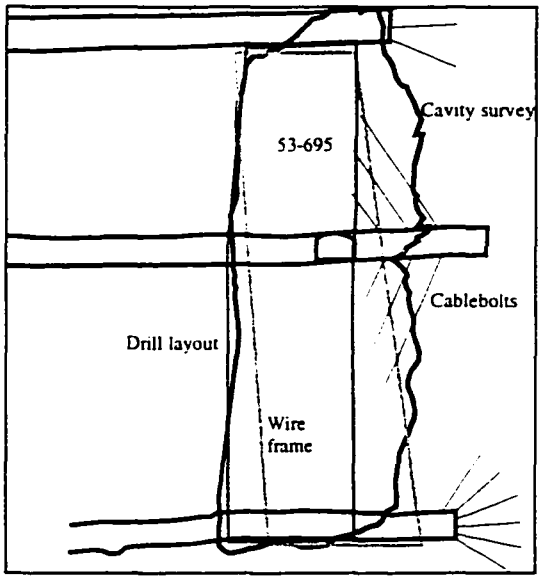


Figure 6.23 Section through the centre of 53-695 stope looking NW - Poorly performed tall stope hangingwall with 7.5 m overbreak

The stability of 48 stopes was assessed using the same procedure as in Figure 6.22 and Figure 6.23, and from drilling logbooks. A total of 112 cases with known performance of stope walls were obtained. A summary of the results is included in Appendix C.

Figure 6.24 presents the results of depths of failures superimposed on a longitudinal section of the #3 Mine, showing the stope layouts. The figure shows that most problem stopes are in the massive sulphide orebody and tend to occur in taller stopes. Sidewall failures in the ore were not common. Significant footwall failures were also rare, but occur in the copper stringer orebody. Majority of the failures occurred in the

5100 level, and in panels 735 and 750. Figure 6.10 showed that the Gouge Fault and the Gouge Fault Splays converged on the 5100 level and in panels 735 and 750. The faults are most likely to be responsible for the overbreaks in the 5100 level and panels 735 and 750. Example stopes with faults near the footwalls and hangingwalls are shown in Figure 6.31.

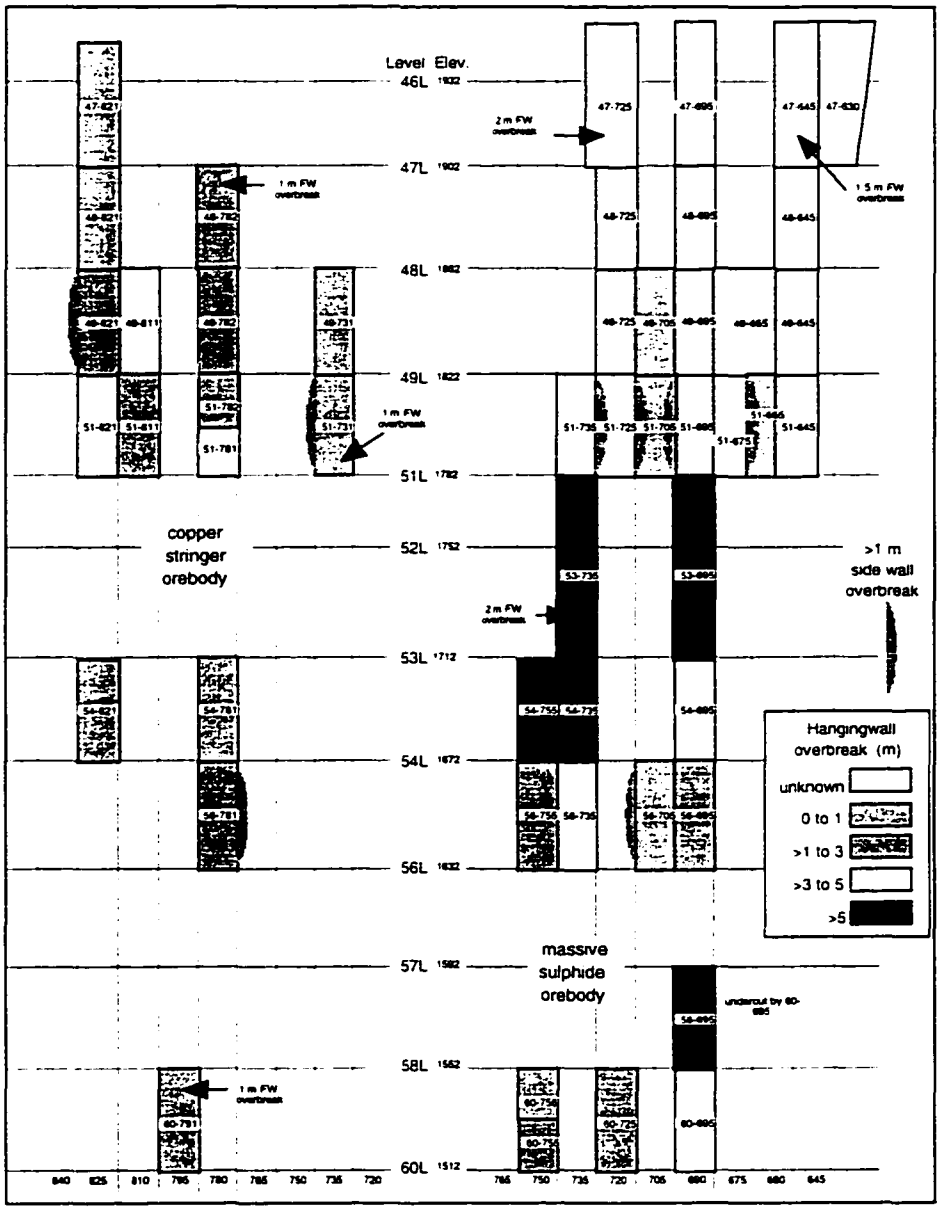


Figure 6.24 Overbreak distribution throughout #3 Mine

6.6 Kidd Mine Stability Graph

Previous sections have been devoted to the establishment of procedures and collection of data relevant for the development of the stability graph. Appendix C contains a summary of all data for all stopes examined, and gives the details of all stope walls and factors.

All the stope surfaces analyzed at Kidd Mine are walls. The stope wall statistics are shown in Figure 6.25.

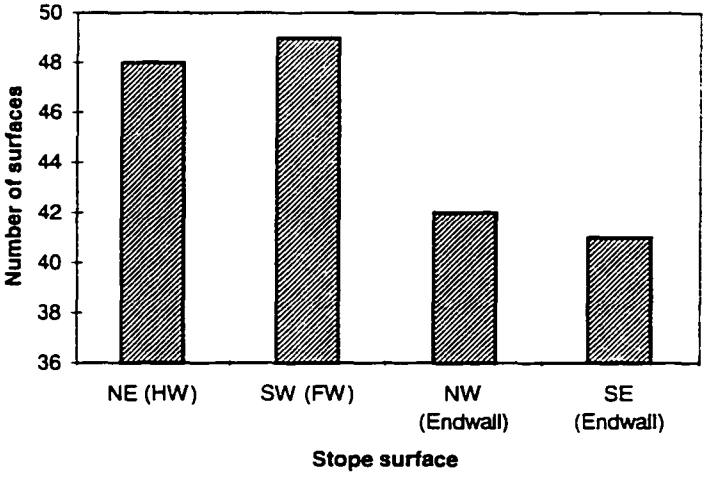


Figure 6.25 Distribution of stope surfaces in the database

In the conventional stability graph, stope performances are classified as stable, unstable or caved. With the introduction of cavity surveys, average depths of failure can be determined. The stability graph can therefore be presented in terms of average depth of failure referred to as *ELOS* (dilution), or the *ELOS* can be classified into stable, unstable and cave to be commensurate with the traditional stability graph terminology.

Stope performances at Kidd were based on average depths of failure. From Figure 6.26, the average depths of failure are classified into stable, unstable and caved as given in Table 6.12.

Table 6.12 Classification of *ELOS* into stability graph terminology

Stope performance: Average depth of failure (m)	Classification
ELOS ≤0.5	Stable
1≤*ELOS*<5	Unstable
ELOS ≥5	Cave

These classifications are adopted in the subsequent plots of the stability graph for Kidd Mine.

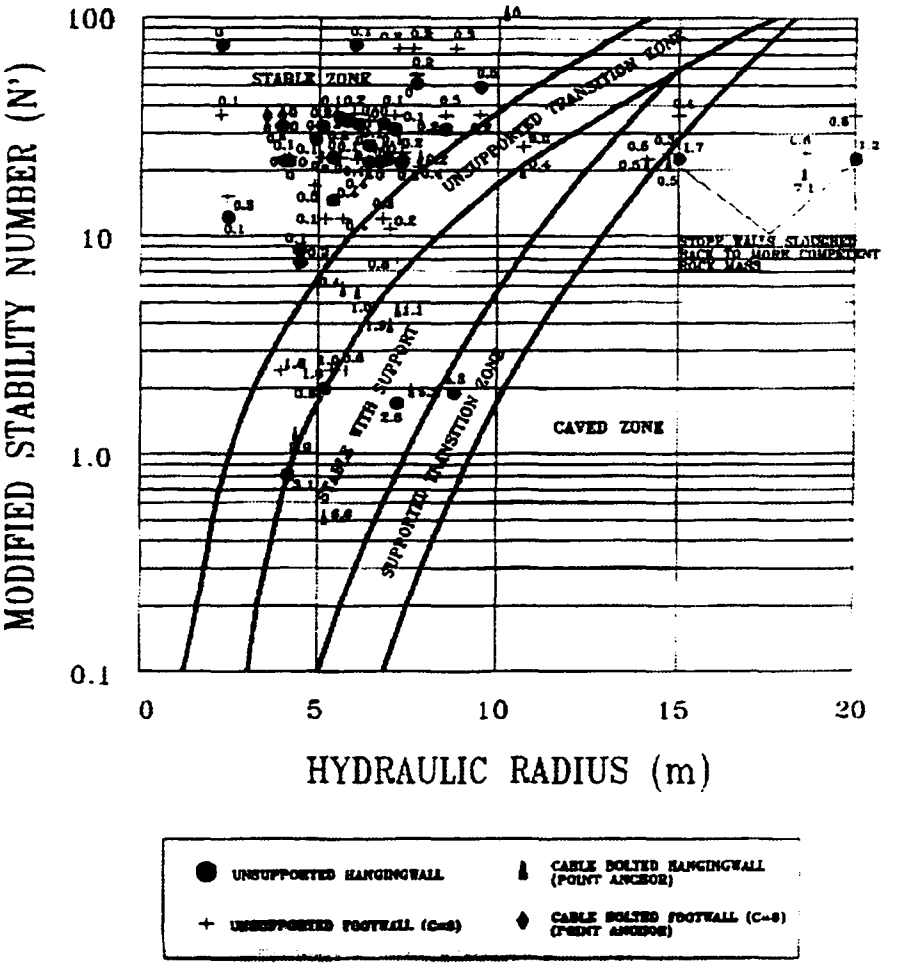


Figure 6.26 *EIOS* stability graph with transition zones as defined by Potvin (1988) and Nickson (1992) (after Clark and Pakalnis, 1997)

6.6.1 Stope wall hydraulic radii

In the stability graph, a stability number is plotted against a wall or back shape factor *S*, often referred to as hydraulic radius *HR*. Stopes at Kidd Mine have regular geometries and hydraulic radius is a good measure of stope surface shape. Thus, stope surface shape effects do not affect stability, and the radius factor *RF* (Milne 1997) is not used.

Geometric information about size, shape and orientation of each stope wall was determined from wire-frame coordinates obtained from the mine. Stope surface dimensions determined by the procedures presented in Appendix B, are used to determine the stope wall hydraulic radii and attitudes (dip and dip directions). Details of the stope dimensions and orientations are given in Appendix C. The wall orientations and included angles between the walls and critical joints were then used to determine the joint orientation factor *B* and the gravity factor *C*. The results are included in Appendix C.

6.6.2 Selecting a stability graph data analysis procedure

There are two schools of thought in analyzing open stopes performance using the stability graph method:

- Use the calibration database stability graph with the established boundaries, by superimposing on it your mine open stope performance data, and
- Establish mine specific transition boundaries with site data.

For most individual mines, particularly new mines, data is limited. Also, for individual mines the range of hydraulic radii is limited, as a consequence of the unique stope sizes often planned for the, mine based on the mine rockmass qualities Q'. For cases of this type statistical applications may give controversial results. A boundary between data groups defined by statistical discrimination, may be statistically well accepted but would have no physical meaning in the engineering sense. For example, the top diagram in Figure 6.27 shows that hydraulic radius decreases with increasing stability number N', which is incorrect since good higher stability numbers should contain relatively bigger stopes. The bottom diagram in the figure shows that the boundary between stable and failed stopes is approximately horizontal, giving the wrong impression that a given N' can take a stope of infinite size.

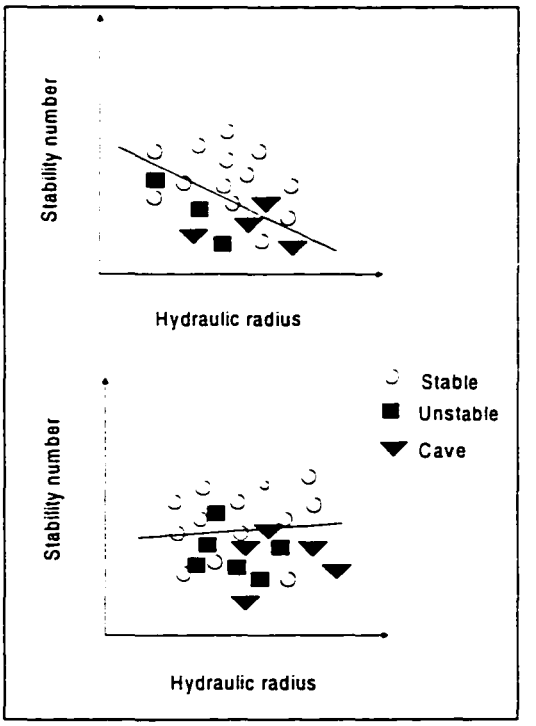
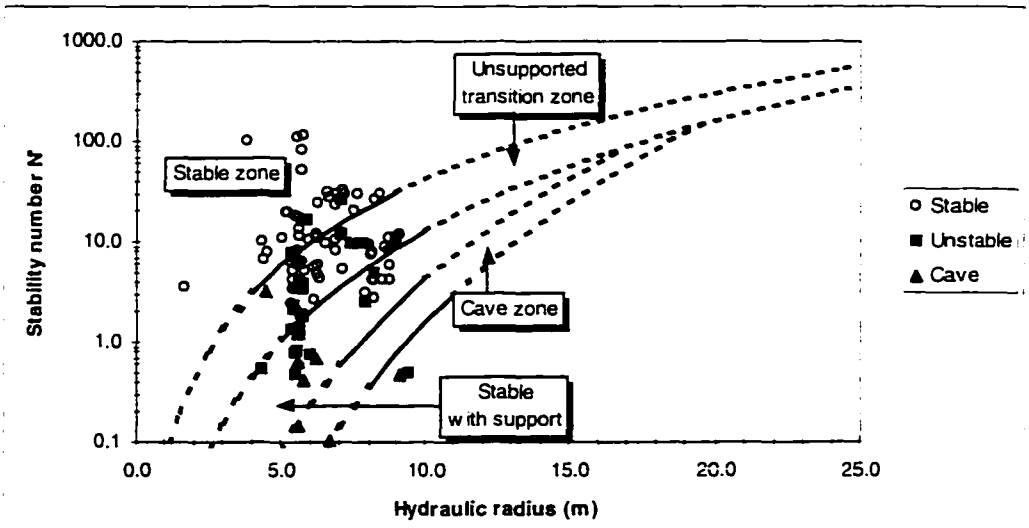


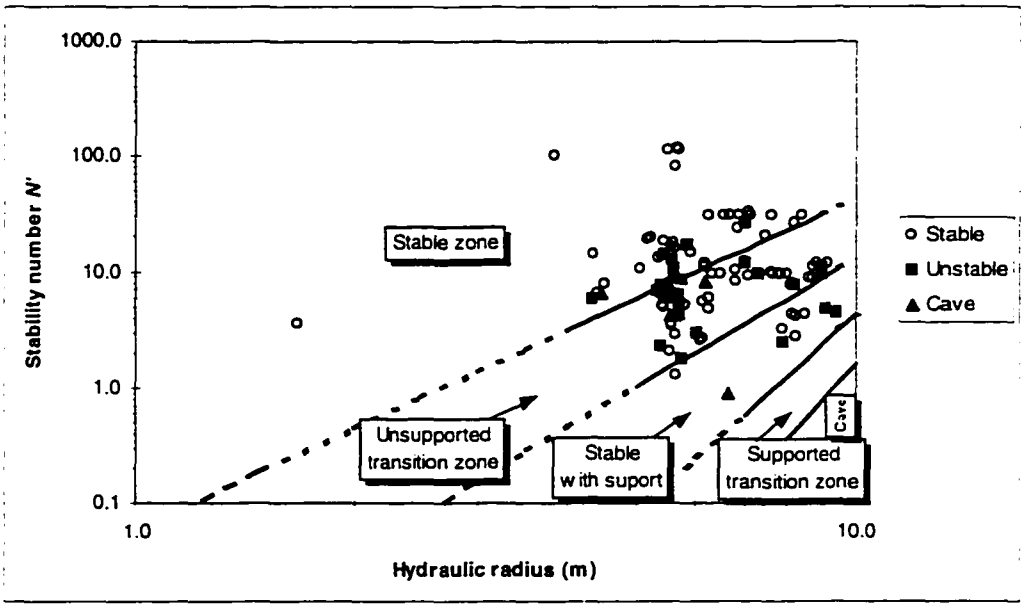
Figure 6.27 Illustrations of problems in statistical discrimination with respect to individual mine data

In Figure 6.28 to Figure 6.29, there is high overlap and no correlation. Statistical discrimination of the data into zones is bound to be erratic, and predictions of stope performance based on them will be spurious. For data distributions of the type shown in Figure 6.27, Figure 6.28 and Figure 6.29, it is better to use boundaries from the calibration database (general stability graph boundaries), and calibrate or optimize

these general stability graph boundaries if necessary, based on local experience as discussed in the following sections.



(a) Conventional stability graph for Kidd Mine on a semi-log scale without corrections for faults



(b) Conventional stability graph re-plotted on log-log scale without corrections for faults

Figure 6.28 Conventional Kidd Mine modified stability graph with Potvin (1988) "unsupported transition zone" and Nickson (1992) "supported transition zone" (a) Semi-log scale (b) Log-log scale.

The distribution of the data in Figure 6.28 to Figure 6.29 is partly a consequence of not accounting for all factors, such as faults, in the stability graph method.

In old operating mines with varied ground conditions, databases could be large, and hydraulic radii will vary in a reasonably large range with changing ground conditions. These ranges of data will more readily

enable statistical discrimination between stope performance data groups that are reasonably accurate. For such cases, the best option of analysis is to establish transition boundaries using the data. The boundaries should then be optimized to account for misclassification costs. Statistical procedures as shown in Chapters 3 of this thesis can be applied.

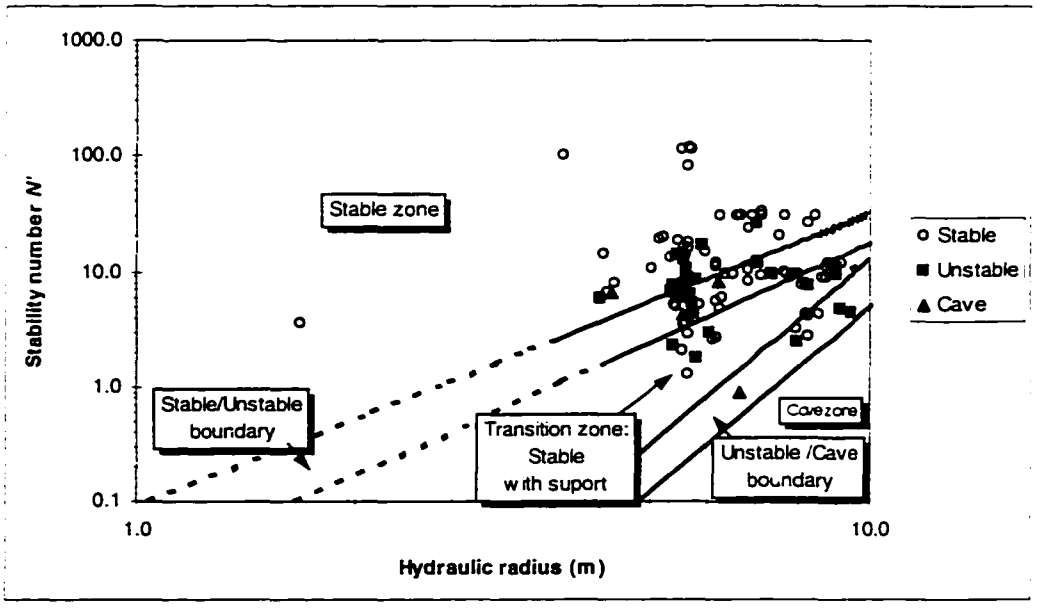


Figure 6.29 Data in Figure 6.28 re-plotted with boundaries as redefined in the thesis, on a log-log scale

In Chapter 3, a method for determining the viability of statistically discriminating between data subgroups was discussed. A parameter for determining data discriminability was presented in Section 3.5.2 of Chapter 3, and is defined as the ratio of the distance between the mean vectors of the data subgroups, to the data subgroups pooled covariance (Equation 6.1). The higher the discriminability index the more viable is the application of a classification procedure.

$$\upsilon = S^{-1}\left(\overline{X}_1 - \overline{X}_2\right) \qquad 6.1$$

where,

S^{-1} = Inverse pooled covariance of the subgroups

$\overline{X}_1$ = Mean vector of data subgroup 1

$\overline{X}_2$ = Mean vector of data subgroup 2

The discriminability indices for the calibration database data, the Kidd Mine conventional stability graph database, and the corrected Kidd Mine database, are given in Table 6.13. The calibration database discriminability indices are included as a basis for comparison. The boundaries between the data subgroups in the calibration database were defined statistically.

Table 6.13 Data discriminability indices as a measure of data overlap

Data sub groups	Discriminability index ϑ	Comment
Calibration database - Stable/Unstable	0.62	Good separation, small overlap
Calibration database - Stable/Cave	0.75	Good separation, see Chapter 3, little overlap
Kidd conventional database - stable/unstable	0.23	High overlap, Very poor separation, see Figure 6.28 and Figure 6.29
Kidd corrected (for faults) database - stable/unstable	0.69	Good separation, see Figure 6.35b and Figure 6.36

The discriminability index is a measure of how well data zone out into groups of similar performance. It is a measure of data separability. Therefore, like the apparent error rate *APER*, the data separability or disciminatability index can be used as a measure of improvement to the quality of data in a database, for reliable prediction of stope performance. Improvement in this sense refers to a reduction in overlap of the data groups. A small discriminability index such as 0.23 implies high overlap of data groups while a high discriminability index means small overlap of the data groups. When the data discriminability index is used together with the stability graph boundaries, improvement in data zoning according to stope performance can be assessed. The apparent error rate *APER* discussed in Chapter 3 gives a direct assessment of how points in the stability graph are well located in the correct zones.

Many of the open stopes at Kidd Mine in the study area are affected by faults. The effects of weak zones such as faults on the stability graph have not been accounted for in the stability graph. Figure 6.30 illustrates the problem. The three stope surfaces in Figure 6.30 plot as transition points between stable and unstable cases, but these stopes caved. The conventional stability graph could not capture the effect of the soft zones. Procedures for correcting for faults in the stability graph were developed in Chapter 5, and a fault factor chart established. In the next section the fault factor is applied to the Kidd database.

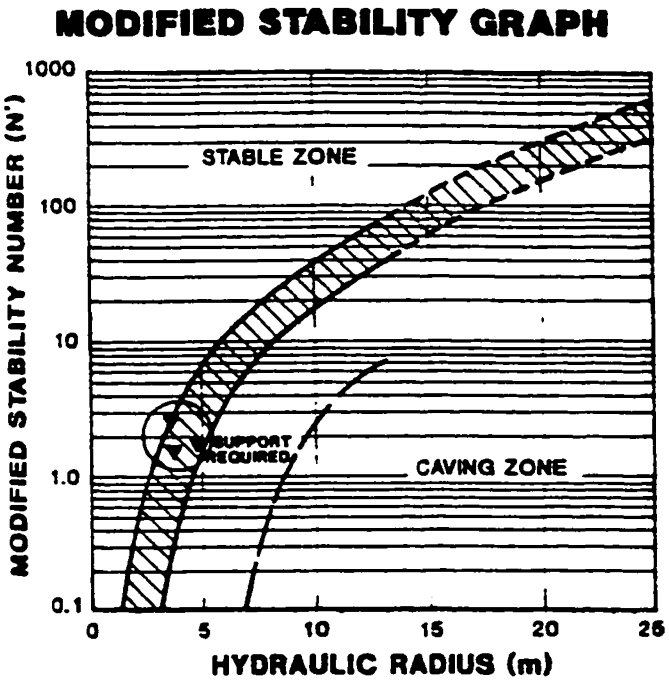


Figure 6.30 Modified stability graph showing three case histories of back failure where soft inclusions of weak material were present (after Potvin and Milne, 1992)

6.7 Application of Fault Factor

Nine typical case examples of stopes with faults are shown in Figure 6.31. Details of the stope surfaces and faults are given in Appendix C. The stability graphs, for these stope surfaces without any corrections, are presented in Figure 6.32.

The fault factors developed in Chapter 5 are determined for the given faults and stope geometries and estimated K-ratio for the 9 cases in Figure 6.31. When the fault factor is known, the stability number N' is given by:

$$N' = Q' \bullet B \bullet C \bullet F_W \qquad 6.2$$

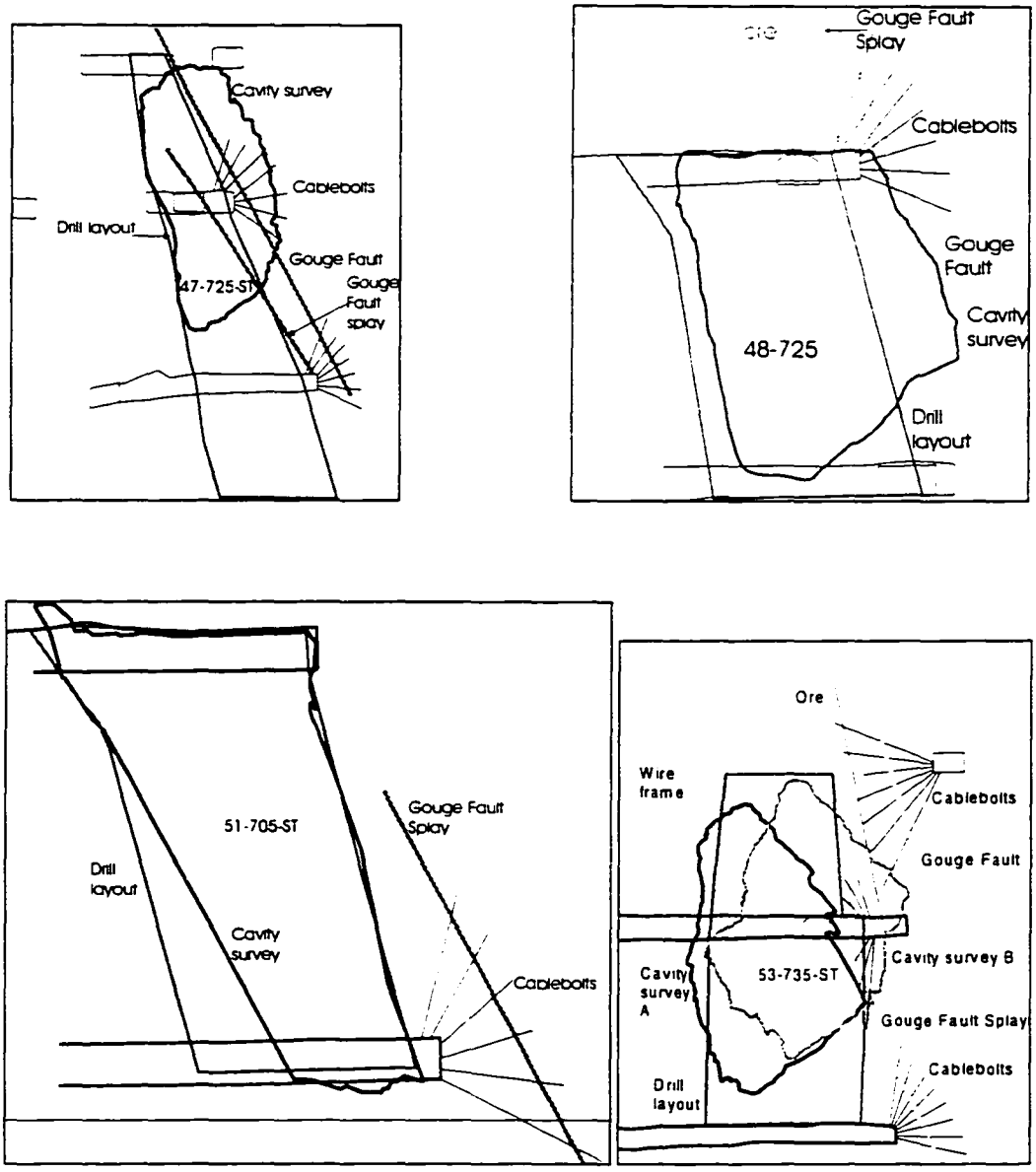


Figure 6.31 Sections of stopes with faults close to or intersecting hangingwalls and or footwalls (cont. next page)

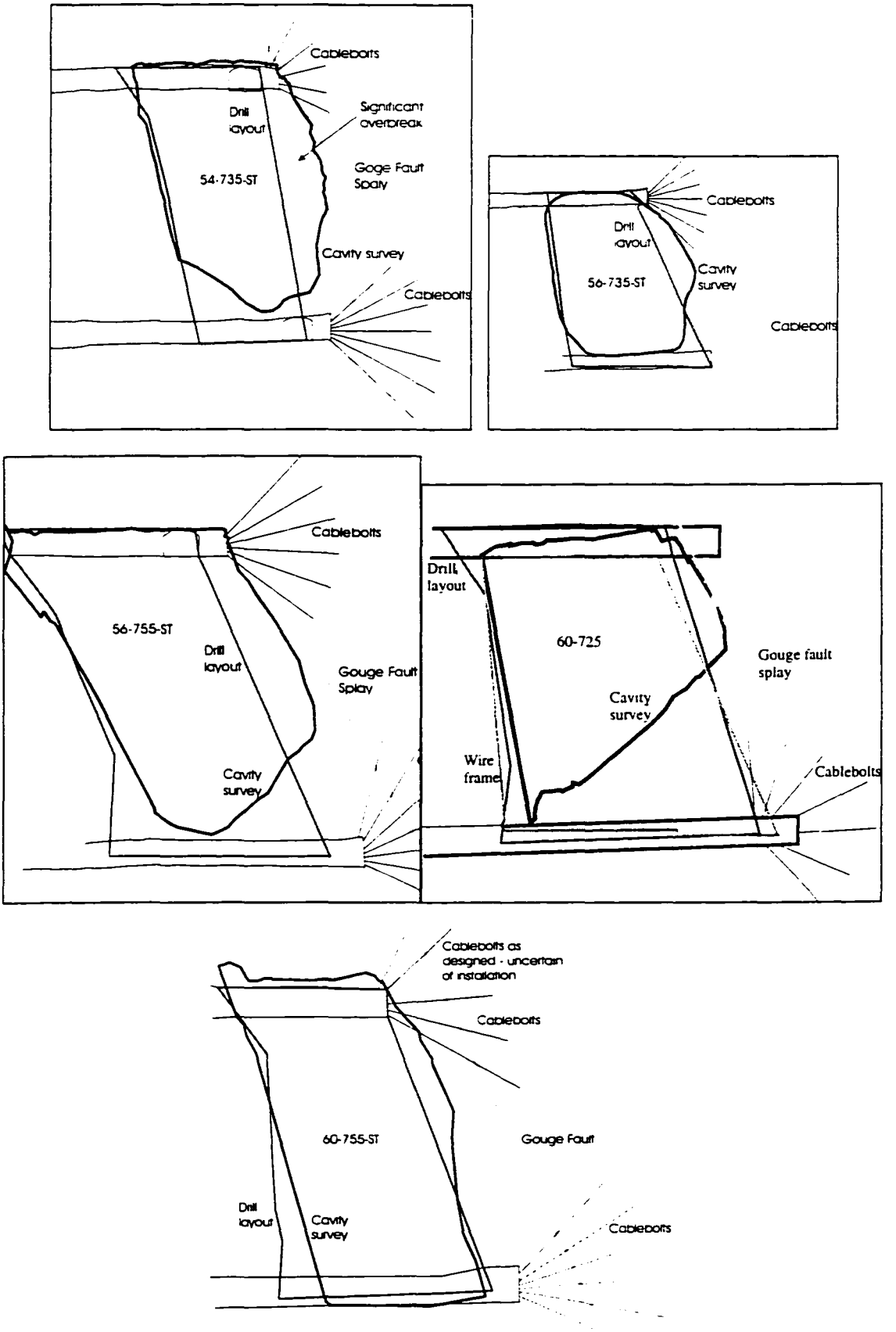
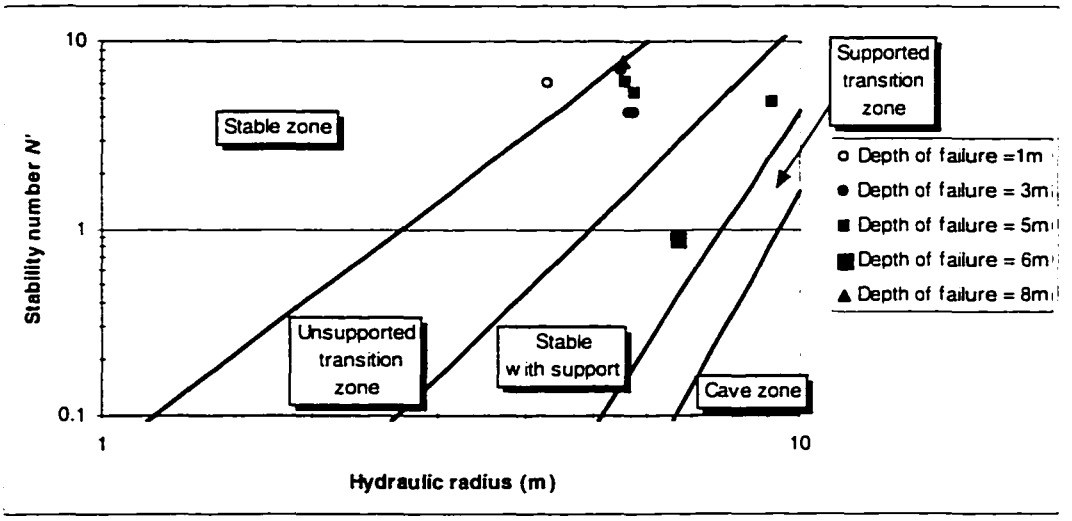
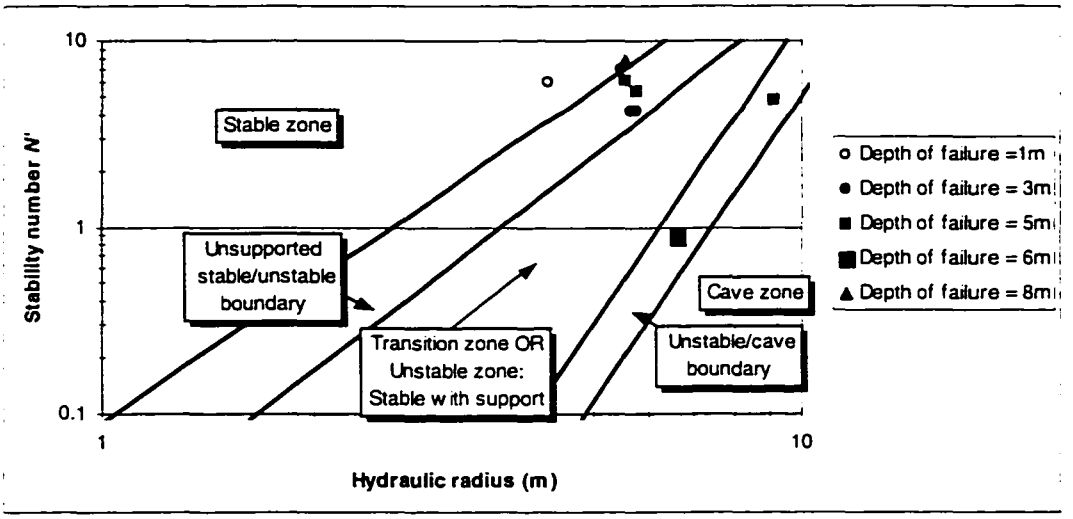


Figure 6.31 (cont.)



(a) Potvin and Nickson defined transition zones (log-log scale)

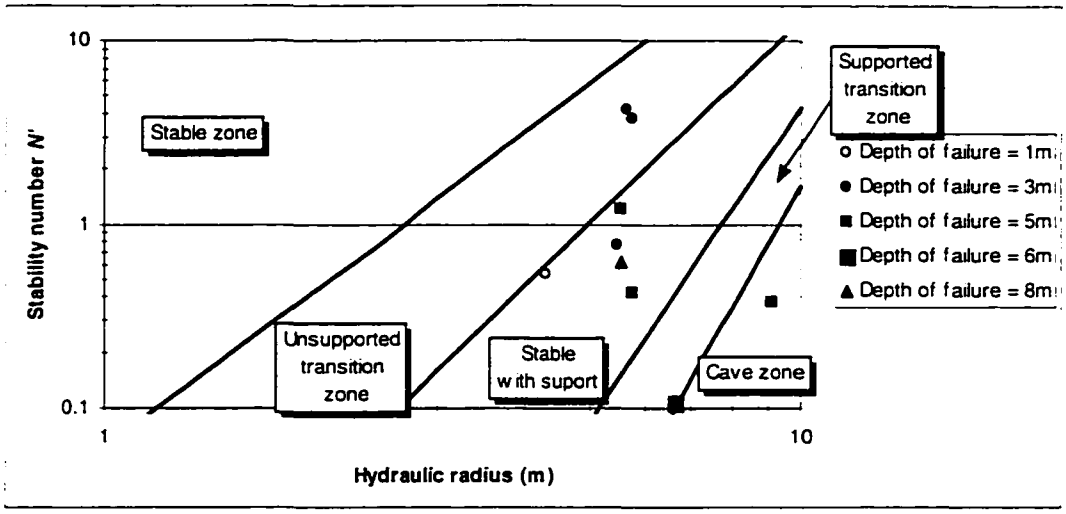


(b) Boundaries and transition zone as defined in the thesis (log-log scale) (Detail of Figure 6.28 and Figure 6.29)

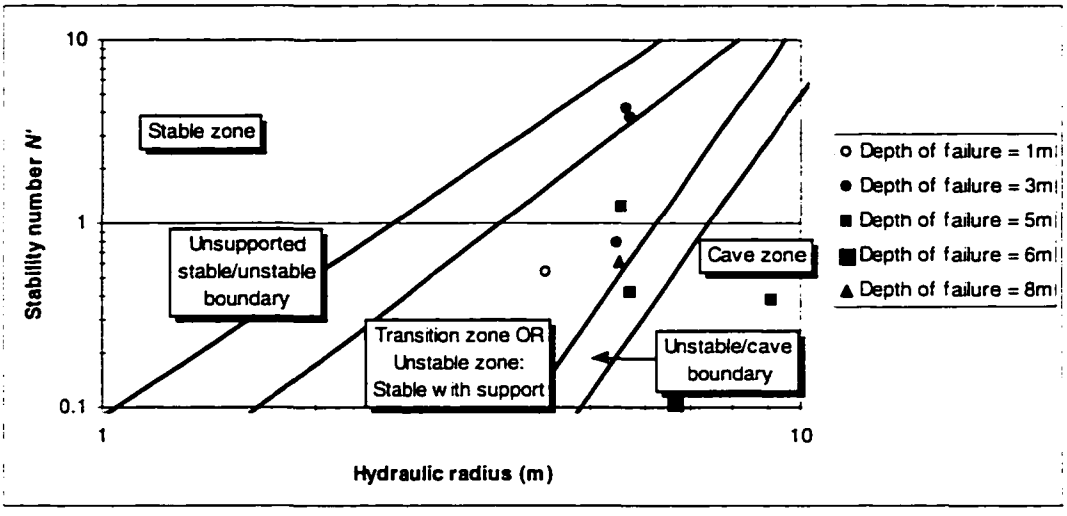
Figure 6.32 Conventional stability graphs without fault factor corrections for the nine stope surfaces

The same problem as shown in Figure 6.30 is shown in Figure 6.32. Caved stopes plot as supportable in stopes both cases.

The stability numbers for the nine stopes are corrected for fault effects using the fault factor graphs presented in Chapter 5. The fault factors determined for the nine stope surfaces are given in Appendix C. The stability graphs for the stability numbers corrected for faults are shown in Figure 6.33.



(a) Potvin and Nickson defined transition zones (log-log scale)



(b) Boundaries and transition zone as defined in the thesis (log-log scale)

Figure 6.33 Re-plotted stability graph for the nine stope surfaces corrected for fault effects

Figure 6.33 shows a marked improvement in the data zoning. The supported (unstable \ cave) boundary defined by Nickson is over estimated. Using this boundary, caved stopes plot as stable if supported, but which are actually not supportable. Figure 6.33b tends to be better in separating the stopes into their correct performance zones and is less conservative, compared to Figure 6.33a. In particular, it separates unstable and caved stopes better. However, adjustment for faults must be made before plotting a stope.

For the same stopes, the depths of failures were estimated from the corresponding curves in the $ELOS_f$ chart in Chapter 5. The results are shown in Table 6.14. All 9 stopes except 56-755-NE and 56-735-NE stopes were supported with cablebolts, and yet they caved. The table shows a comparison of overbreaks in stopes as determined from cavity survey profiles with predicted $ELOS_f$ values from the $ELOS_f$ curves from the procedure that was presented in Chapter 5.

Table 6.14 Comparison of measured average overbreak with predicted $ELOS_f$

Stope surface	Measured average overbreak - $ELOS$ (m)	Predicted $ELOS_f$ (m)
51-705-NE	1	4
56-755-NE	3	1.5
60-725-NE	3	4.5
60-755-NE	3	1.5
47-725-NE	5	5.2
48-725-NE	5	6
56-735-NE	5	8.1
53-735-NE	6	3.3
54-735-NE	8	8.1

Sloughage of 54-735 NE stope surface is a well-known case at Kidd Mine because it resulted in dilution of approximately 30%, with an average depth of failure of 8 m. The distance of the fault to the stope surface as determined using procedures in Appendix B, is 7 m. The predicted overbreak from $ELOS_f$ chart as shown in Table 15 is 8.1m, with a fault factor of 0.08. The overbreak occurred to a depth approximately equal to the distance of the fault from the stope surface, and terminated at the fault. Therefore, the procedures presented in Chapter 5 can be applied to predict fault related overbreak, and to the stability graph, but may require further calibration.

The procedure developed for determining the fault factor F_w can be applied to specific cases. However, the fault factor chart presented in Chapter 5, is applied in a generic form to the Kidd Mine database. Guidelines for general application of the fault factor chart are as follows:

- Determine the included angle ξ between the fault and stope surface using procedures in Appendix B;
- Determine the distance d between the fault and the stope surface from procedures in Appendix B;
- Determine the stope aspect ratio A_r;
- Estimate the in situ stress ratio K;
- If the fault intersects the stope surface, use the stope aspect ratio A_r, K-ratio, and fault friction angle ϕ to select appropriate curve in fault factor chart. Using the included angle ξ determine the fault factor F_w from the selected curve;
- If the fault does not intersect the stope surface, determine the normalized fault distance d/h from the stope surface. If the included angle is $\xi<30°$, use curve for non-intersecting faults to determine fault factor F_w. An included angle $\xi<30°$ is considered sufficiently small for the stope surface and fault to be assumed approximately parallel.
- When the included angle $\xi\geq30°$, use A_r, K, and ϕ to select curve from fault factor chart. Using the included angle, determine fault factor F_w from selected curve.
- In most cases the stope aspect ratio A_r is sufficient in selecting the appropriate curve when the fault intersects the stope surface, or when the included angle $\xi\geq30°$ for non-intersecting faults.

- However, an intersecting fault may fall entirely within the ore rock that is mined (Figure 6.34), and therefore does not affect the stability of the stope surface. In this case the fault factor should be set to one. Stope plans and sections are useful in checking cases of this type.

This procedure has been found to be adequate in assessing the fault factor in a general manner from the fault factor chart in Chapter 5.

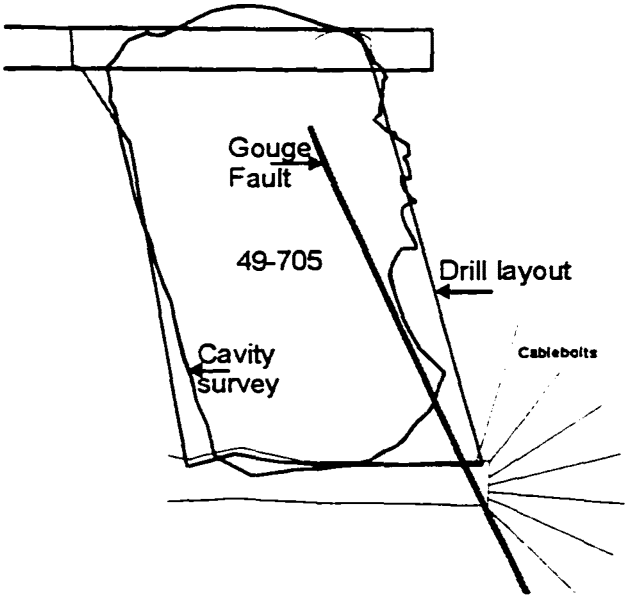
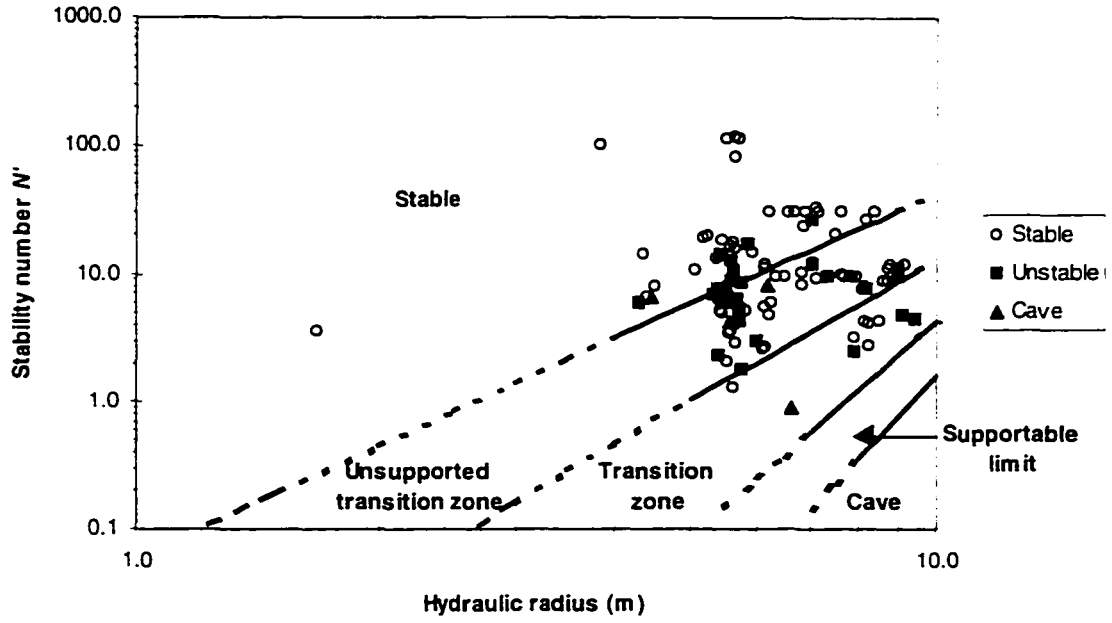
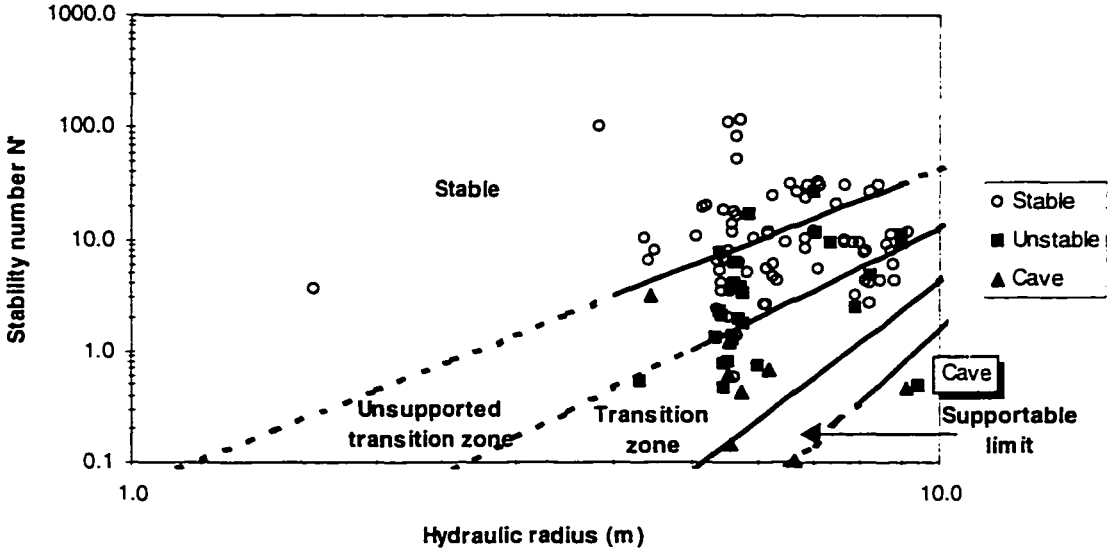


Figure 6.34 Stope section showing fault intersecting stope surface but lying entirely in ore that is mined, and therefore does not affect stability of stope surface - F_s=1

Considering the significant improvement gained by application of the fault factor showed in the specific cases in Figure 6.32a and b, the procedure was applied to the entire Kidd Mine database (Appendix C). The results are shown in Figure 6.35 and Figure 6.36 for both the uncorrected and corrected data.



(a) Uncorrected



(b) Corrected for faults

Figure 6.35 Modified stability graph for (a) uncorrected stability numbers for fault effects (b) corrected stability numbers for fault effects, with boundaries as defined by Potvin (1988) and Nickson (1992)

The better separation of stope performances into their correct zones in the stability graph in Figure 6.36, compared with Figure 6.35b is qualitatively obvious, particularly between unstable and cave stopes.

From Table 6.13, the fault factor has improved the data separability by 67% on the basis of Equation 6.1. This implies that the separation of stope surface performances is improved by 67%, compared to the uncorrected data.

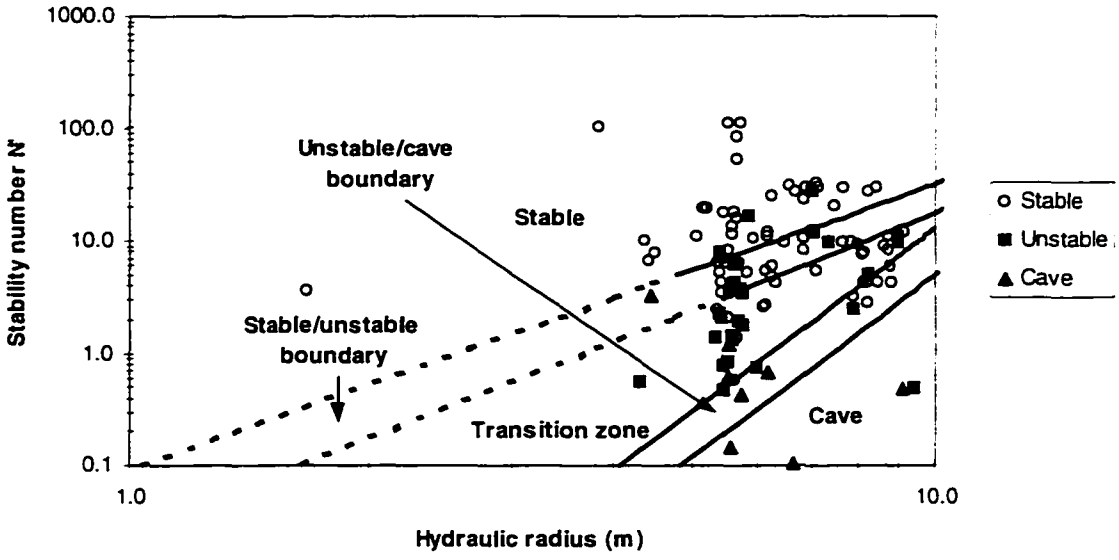


Figure 6.36 Modified stability graph for corrected stability numbers for fault effects, with boundaries as defined in Chapter 3 of thesis

Performance of the classification criteria defined by Potvin and Nickson can be compared with those defined in Chapter 3 of the thesis using Apparent Error Rate *APER* method (Table 6.15). The size of boundary between stable and unstable stopes in Potvin-Nickson is much larger than thesis boundary. The fact that the Potvin-Nickson boundary for "supported stopes" (unstable\cave boundary) over predicts the range of supportable stopes is significant for open stope design. Stopes supported in the overpredicted range of supportable stopes still cave.

Table 6.15 Comparison of performances of stope performance classification criteria

Case	Performance prediction errors (%)		Remarks
	Potvin/Nickson	This thesis	
P(Stable|Unstable)	11	11	No difference
P(Unstable|Stable)	58	51	Thesis approach better
P(Unstable|Cave)	14	14	No difference
P(Cave|Unstable)	57	29	Thesis approach predicts caving much better
APER	47	40	Thesis method better overall

In Chapter 2 of the thesis, it was shown that plots of the stability graph using hydraulic radius and modified span were similar. Figure 6.37 is a plot of modified span versus the re-defined stability index, mine excavation stability index, *MESI*. The mine excavation stability index is defined as:

$$MESI = Q'_m \bullet B \bullet C \bullet F_s \qquad 6.3$$

where, Q'_m = rockmass quality taking into account any soft zones (see Chapter 7) or the other parameters are as defined earlier. For discrete faults as found in Kidd mine, $Q'_m = Q'$.

Span in the context of this thesis is the modified span or equivalent dimension of the stope surface analyzed.

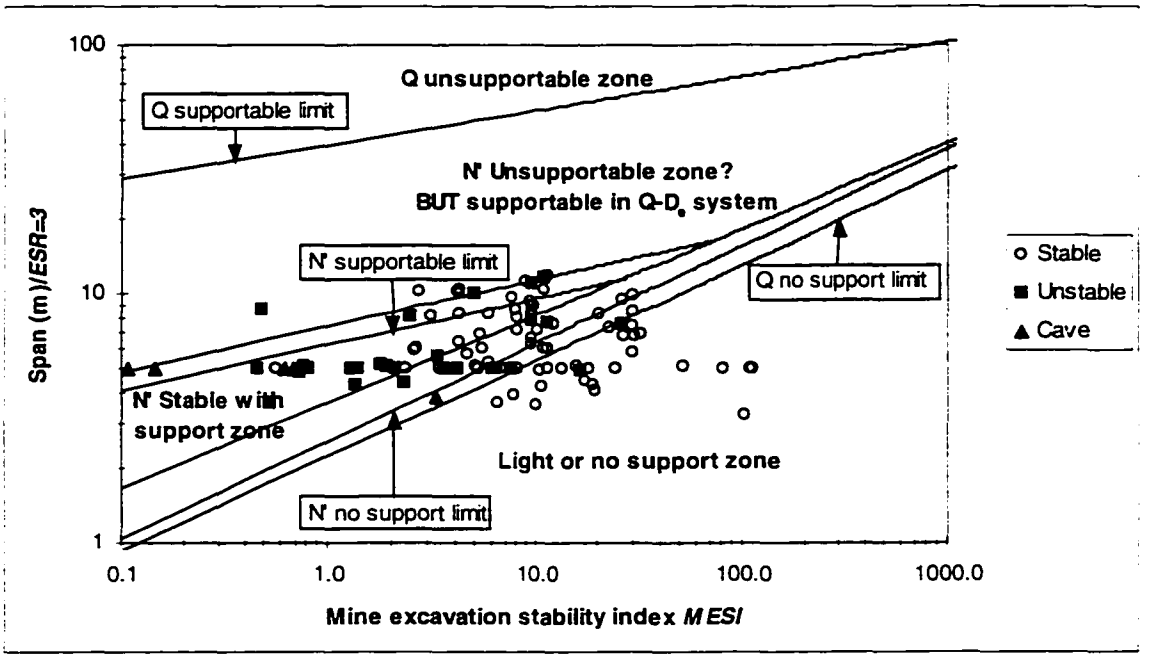


Figure 6.37 Mine excavation stability index graph for Kidd Mine, (ESR = 3)

Figure 6.37 shows a similarity to the stability graph when plotted on a log-log scale with hydraulic radius as vertical axis and stability number as horizontal axis. Figure 6.37 can be used for the design of open stopes, and has the advantage of giving specific stope dimensions such as strike lengths and spans of endwalls in ore or waste rock. The Q-D_e support boundaries (Barton et al., 1974) are superimposed on the plot. Again, there is a large difference between mine environment support limit, and civil engineering excavations support limit as depicted by the Barton Q-D_e graph is evident in this graph. Reasons for the large difference in supportable limits are attributed to relaxation (Kaiser et al. 1997). Another reason is that in civil engineering a wide range of supports are available while in mining only a limited range of supports are used. Furthermore, the data plotted in Figure 6.37, suggests that ground with $MESI \leq 1$, cannot be effectively stabilized with support (cablebolts) at standard support densities (cablebolt spacing).

Another alternative method of presenting the stability graph is in terms of multiple design curves using likelihood ratio Λ. The procedure was proposed and verified in Chapter 3. The likelihood ratio is a

measure of the risk of stability against instability under given conditions. Figure 6.38 is a plot of the likelihood ratios calculated from the corrected Kidd database using Equation 3.31, against average depth of failure from overbreaks from cavity surveys. The figure shows that the higher the likelihood ratio the smaller the depth of overbreak. Most stopes are stable for likelihood ratios greater than one. Stopes with likelihood ratios less than one are prone to large overbreaks. Therefore, the likelihood ratio can be used to predict stope performance.

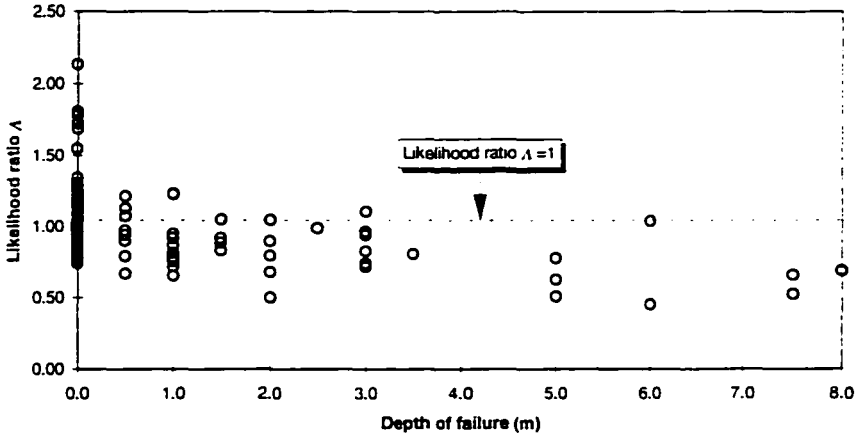


Figure 6.38 Plot of likelihood ratio against average depth of failure

The distribution of data in Figure 6.35 and Figure 6.36 show significant overlaps, implying that the application of the likelihood ratio concept to the Kidd data should be useful, since stability in this case is not absolute but probable. Figure 6.39 is a re-plot of the database as a multiple design-curve stability graph. The Mine Engineer can choose a design curve in Figure 6.39 based on acceptable risk in terms of stope performance.

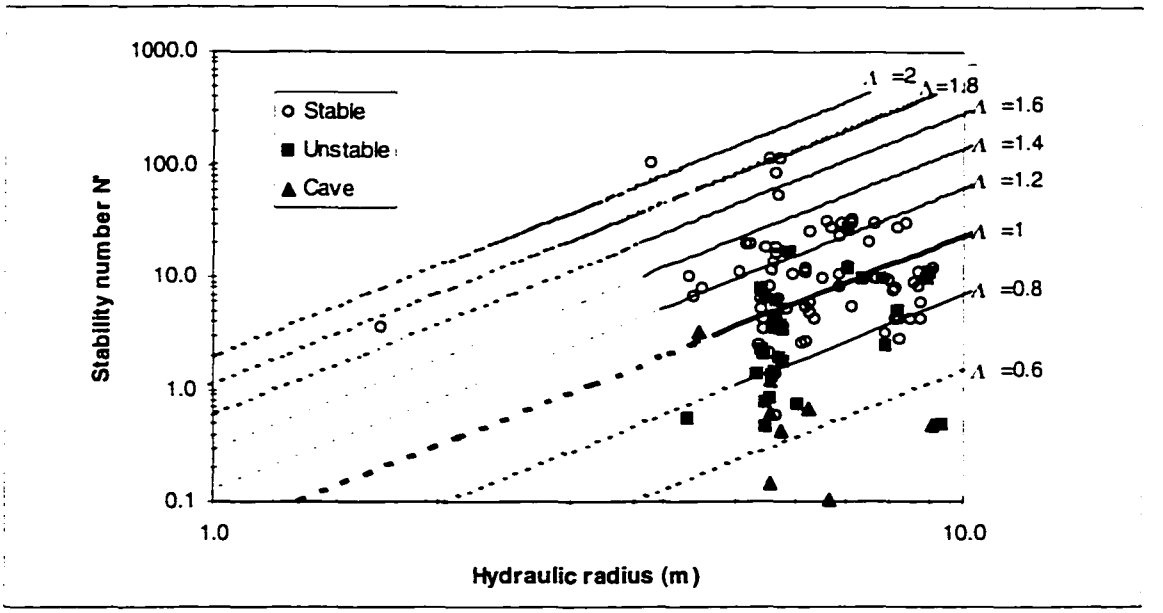


Figure 6.39 Likelihood-based multiple design curves stability graph using hydraulic radius

Figure 6.39 offers the additional advantage that a mine only has to decide which curve it wishes to use for a given ground condition. Therefore, Figure 6.39 is a dynamic design-curve stability graph that may be used for on-the-spot design. An alternative likelihood-based multiple design curves using modified span is presented in Figure 6.40.

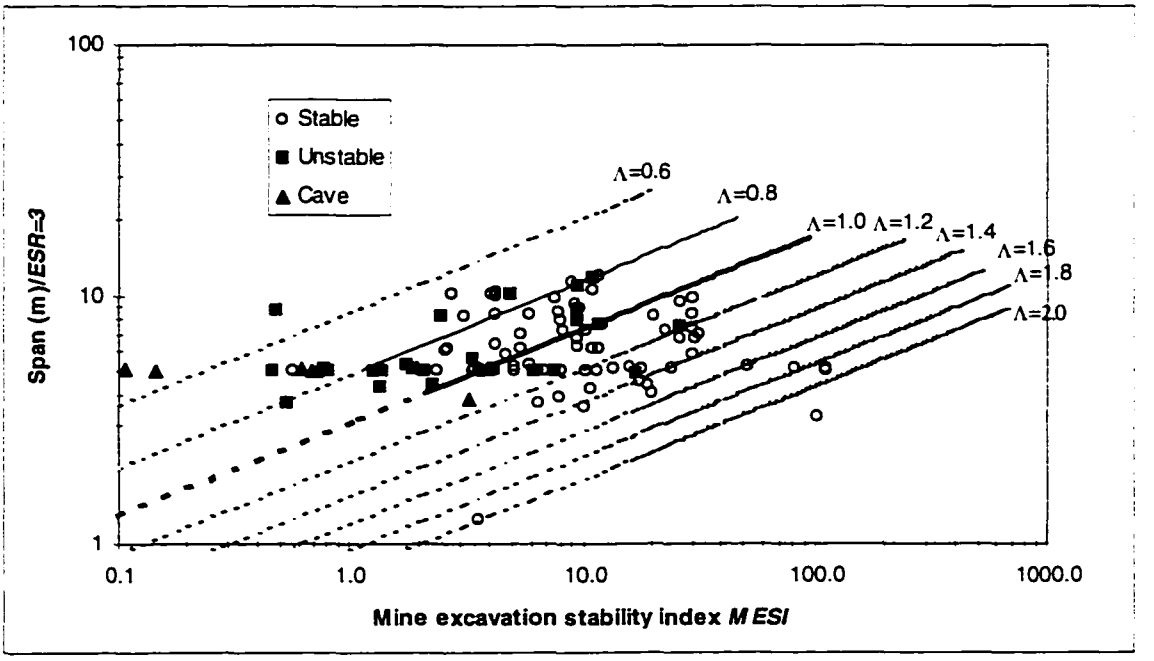


Figure 6.40 Likelihood-based multiple design curves stability graph using modified span

The statistical concepts used in the thesis to develop the boundaries between the different classes of stope performance are used to optimize the boundaries, and to determine risk cost of misclassification or wrong predictions.

6.8 Optimization of Stability Graph Boundaries and Risk Cost

A Mine Engineer can make two types of errors in the stability graph when used as a stope performance prediction tool. A stable stope can be misclassified as a failed or unstable stope, and a failed or unstable stope may be classified as a stable stope. Both errors imply cost to the mine. We need to know the relative cost of these two errors, in order to account for it in the stability graph. The objective is to minimize the probability of misclassification so that for example the prediction of a stope surface performance in design is reliable.

The database is divided into only stable and unstable or failed stopes. The general equation for classifying a stope as stable, as against unstable or failed was derived in Chapter 3. The optimization equation is:

$$HR = 10^{\left[0.4905 - 2\log(A) + 2\log(\xi) + 0.3738\log(N)'\right]}$$

The following is the scenario:

Large span stopes are designed based on the assumption that they will be stable to optimize profit. However, experiences with these stope sizes show unacceptable dilution levels, and future stopes must be cablebolted. This is the P(StablelUnstable) situation. An alternative design is smaller stopes to avoid support cost, assuming that such stopes will be self-supporting. This is the P(UnstablelStable) case.

P(StablelUnstable) - A large stope is considered to be one that is at least +2HR from the design curve (e.g. 50,000) tons). This puts the stope in the caving zone of the modified stability graph. No cables are installed because of the assumption that failure will not occur. The hangingwall caves and gives dilution costing $300,000 (1998 $). Tannant and Diederichs (1997) estimate average dilution at Kidd around this value.

P(UnstablelStable) - For this scenario cablebolts are installed at a cost of $24,000 since likely failure was assumed. However, in service, the stope remains stable. Only acceptable dilution occurs because of irregular orebody geometry, at a cost of $150,000.

The misclassification cost matrix for the scenario for the example case is given below:

Table 6.16 Cost matrix for misclassification risk cost determination

Actual membership	Predicted stable	Predicted unstable
Stable	0	174000.0
Unstable	300000.0	0

The relative cost factor ξ_r for Kidd then becomes:

$$\xi_r = \frac{C(Unstable|Stable)}{C(Stable|Unstable)} = \frac{24000+150000}{300000} = 0.58$$

The confusion matrix for the classification rule is given as:

Table 6.17 Confusion matrix for Kidd Mine database

Actual membership	Predicted membership		Total number of casescases
	Stable	Unstable	
Stable	46	31	77
Unstable	6	29	35

The following are the corresponding probabilities:

P(Stable)=77/112

P(Unstable)=35/112

P(StablelUnstable)=6/35

P(UnstablelStable)=31/77

The total expected cost of misclassification *ECM* is given by the product of the off-diagonal entries in the cost matrix and their respective probabilities of occurrence:

ECM=6/35*300000*77/112+31/77*39000*35/112=$40263

The misclassification cost is significant, and points out the importance of having unbiased and ambiguous boundaries between the stope performance zones of the stability graph.

The misclassification risk cost ratio ξ_r is 0.58, giving a risk cost factor ξ of 0.90. The general boundary between stable and unstable stopes can thus be optimized to account for misclassification cost for Kidd. Figure 6.41 shows the shift in the boundary.

The optimized boundary gives a misclassification risk cost of $23060. The optimization, thus, would save the mine an amount of $17203 per stope.

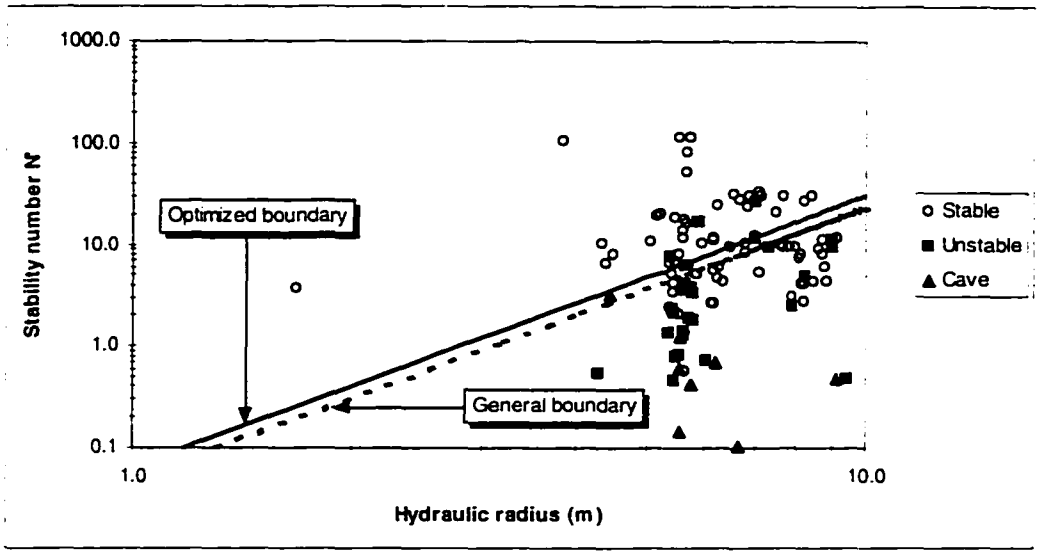


Figure 6.41 Optimized boundary between stable and unstable stopes

The procedure can be applied to the boundaries with upper and lower limits as well, including all boundaries. If desired, the cost associated with each likelihood ratio design curve in Figure 6.39 can be determined and superimposed on the curves. The graph then becomes mine specific, since cost and other conditions vary from mine to mine. Finally, as more data is collected, this procedure can be utilized to further fine-tune the design curves.

6.9 Summary

Mathematical formulae developed in Chapter 5 for calculation of stope surface dimensions, dip and dip directions, distance of faults to stope surfaces, and included angles between faults and stope surfaces have been applied to Kidd Mine. These equations can be applied at any other mine that uses AMINE, DATAMINE, VULCAN and GEMCOM for mine planning and design purposes to determine stope surface geometries and distances of faults to stope surfaces.

A discriminability index was applied to the Kidd database and found to give a good description of the behaviour of the data. The data discriminability index is a useful parameter for determining data overlap, and for assessing data improvement from variation of input parameters when used with the stability graph boundaries.

Statistical discriminant analysis was used together with the calibration database to determine boundaries between the stable\unstable, and unstable\cave data groups, using from the unsupported stopes. The zone between these boundaries is defined as the transition zone. The boundaries are superimposed on the Kidd data and found to perform better compared to the conventional boundaries of Potvin (1988) and Nickson

(1992) boundaries, in separating supportable from unsupportable stopes. The boundary between unstable and cave stopes is particularly better defined, and effectively separates caving and unstable stopes.

The Potvin-Nickson boundaries appear to over estimate the performance of stopes in the transition zone, particularly, their supported transition zone between unstable and cave stopes. Supported stopes in the Kidd database have caved with overbreaks in excess of 5 m, but plotted as supportable compared to the Nickson (1992) supportable stope boundary. The Clark and Pakalnis (1997) *ELOS* stability graph also over estimates of the Potvin-Nickson boundaries by showing all overbreaks in excess of 5 m (caved stopes) in the transition zone, and therefore supports this conclusion.

A fault factor was developed in Chapter 5 and applied to the Kidd Mine database with 67% relative improvement to the separability of the data. Figure 6.32 and Figure 6.33 show that the fault factor graphs developed in Chapter 5 can be applied to the modified stability graph to obtain better prediction of stope performance when faults are present.

The $ELOS_f$ chart developed from modelling stopes with faults has shown good promise as a means of predicting overbreak in open stopes when faults are close to or intersect the stope surface. The $ELOS_f$ chart has been applied to predict overbreak in the nine selected stopes in the Kidd database with about 60% correlation. Further calibration is required to improve the successful prediction rate.

The issue of using the calibration database stability graph at specific mines as against those mines developing their own stability graph with their own boundaries depends on the variability or dispersion of the data. The general modified stability graph stope performance boundaries become useful when data is limited to only a narrow range. Optimizing the general boundaries according to specific mine costs is an economic and viable method. The statistical procedures developed should be applied to define design boundaries for the particular mine, when data are sufficiently dispersed, separability high, and variances of data subgroups well above zero.

Misclassification risk cost has been introduced into the stability graph. This is significant for planning of open stope mines.

CHAPTER 7

EVALUATION OF ASHANTI OPEN STOPE PERFORMANCE

7.1 Introduction

In the past few years, Ashanti Goldfields Mine embarked on a mine-wide expansion program to boost production. The main objective of the mine was to produce one million ounces of gold per annum by February 1997.

With the fast depletion of high-grade ore, a suitable mining method was required to produce a high tonnage to meet the management target. Open stope and mechanized cut-and-fill mining methods were compared for their cost effectiveness. Average cost of underground mining at Ashanti is US$45.00 per ton. The study revealed that average cost of open stope mining including backfill is US$12.00, compared to US$28.00 for mechanized cut-and-fill mining (Amponsah, per comm.). Hence, open stope mining was adopted as the preferred mining method.

Preparations for open stope mining in Ashanti started in March 1991, with production from open stopes beginning in December 1992. Stope sizes of 15 m strike length by 10 to 30 m widths with 24 m-sublevels were based on the recommendations of a team of mining engineers, after touring mining companies practicing open stope mining in Canada and Australia (Craig, per. Comm).

The orebody at Ashanti is divided into mining blocks (Figure 7.1), and the details of the stoping procedure differ from block to block. In this research, Blocks 2 (Kwesi Mensah Shaft - KMS), 7 (Kwesi Mensah Shaft - KMS), 8 (George Cappendell Shaft - GCS) and Eaton Turner Shaft (ETS) shaft pillar were studied. These blocks span a good length of the Ashanti orebody (Figure 7.1).

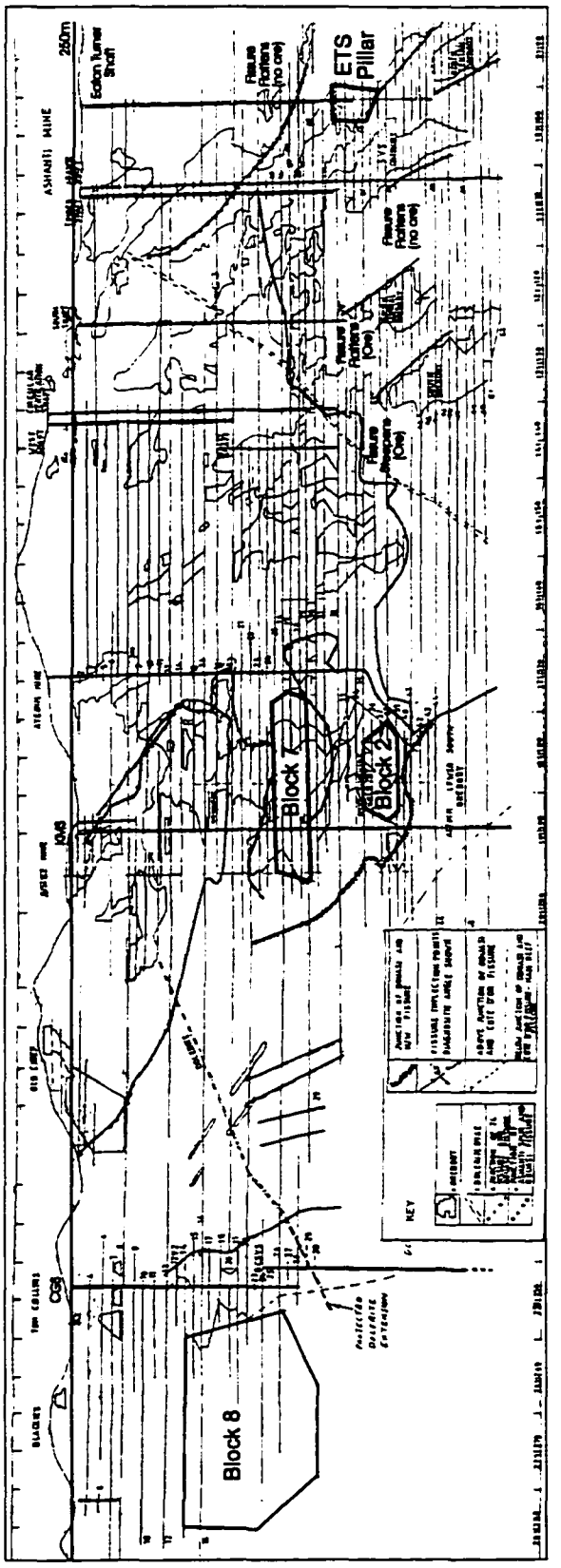


Figure 7.1 Longitudinal section of part of Ashanti Goldfields mine at Obuasi showing the blocks studied

7.2 Objectives

The stability graph method for open stope design is largely based on Canadian underground mines with relatively competent rocks at depths below 1,000 m. In the Ashanti Goldfields mine, the rocks classify as poor to good in the Q-system (Q' is between 0.9 and 20).

The objectives of the investigation are:

- To investigate the applicability of the stability graph method at Ashanti, and
- To investigate the effectiveness of incorporating a correction for the presence of faults, fissures and shears into the stability graph method.

The procedures for achieving the objectives consist of data collection at the mine and developing a correction method in the stability number of the modified stability graph for soft zones. In Chapter 5, a procedure for correcting for discrete faults was presented. It was stated that where faults are wide the gouge material quality is important, as any caving is likely to involve the gouge material. The fault factor concept will therefore be extended to cover the soft fault gouges in wide faults. The graphitic shear zones at Ashanti are an excellent case for the application of this theory. The procedure is discussed in Section 7.10 of this chapter and applied to the Ashanti database.

7.3 Geology

7.3.1 General geology

Ashanti Goldfields Company is located at Obuasi in the Ashanti Region of Ghana. The mine is situated on the main gold belt stretching from south of Prestea in the south to beyond Konongo in the north, along a NE-SW trend. Figure 7.2 shows the geology of Ghana, and the location of the mine.

Numbers on the map are explained below:

- 1 Ntubia-Sunyani-Bombiri-Nangodi zone,
- 2 Siwum-Bibiani North-Chichiwere zone,
- 3 Akanko-Prestea-Bogoso-Obuasi-Obuom-Konongo-Agogo zone,
- 4 Mangoadze-Kibi-Begoro zone, and
- 5 Akoko-Kanyankaw-Nkawkaw-Obemeng zone.

The auriferous reef system in the Obuasi area has a proven lateral extent of over 7.6-km distance, and is persistent at depth to the lower explored level of 1.6 km below surface.

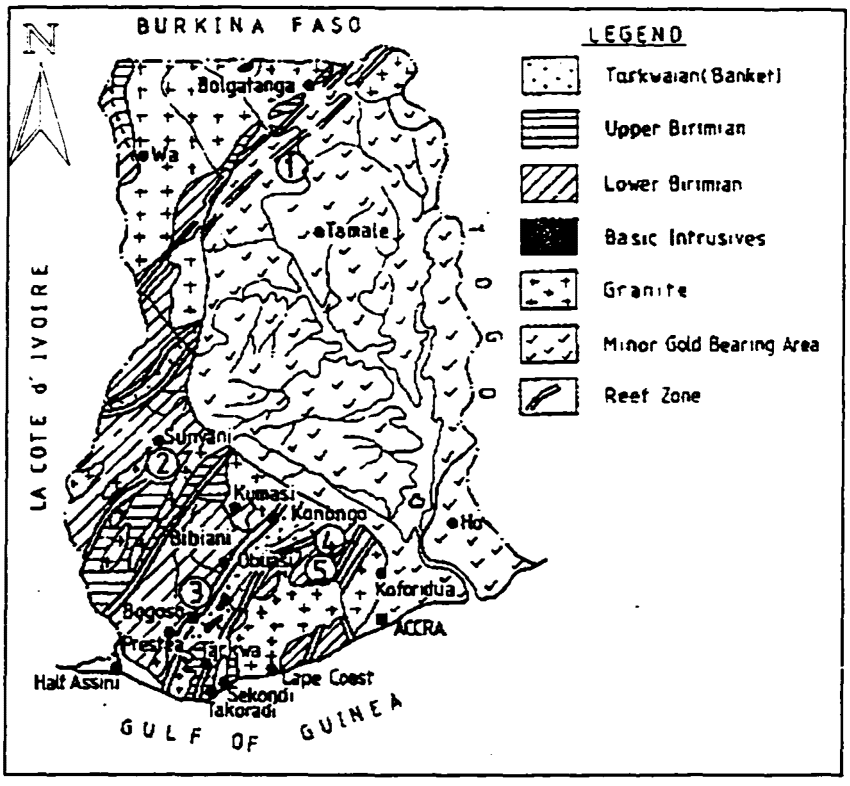


Figure 7.2 Map of Ghana showing geology and location of Obuasi - Ashanti Goldfields mine

The Ashanti orebodies are located in extensive shear zones characteristically associated with carbonaceous schists and phyllites. Two major shears are well known at the mine. They are the steeply dipping Obuasi Fissure, and the flatter dipping Cote d'Or Fissure (Figure 7.3). The two zones join at depth on a southerly pitching intersection to form the Main Reef Fissure. A third prominent fissure is the Ashanti Spur, which occurs at the north of the mine, branching off at the Obuasi Fissure. The fissures are the sources of the ore, having served as channels of the mineralizing solutions that formed the orebody.

The major rock units at the mine are Birimian phyllites, siltstones, greywacke, hornstones and metavolcanics. Greywackes, phyllites and schists are the most prominent.

Jointing is prevalent in the mine especially in the more competent meta-greywackes and meta-volcanics. Sinclare et al. (1978) identified two sets of joints with strikes and dips of 310°/75°SW and 290°/72°NE respectively, and classified them as shear joints.

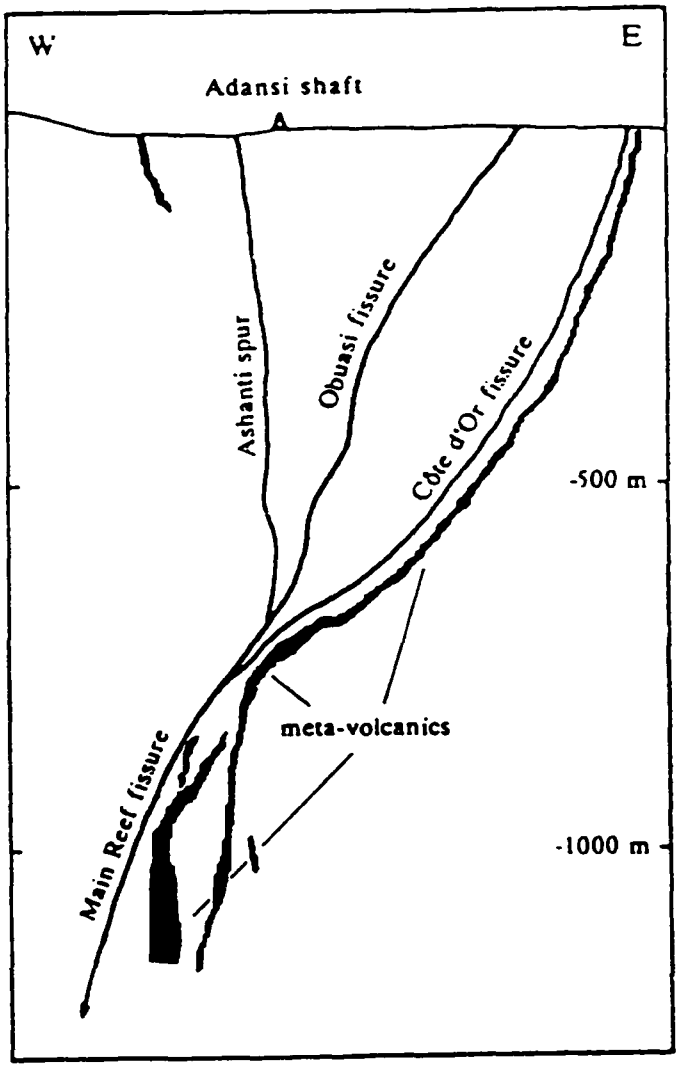


Figure 7.3 Main fissures and shears at Ashanti as observed near Adansi shaft (after Amanor and Gyapong, 1988)

The site-specific geology of the mine blocks often controls the stability of open stopes, depending on the abundance of graphite. The site-specific geology of Blocks 2, 7, and ETS shaft pillar are presented in the following sections.

7.3.2 Geology of Blocks 2 and 7 - Kwesi Mensah Shaft (KMS)

Block 2 is located at the central section of the Ashanti mine between 175/176 and 188/199 mine grids from 35 to 39 levels. Block 2 is part of the Anyinam Lower South Orebody.

Gyapong (1993) presents the geology of Block 2. The description includes Block 7, which is above Block 2, from 26 level to 34 level. The orebodies of Block 2 consist of quartz lenses within the Obuasi Fissure, and disseminated footwall sulphides closely associated with the Obuasi Shear.

The quartz orebody is generally sheared and exhibits banded structure. It is commonly associated with graphitic schist at the contacts, and partings within the quartz. The rich quartz orebodies are mined out below (39 to 41 levels) by cut and fill mining. Block 2 is thus undercut. Disseminated sulphides have become the principal ore-type of the block after the rich quartz orebodies got mined out. The sulphides are largely associated with a lenticular meta-volcanic body, at the footwall side of the Obuasi shear, and the meta-sediments. Sandwiched between the quartz body and the meta-volcanic sulphides at several localities is a carbonaceous sheared pelitic zone that is low grade to barren.

Located to the east of the ore zone is the Cote d'Or Fissure. This fissure is characterized by carbonaceous to graphitic schist gouge. The fissure is between a few metres to 75 m from the orebody. The Cote d'Or Fissure is thus likely to constitute a considerable weakness in the footwall of the orebody (Gyapong, 1993), particularly at the north section where it is very close to the Obuasi system.

The orebodies in the Block 2 area have a general strike of N30°E with dips ranging from 65° to sub-vertical, to the West.

Limited joint surveys (Gyapong, 1993) suggests two major sets, one trending 145° and dipping 78°W. The second joint set is more steeply dipping and trends 170°.

The zone of mineralization in Block 7 lies between the Obuasi Fissure and the 12/74 Fissure. Both fissures are distinctively lined with graphitic gouge ranging in thickness from a few centimetres to metres. This block lies above Block 2 from 26 level to 34 level and has similar characteristics to that block. In Block 7, the dips of both the Obuasi and12/74 fissures are approximately 70°W and 55°W respectively. The quartz and meta-volcanic sulphides dip between 60° to 80° to the east, with a reversal of dip occurring between 34 and 36 Levels.

7.3.3 ETS shaft pillar geology

This summary is based on a discussion with the sectional geologists in charge of ETS. The ETS pillar extents vertically from 7.62 m above 32 level to 36 level, and has an average strike length and width of 62.7 m and 4.0 m respectively.

The orebody consists of main reef quartz. It is white to grey in colour, banded and strongly fractured with abundant visible gold (Kumi, per.comm.). On both footwall and hangingwall contacts with the orebody are strong graphitic shears varying in thickness from 0.5 m to 2.5 m.

The main reef body is steeply dipping, with an average dip of about 75° W, and continuous along strike and dip. However, on 32 level, the main reef body bifurcates into the Main and Hangingwall Shears from 32N 20W crosscut striking southwest to about the 15 crosscut position. The hangingwall has an average dip of

about 72° W. To the east of the footwall graphitic shear lies the meta-volcanics with occasional lenses of meta-sediments. West of the reef is the meta-sedimentary sequence, constituting the country rock.

Current developments further west into the meta-sediments, by a ramp access from 35 level has exposed a strongly sheared graphitic meta-sedimentary sequence dipping west, and averaging in thickness of about 12.0 m.

7.4 Implications of Geologic Structure to Open Stope Mining

The Ashanti Goldfields mine orebodies are associated with fissures, shear zones and faults. These structures often contain very weak graphitic and carbonaceous gouge. The orebodies also bifurcate with intercalating pelitic and graphitic units.

The graphite should be an important consideration in any investigation related to stability of open stopes. The graphitic and carbonaceous materials deteriorate quickly with moisture on exposure and tend to run (Suorineni and Tidzi, 1990). The graphite and carbonaceous rocks are also known to have very low compressive strengths in the range of 5 to 100 MPa.

Both the orebodies and host rocks are strongly fractured and jointed. Joints in the orebody are generally filled with the graphitic material. Major faults and shears run close to the orebodies and affect stability of stope surfaces in their proximity.

Bifurcation of orebodies into two or more lenses with intercalating soft materials is another source of instability, particularly in stope crowns. The variation in orebody dip with depth also seems to constitute an instability problem. These characteristics of the orebodies and host rocks should form the basis for stability assessment of open stopes in the blocks under study.

7.5 Mining Methods

Mireku-Gyimah and Suglo (1993) discussed underground mining methods practiced in the various underground mines in Ghana. Table 7.1 is a summary of current mining methods at Ashanti Goldfields mine in Obuasi.

Table 7.1 Summary of mining methods at Ashanti Goldfields Company underground mines (after Mireku-Gyimah and Suglo, (1993)

Mining method	Stoping efficiency, t/man shift	Recovery (%)	Dilution (%)	Proportion of mine production (%)
Cut and fill (Hydraulic fill - hydrafill)	6-8	80-90	5-10	10-15
Cut and fill (waste rock fill)	8-10* 30-32**	80-90	5-10	25-35
Square-set stoping	1.5-5	80-90	5-10	8-12
Sub-level caving	30-40	70-80	20-30	45-55
Shrinkage stoping	5-8+ 25-30++	80-90	10-15	2-5

*Unmechanized cut and fill stopes.
**Mechanized cut and fill stopes
+Stoping efficiency when stoping
++Stoping efficiency when drawing ore from stopes

Open stoping has only been recently introduced and is targeted to become the major method of ore extraction at the mine. Longitudinal open stoping is the common practice, at Ashanti Goldfields mine. The stopes are designed for 10 to 20 thousand tons of ore. Each stope is designed to be depleted and filled within three months. Filling is immediate, with waste rock or cemented waste rock fill. Figure 7.4 is a typical stope design for Block 8 of GCS.

The open stoping method practiced in Block 8 of GCS is different from the other blocks as shown in Figure 7.5, and deviates from normal open stope design. Figure 7.5 shows a longitudinal section of a typical open stope layout in Block 8. Seven-metre pillars are left on both sides of a stope to prevent dilution from inflow of waste rock fill from adjacent mined and filled stopes (Decker, per. comm.). Waste rock fill is the main source of fill in Block 8 to help dispose of the large volume of waste rock from developments.

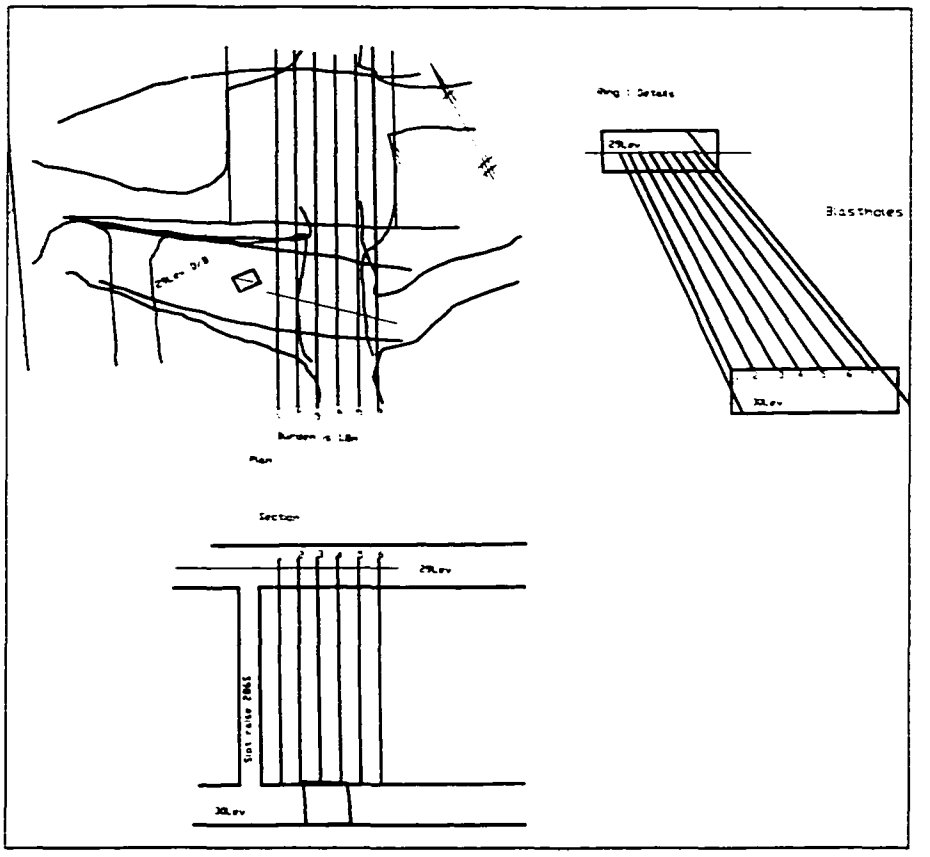


Figure 7.4 Open stope design at Ashanti for GCS Block 8, showing a plan view of blast rings

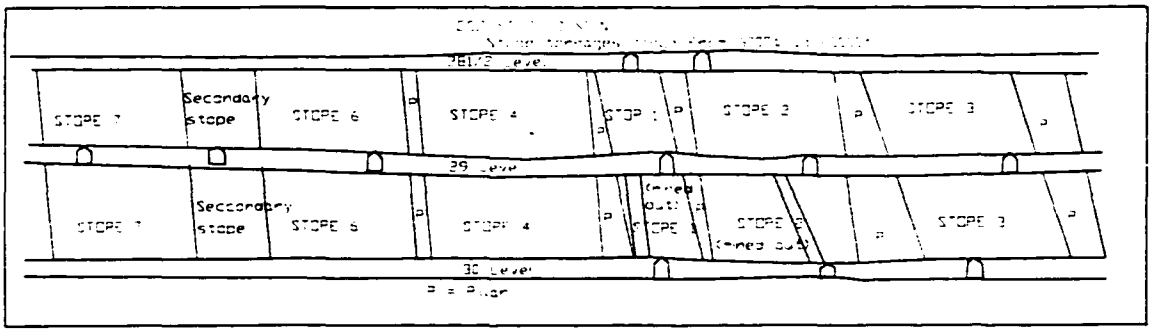


Figure 7.5 Longitudinal section showing open stope design in Block 8 of GCS

The disadvantage of the practice of leaving pillars is that in the case of high-grade ore the practice becomes expensive, if for some reason pillar recovery is not possible at some later date.

The ore body at ETS shaft pillar is given in Figure 7.6. Figure 7.7 shows stope sequencing at ETS shaft pillar. The plan view of the orebody in relation to the shaft is shown in Figure 7.8.

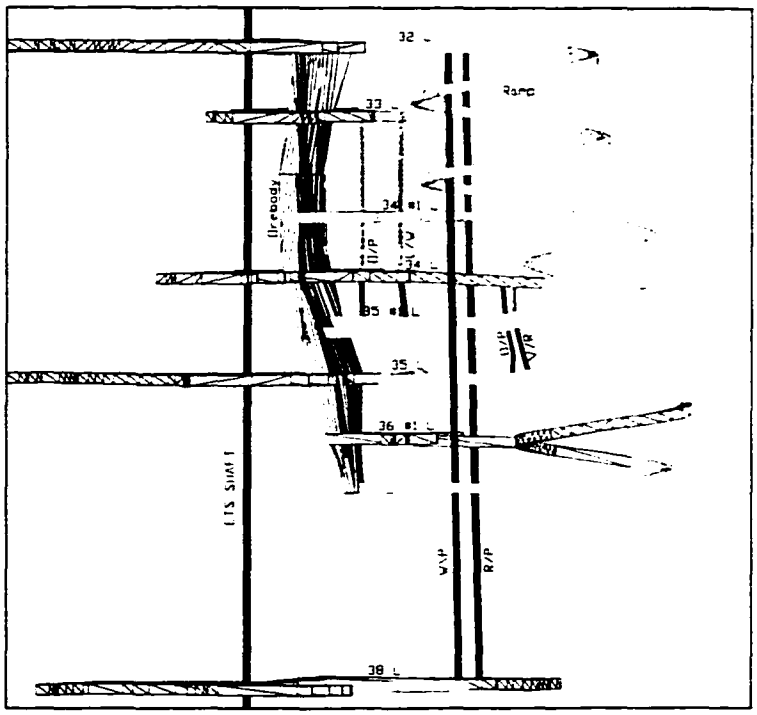


Figure 7.6 3D-wire frame of ETS shaft pillar orebody viewed along strike, with ramp and main levels

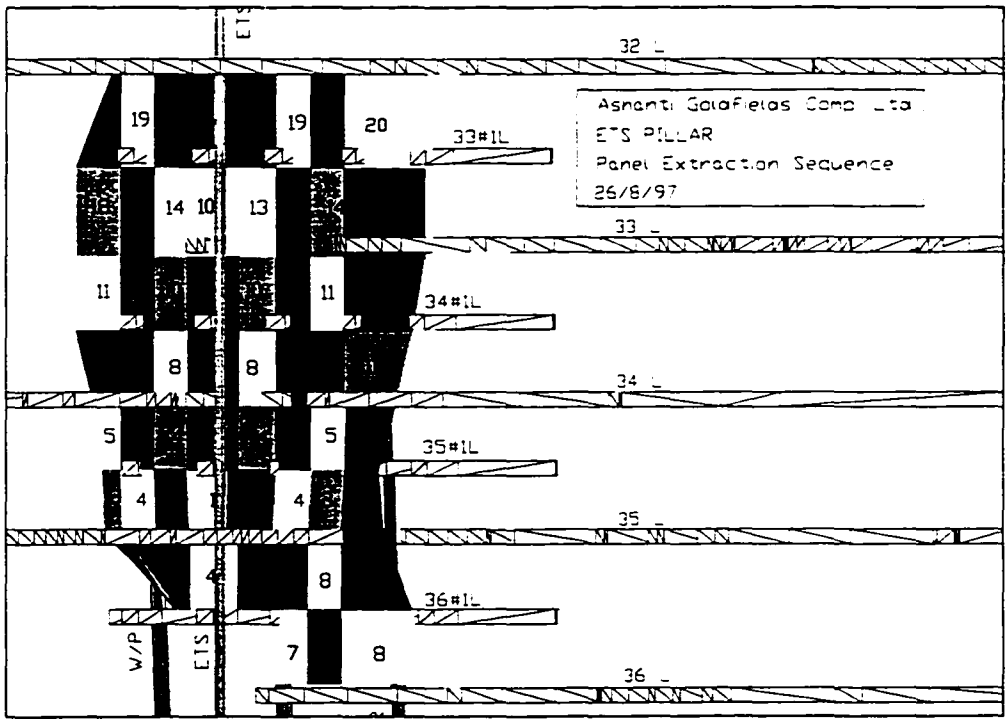


Figure 7.7 Longitudinal section showing stope sequence at ETS shaft pillar.

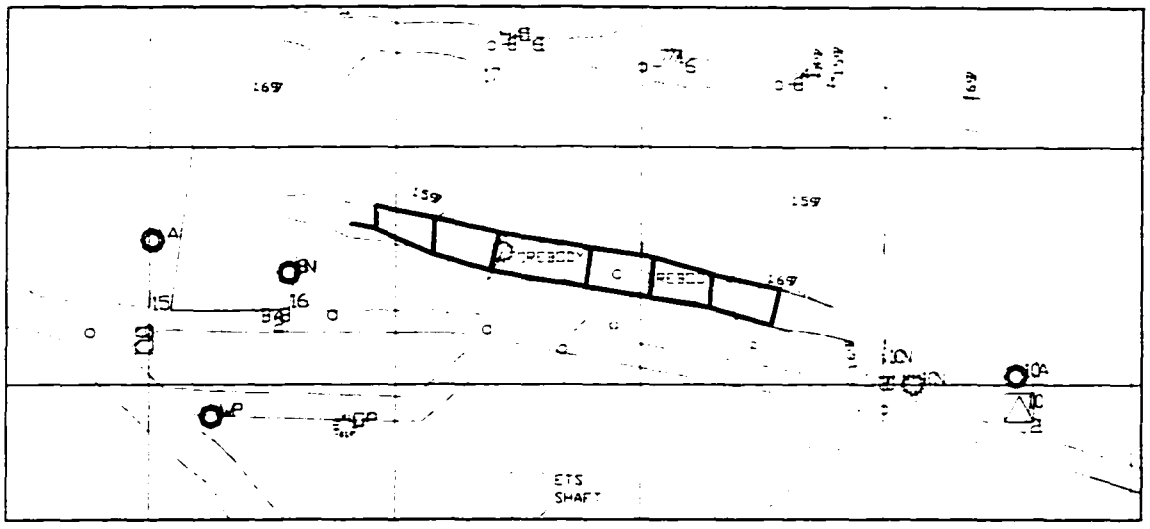


Figure 7.8 Plan view of the ETS shaft pillar orebody as seen on 35 level

In Block 2, development drifts are located in the hangingwall because of the ground weakening effects of Cote d'Or Fissure in the footwall (Craig, per. comm.). Also, because of the ground weakening effects of the Cote d'Or Fissure on the footwall, longitudinal stoping was chosen rather than transverse stoping (Craig, per. comm.). However, due to poor performance of the first four stopes (39L-39S/1 - stopes 1, 2, 3 and 4), mined by the longitudinal method, transverse stoping was adopted. Stope 2 reef drive failed before mining could start. It was not mined.

7.6 Rock Properties

The following data were collected for assessing intact rock properties, rockmass quality determination and in situ stresses in the study areas:

- Intact rock and rockmass properties as used by the mine, and
- Discontinuity data - Self-verifying underground geotechnical discontinuity mapping was conducted.

Management and technical staff was also interviewed for their views on the open stope mining method.

7.6.1 Rock material and rockmass properties

The mechanical properties of Ashanti Goldfields mine rock materials and rockmasses are summarized in Table 7.2.

Table 7.2 Summary of rock material and rockmass properties

Rock type	*UCS* (MPa)	Friction angle (°)	Cohesion *c* (MPa)	*RMR*	*Q*	Source
Meta-greywacke	90	54	30	36 – 41	1.7-2.4	Suorineni (1990)
Carbonaceous phyllite	67	22	15			Suorineni and Borsah (1993)
Graphitic schist	92	20	27			Suorineni and Borsah (1993)
Graphite	5-10	0-10	0			
Meta-volcanic (dolerite)	168	26	45			
Meta-volcanic (Green dyke with quartz)	58	15	45			Suorineni and Borsah (1993)
Hangingwall**	80-150				55 (34*,34†)	Anon. (1993)
Graphite/quartz**	15-150				34 (22*,12†)	Anon. (1993)
Schist/dyke**	60-150				60 (41*,42†)	Anon. (1993)
Footwall**	80-150				55 (36*,37†)	Anon. (1993)
Quartz	50-100					Udo (1996)
Graphite	5-15					Udo (1996)
Meta-sediments	100					Udo (1996)
Meta-volcanics	150					Udo (1996)

*MRMR - Mining Rock Mass Rating
**Block 2 data
†DRMS - Design Rockmass strength

Triaxial tests were used to determine rock cohesion and friction angles. All tests were conducted in accordance with the ISRM Suggested Methods for Rock Testing (Brown, 1981). Confining pressures of between 0 and 25 MPa were used.

7.6.2 Geotechnical discontinuity mapping

Limited records on geotechnical discontinuity surveys were available from the Geotechnical Department of the Mine. Discontinuity survey results for Block 2 were obtained from the Geotechnical Department. A summary of the results is included in Appendix D. The results are based on a small number of joint measurements from the geologists (Agongo, per. comm.), and restricted to Block 2.

Because of the small quantity of data, the restricted areal coverage with respect to the four blocks, and the mine in general, and the uncertainty of the geotechnical relevance of the data, an independent discontinuity survey was conducted by the author in Blocks 2 and 7. Block 8 and the ETS shaft pillar were also covered, but not in detail.

7.6.2.1 Block 2

Figure 7.9 and Figure 7.10 compare results for Block 2 orebody as obtained from the verification mapping and the mine. There is significant difference in the discontinuity structure from the 2 independent surveys. Therefore, the verification mapping was justified. The mine used 53 data points, and the verification data points are 149.

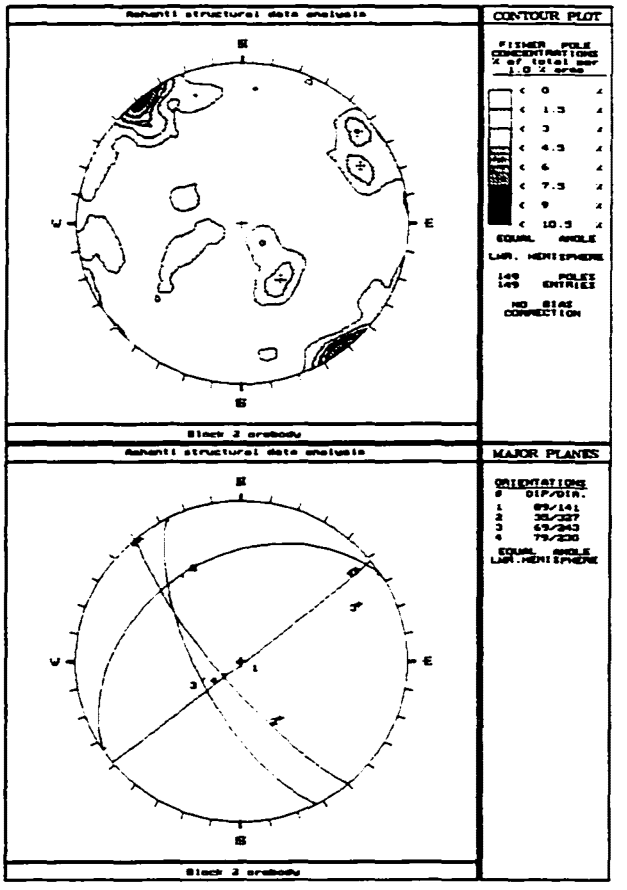


Figure 7.9 Contour plot of discontinuity poles and major planes showing discontinuity structure in KMS Block 2 orebody as obtained from verification survey

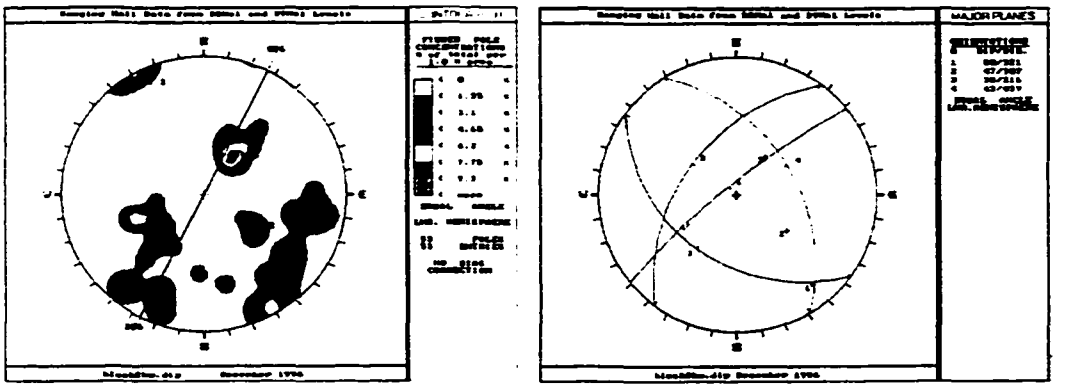


Figure 7.10 Contour plots of discontinuity poles and major planes showing discontinuity structure in KMS Block 2 orebody (after Udo, 1996) as obtained from mine

The discontinuity structures of the hangingwall and footwall of the Block 2 orebody are shown in Figure 7.11 and Figure 7.12 respectively, and the discontinuity patterns in KMS Block 2 are summarized in Table 7.3.

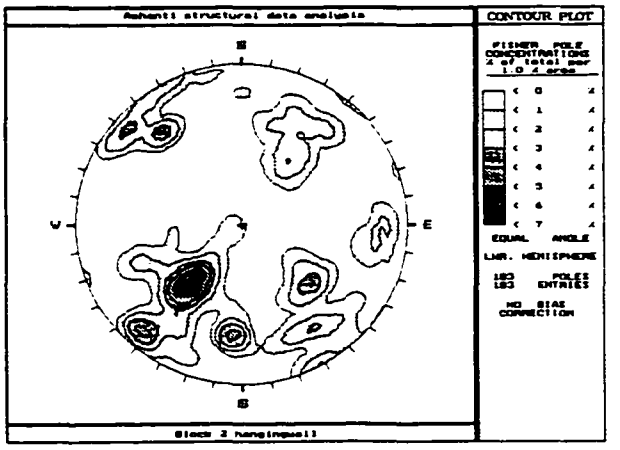


Figure 7.11 Contour plots of discontinuity poles showing discontinuity structure in KMS Block 2 hangingwall

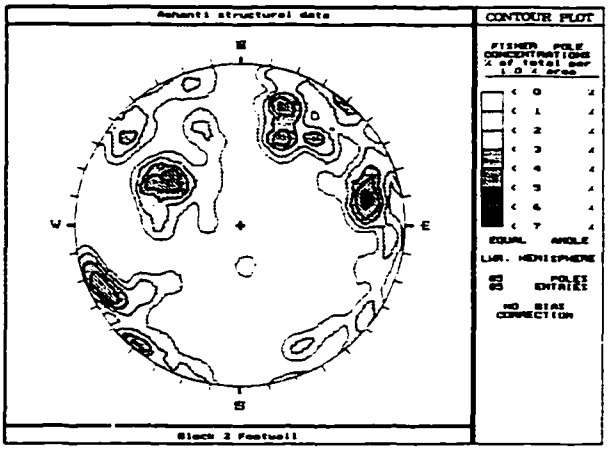


Figure 7.12 Contour plot of discontinuity poles showing discontinuity structure in KMS Block 2 footwall

Table 7.3 Summary of KMS Block 2 rockmasses discontinuity characteristics

Stope surface	Discontinuity characteristics	Number of joint sets	Comments
Hangingwall	1 discontinuity set parallel to orebody dipping between 56° - 90°. 2 discontinuity sets perpendicular to orebody. 1 discontinuity set oblique to orebody. Discontinuities are moderate to steeply dipping	4 discontinuity sets plus random	One very prominent set, which is perpendicular to the orebody, has a low dip of 40°.
Orebody	1 discontinuity set sub-parallel to orebody and near horizontal 1 discontinuity set sub-perpendicular to orebody. 1 discontinuity set oblique to orebody and subvertical.	3 discontinuity sets plus random	Orebody strikes N30°E and dips at 65° to sub-vertical to the west
Footwall	3 discontinuities sets are sub-vertical, 2 discontinuity sets parallel to orebody 2 discontinuity sets oblique to orebody and 1 discontinuity set perpendicular to orebody. Discontinuity dips are moderate to subvertical.	5 discontinuity sets plus random	

7.6.2.2 Block 7

The following figures give the discontinuity structures of the orebody, hangingwall and footwall of Block 7.

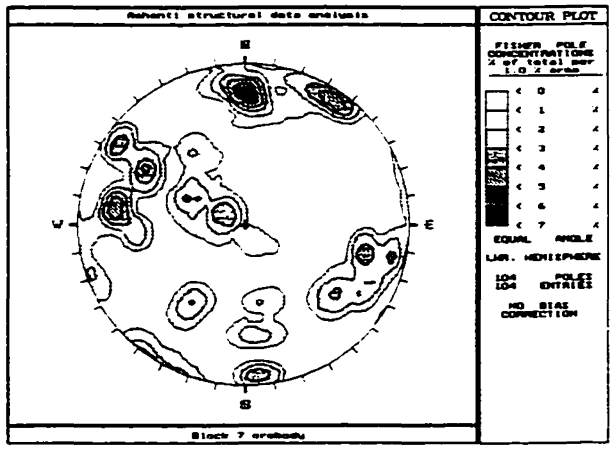


Figure 7.13 Contour plot of discontinuity poles showing discontinuity structure in KMS Block 7 orebody

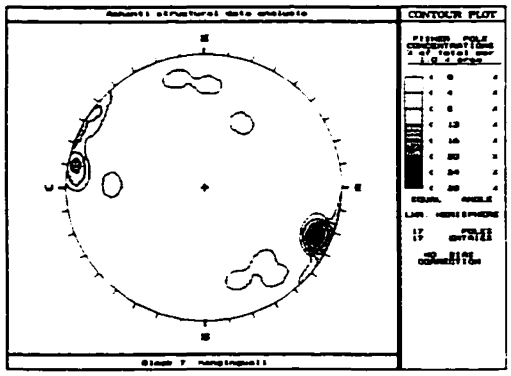


Figure 7.14 Contour plot of discontinuity poles in KMS Block 7 hangingwall

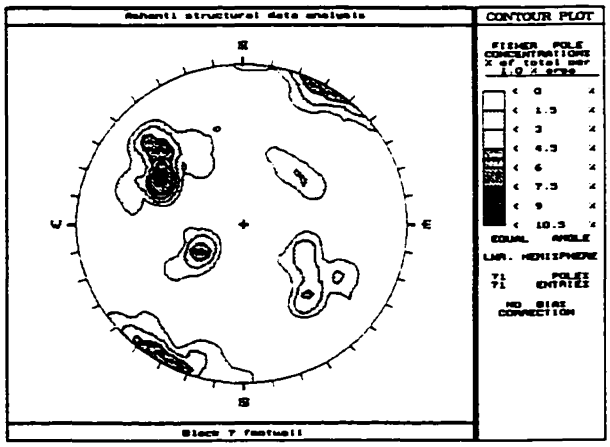


Figure 7.15 Contour plot of discontinuity poles showing discontinuity structure in KMS Block 7 footwall

Table 7.4 Summary of discontinuity characteristics of KMS Block 7 rock units

Stope surface	Discontinuity characteristics	Number of joint sets	Comments
Hangingwall	1 sub-vertical discontinuity set parallel to orebody.	Assume 4 discontinuity sets plus random.	Limited data, low confidence It is justified to assume same discontinuity sets for Block 2 hangingwall for Block 7 hangingwall.
Orebody	1 sub-horizontal discontinuity set parallel to the orebody, 3 discontinuity sets are parallel to the orebody. 2 discontinuity sets perpendicular to orebody. 3 sub-vertical discontinuity sets.	5 discontinuity sets plus random	Orebody attitude as for Block 7
Footwall	2 discontinuity sets parallel to orebody, and 1 discontinuity set perpendicular to it. 1 discontinuity set is oblique to the orebody. 1 discontinuity set is near horizontal and 1 is vertical. 1 discontinuity set is oblique to the orebody.	4 discontinuity sets plus random	

7.6.2.3 Block 8

The following figures show the discontinuity structure in GCS Block 8 hangingwall and footwall.

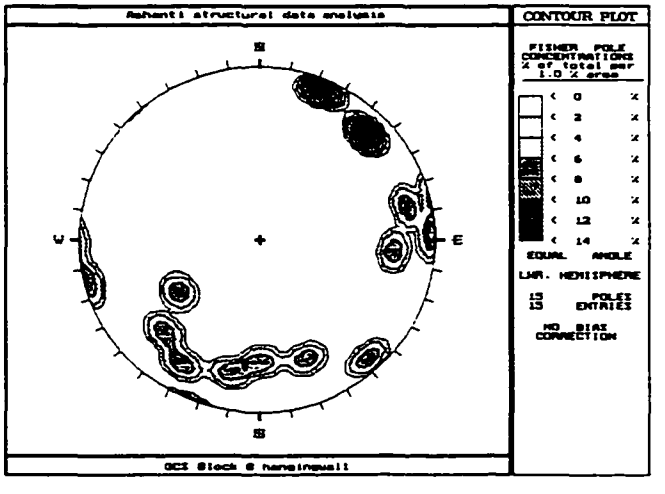


Figure 7.16 Contour plot of discontinuity poles in GCS Block 8 hangingwall

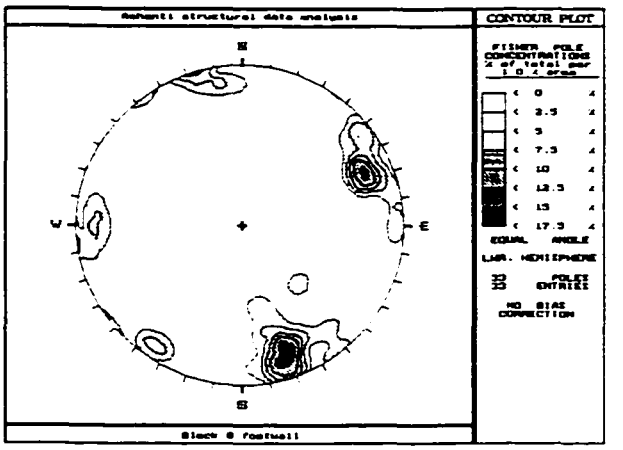


Figure 7.17 Contour plot of discontinuity poles showing discontinuity structure in GCS Block 8 footwall

Table 7.5 Summary of discontinuity characteristics of GCS Block 8 rock units

Stope surface	Discontinuity characteristics	Number of joint sets	Comments
Hangingwall	1 discontinuity set sub-parallel to orebody. 1discontinuity set perpendicular to orebody. 2 discontinuity set oblique to orebody. 3 sub-vertical discontinuity sets. The 4th discontinuity set is moderately dipping.	4 discontinuity sets plus random	Limited data due to lack of sufficient exposure of hangingwall, low confidence
Footwall	2 sub-vertical discontinuity sets	2 sets plus random	Small number of data points but reflects ground condition. Ground is generally competent in this area.

7.6.3 Implications of discontinuity patterns

Discontinuity patterns are as important as discontinuity intensity with reference to mining practice. The stereonets of discontinuities in the orebodies show at least one set parallel and one perpendicular to the orebody. Joints sub parallel to the orebody and dipping in the same direction will cause orebody slabbing if blasting rings are parallel to orebody (Figure 7.4). Slabbing of ore is one problem in Block 2 (Craig, per. comm.)

Sub-horizontal and sub-vertical joints characterize the rockmasses in the study areas. Discontinuity patterns of this type favour rock caving (Mahtab and Dixon, 1976; McMahon and Kendrick, 1969; Cummings et al., 1982; Ferguson 1993). There is strong evidence of rock caving in all the sites visited as seen in Figure 7.23, and Figure 7.24.

It follows on the basis of the rockmass structure at Block 2 and Block 7, that it may be difficult to use open stoping mining method at these locations.

7.6.4 Rock quality designation *RQD*

RQD measurements are not routinely carried out at mines in Ghana, even though *RQD* is one of the most useful parameters for engineering rockmass characterization for mining purposes (Suorineni, 1988). Some small quantity of *RQD* data were obtained from 2 locations, ETS 42L-14NW bypass and GCS 26L-303E and 26S 305E. The *RQD* values give a rough guide as to the general trend of *RQD* values on the mine. Figure 7.18 shows a histogram of the *RQD* values from ETS (North of mine) compared with those from GCS (South of mine).

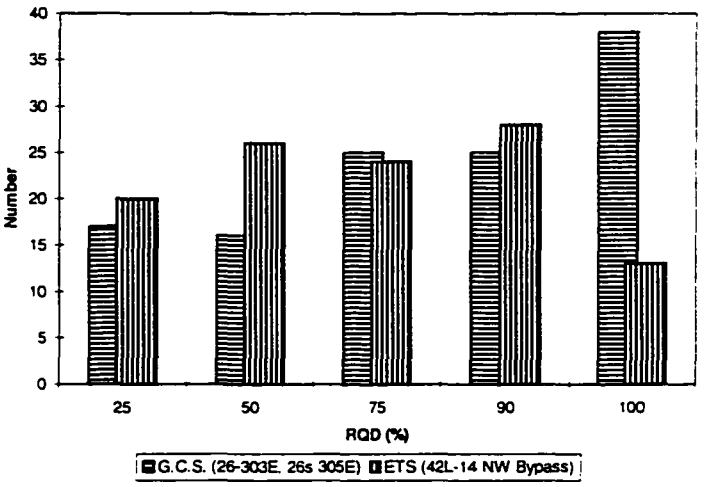


Figure 7.18 Comparison of GCS (South) and ETS (North) *RQD* values

Figure 7.18 supports the view held at the mine that the ground condition improves from North towards the South of the mine. Median *RQD* for GCS is 78% and for ETS, is 64%. Low *RQD* values represent shears, faults and orebodies.

The *RQD*s used in this analysis were estimated from fracture frequencies *FF* measured during mapping. The relationship by Priest and Hudson (1976) was used to convert the fracture frequencies to *RQD*s.

The *RQD* values obtained from the mine for ETS and GCS had corresponding fracture frequencies. Analysis of the fracture frequencies and *RQD* values give somewhat different results (Figure 7.19), when compared with Priest and Hudson (1976).

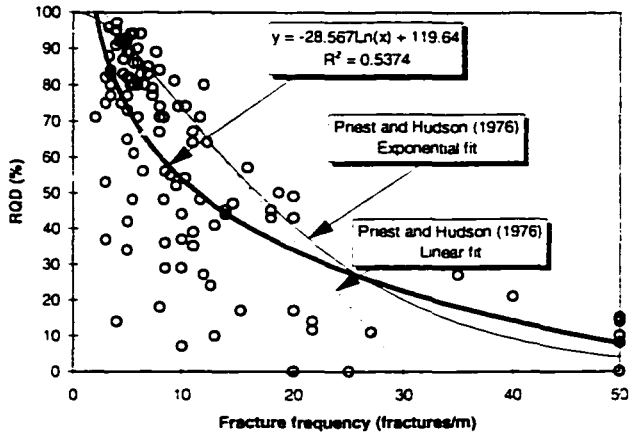


Figure 7.19 *RQD* and fracture frequency relationship for Ashanti data

It is evident from Figure 7.19 that the Priest and Hudson equations do not fit the Ashanti data, but generally provide an upper limit for *RQD* at the Ashanti mine. Equation 7.1 was fitted to the data and compared with the Priest and Hudson (1976) equation (Equation 7.2), with the Ashanti fitted equation somehow approaching more realistic values at the centre of the graph than the Priest and Hudson (1976) equation.

$$RQD = -28.6\ln(FF) + 119.4 \qquad 7.1$$

$$RQD = 100e^{-0.1\lambda}(0.1\lambda + 1) \qquad 7.2$$

Equation 7.1 was used to estimate *RQD*s for ETS.

Table 7.6 Estimated *RQD*s from fracture frequencies

Block	Stope surface/rock type	Fracture frequency FF	Estimated *RQD*	Remarks
KMS Block 2	Hangingwall	12	65	
	Ore	21	40	Fissured
	Footwall	13	60	and sheared
KMS Block 7	Hangingwall	13	60	
	Ore	20	40	Fissured and
	Footwall	10	70	sheared
GCS Block 8	Hangingwall	11	70	Stress
	Ore	8	80	fractured
	Footwall	10	70	Generally good some graphite
ETS shaft pillar	Hangingwall	22	30	
	Ore	33	20	Extremely
	Footwall	23	30	poor-graphitic

7.6.5 Modified rockmass quality *Q'*

The modified rockmass quality *Q'*, is the rockmass property required as input for calculating the modified stability number *N'* that is used in the stability graph for open stope stability assessment. Considering the discontinuity structure discussed in Section 7.6.2, and the *RQD* values in Table 7.6, the modified rockmass qualities at Ashanti Goldfields mine are summarized in Table 7.7.

Table 7.7 Modified rockmass qualities *Q'* at Ashanti Goldfields mine

Block	Stope surface/rock type	*RQD* (%)	Joint set number J_n	Joint roughness J_r	Joint alteration number J_a	Modified rockmass quality *Q'*
2 – KMS	Hangingwall	65	15	1.5	4	1.6
	Orebody	40	12	1.5	4	1.3
	Footwall	60	15	1.5	2	3
7 – KMS	Hangingwall	60	15	1.5	4	1.5
	Orebody	40	15	1.5	4	1
	Footwall	70	15	1.5	2	3.5
8 – GCS	Hangingwall	70	15	1.5	2	3.5
	Orebody	80	6	3	2	20
	Footwall	70	6	1.5	2	8.8
ETS Shaft Pillar	Hangingwall	30	12	1.5	4	0.9
	Orebody	20	15	3	2	2
	Footwall	30	15	1.5	2	1.5
Graphite		10	20	1	4	0.1

Table 7.7 shows that the rocks at Ashanti Goldfields mine classify as poor to good, depending on the mining block. Good rockmass qualities are found in block 8 of GCS. Ignoring rockmass qualities in Block 8, the rockmass qualities in Blocks 2, 7, and ETS shaft pillar classify as poor with *Q'* between 1 and 3.5. The rockmass qualities are further reduced when the graphite zones intersecting the stope surfaces are considered. This is discussed in Section 7.10.1.

7.7 Shape Factors

Stope surface shape factors are the hydraulic radii and spans. The radius factor (Milne, 1997) and volumetric index (Germain et al., 1996) are not considered in this analysis because open stope surfaces at Ashanti mine are relatively simple.

Geometric information on stopes was collected from the mine for use in estimating the shape factors of the stope surfaces. Table 7.8 is a summary of the data. Shape factors of the stope surfaces are required as input for the development of the stability graph. The stope geometric data in Table 7.8 are cross checked with stope and geologic sections from the mine, and where appropriate, corrected values are used rather than the mine value, which are rather more global block wise.

Table 7.8 Geometric information on stopes as obtained from the mine

Block	Panel	Bottom level	Top level	Width at stope bottom (m)	Width at stope top (m)	Average width (m)	Stope height (m)	Stope length (m)	Orebody dip at stope position (°)
Block 2	Stope 1	39L	39#1S/L	12.4	16.8	14.6	24	15.2	70
	Stope 2	39L	39#1S/L	15.5	29.2	22.4	24	18.2	70
	Stope 3	39L	39#1S/L	7.8	28.3	18.1	24	15.2	70
	Stope 4	39L	39#1S/L	21	15.6	18.3	24	15.2	70
	Stope 5	39L	39#1S/L	12.7	17.3	15	24	15.2	70
	Pillar 7	39L	39#1S/L	19	15.9	17.5	24	15.2	70
	Pillar 8	39L	39#1S/L	16.6	32.2	24.4	24	15.2	70
	Pillar 7	39#1S/L	38#1S/L	15.9	18.9	17.4	24	15.2	70
	Stope 2	39#1S/L	38#1S/L	29.2	12.7	21	24	15.2	70
Block 7	Stope 1	28L	27L	18.2	31.9	25.1	30	21	70
	Pillar 1	28L	27L	15.2	27.4	21.3	30	21.3	70
	Stope 2	28L	27L	9.1	22.8	16	30	18.8	70
	Pillar 2	28L	27L	9.1	15.2	12.2	30	15.5	70
	Stope 3	28L	27L	13.7	15.2	14.4	30	27.4	70
	Pillar 3	28L	27L	12.2	16.7	14.4	30	17	70
	Stope 4	28L	27L	12.2	19.8	16	30	27.1	70
	Pillar 4	28L	27L	13.7	18.2	16	30	24.3	70
	Stope 5	28L	27L	10.6	13.7	12.2	30	24.3	70
	Pillar 5	28L	27L	9.1	12.2	10.6	30	26.4	70
	Stope 6	28L	27L	9.1	9.1	9.1	30	16.7	70
	Stope 7	28L	27L	24.9	29.9	27.4	30	26.4	70
	Pillar 7	28L	27L	23.9	10	16.9	30	15	70
	Stope 8	28L	27L	23.9	10	17	30	15	70
ETS shaft pillar		35L	35#1S/L	7.5	5.5	6	15	10	70
Block 8	Stope 1	30L	29L	5	11.4	8.2	17.8	15.5	85
	Stope 2	30L	29L	10	9	9.5	20	25	85

The hydraulic radii and spans are included in the summary sheet for the development of the stability graph, and are given in Appendix D.

7.8 In situ Stresses

There has been only one location in the mine, and the first in Ghana, where in situ stresses have been measured. An Australian mining consultant (Anon., 1993) used the overcoring method of in situ stress measurement on the 26 Level 333 crosscut of the mine to determine the in situ stresses. Three separate measurements were made on the 26 Level. The results are summarized in Table 7.9.

Table 7.9 Summary of in situ stress measurement results

Test #	Principal stress	Magnitude (MPa)	Dip (°)	Bearing (°)
	Major	34.7	24	279
1	Intermediate	27.7	25	021
	Minor	20.9	55	152
	Major	46.1	10	279
2	Intermediate	37.9	36	017
	Minor	26.2	52	176
	Major	46.4	10	303
3	Intermediate	19.5	36	040
	Minor	11.8	53	200
Combined	Major	39.1	21	292
results	Intermediate	28.3	11	026
	Minor	20.8	66	142

Dip is positive downwards; Bearings are positive clockwise from Mine North

The Ashanti mine in situ stress data are superimposed in the general world in situ stress measurement graphs (Hoek and Brown, 1980) as shown in Figure 7.20 and Figure 7.21. The depth below surface at which the stress measurements were conducted at Ashanti is the 2600 Level that is 792.5 m below surface.

According to the world stress map (Zoback, 1992), Ghana falls in a region of strike-slip faulting stress regime in which $\sigma_{hmax} > \sigma_v > \sigma_{hmin}$. The in situ stress measurement results at Ashanti puts Ghana in a region of thrust faulting stress regime in which $\sigma_{hmax} > \sigma_{hmin} > \sigma_v$.

If the rock unit weight at Ashanti is assumed to be 0.027 MN/m^3, the vertical stress at the depth of stress measurement is 21.4 MPa, which compares favourably with the average of 20.8 MPa obtained from the in situ stress measurements.

The ratio of the in situ measured average horizontal stresses to the in situ measured vertical stress is 1.62. It is consistent with worldwide observations collected by Hoek and Brown (1980) as shown in Figure 7.21.

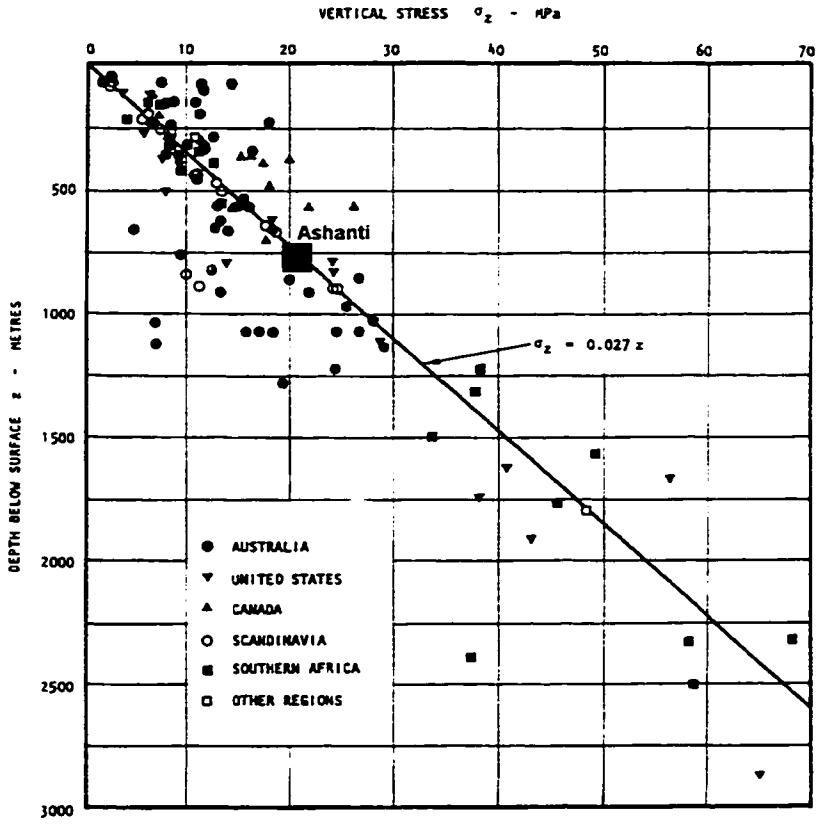


Figure 7.20 Plot of vertical stresses against depth below surface (after Hoek and Brown, 1980) with Ashanti data superimposed

It is concluded from the above comparisons that the single in situ stress measurement result is acceptable and constitutes the best available information of the in situ stress state at Ashanti. The following graph is used in estimating in situ stresses at Ashanti at shallow depths (≤ 1000 m). It is not applicable for greater depths where all three stresses tend to equalize rather than diverge as indicated in Figure 7.22. Figure 7.22 is generated using the in situ principal stress relationships in Equation 7.3 based on the vertical stress σ_v.

$$\sigma_v = 0.027D \text{ MPa} \qquad 7.3$$
$$\sigma_h = 1.33\sigma_v \text{ MPa}$$
$$\sigma_H = 1.82\sigma_v \text{ MPa}$$

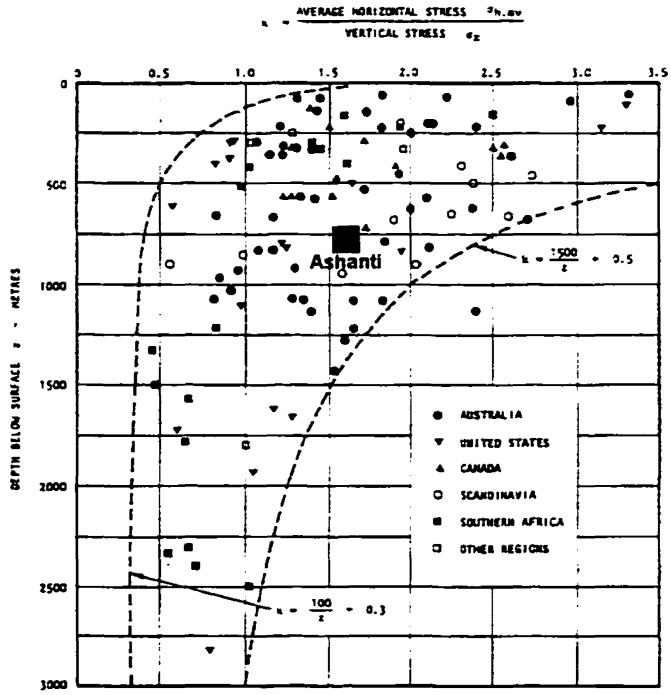


Figure 7.21 Plot of variation of ratio of average horizontal stress to vertical stress with depth below surface (after Hoek and Brown, 1980), with Ashanti data superimposed

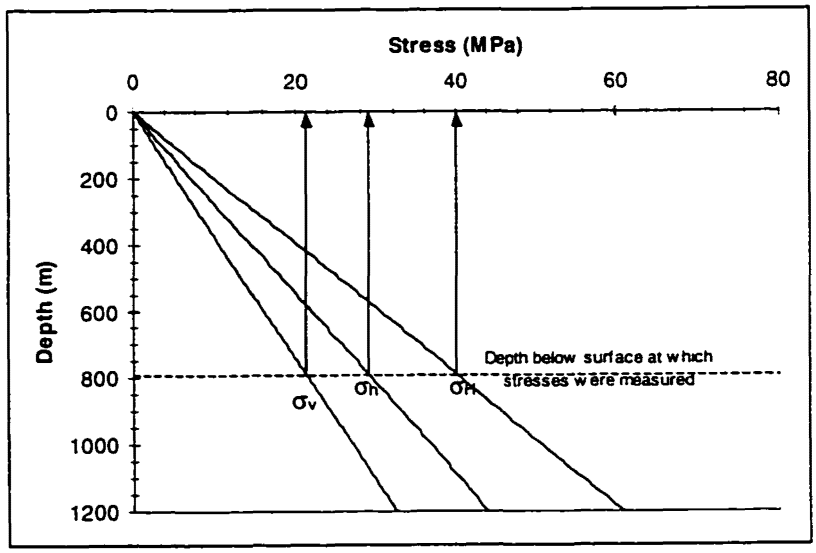


Figure 7.22 Graph for estimating in situ stresses at upper levels in Ashanti

7.9 Stope Performance

The following data were collected for evaluating the performance of the stopes:

- Geological sections and vertical projections,
- Blast design layouts,
- Cablebolt design layouts,
- Cavity survey profiles, and
- Groundfall records detailing extents of falls and approximate dates.

Block 2 has been observed as being problematic. Stope end walls and crowns have failed in almost all the mined stopes. End walls fail progressively, shrinking adjacent pillars. Figure 7.23 shows progressive failure in a stope crown. Sidewall failure was also observed in the 39 Level – 39S/Level stope (Pillar 7) (Figure 7.24) connecting to the adjacent stope.

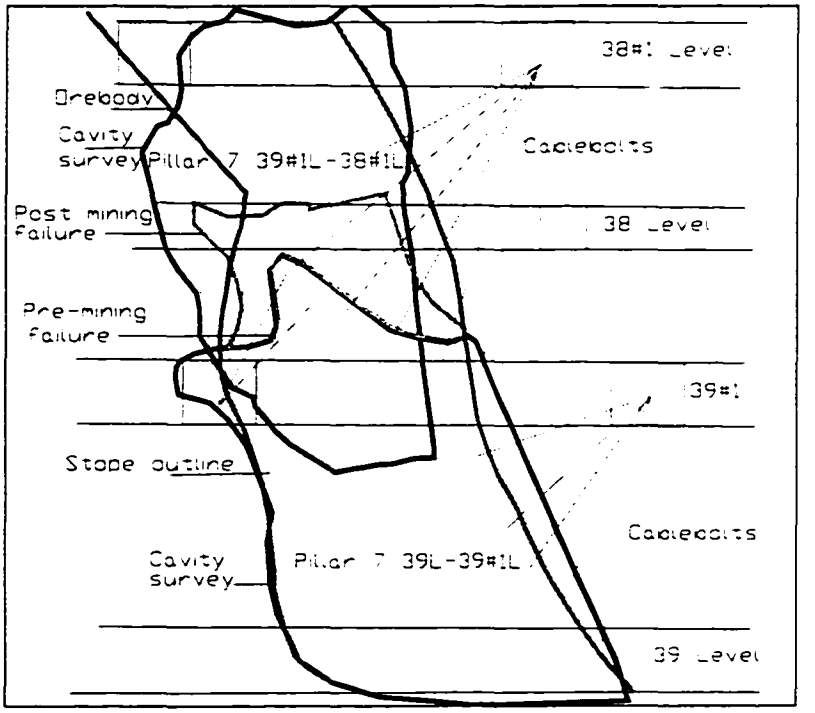


Figure 7.23 Section showing progressive stope failure in pillar 7 of Block 2 Kwesi Mensah Shaft

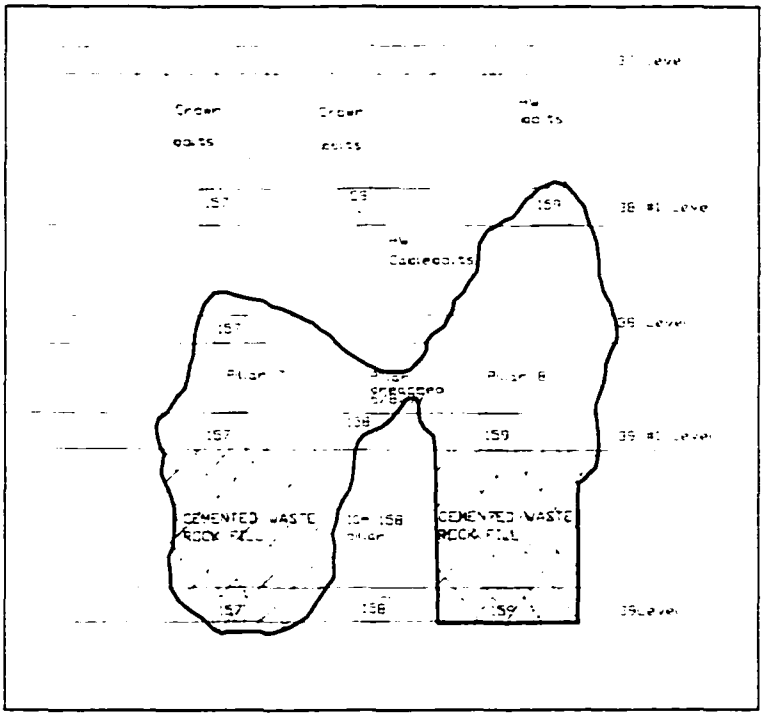


Figure 7.24 Vertical projection, showing sidewall failure in Pillar 7 - 158 pillar breached

Poor performance of stopes in Block 2 is attributed to the following:

- Undercutting by previous mining at the lower levels,
- Delayed mining - developments had being standing for about 10 years before start of mining,
- Rocks classify as poor (Q' is between 1.3 and 3), the rockmass quality is further lowered by the graphitic zones that are not considered in the classification system.
- Presence of graphitic fissures and shears, and
- Bifurcation of the orebody.

One stope had been mined at the ETS pillar block at the time of the visit. A stope of 10 m-length by 5.5 m to 7 m-width and a vertical height of 15 m was designed. The stope caved in the crown including the hangingwall, to a vertical depth of approximately 20 m involving a complete stope above it, immediately following blasting of the fourth blast ring (Figure 7.25). A strike length of 6 m had been achieved at the time of failure. Consequently, the mine now plans 8-m strike lengths instead of 10 m.

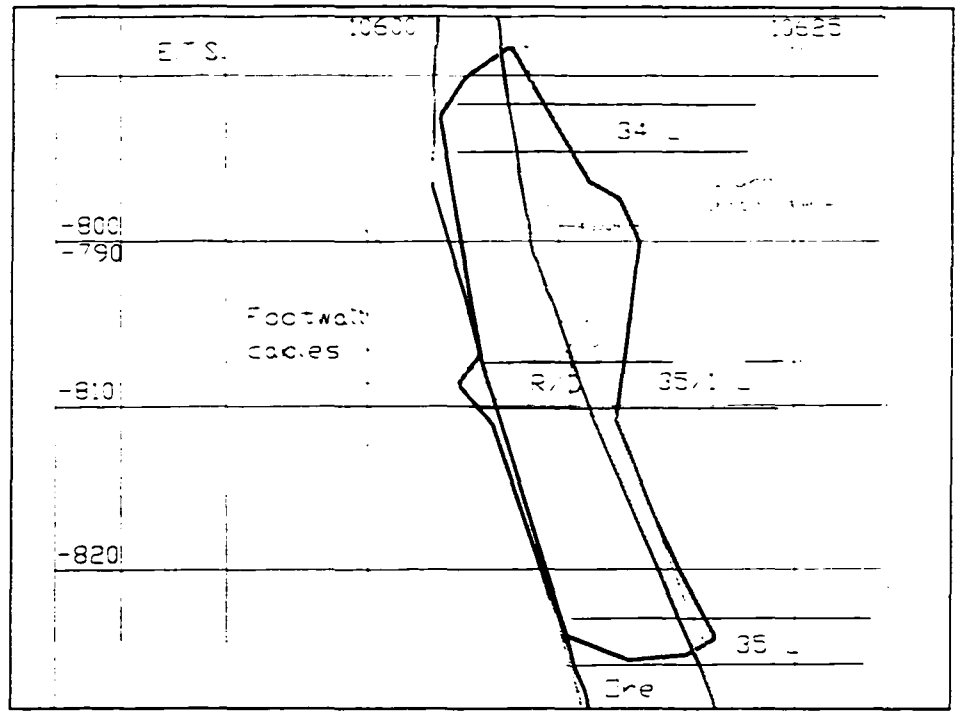


Figure 7.25 ETS shaft pillar stope 1 failure

Block 8 stopes in GCS generally perform better compared with stopes in the other blocks. Some failures still occur in this block if extraction is delayed for more than three months and or when graphite is encountered. Figure 7.26 shows tension fracturing in stope 1 position hangingwall in Block 8.

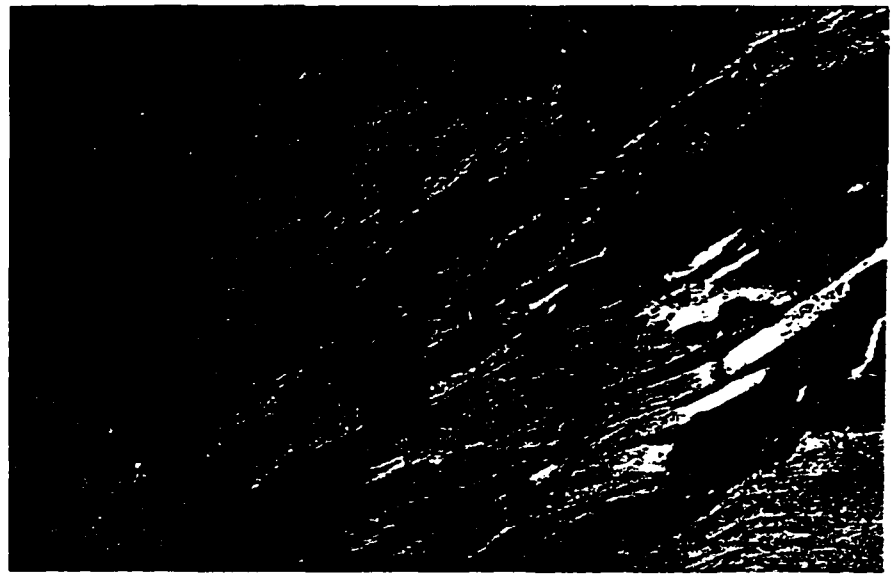


Figure 7.26 Tension fractures as observed in stope 1 position hangingwall



Figure 7.27 Cablebolted back of stope 2 in Block 8, and part of stop1 hangingwall (left) - GCS

Bifurcation seems related to crown failures. The effect of orebody bifurcation on stope stability is summarized in Table 7.10.

Table 7.10 Bifurcation in stopes and association with crown stability

Block	Stope/pillar	Structure of orebody	Comments
KMS Block 2	Stope 1	No bifurcation	Crown and endwalls caved
	Stope 2	Bifurcation within stope	Self collapse - not mined
	Stope 3	Bifurcation at crown	Crown failure - Bad method of dealing with bifurcation in crown (Figure).
	Stope 4	No bifurcation	Satisfactory crown performance -
	Stope 5	Bifurcation at crown	Good way to deal with crown bifurcation
KMS Block 7	Pillar7 (39L-39S/1)	Bifurcation within stope	Crown failure - stope undercut by previous mining
	Pillar 8	No bifurcation	Hangingwall undercut by previous mining
	Pillar 7 (39S/1-38S/1)	No bifurcation	Schist and quartz parallel
	Stope 1	No bifurcation	Several parallel lenses
	Stope 2	Bifurcation	Unstable
	Stope 3	Bifurcation	unstable
	Pillar 3	Bifurcation in crown	Crown failure
	Stope 4	Severe bifurcation	Unstable
	Pillar 4	Bifurcation	Unstable
	Stope 5	Bifurcation	Deep seated crown failure
	Pillar 5	No bifurcation	Unstable
	Stope 6	No bifurcation	Unstable
	Stope 7	Bifurcation	Caved
	Stope 8	No bifurcation	Unstable
ETS shaft pillar	Stope 1	Bifurcation	Deep seated crown failure
GCS Block 8	Stope 1	No bifurcation	Stable
	Stope 2	No bifurcation	Stable

Details of stope failures, and geometries at the research sites are included in Appendix D.

7.10 Fault Gouge Rockmass Quality Correction

7.10.1 Fault gouge rockmass correction factor Q'_m

When a soft fault gouge is exposed in a stope surface, it affects the overall quality of the surface rockmass and its stability. Among the limitations of the stability graph method is the fact that it does not account for such soft zones in the stope surface (Potvin and Milne, 1992).

Some researchers (Quesnel and Ley, 1991; Speight, 1992) have shown that current rockmass classification systems do not apply when soft zones are encountered. They developed different in-house rockmass rating procedures to account for the soft zones.

Løset (1990) proposed the following equation to account for soft zones in the Q-system:

$$Q = \frac{T \log(Q_z) + \log(Q_a)}{T + 1} \qquad 7.4$$

where, T = Thickness of soft zone in metres, Q_z = Rockmass quality of thickness zone, Q_a = Rockmass quality of adjacent competent rockmass, and Q = Resultant surface rockmass quality.

Equation 7.4 does not relate the soft zone thickness to the excavation surface. The ratio of the soft zone thickness to the stope surface thickness (defined below, Figure 7.28) is a measure of the severity of slough in the stope surface due to the soft zone. In this thesis, it is hypothesized that the rockmass quality of a stope surface in which a soft zone is exposed should be related to the adjacent rockmass quality in the stope surface, the soft zone rockmass quality, the stope surface width, and the width of the soft zone. Equation 7.4 is rewritten to include the width of the intersected stope surface:

$$Q'_m = 10^{\frac{\left[\omega \log(Q'_w) + \log(Q'_a)\right]}{\omega + 1}} \qquad 7.5$$

where, Q'_m = adjusted rockmass quality, ω = Ratio of soft zone thickness to stope surface width, Q'_w = Soft zone gouge quality, and Q'_a = Quality of adjacent rockmass.

Figure 7.28 is drawn to illustrate the concept, and shows the various scenarios of soft zones intersecting different stope surfaces, and the determination of ω. Notice that the minimum length for surface 1b is used in calculating ω, since this gives the worst case. The figure shows the relationship between the soft zone in a fault and stope surface.

Terzaghi (1946) observed that the loose rock load (dead weight) on roof support is only a small fraction of the weight of the rock located above the tunnel due to arching or silo effect. Arching is effective when the adjacent rockmass is competent and provides rigid abutments. Therefore, arching can enhance the stability

of a soft zone between relatively competent rock when the width of the soft zone is less than the width of the stope surface.

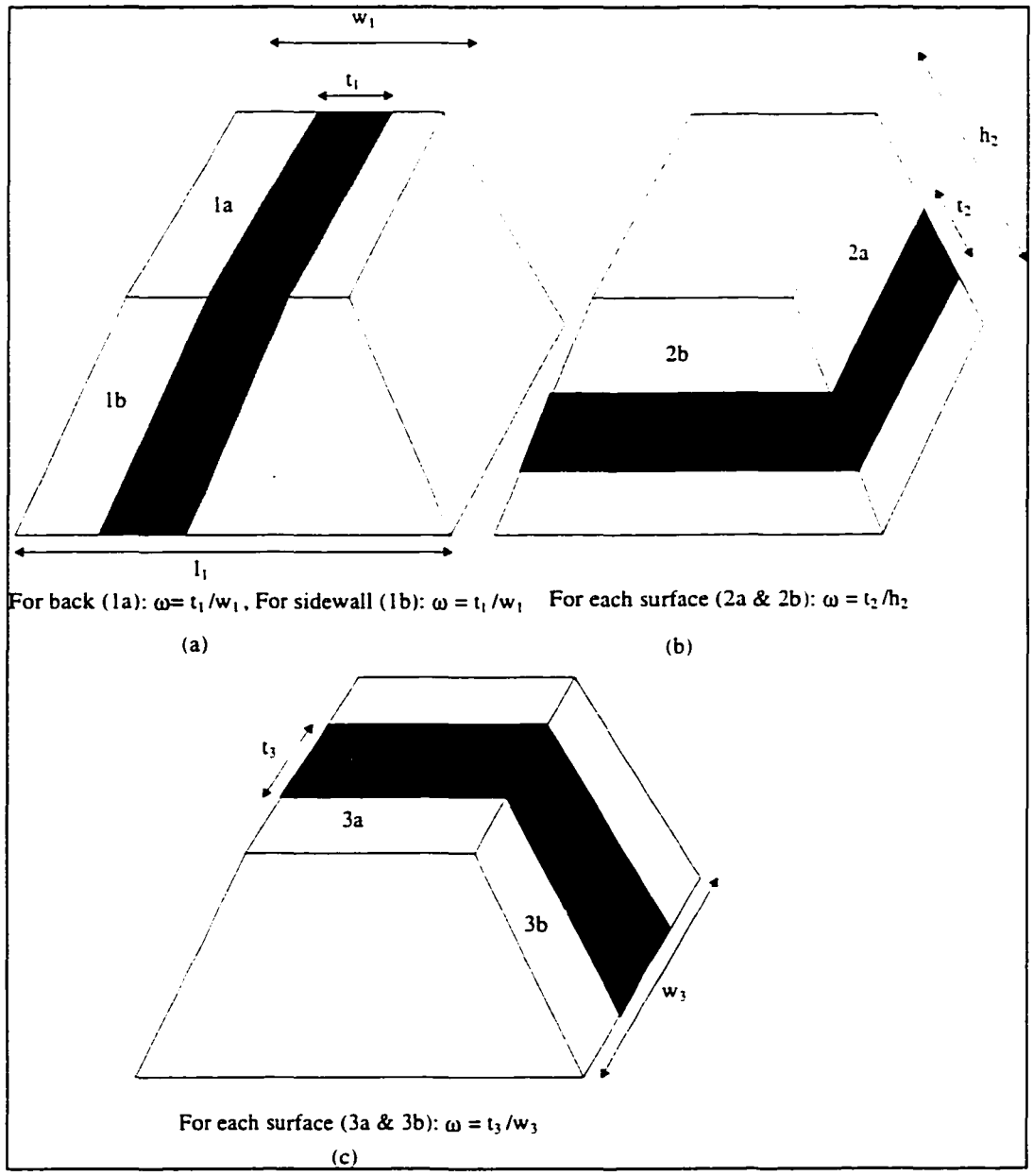


Figure 7.28 Illustration of soft zones (black band) in faults, in various stope surfaces and the calculation of ω

Whether or not the soft zone rockmass quality will have a significant impact on Q'_m, is dependent on ω. For a weakness zone rockmass quality of $Q_w' = 0.02$ and adjacent rockmass quality $Q'_a = 2$. Figure 7.29 shows the limits when Q'_w or Q'_a is dominant, and when Q'_m should be applied. In general, for $\omega <= 0.15$ $Q'_m = Q_a$ and for $\omega \geq 20$, $Q'_m = Q_w$. In between these values Q'_m should be determined and used in place of Q' for the assumed values.

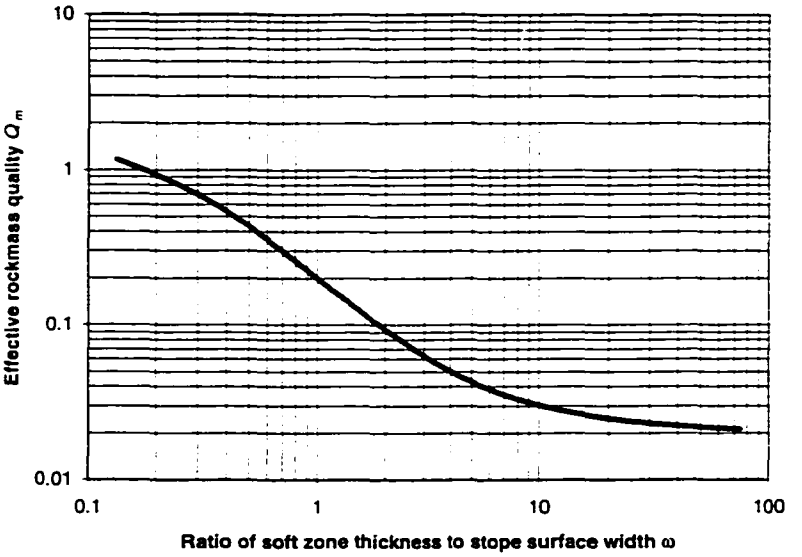


Figure 7.29 Effect of weakness zone gouge quality on adjacent rockmass quality

Equation 7.5 is applied to the Ashanti database to correct for the presence of graphite in the stope surfaces.

7.10.2 Estimation of fault gouge (graphite) thickness

Field observations revealed that failures at Ashanti are related to the thickness of the graphitic zones in the stope surfaces (Figure 7.30 and Figure 7.31).



Figure 7.30 Graphite (dark) in crown with quartz (light)



Figure 7.31 Gravity related failure due to graphite

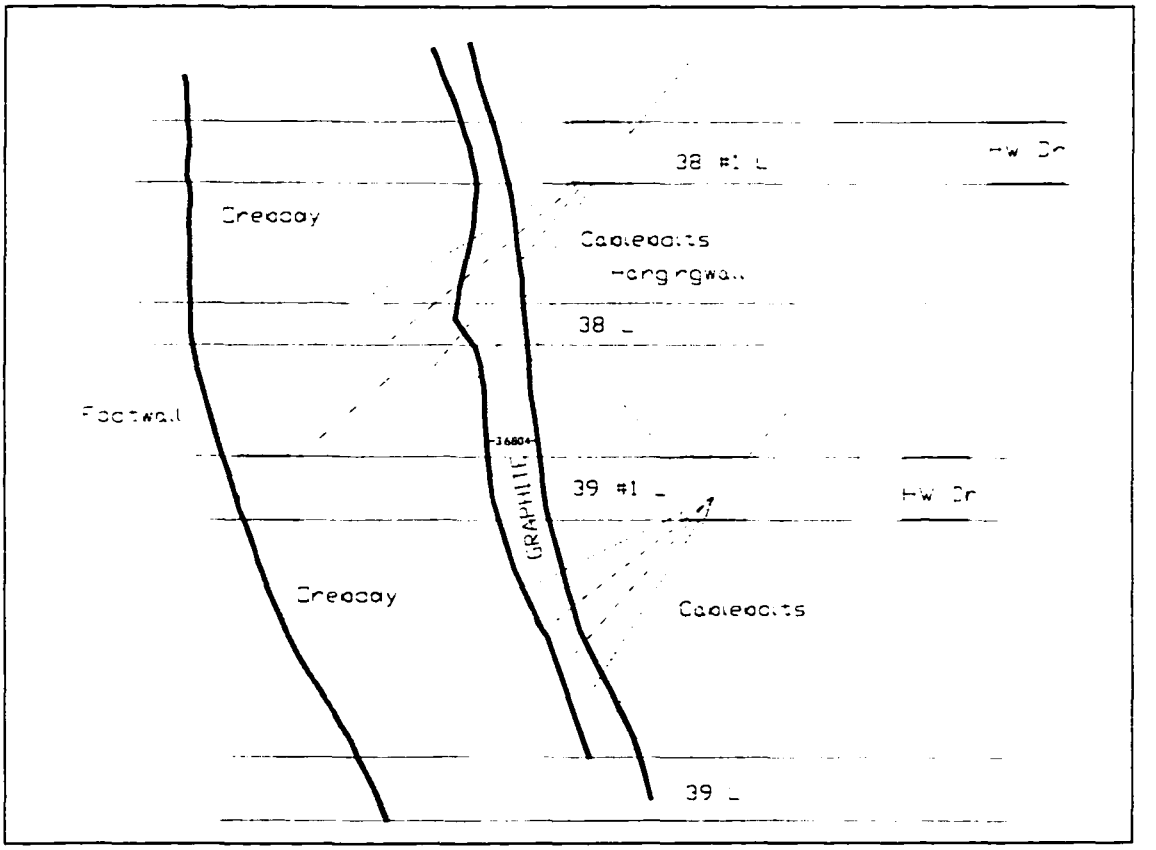


Figure 7.32 Longitudinal section of pillar 8 showing graphite in hangingwall

The failure in ETS shaft pillar stope 1 that occurred, seems graphite related. Figure 7.33 shows graphite occurrence with the orebody of stope 1 in the ETS shaft pillar, and the failure that occurred.

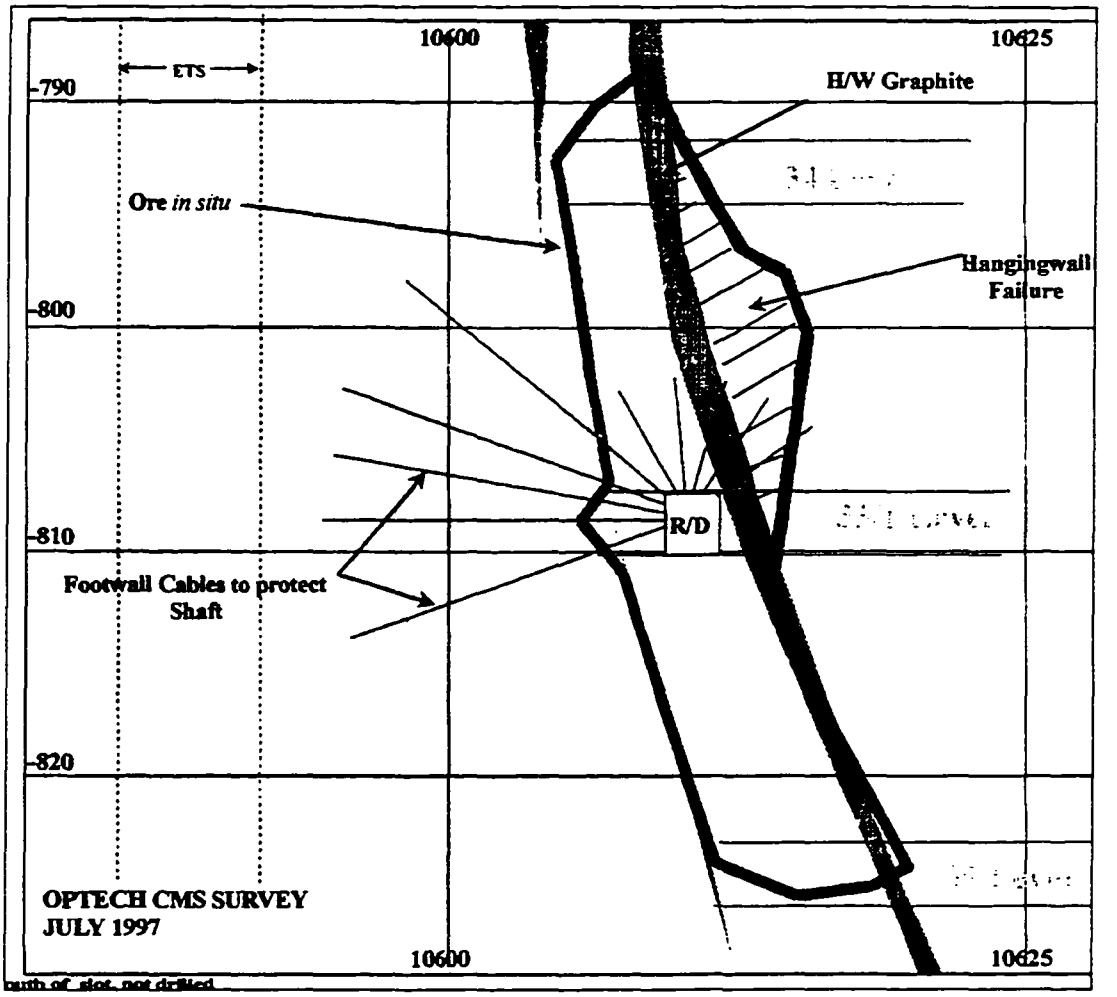


Figure 7.33 Longitudinal section of stope 1 at ETS shaft pillar showing graphite in hangingwall and footwall, and the failure that occurred

The effective thicknesses of graphite in various stope surfaces were determined in field studies and from geological sections and plans obtained from the mine. The thickness of the graphite zone in each stope surface is used to determine a correction factor to the stope surfaces' rockmass quality. Table 7.11 shows the thicknesses of graphite in the various stope surfaces.

Table 7.11 Estimated effective graphite thicknesses (m) in stope surfaces

Block	Stope / pillar	HW graphite thickness (m)	FW graphite thickness (m)	End walls graphite thickness (m)	Crown graphite thickness (m)
	Stope1	Nil	nil	Nil	nil
	Stope2	Nil	nil	Nil	nil
	Stope3	1.2	2.4	3.6	3.6
	Stope 4	30% graphite			
KMS	Stope 5	3.6	nil	3.6	3.6
Block 2	Pillar 7 (39L-39S/L	nil	nil	nil	nil
	Pillar 8	nil	nil	3.5	3.5
	Pillar 7 (39S/1--38S/1)	nil	nil	2.4	2.4
	Stope 1	2.4	1.2	3.6	3.6
	Pillar 1	not mined			
	Stope 2	1.2	1.2	3.6	3.6
	Pillar 2	not mined			
	Stope 3	3.6	1.2	4.8	4.8
	Pillar 3	2.4	1.2	3.6	3.6
	Stope 4	1.2	1.2	2.4	2.4
KMS	Pillar 4	2.4	nil	2.4	2.4
Block 7	Stope 5	3.6	nil	3.6	3.6
	Pillar5	1.2	1.2	2.4	2.4
	Stope 6	1.2	1.2	2.4	2.4
	Stope 7	1.2	2.4	3.6	3.6
	Pillar 7	not mined			
	Stope 8	1.2	2.4	3.6	3.6
ETS shaft pillar	Stope 1	2.5	0.5	3	3
GCS	Stope 1	No information			
Block 8	Stope 2	Nil	3.5	3.5	3.5

7.11 Ashanti Stability Graph

In this section, the stability graph for Ashanti is presented for a case where the soft graphite zones intersecting stope surfaces are not taken into account in the rockmass quality assessment, and for a case where the soft graphite zones are considered by applying Equation 7.5. The rockmass qualities at Ashanti were presented in Section 7.6.5. The modified rockmass qualities Q' for Ashanti rocks range between 1 and 20, with the majority of rockmasses in the range 0.9 to 3.5. When the soft zones in the stope surfaces are taken into account, the rockmass qualities Q' decrease to between 0.7 and 20, with a majority of the rockmasses in the range 0.7 to 1.6.

The stress factor in this study is set to 1 because stope walls are typically in relaxed ground conditions.

Stope surface geometries as obtained from Ashanti mine documents, are included in Appendix D, together with the complete table of data used for the development of the stability graphs. The stope surface hydraulic radii were presented in Section 7.7, and range between 2.4 and 7.8.

The joint orientation factor B and gravity factor C were determined from the joint characteristics of the Ashanti rocks and stope orientation data presented in Sections 7.6.2, and 7.7 respectively.

Figure 7.34 is the modified stability graph without correction for graphite zones. The boundaries separating stable unsupported stopes from unstable stopes, and unstable from caved stopes are those developed with the statistical tools discussed in Chapter 3 using the unsupported calibration database. The two boundaries define the transition zone, and are shown in the plot.

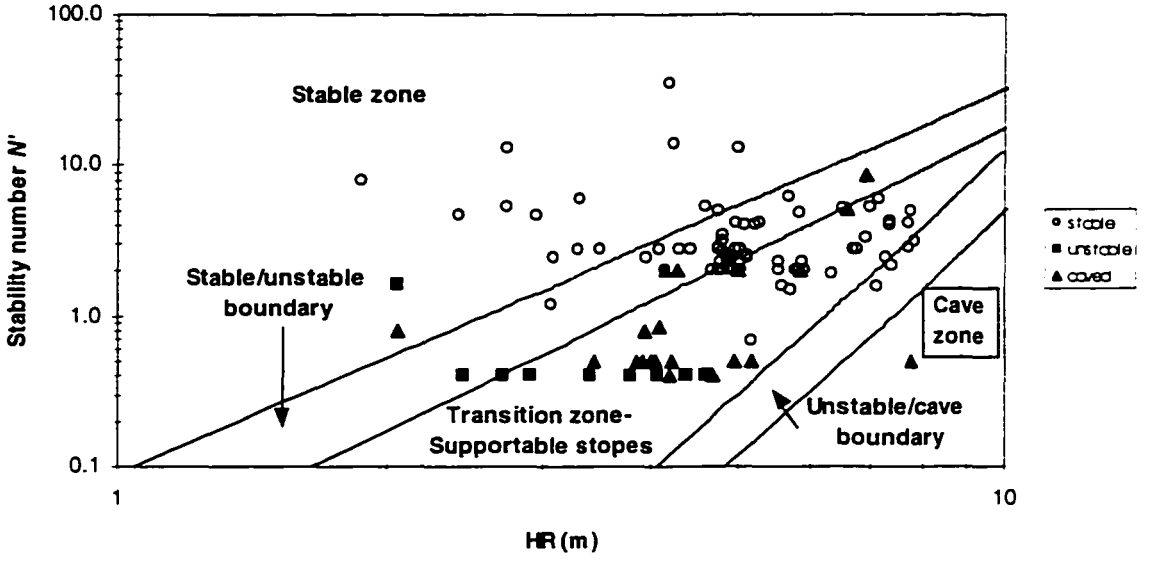


Figure 7.34 Conventional stability graph for Ashanti (with transition zone statistically defined using the unsupported calibration database) on a log-log scale - no correction for graphite

Figure 7.34 shows that all but one unstable and one caved stope fall below the transition zone.

Open stopes in Ashanti are cablebolted before mining. Many (almost half) of the stable stopes fall above $N' = 1$, and plot below the transition zone for unsupported stopes. This suggests that the cablebolting at Ashanti is effective for $N' > 1$, when HR is less than 8.

The boundary between stable and failed stopes, based on the Ashanti data alone, seems to be a horizontal line, and fall near $N' = 1$, suggesting that the conventional stability graph boundaries may not be applicable to Ashanti, and therefore that the stability graph and for that matter open stope mining may not be applicable. The author does not subscribe to this interpretation, and suggests that it is an artifact due to lack of stable small stopes in poor ground ($N'<1$). Furthermore, it is interpreted as an indirect support of the

fault factor concept: i.e., if soft zones in wide faults have little effect, stability can be assessed by the stability graph, and conditions that are supportable can be properly identified. However, if soft zones in wide faults dominate, stopes become quickly unstable or cave.

The fault factor concept was applied to Ashanti to correct for the soft graphite zones intersecting stopes. Only the unstable and caved points are re-plotted in Figure 7.35 after applying the correction procedure. The correction procedure takes into account the thickness of the graphite, the stope surface width, the rockmass qualities of the graphite zone, and the adjacent rockmass. The lines connecting to the data points show the movement of the points from their original positions downwards to the final position indicated by the corresponding symbol. Even though the points moved in the right direction, it seems that the amount of movement is still insufficient to plot caved stopes in the caved zone, and they still plot in the transition zone.

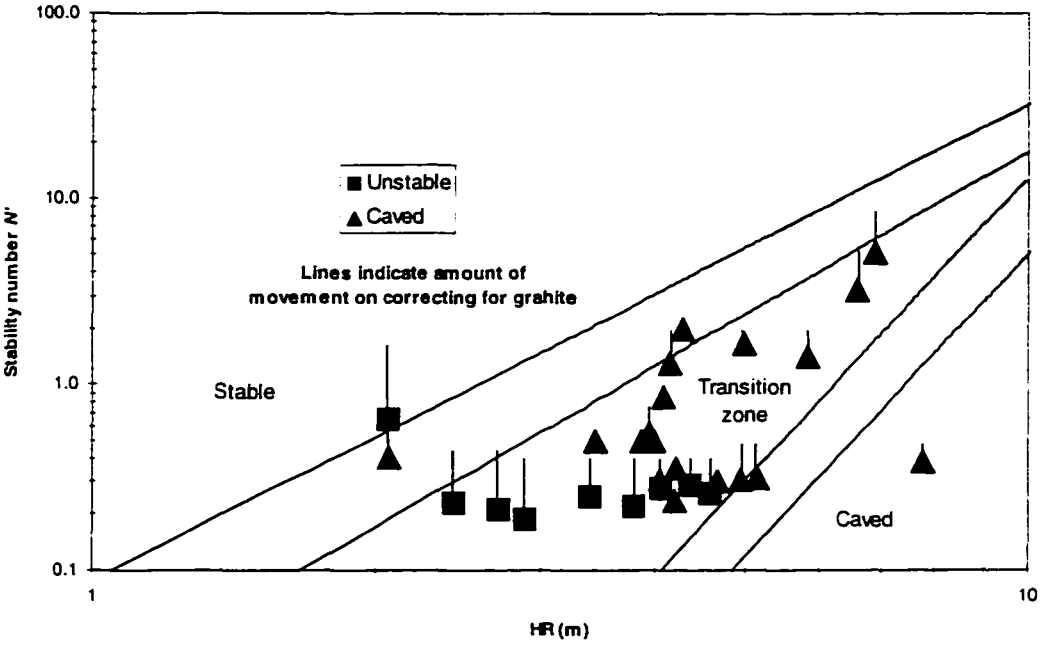


Figure 7.35 Stability graph showing examples of movement of points after correcting for graphitic zones in stope surfaces

Because of the combined effects of faults and relatively poor ground, the results of corrections for soft zones (graphitic zones) using the approach presented in the thesis is minor. However, the method removes outliers from the stable data zone. Thus the thesis approach to accounting for soft zone influences is confirmed.

Figure 7.35 clearly demonstrates that (a) an $N' = 1$ threshold would not properly identify unstable or caving conditions, (b) the general transition zone seems to be applicable, and (c) that the unstable and caved cases could not be controlled by the applied rock support systems.

The graphite zone correction criterion applied to obtain Figure 7.35, was applied to the whole database and Figure 7.36 presents the stability graph after correcting for the graphite zones in the stope surfaces.

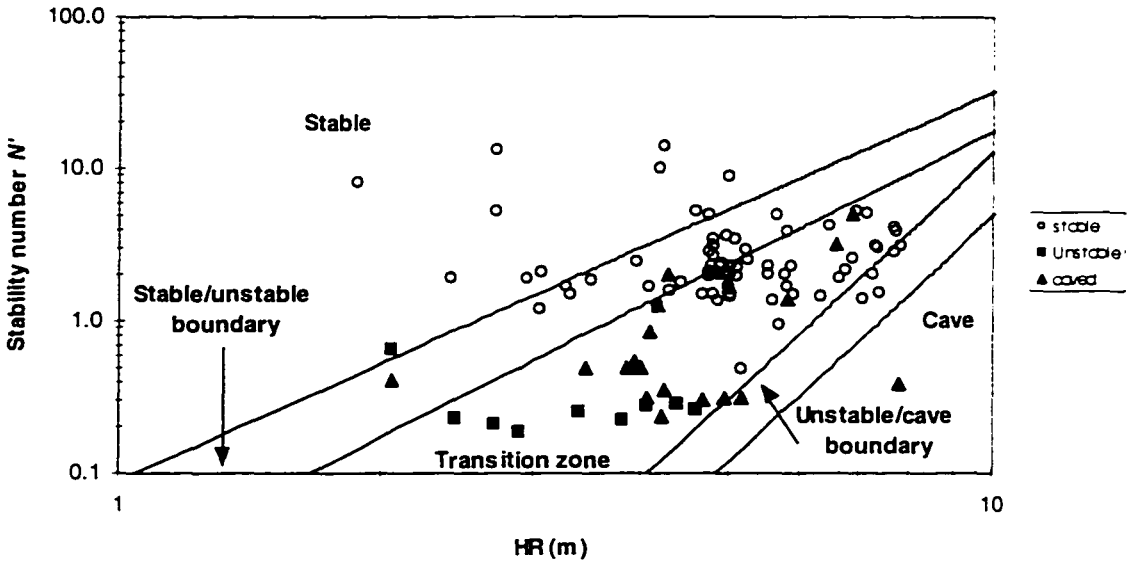


Figure 7.36 Ashanti stability graph after correcting for graphite zones

Again, the boundaries between unsupported stable and unstable stopes, unstable and caved stopes are the same as for Figure 7.35. The boundary between stable and failed stopes still appears to be horizontal even after correcting for the soft graphite zones, suggesting either that other factors such as time, blasting and water may be affecting stope stability but are not accounted for in the plot or that conditions involving faults in ground with $N' \leq 1$ are not supportable (at least with support type adopted at Ashanti).

Whereas there may be insufficient data to conclusively justify the following conclusion, the stability graph presented in Figure 7.36 strongly suggests that stopes are unsupportable if graphitic shears exist and results in ground with $N' < 1$. Hence the stability graph boundaries shown in Figure 7.37 are recommended for verification at Ashanti.

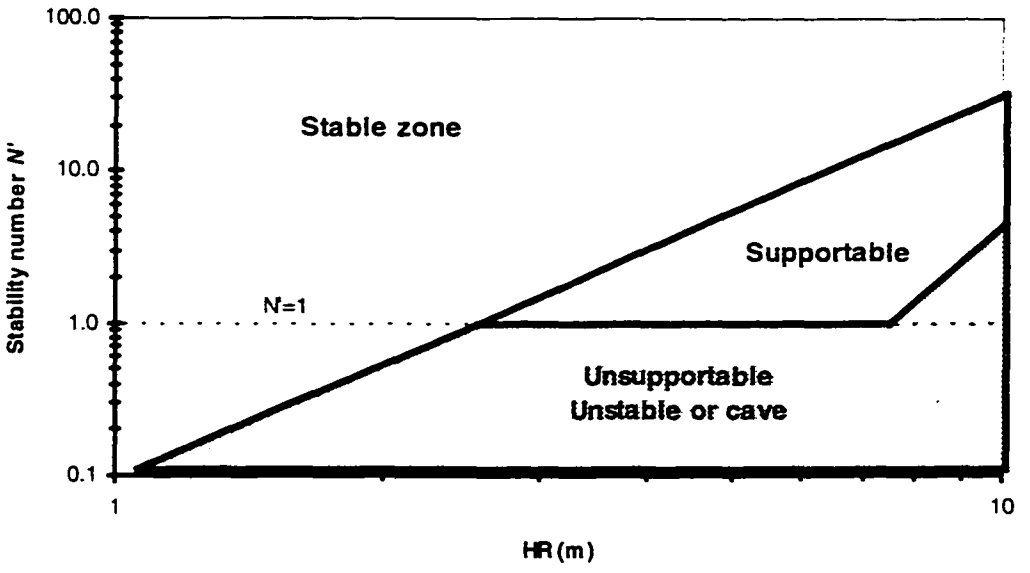


Figure 7.37 Recommended stability graph for Ashanti

To operate unsupported stopes at Ashanti, one would have to use stopes with hydraulic radii of less than 4. This range of hydraulic radii should only be applicable at locations where N' is at least one, taking into account corrections for graphite. Support seems effective up to hydraulic radius of 8 if N' is greater than one.

The zone identified as Unsupportable in Figure 7.37 implies that at Ashanti, when N'<1 no open stopes can be mined even with support.

The modified span concept has been shown in this thesis to be applicable to open stope design, and is applied to the Ashanti database. Figure 7.38 is a plot of the Ashanti data using the modified span or equivalent dimension and the mine excavation stability index *MESI* (with Q'_m for soft zones but with F_w = 1 for discrete faults).

$$MESI = Q'_m \bullet B \bullet C \bullet F_w$$

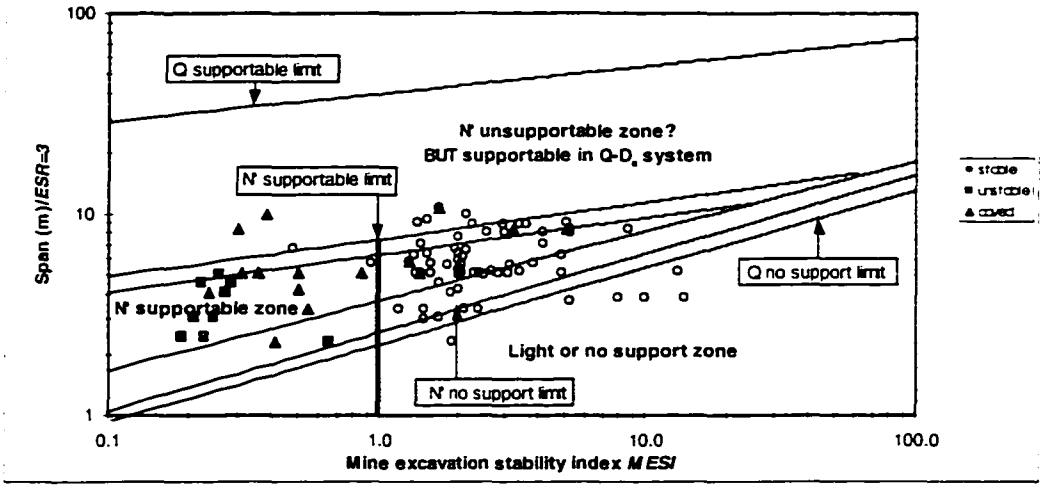


Figure 7.38 Plot of modified span versus mine excavation stability index *MESI*.

Figure 7.38 can be used as an alternative to the stability graph for open stope design, and has the advantage of giving specific stope dimensions such as strike lengths and endwall widths in the orebody. Hydraulic radius does not give specific stope surface dimensions, and often require further analysis for the specific stope surface dimensions. Figure 7.38 also has the advantage over the traditional Q-D_e graph because it accounts for gravity, joint orientation and faults and soft zones. For Ashanti, *MESI* less than one defines conditions that are difficult to support, as discussed in previous section.

7.12 Evaluation of Mining Methods in Ashanti

7.12.1 Accounting for bifurcations in design

A bifurcation of the orebody creates a potential wedge problem, and is most critical when associated with graphite in stope backs (Figure 7.39).

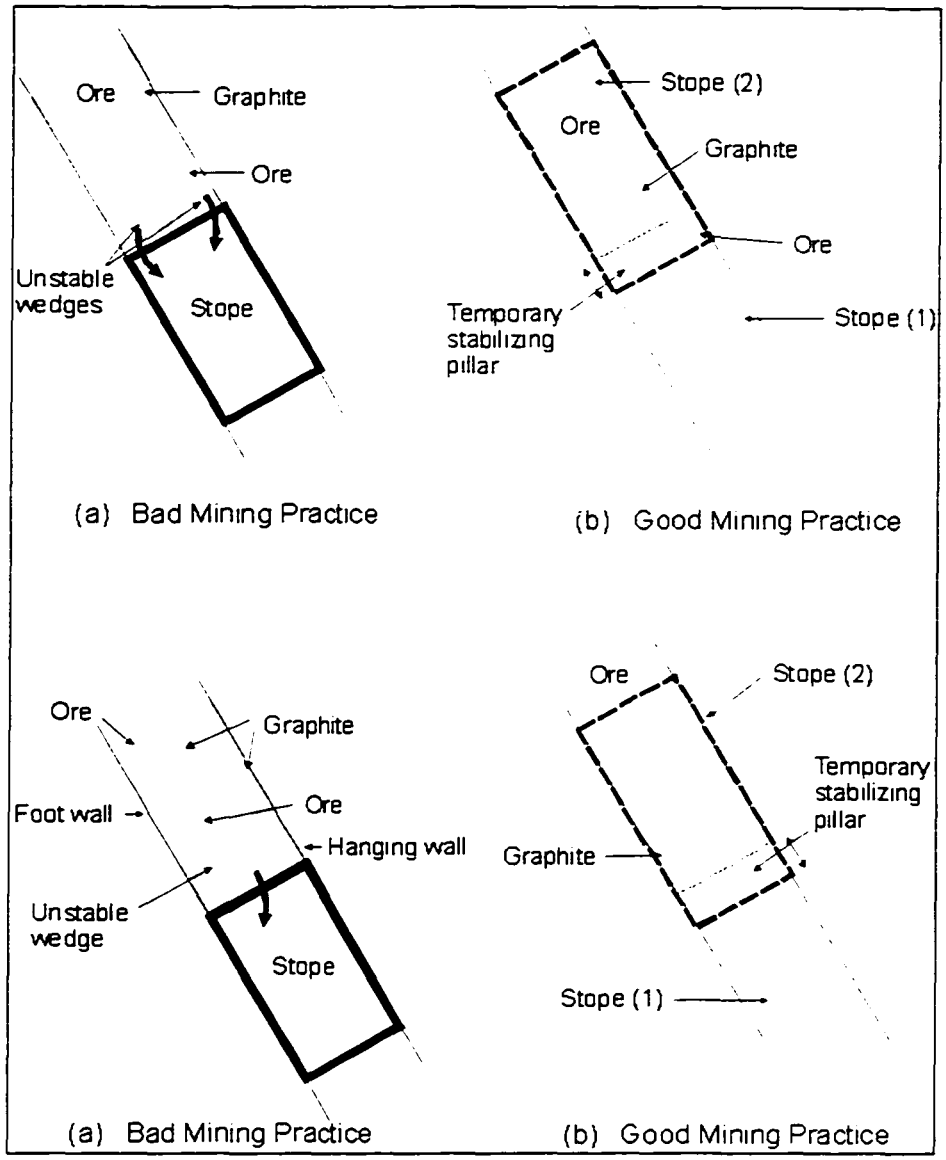


Figure 7.39 Bifurcation of orebody and mining practice

Figure 7.39 is based on field observation of failures and analysis of bifurcation cases, and qualitatively shows the difference between bad and good stope design when orebody bifurcates. When stopes terminate with their crowns at the "V" or inverted "V" nodes of bifurcation shown as bad mining practice, such crowns were noted to cave more frequently compared to cases where the bifurcation occurred within the stope called good mining practice. Also, when the stope crown is at some distance from the "V" junction or inverted "V" nodes (good mining practice) such crowns were observed to perform satisfactorily.

7.12.2 Alternative mining methods for Ashanti

The previous chapters demonstrated that the applicability of the stability graph at Ashanti appears to be limited, and that use of the open stope mining method at the mine seems not to be the right mining method,

particularly where N'<1. This section examines alternative mining methods for the sites studied at Ashanti based only on geomechanics constraints.

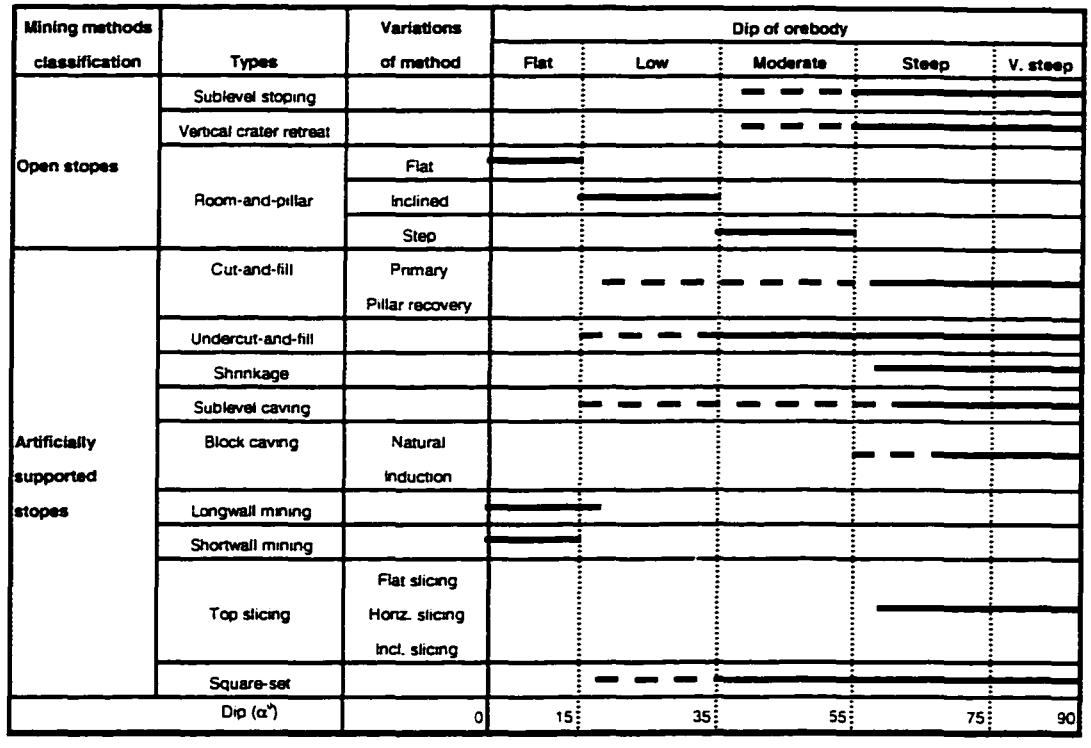
In Sections 7.6.5 and 7.7 both rockmass characteristics and orebody geometries at the research sites were discussed. It seemed that the structure of the rockmasses does not favour the use of open stope mining at least for Blocks 2, 7 and ETS shaft pillar. Much improved support would be required for the open stopes of current sizes to be stable, particularly if *MESI* is less than one. Smaller stope sizes with hydraulic radii between 2.5 and 4 for *MESI* of at least 1 are required if they were to be unsupported. Such sizes would most likely be uneconomic. Other mining methods are examined as alternatives that could be used at increased profit without increased risk.

Dips of orebodies, even though critical for mining method selection, are still inadequately classified. Table 7.12 is an attempt to classify orebody dips with reference to mining demands. Table 7.12 presents the results of a literature survey including Cummins and Givens (1973). Stress factor *A* in the Table 7.12 is taken as 1.

Table 7.12 Classification of dips of orebodies and discontinuities for mining method selection and stability considerations - stress factor $A = 1$

Dip α° of orebody or discontinuity	Classification	Remarks
0-15	Flat	Optimum performance of mining equipment. Power shovels and scrapers required to move ore. Stability of walls not affected by discontinuities in this dip range, but are critical for crown stability.
15-35	Low	Critical for ore flow. Scrapers may be required to move ore. Range for angles of internal friction of most rock joints. Failure in walls by sliding is critical for joints with dips in this range.
35-55	Moderate	Above critical angle for ore flow. Ore flows but may require use of scrapers. Joints in this dip range may cause sliding failure in walls. Crowns may fail.
55-75	Steep	Scrapers are not required. Stability of walls improved, failure may be by buckling. Some sliding is possible.
75-90	Very steep	Ore flows under total gravity or nearly so. No scrapers required. Stability of walls optimum. Crowns without flat to low dipping joints will be stable.

Table 7.12 is related to mining methods in Figure 7.40, which gives a relationship between orebody dip and mining methods.



Symbol	Meaning
▬▬▬	Effective dip range for optimizing method
▬ ▬ ▬	Method applied under special circumstances

Figure 7.40 Relationship between orebody dips and mining methods

Figure 7.41 presents the relationship between rockmass quality and mining methods. Figure 7.41 is developed from published case histories including those in Hustrulid (1985), Cummins and Givens (1973) and Hudson (1993). Used together, Figure 7.40 and Figure 7.41 can effectively assist in selecting a suitable mining method for a given situation based on geomechanical requirements only.

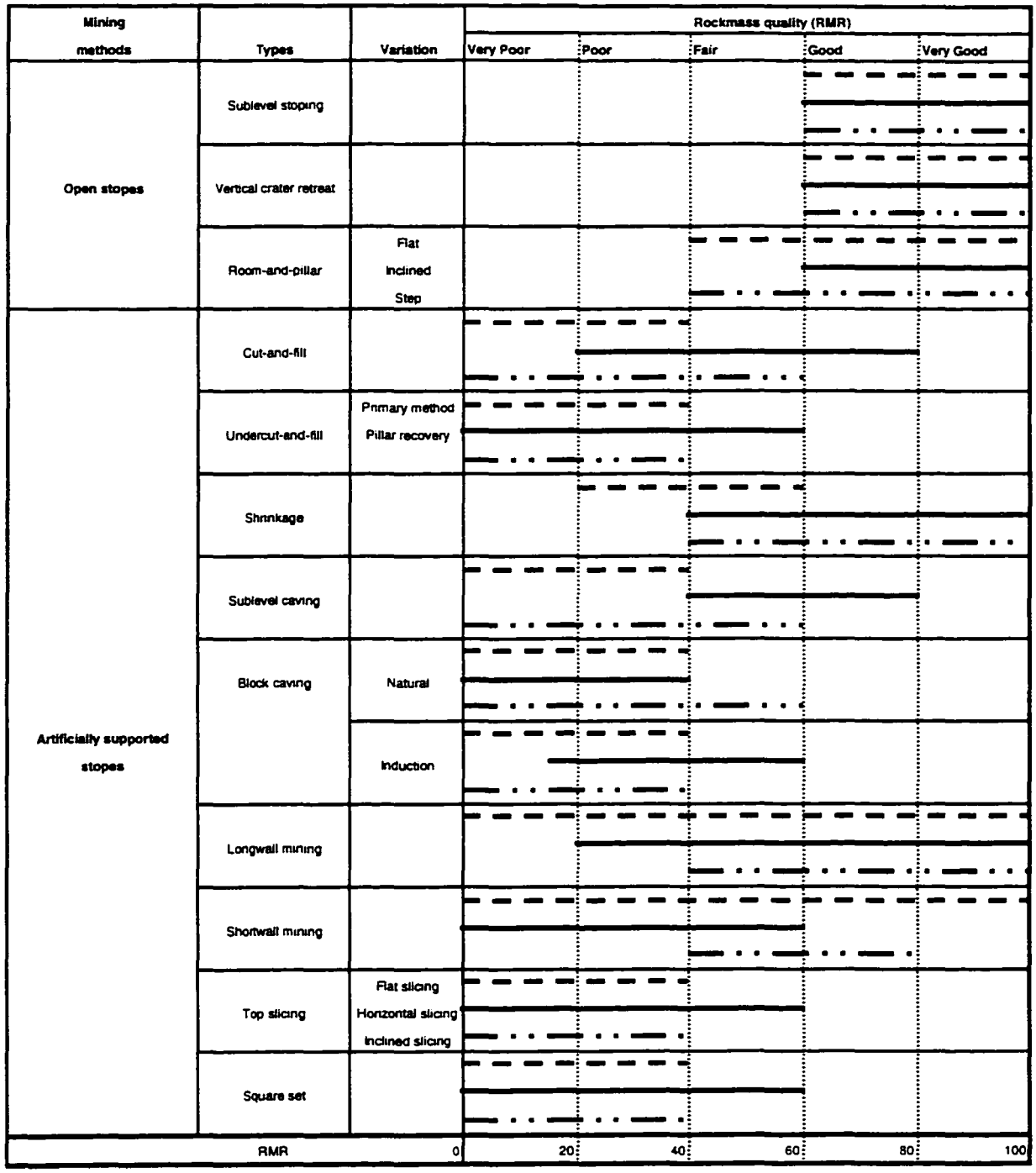


Figure 7.41 Relationship between rockmass quality and mining methods

Orebodies at Ashanti typically dip between 60° and 80°. Possible mining methods, based on orebody dip, for this orebody dip range are:

- Sub-level stoping,
- Vertical crater retreat,
- Cut and fill,
- Shrinkage,
- Square set,
- Block caving,
- Sub-level caving,
- Top slicing, and
- Undercut and fill.

Rockmass qualities in the study areas at Ashanti range from Q' of 0.9 to 20 (*RMR* between 45 and 88), and classify as very poor to good rocks (not considering graphite). Good quality rocks are generally found in Block 8 of GCS. For Blocks 2, 7 and ETS shaft pillar, rockmass quality Q' is between 1 and 3.5 (*RMR* between 46 and 61). When the soft zones are considered Q'_m is lower for the rockmasses. Thus the rockmasses classify as poor in Q-system in Blocks 2, 7 and ETS shaft pillar. This range is reduced further when the thickness of graphite in the shear or fault zones is taken into account. Possible mining methods, based on rockmass quality, for this class of rockmasses as shown in Figure 7.41 are:

- Cut and fill,
- Undercut and fill,
- Block caving,
- Top slicing,
- Square set, and
- Shrinkage.

The final alternative mining methods, considering both rockmass quality and orebody geometry are:

- Block caving,
- Cut and fill,
- Square set,
- Shrinkage, and
- Top slicing.

A review of the mining methods at Ashanti (Section 7.5) shows that in the Ashanti practices, cut and fill (cut and fill, undercut and fill), shrinkage, square set, and sub-level caving, which agrees well with the methods identified with the procedure discussed in this thesis. They only recently introduced open stope mining, and this analysis has shown that it is not an appropriate mining method for the sites studied.

Indeed, the bottom part of Block 2 was mined by cut and fill before management decided to opt for open stoping, because of large tonnage and lower production cost requirements. It would appear that on the basis of geomechanics with good mining practice, block caving and cut and fill are the most promising mining methods for Blocks 2, 7 and the ETS shaft pillar.

7.13 Summary

Rockmasses at Ashanti are highly jointed, and classify as poor to good with Q' between 0.9 and 20. The good quality rockmasses are in Block 8 of GCS. Ignoring GCS, rockmasses in Blocks 2, 7 and ETS shaft pillar classify as poor with Q' between 1 and 3.5. Rockmass quality is further lowered when the graphite layers intersecting the stope surfaces are considered in Q', and the stability index *MESI* is further reduced.

The orebody contains discontinuities that are sub-parallel and perpendicular to it. Blast rings parallel to the discontinuity patterns are the cause of blast ring slabbing, as experienced in Block 2.

The stability graph method's applicability is limited for ground conditions encountered at Ashanti. The conventional stability graph boundaries do not fit the Ashanti data when $N'<1$. Hydraulic radii less than 4 for N' greater than or equal to one are required, only stopes with hydraulic radii less than 8 for N' greater than one are supportable.

At the study sites in Ashanti, open stopes are not recommended at locations where $N'<1$.

A procedure is presented and applied to case histories to account for the presence of soft gouge zones in wide faults and shear zones intersecting stope surfaces. The procedure relates the stope surface rockmass quality to the thickness of fault gouge, stope surface width, adjacent rockmass quality and gouge rockmass quality. The resultant stability graph shows less overlap by about 12% and thus is slightly improved.

The orebody at Ashanti bifurcates with intercalating graphitic bands. Birfurcation adversely affects the stability of open stope backs. Crown stability is correlated with orebody bifurcation. Stope crowns cave progressively due to the presence of low and high dipping graphite filled discontinuities in the orebody. When orebody bifurcates, stope design should be such that stope backs do not terminate at bifurcation nodes.

Stope stability is strongly influenced by the amount of graphite and the thickness of graphitic shears. Stope crown caving is aggravated by the presence of graphite in bifurcation zones.

Block caving and cut and fill mining seem more appropriate for Ashanti mine Blocks 2, 7, and ETS. Charts are presented for quick determination of mining methods on the basis of geomechanics requirements and orebody geometry.

CHAPTER 8

CONCLUSIONS AND RECOMMENDATIONS

8.1 Conclusions

The thesis is focused on evaluating the effects of faults on the stability of open stopes. Faults are often the source of open stope overbreak and dilution. How faults affect stope stability was not well understood. This thesis identifies and evaluates the fault characteristics that adversely affect stope stability. The modified stability graph method (Mathews et al. 1980, Potvin 1988) was developed in Canada as an empirical design tool for stope design and is now used throughout the world. However, this design method does not include a factor to account for the presence of faults or soft zones on excavation stability. Substantial effort was devoted in this thesis to improve the applicability of the stability graph method by accounting for the destabilizing effects associated with faults.

When stopes are intersected by a fault, or near such a weakness zone, this thesis shows that modifications to the conventional stability number yield better empirical design results for open stopes. To determine the modified stability number, a decision is made whether the fault is a discrete structure or a wide zone. When the fault is a wide zone, then a weighted rockmass quality Q'_m that captures the lower rockmass quality of the gouge is used. For discrete faults, the Q' of the host rockmass quality is used. For all faults, a fault factor is introduced to account for the de-stabilizing effects of these faults. The fault factor is a function of stope geometry, fault characteristics and the in situ stress state. The stability number modified for the influence of faults is then used in a similar manner as for the conventional stability graph method. The empirical design of stopes without faults is unchanged.

8.1.1 Fault effects

First a methodology was developed for determining overbreak or $ELOS_f$ (equivalent linear sloughage) due to faults near stopes. The approach is based on the theory that a fault near a stope increases the zone of low stress. When the stresses fall below some critical value, which is on the order of 100 kPa or near zero, unravelling possibly leading to caving occurs. Two-dimensional finite element simulations using PHASE^2 was used to demonstrate that the presence of a fault increases the volume or area of low stress. For 2-dimensional modelling, $ELOS_f$ is given by the increase in the area of low stress divided by the height of the stope, when the stope is modelled with a fault compared to a stope modelled without a fault. This methodology is applicable to excavations in discontinuous (jointed or blocky) rockmasses and can be used to analyze other scenarios beyond those presented in this thesis.

Numerical modelling, analytical methods and an observational approach, have shown that the following fault characteristics have greatest influence on stope stability:

- Included angle between the stope surface and the fault,
- Location of fault intersection on a stope wall,
- Distance of the fault from the stope surface, for non-intersecting faults,
- Fault shear strength, and
- Rockmass quality of the gouge, for wide faults and shear zones.

The shape and extent of the zone of low stress also depend on:

- The stope geometry (stope surface dip and stope aspect ratio), and, for stress levels below the yield point of the host rock.

For example, the importance of included angle and fault position on $ELOS_f$ is illustrated in Figure 8.1. If the assumptions for the creation of this graph are applicable, it can be used to estimate the support length and capacity requirements.

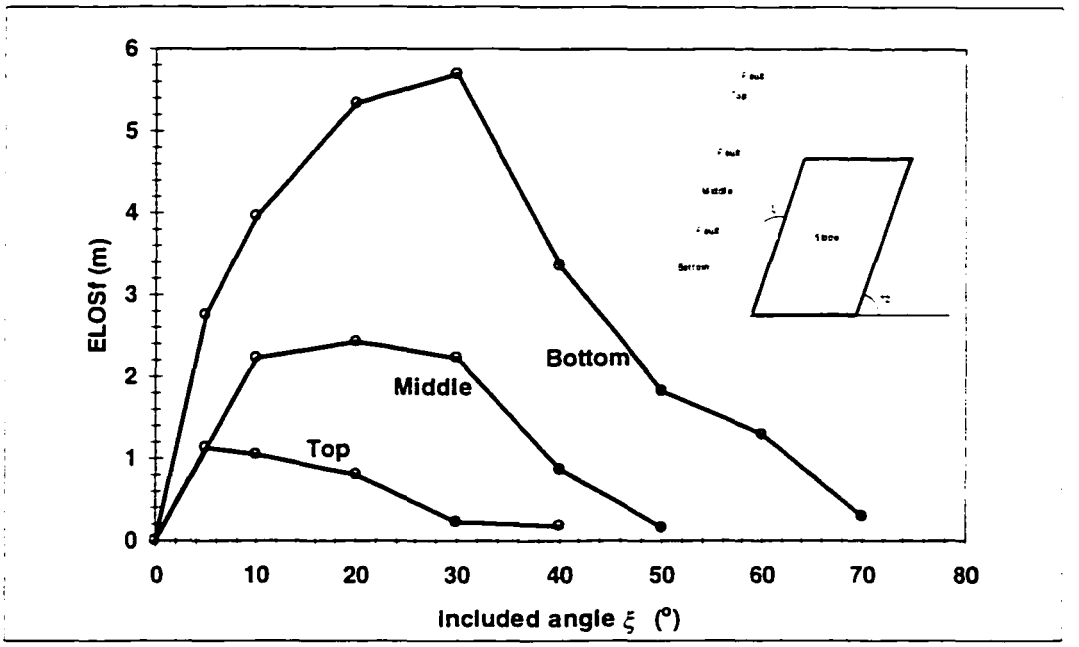


Figure 8.1 Effect of included angle and location of fault (bottom, middle and top) on $ELOS_f$: $K = 2.1$, $\phi^* = 20°$, $\alpha = 72°$, $Ar = 0.4$

An important contribution of this thesis was to identify that the lack of a correction factor for faults was a deficiency in the stability graph method. A procedure was developed for determining a fault factor for incorporation into the stability number N'. The procedure combines the predicted $ELOS_f$ from the numerical modelling with the empirical $ELOS$ contours plotted on the stability graph by Clark and Pakalnis (1997). $ELOS_f$ values from 0 to 0.5 m are considered to represent stable stope conditions, and the $ELOS$ = 0.5 m-contour is used as the basis for calculating a fault factor F_f. The fault factor is given by the stability number N_f corresponding to $ELOS_f$ divided by the stability number N_0 corresponding $ELOS$ = 0.5 m-contour for a given stope geometry (hydraulic radii) and fault condition. The fault factor graph for conditions corresponding to those in Figure 8.1 is presented as an example in Figure

The fault factor can reduce the stability number N, by one to about three orders of magnitude, compared to the effects of the stress factor A, joint orientation defect factor B and gravity factor C. A, B and C affect N' by a maximum of one order of magnitude. Therefore, when faults are near stopes they control the stability of the stope surface.

When a wide fault or shear zone with soft gouge intersects the stope surface, the rockmass quality of the soft zone is important for the stability of the stope surface. The effect of the poor rockmass quality in the fault can be accounted for by using a weighted rockmass quality, which is based on the rockmass qualities of the soft zone, the adjacent rockmass, and the relative thickness of the fault to the stope surface.

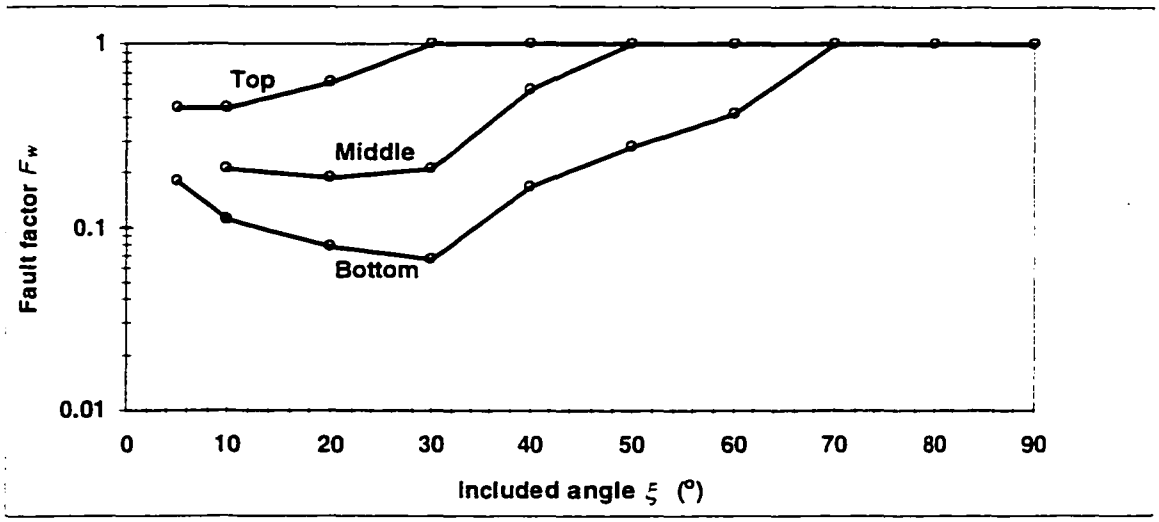


Figure 8.2 Example fault factor graph for conditions corresponding to those in Figure 8.1

8.1.2 Case histories

Kidd Mine in Timmins, Canada, is one of the research case study sites. The mine uses the open stope mining method and has experienced significant dilution from hangingwalls (Tannant et al., 1997). The orebodies at the mine are associated with major and minor faults. The major faults are the Gouge Fault and Gouge Fault Splay. A total of 48 stopes were studied in #3 mine resulting in 112 stope wall stability assessments. Sixty-nine percent of the stope walls analyzed were associated with either a major or a minor fault.

Application of the conventional stability graph method was unable to adequately differentiate between stable and caved stopes, because it did not account for the adverse effects of faults. Cavity surveys were used to assess the performance of the stopes, and to quantify overbreak. A detailed review of geological sections and stope designs was undertaken to characterize the locations and orientations of faults relative to each stope surface. Using this information fault factors were calculated and applied to the database. With the stability number modified to account for the presence of faults, the stability graph method was able to better differentiate stable and caved stopes (with a data separability index of 67%). Based on this evidence, the use of a fault factor to revise the conventional stability number N' is recommended.

Ashanti Goldfields mine in Ghana was the second case study site for the research. Data were collected from the mine to develop a database consisting of 130 cases of stope walls. Ashanti Goldfields mine rocks are characterized by many shear zones filled with graphite. Faults or large shear zones containing soft gouge often intersect stope surfaces. The soft gouge largely controls stope back stability.

The quality of the rockmass containing a soft zone in a stope surface is adjusted by taken into account the rockmass quality of the soft zone, the adjacent rockmass quality, the width of the stope surface intersected,

and the thickness of the soft zone. The method is applied to the case histories at Ashanti, and was found to slightly improve the differentiation between stable and caved cases. It is recommended that where wide soft zones intersect stope surfaces, this method be used. It is shown that the fault factor approach removes outliers from the stable data zone.

It is concluded from the Ashanti stability graphs that the general transition zone developed using statistics and the calibration database are applicable, but that unstable and caving cases below $N' = 1$ could not be controlled by the applied rock support systems at Ashanti. Hence, for locations at Ashanti, where $N' < 1$, open stopes are not recommended.

To operate unsupported stopes, Ashanti would have to use stopes with hydraulic radii of less than 4, and only where N' is at least one, taking into account corrections for graphite. Support seems effective up to a hydraulic radius of 8 if N' is greater than one. The stability graph method that accounts for wide fault zones presented in the thesis, suggests that stopes are unsupportable if graphitic shears exist and result in ground with $N' < 1$.

8.1.3 Stability graph and applications of statistics

It is often recommended that individual mines calibrate their own stability graphs. The distribution of points in the zones of the stability graph, and boundaries between stable \ unstable, and unstable \ cave, are amenable to statistical treatment. Potvin (1988) recommended use of statistics to define the boundaries between stable and caved stopes. Application of statistics to the stability graph has several advantages as discussed in the thesis. The implication of the location of a point on the stability graph, and the relationship between zones of the stability graph, have statistical and physical significance. The thesis presents statistical tools relevant to the interpretation of empirical data, and applicable to the stability graph method.

The likelihood ratio was found to provide an excellent statistical tool for use in interpreting the stability graph. The likelihood method can be used to optimally define the boundaries between zones in the stability graph based on misclassification risk cost and inequality in data subgroups.

The stable, unstable and cave zones of the stability graph overlap. An index for determining the amount of overlap is defined as the separability index. It can be used to determine the improvement to the stability graph when a new parameter is introduced, or when an existing parameter in the stability graph parameters is modified, as is the case in the fault factor development.

There is a transition zone in the stability graph, defined by the boundary between stable and unstable stopes, and the boundary between unstable and caved stopes. In the transition zone, stable, unstable, and caved stopes are all possibilities. Unstable stopes in the transition zone are supportable.

It was found that the use of statistics to define boundaries for the zones in the stability graph for an individual mine is difficult, if not impossible, because of the restricted dispersion of data. Individual mines have unique rockmass qualities and stope sizes that often restrict variability in the data.

The boundaries defined by statistical methods using the calibration database are applicable to individual mines, and if required, should be optimized to individual mine conditions depending on cost and difference between number of stable and unstable cases.

8.1.4 Alternative stability graphs

The likelihood-based stability graph and the stability graph method that uses the stability number and a critical span, are useful alternative open stope design tools to the conventional stability graph method. The revised stability index – modified span graph includes rockmass parameters not included in the conventional stability graph.

A likelihood-based stability graph with multiple design curves is presented. Based on the experiences of a mine, a specific likelihood ratio curve can be selected according to a desired level of risk. The graph is ideal for making on the spot design decisions based on exposed ground conditions, and for new mines that intend to use open stope mining but have little data.

A modified stability number N' taking into account fault factors provides an improved rockmass quality rating when compared to the $Q - D_e$ method of underground excavation design or the conventional stability graph method. Rock defect orientation and gravity are better accounted for.

The stress factor A is set to unity because hangingwalls are typically located in relaxed ground in open stope mining. For the investigated mine sites, 70% of the cases in the calibration database are in relaxed stress conditions.

Mathematical equations are presented in the Appendix for determining stope surface and fault geometries. The geometry of stopes and faults are required for determining fault-related overbreak, the fault factor, and stope surface hydraulic radius. The equations are verified with the Kidd database, and are recommended for mine design and planning purposes.

8.2 Recommendations For Future Research

Factors affecting the stability of open stopes are many. Faults and stress are only some of the factors that affect open stope stability. This research contributed to the understanding fault effects and stress on open stope design. The work can be further advanced to improve open stope stability by researching some of the following.

- More parametric studies are required to determine the effects of faults on squat stopes.
- The effect of non-intersecting and non-parallel faults, utilizing 3-dimensional models on open should be investigated.
- A gravity factor that takes into account both stope surface rockmass quality and stope surface orientation is more realistic than one that considers only stope surface orientation as in the stability number N' or only rockmass quality as in the Q-system. Further work is required in this direction.
- The Q-system shows that larger spans can be supported than implied by the stability graph method. A possibility of exploiting this advantage for mining applications requires further investigation.
- Field evidence and numerical modelling are required to define critical span for use in open stope design. It is shown that modified span and hydraulic radius, could both be used for open stope design. Stress may be an important factor in defining critical span.
- Effect of stope life span on its performance relative to the rockmass stand-up time, is an important area of further study. A good starting point is the span stand-up time graph. It is recognized that planned stope lives are rarely achieved in practice. It is important to adjust stope sizes to account for dilution due to time effects from delays in mining.

APPENDIX A

STATISTICAL MODELS FOR EMPIRICAL DATA INTERPRETATION

A.1 Bayes' theorem and the likelihood statistic

The principle of likelihood in discriminant analysis can be related to Bayes' theorem. Bayes' theorem is an extension of Bayes' rule which states that "assign the object to the group (unstable or stable) with the highest conditional probability". The Bayes' classification rule is defined in terms of discriminant functions or discriminant scores of the data groups concerned. The ratio of the conditional probabilities of the data groups treated is the likelihood ratio. The theory of Bayes' classification rule in terms of the likelihood ratio is presented below for application to the interpretation of the open stopes' stability graph database.

The theory of the likelihood ratio approach to data classification is developed as follows:

Let

P(U|X) = probability that a stope is truly unstable in **X** data collected is true (**a posteriori** probability)

P(S|X) = probability that the stope is truly stable in **X** data collected is true (**a posteriori** probability)

P(X|U) = conditional probability that **X** data is observed if the stope is unstable (**a priori** probability)

P(X|S) = conditional probability that **X** data is observed if the stope is stable (**a priori** probability)

P(U) = probability of stope being selected from the database is unstable (**a priori** probability)

P(S) = probability of stope being selected from the database is stable (**a priori** probability)

Bayes' rule is expressed mathematically as:

$$\mathbf{P(U|X) > P(S|X)} \qquad \text{A.1}$$

Equation A.1 implies assign the stope surface to the unstable stopes cluster if its **a posteriori** probability of being unstable is greater than its **a posteriori** probability of its being stable.

From probability calculus,

$$\mathbf{P(U,X) = P(U)P(X|U) = P(X)P(U|X)} \qquad \text{A.2}$$

P(U,X) is the probability that instability is true and **X** stopes is observed. From Equation A.2,

$$\mathbf{P(U|X) = \frac{P(U)P(X|U)}{P(X)}} \qquad \text{A.3}$$

If the whole database consisting of stable and failed (failed stopes = unstable plus caved stopes) stopes is represented by the space Ω, then:

$$\mathbf{P(\Omega|X) = 1} \qquad \text{A.4}$$

$$\mathbf{\frac{P(\Omega)P(X|\Omega)}{P(X)} = 1}$$

$$\mathbf{P(X) = P(\Omega)P(X|\Omega)}$$

The probability that *U* stopes are unstable given that **X** stopes are studied, and the probability that *S* stopes are stable given that **X** are observed, are given by Equations A.2 and A.3 given that for the whole database,

$$\mathbf{P(U|X) = \frac{P(X|U)P(U)}{P(\Omega)P(X|\Omega)}} \qquad \text{A.5}$$

$$\mathbf{P(S|X) = \frac{P(X|S)P(S)}{P(\Omega)P(X|\Omega)}} \qquad \text{A.6}$$

Bayes' classification rule is now related to **a priori** probability and conditional probability in Bayes' theorem by dividing Equation A.5 by Equation A.6 as follows:

$$\mathbf{\frac{P(U|X)}{P(S|X)} = \left[\frac{P(U)}{P(S)}\right]\left[\frac{P(X|U)}{P(X|S)}\right]} \qquad \text{A.7}$$

Equation A.7 is the Bayes' classification theorem, and relates **a posteriori** probabilities to **a priori** probabilities and conditional probabilities. It allows **a priori** probabilities or odds to be corrected on the basis of a new observation **X** to obtain **a posteriori** probabilities.

The term on the left of Equation A.7 is the ratio of **a posteriori** probabilities. The first term on the right is the ratio of **a priori** probabilities, and the second term is the ratio of conditional probabilities known as the likelihood ratio.

The likelihood ratio is often expressed as a logarithm. Equation A.7 is rewritten as in Equation A.8:

$$log\left[\frac{\mathbf{P(U|X)}}{\mathbf{P(S|X)}}\right] = log\left[\frac{\mathbf{P(U)}}{\mathbf{P(S)}}\right] + log(\Lambda) \tag{A.8}$$

The likelihood functions for the stable $f_s(HR,N')$ and unstable $f_u(HR,N')$ classes are of the general form:

$$f(\mathrm{HR},\mathrm{N}) = \frac{1}{2\pi\sigma_{HR}\sigma_{N'}\sqrt{1-\rho_{HRN'}}} \tag{A.9}$$

$$\bullet \exp\left\{-\frac{1}{2\left(1-\rho^2\right)}\left[\frac{\left(\mathrm{HR}-\overline{\mathrm{HR}}\right)^2}{\sigma^2_{HR}} - \frac{2\rho\left(\mathrm{HR}-\overline{\mathrm{HR}}\right)\left(\mathrm{N'}-\overline{\mathrm{N'}}\right)}{\sigma_{HR}\sigma_{N'}} + \left(\frac{\left(\mathrm{N'}-\overline{\mathrm{N'}}\right)^2}{\sigma^2_{N'}}\right)\right]\right\}$$

Where $\rho_{HR,N'}$ is the product moment correlation coefficient given by:

$$\rho_{HRN'} = \frac{\sigma_{HRN'}}{\sqrt{\sigma_{HR}}\sqrt{\sigma_{N'}}} \tag{A.10}$$

The expression in the square bracket in Equation A.9 is rewritten as:

$$\left(\mathbf{X}-\overline{\mathbf{X}}\right)\mathbf{S}^{-1}\left(\mathbf{X}-\overline{\mathbf{X}}\right) \tag{A.11}$$

Where **X** is a row vector given by,

$$\mathbf{X} = (HR \quad N') \tag{A.12}$$

And

$$\mathbf{X}-\overline{\mathbf{X}} = \left(HR-\overline{HR} \quad N'-\overline{N'}\right) \tag{A.13}$$

When the within variance-covariance matrices for the stable and unstable classes are different, each distribution is unique in its own right. The normal density functions for the unstable and stable classes are then given in Equations A.14 and A.15 in terms of discriminant functions.

$$ln[f_u(X)] = -\left(\frac{1}{2}mln(2\Pi)\right) - \frac{1}{2}ln(|\mathbf{S_u}|) - \frac{1}{2}(\mathbf{X} - \overline{\mathbf{X}}_u)\mathbf{S_u^{-1}}(\mathbf{X} - \mathbf{X}_u) \quad \text{A.14}$$

$$ln[f_S(X)] = -\left(\frac{1}{2}mln(2\Pi)\right) - \frac{1}{2}ln(|\mathbf{S}_S|) - \frac{1}{2}(\mathbf{X} - \overline{\mathbf{X}}_S)\mathbf{S}_S^{-1}(\mathbf{X} - \overline{\mathbf{X}}_S) \quad \text{A.15}$$

Where, $\mathbf{S_u}$ and $\mathbf{S_s}$ are the class within variance-covariance matrices for the stable and stable classes respectively.

If the within subgroups variance-covariance matrices are equal, i.e.,

$$\mathbf{S}_u = \mathbf{S}_s = \mathbf{S} \quad \text{A.16}$$

The likelihood ratio is also equal to the ratio of the bivariate normal density functions or likelihoods (Equations A.14 and A.15) as shown in Equation A.17.

$$\frac{f_u(HR, N')}{f_S(HR, N')} = \frac{\mathbf{P(X|U)}}{\mathbf{P(X|S)}} = \Lambda \quad \text{A.17}$$

The subscripts u and s in Equation A.17 stand for unstable and stable respectively.

Therefore, by definition the likelihood ratio Λ is given by,

$$\Lambda = \frac{f_u(\mathbf{X})}{f_s(\mathbf{X})} \quad \text{A.18}$$

Taking logarithms of both sides of Equation A.18, substituting for $f_u(\mathbf{X})$, $f_s(\mathbf{X})$, and simplifying gives Equation A.19 as follows:

$$ln(\Lambda) = \mathbf{X}^{\mathbf{T}}\mathbf{S}^{-1}\mathbf{d} - \frac{1}{2}\left(\overline{\mathbf{X}}_{\mathbf{u}}^{\mathbf{T}}\mathbf{S}^{-1}\overline{\mathbf{X}}_{\mathbf{u}} - \overline{\mathbf{X}}_{\mathbf{S}}^{\mathbf{T}}\mathbf{S}^{-1}\overline{\mathbf{X}}_{\mathbf{S}}\right) \quad \text{A.19}$$

Where, $\mathbf{d}$ is the mean difference vector given by:

$$\mathbf{d} = \overline{\mathbf{X}}_{\mathbf{u}} - \overline{\mathbf{X}}_{\mathbf{s}} \quad \text{A.20}$$

Equation A.19 is an important equation. It is the Bayes' rule related to the general likelihood ratio. It is a practical form of Bayes' rule in that all the parameters in the equation are known. When the likelihood ratio is 1, implying equal conditional probabilities, Equation A.21 becomes:

$$\mathbf{X}^{\mathrm{T}}\mathbf{S}^{-1}\mathbf{d} - \frac{1}{2}\left(\overline{\mathbf{X}}_{\mathbf{u}}^{\mathrm{T}}\mathbf{S}^{-1}\overline{\mathbf{X}}_{\mathbf{u}} - \overline{\mathbf{X}}_{\mathbf{S}}^{\mathrm{T}}\mathbf{S}^{-1}\overline{\mathbf{X}}_{\mathbf{S}}\right) = 0 \qquad \text{A.21}$$

Equation A.21 is a special case of the likelihood ratio criterion commonly referred to as Mahalanobis distance criterion. The Mahalanobis distance criterion is discussed in section A.2

Equation A.19 has another significant implication. It shows that the likelihood functions for the two or more groups of data are equal, i.e.,

$$f_u(\mathbf{X}) = f_s(\mathbf{X}) \qquad \text{A.22}$$

This means that an object with this characteristic can neither be assigned to the unstable or the stable group. A curve defining all such objects is the discriminating curve between the stable and unstable clusters. Above this curve the likelihood of having a stable stope surface increases, and below it the possibility of an unstable stope increases.

The analysis to this point assumes that **a priori** probabilities for stable and unstable stopes (equal numbers of stable and unstable stopes in the database) are equal. Therefore, the likelihood ratio is equal to the ratio of **a posteriori** probabilities. When **a priori** probabilities are not equal, then the likelihood ratio is given by Equation A.23:

$$\Lambda = \frac{\mathbf{P(S)}}{\mathbf{P(U)}} \cdot \frac{\mathbf{P(U|X)}}{\mathbf{P(S|X)}} \qquad \text{A.23}$$

Another meaningful inference from Equation A.19 is that the discriminating curve will pass through the intersection of the equiprobability contours of the data groups as explained in the following section.

A.2 Mahalanobis Distance Method

The Mahalanobis distance method is a special case of the likelihood ratio discriminant function. The Mahalanobis method is a corrected version of the Euclidean distance approach when the variables are correlated. If there is no correlation between the variables the Mahalanobis and Euclidean distance methods give identical results. Also, for uncorrelated variables, discriminant scores methods and the distance methods give similar results.

In defining the Mahalanobis distance lets consider two groups of data. Let $\mathbf{X_u}$ and $\mathbf{X_s}$ be vectors of coordinates for two points in a sampling space Ω, and let the coordinates of the whole set of points in the sampling space have a variance-covariance matrix S. Then by definition, the square Mahalanobis distance is given by:

$$D_{ij}^2 = (\mathbf{X_i} - \mathbf{X_j})^T \mathbf{S}^{-1} (\mathbf{X_i} - \mathbf{X_j}) \qquad \text{A.24}$$

The classical squared distance between two points Y_i and Y_j is given by:

$$(\mathbf{Y_i} - \mathbf{Y_j})^T (\mathbf{Y_i} - \mathbf{Y_j}) = (\mathbf{X_i} - \mathbf{X_j})^T \mathbf{S}^{-1} (\mathbf{X_i} - \mathbf{X_j}) \qquad \text{A.25}$$

The Mahalanobis' rule states that a vector $\mathbf{X_i}$ will be assigned to the first subgroup if it's squared Mahalanobis distance to the first subgroup average is smaller than it's squared Mahalanobis distance to the second subgroup average. This statement is expressed as:

$$(\mathbf{X_i} - \mathbf{X_u})^T \mathbf{S}^{-1} (\mathbf{X_i} - \mathbf{X_u}) < (\mathbf{X_i} - \mathbf{X_s})^T \mathbf{S}^{-1} (\mathbf{X_i} - \mathbf{X_s}) \qquad \text{A.26}$$

Expanding Equation A.26 and rearranging gives Equation A.27:

$$\mathbf{X_i^T S^{-1} d} > \frac{1}{2} (\mathbf{X_i S^{-1} \bar{X}_u} - \mathbf{X_s^T S^{-1} \bar{X}_s}) \qquad \text{A.27}$$

Equation A.21 compares well with Equation A.27, and is only a special case of the more general form of Bayes' classification rule.

A.3 Calibration database

Table A.1 Summary of the unsupported calibration database

Mine #	Case #	Plane	RQD/Jn	Stress factor	Crit. Dip diff.	Strike diff.	Shear Jr/Ja	Sliding Crit.jt.dip	F-fall S-surf.dip	Gravity Factor	Hydra. rad.	Span/3 (S)	Perf.	Q'	A	B	N'
3	3	wall	6.0	comp.	5.0	0.0	1.0	85.0	90.0	2.5	7.7	8.9	cave	6.0	0.1	0.2	0.3
9	16	back	25.0	comp.	70.0	0.0	0.3	70.0	0.0	2.0	5.8	6.7	cave	6.3	0.1	0.9	1.1
28	159	back	8.0	comp.	0.0	0.0	2.0	0.0	0.0	2.0	7.6	8.7	cave	16.0	0.1	0.2	0.6
30	164	back	14.0	comp.	60.0	0.0	1.5	60.0	0.0	2.0	8.6	9.9	cave	21.0	0.1	0.8	3.3
17	47	back	9.0	comp.	90.0	0.0	2.0	90.0	0.0	2.0	7.3	8.4	cave	18.0	0.3	1.0	11.0
17	50	back	9.0	comp.	90.0	0.0	2.0	90.0	0.0	2.0	6.8	7.8	cave	18.0	0.4	1.0	14.0
27	151	back	15.0	comp.	10.0	0.0	2.0	10.0	0.0	2.0	10.0	11.5	cave	30.0	0.4	0.2	4.8
16	43	back	14.0	comp.	0.0	0.0	1.3	0.0	0.0	2.0	15.2	17.5	cave	18.2	0.5	0.3	5.5
19	54	back	29.0	comp.	10.0	0.0	1.5	10.0	0.0	2.0	6.8	7.8	cave	43.5	0.5	0.2	8.8
19	55	back	29.0	comp.	10.0	0.0	1.5	10.0	0.0	2.0	8.0	9.2	cave	43.5	0.5	0.2	8.8
34	204	back		comp.						1.0	15.2	17.5	cave	20.0	0.5	0.5	5.1
15	35	back	6.0	comp.	0.0	0.0	1.5	20.0	20.0	2.3	10.5	12.1	cave	9.0	0.6	0.3	3.9
34	206	back		comp.						1.0	17.4	20.0	cave	13.0	0.7	0.5	4.7
35	207	back		comp.						1.0	9.9	11.4	cave	10.3	1.0	1.0	10.3
23	150	hw	5.0	comp.	0.0	0.0	0.1	70.0	70.0	6.0	11.3	13.0	cave	0.5	1.0	0.2	0.8
29	161	wall	3.0	comp.	20.0	0.0	1.0	70.0	90.0	8.0	20.0	23.0	cave	3.0	1.0	0.2	4.8
17	49	back	9.0	comp.	90.0	0.0	2.0	90.0	0.0	2.0	9.9	11.4	cave	18.0	1.0	1.0	36.0
31	170	back	18.0	comp.	35.0	60.0	1.5	65.0	30.0	2.8	12.5	14.4	cave	27.0	1.0	0.8	60.0
31	171	back	18.0	comp.	35.0	60.0	1.5	65.0	30.0	2.8	15.0	17.2	cave	27.0	1.0	0.8	60.0
31	172	back	18.0	comp.	35.0	60.0	1.5	65.0	30.0	2.8	15.9	18.3	cave	27.0	1.0	0.8	60.0
13	24	back	17.0	comp.	30.0	0.0	2.0	30.0	0.0	2.0	10.5	12.1	cave	34.0	1.0	0.2	14.0
13	25	back	17.0	comp.	30.0	0.0	2.0	30.0	0.0	2.0	11.3	13.0	cave	34.0	1.0	0.2	14.0
13	26	back	17.0	comp.	30.0	0.0	2.0	30.0	0.0	2.0	12.2	14.0	cave	34.0	1.0	0.2	14.0
21	72	hw	1.0	relax	0.0	0.0	0.3	75.0	75.0	6.5	16.0	18.4	cave	0.3	1.0	0.3	0.5
21	80	hw	1.0	relax	0.0	0.0	0.3	75.0	75.0	6.5	11.0	12.6	cave	0.3	1.0	0.3	0.5
21	96	hw	1.0	relax	0.0	0.0	0.3	78.0	78.0	7.0	8.0	9.2	cave	0.3	1.0	0.3	0.5
21	98	hw	1.0	relax	0.0	0.0	0.3	90.0	90.0	8.0	5.0	5.7	cave	0.3	1.0	0.3	0.6
21	119	hw	1.0	relax	0.0	0.0	0.3	76.0	76.0	6.5	9.0	10.3	cave	0.3	1.0	0.3	0.5
21	122	hw	1.0	relax	0.0	0.0	0.3	60.0	60.0	5.0	13.0	14.9	cave	0.3	1.0	0.3	0.4

21	124	hw	1.0	relax	0.0	0.0	0.3	65.0	65.0	5.5	10.0	11.5	cave	0.3	1.0	0.3	0.4
21	127	hw	1.0	relax	0.0	0.0	0.3	71.0	71.0	6.0	13.0	14.9	cave	0.3	1.0	0.3	0.5
23	149	hw	5.0	relax	0.0	0.0	0.1	70.0	70.0	6.0	9.0	10.3	cave	0.5	1.0	0.2	0.8
21	77	hw	3.0	relax	0.0	0.0	0.3	90.0	90.0	8.0	14.0	16.1	cave	0.8	1.0	0.3	1.8
21	78	hw	3.0	relax	0.0	0.0	0.3	80.0	80.0	7.0	6.0	6.9	cave	0.8	1.0	0.3	1.6
21	79	hw	3.0	relax	0.0	0.0	0.3	80.0	80.0	7.0	10.0	11.5	cave	0.8	1.0	0.3	1.6
21	91	hw	3.0	relax	0.0	0.0	0.3	52.0	52.0	4.0	11.0	12.6	cave	0.8	1.0	0.3	0.9
21	93	hw	3.0	relax	0.0	0.0	0.3	65.0	65.0	5.5	7.0	8.0	cave	0.8	1.0	0.3	1.2
21	94	hw	3.0	relax	0.0	0.0	0.3	65.0	65.0	5.5	9.0	10.3	cave	0.8	1.0	0.3	1.2
21	95	hw	3.0	relax	0.0	0.0	0.3	65.0	65.0	5.5	16.0	18.4	cave	0.8	1.0	0.3	1.2
21	113	hw	2.0	relax	0.0	0.0	0.5	72.0	72.0	6.0	14.0	16.1	cave	1.0	1.0	0.3	1.8
21	105	hw	6.0	relax	0.0	0.0	0.3	63.0	63.0	5.5	13.0	14.9	cave	1.5	1.0	0.3	2.5
21	107	hw	2.0	relax	0.0	0.0	0.8	80.0	80.0	7.0	4.0	4.6	cave	1.6	1.0	0.3	3.4
21	108	hw	2.0	relax	0.0	0.0	0.8	80.0	80.0	7.0	10.0	11.5	cave	1.6	1.0	0.3	3.4
19	56	wall	4.0	relax	0.0	0.0	0.5	90.0	90.0	8.0	19.0	21.8	cave	2.0	1.0	0.3	5.2
21	83	hw	1.5	relax	0.0	0.0	1.5	62.0	62.0	5.0	13.0	14.9	cave	2.3	1.0	0.3	3.4
21	68	hw	3.0	relax	0.0	0.0	0.8	82.0	82.0	7.0	12.0	13.8	cave	2.4	1.0	0.3	5.0
21	102	hw	3.0	relax	0.0	0.0	1.0	60.0	60.0	5.0	14.0	16.1	cave	3.0	1.0	0.3	4.5
21	110	hw	3.0	relax	0.0	0.0	1.0	60.0	60.0	5.0	12.0	13.8	cave	3.0	1.0	0.3	4.5
8	14	hw	9.0	relax	6.0	0.0	0.5	78.0	72.0	6.0	8.8	10.1	cave	4.5	1.0	0.2	5.4
8	15	hw	9.0	relax	0.0	0.0	0.5	78.0	78.0	7.0	8.8	10.1	cave	4.5	1.0	0.3	9.5
21	71	hw	6.0	relax	0.0	0.0	0.8	90.0	90.0	8.0	8.0	9.2	cave	4.8	1.0	0.3	12.0
21	65	hw	4.0	relax	0.0	0.0	1.5	65.0	65.0	5.5	12.0	13.8	cave	6.0	1.0	0.3	10.0
33	185	back		comp.						2.0	6.2	7.1	caved	13.3	0.1	0.2	0.5
33	186	back		Comp.						2.0	5.2	6.0	caved	13.3	0.1	0.2	0.5
33	187	hw		Relax						5.0	10.3	11.8	caved	10.0	1.0	0.3	15.0
33	188	hw		Relax						5.5	16.4	18.9	caved	5.9	1.0	0.2	6.5
33	195	hw		Relax						5.0	5.9	6.8	caved	7.2	1.0	0.2	7.2
22	146	back	8.0	Comp.	10.0	0.0	1.0	10.0	0.0	2.0	2.1	2.4	unstable	8.0	0.1	0.2	0.3
22	147	back	8.0	Comp.	10.0	0.0	1.0	10.0	0.0	2.0	2.3	2.6	unstable	8.0	0.1	0.2	0.3
17	48	back	9.0	Comp.	90.0	0.0	2.0	90.0	0.0	2.0	5.0	5.7	unstable	18.0	0.1	1.0	3.6
11	19	back	30.0	Comp.	40.0	0.0	1.0	40.0	0.0	2.0	3.5	4.0	unstable	30.0	0.1	0.4	2.4
28	154	back	16.0	Comp.	0.0	0.0	2.0	0.0	0.0	2.0	5.2	6.0	unstable	32.0	0.1	0.3	1.9
3	2	wall	6.0	Comp.	5.0	0.0	1.0	85.0	90.0	2.5	8.9	10.2	unstable	6.0	0.2	0.3	0.7
34	205	back		Comp.						1.0	6.4	7.4	unstable	20.0	0.3	0.5	2.7
6	10	end	4.0	Comp.	15.0	0.0	0.8	75.0	90.0	3.5	4.7	5.4	unstable	3.2	0.3	0.2	0.7
16	44	back	14.0	Comp.	0.0	0.0	1.3	0.0	0.0	2.0	6.4	7.4	unstable	18.2	0.3	0.3	3.3

16	38	back	45.0	Comp.	90.0	0.0	2.7	90.0	0.0	2.0	6.1	7.0	unstable	121.5	0.4	1.0	97.0
34	203	back		Comp.						1.0	6.1	7.0	unstable	20.0	0.5	0.5	4.9
16	42	back	14.0	Comp.	0.0	0.0	1.3	0.0	0.0	2.0	6.1	7.0	unstable	18.2	0.5	0.3	5.5
31	175	wall	18.0	Comp.	20.0	25.0	1.5	70.0	90.0	8.0	11.6	13.3	unstable	27.0	0.5	0.3	32.0
31	178	back	18.0	Comp.	45.0	60.0	1.5	65.0	20.0	2.5	11.1	12.8	unstable	27.0	0.5	0.9	29.0
34	201	back		Comp.						1.0	8.8	10.1	unstable	40.0	0.5	1.0	21.6
34	202	back		Comp.						1.0	13.4	15.4	unstable	40.0	0.6	1.0	21.6
34	200	back		Comp.						1.0	7.6	8.7	unstable	100.0	0.6	1.0	60.0
16	41	back	15.0	Comp.	90.0	0.0	2.6	90.0	0.0	2.0	13.4	15.4	unstable	39.0	0.6	1.0	47.0
16	39	back	45.0	Comp.	90.0	0.0	2.7	90.0	0.0	2.0	7.6	8.7	unstable	121.5	0.6	1.0	146.0
32	180	hw	6.0	Comp.	0.0	0.0	1.0	70.0	70.0	6.0	6.9	7.9	unstable	6.0	1.0	0.3	10.0
22	141	hw	8.0	Comp.	0.0	0.0	1.0	70.0	70.0	6.0	8.1	9.3	unstable	8.0	1.0	0.3	15.0
21	97	hw	1.0	Relax	0.0	0.0	0.3	90.0	90.0	8.0	3.0	3.4	unstable	0.3	1.0	0.3	0.6
21	118	hw	1.0	Relax	0.0	0.0	0.3	76.0	76.0	6.5	6.0	6.9	unstable	0.3	1.0	0.3	0.5
21	121	hw	1.0	Relax	0.0	0.0	0.3	60.0	60.0	5.0	2.0	2.3	unstable	0.3	1.0	0.3	0.4
21	123	hw	1.0	relax	0.0	0.0	0.3	65.0	65.0	5.5	6.0	6.9	unstable	0.3	1.0	0.3	0.4
21	126	hw	1.0	relax	0.0	0.0	0.3	71.0	71.0	6.0	2.0	2.3	unstable	0.3	1.0	0.3	0.5
21	130	hw	1.0	relax	0.0	0.0	0.3	60.0	60.0	5.0	4.0	4.6	unstable	0.3	1.0	0.3	0.4
21	131	hw	1.0	relax	0.0	0.0	0.3	65.0	65.0	5.5	3.0	3.4	unstable	0.3	1.0	0.3	0.4
21	112	hw	2.0	relax	0.0	0.0	0.5	72.0	72.0	6.0	8.0	9.2	unstable	1.0	1.0	0.3	1.8
21	104	hw	6.0	relax	0.0	0.0	0.3	63.0	63.0	5.5	8.0	9.2	unstable	1.5	1.0	0.3	2.5
21	129	hw	6.0	relax	0.0	0.0	0.3	65.0	65.0	5.5	12.0	13.8	unstable	1.5	1.0	0.3	2.5
21	67	hw	3.0	relax	0.0	0.0	0.8	82.0	82.0	7.0	9.0	10.3	unstable	2.4	1.0	0.3	5.0
21	82	hw	3.0	relax	0.0	0.0	0.8	65.0	65.0	5.5	6.0	6.9	unstable	2.4	1.0	0.3	4.0
21	115	hw	3.0	relax	0.0	0.0	0.8	65.0	65.0	5.5	8.0	9.2	unstable	2.4	1.0	0.3	4.0
21	116	hw	3.0	relax	0.0	0.0	0.8	65.0	65.0	5.5	10.0	11.5	unstable	2.4	1.0	0.3	4.0
21	101	hw	3.0	relax	0.0	0.0	1.0	60.0	60.0	5.0	6.0	6.9	unstable	3.0	1.0	0.3	4.5
21	109	hw	3.0	relax	0.0	0.0	1.0	60.0	60.0	5.0	6.0	6.9	unstable	3.0	1.0	0.3	4.5
7	12	hw	7.0	relax	0.0	0.0	0.6	75.0	75.0	6.5	9.1	10.5	unstable	4.2	1.0	0.2	5.5
21	70	hw	6.0	relax	0.0	0.0	0.8	90.0	90.0	8.0	5.0	5.7	unstable	4.8	1.0	0.3	12.0
4	4	hw	7.0	relax	15.0	0.0	1.5	30.0	45.0	3.7	7.1	8.2	unstable	10.5	1.0	0.2	7.8
30	166	fw	9.0	relax	10.0	0.0	1.5	80.0	90.0	3.0	9.9	11.4	unstable	13.5	1.0	0.2	8.3
21	69	hw	18.0	relax	0.0	0.0	3.0	55.0	55.0	4.5	16.0	18.4	unstable	54.0	1.0	0.3	73.0
21	87	hw	20.0	relax	0.0	0.0	3.0	66.0	66.0	4.5	12.0	13.8	unstable	60.0	1.0	0.3	81.0
33	197	hw		relax						6.0	4.9	5.6	unstable	3.1	1.0	0.3	5.6
22	134	back	5.0	comp.	30.0	0.0	1.0	30.0	0.0	2.0	1.9	2.2	stable	5.0	0.1	0.2	0.2
9	17	back	25.0	comp.	70.0	0.0	0.3	70.0	0.0	2.0	4.2	4.8	stable	6.3	0.1	0.9	1.1

22	144	back	8.0	comp.	10.0	0.0	1.0	10.0	0.0	2.0	1.9	2.2	stable	8.0	0.1	0.2	0.3
32	179	back	15.0	comp.	70.0	0.0	1.5	70.0	0.0	2.0	4.1	4.7	stable	22.5	0.1	0.9	3.8
32	181	back	15.0	comp.	70.0	0.0	1.5	70.0	0.0	2.0	4.0	4.6	stable	22.5	0.1	0.9	3.8
32	183	wall	16.0	comp.	0.0	0.0	1.5	90.0	90.0	8.0	4.9	5.6	stable	24.0	0.1	0.3	5.8
28	158	back	10.0	comp.	20.0	0.0	2.5	20.0	0.0	2.0	3.4	3.9	stable	25.0	0.1	0.2	1.0
28	156	end	16.0	comp.	10.0	75.0	2.0	80.0	90.0	3.0	5.6	6.4	stable	32.0	0.1	1.0	10.0
14	32	back	90.0	comp.	90.0	n/a	1.0	n/a	0.0	2.0	4.0	4.6	stable	90.0	0.1	1.0	18.0
33	191	back		comp.						2.0	1.3	1.5	stable	15.8	0.1	0.2	0.6
33	193	back		comp.						2.0	1.8	2.1	stable	15.8	0.1	0.2	0.6
36	210	back		comp.						1.0	5.0	5.7	stable	85.0	0.2	0.5	6.4
36	209	back		comp.						1.0	8.4	9.7	stable	85.0	0.2	0.5	6.8
19	57	back	29.0	comp.	10.0	0.0	1.5	10.0	0.0	2.0	3.7	4.3	stable	43.5	0.2	0.2	3.5
36	208	back		comp.						1.0	7.0	8.0	stable	85.0	0.2	0.5	9.4
6	9	wall	12.0	comp.	10.0	0.0	2.0	80.0	90.0	8.0	4.7	5.4	stable	24.0	0.3	0.2	12.0
22	145	back	8.0	comp.	10.0	0.0	1.0	10.0	0.0	2.0	1.8	2.1	stable	8.0	0.3	0.2	1.0
30	169	back	15.0	comp.	0.0	0.0	1.5	0.0	0.0	2.0	5.0	5.7	stable	22.5	0.3	0.3	4.1
22	139	back	13.0	comp.	50.0	0.0	2.0	50.0	0.0	2.0	3.0	3.4	stable	26.0	0.3	0.6	10.0
22	137	back	13.0	comp.	50.0	0.0	2.0	50.0	0.0	2.0	2.9	3.3	stable	26.0	0.4	0.6	13.0
22	138	back	13.0	comp.	50.0	0.0	2.0	50.0	0.0	2.0	3.1	3.6	stable	26.0	0.4	0.6	13.0
14	34	back	90.0	comp.	90.0	n/a	1.0	n/a	0.0	2.0	10.7	12.3	stable	90.0	0.4	1.0	72.0
16	37	back	45.0	comp.	90.0	0.0	2.7	90.0	0.0	2.0	2.7	3.1	stable	121.5	0.4	1.0	97.0
22	136	back	13.0	comp.	50.0	0.0	2.0	50.0	0.0	2.0	2.4	2.8	stable	26.0	0.5	0.6	16.0
31	176	back	18.0	comp.	45.0	60.0	1.5	65.0	20.0	2.5	7.3	8.4	stable	27.0	0.5	0.9	29.0
31	177	back	18.0	comp.	45.0	60.0	1.5	65.0	20.0	2.5	9.9	11.4	stable	27.0	0.5	0.9	29.0
19	53	back	29.0	comp.	10.0	0.0	1.5	10.0	0.0	2.0	2.4	2.8	stable	43.5	0.5	0.2	8.8
22	135	back	13.0	comp.	50.0	0.0	2.0	50.0	0.0	2.0	2.1	2.4	stable	26.0	0.6	0.6	19.0
23	148	back	11.0	comp.	0.0	0.0	2.0	0.0	0.0	2.0	5.0	5.7	stable	22.0	0.7	0.2	5.9
15	36	hw	6.0	comp.	20.0	25.0	1.5	80.0	60.0	5.0	9.0	10.3	stable	9.0	0.9	0.3	13.0
5	7	hw	40.0	comp.	15.0	90.0	1.0	90.0	75.0	6.5	5.2	6.0	stable	40.0	1.0	1.0	260.0
19	59	wall	4.0	comp.	0.0	0.0	0.5	90.0	90.0	8.0	4.5	5.2	stable	2.0	1.0	0.3	5.2
22	133	hw	6.0	comp.	10.0	20.0	1.0	80.0	90.0	8.0	6.7	7.7	stable	6.0	1.0	0.2	9.4
32	184	hw	6.0	comp.	0.0	0.0	1.0	80.0	80.0	7.0	6.7	7.7	stable	6.0	1.0	0.3	12.0
22	140	hw	8.0	comp.	0.0	0.0	1.0	70.0	70.0	6.0	7.5	8.6	stable	8.0	1.0	0.3	15.0
22	142	hw	8.0	comp.	4.0	0.0	1.0	70.0	66.0	5.5	5.3	6.1	stable	8.0	1.0	0.2	9.2
22	143	hw	8.0	comp.	7.0	0.0	1.0	70.0	63.0	5.5	5.7	6.6	stable	8.0	1.0	0.2	9.2
28	157	fw	9.0	comp.	10.0	25.0	1.8	80.0	90.0	8.0	8.4	9.7	stable	16.2	1.0	0.2	26.0
12	20	back	11.0	comp.	20.0	0.0	1.5	20.0	0.0	2.0	1.8	2.1	stable	16.5	1.0	0.2	6.6

12	23	back	11.0	comp.	20.0	0.0	1.5	20.0	0.0	2.0	2.1	2.4	stable	16.5	1.0	0.2	6.6
20	61	hw	17.0	comp.	0.0	0.0	1.5	70.0	70.0	6.0	7.5	8.6	stable	25.5	1.0	0.3	45.0
20	62	fw	17.0	comp.	0.0	0.0	1.5	70.0	70.0	4.0	7.5	8.6	stable	25.5	1.0	0.3	30.0
31	173	back	18.0	comp.	35.0	60.0	1.5	65.0	30.0	2.8	7.7	8.9	stable	27.0	1.0	0.8	60.0
31	174	back	18.0	comp.	35.0	60.0	1.5	65.0	30.0	2.8	5.4	6.2	stable	27.0	1.0	0.8	60.0
27	152	back	15.0	comp.	10.0	0.0	2.0	10.0	0.0	2.0	6.7	7.7	stable	30.0	1.0	0.2	12.0
13	27	back	17.0	comp.	30.0	0.0	2.0	30.0	0.0	2.0	4.1	4.7	stable	34.0	1.0	0.2	14.0
19	58	wall	29.0	comp.	80.0	90.0	1.5	8.0	90.0	8.0	8.4	9.7	stable	43.5	1.0	1.0	352.0
1	1	hw	18.0	comp.	45.0	35.0	3.0	45.0	90.0	6.5	5.0	5.7	stable	54.0	1.0	0.7	228.0
21	120	hw	1.0	relax	0.0	0.0	0.3	60.0	60.0	5.0	1.0	1.1	stable	0.3	1.0	0.3	0.4
21	125	hw	1.0	relax	0.0	0.0	0.3	71.0	71.0	6.0	1.0	1.1	stable	0.3	1.0	0.3	0.5
21	90	hw	3.0	relax	0.0	0.0	0.3	52.0	52.0	4.0	3.0	3.4	stable	0.8	1.0	0.3	0.9
21	92	hw	3.0	relax	0.0	0.0	0.3	65.0	65.0	5.5	2.0	2.3	stable	0.8	1.0	0.3	1.2
21	111	hw	2.0	relax	0.0	0.0	0.5	72.0	72.0	6.0	3.0	3.4	stable	1.0	1.0	0.3	1.8
21	103	hw	6.0	relax	0.0	0.0	0.3	63.0	63.0	5.5	3.0	3.4	stable	1.5	1.0	0.3	2.5
21	66	hw	3.0	relax	0.0	0.0	0.8	82.0	82.0	7.0	3.0	3.4	stable	2.4	1.0	0.3	5.0
21	114	hw	3.0	relax	0.0	0.0	0.8	65.0	65.0	5.5	2.0	2.3	stable	2.4	1.0	0.3	4.0
21	100	hw	3.0	relax	0.0	0.0	1.0	60.0	60.0	5.0	3.0	3.4	stable	3.0	1.0	0.3	4.5
7	11	hw	5.0	relax	10.0	0.0	0.6	70.0	80.0	7.0	7.9	9.1	stable	3.0	1.0	0.2	4.2
22	132	hw	6.0	relax	10.0	20.0	1.0	80.0	90.0	8.0	5.6	6.4	stable	6.0	1.0	0.2	10.0
21*	64	hw	4.0	relax	0.0	0.0	1.5	65.0	65.0	6.0	6.0	6.9	stable	6.0	1.0	0.3	10.0
21	117	hw	4.0	relax	0.0	0.0	1.5	65.0	65.0	5.5	10.0	11.5	stable	6.0	1.0	0.3	10.0
6	8	hw	6.0	relax	30.0	30.0	1.5	60.0	90.0	5.0	8.5	9.8	stable	9.0	1.0	0.4	18.0
21	128	hw	12.0	relax	0.0	0.0	0.8	65.0	65.0	4.5	7.0	8.0	stable	9.6	1.0	0.3	13.0
13	28	wall	8.0	relax	0.0	10.0	1.5	90.0	90.0	2.0	7.6	8.7	stable	12.0	1.0	0.3	6.9
21	74	hw	8.0	relax	0.0	0.0	1.5	55.0	55.0	4.5	2.0	2.3	stable	12.0	1.0	0.3	16.0
21	75	hw	8.0	relax	0.0	0.0	1.5	55.0	55.0	4.5	11.0	12.6	stable	12.0	1.0	0.3	16.0
30	167	hw	9.0	relax	20.0	0.0	1.5	70.0	90.0	8.0	7.8	9.0	stable	13.5	1.0	0.2	22.0
21	88	hw	20.0	relax	0.0	0.0	0.8	90.0	90.0	8.0	4.0	4.6	stable	16.0	1.0	0.3	38.0
21	89	hw	20.0	relax	0.0	0.0	0.8	90.0	90.0	8.0	11.0	12.6	stable	16.0	1.0	0.3	38.0
21	99	hw	8.0	relax	0.0	0.0	2.0	65.0	65.0	5.5	3.0	3.4	stable	16.0	1.0	0.3	26.0
12	21	hw	11.0	relax	10.0	0.0	1.5	65.0	55.0	4.5	4.7	5.4	stable	16.5	1.0	0.2	15.0
12	22	hw	11.0	relax	10.0	0.0	1.5	65.0	55.0	4.5	8.8	10.1	stable	16.5	1.0	0.2	15.0
30	165	hw	14.0	relax	0.0	0.0	1.5	90.0	90.0	8.0	9.9	11.4	stable	21.0	1.0	0.2	33.0
21	85	hw	7.0	relax	0.0	0.0	3.0	65.0	65.0	5.5	4.0	4.6	stable	21.0	1.0	0.3	35.0
30	168	hw	15.0	relax	20.0	0.0	1.5	70.0	90.0	8.0	6.0	6.9	stable	22.5	1.0	0.2	36.0
32	182	hw	15.0	relax	0.0	0.0	1.5	90.0	90.0	8.0	4.9	5.6	stable	22.5	1.0	0.3	54.0

8	13	hw	15.0	relax	0.0	0.0	2.0	80.0	80.0	7.0	8.3	9.5	stable	30.0	1.0	0.2	42.0
11	18	hw	30.0	relax	50.0	0.0	1.0	40.0	90.0	8.0	8.8	10.1	stable	30.0	1.0	0.6	144.0
27	153	wall	15.0	relax	0.0	45.0	2.0	90.0	90.0	8.0	18.0	20.7	stable	30.0	1.0	0.5	120.0
21	106	hw	15.0	relax	0.0	0.0	2.0	70.0	70.0	6.0	10.0	11.5	stable	30.0	1.0	0.3	54.0
28	155	hw	16.0	relax	10.0	15.0	2.0	80.0	90.0	3.0	9.7	11.1	stable	32.0	1.0	0.2	19.0
13	29	wall	17.0	relax	10.0	10.0	2.0	80.0	90.0	3.0	7.6	8.7	stable	34.0	1.0	0.2	20.0
13	30	hw	17.0	relax	20.0	10.0	2.0	80.0	60.0	5.0	9.0	10.3	stable	34.0	1.0	0.2	34.0
16	46	hw	30.0	relax	0.0	0.0	1.3	90.0	90.0	8.0	13.1	15.1	stable	39.0	1.0	0.3	94.0
5	5	hw	40.0	relax	0.0	90.0	1.0	90.0	90.0	8.0	14.0	16.1	stable	40.0	1.0	1.0	320.0
5	6	hw	40.0	relax	0.0	90.0	1.0	90.0	90.0	8.0	11.0	12.6	stable	40.0	1.0	1.0	320.0
21	73	hw	16.0	relax	0.0	0.0	3.0	90.0	90.0	8.0	7.0	8.0	stable	48.0	1.0	0.3	115.0
21	76	hw	18.0	relax	0.0	0.0	3.0	60.0	60.0	5.0	5.0	5.7	stable	54.0	1.0	0.3	81.0
21	81	hw	18.0	relax	0.0	0.0	3.0	60.0	60.0	5.0	9.0	10.3	stable	54.0	1.0	0.3	81.0
21	84	hw	18.0	relax	0.0	0.0	3.0	55.0	55.0	4.5	10.0	11.5	stable	54.0	1.0	0.3	73.0
21	86	hw	20.0	relax	0.0	0.0	3.0	66.0	66.0	4.5	1.0	1.1	stable	60.0	1.0	0.3	81.0
14	31	hw	90.0	relax	90.0	n/a	1.0	n/a	90.0	8.0	16.6	19.1	stable	90.0	1.0	1.0	720.0
14	33	hw	90.0	relax	90.0	n/a	1.0	n/a	90.0	8.0	23.0	26.4	stable	90.0	1.0	1.0	720.0
33	189	hw		relax						8.0	7.0	8.0	stable	13.1	1.0	0.2	21.0
33	190	hw		relax						5.0	5.2	6.0	stable	7.2	1.0	0.2	7.2
33	192	hw		relax						6.0	6.1	7.0	stable	21.5	1.0	0.3	38.7
33	196	hw		relax						5.0	10.4	12.0	stable	8.3	1.0	0.3	12.5
34	198	wall		relax						8.0	13.1	15.1	stable	40.0	1.0	0.5	160.0
36	211	wall		relax						6.8	16.1	18.5	stable	85.0	1.0	0.5	289.0
36	222	fw		relax						6.8	21.3	24.5	stable	85.0	1.0	0.5	289.0

Table A.2 Summary of supported case histories database

Mine	Case #	Plane	RQD/Jn	Stress state	Crit.jt. dip diff.	Crit.jt. strk diff.	Block shape	Jr/Ja	Sliding Crit.jt. dip	Fall/b'kling S.pl-dip	HR	Assess.	A	B	C	Q'	N'
1	251	Back	25	Comp	20	0	Blocky	0.75	20	0	8.4	Cave	0.25	0.2	2	40	1.9
1	252	Back	25	Comp	20	0	Blocky	0.75	20	0	8.4	Cave	0.50	0.2	2	18.75	3.8
2	262	Back	14	Comp	40	0	Blocky	0.5	40	25	16	Cave	0.10	0.4	2.6	7	0.7
2	266	Back	6	Comp	22	0	Blocky	0.7	22	20	14.8	Cave	0.77	0.2	2.4	4.2	1.6
2	267	Back	4	Comp	66	0	Blocky	0.2	66	0	7.8	Cave	0.10	0.85	2	0.8	0.1
7	279	Back	4	Comp	20	0	Blocky	0.8	20	0	7.5	Cave	0.20	0.2	2	3.2	0.3
15	290	Back	6	Comp	0	0	Blocky	1.5	20	20	11.4	Cave	0.60	0.3	2.4	9	3.9
15	292	Back	6	Comp	0	0	Blocky	1.5	20	20	20	Cave	1.00	0.3	2.4	9	6.5
22	301	Back	9	Comp	10	0	Foliated	1.8	10	0	7.7	Cave	0.10	0.2	2	16.2	0.6
26	305	Back	2	Comp	20	0	Blocky	1	20	0	14	Cave	1.00	0.2	2	2	0.8
26	307	Back	1	Comp	20	0	Blocky	1	20	0	12.7	Cave	1.00	0.2	2	1	0.4
26	312	Back	5	Comp	20	0	Blocky	1	20	0	13.7	Cave	0.70	0.2	2	5	1.4
93	366	end		comp							10.5	cave	0.35	0.5	8	5.3	7.4
97	370	back		comp							6.7	cave	0.35	0.3	1	5.3	0.56
19	294	Wall	4	Relax	0	0	Blocky	0.5	90	90	19	Cave	1.00	0.3	8	2	4.8
92	365	hw		relax							11.9	cave	1.00	0.5	0.5	5.3	13.3
95	368	hw		relax							10.2	cave	1.00	0.5	5	5.3	13.3
57	341	Back	13.3	Comp				1		70	6.4	Caved	0.10	0.2	2	13.3	0.53
	25	back	13.3	comp							6.4	caved	0.10	0.2	2	13.3	0.53
33	319	HW	11.7	Relax				1		74	10	Caved	1.00	0.2	6	11.7	14
36	322	HW	6.7	Relax				0.38		80	19.1	Caved	1.00	0.3	7.5	2.5	5.6
38	324	HW	13.7	Relax				2		82	17.1	Caved	1.00	0.3	7.5	27.3	61.4
48	334	Back	2.5	Relax				0.38		35	11.2	Caved	1.00	0.3	3	0.5	0.45
49	335	Back	1.67	Relax				0.38	35		8.6	Caved	1.00	0.2	2	0.6	0.24
52	338	HW	15.8	Relax				1		62	12.4	Caved	1.00	0.2	5	15.8	15.8
82	357	HW	8.3	Relax				0.38		62	17	Caved	1.00	0.3	4.7	3.1	4.4
	1	hw	11.7	relax							10	caved	1.00	0.2	6	11.7	14
	4	hw	6.7	Relax							19.1	caved	1.00	0.3	7.5	2.5	5.6
	6	hw	13.7	relax							17.1	caved	1.00	0.3	7.5	27.3	61.4
	16	back	2.5	relax							11.2	caved	1.00	0.3	3	0.5	0.45
	17	back	1.67	relax							8.6	caved	1.00	0.2	2	0.6	0.24
	20	hw	15.8	relax							12.4	caved	1.00	0.2	5	15.8	15.8

	50	hw	8.3	relax							17	caved	1.01	0.3	4.7	3.1	4.4
10	285	Back	8	Comp	15	0	Blocky	0.75	15	0	6.3	Unstable	0.50	0.2	2	6	1.2
26	306	Back	5	Comp	20	0	Blocky	1	20	0	9.3	Unstable	1.00	0.2	2	5	2
30	317	Back	14	Comp	60	0	Blocky	1.5	60	0	8.6	Unstable	0.10	0.8	2	21	3.4
51	337	Back	13.3	Comp				1		70	5.2	Unstable	0.10	0.3	2	13.3	0.8
66	348	Back	4.7	Comp				1.79		90	5.1	Unstable	0.10	0.2	2	8.3	0.33
	19	back	13.3	comp							5.2	Unstable	0.10	0.3	2	13.3	0.8
	34	back	4.7	comp							5.1	Unstable	0.10	0.2	2	8.3	0.33
39	325	HW	6.7	Relax				0.38		85	10.9	Unstable	1.00	0.2	7.5	2.5	3.8
40	326	HW	6.7	Relax				0.38		84	12.7	Unstable	1.00	0.3	7.5	2.5	5.6
	7	hw	6.7	relax							10.9	Unstable	1.01	0.2	7.5	2.5	3.8
	8	hw	6.7	relax							12.7	Unstable	1.00	0.3	7.5	2.5	5.6
1	253	Back	25	Comp	20	0	Blocky	0.75	20	0	5.3	Stable	0.25	0.2	2	18.75	1.9
1	254	Back	18	Comp	20	0	Blocky	3	20	0	6.4	Stable	0.10	0.2	2	54	2.2
1	256	Back	18	Comp	20	0	Blocky	3	20	0	5.9	Stable	0.10	0.2	2	54	2.2
1	257	Back	18	Comp	20	0	Blocky	3	20	0	6.7	Stable	0.10	0.2	2	54	2.2
1	258	Back	18	Comp	20	0	Blocky	3	20	0	7.1	Stable	0.10	0.2	2	54	2.2
1	259	Back	18	Comp	20	0	Blocky	3	20	0	4.6	Stable	0.10	0.2	2	54	2.2
1	260	Back	18	Comp	20	0	Blocky	3	20	0	5	Stable	0.10	0.2	2	54	2.2
2	261	Back	14	Comp	40	0	Blocky	0.5	40	25	13.9	Stable	0.10	0.4	2.6	7	0.7
2	263	Back	6	Comp	22	0	Blocky	0.7	22	20	7.3	Stable	0.36	0.2	2.4	4.2	0.7
2	264	Back	4	Comp	42	0	Blocky	0.2	42	0	6	Stable	0.10	0.4	2	0.8	0.1
2	265	Back	6	Comp	22	0	Blocky	0.7	22	20	8	Stable	0.35	0.2	2.4	4.2	0.7
3	269	Back	6	Comp	24	0	Blocky	1	24	0	4.4	Stable	0.20	0.2	2	6	0.5
3	270	Back	6	Comp	24	0	Blocky	1	24	0	5.3	Stable	0.10	0.2	2	6	0.2
4	271	Back	7	Comp	45	0	Foliated	1.5	45	0	5.3	Stable	0.10	0.5	2	10.5	1.1
5	272	Back	40	Comp	90	0	Blocky	1	90	0	6.2	Stable	0.10	1	2	40	8
6	273	Back	6	Comp	20	0	Blocky	1.5	20	0	2.6	Stable	0.10	0.2	2	9	0.4
6	274	Back	6	Comp	20	0	Blocky	1.5	20	0	4.2	Stable	0.10	0.2	2	9	0.4
6	275	End	6	Comp	30	30	Foliated	1.5	30	90	4.7	Stable	0.10	0.4	5	9	1.8
6	276	End	6	Comp	5	0	Foliated	1.5	5	55	6.1	Stable	0.23	0.25	4.6	9	2.4
6	277	Back	6	Comp	20	0	Blocky	1.5	20	0	5.2	Stable	0.10	0.2	2	9	0.4
7	278	Back	4	Comp	20	0	Blocky	0.8	20	0	2.5	Stable	0.10	0.2	2	3.2	0.1
8	280	Back	15	Comp	20	0	Blocky	2	20	0	2.7	Stable	0.60	0.2	2	30	7.2
8	281	Back	15	Comp	20	0	Blocky	2	20	0	3.6	Stable	0.80	0.2	2	30	9.6
9	282	Back	25	Comp	70	0	Blocky	0.25	70	0	4.1	Stable	0.10	0.9	2	6.25	1.1
13	289	Back	17	Comp	20	0	Blocky	2	20	0	6.2	Stable	1.00	0.2	2	34	14

15	291	Back	6	Comp	0	0	Blocky	1.5	20	20	8	Stable	1.00	0.3	2.4	9	6.5
15	293	Back	6	Comp	0	0	Blocky	1.5	20	20	9.2	Stable	1.00	0.3	2.4	9	6.5
19	295	Back	29	Comp	0	0	Blocky	1.5	0	0	3.7	Stable	0.20	0.3	2	43.5	5.2
20	296	Back	17	Comp	20	0	Foliated	1.5	20	0	5.3	Stable	0.10	0.2	2	25.5	1
20	297	Back	25	Comp	20	0	Foliated	2	20	0	9	Stable	0.30	0.2	2	50	6
20	298	Back	25	Comp	20	0	Foliated	2	20	0	3.9	Stable	0.10	0.2	2	50	2
20	299	Back	17	Comp	70	0	Foliated	1.5	70	0	8	Stable	0.30	0.9	2	25.5	11
22	300	Back	9	Comp	10	0	Foliated	1.8	10	0	4.7	Stable	0.10	0.2	2	16.2	0.6
26	302	Back	2	Comp	20	0	Blocky	1	20	0	5.6	Stable	1.00	0.2	2	2	0.8
26	303	Back	10	Comp	20	0	Blocky	1	20	0	4.3	Stable	1.00	0.2	2	10	4
26	304	Back	5	Comp	70	0	Blocky	1	70	0	2.7	Stable	1.00	0.9	2	5	9
26	308	Back	8	Comp	20	0	Blocky	1	20	0	14.6	Stable	1.00	0.2	2	8	3.2
26	309	Back	15	Comp	20	0	Blocky	1	20	0	7.1	Stable	0.70	0.2	2	15	4.2
26	310	Back	25	Comp	20	0	Blocky	1	20	0	8	Stable	0.70	0.2	2	25	7
26	311	Back	20	Comp	20	0	Blocky	1	20	0	7.4	Stable	0.70	0.2	2	20	5.6
26	313	Back	10	Comp	20	0	Blocky	1	20	0	10	Stable	0.70	0.2	2	10	2.8
26	314	Back	20	Comp	20	0	Blocky	1	20	0	5.3	Stable	0.50	0.2	2	20	4
26	315	Back	20	Comp	20	0	Blocky	1	20	0	6.9	Stable	0.50	0.2	2	20	4
32	318	Back	13	Comp	70	0	Blocky	1.8	70	0	5.9	Stable	0.10	0.9	2	23.4	4.2
42	328	Back	12.5	Comp				1.5		85	5	Stable	0.20	0.3	2	18.8	2.3
44	330	Back	12.5	Comp				1.5		0	1.6	Stable	0.10	0.2	2	18.8	0.75
50	336	Back	13.3	Comp				1		68	4.2	Stable	0.10	0.3	2	13.3	0.8
55	340	Back	13.3	Comp				1		69	5.2	Stable	0.10	0.2	2	13.3	0.53
61	344	Back	2.5	Comp				0.38		70	2.1	Stable	0.10	0.8	2	0.9	0.14
62	345	Back	6.6	Comp				1.77		60	2	Stable	0.10	0.2	2	11.6	0.46
65	347	Back	8.9	Comp				1		0	1.7	Stable	0.10	0.4	2	8.9	0.71
69	350	Back	5.8	Comp				2.1		54	2.3	Stable	0.10	0.2	2	12.3	0.49
75	351	Back	6.25	Comp				1.77		56	2.4	Stable	0.10	0.2	2	11.1	0.44
77	352	Back	9.8	Comp				2.67		33	3.6	Stable	0.10	0.3	2	26.1	1.6
78	353	Back	10.8	Comp				0.5		68	5	Stable	0.10	0.2	2	5.4	0.22
79	354	Back	10.8	Comp				0.5		75	5.1	Stable	0.10	0.2	2	5.4	0.22
80	355	Back	16.7	Comp				1.5		75	5	Stable	0.40	0.2	2	25	4
84	358	Back	15.5	Comp				1		60	5.2	Stable	0.10	0.2	2	15.5	0.62
85	359	Back	10.8	Comp				0.5		60	3.8	Stable	0.10	0.2	2	5.4	0.22
87	361	Back	16.7	Comp				1.5		60	6.2	Stable	0.20	0.2	2	25	2
89	363	Back	10.8	Comp				0.5		70	5.4	Stable	0.10	0.2	2	5.4	0.22
91	364	Back	12.9	Comp				2.1		20	5.6	Stable	0.40	0.3	2.2	25	6.6

94	367	back		comp							6	stable	0.35	0.3	1	5.3	0.56
96	369	end		comp							9.9	stable	0.35	0.5	8	5.3	7.4
99	372	end		comp							9.9	stable	0.35	0.5	8	5.3	7.4
100	373	back		comp							5.7	stable	0.35	0.3	1	5.3	0.56
101	374	back		comp							6	stable	0.25	0.3	1	7.8	0.59
103	376	end		comp							8.6	stable	0.25	0.5	8	7.8	7.8
104	377	end		comp							8.2	stable	0.17	0.5	8	7.8	5.3
105	378	back		comp							4.6	stable	0.25	0.3	1	7.8	0.59
107	380	end		comp							7.1	stable	0.25	0.5	8	7.8	7.8
108	381	back		comp							8.9	stable	0.17	0.3	1	7.8	0.4
	10	back	12.5	comp							5	stable	0.20	0.3	2	18.8	2.3
	12	back	12.5	comp							1.6	stable	0.10	0.2	2	18.8	0.75
	18	back	13.3	comp							4.2	stable	0.10	0.3	2	13.3	0.8
	23	back	13.3	comp							5.2	stable	0.10	0.2	2	13.3	0.53
	29	back	2.5	comp							2.1	stable	0.10	0.8	2	0.9	0.14
	30	back	6.6	comp							2	stable	0.10	0.2	2	11.6	0.46
	33	back	8.9	comp							1.7	stable	0.10	0.4	2	8.9	0.71
	37	back	5.8	comp							2.3	stable	0.10	0.2	2	12.3	0.49
	43	back	6.25	comp							2.4	stable	0.10	0.2	2	11.1	0.44
	45	back	9.8	comp							3.6	stable	0.10	0.3	2	26.1	1.6
	46	back	10.8	comp							5	stable	0.10	0.2	2	5.4	0.22
	47	back	10.8	comp							5.1	stable	0.10	0.2	2	5.4	0.22
	48	back	16.7	comp							5	stable	0.40	0.2	2	25	4
	52	back	15.5	comp							5.2	stable	0.10	0.2	2	15.5	0.62
	53	back	10.8	comp							3.8	stable	0.10	0.2	2	5.4	0.22
	55	back	16.7	comp							6.2	stable	0.20	0.2	2	25	2
	57	back	10.8	comp							5.4	stable	0.10	0.2	2	5.4	0.22
	59	back	12.9	comp							5.6	stable	0.40	0.3	2.2	25	6.6
1	255	HW	25	Relax	20	0	Foliated	0.75	20	90	5	Stable	1.00	0.2	8	18.75	30
3	268	Wall	6	Relax	15	0	Blocky	1	15	90	8.9	Stable	1.00	0.2	3.5	6	4.2
9	284	HW	9	Relax	0	0	Blocky	0.5	0	70	7.5	Stable	0.45	0.3	6	4.5	3.6
10	286	HW	8	Relax	0	0	Foliated	0.75	70	70	10	Stable	1.00	0.3	6	6	11
11	287	HW	30	Relax	0	0	Foliated	1	90	90	19.7	Stable	1.00	0.3	8	30	72
28	316	HW	9	Relax	15	0	Blocky	1.8	80	65	8.4	Stable	1.00	0.2	5.5	16.2	18
34	320	Back	11.7	Relax				1		0	2.3	Stable	1.00	0.2	2	11.7	4.7
35	321	HW	6.7	Relax				0.38		80	11.7	Stable	1.00	0.3	7.5	2.5	5.6
37	323	Back	11.7	Relax				1		76	2.6	Stable	1.00	0.2	2	11.7	4.7

41	327	HW	11.8	Relax	2	87	13.2	Stable	1.00	0.3	8	23.7	56.9
43	329	HW	15	Relax	2	85	10.8	Stable	1.00	0.3	7.5	30	67.5
45	331	Back	11.7	Relax	1	84	3.6	Stable	1.00	0.2	2	11.7	4.7
46	332	Back	1.67	Relax	0.38	15	4.3	Stable	1.00	0.4	2	0.6	0.48
47	333	Back	2.5	Relax	0.38	35	7.6	Stable	1.00	0.3	3	0.5	0.45
53	339	HW	15.8	Relax	1	72	10.8	Stable	1.00	0.3	6	15.8	28.4
58	342	back	15.8	Relax	1	79	11.5	Stable	1.00	0.3	7	15.8	33.2
59	343	HW	15.8	Relax	1	74	10.7	Stable	1.00	0.3	6.5	15.8	30.8
64	346	HW	6.9	Relax	1.5	83	4.9	Stable	1.00	0.2	5	10.4	10.4
68	349	Back	11.1	Relax	2.63	0	1.8	Stable	1.00	0.5	2	29.2	29.2
81	356	HW	13.1	Relax	0.75	62	15.5	Stable	1.00	0.3	4.7	9.9	14
86	360	HW	8.3	Relax	0.38	60	7.9	Stable	1.00	0.3	5	3.1	4.7
88	362	HW	8.3	Relax	0.38	60	10.9	Stable	1.00	0.3	5	3.1	4.7
98	371	hw		relax			9.2	stable	1.00	0.5	5	5.3	13.3
102	375	hw		relax			7.3	stable	1.00	0.5	5	6.8	17.9
106	379	hw		relax			5.9	stable	1.00	0.5	5	6.8	17
109	382	hw		relax			9.5	stable	1.00	0.5	5	6.8	17
	2	back	11.7	relax			2.3	stable	1.00	0.2	2	11.7	4.7
	3	hw	6.7	relax			11.7	stable	1.00	0.3	7.5	2.5	5.6
89,93	5	back	11.7	relax			2.6	stable	1.00	0.2	2	11.7	4.7
	9	hw	11.8	relax			13.2	stable	1.00	0.3	8	23.7	56.9
	11	hw	15	relax			10.8	stable	1.00	0.3	7.5	30	67.5
	13	back	11.7	relax			3.6	stable	1.00	0.2	2	11.7	4.7
	14	back	1.67	relax			4.3	stable	1.00	0.4	2	0.6	0.48
	15	back	2.5	relax			7.6	stable	1.00	0.3	3	0.5	0.45
	21	hw	15.8	relax			10.8	stable	1.00	0.3	6	15.8	28.4
	26	hw	15.8	relax			11.5	stable	1.00	0.3	7	15.8	33.2
	27	hw	15.8	relax			10.7	stable	1.00	0.3	6.5	15.8	30.8
	32	hw	6.9	relax			4.9	stable	1.00	0.2	5	10.4	10.4
	36	back	11.1	relax			1.8	stable	1.00	0.5	2	29.2	29.2
	49	hw	13.1	relax			15.5	stable	1.00	0.3	4.7	9.9	14
	54	hw	8.3	relax			7.9	stable	1.01	0.3	5	3.1	4.7
	56	hw	8.3	relax			10.9	stable	1.01	0.3	5	3.1	4.7

A.4 Verification of the bivariate normality assumption

Two procedures are used to verify the bivariate normal distribution assumption. Quantile plots are special plots applicable to both univariate and bivariate distributions to assess normality. For univariate normality the quantile plot is a plot of sample values against their respective quantiles. For normality the plot has an "S" shape.

Bivariate normality is justified when quantiles of one variable plotted against quantiles of the second variable form a straight line. Quantile - quantile plots for the logarithmic (base 10) transformed variables for the stable, unstable and caving classes are made with SYSTAT (Wilkinson, 1990a,b), a statistical package. The plots are shown in Figure A.1 to Figure A.6 for the stable, unstable and caving classes respectively. The plots for all three classes approximate straight-lines, and the normality assumption is justified.

A second procedure typically for investigating multivariate normality is the chi-square plot. When the number of observations n, and the number of variables p is such that n - p is greater than 25, each of the squared distances d_j^2 defined in Equation A.28, behave as a chi-square variable. A plot of the ordered distances versus chi-square should approximate a straight line for bivariate normality. Points deviating from the straight line are outliers, and normally merit further investigation.

$$d_i^2 = \left(\mathbf{X}_i - \overline{\mathbf{X}}\right)^T \mathbf{S}^{-1} \left(\mathbf{X}_i - \overline{\mathbf{X}}\right) \qquad \text{A.28}$$

Where i = 1, 2, 3, etc.

Chi-square plots for the stable, unstable, and caving data groups are presented in Figure A.4 to Figure A.6, respectively.

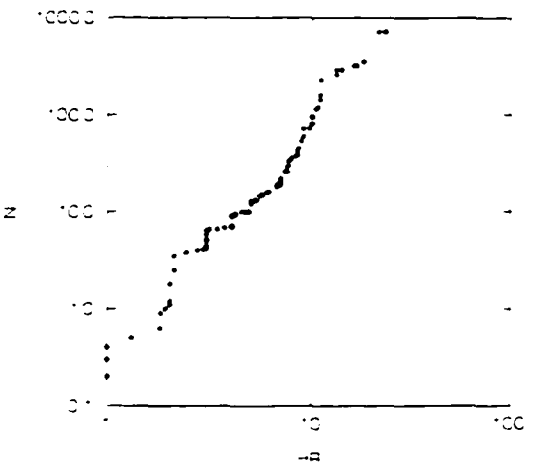


Figure A.1 Quantile-quantile plot for the stable class in the calibration database

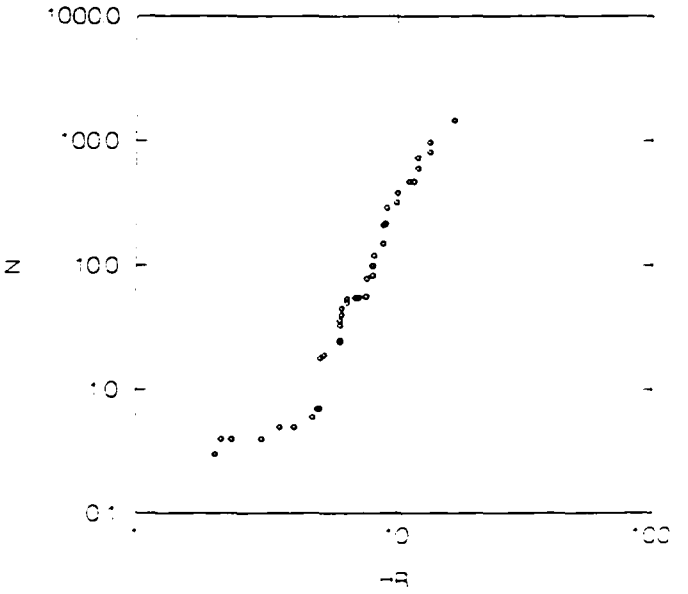


Figure A.2 Quantile-quantile plot for the unstable class in the calibration database

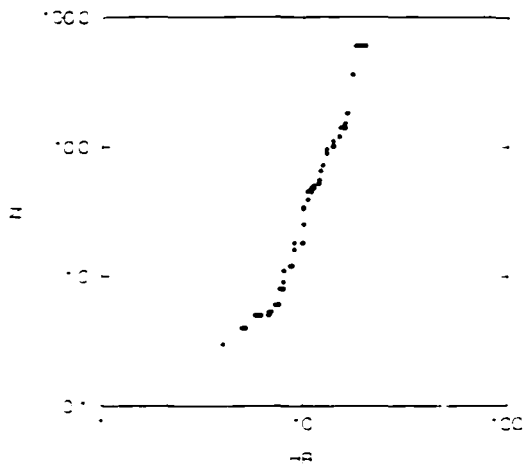


Figure A.3 Quantile-quantile plot for the caving class in the calibration database

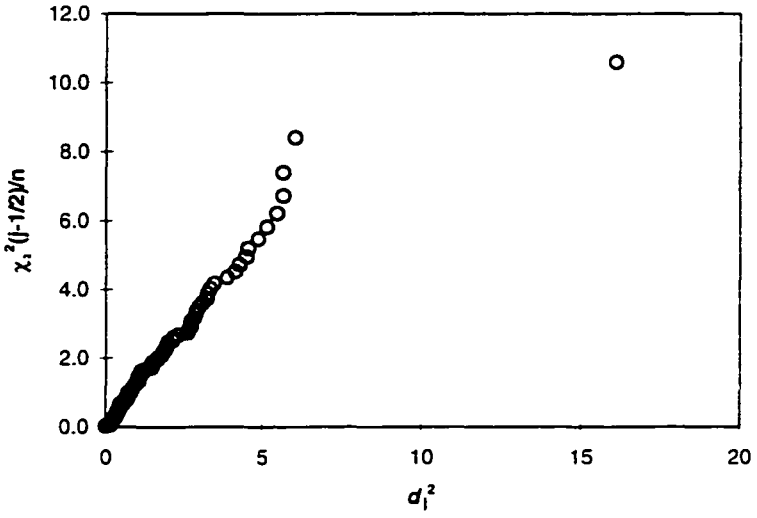


Figure A.4 Chi-square plot for the stable class of data

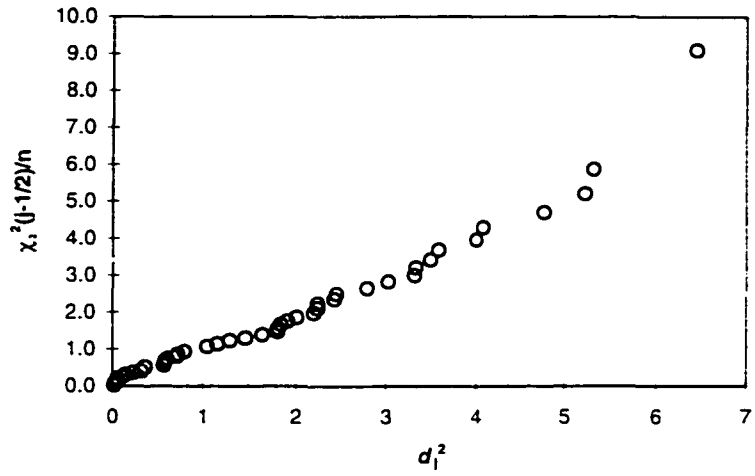


Figure A.5 Chi-square plot for the unstable class of data

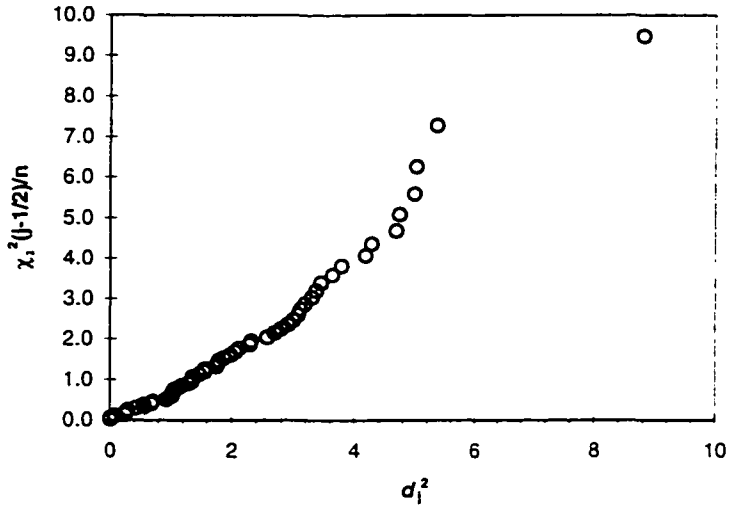


Figure A.6 Chi-square plot for the caving class of data

APPENDIX B

OVERBREAK AND FAULT FACTOR

B.1 Influence of Fault Shear Strength on Fault Effect on Stope Stability

B.1.1 Fault friction angle is 15° - Shear strength (i)

Model out puts for strength effects on the influence of faults on stope stability for a fault with friction angle of 15°.

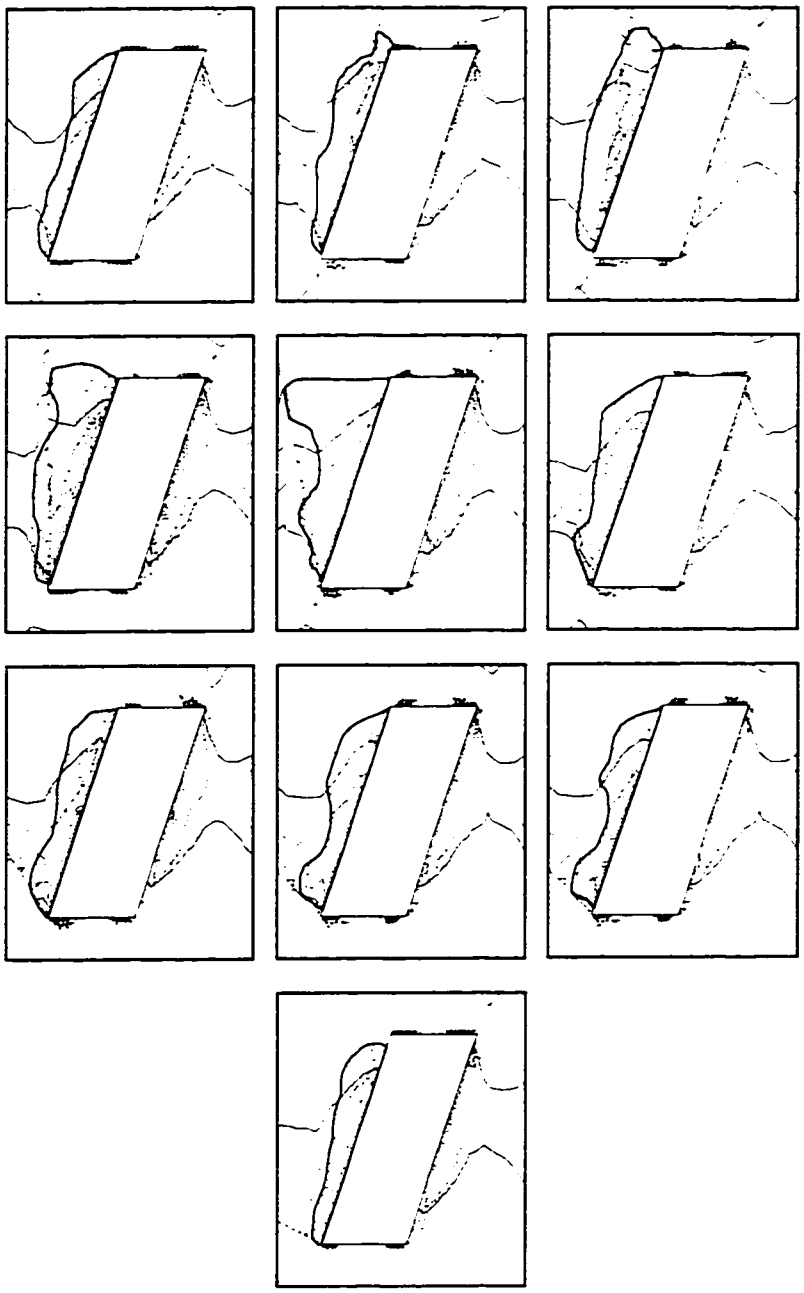


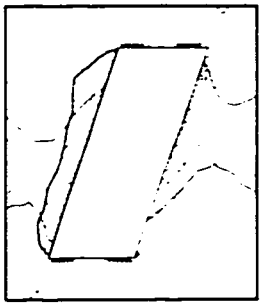
Figure B.1 Effect of fault with friction angle 15° on stope stability: Stress ratio K=2.1, Stope aspect ratio A_r=0.4, fault friction angle ϕ=15°, stope dip α=72°

B.1.2 Fault friction is 20° - Shear strength (ii)

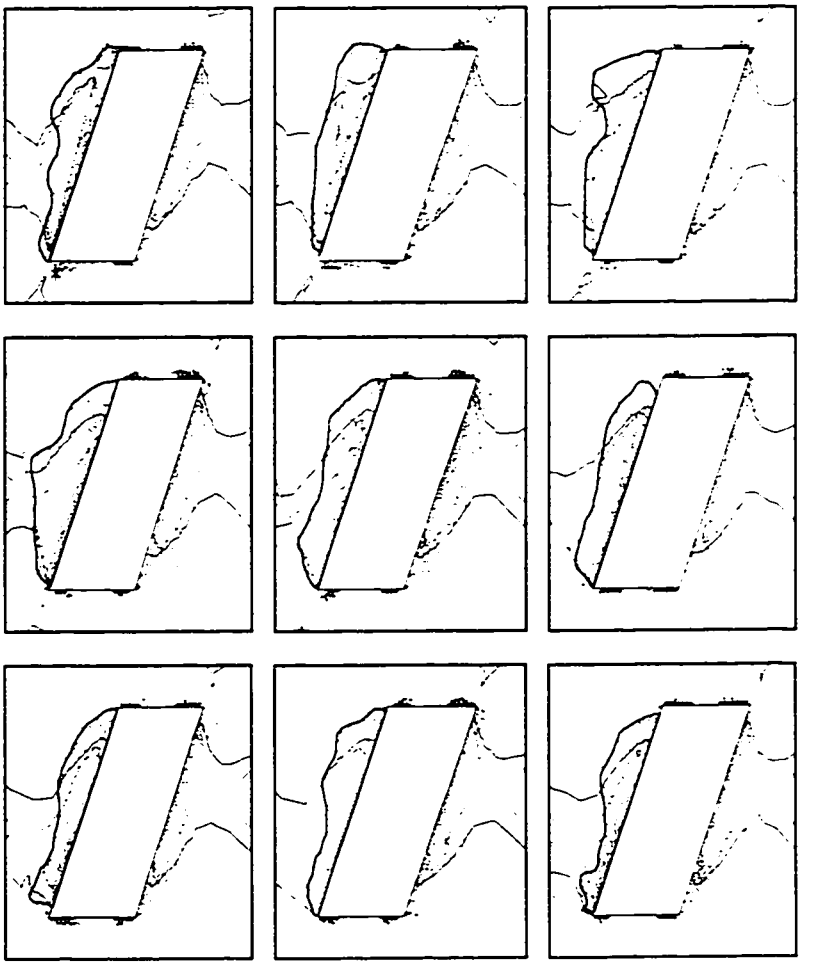
See Figure 7.10 in main text for model outputs for a fault with friction angle of 20°.

B.1.3 Fault friction is 30° - Shear strength (iii)

Model outputs for a fault with a friction angle of 30°.



(a) No fault



(h) Fault at included angle 60° (i) Fault at included angle 70° (j) Fault at included angle 80°

Figure B.2 Effect of fault with friction angle 30° on stope stability: Stress ratio K=1.8, Stope aspect ratio A_r=0.4, fault friction angle ϕ=30°, stope dip α=72°

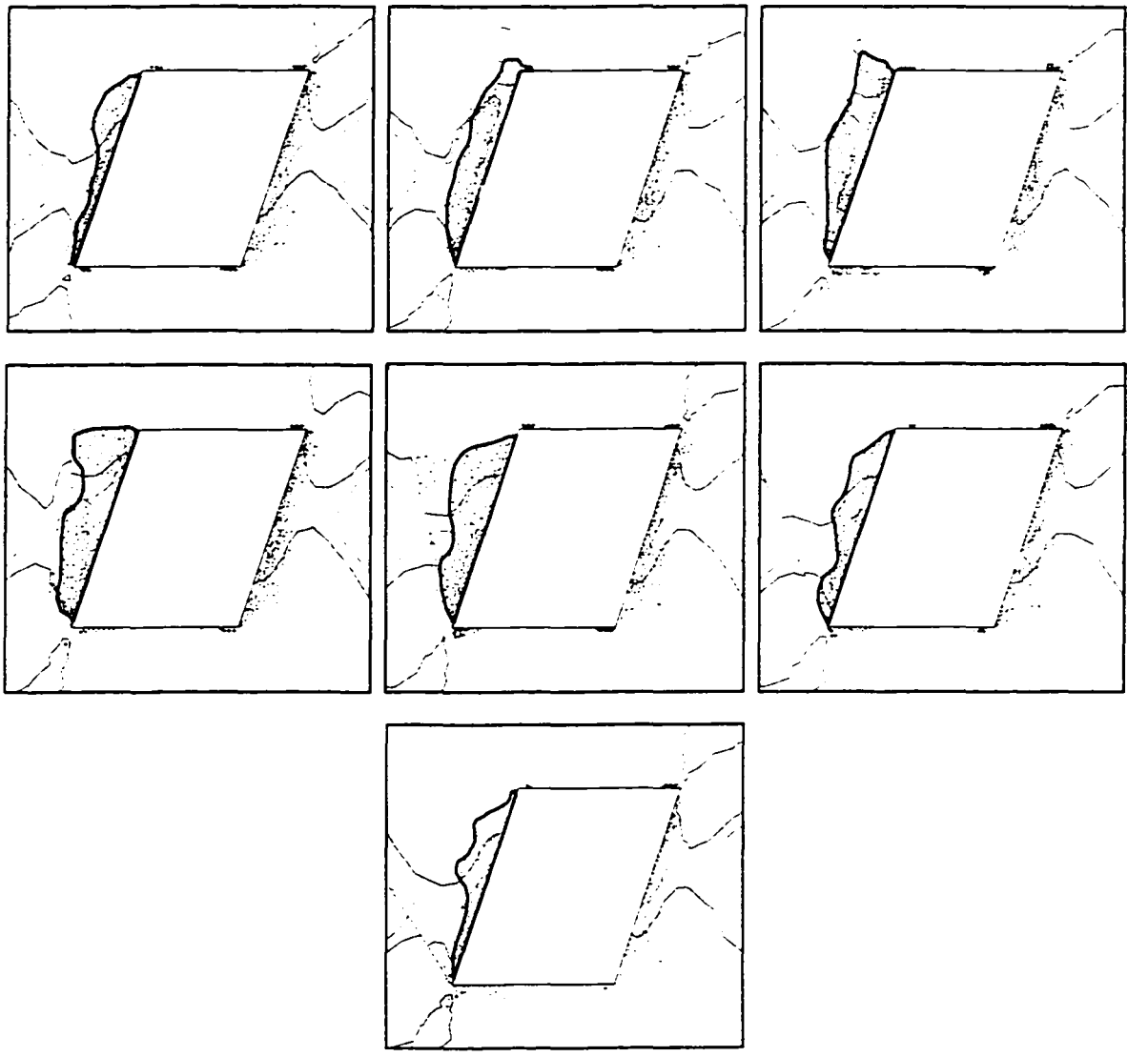
B.2 Influence of stope aspect ratio on fault effect on stope stability

B.2.1 Effect of A_r = 0.4

The modelling results for this stope aspect ratio are given in Figure B.2 in the main text

B.2.2 Effect of A_r = 0.8

Figure B.3 pictorially shows the effect of a fault on a stope with an aspect ratio A_r of 0.8.



(f) Fault at included angle 50°

Figure B.3 Effect of stope aspect ratio Ar =0.8 on the influence of faults on stope stability: Stress ratio K=2.1, stope aspect ratio A_r=0.8, fault friction angle ϕ=20°; stope dip α=72°

B.2.3 Effect of $A_r = 1.5$

Graphical model results are given in Figure B.3 below:

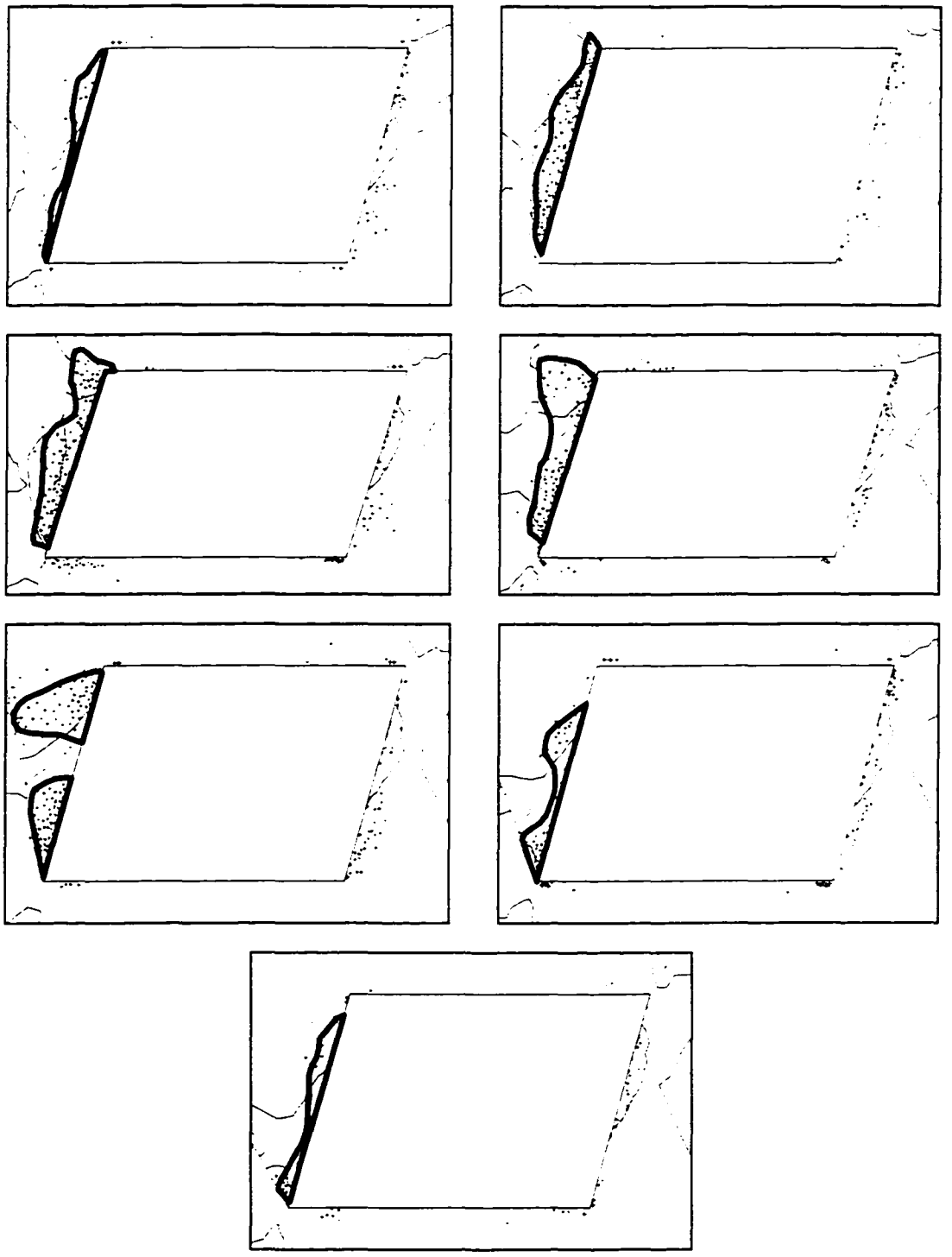
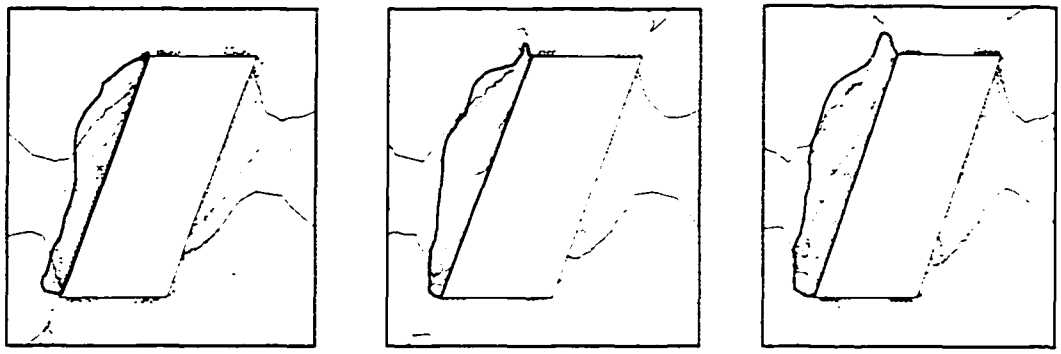
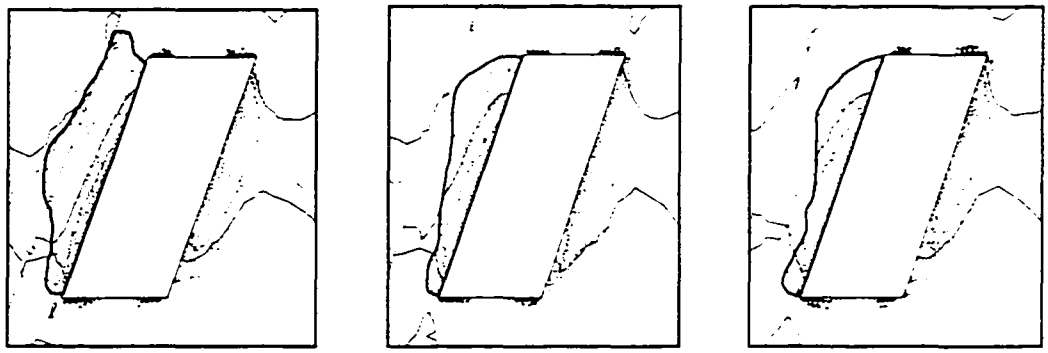


Figure B.4 Effect of stope aspect ratio $Ar = 1.5$ on the influence of faults on stope stability: Stress ratio K=2.1, stope aspect ratio A_r=1.5, fault friction ϕ=20°; stope dip α=72°

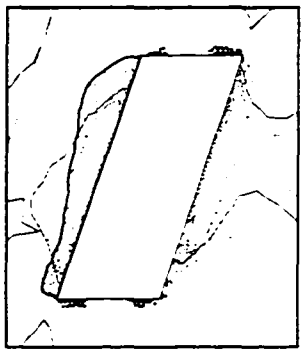
Figure B.5 shows the modelling results in graphic form.



(a) Fault distance to stope = 1m (b) Fault distance to stope = 3m (c) Fault distance to stope = 6m



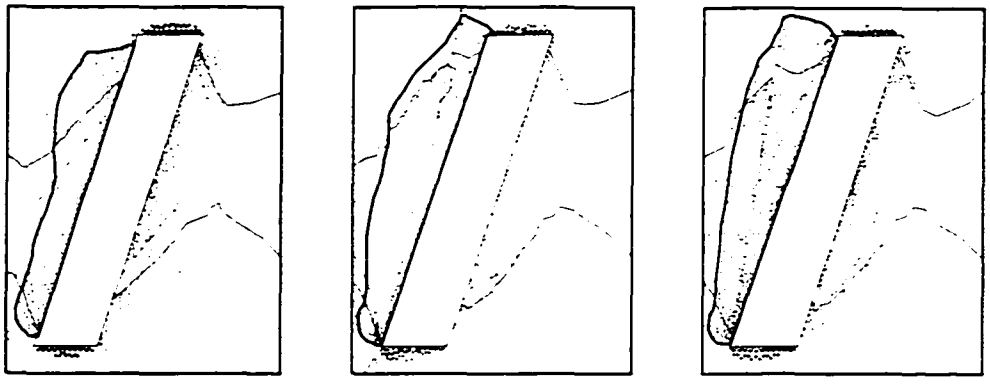
(d) Fault distance to stope = 10m (e) Fault distance to stope = 15m (g) Fault distance to stope = 20m



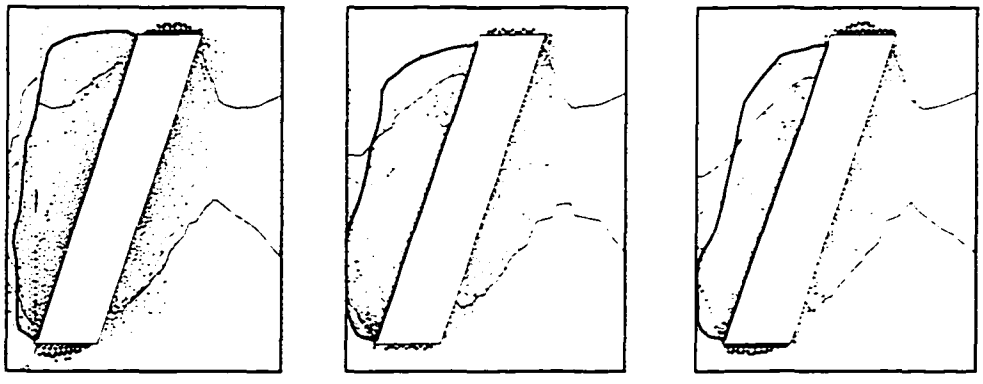
(h) Fault distance from stope surface = 25m

Figure B.5 Effect of fault distance to stope on the influence of the fault on stope stability: Stress ratio K=2.1, stope aspect ratio A_r=0.4, fault friction angle ϕ=20°; stope dip α=72°

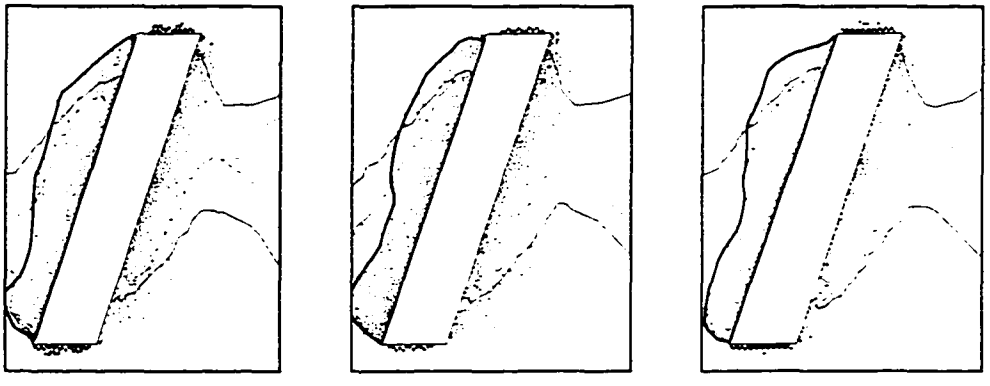
B.2.4 Effect of Ar=0.2



(a) No fault (b) Included angle 5° (c) Included angle 10°



(d) Included angle 20° (e) Included angle 30° (f) Included angle 40°



(g) Included angle 50° (h) Included angle 60° (i) Included angle 70°

Figure B.6 Influence of stope aspect ratio Ar on fault effect on stope stability: K=2.1, fault friction angle ϕ=20°, stope dip α=72°

B.3 Analytical procedures for Fault and Stope Geometry Determination

To determine the included angles between planes and the distance between planes, the equations of the two planes must be known. Various methods are given below for the determination of the equations of given stope and discrete discontinuity surfaces depending on the data available.

B.3.1 Method 1: Using three coordinates on the plane

Many mining companies now use DataMine, Vulcan and AutoCAD for grade control stope design and other mine planning procedures. Wire-frame models in these programs represent the planned stope geometry in three-dimensional space. The coordinates defining the stope model can be used to determine the geometry of the stope surfaces.

The general form of the equation of a plane is:

$$ax + by + cz + k = 0 \qquad \text{B.1}$$

Where a, b, c, and k are constants.

Three points on a plane can be used to uniquely define the plane. Three points (O, A, and B) on the stope wall are selected to determine the equation of a plane representing the wall. The point O is taken as the average between two corners coordinates while A and B are the two other coordinates (Figure B.7). From these three known points on the plane, the constants a, b, c, and k in Equation i can be determined.

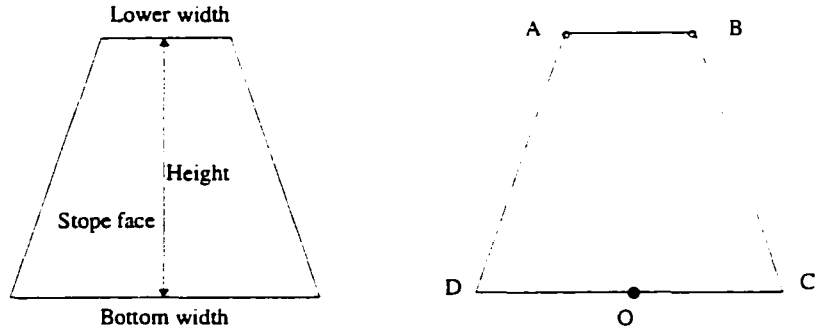


Figure B.7 Plane representing stope face showing geometry (left) and three points (right) for determination of stope plane equation

The equation of a plane passing through three points A = (x_1, y_1, z_1), B = (x_2, y_2, z_2), and O = (x_3, y_3, z_3) is given by:

$$\begin{vmatrix} y_2 - y_1 & z_2 - z_1 \\ y_3 - y_1 & z_3 - z_1 \end{vmatrix}(x - x_1) + \begin{vmatrix} z_2 - z_1 & x_2 - x_1 \\ z_3 - z_1 & x_3 - x_1 \end{vmatrix}(y - y_1) + \begin{vmatrix} x_2 - x_1 & y_2 - y_1 \\ x_3 - x_1 & y_3 - y_1 \end{vmatrix}(z - z_1) = 0 \qquad \text{B.2}$$

Where

$$a = \begin{vmatrix} y_2 - y_1 & z_2 - z_1 \\ y_3 - y_1 & z_3 - z_1 \end{vmatrix} = (y_2 - y_1)(z_3 - z_1) - (z_2 - z_1)(y_3 - y_1) \quad \text{B.3}$$

$$b = \begin{vmatrix} z_2 - z_1 & x_2 - x_1 \\ z_3 - z_1 & x_3 - x_1 \end{vmatrix} = (z_2 - z_1)(x_3 - x_1) - (x_2 - x_1)(z_3 - z_1)$$

$$c = \begin{vmatrix} x_2 - x_1 & y_2 - y_1 \\ x_3 - x_1 & y_3 - y_1 \end{vmatrix} (x_2 - x_1)(y_3 - y_1) - (y_2 - y_1)(x_3 - x_1)$$

And

$$k = ax_1 + by_1 + cz_1 \quad \text{B.4}$$

B.3.2 Method 2: When dip and dip direction of the plane are known

The orientation of a plane is defined in terms of the normal vector to the plane. Figure B.8 shows the direction cosines of the normal to a plane.

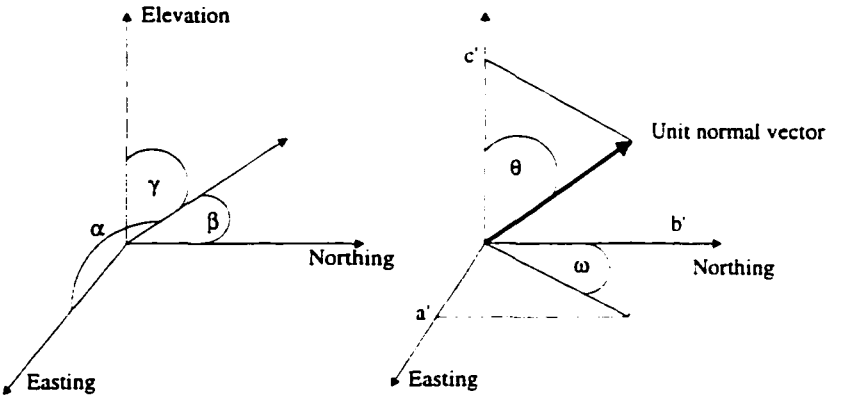


Figure B.8 Normal vector to plane showing direction cosines (left) and dip and dip direction of a plane (right)

These direction cosines can be expressed in the form:

$$\cos\alpha = \frac{a}{\sqrt{a^2 + b^2 + c^2}} = a' \quad \text{B.5}$$

$$\cos\beta = \frac{b}{\sqrt{a^2 + b^2 + c^2}} = b'$$

$$\cos\gamma = \frac{c}{\sqrt{a^2 + b^2 + c}} = c'$$

Where a',b' and c' are as defined in Equation B.3

Given the direction cosines it is easy to calculate the dip and dip direction of the plane or conversely determine the direction cosines from known values of dip and dip direction. This method is particularly useful in determining the equation of a fault or joint, where the dip and dip direction can be obtained from geological maps or in the field. The coordinate of one point on the fault plane is also needed to fully define the equation of the plane. In Figure B.8, θ and ψ are the dip and dip direction of a fault respectively, shown relative to the unit vector normal to the fault. The right-hand coordinate system used in Figure B.8 is based on x = easting, y = northing, and z = elevation. The parameters defining the equation of the plane representing a fault or other planar features are then determined from the following equations:

$$\sin\theta \sin\psi = \frac{a}{\sqrt{a^2 + b^2 + c^2}} = a' \qquad \text{B.6}$$

$$\cos\psi \sin\theta = \frac{b}{\sqrt{a^2 + b^2 + c^2}} = b'$$

$$\cos\theta = \frac{c}{\sqrt{a^2 + b^2 + c^2}} = c'$$

$$ax_f + by_f + cz_f = \frac{k}{\sqrt{a^2 + b^2 + c^2}} = k'$$

Where, for example, (x_f, y_f, z_f) are known coordinates on the fault plane. Therefore, the dip and dip direction of the plane are:

$$dip = \cos^{-1}\left(\frac{c}{\sqrt{a^2 + b^2 + c^2}}\right) = \cos^{-1} c' \qquad \text{B.7}$$

And

$$dip\ direction = \tan^{-1}\left(\frac{a}{b}\right) = \tan^{-1}\left(\frac{a'}{b'}\right) \quad \text{if} \quad a \geq 0 \quad \text{and} \quad b \geq 0 \qquad \text{B.8}$$

$$dip\ direction = 90 + \tan^{-1}\left(\frac{a}{b}\right) = 90 + \tan^{-1}\left(\frac{a'}{b'}\right) \quad \text{if} \quad a \geq 0 \quad \text{and} \quad b < 0$$

$$dip\ direction = 180 + \tan^{-1}\left(\frac{a}{b}\right) = 180 + \tan^{-1}\left(\frac{a'}{b'}\right) \quad \text{if} \quad a < 0 \quad \text{and} \quad b < 0$$

$$dip\ direction = 360 - \tan^{-1}\left(\frac{a}{b}\right) = 360 - \tan^{-1}\left(\frac{a'}{b'}\right) \quad \text{if} \quad a < 0 \quad \text{and} \quad b \geq 0$$

The convention for dip direction is that positive angles are measured clockwise from north. Note that the direction cosine between the normal vector and the positive z-direction (elevation) is equivalent to the dip of the plane as measured downwards from a horizontal plane.

B.3.3 Method 3: Cross product of two vectors in the plane

This method is similar to method one except vectors are used. If **OA** and **OB** are vectors in the plane with local coordinates in the plane zeroed at point O, then the vector to the plane is given by the cross product of these two vectors (Figure B.9).

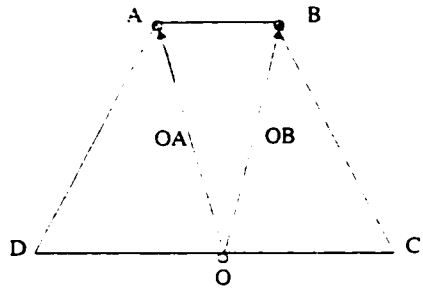


Figure B.9 Two vectors on a stope plane for defining normal vector to plane

The normal vector or cross product is given by:

$$\mathbf{N} = \mathbf{OA} \times \mathbf{OB} \tag{B.9}$$

Where

$$\mathbf{OA} = A_x\mathbf{i} + A_y\mathbf{j} + A_z\mathbf{k} \tag{B.10}$$

$$\mathbf{OB} = B_x\mathbf{i} + B_y\mathbf{j} + B_z\mathbf{k}$$

With known coordinates at O, A, and B, Equation B.10 is fully written as:

$$\mathbf{N} = \begin{vmatrix} A_y & A_z \\ B_y & B_z \end{vmatrix}\mathbf{i} + \begin{vmatrix} A_z & A_x \\ B_z & B_x \end{vmatrix}\mathbf{j} + \begin{vmatrix} A_x & A_y \\ B_x & B_y \end{vmatrix}\mathbf{k} \tag{B.11}$$

And

$$\mathbf{N} = \left(A_yB_z - A_zB_y\right)\mathbf{i} + \left(A_zB_x - A_xB_z\right)\mathbf{j} + \left(A_xB_y - A_yB_x\right)\mathbf{k} \tag{B.12}$$

The coordinate system convention is: i = easting, j = northing, and k = elevation. The three components of normal vector N to the plane can be used to define dip and dip direction of the plane as follows:

$$dip = cos^{-1}\left[\frac{\left(A_x B_y - A_y B_x\right)}{\sqrt{\left(A_y B_z - A_z B_y\right)^2 + \left(A_z B_x - A_x B_z\right)^2 + \left(A_x B_y - A_y B_x\right)^2}}\right] \quad \text{B.13}$$

And

$$dip\ direction = tan^{-1}\left(\frac{A_y B_z - A_z B_y}{A_z B_x - A_x B_z}\right) \quad \text{B.14}$$

B.3.4 Included Angle Between Fault or Joint Set and a Stope Surface

In order to determine the fault factor F_w the included angle ξ between the fault plane and the stope surface is required. The included angle is also needed to determine the critical joint orientation factor B in the determination of the stability number N'. Hutchinson and Diederichs (1996) noted that the included angle is not the difference between the dips of the critical joint and stope surface planes. From the equations of the planes representing the stope surface and a fault or critical joint, the included angle is given by:

$$\xi = cos^{-1}\left[\frac{a_s a_f + b_s b_f + c_s c_f}{\left(\sqrt{a_s^2 + b_s^2 + c_s^2}\right) * \left(\sqrt{a_f^2 + b_f^2 + c_f^2}\right)}\right] = cos^{-1}\left(a'_s\, a'_f + b'_s\, b'_f + c'_s\, c'_f\right) \quad \text{B.15}$$

The subscripts "s" and "f" refer to the stope face and fault plane respectively. Note that k_s and k_f are not needed in order to determine the angles between planes.

B.3.5 Distance Between a Fault and a Point on a Stope Surface

Determination of the fault factor demands that the distance of the fault to the stope surface be known. The following procedure can be used to compute the distance of a fault from specific points on a stope surface. The procedure uses the stope surface coordinates and the equation of the fault plane. The distance d_f (Figure B.10) from an arbitrary point Q (x_s, y_s, z_s) on the stope surface to the fault plane measured perpendicular to the fault plane is given by:

$$d_f = \left(a'_f\, x_s + b'_f\, y_s - + c'_f\, z_s\right) - \left(a'_f\, x_f + b'_f\, y_f + c'_f\, z_f\right) \quad \text{B.16}$$

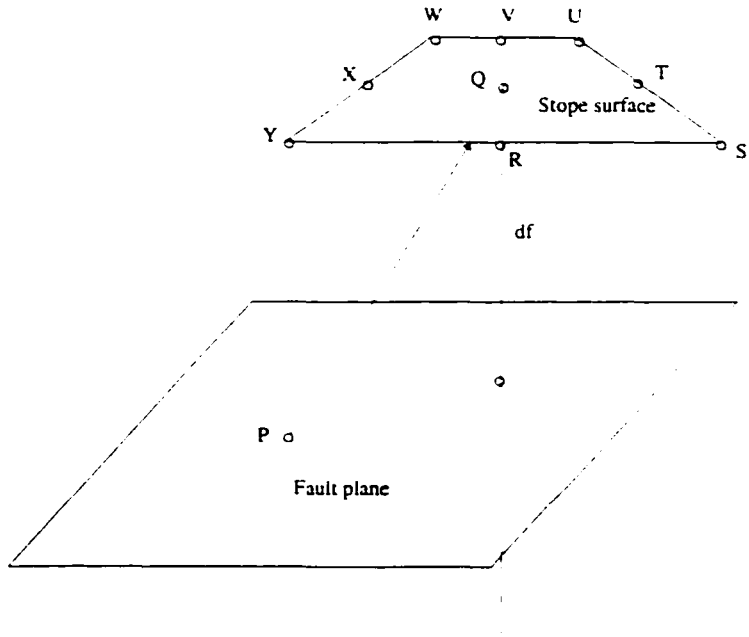


Figure B.10 Determination of distance of fault to a point on a stope surface

A number of points (for example: Q, R, S, T, U, V, W, X, and Y) are selected on the stope surface and their distances to the fault plane computed. The computed distances are then sorted to find the shortest distance. If more than one fault is present, the fault making the smallest included angle with the stope surface should be used in determining the fault distance. This is because the fault making the smallest included angle with the stope surface is the most critical fault.

The fault-stope distance can be used in determining suitable cablebolt lengths, in order to adequately anchor the wedge between a stope surface and a fault. In this case the longest distance determined might be more useful.

It is important to note that the distance d_f in Equation B.16 may be positive or negative. A series of distances from a given stope surface to a fault plane may be all positive, all negative or a mixture of positives and negatives. A mixture of positive and negative distances implies intersection of the fault surface to the stope surface, while all positive or all negative distances imply non-intersection.

APPENDIX C

DETAILS OF STOPES AND FAULTS IN KIDD DATABASE

Table C.1 Stope surface dimensions and orientations

Stope	Easting	Northing	Elevation		x	y	z	L	s-face-dip	s-face-D.dir	S.Face	per.	Area	S_Hgt.	L	HR	H/L
47-630-ST	65763.2	65568.6	1902.5	WL	583	346	104	686	81	59	NE	154.4	1075.8	58.2	18.0	7.0	3.2
47-630-ST	65778.1	65557.4	1902.5	EL	636	-124	64	651	84	101	SE	130.2	412.3	57.8	6.9	3.2	8.3
47-630-ST	65776.0	65555.3	1902.5	SL	-447	-994	-193	1107	100	204	SW	154.8	1097.2	58.6	18.4	7.1	3.2
47-630-ST	65777.1	65582.5	1902.5	NL	-772	772	0	1091	90	315	NW	157.5	1112.0	59.4	19.3	7.1	3.1
47-630-ST	65752.9	65558.3	1960.0	WU													
47-630-ST	65772.3	65561.6	1960.0	EU													
47-630-ST	65770.1	65550.5	1960.0	SU													
47-630-ST	65766.3	65571.7	1960.0	NU	x	y	z	L	s-face-dip	s-face-D.dir	S.Face	per.	Area	S_Hgt.	L	HR	H/L
47-645-ST	65761.5	65582.8	1902.3	WL	657	549	302	908	71	50	NE	154.4	825.1	64.4	12.8	5.3	5.0
47-645-ST	65779.2	65584.6	1902.3	EL	493	-493	0	698	90	135	SE	154.8	848.1	63.4	14.0	5.5	4.5
47-645-ST	65767.5	65573.0	1902.3	SL	-756	-450	-221	907	104	239	SW	151.4	817.1	62.6	13.1	5.4	4.8

47-645-ST	65772.9	65594.3	1902.3	NL	-395	395	-25	559	93	315	NW	152.6	771.7	63.5	12.7	5.1	5.0
47-645-ST	65748.9	65574.2	1963.0	WU													
47-645-ST	65764.5	65569.9	1963.0	EU													
47-645-ST	65756.4	65561.8	1963.0	SU													
47-645-ST	65755.4	65580.7	1963.0	NU	x	y	z	L	s-face-dip	s-face-D.dir	S.Face	per.	Area	S_Hgt.	L	HR	H/L
47-690A-ST	65723.7	65602.3	1935.7	WL	320	246	-110	418	105	52	NE	85.5	416.9	27.7	15.0	4.9	1.8
47-690A-ST	65737.6	65595.0	1935.7	EL	390	-390	0	552	90	135	SE	81.1	337.3	26.7	12.6	4.2	2.1
47-690A-ST	65734.3	65591.7	1935.7	SL	-232	-232	-119	349	110	225	SW	84.2	387.2	28.4	13.6	4.6	2.1
47-690A-ST	65727.0	65605.6	1935.7	NL	-478	376	29	609	87	308	NW	83.9	366.0	26.7	13.7	4.4	2.0
47-690A-ST	65718.8	65593.5	1962.3	WU													
47-690A-ST	65742.1	65599.5	1962.3	EU													
47-690A-ST	65727.5	65584.9	1962.3	SU													
47-690A-ST	65732.9	65611.5	1962.3	NU													
47-690-ST	X	Y	Z		x	y	Z	L	s-face-dip	s-face-D.dir	S.Face	per.	Area	S_Hgt.	L	HR	H/L
47-690-ST	65727.3	65605.9	1905.2	WL	524	335	265	676	67	57	NE	118.9	671.8	44.2	15.2	5.7	2.9
47-690-ST	65759.2	65616.6	1905.2	EL	117	-117	0	166	90	135	SE	125.2	779.4	40.6	19.2	6.2	2.1
47-690-ST	65734.9	65592.3	1905.2	SL	-430	-430	149	626	76	225	SW	114.1	637.6	41.7	15.1	5.6	2.8
47-690-ST	65750.0	65628.6	1905.2	NL	-212	212	0	300	90	315	NW	124.8	801.9	40.8	19.8	6.4	2.1
47-690-ST	65732.8	65611.4	1945.7	WU													
47-690-ST	65746.3	65603.7	1945.7	EU													
47-690-ST	65743.4	65600.8	1945.7	SU													
47-690-ST	65738.0	65616.6	1945.7	NU	x	y	z	L	s-face-dip	s-face-D.dir	S.Face	per.	Area	S_Hgt.	L	HR	H/L
47-725-ST	65719.7	65652.0	1899.9	WL	1233	1143	642	1800	69	47	NE	185.8	1691.5	67.9	24.8	9.1	2.7
47-725-ST	65741.1	65640.9	1899.9	EL	269	-269	0	380	90	135	SE	159.5	824.0	66.4	13.0	5.2	5.1
47-725-ST	65727.0	65626.8	1899.9	SL	-1300	-1076	-479	1754	106	230	SW	185.1	1741.4	65.9	25.9	9.4	2.5
47-725-ST	65721.8	65654.2	1899.9	NL	-202	202	-16	286	93	315	NW	142.1	238.2	67.3	3.8	1.7	17.9
47-725-ST	65701.0	65638.3	1963.3	WU													
47-725-ST	65722.2	65622.0	1963.3	EU													
47-725-ST	65718.0	65617.8	1963.3	SU													
47-725-ST	65704.2	65641.4	1963.3	NU	x	y	z	L	s-face-dip	s-face-D.dir	S.Face	per.	Area	S_Hgt.	L	HR	H/L
48-635-ST	65776.3	65581.4	1860.6	WL	310	310	197	480	66	45	NE	99.3	499.8	35.5	14.0	5.0	2.5
48-635-ST	65794.6	65579.4	1860.6	EL	183	-183	7	259	89	135	SE	88.1	312.6	34.4	9.6	3.5	3.6
48-635-ST	65786.6	65571.4	1860.6	SL	-310	-310	-132	457	107	225	SW	95.6	471.5	33.8	13.9	4.9	2.4
48-635-ST	65786.4	65591.5	1860.6	NL	-183	183	0	259	90	315	NW	92.2	361.3	34.8	11.2	3.9	3.1

48-635-ST	65769.5	65574.6	1893.0	WU												
48-635-ST	65784.7	65570.7	1893.0	EU												
48-635-ST	65779.0	65565.0	1893.0	SU												
48-635-ST	65775.1	65580.2	1893.0	NU	x	y	z	L	s-face-dip	s-face-D.dir	S.Face	per.	Area	S_Hgt.	L	HR	H/L
48-645-ST	65769.0	65590.2	1860.7	WL	409	262	157	510	72	57	NE	111.0	510.1	43.8	11.7	4.6	3.8
48-645-ST	65789.3	65594.4	1860.7	EL	520	-520	0	736	90	135	SE	122.9	733.9	43.8	17.6	6.0	2.5
48-645-ST	65776.9	65582.0	1860.7	SL	-530	-140	-122	562	102	255	SW	110.7	526.4	42.9	11.9	4.8	3.6
48-645-ST	65783.0	65604.2	1860.7	NL	-399	399	0	564	90	315	NW	119.4	693.9	42.9	16.7	5.8	2.6
48-645-ST	65763.7	65584.9	1902.3	WU												
48-645-ST	65779.6	65584.7	1902.3	EU												
48-645-ST	65767.1	65572.2	1902.3	SU												
48-645-ST	65773.3	65594.5	1902.3	NU	x	y	z	L	s-face-dip	s-face-D.dir	S.Face	per.	Area	S_Hgt.	L	HR	H/L
48-690-ST	65744.5	65623.1	1862.0	WL	312	286	183	461	67	47	NE	91.5	461.2	30.7	15.0	5.0	2.0
48-690-ST	65770.9	65628.3	1862.0	EL	514	-514	0	727	90	135	SE	111.3	678.0	31.6	24.0	6.1	1.3
48-690-ST	65755.2	65612.5	1862.0	SL	-299	-299	-240	486	120	225	SW	94.9	486.5	32.4	15.0	5.1	2.2
48-690-ST	65760.3	65638.9	1862.0	NL	-527	527	0	745	90	315	NW	111.7	687.1	31.5	24.3	6.1	1.3
48-690-ST	65733.2	65611.8	1890.2	WU												
48-690-ST	65762.1	65619.5	1890.2	EU												
48-690-ST	65743.9	65601.2	1890.2	SU												
48-690-ST	65751.9	65630.5	1890.2	NU	x	y	z	L	s-face-dip	s-face-D.dir	S.Face	per.	Area	S_Hgt.	L	HR	H/L
48-725-ST	65723.1	65639.2	1859.0	WL	434	434	179	639	74	45	NE	115.2	639.3	42.6	15.0	5.5	2.8
48-725-ST	65749.6	65649.3	1859.0	EL	578	-578	0	818	90	135	SE	125.5	826.0	42.5	20.2	6.6	2.1
48-725-ST	65735.1	65634.9	1859.0	SL	-737	-130	-71	752	95	260	SW	114.8	647.3	41.1	13.5	5.6	3.0
48-725-ST	65739.0	65660.0	1859.0	NL	-275	275	-17	389	92	315	NW	119.7	732.0	41.1	17.8	6.1	2.3
48-725-ST	65723.8	65644.8	1899.9	WU												
48-725-ST	65741.1	65640.9	1899.9	EU												
48-725-ST	65727.0	65626.8	1899.9	SU												
48-725-ST	65730.5	65651.6	1899.9	NU	x	y	z	L	s-face-dip	s-face-D.dir	S.Face	per.	Area	S Hgt.	L	HR	H/L
48-821-ST	65688.8	65758.3	1858.6	WL	434	434	110	623	80	45	NE	114.0	496.2	46.2	10.8	4.4	4.3
48-821-ST	65718.5	65766.8	1858.6	EL	738	-739	-102	1049	96	135	SE	141.3	1117.9	46.1	24.5	7.9	1.9
48-821-ST	65700.1	65748.4	1858.6	SL	-626	-626	-93	890	96	225	SW	126.0	787.7	45.7	17.2	6.3	2.7
48-821-ST	65712.6	65772.2	1858.6	NL	-546	931	24	1080	89	330	NW	143.1	1166.0	45.8	25.7	8.2	1.8
48-821-ST	65685.7	65755.3	1904.0	WU												
48-821-ST	65715.8	65757.8	1904.0	EU												

48-821-ST	65699.5	65741.5	1904.0	SU													
48-821-ST	65706.2	65767.3	1904.0	NU	x	y	z	L	s-face-dip	s-face-D.dir	S.Face	per.	Area	S_Hgt.	L	HR	H/L
49-635-ST	65788.1	65594.3	1822.0	WL	495	331	189	625	72	56	NE	106.8	502.3	40.9	12.4	4.7	3.3
49-635-ST	65799.5	65593.0	1822.0	EL	308	-308	-69	442	99	135	SE	99.8	264.3	42.9	6.8	2.6	6.3
49-635-ST	65798.0	65591.4	1822.0	SL	-416	-410	-298	656	117	225	SW	112.7	550.0	43.5	12.3	4.9	3.5
49-635-ST	65795.2	65601.4	1822.0	NL	-388	388	0	548	90	315	NW	107.2	467.0	41.4	12.1	4.4	3.4
49-635-ST	65775.9	65582.1	1860.6	WU													
49-635-ST	65794.6	65579.4	1860.6	EU													
49-635-ST	65786.6	65571.4	1860.6	SU													
49-635-ST	65786.0	65592.2	1860.6	NU	x	y	z	L	s-face-dip	s-face-D.dir	S.Face	per.	Area	S_Hgt.	L	HR	H/L
49-645-ST	65777.3	65601.9	1819.7	WL	377	377	201	570	69	45	NE	113.7	569.7	43.8	13.0	5.0	3.4
49-645-ST	65800.2	65606.4	1819.7	EL	536	-536	0	758	90	135	SE	125.3	779.0	43.7	19.0	6.2	2.3
49-645-ST	65786.5	65592.7	1819.7	SL	-377	-377	-188	565	109	225	SW	113.0	565.4	43.5	13.0	5.0	3.3
49-645-ST	65791.1	65615.6	1819.7	NL	-536	536	0	758	90	315	NW	125.3	778.9	43.7	19.0	6.2	2.3
49-645-ST	65767.0	65591.6	1860.7	WU													
49-645-ST	65789.3	65595.5	1860.7	EU													
49-645-ST	65776.2	65582.4	1860.7	SU													
49-645-ST	65780.1	65604.7	1860.7	NU	x	y	z	L	s-face-dip	s-face-D.dir	S.Face	per.	Area	S_Hgt.	L	HR	H/L
49-665-ST	65764.9	65622.2	1819.5	WL	913	540	258	1092	76	59	NE	138.2	1074.4	45.4	23.5	7.8	1.9
49-665-ST	65791.9	65616.4	1819.5	EL	218	-218	0	308	90	135	SE	118.2	616.0	44.6	14.0	5.2	3.2
49-665-ST	65777.0	65601.6	1819.5	SL	-733	-733	-71	1040	94	225	SW	135.9	1050.1	44.1	23.6	7.7	1.9
49-665-ST	65775.5	65632.8	1819.5	NL	-398	411	-2	572	90	316	NW	117.1	616.1	44.6	14.0	5.3	3.2
49-665-ST	65760.3	65618.3	1863.5	WU													
49-665-ST	65782.0	65606.5	1863.5	EU													
49-665-ST	65777.0	65601.6	1863.5	SU													
49-665-ST	65769.7	65627.3	1863.5	NU	x	y	z	L	s-face-dip	s-face-D.dir	S.Face	per.	Area	S_Hgt.	L	HR	H/L
49-690-ST	65754.5	65633.1	1820.7	WL	438	438	91	626	82	45	NE	113.7	630.1	41.8	15.0	5.5	2.8
49-690-ST	65774.4	65631.8	1820.7	EL	652	-651	0	921	90	135	SE	120.9	739.5	42.4	17.9	6.1	2.4
49-690-ST	65764.8	65622.2	1820.7	SL	-438	-438	-208	654	109	225	SW	117.2	653.8	43.6	15.0	5.6	2.9
49-690-ST	65765.4	65644.0	1820.7	NL	-651	652	0	921	90	315	NW	123.4	780.7	42.7	18.9	6.3	2.3
49-690-ST	65744.5	65623.1	1862.0	WU													
49-690-ST	65770.9	65628.3	1862.0	EU													
49-690-ST	65755.2	65612.5	1862.0	SU													
49-690-ST	65760.3	65638.9	1862.0	NU	x	y	z	L	s-face-dip	s-face-D.dir	S.Face	per.	Area	S_Hgt.	L	HR	H/L

49-705-ST	65737.1	65636.8	1819.6	WL	407	407	151	595	75	45	NE	109.8	598.6	39.9	15.0	5.4	2.7
49-705-ST	65766.0	65644.6	1819.6	EL	601	-601	0	849	90	135	SE	122.5	829.7	39.8	21.5	6.8	1.8
49-705-ST	65751.2	65629.8	1819.6	SL	-476	-339	-93	591	99	235	SW	109.4	605.7	39.1	15.0	5.5	2.6
49-705-ST	65757.0	65656.7	1819.6	NL	-532	532	0	753	90	315	NW	126.6	920.6	39.2	23.9	7.3	1.6
49-705-ST	65735.3	65635.0	1858.2	WU													
49-705-ST	65759.7	65638.3	1858.2	EU													
49-705-ST	65744.1	65622.7	1858.2	SU													
49-705-ST	65749.1	65648.8	1858.2	NU	x	y	z	L	s-face-dip	s-face-D.dir	S.Face	per.	Area	S_Hgt.	L	HR	H/L
49-720-ST	65726.3	65647.2	1820.0	WL	303	414	88	520	80	36	NE	113.3	666.1	39.7	16.8	5.9	2.4
49-720-ST	65755.6	65655.3	1820.0	EL	800	-800	0	1131	90	135	SE	135.5	1082.4	40.0	27.8	8.0	1.4
49-720-ST	65736.9	65636.6	1820.0	SL	-276	-276	-100	403	104	225	SW	105.8	503.3	40.3	12.5	4.8	3.2
49-720-ST	65738.3	65666.3	1820.0	NL	-827	662	140	1069	82	309	NW	130.2	977.0	40.2	24.8	7.5	1.6
49-720-ST	65722.7	65636.6	1859.0	WU													
49-720-ST	65750.3	65650.0	1859.0	EU													
49-720-ST	65729.8	65629.5	1859.0	SU													
49-720-ST	65739.7	65657.8	1859.0	NU	x	y	z	L	s-face-dip	s-face-D.dir	S.Face	per.	Area	S_Hgt.	L	HR	H/L
49-731-ST	65745.7	65688.1	1823.2	WL	419	419	235	637	68	45	NE	115.5	646.9	42.5	15.1	5.6	2.8
49-731-ST	65783.6	65704.8	1823.2	EL	807	-807	-6	1142	90	135	SE	144.6	1228.7	41.1	31.1	8.5	1.3
49-731-ST	65760.0	65681.2	1823.2	SL	-419	-419	-100	601	100	225	SW	111.2	620.0	40.1	15.2	5.6	2.6
49-731-ST	65775.7	65718.1	1823.2	NL	-807	807	6	1142	90	315	NW	154.3	1410.1	40.9	35.7	9.1	1.1
49-731-ST	65743.0	65685.1	1862.7	WU													
49-731-ST	65774.0	65694.9	1862.7	EU													
49-731-ST	65753.6	65674.5	1862.7	SU													
49-731-ST	65763.4	65705.5	1862.7	NU	x	y	z	L	s-face-dip	s-face-D.dir	S.Face	per.	Area	S_Hgt.	L	HR	H/L
49-782-ST	65743.2	65749.1	1822.5	WL	397	397	123	574	78	45	NE	106.6	574.2	38.3	15.0	5.4	2.6
49-782-ST	65770.1	65754.8	1822.5	EL	597	-597	0	845	90	135	SE	122.1	852.6	38.2	22.8	7.0	1.7
49-782-ST	65753.8	65738.5	1822.5	SL	-397	-397	-117	573	102	225	SW	106.4	573.0	38.2	15.0	5.4	2.5
49-782-ST	65759.5	65765.4	1822.5	NL	-597	597	0	845	90	315	NW	122.1	852.4	38.2	22.8	7.0	1.7
49-782-ST	65737.7	65743.6	1859.9	WU													
49-782-ST	65764.3	65749.0	1859.9	EU													
49-782-ST	65748.3	65733.0	1859.9	SU													
49-782-ST	65753.7	65759.6	1859.9	NU	x	y	z	L	s-face-dip	s-face-D.dir	S.Face	per.	Area	S_Hgt.	L	HR	H/L
49-821-ST	65696.2	65765.7	1821.0	WL	383	415	50	567	85	43	NE	105.5	566.5	37.7	15.0	5.4	2.5
49-821-ST	65720.6	65768.9	1821.0	EL	691	-691	0	978	90	135	SE	122.0	855.4	38.1	22.8	7.0	1.7

49-821-ST	65706.8	65755.1	1821.0	SL	-372	-426	-151	585	105	221	SW	107.9	584.6	38.9	15.0	5.4	2.6
49-821-ST	65710.0	65779.5	1821.0	NL	-702	702	0	993	90	315	NW	122.7	863.0	38.3	23.0	7.0	1.7
49-821-ST	65688.8	65758.3	1858.6	WU													
49-821-ST	65718.5	65766.8	1858.6	EU													
49-821-ST	65700.1	65748.4	1858.6	SU													
49-821-ST	65707.4	65777.0	1858.6	NU	x	y	z	L	s-face-dip	s-face-D.dir	S.Face	per.	Area	S Hgt.	L	HR	H/L
51-645-ST	65782.9	65608.3	1779.7	WL	283	283	21	401	87	45	NE	108.4	551.9	40.1	13.2	5.1	3.0
51-645-ST	65799.5	65604.4	1779.7	EL	566	-311	55	648	85	119	SE	99.4	350.1	40.3	8.7	3.5	4.6
51-645-ST	65798.6	65603.5	1779.7	SL	-254	-566	-150	638	104	204	SW	114.6	657.1	41.3	16.0	5.7	2.6
51-645-ST	65796.2	65621.6	1779.7	NL	-594	594	0	840	90	315	NW	121.5	796.1	40.8	19.9	6.6	2.1
51-645-ST	65776.4	65601.8	1819.7	WU													
51-645-ST	65798.3	65609.5	1819.7	EU													
51-645-ST	65790.5	65595.4	1819.7	SU													
51-645-ST	65791.2	65616.6	1819.7	NU	x	y	z	L	s-face-dip	s-face-D.dir	S.Face	per.	Area	S_Hgt.	L	HR	H/L
51-665-ST	65771.5	65613.4	1780.5	WL	328	316	81	462	80	46	NE	102.6	462.2	39.6	11.7	4.5	3.4
51-665-ST	65796.2	65621.6	1780.5	EL	579	-579	0	819	90	135	SE	119.5	776.2	39.8	19.9	6.5	2.0
51-665-ST	65782.9	65608.3	1780.5	SL	-631	-12	-16	631	91	269	SW	108.2	565.9	39.0	12.2	5.2	3.2
51-665-ST	65788.0	65629.9	1780.5	NL	-276	276	0	390	90	315	NW	112.4	649.4	39.0	16.7	5.8	2.3
51-665-ST	65776.0	65617.9	1819.5	WU													
51-665-ST	65791.2	65616.6	1819.5	EU													
51-665-ST	65776.4	65601.8	1819.5	SU													
51-665-ST	65783.1	65625.0	1819.5	NU	x	y	z	L	s-face-dip	s-face-D.dir	S.Face	per.	Area	S_Hgt.	L	HR	H/L
51-675-SLF	65769.4	65626.8	1800.0	WL	97	223	54	249	77	24	NE	66.0	245.8	21.3	11.0	3.7	1.9
51-675-SLF	65777.2	65619.1	1800.0	EL	86	-86	0	122	90	135	SE	48.7	61.1	21.2	3.0	1.3	7.2
51-675-SLF	65777.2	65619.1	1800.0	SL	-160	-160	-82	241	110	225	SW	65.9	241.0	22.0	10.9	3.7	2.0
51-675-SLF	65771.1	65628.5	1800.0	NL	-24	24	0	33	90	315	NW	48.2	40.7	22.1	2.0	0.8	11.2
51-675-SLF	65764.1	65621.5	1820.7	WU													
51-675-SLF	65776.0	65617.9	1820.7	EU													
51-675-SLF	65771.9	65613.8	1820.7	SU													
51-675-SLF	65765.3	65622.6	1820.7	NU	x	y	z	L	s-face-dip	s-face-D.dir	S.Face	per.	Area	S_Hgt.	L	HR	H/L
51-675-ST	65767.3	65624.7	1777.7	WL	327	308	90	458	79	47	NE	106.3	462.3	41.8	11.1	4.4	3.8
51-675-ST	65788.0	65629.9	1780.5	EL	276	-276	0	390	90	135	SE	112.4	649.4	39.0	16.7	5.8	2.3
51-675-ST	65771.5	65613.4	1780.5	SL	-191	-443	19	483	88	203	SW	106.8	491.0	41.0	11.0	4.6	3.7
51-675-ST	65782.2	65639.5	1777.7	NL	-438	437	0	619	90	315	NW	122.5	760.7	43.4	17.7	6.2	2.5

51-675-ST	65765.3	65622.6	1820.7	WU												
51-675-ST	65783.1	65625.0	1819.5	EU												
51-675-ST	65776.0	65617.9	1819.5	SU												
51-675-ST	65775.4	65632.8	1820.7	NU	x	y	z	L	s-face-dip	s-face-D.dir	S.Face	per.	Area	S_Hgt.	L	HR	H/L
51-690-ST	65761.2	65639.8	1777.7	WL	526	385	138	667	78	54	NE	118.2	664.6	43.9	15.0	5.6	2.9
51-690-ST	65782.2	65639.5	1777.7	EL	410	-410	0	580	90	135	SE	123.3	771.9	43.5	18.0	6.3	2.4
51-690-ST	65766.3	65623.7	1777.7	SL	-466	-446	-88	651	98	226	SW	119.0	693.5	43.4	15.5	5.8	2.8
51-690-ST	65770.6	65649.2	1777.7	NL	-471	471	0	666	90	315	NW	116.4	617.3	43.8	14.4	5.3	3.0
51-690-ST	65754.5	65633.1	1820.7	WU												
51-690-ST	65774.4	65631.8	1820.7	EU												
51-690-ST	65764.8	65622.2	1820.7	SU												
51-690-ST	65765.4	65644.0	1820.7	NU	x	y	z	L	s-face-dip	s-face-D.dir	S.Face	per.	Area	S_Hgt.	L	HR	H/L
51-705-ST	65749.3	65643.3	1780.0	WL	337	271	61	437	82	51	NE	102.0	439.2	40.0	11.0	4.3	3.6
51-705-ST	65772.0	65650.6	1780.0	EL	639	-639	0	903	90	135	SE	124.2	871.8	40.1	22.0	7.0	1.8
51-705-ST	65757.0	65635.6	1780.0	SL	-304	-304	-74	436	100	225	SW	102.1	436.5	40.2	10.9	4.3	3.7
51-705-ST	65765.8	65659.7	1780.0	NL	-672	672	0	950	90	315	NW	127.4	934.7	40.1	23.6	7.3	1.7
51-705-ST	65744.5	65638.5	1819.6	WU												
51-705-ST	65768.4	65646.9	1819.6	EU												
51-705-ST	65752.2	65630.8	1819.6	SU												
51-705-ST	65761.5	65655.5	1819.6	NU	x	y	z	L	s-face-dip	s-face-D.dir	S.Face	per.	Area	S_Hgt.	L	HR	H/L
51-725-ST	65736.7	65647.3	1780.0	WL	301	359	102	479	78	40	NE	105.5	493.2	40.5	11.9	4.7	3.4
51-725-ST	65765.8	65659.7	1780.0	EL	672	-672	0	950	90	135	SE	127.4	934.7	40.1	23.6	7.3	1.7
51-725-ST	65749.3	65643.3	1780.0	SL	-82	-578	-96	591	99	188	SW	108.9	563.1	40.4	14.0	5.2	2.9
51-725-ST	65760.4	65671.0	1780.0	NL	-891	891	0	1260	90	315	NW	147.3	1294.1	40.9	32.7	8.8	1.3
51-725-ST	65730.0	65640.6	1819.6	WU												
51-725-ST	65761.5	65655.5	1819.6	EU												
51-725-ST	65744.5	65638.5	1819.6	SU												
51-725-ST	65752.5	65663.1	1819.6	NU	x	y	z	L	s-face-dip	s-face-D.dir	S.Face	per.	Area	S_Hgt.	L	HR	H/L
51-731-ST	65760.9	65703.3	1783.2	WL	534	314	151	638	76	60	NE	113.5	635.0	41.3	15.0	5.6	2.7
51-731-ST	65793.0	65714.2	1783.2	EL	942	-942	0	1332	90	135	SE	146.8	1195.9	43.4	29.9	8.1	1.5
51-731-ST	65774.3	65695.5	1783.2	SL	-274	-574	-313	709	116	206	SW	121.7	702.2	45.1	15.7	5.8	2.9
51-731-ST	65780.5	65722.9	1783.2	NL	-1202	1202	0	1700	90	315	NW	156.3	1406.0	42.4	35.2	9.0	1.2
51-731-ST	65745.7	65688.1	1823.2	WU												
51-731-ST	65783.6	65704.8	1823.2	EU												

51-731-ST	65760.0	65681.2	1823.2	SU												
51-731-ST	65775.7	65718.1	1823.2	NU	x	y	z	L	s-face-dip	s-face-D.dir	S.Face	per.	Area	S_Hgt.	L	HR	H/L
51-735-ST	65730.0	65668.8	1778.5	WL	150	396	103	436	76	21	NE	121.8	748.4	42.8	17.5	6.1	2.4
51-735-ST	65760.7	65671.3	1778.5	EL	933	-933	0	1320	90	135	SE	151.2	1357.1	42.9	32.7	9.0	1.3
51-735-ST	65737.0	65647.6	1778.5	SL	-414	-27	-47	417	96	266	SW	120.5	681.0	43.6	16.1	5.7	2.7
51-735-ST	65737.0	65678.7	1778.5	NL	-669	564	248	909	74	310	NW	122.3	715.7	44.3	16.6	5.9	2.7
51-735-ST	65729.2	65650.5	1820.0	WU													
51-735-ST	65752.4	65663.0	1820.0	EU													
51-735-ST	65729.9	65640.5	1820.0	SU													
51-735-ST	65742.8	65666.6	1820.0	NU	x	y	z	L	s-face-dip	s-face-D.dir	S.Face	per.	Area	S_Hgt.	L	HR	H/L
51-781-ST	65766.8	65772.9	1781.0	WL	362	507	0	623	90	36	NE	112.4	623.4	41.0	15.2	5.5	2.7
51-781-ST	65795.0	65779.9	1781.0	EL	722	-722	0	1021	90	135	SE	131.8	1021.1	41.0	24.9	7.7	1.6
51-781-ST	65777.4	65762.3	1781.0	SL	-435	-435	0	615	90	225	SW	112.0	614.9	41.0	15.0	5.5	2.7
51-781-ST	65782.6	65788.8	1781.0	NL	-649	649	0	918	90	315	NW	126.8	918.4	41.0	22.4	7.2	1.8
51-781-ST	65766.8	65772.9	1822.0	WU													
51-781-ST	65795.0	65779.9	1822.0	EU													
51-781-ST	65777.4	65762.3	1822.0	SU													
51-781-ST	65782.6	65788.8	1822.0	NU	x	y	z	L	s-face-dip	s-face-D.dir	S.Face	per.	Area	S_Hgt.	L	HR	H/L
51-782-SLF	65753.4	65766.2	1783.0	WL	138	137	27	196	82	45	NE	89.6	196.3	39.9	4.9	2.2	8.1
51-782-SLF	65762.9	65768.8	1783.0	EL	293	-293	0	415	90	135	SE	99.1	375.2	40.0	9.5	3.8	4.2
51-782-SLF	65756.8	65762.8	1783.0	SL	-138	-137	-37	198	101	225	SW	90.3	197.9	40.2	4.9	2.2	8.2
51-782-SLF	65759.5	65772.3	1783.0	NL	-293	293	0	415	90	315	NW	99.2	377.2	40.0	9.5	3.8	4.2
51-782-SLF	65748.1	65760.9	1822.5	WU													
51-782-SLF	65759.0	65764.9	1822.5	EU													
51-782-SLF	65751.5	65757.5	1822.5	SU													
51-782-SLF	65755.5	65768.4	1822.5	NU	x	y	z	L	s-face-dip	s-face-D.dir	S.Face	per.	Area	S_Hgt.	L	HR	H/L
51-782-ST	65750.8	65756.7	1783.0	WL	419	419	83	598	82	45	NE	109.8	598.1	39.9	15.0	5.4	2.7
51-782-ST	65773.5	65758.2	1783.0	EL	545	-545	0	770	90	135	SE	116.7	720.9	40.1	18.3	6.2	2.2
51-782-ST	65761.4	65746.1	1783.0	SL	-419	-419	-120	604	101	225	SW	110.6	604.5	40.3	15.0	5.5	2.7
51-782-ST	65762.9	65768.8	1783.0	NL	-545	545	0	770	90	315	NW	116.7	720.9	40.1	18.3	6.2	2.2
51-782-ST	65745.2	65751.1	1822.5	WU													
51-782-ST	65769.6	65754.3	1822.5	EU													
51-782-ST	65755.8	65740.5	1822.5	SU													
51-782-ST	65759.0	65764.9	1822.5	NU	x	y	z	L	s-face-dip	s-face-D.dir	S.Face	per.	Area	S_Hgt.	L	HR	H/L

51-811-ST	65707.4	65755.7	1783.8	WL	426	426	79	608	83	45	NE	112.4	636.0	40.3	15.4	5.7	2.6
51-811-ST	65743.8	65770.8	1783.8	EL	736	-736	0	1040	90	135	SE	143.5	1250.2	40.1	31.3	8.7	1.3
51-811-ST	65718.0	65745.0	1783.8	SL	-426	-426	30	603	87	225	SW	110.2	603.3	40.0	15.1	5.5	2.7
51-811-ST	65728.6	65776.9	1783.8	NL	-735	736	0	1040	90	315	NW	136.1	1120.1	40.0	28.0	8.2	1.4
51-811-ST	65708.8	65757.1	1823.8	WU													
51-811-ST	65737.8	65764.8	1823.8	EU													
51-811-ST	65719.4	65746.4	1823.8	SU													
51-811-ST	65727.2	65775.5	1823.8	NU	x	y	z	L	s-face-dip	s-face-D.dir	S.Face	per.	Area	S_Hgt.	L	HR	H/L
51-821-ST	65699.1	65768.6	1791.4	WL	314	314	9	444	89	45	NE	89.7	450.8	29.6	15.1	5.0	2.0
51-821-ST	65719.8	65768.1	1791.4	EL	408	-408	0	577	90	135	SE	93.2	499.9	29.6	16.9	5.4	1.8
51-821-ST	65709.7	65758.0	1791.4	SL	-314	-314	-60	448	98	225	SW	89.7	447.7	29.8	15.0	5.0	2.0
51-821-ST	65711.7	65781.2	1791.4	NL	-408	408	0	577	90	315	NW	96.9	553.0	29.7	18.7	5.7	1.6
51-821-ST	65696.2	65765.7	1821.0	WU													
51-821-ST	65720.6	65768.9	1821.0	EU													
51-821-ST	65706.8	65755.1	1821.0	SU													
51-821-ST	65710.0	65779.5	1821.0	NU	x	y	z	L	s-face-dip	s-face-D.dir	S.Face	per.	Area	S_Hgt.	L	HR	H/L
53-695-ST	65763.3	65641.9	1708.4	WL	670	801	142	1054	82	40	NE	170.2	1056.5	70.0	15.0	6.2	4.7
53-695-ST	65787.7	65645.1	1708.4	EL	890	-884	0	1255	90	135	SE	177.0	1303.5	69.7	18.8	7.4	3.7
53-695-ST	65773.9	65631.3	1708.4	SL	-911	-566	-70	1075	94	238	SW	169.5	1058.8	69.5	15.1	6.2	4.6
53-695-ST	65778.5	65657.1	1708.4	NL	-649	649	0	918	90	315	NW	174.4	1204.2	69.7	17.4	6.9	4.0
53-695-ST	65761.2	65639.8	1777.7	WU													
53-695-ST	65782.2	65639.5	1777.7	EU													
53-695-ST	65769.4	65626.7	1777.7	SU													
53-695-ST	65770.6	65649.2	1777.7	NU	x	y	z	L	s-face-dip	s-face-D.dir	S.Face	per.	Area	S_Hgt.	L	HR	H/L
53-735-ST	65736.6	65679.0	1711.0	WL	209	1176	185	1208	81	10	NE	171.1	1135.5	68.7	15.1	6.6	4.5
53-735-ST	65758.5	65679.7	1711.0	EL	1357	-1357	0	1920	90	135	SE	184.6	1611.4	68.3	23.9	8.7	2.9
53-735-ST	65744.9	65666.1	1711.0	SL	-898	-296	-159	959	100	252	SW	167.1	1006.9	68.8	14.6	6.0	4.7
53-735-ST	65750.4	65692.8	1711.0	NL	-668	477	-13	821	91	306	NW	170.5	1068.8	69.3	15.8	6.3	4.4
53-735-ST	65730.0	65668.8	1778.5	WU													
53-735-ST	65754.4	65675.7	1778.5	EU													
53-735-ST	65734.3	65655.5	1778.5	SU													
53-735-ST	65737.0	65678.7	1778.5	NU	x	y	z	L	s-face-dip	s-face-D.dir	S.Face	per.	Area	S_Hgt.	L	HR	H/L
54-695-ST	65776.4	65655.0	1672.0	WL	437	334	245	602	66	53	NE	105.0	501.0	39.8	12.6	4.8	3.2
54-695-ST	65799.3	65656.7	1672.0	EL	502	-502	0	709	90	135	SE	121.1	772.9	39.2	21.3	6.4	1.8

54-695-ST	65783.1	65640.5	1672.0	SL	-386	-386	-236	594	113	225	SW	110.4	611.7	39.6	15.3	5.5	2.6
54-695-ST	65793.0	65664.5	1672.0	NL	-553	553	-54	784	94	315	NW	121.3	739.5	40.2	20.2	6.1	2.0
54-695-ST	65763.3	65641.9	1708.4	WU													
54-695-ST	65787.7	65645.1	1708.4	EU													
54-695-ST	65773.9	65631.3	1708.4	SU													
54-695-ST	65778.5	65657.1	1708.4	NU	x	y	z	L	stp-face-dip	stp-face-dip-dir	Stp.Face	perimeter	Area	Height	Length	HR	H/L
54-735-ST	65739.3	65681.8	1671.2	WL	521	324	111	623	80	58	NE	111.5	615.9	40.5	15.1	5.5	2.7
54-735-ST	65765.1	65686.4	1671.2	EL	543	-543	0	768	90	135	SE	120.2	762.2	40.9	19.2	6.3	2.1
54-735-ST	65751.7	65672.9	1671.2	SL	-515	-329	-102	620	99	237	SW	111.5	618.2	40.4	15.0	5.5	2.7
54-735-ST	65754.2	65696.6	1671.2	NL	-549	549	0	776	90	315	NW	120.7	806.0	40.1	20.3	6.7	2.0
54-735-ST	65736.6	65679.0	1711.0	WU													
54-735-ST	65758.5	65679.7	1711.0	EU													
54-735-ST	65744.9	65666.1	1711.0	SU													
54-735-ST	65750.4	65692.8	1711.0	NU	x	y	z	L	stp-face-dip	stp-face-dip-dir	Stp.Face	perimeter	Area	S_Height	Length	HR	H/L
54-781-ST	65765.9	65771.7	1674.5	WL	419	419	157	613	75	45	NE	111.7	613.0	40.9	15.0	5.5	2.7
54-781-ST	65793.1	65777.7	1674.5	EL	363	-363	0	513	90	135	SE	116.9	720.9	39.8	18.3	6.2	2.2
54-781-ST	65776.5	65761.1	1674.5	SL	-419	-419	0	593	90	225	SW	109.0	592.7	39.5	15.0	5.4	2.6
54-781-ST	65782.5	65788.3	1674.5	NL	-363	363	0	514	90	315	NW	116.9	720.9	39.8	18.3	6.2	2.2
54-781-ST	65765.9	65771.7	1714.0	WU													
54-781-ST	65785.7	65770.3	1714.0	EU													
54-781-ST	65776.5	65761.1	1714.0	SU													
54-781-ST	65775.1	65780.9	1714.0	NU	x	y	z	L	s-face-dip	s-face-D.dir	S.Face	per.	Area	S_Hgt.	L	HR	H/L
54-821-ST	65725.8	65795.5	1674.0	WL	420	420	98	602	81	45	NE	110.3	602.0	40.1	15.0	5.5	2.7
54-821-ST	65752.3	65800.8	1674.0	EL	1078	-1078	0	1524	90	135	SE	146.7	1207.7	42.2	30.5	8.2	1.4
54-821-ST	65736.4	65784.9	1674.0	SL	-420	-420	-338	683	120	225	SW	121.1	683.4	45.5	15.0	5.6	3.0
54-821-ST	65741.7	65811.4	1674.0	NL	-1078	1078	0	1525	90	315	NW	146.7	1207.8	42.2	30.5	8.2	1.4
54-821-ST	65709.9	65779.6	1713.6	WU													
54-821-ST	65747.7	65796.2	1713.6	EU													
54-821-ST	65720.5	65769.0	1713.6	SU													
54-821-ST	65737.1	65806.8	1713.6	NU	x	y	z	L	s-face-dip	s-face-D.dir	S.Face	per.	Area	S_Hgt.	L	HR	H/L
56-695-ST	65774.8	65653.4	1630.0	WL	374	517	271	693	67	36	NE	121.8	693.4	45.7	15.2	5.7	3.0
56-695-ST	65812.2	65669.6	1630.0	EL	665	-665	0	941	90	135	SE	146.6	1232.6	43.5	29.3	8.4	1.5
56-695-ST	65786.5	65643.9	1630.0	SL	-594	-297	-14	664	91	243	SW	115.2	650.5	42.0	15.1	5.6	2.8

56-695-ST	65799.8	65678.4	1630.0	NL	-446	446	0	630	90	315	NW	138.1	1056.4	42.7	25.2	7.7	1.7
56-695-ST	65776.5	65655.1	1672.0	WU													
56-695-ST	65799.4	65656.8	1672.0	EU													
56-695-ST	65783.5	65640.9	1672.0	SU													
56-695-ST	65787.1	65665.7	1672.0	NU	x	y	z	L	s-face-dip	s-face-D.dir	S.Face	per.	Area	S_Hgt.	L	HR	H/L
56-705-ST	65773.0	65672.8	1629.0	WL	426	486	292	709	66	41	NE	124.5	708.8	47.2	15.0	5.7	3.1
56-705-ST	65801.3	65679.9	1629.0	EL	639	-639	0	903	90	135	SE	140.6	1053.2	45.7	24.5	7.5	1.9
56-705-ST	65781.5	65660.1	1629.0	SL	-456	-456	-203	676	107	225	SW	120.5	682.5	45.1	15.1	5.7	3.0
56-705-ST	65790.7	65690.5	1629.0	NL	-608	608	0	860	90	315	NW	138.0	967.7	46.4	22.5	7.0	2.1
56-705-ST	65762.4	65662.2	1672.0	WU													
56-705-ST	65787.9	65666.5	1672.0	EU													
56-705-ST	65773.0	65651.6	1672.0	SU													
56-705-ST	65776.5	65676.4	1672.0	NU	x	y	z	L	s-face-dip	s-face-D.dir	S.Face	per.	Area	S_Hgt.	L	HR	H/L
56-735-ST	65747.1	65689.5	1628.0	WL	443	473	330	727	63	43	NE	127.0	727.5	48.5	15.0	5.7	3.2
56-735-ST	65780.4	65701.6	1628.0	EL	581	-580	0	821	90	135	SE	147.8	1214.1	45.0	28.1	8.2	1.6
56-735-ST	65754.1	65675.3	1628.0	SL	-382	-535	-108	666	99	216	SW	119.0	681.7	43.8	15.1	5.7	2.9
56-735-ST	65770.0	65712.4	1628.0	NL	-642	642	0	907	90	315	NW	146.6	1153.5	46.3	26.7	7.9	1.7
56-735-ST	65739.3	65681.8	1671.2	WU													
56-735-ST	65765.1	65686.4	1671.2	EU													
56-735-ST	65751.7	65672.9	1671.2	SU													
56-735-ST	65754.2	65696.6	1671.2	NU	x	y	z	L	s-face-dip	s-face-D.dir	S.Face	per.	Area	S_Hgt.	L	HR	H/L
56-781-ST	65764.4	65770.2	1630.0	WL	472	472	0	667	90	45	NE	119.0	667.4	44.5	15.0	5.6	3.0
56-781-ST	65792.1	65776.7	1630.0	EL	635	-887	0	1091	90	144	SE	138.1	1091.4	44.5	24.5	7.9	1.8
56-781-ST	65772.2	65762.4	1630.0	SL	-346	-346	0	490	90	225	SW	111.0	489.6	44.5	11.0	4.4	4.0
56-781-ST	65781.5	65787.3	1630.0	NL	-761	762	0	1077	90	315	NW	137.4	1077.1	44.5	24.2	7.8	1.8
56-781-ST	65764.4	65770.2	1674.5	WU													
56-781-ST	65792.1	65776.7	1674.5	EU													
56-781-ST	65772.2	65762.4	1674.5	SU													
56-781-ST	65781.5	65787.3	1674.5	NU	x	y	z	L	s-face-dip	s-face-D.dir	S.Face	per.	Area	S_Hgt.	L	HR	H/L
58-695-ST	65801.1	65679.7	1552.5	WL	488	349	241	646	68	54	NE	109.2	486.2	43.0	11.4	4.5	3.8
58-695-ST	65827.9	65695.9	1552.5	EL	837	-837	-112	1189	95	135	SE	147.3	1209.8	43.2	30.1	8.2	1.4
58-695-ST	65812.2	65669.6	1552.5	SL	-349	-488	-273	659	115	216	SW	117.1	655.9	43.4	15.1	5.6	2.9
58-695-ST	65823.9	65702.5	1552.5	NL	-976	976	0	1380	90	315	NW	153.7	1325.1	43.2	33.6	8.6	1.3
58-695-ST	65787.6	65666.2	1591.9	WU													

58-695-ST	65821.2	65678.6	1591.9	EU												
58-695-ST	65800.0	65657.4	1591.9	SU												
58-695-ST	65812.3	65690.9	1591.9	NU	x	y	z	L	s-face-dip	s-face-D.dir	S.Face	per.	Area	S_Hgt.	L	HR	H/L
60-695-ST	65813.6	65692.2	1511.6	WL	268	165	43	318	82	58	NE	108.5	520.1	41.4	12.6	4.8	3.3
60-695-ST	65837.0	65691.6	1511.6	EL	1105	-372	227	1188	79	109	SE	123.6	718.0	43.1	16.3	5.8	2.6
60-695-ST	65832.0	65689.3	1511.6	SL	-444	-721	-431	951	117	212	SW	131.3	894.4	45.9	19.3	6.8	2.4
60-695-ST	65828.1	65706.7	1511.6	NL	-929	929	0	1314	90	315	NW	138.5	1075.6	42.5	26.4	7.8	1.6
60-695-ST	65801.1	65679.7	1552.5	WU												
60-695-ST	65827.9	65695.9	1552.5	EU												
60-695-ST	65818.8	65668.8	1552.5	SU												
60-695-ST	65823.9	65702.5	1552.5	NU	x	y	z	L	s-face-dip	s-face-D.dir	S.Face	per.	Area	S_Hgt.	L	HR	H/L
60-725-ST	65804.5	65718.1	1510.1	WL	277	507	177	604	73	29	NE	108.4	594.2	38.8	15.2	5.5	2.6
60-725-ST	65834.0	65733.8	1510.1	EL	675	-675	-68	957	94	135	SE	133.9	1083.7	37.7	29.0	8.1	1.3
60-725-ST	65807.7	65715.0	1510.1	SL	-393	-393	-52	558	95	225	SW	94.6	362.6	37.2	9.8	3.8	3.8
60-725-ST	65823.4	65744.5	1510.1	NL	-560	560	-56	794	94	315	NW	130.9	1000.2	38.1	26.8	7.6	1.4
60-725-ST	65798.4	65719.4	1547.1	WU												
60-725-ST	65827.2	65727.1	1547.1	EU												
60-725-ST	65809.0	65708.8	1547.1	SU												
60-725-ST	65813.5	65734.6	1547.1	NU	x	y	z	L	s-face-dip	s-face-D.dir	S.Face	per.	Area	S_Hgt.	L	HR	H/L
60-755-ST	65777.4	65740.9	1511.7	WL	404	461	274	671	66	41	NE	119.6	674.4	44.7	15.1	5.6	3.0
60-755-ST	65809.5	65751.8	1511.7	EL	375	-375	0	530	90	135	SE	129.1	884.2	42.0	21.7	6.8	1.9
60-755-ST	65788.0	65730.3	1511.7	SL	-432	-432	-24	612	92	225	SW	111.6	611.8	40.8	15.0	5.5	2.7
60-755-ST	65797.1	65760.6	1511.7	NL	-346	346	0	489	90	315	NW	125.1	813.2	41.9	20.0	6.5	2.1
60-755-ST	65776.3	65739.7	1552.5	WU												
60-755-ST	65796.1	65738.3	1552.5	EU												
60-755-ST	65786.9	65729.1	1552.5	SU												
60-755-ST	65784.8	65748.2	1552.5	NU	x	y	z	L	s-face-dip	s-face-D.dir	S.Face	per.	Area	S_Hgt.	L	HR	H/L
60-756-ST	65763.5	65727.0	1510.5	WL	435	435	20	616	88	45	NE	112.1	615.4	41.0	15.0	5.5	2.7
60-756-ST	65787.9	65730.1	1510.5	EL	713	-716	0	1010	90	135	SE	132.6	1037.5	41.0	25.3	7.8	1.6
60-756-ST	65769.5	65711.8	1510.5	SL	-435	-435	-49	617	95	225	SW	113.9	646.1	41.1	15.3	5.7	2.7
60-756-ST	65777.3	65740.7	1510.5	NL	-713	716	0	1010	90	315	NW	126.6	904.0	41.2	22.0	7.1	1.9
60-756-ST	65758.9	65722.4	1551.5	WU												
60-756-ST	65787.0	65729.2	1551.5	EU												
60-756-ST	65769.5	65711.8	1551.5	SU												

60-756-ST	**65776.4**	**65739.8**	**1551.5**	**NU**	**x**	**y**	**z**	**L**	**s-face-dip**	**s-face-D.dir**	**S.Face**	**per.**	**Area**	**S_Hgt.**	**L**	**HR**	**H/L**
60-791-ST	**65767.0**	**65794.2**	**1511.3**	**WL**	435	435	240	660	69	45	NE	118.0	660.1	44.0	15.0	**5.6**	**2.9**
60-791-ST	**65794.6**	**65800.6**	**1511.3**	**EL**	554	-554	0	783	90	135	SE	129.7	885.4	43.2	21.6	**6.8**	**2.0**
60-791-ST	**65777.6**	**65783.6**	**1511.3**	**SL**	-435	-435	-165	637	105	225	SW	114.9	636.7	42.5	15.0	**5.5**	**2.8**
60-791-ST	**65784.0**	**65811.2**	**1511.3**	**NL**	-554	554	0	783	90	315	NW	129.7	885.7	43.2	21.6	**6.8**	**2.0**
60-791-ST	**65759.2**	**65786.4**	**1552.3**	**WU**													
60-791-ST	**65783.3**	**65789.3**	**1552.3**	**EU**													
60-791-ST	**65769.8**	**65775.8**	**1552.3**	**SU**													
60-791-ST	**65772.7**	**65799.9**	**1552.3**	**NU**													

Table C.2 Summary of fault database relating fault to stope surface

STOPE	X	Y	Z	Point	F-faults	Fault-dip	Dip_Direct.	Alpha	L_Left	L_Mid	L_Right	Mid_right	Mid_Left	Mid_Mid	U-Right	U_mid	U_left	Crit._Dist.
47-630-ST	65763.2	65568.6	1902.5	WL	NE wall	62	49	22	-38.0	-31.1	-24.2	-17.4	-25.2	-21.3	-10.6	-11.5	-12.5	10.6
47-630-ST	65778.1	65557.4	1902.5	EL	SE wall													
47-630-ST	65776.0	65555.3	1902.5	SL	SW wall	30	245	77	-29.2	-30.7	-32.2	-5.5	-0.9	-3.2	21.3	24.4	27.5	intersect
47-630-ST	65777.1	65582.5	1902.5	NL	NW wall	30	245	80	-38.4	-33.8	-29.2	-0.9	-9.9	-5.4	27.5	23.0	18.5	intersect
47-630-ST	65752.9	65558.3	1960.0	WU														
47-630-ST	65772.3	65561.6	1960.0	EU														
47-630-ST	65770.1	65550.5	1960.0	SU														
47-630-ST	65766.3	65571.7	1960.0	NU	F-faults	Fault-dip	Dip_Direct.	Alpha	L_Left	L_Mid	L_Right	Mid_right	Mid_Left	Mid_Mid	U-Right	U_mid	U_left	Crit._Dist.
47-645-ST	65761.5	65582.8	1902.3	WL	NE wall	62	50	9	-10.1	-9.4	-8.8	-4.3	-5.0	-4.6	0.2	0.2	0.1	intersect
47-645-ST	65779.2	65584.6	1902.3	EL	SE wall	62	20	112	-14.9	-11.8	-8.7	-2.8	-9.0	-5.9	3.2	0.1	-3.0	intersect
47-645-ST	65767.5	65573.0	1902.3	SL	SW wall	30	257	75	-3.7	-4.6	-5.6	24.1	26.1	25.1	53.7	54.8	55.9	intersect
47-645-ST	65772.9	65594.3	1902.3	NL	NW wall													
47-645-ST	65748.9	65574.2	1963.0	WU														
47-645-ST	65764.5	65569.9	1963.0	EU														
47-645-ST	65756.4	65561.8	1963.0	SU														
47-645-ST	65755.4	65580.7	1963.0	NU	F-faults	Fault-dip	Dip_Direct.	Alpha	L_Left	L_Mid	L_Right	Mid_right	Mid_Left	Mid_Mid	U-Right	U_mid	U_left	Crit._Dist.
47-690-ST	65727.3	65605.9	1905.2	WL	NE wall	65	52	5	-0.4	-0.3	-0.2	0.7	-0.1	0.3	1.6	0.9	0.3	intersect
47-690-ST	65759.2	65616.6	1905.2	EL	NE wall	70	41	16	-10.3	-8.9	-7.5	-8.5	-12.0	-10.3	-9.6	-11.6	-13.6	7.5
47-690-ST	65734.9	65592.3	1905.2	SL	SE wall													
47-690-ST	65750.0	65628.6	1905.2	NL	SW wall													
47-690-ST	65732.8	65611.4	1945.7	WU	NW wall													
47-690-ST	65746.3	65603.7	1945.7	EU														
47-690-ST	65743.4	65600.8	1945.7	SU														
47-690-ST	65738.0	65616.6	1945.7	NU	F-faults	Fault-dip	Dip_Direct.	Alpha	L_Left	L_Mid	L_Right	Mid_right	Mid_Left	Mid_Mid	U-Right	U_mid	U_left	Crit. Dist.
47-725-ST	65719.7	65652.0	1899.9	WL	NE wall	75	39	10	-61.9	-62.8	-63.7	-65.7	66.6	-66.1	-67.6	-69.4	-71.2	62.8
47-725-ST	65741.1	65640.9	1899.9	EL	NE wall	60	39	12	-6.8	-7.7	23.2	-1.7	-2.5	-2.1	5.0	3.4	1.8	intersect
47-725-ST	65727.0	65626.8	1899.9	SL	SE wall	52	39	19	-19.1	-4.2	14.0	6.3	5.6	5.9	17.6	16.1	9.9	intersect
47-725-ST	65721.8	65654.2	1899.9	NL	SW wall													
47-725-ST	65701.0	65638.3	1963.3	WU	NW wall													
47-725-ST	65722.2	65622.0	1963.3	EU														
47-725-ST	65718.0	65617.8	1963.3	SU														

47-725-ST	65704.2	65641.4	1963.3	NU	F-faults	Fault-dip	Dip_Direct.	Alpha	L_Left	L_Mid	L_Right	Mid_right	Mid_Left	Mid_Mid	U-Right	U_mid	U_left	Crit._Dist.
47-725-ST	65720	65652	1900	WL														
47-725-ST	65741	65641	1900	EL														
47-725-ST	65727	65627	1900	SL	SW wall	75	39	169	9.4	2.1	-5.2	-3.1	6.7	1.8	-1.0	1.5	4.0	intersect
47-725-ST	65722	65654	1900	NL	NWwall	75	39	85	12.2	10.8	9.4	6.7	10.3	8.5	4.0	6.2	8.4	4.0
47-725-ST	65701	65638	1963	WU														
47-725-ST	65722	65622	1963	EU														
47-725-ST	65718	65618	1963	SU														
47-725-ST	65704	65641	1963	NU														
47-821-ST	65685	65754	1904	WL	F-faults	Fault-dip	Dip_Direct.	Alpha	L_Left	L_Mid	L_Right	Mid_right	Mid_Left	Mid_Mid	U-Right	U_mid	U_left	Crit._Dist.
47-821-ST	65713	65761	1904	EL	SE wall	88	20	65	8.1	18.4	28.6	29.7	7.1	18.4	30.7	18.4	6.1	6.1
47-821-ST	65695	65744	1904	SL	SEwall	65	45	90	55.3	54.0	52.7	65.3	42.7	54.0	77.9	54.0	30.1	30.1
47-821-ST	65703	65772	1904	NL	NW wall	50	29	78	-14.3	-23.5	-32.7	-13.6	4.8	-4.4	5.5	14.7	23.9	intersect
47-821-ST	65685	65754	1964	WU	NW wall	75	30	75	-10.4	-14.1	-6.1	-18.1	5.2	-6.4	-10.4	1.3	-25.8	intersect
47-821-ST	65713	65761	1964	EU	NW wall	85	197	118	11.9	10.9	28.8	24.4	2.5	13.4	27.0	16.0	6.7	2.5
47-821-ST	65695	65744	1964	SU	NWwall	88	205	110	16.2	-2.7	-14.4	10.0	-13.4	-1.7	11.1	-0.6	14.1	intersect
47-821-ST	65703	65772	1964	NU	F-faults	88	20	65	30.7	17.4	8.1	7.1	29.7	18.4	8.1	19.4	28.6	7.1
47-821-ST	65685	65754	1904	WL	NWwall	70	35	80	-29.5	-18.0	11.6	-19.4	3.7	-7.8	-9.2	2.4	-9.2	intersect
47-821-ST	65713	65761	1904	EL	SE wall	50	29	102	-36.0	-26.8	-17.6	1.5	-16.9	-7.7	20.7	11.4	2.2	intersect
47-821-ST	65695	65744	1904	SL	SE wall	75	30	104	-2.9	-18.2	-29.9	1.2	-22.2	-10.5	8.9	-2.8	12.5	intersect
47-821-ST	65703	65772	1904	NL	SE wall	88	205	70	11.1	2.3	-14.4	-8.4	15.1	3.3	-7.4	4.4	48.3	intersect
47-821-ST	65685	65754	1964	WU	SE wall	88	20	115	24.6	11.2	8.1	23.6	0.8	12.2	24.6	13.2	-45.2	intersect
47-821-ST	65713	65761	1964	EU	SE wall	85	197	62	33.9	17.7	11.9	9.3	31.4	20.3	11.9	22.9	71.3	9.3
47-821-ST	65695	65744	1964	SU	SE wall	70	35	99	25.8	-8.4	0.3	13.3	-9.9	1.7	23.5	11.9	-95.4	intersect
47-821-ST	65703	65772	1964	NU	F-faults	Fault-dip	Dip_Direct.	Alpha	L_Left	L_Mid	L_Right	Mid_right	Mid_Left	Mid_Mid	U-Right	U_mid	U_left	Crit._Dist.
48-690-ST	65744.5	65623.1	1862.0	WL	NE wall	75	32	17	-10.2	-8.5	-6.9	-8.8	-12.4	-10.6	-10.8	-12.7	-14.6	6.9
48-690-ST	65770.9	65628.3	1862.0	EL	NE wall	65	41	6	-15.3	-14.8	-2.4	-13.8	-15.0	-14.4	-13.2	-13.9	-14.7	2.4
48-690-ST	65755.2	65612.5	1862.0	SL	NE wall	64	56	8	0.6	-0.7	-2.0	-1.0	1.3	0.1	-0.1	0.9	1.9	intersect
48-690-ST	65760.3	65638.9	1862.0	NL	SE wall													
48-690-ST	65733.2	65611.8	1890.2	WU	SW wall													
48-690-ST	65762.1	65619.5	1890.2	EU	NW wall													
48-690-ST	65743.9	65601.2	1890.2	SU														
48-690-ST	65751.9	65630.5	1890.2	NU	F-faults	Fault-dip	Dip_Direct.	Alpha	L_Left	L_Mid	L_Right	Mid_right	Mid_Left	Mid_Mid	U-Right	U_mid	U_left	Crit._Dist.
48-725-ST	65723.1	65639.2	1859.0	WL	NE wall	75	31	14	-6.6	-4.8	-3.0	-3.3	-6.8	-5.1	-3.6	-5.4	-7.1	3.0

48-725-ST	65749.6	65649.3	1859.0	EL	NE wall	55	41	19	-11.1	-10.6	13.3	-3.3	-4.2	-3.7	3.5	3.1	2.7	intersect
48-725-ST	65735.1	65634.9	1859.0	SL	SE wall													
48-725-ST	65739.0	65660.0	1859.0	NL	SW wall													
48-725-ST	65723.8	65644.8	1899.9	WU	NW wall													
48-725-ST	65741.1	65640.9	1899.9	EU														
48-725-ST	65727.0	65626.8	1899.9	SU														
48-725-ST	65730.5	65651.6	1899.9	NU	F-faults	Fault-dip	Dip_Direct.	Alpha	L_Left	L_Mid	L_Right	Mid_right	Mid_Left	Mid_Mid	U-Right	U_mid	U_left	
48-782-ST	65751	65757	1905	NU	NEwall	80	175	128	-5.2	-13.9	6.1	-14.5	-3.2	-8.9	-9.6	-3.9	2.5	intersect
48-782-ST	65738	65744	1860	WL	NE wall	65	357	51	-11.5	-6.4	-1.4	7.1	-3.0	2.1	15.6	10.6	5.5	intersect
48-782-ST	65764	65749	1860	EL	NE wall	80	175	128	6.1	-13.9	2.5	-14.5	-3.2	-8.9	-9.6	-3.9	13.8	intersect
48-782-ST	65748	65733	1860	SL	SW wall	55	61	103	39.7	20.2	36.3	34.9	31.5	33.2	47.9	46.2	62.8	20.2
48-782-ST	65754	65760	1860	NL	SW wall	70	68	112	26.4	23.6	36.4	34.2	28.7	31.4	41.9	39.2	41.9	23.6
48-782-ST	65738	65744	1905	WU	NWwall	70	25	71	8.1	-1.9	-11.9	-4.1	14.3	5.1	3.7	12.1	20.5	intersect
48-782-ST	65762	65747	1905	EU														
48-782-ST	65748	65733	1905	SU														
48-782-ST	65751	65757	1905	NU	F-faults	Fault-dip	Dip_Direct.	Alpha	L_Left	L_Mid	L_Right	Mid_right	Mid_Left	Mid_Mid	U-Right	U_mid	U_left	Crit._Dist.
48-821-ST	65688.8	65758.3	1858.6	WL	SE wall	50	29	106	14.5	-4.4	10.3	16.2	-1.8	7.2	27.3	18.8	-99.6	intersect
48-821-ST	65718.5	65766.8	1858.6	EL	SE wall	75	30	106	-6.1	-4.5	-10.9	9.1	-13.8	-2.4	10.5	-0.2	-101.0	intersect
48-821-ST	65700.1	65748.4	1858.6	SL	NW wall	50	29	66	6.8	-2.3	-11.4	1.6	18.5	10.1	14.6	22.5	30.3	intersect
48-821-ST	65712.6	65772.2	1858.6	NL	NW wall	75	30	61	9.7	-1.8	-13.4	-9.5	12.0	1.2	-5.7	4.3	14.3	intersect
48-821-ST	65685.7	65755.3	1904.0	WU	NW wall	85	197	132	-1.3	8.8	18.9	22.7	3.9	13.3	26.6	17.9	9.1	intersect
48-821-ST	65715.8	65757.8	1904.0	EU														
48-821-ST	65699.5	65741.5	1904.0	SU														
48-821-ST	65706.2	65767.3	1904.0	NU	F-faults	Fault-dip	Dip_Direct.	Alpha	L_Left	L_Mid	L_Right	Mid_right	Mid_Left	Mid_Mid	U-Right	U_mid	U_left	Crit._Dist.
48-821-ST	65689	65758	1859	WL	NE wall													
48-821-ST	65718	65767	1859	EL	SE wall													
48-821-ST	65700	65748	1859	SL	SW wall	88	20	155	11.7	9.0	6.3	3.7	10.6	7.1	1.2	5.3	9.4	1.2
48-821-ST	65713	65772	1859	NL	NW wall	65	45	161	62.9	38.9	62.6	46.5	46.1	46.3	53.7	53.7	74.6	38.9
48-821-ST	65686	65755	1904	WU														
48-821-ST	65716	65758	1904	EU														
48-821-ST	65699	65742	1904	SU														
48-821-ST	65706	65767	1904	NU	F-faults	Fault-dip	Dip_Direct.	Alpha	L_Left	L_Mid	L_Right	Mid_right	Mid_Left	Mid_Mid	U-Right	U_mid	U_left	Crit._Dist.
49-665-ST	65764.9	65622.2	1819.5	WL	NE wall	64	55	13	-2.4	-4.2	-6.0	0.0	1.0	0.5	6.1	5.3	4.5	intersect
49-665-ST	65791.9	65616.4	1819.5	EL	NE wall	65	41	21	-17.8	-17.1	-16.3	-10.6	-14.8	-12.7	-5.0	-8.4	-11.9	5.0

49-665-ST	65777.0	65601.6	1819.5	SL	SE wall												
49-665-ST	65775.5	65632.8	1819.5	NL	SW wall												
49-665-ST	65760.3	65618.3	1863.5	WU	NW wall												
49-665-ST	65782.0	65606.5	1863.5	EU													
49-665-ST	65777.0	65601.6	1863.5	SU													
49-665-ST	65769.7	65627.3	1863.5	NU	F-faults	Fault-dip	Dip_Direct.	Alpha	L_Left	L_Mid	L_Right	Mid_right	Mid_Left	Mid_Mid	U-Right	U_mid	U_left	Crit._Dist.
49-690-ST	65754.5	65633.1	1820.7	WL	NE wall	65	45	17	-17.2	-16.1	-15.0	-9.6	-10.6	-10.1	-4.1	-4.1	-4.1	4.1
49-690-ST	65774.4	65631.8	1820.7	EL	NE wall	65	45	17	-25.3	-24.3	-5.8	-17.8	-18.8	-18.3	-12.3	-12.3	-12.3	5.8
49-690-ST	65764.8	65622.2	1820.7	SL	NE wall	64	50	18	-5.9	-5.5	-5.0	0.8	1.0	0.9	6.6	7.2	7.8	intersect
49-690-ST	65765.4	65644.0	1820.7	NL	SE wall													
49-690-ST	65744.5	65623.1	1862.0	WU	SW wall													
49-690-ST	65770.9	65628.3	1862.0	EU	NW wall													
49-690-ST	65755.2	65612.5	1862.0	SU														
49-690-ST	65760.3	65638.9	1862.0	NU	F-faults	Fault-dip	Dip_Direct.	Alpha	L_Left	L_Mid	L_Right	Mid_right	Mid_Left	Mid_Mid	U-Right	U_mid	U_left	Crit._Dist.
49-705-ST	65737.1	65636.8	1819.6	WL	NE wall	65	45	10	-14.3	-13.3	-12.3	-9.2	-10.2	-9.7	-6.1	-6.1	-6.1	6.1
49-705-ST	65766.0	65644.6	1819.6	EL	NE wall	65	42	11	-22.7	-21.3	-3.6	-16.9	-18.6	-17.7	-13.8	-14.1	-14.5	3.6
49-705-ST	65751.2	65629.8	1819.6	SL	NE wall	65	45	10	-20.8	-19.8	-18.8	-15.7	-16.7	-16.2	-12.7	-12.7	-12.7	12.7
49-705-ST	65757.0	65656.7	1819.6	NL	SE wall													
49-705-ST	65735.3	65635.0	1858.2	WU	SW wall	70	45	70	57.5	57.5	57.5	83.4	81.6	82.5	109.3	107.5	105.6	57.5
49-705-ST	65759.7	65638.3	1858.2	EU	NW wall													
49-705-ST	65744.1	65622.7	1858.2	SU														
49-705-ST	65749.1	65648.8	1858.2	NU	F-faults	Fault-dip	Dip_Direct.	Alpha	L_Left	L_Mid	L_Right	Mid_right	Mid_Left	Mid_Mid	U-Right	U_mid	U_left	Crit._Dist.
49-705-ST	65737	65637	1820	WL	NE wall													
49-705-ST	65766	65645	1820	EL	SE wall													
49-705-ST	65751	65630	1820	SL	SW wall	70	45	166	28.3	30.7	33.1	35.0	33.8	34 4	36.8	38.0	39.2	28.3
49-705-ST	65757	65657	1820	NL	NW wall													
49-705-ST	65735	65635	1858	WU														
49-705-ST	65760	65638	1858	EU														
49-705-ST	65744	65623	1858	SU														
49-705-ST	65749	65649	1858	NU	F-faults	Fault-dip	Dip_Direct.	Alpha	L_Left	L_Mid	L_Right	Mid_right	Mid_Left	Mid_Mid	U-Right	U_mid	U_left	Crit._Dist.
49-720-ST	65726.3	65647.2	1820.0	WL	NE wall	65	45	17	-3.2	-5.3	-7.3	-1.3	1.6	0.1	4.6	5.5	6.4	intersect
49-720-ST	65755.6	65655.3	1820.0	EL	NE wall	65	42	16	-13.2	-14.7	0.2	-10.5	-8.3	-9.4	-4.7	-4.1	-3.5	intersect
49-720-ST	65736.9	65636.6	1820.0	SL	NE wall	65	45	17	-22.6	-24.7	-26.7	-20.8	-17.8	-19.3	-14.8	-13.9	-13.0	13.0
49-720-ST	65738.3	65666.3	1820.0	NL	SE wall													

49-720-ST	65722.7	65636.6	1859.0	WU	SW wall												
49-720-ST	65750.3	65650.0	1859.0	EU	NW wall												
49-720-ST	65729.8	65629.5	1859.0	SU													
49-720-ST	65739.7	65657.8	1859.0	NU	F-faults	Fault-dip	Dip_Direct.	Alpha	L_Left	L_Mid	L_Right	Mid_right	Mid_Left	Mid_Mid	U-Right	U_mid	U_left	Crit._Dist.
49-720-ST	65726	65647	1820	WL														
49-720-ST	65756	65655	1820	EL														
49-720-ST	65737	65637	1820	SL	SW wall	71	49	174	2.3	2.8	3.3	5.0	4.1	4.6	6.6	6.3	5.9	2.3
49-720-ST	65738	65666	1820	NL														
49-720-ST	65723	65637	1859	WU														
49-720-ST	65750	65650	1859	EU														
49-720-ST	65730	65630	1859	SU														
49-720-ST	65740	65658	1859	NU	F-faults	Fault-dip	Dip_Direct.	Alpha	L_Left	L_Mid	L_Right	Mid_right	Mid_Left	Mid_Mid	U-Right	U_mid	U_left	Crit._Dist.
49-731-ST	65745.7	65688.1	1823.2	WL	NE wall	65	42	4	36.3	38.4	40.6	40.9	38.5	39.7	41.3	41.0	40.6	36.3
49-731-ST	65783.6	65704.8	1823.2	EL	SE wall	71	42	93	-34.1	-18.4	-2.7	-2.7	-32.1	-17.4	-2.8	-16.4	-30.1	2.7
49-731-ST	65760.0	65681.2	1823.2	SL	SW wall	66	45	166	-45.0	-42.6	-40.2	-36.4	-38.8	-37.6	-32.6	-32.6	-32.6	32.6
49-731-ST	65775.7	65718.1	1823.2	NL	SW wall	67	45	167	-25.4	-23.0	-20.6	-17.1	-19.6	-18.3	-13.7	-13.7	-13.7	13.7
49-731-ST	65743.0	65685.1	1862.7	WU	SW wall													
49-731-ST	65774.0	65694.9	1862.7	EU	NW wall													
49-731-ST	65753.6	65674.5	1862.7	SU														
49-731-ST	65763.4	65705.5	1862.7	NU	F-faults	Fault-dip	Dip_Direct.	Alpha	L_Left	L_Mid	L_Right	Mid_right	Mid_Left	Mid_Mid	U-Right	U_mid	U_left	Crit._Dist.
49-731-ST	65746	65688	1823	WL														
49-731-ST	65784	65705	1823	EL														
49-731-ST	65760	65681	1823	SL														
49-731-ST	65776	65718	1823	NL	NWwall	71	42	87	1.7	-18.3	-38.4	-33.9	-0.1	-17.0	-29.3	-15.7	-2.0	0.1
49-731-ST	65743	65685	1863	WU														
49-731-ST	65774	65695	1863	EU														
49-731-ST	65754	65675	1863	SU														
49-731-ST	65763	65706	1863	NU	F-faults	Fault-dip	Dip_Direct.	Alpha	L_Left	L_Mid	L_Right	Mid_right	Mid_Left	Mid_Mid	U-Right	U_mid	U_left	Crit._Dist.
49-782-ST	65743.2	65749.1	1822.5	WL	NE wall	70	45	8	-33.0	-33.0	-33.0	-30.5	-30.5	-30.5	-28.0	-28.0	-28.0	28.0
49-782-ST	65770.1	65754.8	1822.5	EL	SE wall													
49-782-ST	65753.8	65738.5	1822.5	SL	SW wall													
49-782-ST	65759.5	65765.4	1822.5	NL	NW wall													
49-782-ST	65737.7	65743.6	1859.9	WU														
49-782-ST	65764.3	65749.0	1859.9	EU														

49-782-ST	65748.3	65733.0	1859.9	SU													
49-782-ST	65753.7	65759.6	1859.9	NU	F-faults	Fault-dip	Dip_Direct.	Alpha	L_Left	L_Mid	L_Right	Mid_right	Mid_Left	Mid_Mid	U-Right	U_mid	U_left	Crit._Dist.
49-821-ST	65696.2	65765.7	1821.0	WL	NE wall	65	45	20	-21.9	-32.7	-21.9	-61.4	-61.9	-61.6	-90.5	-90.5	-8.7	8.7
49-821-ST	65720.6	65768.9	1821.0	EL	SE wall	25	221	88	4.0	42.1	42.1	25.5	25.3	25.4	8.9	8.7	42.1	4.0
49-821-ST	65706.8	65755.1	1821.0	SL	SW wall	88	20	155	58.8	55.6	52.5	48.8	54.7	51.8	45.2	47.9	50.6	45.2
49-821-ST	65710.0	65779.5	1821.0	NL	SW wall	70	45	174	18.7	18.7	18.7	20.6	20.2	20.4	22.6	22.1	21.6	18.7
49-821-ST	65688.8	65758.3	1858.6	WU	NWwall													
49-821-ST	65718.5	65766.8	1858.6	EU														
49-821-ST	65700.1	65748.4	1858.6	SU														
49-821-ST	65707.4	65777.0	1858.6	NU	F-faults	Fault-dip	Dip_Direct.	Alpha	L_Left	L_Mid	L_Right	Mid_right	Mid_Left	Mid_Mid	U-Right	U_mid	U_left	Crit._Dist.
49-821-ST	65696	65766	1821	WL	NEwall	65	45	20	-21.9	-21.9	-21.9	-15.6	-15.3	-15.4	-9.3	-9.0	-8.7	8.7
49-821-ST	65721	65769	1821	EL	SEwall													
49-821-ST	65707	65755	1821	SL	SWwall													
49-821-ST	65710	65780	1821	NL	NWwall	50	17	69	21.0	14.4	7.8	16.4	31.9	24.1	24.9	33.8	42.7	7.8
49-821-ST	65689	65758	1859	WU	NWwall	75	30	75	9.3	18.5	23.9	9.4	30.8	20.1	9.3	21.6	-85.5	intersect
49-821-ST	65718	65767	1859	EU		70	35	70	32.7	16.1	4.6	8.6	29.8	19.2	10.2	22.4	-61.9	intersect
49-821-ST	65700	65748	1859	SU														
49-821-ST	65707	65777	1859	NU	F-faults	Fault-dip	Dip_Direct.	Alpha	L_Left	L_Mid	L_Right	Mid_right	Mid_Left	Mid_Mid	U-Right	U_mid	U_left	Crit._Dist.
51-645-ST	65782.9	65608.3	1779.7	WL	NE wall													
51-645-ST	65799.5	65604.4	1779.7	EL	SE wall													
51-645-ST	65798.6	65603.5	1779.7	SL	SW wall													
51-645-ST	65796.2	65621.6	1779.7	NL	NW wall													
51-645-ST	65776.4	65601.8	1819.7	WU														
51-645-ST	65798.3	65609.5	1819.7	EU														
51-645-ST	65790.5	65595.4	1819.7	SU														
51-645-ST	65791.2	65616.6	1819.7	NU	F-faults	Fault-dip	Dip_Direct.	Alpha	L_Left	L_Mid	L_Right	Mid_right	Mid_Left	Mid_Mid	U-Right	U_mid	U_left	Crit._Dist.
51-665-ST	65771.5	65613.4	1780.5	WL	NE wall	65	45	15	-26.6	-26.5	-26.5	-21.4	-21.5	-21.4	-16.3	-16.3	-16.4	16.3
51-665-ST	65796.2	65621.6	1780.5	EL	SE wall													
51-665-ST	65782.9	65608.3	1780.5	SL	SW wall													
51-665-ST	65788.0	65629.9	1780.5	NL	NW wall													
51-665-ST	65776.0	65617.9	1819.5	WU														
51-665-ST	65791.2	65616.6	1819.5	EU														
51-665-ST	65776.4	65601.8	1819.5	SU														
51-665-ST	65783.1	65625.0	1819.5	NU	F-faults	Fault-dip	Dip_Direct.	Alpha	L_Left	L_Mid	L_Right	Mid_right	Mid_Left	Mid_Mid	U-Right	U_mid	U_left	Crit._Dist.

51-675-SLF	65769.4	65626.8	1800.0	WL	NE wall													
51-675-SLF	65777.2	65619.1	1800.0	EL	SE wall													
51-675-SLF	65777.2	65619.1	1800.0	SL	SW wall													
51-675-SLF	65771.1	65628.5	1800.0	NL	NW wall													
51-675-SLF	65764.1	65621.5	1820.7	WU	F-faults	Fault-dip	Dip_Direct.	Alpha	L_Left	L_Mid	L_Right	Mid_right	Mid_Left	Mid_Mid	U-Right	U_mid	U_left	Crit._Dist.
51-675-SLF	65776.0	65617.9	1820.7	EU	NE wall	25	217	105	-1.5	-5.3	5.3	16.7	17.3	17.0	38.9	39.3	5.7	intersect
51-675-SLF	65771.9	65613.8	1820.7	SU	NE wall													
51-675-SLF	65765.3	65622.6	1820.7	NU	NE wall													
51-675-ST	65767.3	65624.7	1777.7	WL	NE wall	65	45	14	-17.0	-16.3	-15.7	-10.9	-11.9	-11.4	-6.2	-6.5	-6.8	6.2
51-675-ST	65788.0	65629.9	1780.5	EL	NEwall	64	47	88	-28.0	-6.6	-8.8	-1.0	-1.6	-1.3	4.1	4.0	-5.1	intersect
51-675-ST	65771.5	65613.4	1780.5	SL	SWwall													
51-675-ST	65782.2	65639.5	1777.7	NL	NW wall	64	47	92	-6.2	-15.6	-25.1	-16.9	-1.0	-9.0	-8.8	-2.4	4.1	intersect
51-675-ST	65765.3	65622.6	1820.7	WU														
51-675-ST	65783.1	65625.0	1819.5	EU														
51-675-ST	65776.0	65617.9	1819.5	SU														
51-675-ST	65775.4	65632.8	1820.7	NU	F-faults	Fault-dip	Dip_Direct.	Alpha	L_Left	L_Mid	L_Right	Mid_right	Mid_Left	Mid_Mid	U-Right	U_mid	U_left	Crit._Dist.
51-675-ST	65767	65625	1778	WL	NEwall													
51-675-ST	65788	65630	1781	EL	SEwall	64	47	88	-28.0	-17.5	-7.1	-1.6	-16.6	-9.1	3.8	-0.6	-5.1	intersect
51-675-ST	65772	65613	1781	SL	SWwall	58	78	62	-15.0	-21.0	-27.0	-14.4	-7.0	-10.7	-1.8	-0.4	1.0	intersect
51-675-ST	65782	65640	1778	NL	NWwall													
51-675-ST	65765	65623	1821	WU														
51-675-ST	65783	65625	1820	EU														
51-675-ST	65776	65618	1820	SU														
51-675-ST	65775	65633	1821	NU	F-faults	Fault-dip	Dip_Direct.	Alpha	L_Left	L_Mid	L_Right	Mid_right	Mid_Left	Mid_Mid	U-Right	U_mid	U_left	Crit._Dist.
51-690-ST	65761.2	65639.8	1777.7	WL	NE wall	25	310	85	-6.6	-3.4	-0.2	19.4	13.1	16.2	39.0	35.9	32.7	intersect
51-690-ST	65782.2	65639.5	1777.7	EL	SE wall	25	310	115	-5.8	-6.2	-6.6	13.1	13.7	13.4	32.7	33.0	33.2	intersect
51-690-ST	65766.3	65623.7	1777.7	SL	SW wall	25	310	94	0.2	-2.8	-5.8	13.7	19.9	16 8	33.2	36.4	39.5	intersect
51-690-ST	65770.6	65649.2	1777.7	NL	NW wall	25	310	65	-0.2	0.0	0.2	19.9	19.4	19.6	39.5	39.3	39.0	intersect
51-690-ST	65754.5	65633.1	1820.7	WU														
51-690-ST	65774.4	65631.8	1820.7	EU														
51-690-ST	65764.8	65622.2	1820.7	SU														
51-690-ST	65765.4	65644.0	1820.7	NU	F-faults	Fault-dip	Dip_Direct.	Alpha	L_Left	L_Mid	L_Right	Mid_right	Mid_Left	Mid_Mid	U-Right	U_mid	U_left	Crit._Dist.
51-705-ST	65749.3	65643.3	1780.0	WL	NE wall	65	50	17	-10.9	-10.5	-10.0	-4.3	-4.9	-4.6	1.3	1.2	1.1	intersect
51-705-ST	65772.0	65650.6	1780.0	EL	SE wall	88	53	6	-12.4	8.8	-19.3	6.7	6.7	6.7	4.4	4.6	-17.8	intersect

51-705-ST	65757.0	65635.6	1780.0	SL	SW wall												
51-705-ST	65765.8	65659.7	1780.0	NL	NW wall												
51-705-ST	65744.5	65638.5	1819.6	WU													
51-705-ST	65768.4	65646.9	1819.6	EU													
51-705-ST	65752.2	65630.8	1819.6	SU													
51-705-ST	65761.5	65655.5	1819.6	NU	F-faults	Fault-dip	Dip_Direct.	Alpha	L_Left	L_Mid	L_Right	Mid_right	Mid_Left	Mid_Mid	U-Right	U_mid	U_left	Crit._Dist.
51-725-ST	65736.7	65647.3	1780.0	WL	NE wall	65	50	16	-7.5	-6.0	-4.6	-1.3	-1.8	-1.6	2.0	2.9	3.8	intersect
51-725-ST	65765.8	65659.7	1780.0	EL	SE wall	62	40	94	-1.3	8.9	19.1	25.8	5.0	15.4	32.4	21.9	11.3	intersect
51-725-ST	65749.3	65643.3	1780.0	SL	SE wall	74	37	98	24.5	7.9	-3.2	21.5	-1.0	10.3	24.1	12.7	24.7	intersect
51-725-ST	65760.4	65671.0	1780.0	NL	SE wall	65	37	97	5.9	12.2	27.8	28.2	7.1	17.6	33.9	23.1	-7.6	intersect
51-725-ST	65730.0	65640.6	1819.6	WU	SE wall	80	40	95	26.4	14.0	-4.8	25.9	2.7	14.3	26.4	14.6	15.9	intersect
51-725-ST	65761.5	65655.5	1819.6	EU	SE wall	76	88	49	3.8	7.2	20.8	18.1	1.4	9.7	20.8	12.3	30.4	1.4
51-725-ST	65744.5	65638.5	1819.6	SU														
51-725-ST	65752.5	65663.1	1819.6	NU	F-faults	Fault-dip	Dip_Direct.	Alpha	L_Left	L_Mid	L_Right	Mid_right	Mid_Left	Mid_Mid	U-Right	U_mid	U_left	Crit._Dist.
51-725-ST	65737	65647	1780	WL														
51-725-ST	65766	65660	1780	EL														
51-725-ST	65749	65643	1780	SL	SW wall	80	45	144	1.4	4.4	7.4	7.5	0.1	3.8	7.6	3.2	-1.1	intersect
51-725-ST	65760	65671	1780	NL	NW wall	62	40	86	23.7	9.0	-5.8	-0.7	28.1	13.7	4.4	18.4	32.4	intersect
51-725-ST	65730	65641	1820	WU	NW wall	74	37	82	-5.6	8.5	18.9	-6.5	24.6	9.0	-5.6	9.5	4.8	intersect
51-725-ST	65762	65655	1820	EU	NW wall	65	37	83	33.9	12.8	1.7	1.8	31.2	16.5	5.9	20.2	27.6	1.7
51-725-ST	65745	65638	1820	SU														
51-725-ST	65752	65663	1820	NU	F-faults	Fault-dip	Dip_Direct.	Alpha	L_Left	L_Mid	L_Right	Mid_right	Mid_Left	Mid_Mid	U-Right	U_mid	U_left	Crit._Dist.
51-731-ST	65760.9	65703.3	1783.2	WL	NE wall	60	42	93	-6.1	-11.0	-3.3	-3.9	-6.1	-5.0	1.8	1.0	-4.6	intersect
51-731-ST	65793.0	65714.2	1783.2	EL	SE wall	60	41	93	45.4	13.7	43.9	20.8	18.5	19.7	26.6	25.7	53.8	13.7
51-731-ST	65774.3	65695.5	1783.2	SL	SW wall	60	42	165	-6.1	-4.7	-3.3	-2.0	-5.3	-3.7	-0.7	-2.7	-4.6	0.7
51-731-ST	65780.5	65722.9	1783.2	NL	SW wall	60	41	166	19.9	21.2	22.5	23.7	20.6	22.2	25.0	23.2	21.3	19.9
51-731-ST	65745.7	65688.1	1823.2	WU	NW wall	65	16	64	20.8	1.5	25.2	0.2	3.1	1.7	0.7	1.9	27.1	0.2
51-731-ST	65783.6	65704.8	1823.2	EU														
51-731-ST	65760.0	65681.2	1823.2	SU														
51-731-ST	65775.7	65718.1	1823.2	NU	F-faults	Fault-dip	Dip_Direct.	Alpha	L_Left	L_Mid	L_Right	Mid_right	Mid_Left	Mid_Mid	U-Right	U_mid	U_left	Crit._Dist.
51-731-ST	65761	65703	1783	WL	NE wall	35	271	106	4.8	8.4	12.1	29.8	23.9	26.8	47.5	45.2	42.9	4.8
51-731-ST	65793	65714	1783	EL	SE wall													
51-731-ST	65774	65696	1783	SL	SW wall													
51-731-ST	65781	65723	1783	NL	NW wall	60	39	85	21.8	9.8	-2.2	-1.4	28.8	13.7	-0.7	17.6	35.9	intersect

51-731-ST	65746	65688	1823	WU	NW wall	60	39	85	-0.1	10.3	23.3	-0.9	29.4	14.3	-0.1	18.2	-54.1	intersect
51-731-ST	65784	65705	1823	EU	NW wall	65	16	64	27.1	14.2	-0.2	3.1	31.0	17.1	3.1	19.9	-34.9	intersect
51-731-ST	65760	65681	1823	SU														
51-731-ST	65776	65718	1823	NU	Face faults	Fault-dip	Dip_Direct.	Alpha	L_Left	L_Mid	L_Right	Mid_right	Mid_Left	Mid_Mid	U-Right	U_mid	U_left	Crit._Dist.
51-735-ST	65730.0	65668.8	1778.5	WL	NE wall	70	45	24	-2.1	-7.5	-12.9	-7.9	-0.6	-4.2	-3.0	-1.0	1.0	intersect
51-735-ST	65760.7	65671.3	1778.5	EL	NE wall	70	355	136	-25.8	-1.1	-8.3	4.5	-2.0	1.3	5.7	3.6	-17.7	intersect
51-735-ST	65737.0	65647.6	1778.5	SL	NE wall	70	351	87	1.4	-3.8	-1.3	2.4	-5.1	-1.4	3.5	1.1	3.5	intersect
51-735-ST	65737.0	65678.7	1778.5	NL	NW wall													
51-735-ST	65729.2	65650.5	1820.0	WU														
51-735-ST	65752.4	65663.0	1820.0	EU														
51-735-ST	65729.9	65640.5	1820.0	SU														
51-735-ST	65742.8	65666.6	1820.0	NU	F-faults	Fault-dip	Dip_Direct.	Alpha	L_Left	L_Mid	L_Right	Mid_right	Mid_Left	Mid_Mid	U-Right	U_mid	U_left	Crit._Dist.
51-735-ST	65730	65669	1779	WL														
51-735-ST	65761	65671	1779	EL	SEwall	62	40	94	-6.2	8.6	23.4	27.9	-0.8	13.6	32.5	18.5	4.5	intersect
51-735-ST	65737	65648	1779	SL	SEwall	74	37	98	16.5	8.5	-7.5	24.6	-6.5	9.0	24.7	9.6	21.9	intersect
51-735-ST	65737	65679	1779	NL	SEwall	65	37	97	12.9	12.5	20.0	31.1	1.7	16.4	34.5	20.3	9.0	1.7
51-735-ST	65729	65650	1820	WU	SEwall	75	85	52	24.0	9.6	0.7	23.0	-1.2	10.9	24.0	12.3	22.0	intersect
51-735-ST	65752	65663	1820	EU	NW wall	69	292	18	-4.3	-2.9	-1.6	2.9	-1.5	0.7	7.4	4.4	1.3	intersect
51-735-ST	65730	65640	1820	SU	NW wall	85	148	153	-0.8	1.5	3.8	13.2	7.7	10.4	22.6	19.4	16.1	intersect
51-735-ST	65743	65667	1820	NU	NW wall	70	134	144	4.3	5.1	5.9	18.8	17.3	18.0	31.7	31.0	30.3	4.3
51-735-ST	65730	65669	1779	WL	NW wall	65	70	109	10.7	6.2	1.6	7.3	20.1	13.7	12.9	21.2	29.4	1.6
51-735-ST	65761	65671	1779	EL	NW wall	70	65	107	12.1	7.1	2.2	5.3	19.3	12.3	8.5	17.4	26.4	2.2
51-735-ST	65737	65648	1779	SL	NW wall	75	67	110	18.0	13.0	7.9	9.5	23.6	16.6	11.1	20.2	29.3	7.9
51-735-ST	65737	65679	1779	NL	NW wall	75	140	148	3.6	5.1	6.6	18.5	15.3	16.9	30.5	28.7	27.0	3.6
51-781-ST	65766.8	65772.9	1781.0	WL	NE wall													
51-781-ST	65795.0	65779.9	1781.0	EL	SE wall													
51-781-ST	65777.4	65762.3	1781.0	SL	SW wall	65	45	155	42.8	42.8	42.8	51.5	51.5	51.5	60.1	60.1	60.1	42.8
51-781-ST	65782.6	65788.8	1781.0	NL	NW wall													
51-781-ST	65766.8	65772.9	1822.0	WU														
51-781-ST	65795.0	65779.9	1822.0	EU														
51-781-ST	65777.4	65762.3	1822.0	SU														
51-781-ST	65782.6	65788.8	1822.0	NU	F-faults	Fault-dip	Dip_Direct.	Alpha	L_Left	L_Mid	L_Right	Mid_right	Mid_Left	Mid_Mid	U-Right	U_mid	U_left	Crit._Dist.
51-782-ST	65750.8	65756.7	1783.0	WL	NE wall	70	35	15	-14.1	-12.8	-11.6	-7.4	-9.9	-8.6	-3.2	-4.4	-5.6	3.2
51-782-ST	65773.5	65758.2	1783.0	EL	NE wall	65	45	17	-33.3	-17.9	-23.9	-12.0	-12.0	-12.0	-6.2	-6.2	-23.9	6.2

51-782-ST	65761.4	65746.1	1783.0	SL	SW wall	70	34	166	36.7	35.4	34.0	37.1	39.8	38.5	40.2	41.5	42.9	34.0
51-782-ST	65762.9	65768.8	1783.0	NL	NW wall													
51-782-ST	65745.2	65751.1	1822.5	WU														
51-782-ST	65769.6	65754.3	1822.5	EU														
51-782-ST	65755.8	65740.5	1822.5	SU														
51-782-ST	65759.0	65764.9	1822.5	NU	F-faults	Fault-dip	Dip_Direct.	Alpha	L_Left	L_Mid	L_Right	Mid_right	Mid_Left	Mid_Mid	U-Right	U_mid	U_left	Crit._Dist.
51-811-ST	65707.4	65755.7	1783.8	WL	NE wall	65	45	152	-10.4	-13.3	-16.3	-8.7	-5.8	-7.2	-1.2	-1.2	-1.2	1.2
51-811-ST	65743.8	65770.8	1783.8	EL	SE wall													
51-811-ST	65718.0	65745.0	1783.8	SL	SE wall													
51-811-ST	65728.6	65776.9	1783.8	NL	SW wall	63	48	150	15.0	15.4	15.7	25.7	25.0	25.3	35.7	35.3	35.0	15.0
51-811-ST	65708.8	65757.1	1823.8	WU	SW wall	66	45	153	16.2	16.2	16.2	25.3	25.3	25.3	34.3	34.3	34.3	16.2
51-811-ST	65737.8	65764.8	1823.8	EU	NW wall													
51-811-ST	65719.4	65746.4	1823.8	SU	NW wall													
51-811-ST	65727.2	65775.5	1823.8	NU	F-faults	Fault-dip	Dip_Direct.	Alpha	L_Left	L_Mid	L_Right	Mid_right	Mid_Left	Mid_Mid	U-Right	U_mid	U_left	Crit._Dist.
51-821-ST	65699.1	65768.6	1791.4	WL	NE wall	65	45	24	-18.5	-16.9	-15.3	-10.1	-11.8	-10.9	-5.0	-5.0	-5.0	5.0
51-821-ST	65719.8	65768.1	1791.4	EL	SE wall													
51-821-ST	65709.7	65758.0	1791.4	SL	SW wall	55	44	153	3.2	3.1	3.0	9.9	10.1	10.0	16.7	16.8	16.9	3.0
51-821-ST	65711.7	65781.2	1791.4	NL	NW wall													
51-821-ST	65696.2	65765.7	1821.0	WU														
51-821-ST	65720.6	65768.9	1821.0	EU														
51-821-ST	65706.8	65755.1	1821.0	SU														
51-821-ST	65710.0	65779.5	1821.0	NU	F-faults	Fault-dip	Dip_Direct.	Alpha	L_Left	L_Mid	L_Right	Mid_right	Mid_Left	Mid_Mid	U-Right	U_mid	U_left	Crit._Dist.
53-695-ST	65763.3	65641.9	1708.4	WL	NE wall	80	75	35	4.5	1.6	-1.2	0.0	7.1	3.6	1.3	5.6	9.8	intersect
53-695-ST	65787.7	65645.1	1708.4	EL	SE wall	70	80	41	-6.3	5.5	7.2	9.8	17.6	13.7	17.3	21.9	12.6	intersect
53-695-ST	65773.9	65631.3	1708.4	SL	SW wall	70	10	130	14.2	10.2	6.1	15.5	25.0	20.2	24.9	30.3	35.7	6.1
53-695-ST	65778.5	65657.1	1708.4	NL	NW wall													
53-695-ST	65761.2	65639.8	1777.7	WU														
53-695-ST	65782.2	65639.5	1777.7	EU														
53-695-ST	65769.4	65626.7	1777.7	SU														
53-695-ST	65770.6	65649.2	1777.7	NU	F-faults	Fault-dip	Dip_Direct.	Alpha	L_Left	L_Mid	L_Right	Mid_right	Mid_Left	Mid_Mid	U-Right	U_mid	U_left	Crit._Dist.
53-735-ST	65736.6	65679.0	1711.0	WL	NE wall	65	45	37	-4.2	-2.6	-1.0	4.5	7.5	6.0	10.0	14.6	19.2	intersect
53-735-ST	65758.5	65679.7	1711.0	EL	NE wall	70	62	51	-20.5	-3.6	-8.5	-1.2	5.8	2.3	1.7	8.2	-10.8	intersect
53-735-ST	65744.9	65666.1	1711.0	SL	NE wall	58	2	24	-75.3	-80.7	-53.9	-63.5	-70.0	-66.8	-51.8	-52.9	-51.8	51.8
53-735-ST	65750.4	65692.8	1711.0	NL	NW wall	58	2	63	9.5	3.4	-2.6	10.9	21.2	16.0	24.3	28.6	32.9	intersect

53-735-ST	65730.0	65668.8	1778.5	WU	NW wall	72	37	72	4.7	4.6	8.5	0.1	15.0	7.6	4.7	10.5	-13.2	intersect
53-735-ST	65754.4	65675.7	1778.5	EU	SE wall	72	37	98	-9.7	-0.6	8.5	16.2	-6.3	5.0	23.9	10.5	-2.8	intersect
53-735-ST	65734.3	65655.5	1778.5	SU	SW wall	72	37	145	-4.6	-7.1	-9.7	-6.3	0.1	-3.1	-2.8	1.0	4.7	intersect
53-735-ST	65737.0	65678.7	1778.5	NU	F-faults	Fault-dip	Dip_Direct.	Alpha	L_Left	L_Mid	L_Right	Mid_right	Mid_Left	Mid_Mid	U-Right	U_mid	U_left	Crit._Dist.
54-695-ST	65776.4	65655.0	1672.0	WL	NE wall	65	45	7	-1.9	-1.4	-1.0	-0.3	-1.7	-1.0	0.3	-0.6	-1.5	intersect
54-695-ST	65799.3	65656.7	1672.0	EL	SE wall													
54-695-ST	65783.1	65640.5	1672.0	SL	SW wall	70	9	146	56.6	50.4	44.1	45.4	55.8	50.6	46.7	50.8	55.0	44.1
54-695-ST	65793.0	65664.5	1672.0	NL	NW wall													
54-695-ST	65763.3	65641.9	1708.4	WU														
54-695-ST	65787.7	65645.1	1708.4	EU														
54-695-ST	65773.9	65631.3	1708.4	SU														
54-695-ST	65778.5	65657.1	1708.4	NU	F-faults	Fault-dip	Dip_Direct.	Alpha	L_Left	L_Mid	L_Right	Mid_right	Mid_Left	Mid_Mid	U-Right	U_mid	U_left	Crit._Dist.
54-735-ST	65739.3	65681.8	1671.2	WL	NE wall	60	45	23	-21.5	-21.8	-22.0	-14.4	-15.7	-15.0	-6.7	-8.2	-9.8	6.7
54-735-ST	65765.1	65686.4	1671.2	EL	SE wall	80	84	25	-25.7	-16.0	-33.0	-19.4	-11.3	-15.4	-18.0	-14.7	-26.2	11.3
54-735-ST	65751.7	65672.9	1671.2	SL	SW wall	68	37	157	-32.5	-32.3	-32.2	-29.2	-26.9	-28.0	-26.2	-23.7	-21.2	21.2
54-735-ST	65754.2	65696.6	1671.2	NL	NW wall	80	30	153	-12.2	-29.5	-8.8	-31.4	-27.2	-29.3	-32.5	-29.1	-14.2	8.8
54-735-ST	65736.6	65679.0	1711.0	WU		82	270	37	14.9	21.0	35.4	21.0	31.2	26.1	27.2	31.3	27.2	14.9
54-735-ST	65758.5	65679.7	1711.0	EU														
54-735-ST	65744.9	65666.1	1711.0	SU														
54-735-ST	65750.4	65692.8	1711.0	NU	F-faults	Fault-dip	Dip_Direct.	Alpha	L_Left	L_Mid	L_Right	Mid_right	Mid_Left	Mid_Mid	U-Right	U_mid	U_left	Crit._Dist.
54-735-ST	65739	65682	1671	WL	SEwall	80	30	28	-12.2	-21.2	-28.8	-13.2	-31.4	-22.3	-14.2	-23.4	-14.2	13.2
54-735-ST	65765	65686	1671	EL	SEwall	80	84	25	-25.7	-18.4	-11.2	-11.3	-25.9	-18.6	-11.4	-18.8	-26.2	11.2
54-735-ST	65752	65673	1671	SL	SEwall	68	37	23	-13.2	-23.4	-32.2	-11.6	-29.2	-20.4	-8.4	-17.3	-3.3	3.3
54-735-ST	65754	65697	1671	NL	NWwall	82	270	46	12.4	19.8	27.1	31.2	17.1	24.2	35.4	28.5	21.7	12.4
54-735-ST	65737	65679	1711	WU	NWwall	80	30	75	-25.6	-18.8	-12.2	-27.2	-7.9	-17.6	-25.6	-16.3	6.1	intersect
54-735-ST	65759	65680	1711	EU														
54-735-ST	65745	65666	1711	SU														
54-735-ST	65750	65693	1711	NU	F-faults	Fault-dip	Dip_Direct.	Alpha	L_Left	L_Mid	L_Right	Mid_right	Mid_Left	Mid_Mid	U-Right	U_mid	U_left	Crit._Dist.
54-781-ST	65765.9	65771.7	1674.5	WL	SE wall	65	18	114	-5.5	4.0	13.4	17.6	2.8	10.2	21.7	16.4	11.2	intersect
54-781-ST	65793.1	65777.7	1674.5	EL	SE wall	65	1	129	1.1	8.8	16.4	21.4	9.5	15.4	26.3	22.0	17.8	1.1
54-781-ST	65776.5	65761.1	1674.5	SL	SW wall	65	18	144	-2.1	-5.2	-8.3	0.0	6.2	3.1	8.4	11.5	14.5	intersect
54-781-ST	65782.5	65788.3	1674.5	NL	SW wall	65	29	151	5.2	3.3	1.4	9.8	13.5	11.6	18.1	20.0	21.9	1.4
54-781-ST	65765.9	65771.7	1714.0	WU	SW wall	65	29	151	13.2	11.3	9.4	17.8	21.5	19.6	26.1	28.0	29.8	9.4
54-781-ST	65785.7	65770.3	1714.0	EU	NW wall	65	45	90	16.2	13.9	-5.1	19.8	-2.0	8.9	23.4	3.9	-15.7	intersect

54-781-ST	65776.5	65761.1	1714.0	SU	NW wall	65	45	90	25.8	23.5	4.5	29.4	7.5	18.4	33.0	13.4	-6.2	intersect
54-781-ST	65775.1	65780.9	1714.0	NU	NE wall	65	38	96	-9.1	-8.2	-7.4	-3.8	-5.4	-4.6	-0.2	-1.0	-1.8	0.2
54-821-ST	65725.8	65795.5	1674.0	WL	NE wall	65	40	16	6.2	6.8	7.4	12.8	11.6	12.2	18.3	17.7	17.1	6.2
54-821-ST	65752.3	65800.8	1674.0	EL	NE wall	65	30	21	22.0	23.7	42.2	31.0	27.5	29.3	36.5	34.8	33.0	22.0
54-821-ST	65736.4	65784.9	1674.0	SL	SE wall	65	40	25	7.8	17.9	28.1	33.5	6.0	19.8	39.0	21.6	4.2	4.2
54-821-ST	65741.7	65811.4	1674.0	NL	SE wall	65	30	29	-11.5	-1.6	8.2	13.7	-13.0	0.4	19.2	2.4	-14.4	intersect
54-821-ST	65709.9	65779.6	1713.6	WU	NW wall	65	40	85	17.2	1.6	-13.9	-15.7	-22.3	-19.0	-17.5	-39.7	-61.8	intersect
54-821-ST	65747.7	65796.2	1713.6	EU	NW wall	65	30	76	33.7	18.3	3.0	1.5	-14.2	-6.4	0.0	-31.1	-62.2	intersect
54-821-ST	65720.5	65769.0	1713.6	SU	SWwall	65	40	174	-13.0	-13.6	-14.2	-16.0	-14.8	-15.4	-17.7	-17.1	-16.6	13.6
54-821-ST	65737.1	65806.8	1713.6	NU	SWwall	65	30	166	5.7	4.0	2.2	0.7	4.2	2.5	-0.8	1.0	2.8	intersect
54-821-ST	65726	65796	1674	WL														
54-821-ST	65752	65801	1674	EL	F-faults	Fault-dip	Dip_Direct.	Alpha	L_Left	L_Mid	L_Right	Mid_right	Mid_Left	Mid_Mid	U-Right	U_mid	U_left	Crit._Dist.
54-821-ST	65736	65785	1674	SL	SW wall	65	40	174	-13.0	-13.6	-14.2	-16.0	-14.8	-15.4	-17.7	-17.1	-16.6	13.6
54-821-ST	65742	65811	1674	NL	SW wall	65	30	166	21.9	4.0	25.4	0.7	4.2	2.5	-0.8	1.0	32.9	intersect
54-821-ST	65710	65780	1714	WU														
54-821-ST	65748	65796	1714	EU														
54-821-ST	65721	65769	1714	SU														
54-821-ST	65737	65807	1714	NU	F-faults	Fault-dip	Dip_Direct.	Alpha	L_Left	L_Mid	L_Right	Mid_right	Mid_Left	Mid_Mid	U-Right	U_mid	U_left	Crit._Dist.
56-695-ST	65774.8	65653.4	1630.0	WL	NE wall	80	348	48	-9.6	-4.0	1.5	0.3	-10.8	-5.2	-0.9	-6.4	-12.0	intersect
56-695-ST	65812.2	65669.6	1630.0	EL	SE wall													
56-695-ST	65786.5	65643.9	1630.0	SL	SW wall													
56-695-ST	65799.8	65678.4	1630.0	NL	NW wall	80	348	34	1.5	-8.0	-17.5	-13.2	0.3	-6.4	-8.9	-4.9	-0.9	intersect
56-695-ST	65776.5	65655.1	1672.0	WU	NW wall	65	0	50	19.1	11.1	14.4	9.4	25.6	17.5	19.1	23.9	105.7	9.4
56-695-ST	65799.4	65656.8	1672.0	EU	NW wall	70	0	48	20.6	14.8	-5.9	11.0	27.8	19.4	19.0	24.0	118.9	intersect
56-695-ST	65783.5	65640.9	1672.0	SU	NW wall	68	0	49	7.7	15.1	26.7	12.2	28.7	20.4	20.8	25.7	104.6	7.7
56-695-ST	65787.1	65665.7	1672.0	NU	F-faults	Fault-dip	Dip_Direct.	Alpha	L_Left	L_Mid	L_Right	Mid_right	Mid_Left	Mid_Mid	U-Right	U_mid	U_left	Crit._Dist.
56-695-ST	65775	65653	1630	WL														
56-695-ST	65812	65670	1630	EL														
56-695-ST	65787	65644	1630	SL	SW wall	65	0	114	-0.2	-4.5	-8.8	-1.3	9.4	4.1	6.2	12.7	19.1	intersect
56-695-ST	65800	65678	1630	NL	SW wall	70	0	115	18.2	146.7	26.6	141.0	151.0	146.0	140.3	145.3	20.6	18.2
56-695-ST	65776	65655	1672	WU	SW wall	68	0	115	-5.3	146.9	20.8	142.0	151.8	146.9	142.0	147.0	7.7	intersect
56-695-ST	65799	65657	1672	EU														
56-695-ST	65784	65641	1672	SU														
56-695-ST	65787	65666	1672	NU	F-faults	Fault-dip	Dip_Direct.	Alpha	L_Left	L_Mid	L_Right	Mid_right	Mid_Left	Mid_Mid	U-Right	U_mid	U_left	Crit._Dist.

56-705-ST	65773.0	65672.8	1629.0	WL	NE wall	80	342	58	2.8	9.4	16.0	15.3	2.3	8.8	14.5	8.2	1.8	1.8
56-705-ST	65801.3	65679.9	1629.0	EL	SE wall													
56-705-ST	65781.5	65660.1	1629.0	SL	SW wall													
56-705-ST	65790.7	65690.5	1629.0	NL	NW wall													
56-705-ST	65762.4	65662.2	1672.0	WU														
56-705-ST	65787.9	65666.5	1672.0	EU														
56-705-ST	65773.0	65651.6	1672.0	SU														
56-705-ST	65776.5	65676.4	1672.0	NU	F-faults	Fault-dip	Dip_Direct.	Alpha	L_Left	L_Mid	L_Right	Mid_right	Mid_Left	Mid_Mid	U-Right	U_mid	U_left	Crit._Dist.
56-735-ST	65747.1	65689.5	1628.0	WL	NE wall	65	45	3	-9.7	-9.6	-9.4	-10.4	-10.4	-10.4	-11.5	-11.2	-11.0	9.4
56-735-ST	65780.4	65701.6	1628.0	EL	SE wall	80	79	57	3.7	26.0	-4.3	19.4	24.9	22.2	15.0	18.4	-6.5	intersect
56-735-ST	65754.1	65675.3	1628.0	SL	SWwall	68	47	163	-24.6	-26.7	-28.9	-22.3	-21.6	-22.0	-15.8	-17.2	-18.6	15.8
56-735-ST	65770.0	65712.4	1628.0	NL	SWwall	82	263	50	-12.8	18.8	-3.9	20.5	28.7	24.6	24.9	30.4	10.0	intersect
56-735-ST	65739.3	65681.8	1671.2	WU	SWwall	80	26	171	-27.8	-23.1	-21.0	-25.7	-19.7	-22.7	-23.5	-22.3	-23.5	19.7
56-735-ST	65765.1	65686.4	1671.2	EU	NWwall	82	263	52	-1.0	11.6	24.3	31.6	10.7	21.1	38.9	30.7	22.5	intersect
56-735-ST	65751.7	65672.9	1671.2	SU	NWwall	68	47	92	3.2	-11.8	-26.8	-23.8	0.9	-11.5	-20.8	-11.1	-1.4	intersect
56-735-ST	65754.2	65696.6	1671.2	NU	F-faults	Fault-dip	Dip_Direct.	Alpha	L_Left	L_Mid	L_Right	Mid_right	Mid_Left	Mid_Mid	U-Right	U_mid	U_left	Crit._Dist.
56-755-ST	65724.1	65687.3	1670.0	WL	NE wall	65	45	34	-34.6	-34.0	-33.4	-16.9	-20.7	-18.8	-0.4	-3.5	-6.7	0.4
56-755-ST	65754.2	65697.0	1670.0	EL	SE wall	82	270	134	9.7	20.4	18.8	36.3	28.7	32.5	49.2	44.7	25.3	9.7
56-755-ST	65732.8	65675.7	1670.0	SL	SW wall	80	30	105	-40.6	-52.5	-13.0	-54.7	-59.7	-57.2	-59.6	-61.9	-22.4	13.0
56-755-ST	65745.0	65708.2	1670.0	NL	NW wall	55	45	90	-2.3	80.2	37.2	89.6	88.1	88.9	98.0	97.5	42.9	intersect
56-755-ST	65730.0	65693.4	1750.0	WU	SWwall	75	39	146	-8.7	-10.5	-12.2	0.3	5.7	3.0	12.9	16.5	20.1	intersect
56-755-ST	65749.6	65692.5	1750.0	EU	SWwall	55	45	135	-3.4	-27.3	-2.3	-3.3	0.0	-1.7	21.5	23.9	37.2	intersect
56-755-ST	65736.0	65678.9	1750.0	SU	NE wall	65	45	26	-18.8	-18.7	-18.6	-18.1	-18.3	-18.2	-17.5	-17.7	-17.8	17.5
56-755-ST	65744.3	65707.6	1750.0	NU														
56-781-ST	65764.4	65770.2	1630.0	WL	NE wall	65	29	29	-9.0	-7.1	-5.2	4.2	0.4	2.3	13.6	11.7	9.8	intersect
56-781-ST	65792.1	65776.7	1630.0	EL	SE wall	55	0	132	-11.1	-5.3	0.6	13.3	1.6	7.5	26.1	20.3	14.4	intersect
56-781-ST	65772.2	65762.4	1630.0	SL	SW wall	65	45	155	2.1	2.1	2.1	11.5	11.5	11.5	20.9	20.9	20.9	2.1
56-781-ST	65781.5	65787.3	1630.0	NL	NW wall													
56-781-ST	65764.4	65770.2	1674.5	WU														
56-781-ST	65792.1	65776.7	1674.5	EU														
56-781-ST	65772.2	65762.4	1674.5	SU														
56-781-ST	65781.5	65787.3	1674.5	NU	F-faults	Fault-dip	Dip_Direct.	Alpha	L_Left	L_Mid	L_Right	Mid_right	Mid_Left	Mid_Mid	U-Right	U_mid	U_left	Crit._Dist.
58-695-ST	65801.1	65679.7	1552.5	WL	NE wall	65	45	9	-16.4	-15.6	-14.8	-13.9	-15.8	-14.8	-12.9	-14.0	-15.2	12.9
58-695-ST	65827.9	65695.9	1552.5	EL	SE wall	63	20	40	-5.5	7.9	21.3	21.9	-3.6	9.2	22.6	10.5	-1.6	intersect

58-695-ST	65812.2	65669.6	1552.5	SL	SW wall	63	20	166	-0.5	-3.0	-5.5	-3.6	0.8	-1.4	-1.6	0.2	2.0	intersect
58-695-ST	65823.9	65702.5	1552.5	NL	SW wall	58	55	161	18.8	-6.3	19.2	-1.7	-5.2	-3.5	1.5	-0.6	26.6	intersect
58-695-ST	65787.6	65666.2	1591.9	WU	SW wall	83	3	144	-0.5	4.2	-0.4	-4.5	4.3	-0.1	-8.5	-4.4	-8.5	intersect
58-695-ST	65821.2	65678.6	1591.9	EU														
58-695-ST	65800.0	65657.4	1591.9	SU														
58-695-ST	65812.3	65690.9	1591.9	NU	F-faults	Fault-dip	Dip_Direct.	Alpha	L_Left	L_Mid	L_Right	Mid_right	Mid_Left	Mid_Mid	U-Right	U_mid	U_left	Crit._Dist.
60-725-ST	65804.5	65718.1	1510.1	WL	NE wall	65	20	11	-12.1	-28.1	-6.3	-0.4	-30.9	-15.7	19.0	-3.3	-4.3	intersect
60-725-ST	65834.0	65733.8	1510.1	EL	SE wall	65	24	111	-49.2	-36.5	-23.9	-20.1	-43.7	-31.9	-16.4	-27.3	-38.2	16.4
60-725-ST	65807.7	65715.0	1510.1	SL	SW wall													
60-725-ST	65823.4	65744.5	1510.1	NL	NW wall	65	24	73	-19.0	-33.4	-47.7	-40.5	-17.1	-28.8	-33.3	-24.3	-15.2	15.2
60-725-ST	65798.4	65719.4	1547.1	WU														
60-725-ST	65827.2	65727.1	1547.1	EU														
60-725-ST	65809.0	65708.8	1547.1	SU														
60-725-ST	65813.5	65734.6	1547.1	NU	F-faults	Fault-dip	Dip_Direct.	Alpha	L_Left	L_Mid	L_Right	Mid_right	Mid_Left	Mid_Mid	U-Right	U_mid	U_left	Crit._Dist.
60-755-ST	65777.4	65740.9	1511.7	WL	NE wall	65	45	4	-17.2	-18.3	-19.5	-18.8	-17.2	-18.0	-18.1	-17.6	-17.2	17.2
60-755-ST	65809.5	65751.8	1511.7	EL	SE wall													
60-755-ST	65788.0	65730.3	1511.7	SL	SW wall													
60-755-ST	65797.1	65760.6	1511.7	NL	NW wall													
60-755-ST	65776.3	65739.7	1552.5	WU														
60-755-ST	65796.1	65738.3	1552.5	EU														
60-755-ST	65786.9	65729.1	1552.5	SU														
60-755-ST	65784.8	65748.2	1552.5	NU	F-faults	Fault-dip	Dip_Direct.	Alpha	L_Left	L_Mid	L_Right	Mid_right	Mid_Left	Mid_Mid	U-Right	U_mid	U_left	Crit._Dist.
60-756-ST	65763.5	65727.0	1510.5	WL	NE wall													
60-756-ST	65787.9	65730.1	1510.5	EL	SE wall													
60-756-ST	65769.5	65711.8	1510.5	SL	SW wall	85	225	10	-20.5	-17.3	-14.1	-12.3	-15.5	-13.9	-10.5	-10.5	-10.5	10.5
60-756-ST	65777.3	65740.7	1510.5	NL	NW wall													
60-756-ST	65758.9	65722.4	1551.5	WU														
60-756-ST	65787.0	65729.2	1551.5	EU														
60-756-ST	65769.5	65711.8	1551.5	SU														
60-756-ST	65776.4	65739.8	1551.5	NU	F-faults	Fault-dip	Dip_Direct.	Alpha	L_Left	L_Mid	L_Right	Mid_right	Mid_Left	Mid_Mid	U-Right	U_mid	U_left	Crit._Dist.
60-791-ST	65767.0	65794.2	1511.3	WL	NE wall	65	45	4	27.3	16.4	5.4	9.1	28.7	18.9	12.8	21.4	30.1	5.4
60-791-ST	65794.6	65800.6	1511.3	EL	SE wall													
60-791-ST	65777.6	65783.6	1511.3	SL	SW wall	65	46	170	-24.2	-24.0	-23.9	-20.2	-20.5	-20.4	-16.6	-16.7	-16.8	16.6
60-791-ST	65784.0	65811.2	1511.3	NL	SW wall	65	45	170	15.4	-6.4	15.4	-2.7	-2.7	-2.7	1.0	1.0	18.3	intersect

60-791-ST	65759.2	65786.4	1552.3	WU
60-791-ST	65783.3	65789.3	1552.3	EU
60-791-ST	65769.8	65775.8	1552.3	SU
60-791-ST	65772.7	65799.9	1552.3	NU

Table C.3 Kidd Mine stability graph database

Stope	Face	dip	dip-dir	Ar	span/3	HR	Rock	RQD	Jn	Jr	Ja	Q'	A	B	crit jnt	C	N'	Perform.	O-break	In-angle	Flt Dist	Dist/h	Fw	N'	delta
47-645	NW	93	315	0.2	4.2	5.1	sulphide	93	6	1	1	15	1.0	0.3	85	2.5	10.7	stable	0.0				1.0	10.7	1.2
47-725	NW	93	315	0.1	1.3	1.7	breccia	80	12	1.5	2	5	1.0	0.3	83	2.7	3.6	stable	0.0				1.0	3.6	1.7
47-725	SE	90	135	0.2	4.3	5.2	sulphide	58	6	1	1	10	1.0	0.3	85	8.0	19.2	stable	0.0	85	4	0.06	1.0	19.2	1.3
47-821	NW	90	135	0.4	8.3	8.8	stringer	70	12	1.5	2	4	1.0	0.3	83	8.0	9.3	stable	0.0	62	3	0.04	0.5	4.2	0.8
47-821	SE	90	225	0.2	4.9	5.9	stringer	70	12	1.5	2	4	1.0	0.4	79	8.0	14.9	stable	0.0	62	9	0.16	0.7	10.4	1.1
47-821	SW	90	315	0.4	8.3	8.8	breccia	85	12	1.5	2	5	1.0	0.3	83	8.0	11.7	stable	0.0	65	6	0.10	0.5	5.9	0.8
48-725	NW	92	315	0.4	5.9	6.1	rhyolite	73	12	1.5	2	5	1.0	0.2	82	2.8	2.6	stable	0.0				1.0	2.6	0.8
48-725	SE	90	135	0.5	6.7	6.6	sulphide	93	6	1	1	15	1.0	0.3	85	8.0	30.8	stable	0.0				1.0	30.8	1.3
48-725	SW	95	260	0.3	4.5	5.6	sulphide	60	6	1	1	10	1.0	0.7	85	2.5	17.5	stable	0.0				1.0	17.5	1.3
48-782	NW	90	315	0.5	6.9	7.1	sulphide	85	6	1	1	14	1.0	0.3	85	2.5	9.0	stable	0.0	71	0	0.00	0.6	5.4	0.9
48-782	SE	90	135	0.5	6.9	7.1	sulphide	97	6	1	1	16	1.0	0.3	85	8.0	32.4	stable	0.0				1.0	32.4	1.3
48-821	NE	80	45	0.2	3.6	4.4	breccia	85	12	1.5	2	5	1.0	0.4	79	6.9	14.2	stable	0.0	75	0	0.00	0.7	10.1	1.3
48-821	NW	89	330	0.6	8.6	8.2	stringer	80	12	1.5	2	5	1.0	0.2	87	7.9	7.9	stable	0.0	48	0	0.00	1.0	7.9	0.9
48-821	SE	96	135	0.5	8.2	7.9	stringer	60	12	1.5	2	4	1.0	0.3	83	2.7	3.1	stable	0.0	74	0	0.00	1.0	3.1	0.8
49-705	NE	75	45	0.4	5.0	5.4	rhyolite	60	12	1.5	2	4	1.0	0.2	75	6.5	4.9	stable	0.0	10	13	0.31	0.7	3.4	0.9
49-705	SW	99	235	0.4	5.0	5.5	sulphide	90	6	1	1	15	1.0	0.9	8	7.9	110.7	stable	0.0	14	28	0.71	1.0	110.7	1.8
49-720	SE	90	135	0.7	9.3	8.0	sulphide	89	6	1	1	15	1.0	0.2	85	2.5	9.3	stable	0.0				1.0	9.3	0.9
49-731	NE	68	45	0.3	5.0	5.6	breccia	95	12	1.5	2	6	1.0	0.4	79	5.8	13.5	stable	0.0	4	36	0.79	1.0	13.5	1.2
49-731	NW	90	315	0.9	11.9	9.1	stringer	85	12	1.5	2	5	1.0	0.3	83	8.0	11.6	stable	0.0	87	0	0.00	1.0	11.6	0.9
49-731	SW	100	225	0.4	5.1	5.6	stringer	45	12	1.5	2	3	1.0	0.4	79	3.1	3.4	stable	0.0	14	32	0.79	1.0	3.4	0.9
49-821	NE	85	43	0.4	5.0	5.4	breccia	80	12	1.5	2	5	1.0	0.4	79	7.5	13.3	stable	0.0	20	9	0.23	0.2	2.4	0.9
49-821	SE	90	135	0.6	7.6	7.0	stringer	90	12	1.5	2	6	1.0	0.3	83	8.0	12.3	stable	0.0				1.0	12.3	1.1
49-821	SW	105	221	0.4	5.0	5.4	breccia	85	12	1.5	2	5	1.0	0.3	79	3.1	5.2	stable	0.0	6	20	0.50	1.0	5.2	1.0
51-665	NE	80	46	0.3	3.9	4.5	rhyolite	90	12	1.5	2	6	1.0	0.2	65	6.9	7.8	stable	0.0	15	16	0.40	1.0	7.8	1.2
51-665	SW	91	269	0.3	4.1	5.2	sulphide	90	6	1	1	15	1.0	0.5	85	2.5	19.8	stable	0.0				1.0	19.8	1.3
51-731	NE	76	60	0.4	5.0	5.6	breccia	90	12	1.5	2	6	1.0	0.4	83	6.6	16.4	stable	0.0	74	4	0.09	0.7	11.5	1.2
51-731	SE	90	135	0.7	10.0	8.1	stringer	90	12	1.5	2	6	1.0	0.3	83	2.7	4.2	stable	0.0	77	0	0.00	1.0	4.2	0.8
51-782	NW	90	315	0.5	6.1	6.2	stringer	85	12	1.5	2	5	1.0	0.3	83	8.0	11.6	stable	0.0				1.0	11.6	1.1
51-782	SE	90	135	0.5	6.1	6.2	stringer	80	12	1.5	2	5	1.0	0.3	83	8.0	10.9	stable	0.0				1.0	10.9	1.1
51-782	SW	101	225	0.4	5.0	5.5	breccia	90	12	1.5	2	6	1.0	0.4	79	3.1	6.8	stable	0.0	14	34	0.83	1.0	6.8	1.1
51-811	NE	83	45	0.4	5.1	5.7	breccia	90	12	1.5	2	6	1.0	0.4	79	7.2	15.9	stable	0.0				1.0	15.9	1.2
51-811	SE	90	135	0.8	10.4	8.7	stringer	80	12	1.5	2	5	1.0	0.3	83	8.0	10.9	stable	0.0				1.0	10.9	0.9

51-811	SW	87	225	0.4	5.0	5.5	stringer	85	12	1.5	2	5	1.0	0.4	79	7.7	18.1	stable	0.0	27	16	0.40	1.0	18.1	1.3
53-695	NW	90	315	0.2	5.8	6.9	sulphide	90	6	1	1	15	1.0	0.2	85	8.0	30.0	stable	0.0				1.0	30.0	1.3
53-695	SE	90	135	0.3	6.3	7.4	sulphide	90	6	1	1	15	1.0	0.2	85	2.5	9.5	stable	0.0				1.0	9.5	1.0
Stope	Face	dip	dip-dir	Ar	span/3	HR	Rock	RQD	Jn	Jr	Ja	Q'	A	B	crit jnt	C	N'	Perform.	O-break	In-angle	Flt Dist	Dist/h	Fw	N'	delta
53-695	SW	94	238	0.2	5.0	6.2	sulphide	80	6	1	1	13	1.0	0.9	85	2.5	30.7	stable	0.0	50	0	0.00	0.8	24.6	1.3
53-735	NW	91	306	0.2	5.3	6.3	sulphide	70	6	1	1	12	1.0	0.2	85	2.5	5.9	stable	0.0	63	0	0.00	1.0	5.9	1.0
53-735	SE	90	135	0.3	8.0	8.7	sulphide	85	6	1	1	14	1.0	0.2	85	2.5	8.9	stable	0.0	82	0	0.00	0.9	8.0	0.9
54-735	NW	90	315	0.5	6.8	6.7	sulphide	90	6	1	1	15	1.0	0.2	85	8.0	30.0	stable	0.0	46	12	0.31	0.9	27.0	1.3
54-735	SE	90	135	0.5	6.4	6.3	sulphide	90	6	1	1	15	1.0	0.2	85	2.5	9.5	stable	0.0	25	11	0.27	0.5	4.3	0.9
54-735	SW	99	237	0.4	5.0	5.5	rhyolite	65	12	1.5	2	4	1.0	0.2	85	2.5	2.0	stable	0.0	23	21	0.52	1.0	2.0	0.9
54-755	NW	90	315	0.6	8.3	7.7	sulphide	90	6	1	1	15	1.0	0.3	85	2.5	9.5	stable	0.0				1.0	9.5	1.0
54-755	SW	82	247	0.4	5.0	5.5	rhyolite	90	12	1.5	2	6	1.0	0.2	85	7.1	8.0	stable	0.0				1.0	8.0	1.1
54-781	NE	75	45	0.4	5.0	5.5	rhyolite	80	12	1.5	2	5	1.0	0.2	75	6.5	6.5	stable	0.0	84	0	0.00	1.0	6.5	1.1
54-781	NW	90	315	0.5	6.1	6.2	stringer	40	12	1.5	2	3	1.0	0.3	83	8.0	5.5	stable	0.0	90	0	0.00	1.0	5.5	1.0
54-781	SE	90	135	0.5	6.1	6.2	sulphide	25	6	1	1	4	1.0	0.2	85	2.5	2.6	stable	0.0	90	0	0.00	1.0	2.6	0.8
54-781	SW	90	225	0.4	5.0	5.4	stringer	65	12	1.5	2	4	1.0	0.4	79	8.0	13.8	stable	0.0	25	10	0.25	0.3	4.1	1.0
54-821	NW	90	315	0.7	10.2	8.2	stringer	30	12	1.5	2	2	1.0	0.3	83	8.0	4.1	stable	0.0	76	0	0.00	1.0	4.1	0.8
54-821	SE	90	135	0.7	10.2	8.2	stringer	20	12	1.5	2	1	1.0	0.3	83	8.0	2.7	stable	0.0	76	0	0.00	1.0	2.7	0.7
56-695	NW	90	315	0.6	8.4	7.7	sulphide	90	6	1	1	15	1.0	0.2	85	8.0	30.0	stable	0.0	46	1	0.02	1.0	30.0	1.2
56-695	SE	90	135	0.7	9.8	8.4	sulphide	90	6	1	1	15	1.0	0.3	85	8.0	30.0	stable	0.0				1.0	30.0	1.1
56-695	SW	91	243	0.4	5.0	5.6	rhyolite	90	12	1.5	2	6	1.0	0.2	85	2.5	2.8	stable	0.0	65	0	0.00	0.5	1.4	0.8
56-705	NE	66	41	0.3	5.0	5.7	rhyolite	90	12	1.5	2	6	1.0	0.2	75	5.5	6.2	stable	0.0	58	2	0.04	1.0	6.2	1.0
56-705	SW	107	225	0.3	5.0	5.7	sulphide	70	6	1	1	12	1.0	0.9	8	7.9	81.8	stable	0.0				1.0	81.8	1.7
56-735	NW	90	315	0.6	8.9	7.9	sulphide	90	6	1	1	15	1.0	0.3	85	2.5	9.5	stable	0.0	52	0	0.00	1.0	9.5	1.0
56-735	SE	90	135	0.6	9.4	8.2	sulphide	80	6	1	1	13	1.0	0.3	85	8.0	26.7	stable	0.0	57	0	0.00	1.0	26.7	1.1
56-735	SW	99	216	0.3	5.0	5.7	sulphide	90	6	1	1	15	1.0	0.9	8	7.9	112.6	stable	0.0	9	20	0.45	1.0	112.6	1.8
56-755	SW	112	223	0.3	5.1	5.8	fragmental		12	1.5	2	6	1.0	0.2	65	4.5	5.1	stable	0.0				1.0	5.1	1.0
56-781	NW	90	315	0.5	8.1	7.8	stringer	70	12	1.5	2	4	1.0	0.3	83	8.0	9.6	stable	0.0				1.0	9.6	1.0
56-781	SW	90	225	0.2	3.7	4.4	stringer	78	12	1.5	2	5	1.0	0.4	79	3.1	6.5	stable	0.0				1.0	6.5	1.2
58-695	NW	90	315	0.8	11.2	8.6	sulphide	85	6	1	1	14	1.0	0.3	85	2.5	8.9	stable	0.0				1.0	8.9	0.9
58-695	SW	115	216	0.3	5.0	5.6	rhyolite	80	12	1.5	2	5	1.0	0.2	75	3.6	3.6	stable	0.0				1.0	3.6	0.9
60-725	SW	95	225	0.3	3.3	3.8	sulphide	80	6	1	1	13	1.0	1.0	8	7.9	102.0	stable	0.0				1.0	102.0	2.1
60-755	NW	90	315	0.5	6.7	6.5	sulphide	90	6	1	1	15	1.0	0.3	85	2.5	9.5	stable	0.0				1.0	9.5	1.0
60-756	NW	90	315	0.5	7.3	7.1	sulphide	90	6	1	1	15	1.0	0.2	85	8.0	30.0	stable	0.0				1.0	30.0	1.2
60-756	SE	90	135	0.6	8.4	7.8	sulphide	90	6	1	1	15	1.0	0.2	85	2.5	9.5	stable	0.0				1.0	9.5	1.0

60-756	SW	95	225	0.4	5.1	5.7	sulphide	90	6	1	1	15	1.0	1.0	8	7.9	115.3	stable	0.0	10	11	0.27	0.5	51.9	1.5
60-791	NW	90	315	0.5	7.2	6.8	stringer	60	12	1.5	2	4	1.0	0.3	83	8.0	8.2	stable	0.0				1.0	8.2	1.0
60-791	SE	90	135	0.5	7.2	6.8	stringer	75	12	1.5	2	5	1.0	0.3	83	8.0	10.2	stable	0.0				1.0	10.2	1.0
48-821	SW	96	225	0.4	5.7	6.3	breccia	60	12	1.5	2	4	1.0	0.4	79	3.1	4.7	known failure	0.5	19	39	0.85	1.0	4.7	0.9
Stope	Face	dip	dip-dir	Ar	span/3	HR	Rock	RQD	Jn	Jr	Ja	Q'	A	B	crit jnt	C	N'	Perform.	O-break	In-angle	Flt Dist	Dist/h	Fw	N'	delta
49-720	NW	82	309	0.6	8.3	7.5	sulphide	85	6	1	1	14	1.0	0.2	85	7.2	20.4	known failure	0.5				1.0	20.4	1.1
49-731	SE	90	135	0.8	10.4	8.5	stringer	90	12	1.5	2	6	1.0	0.3	83	2.7	4.2	known failure	0.5	87	3	0.07	1.0	4.2	0.8
49-782	SW	102	225	0.4	5.0	5.4	stringer	85	12	1.5	2	5	1.0	0.4	79	3.1	6.4	known failure	0.5				1.0	6.4	1.1
54-821	SW	120	225	0.3	5.0	5.6	stringer	15	12	1 5	2	1	1.0	0.4	79	3.1	1.3	check	0.5	6	14	0.27	0.5	0.6	0.7
60-725	NW	94	315	0.7	8.9	7.6	sulphide	80	6	1	1	13	1.0	0.3	85	2.5	9.8	known failure	0.5	73	15	0.39	1.0	9.8	1.0
60-725	SE	94	135	0.8	9.7	8.1	sulphide	85	6	1	1	14	1.0	0.2	85	2.5	7.5	known failure	0.5	69	16	0.42	1.0	7.5	0.9
60-755	SE	90	135	0.5	7.2	6.8	sulphide	70	6	1	1	12	1.0	0.3	85	8.0	23.3	known failure	0.5				1.0	23.3	1.2
47-821	NE	90	45	0.2	4.9	5.9	breccia	80	12	1.5	2	5	1.0	0.4	79	8.0	16.8	known failure	1.0	65	0	0.00	1.0	16.8	1.2
48-782	SW	90	225	0.3	5.0	5.6	rhyolite	90	12	1.5	2	6	1.0	0.2	65	8.0	10.6	known failure	1.0	30	20	0.45	0.4	3.7	0.9
51-675	SE	90	135	0.4	5.6	5.8	sulphide	80	6	1	1	13	1.0	0.2	85	2.5	8.4	known failure	1.0	62	0	0.00	0.4	3.4	0.9
51-705	NE	82	51	0.3	3.7	4.3	fragmental	65	12	1.5	2	4	1.0	0.2	65	7.2	6.0	known failure	1.0	17	0	0.00	0.1	0.5	0.8
51-731	SW	116	206	0.3	5.2	5.8	breccia	45	12	1.5	2	3	1.0	0.2	79	3.1	1.8	known failure	1.0	14	20	0.40	1.0	1.8	0.8
51-782	NE	82	45	0.4	5.0	5.4	breccia	80	12	1.5	2	5	1.0	0.4	79	7.2	14.0	known failure	1.0	15	3	0.08	0.2	2.1	0.9
54-821	NE	81	45	0.4	5.0	5.5	rhyolite	70	12	1.5	2	4	1.0	0.2	75	7.0	6.1	check	1.0	16	6	0.15	0.1	0.5	0.7
56-705	NW	90	315	0.5	7.5	7.0	sulphide	80	6	1	1	13	1.0	0.2	85	8.0	26.7	known failure	1.0				1.0	26.7	1.2
60-791	NE	69	45	0.3	5.0	5.6	breccia	90	12	1.5	2	6	1.0	0.4	79	5.8	12.9	known failure	1.0	4	5	0.11	0.1	1.3	0.8
60-791	SW	105	225	0.3	5.0	5.5	stringer	78	12	1.5	2	5	1.0	0.4	79	3.1	5.8	known failure	1.0	10	0	0.00	0.1	0.8	0.7
47-645	SW	104	239	0.2	4.4	5.4	rhyolite	73	12	1.5	2	5	1.0	0.2	85	2.5	2.3	known failure	1.5	75	0	0.00	1.0	2.3	0.9
49-821	NW	90	315	0.6	7.7	7.0	stringer	85	12	1.5	2	5	1.0	0.3	83	8.0	11.6	known failure	1.5	69	8	0.20	1.0	11.6	1.0
51-731	NW	90	315	0.8	11.7	9.0	stringer	80	12	1.5	2	5	1.0	0.3	83	8.0	10.9	known failure	1.5	64	0	0.00	1.0	10.9	0.9

56-695	NE	67	36	0.3	5.1	5.7	rhyolite	90	12	1.5	2	6	1.0	0.2	75	5.7	6.4	known failure	1.5	37	0	0.00	0.3	1.9	0.8
47-725	SW	106	230	0.4	8.6	9.4	rhyolite	78	12	1.5	2	5	1.0	0.2	65	4.5	4.4	known failure	2.0	11	0	0.00	0.1	0.5	0.5
48-782	NE	86	45	0.3	5.0	5.6	rhyolite	93	12	1.5	2	6	1.0	0.2	65	7.5	8.8	known failure	2.0	51	0	0.00	0.7	6.1	1.0
51-735	SE	90	135	0.8	10.9	9.0	sulphide	90	6	1	1	15	1.0	0.2	85	2.5	9.5	known failure	2.0	52	0	0.00	1.0	9.5	0.9
Stope	Face	dip	dip-dir	Ar	span/3	HR	Rock	RQD	Jn	Jr	Ja	Q'	A	B	crit jnt	C	N'	Perform.	O-break	In-angle	Flt Dist	Dist/h	Fw	N'	delta
53-735	SW	100	252	0.2	4.9	6.0	rhyolite	90	12	1.5	2	6	1.0	0.2	85	2.5	2.9	known failure	2.0	35	0	0.00	0.3	0.7	0.7
56-781	NE	90	45	0.3	5.0	5.6	rhyolite	75	12	1.5	2	5	1.0	0.2	65	8.0	8.7	known failure	2.0	29	0	0.00	0.2	1.4	0.8
51-725	SE	90	135	0.6	7.9	7.3	sulphide	90	6	1	1	15	1.0	0.2	85	2.5	9.5	known failure	2.5	49	1	0.03	1.0	9.5	1.0
49-782	NE	78	45	0.4	5.0	5.4	breccia	48	12	1.5	2	3	1.0	0.4	79	6.7	7.6	known failure	3.0	13	25	0.64	1.0	7.6	1.1
56-755	NE	66	46	0.3	5.0	5.7	rhyolite	60	12	1.5	2	4	1.0	0.2	65	5.6	4.2	known failure	3.0	26	18	0.33	0.9	3.8	0.9
56-781	SE	90	144	0.6	8.2	7.9	stringer	80	12	1.5	2	5	1.0	0.2	87	2.3	2.5	known failure	3.0	48	1	0.02	1.0	2.5	0.7
58-695	SE	95	135	0.7	10.0	8.2	sulphide	90	6	1	1	15	1.0	0.2	85	2.5	7.6	known failure	3.0	40	0	0.00	0.7	4.9	0.8
60-725	NE	73	29	0.4	5.1	5.5	breccia	90	12	1.5	2	6	1.0	0.2	79	6.2	7.0	known failure	3.0	11	0	0.00	0.1	0.8	0.7
60-755	NE	66	41	0.3	5.0	5.6	rhyolite	60	12	1.5	2	4	1.0	0.2	75	5.6	4.2	known failure	3.0	4	17	0.35	1.0	4.2	1.0
47-645	NE	71	50	0.2	4.3	5.3	rhyolite	90	12	1.5	2	6	1.0	0.2	65	6.0	6.8	known failure	3.5	9	0	0.00	0.2	1.4	0.8
47-725	NE	69	47	0.3	8.3	9.1	breccia	30	12	1.5	2	2	1.0	0.4	79	5.9	4.7	known failure	5.0	10	0	0.00	0.1	0.5	0.5
48-725	NE	74	45	0.3	5.0	5.5	rhyolite	78	12	1.5	2	5	1.0	0.2	75	6.3	6.1	known failure	5.0	14	3	0.07	0.2	1.2	0.8
56-735	NE	63	43	0.3	5.0	5.7	rhyolite	80	12	1.5	2	5	1.0	0.2	75	5.3	5.3	known failure	5.0	3	9	0.17	0.1	0.4	0.6
53-735	NE	81	10	0.2	5.0	6.6	rhyolite	10	12	1.5	2	1	1.0	0.2	65	7.1	0.9	known failure	6.0	37	0	0.00	0.1	0.1	0.4
58-695	NE	68	54	0.2	3.8	4.5	rhyolite	90	12	1.5	2	6	1.0	0.2	85	5.8	6.5	known failure	6.0	9	13	0.28	0.5	3.2	1.0
53-695	NE	82	40	0.2	5.0	6.2	rhyolite	90	12	1.5	2	6	1.0	0.2	75	7.2	8.1	known failure	7.5	18	0	0.00	0.1	0.7	0.7
54-755	NE	85	71	0.4	5.0	5.6	breccia	40	12	1.5	2	3	1.0	0.2	83	7.5	4.2	known failure	7.5	34	0	0.01	0.0	0.1	0.5
54-735	NE	80	58	0.4	5.0	5.5	rhyolite	90	12	1.5	2	6	1.0	0.2	85	6.9	7.8	known failure	8.0	23	7	0.17	0.1	0 6	0.7

APPENDIX D

ASHANTI GOLDFIELDS CORPORATION (GHANA) LTD.

GEOTECHNICAL ENGINEERING DEPARTMENT
LAUBSCHER'S ROCK MASS CLASSIFICATION SYSTEM

Location: Block 2: Date: 7 December 1993

Table D.1 A Rock Mass Rating

Description	Location and length	Intact rock strength						Fracture frequency per metre					Joint Condition						RMR
		Max. UCS	Min. UCS	% Weak	Factor %	Ave (MPa)	Rating	No. fractures	Length (m)	Factor	FF/m	Rating	A %	B %	C %	D %	Total %	Rating	Total
Hangingwall	38, 39 level	150	80	10	89	134	14	82	5	1.5	10.9	10	95	85	100	95	76.7	31	55
Graphite	38 level	150	15	10	48	72	8	150	5	1.5	20.0	5	90	70	100	85	53.6	31	34
Schist	38, 39 level	150	60	5	91	137	14	50	5	1.5	6.7	12	95	90	100	100	85.5	34	50
Footwall	38 level	150	80	10	89	134	14	82	5	1.5	10.9	10	95	85	100	95	76.7	31	55

Table D.2 A Rock Mass Rating Adjustments

Description	Location and length	Mining Rock Mass Rating							Rock Mass Strength			Design Rock Mass Strength				
		RMR total	Weathering	Joint dip.	Mining stress	Blasting %	Total %	M.R.M.R.	I.R.S. rating	Ave I.R.S.	R.M.S.(MPa)	Weathering	Joint orient.	Blasting %	Total factor	D.R.M.S (MPa)
Hangingwall	38, 39	55	92	75	100	90	62.1	34	14	134	54	94	75	90	63.5	34
Graphite	38 level	34	88	80	100	90	63.4	22	8	72	10	88	80	90	63.4	12
Schist	38, 39	60	94	80	100	90	67.7	41	14	137	63	92	80	90	66.2	42
Footwall	38 level	55	92	80	100	90	66.2	36	14	134	54	95	80	90	68.4	37

Table D.3 A Mining Rock Mass Rating

Description	Location	RMR		MRMR			Comments
		Rating	Class	Rating	Class	Rating Description	
Hangingwall	38, 39 level	55	3A	34	4A	Poor	Blocky hangingwall
Graphite	38 level	34	4A	22	4B	Poor	Graphite/quartz
Schist	38, 39 level	60	3A	41	3B	Fair	Schist/dyke
Footwall	38 level	55	3A	36	4A	Poor	Footwall

Table D.4A. Summary of stope geometry and performance data collected from Ashanti

Mine (Shaft)	Panel Name	Block name	Bottom Level	Top Level	Stope Bottom	Width (m) Top	Average Width	Height (m)	Length (m)	Local dip ore dip	Period of mining	Status	Stope performance
KMS	Stope 1	Block 2	39L	39#1 S/L	12.4	16.8	14.6	24	15.2	62	23/2-26/4/96	Mined &filled	H/W-crown failure up to 38#1 L, across to 162 X-cut
KMS	Stope 2	Block 2	39L	39#1 S/L	15.5	29.2	22.4	24	18.2	71	?	Mined &filled	?
KMS	Stope 3	Block 2	39L	39#1 S/L	7.8	28.3	18.1	24	15.2	65	?	Mined &filled	Connected to a.m stope 1 failure
KMS	Stope 4	Block 2	39L	39#1 S/L	21	15.6	18.3	24	15.2	58	23/11-2/1/97	Mined &filled	Crown failure Up to 38L
KMS	Stope 5	Block 2	39L	39#1 S/L	12.7	17.3	15.0	24	15.2	70	4/2-13/2/97	Mined &filled	?
KMS	Pillar 7	Block 2	39L	39#1 S/L	19	15.9	17.5	24	15.2	69	4/4-18/4/97	Mined &filled	Crown failure up to 38 L and
KMS	Pillar 8	Block 2	39L	39#1 S/L	16.6	32.2	24.4	24	15.2	85	24/5-25/5/97	Mined &filled	Crown failure up to 38 L, cutting to connect 159 void.
KMS	Pillar 7	Block 2	39#1	38#1 S/L	15.9	18.9	17.4	24	15.2	80		Mined/filling	Crown failure above 38#1 L
KMS	Stope 2	Block 2	39#1	38#1 S/L	29.2	12.7	21.0	24	15.2	64		Active	Ground slightly fractured, exposure
KMS	Stope 1	Block 7	28L,	27L	18.2	31.9	25.1	30	21.0	70	6/2-20/8/93	Mined&filled	
KMS	Pillar 1	Block 7	28L	27L	15.2	27.4	21.3	30	21.3	70	-	Intact	
KMS	Stope 2	Block 7	28L	27L	9.1	22.8	16.0	30	18.8	70	27/3/94-16/4/95	Mined&filled	
KMS	Pillar 2	Block 7	28L	27L	9.1	15.2	12.2	30	15.5	70	-	Intact	
KMS	Stope 3	Block 7	28L	27L	13.7	15.2	14.4	30	27.4	70	3/12/93/15/4/94	Mined&filled	
KMS	Pillar 3	Block 7	28L	27L	12.2	16.7	14.4	30	17.0	70	29/5/96-13/6/96	Mined	Failed from 28No.1 to 27No.1 in July 1996
KMS	Stope 4	Block 7	28L	27L	12.2	19.8	16.0	30	27.1	70	16/10/94-9/2/95	Mined&filled	
KMS	Pillar 4	Block 7	28L	27L	13.7	18.2	16.0	30	24.3	70	Mar-96	Mined	
KMS	Stope 5	Block 7	28L	27L	10.6	13.7	12.2	30	24.3	70	28/4-22/9/94	Mined&filled	Crown failed from 27L to 27No.1 in September 1994.
KMS	Pillar 5	Block 7	28L	27L	9.1	12.2	10.6	30	26.4	70	14/8-28/8/95	Mined	
KMS	Stope 6	Block 7	28L	27L	9.1	9.1	9.1	30	16.7	70	25/4/96-	Mined	
KMS	Stope 7	Block 7	28L	27L	24.9	29.9	27.4	30	26.4	70	19/10/96-5/2/97	Mined&filled	
KMS	Pillar 7	Block 7	28L	27L	23.9	10.0	16.9	30	15.0	70	-	Intact	
KMS	Stope 8	Block 7	28L	27L	23.9	10.0	17.0	30	15.0	70	14/3/97	Mined	
ETS	Stope 1	Pillar	35L	35#1			6					mined&filled	Crown failure including hangingwall
GCS	Stop1	Block 8	30L	29L	5	11.4	8.2	17.8	15.5			Mined&filled	Stable
GCS	Stope2	Block 8	30L	29L	10	9	9.5	20	25			Mined/filling	unstable footwall

Table D.5A Ashanti Goldfields Company open stope database

Block name	Bottom Level	Top Level	Panel Name	stope surface	Surface Dip	HR (m)	RQD	Q'	Thickness of graphite(m)	Qm' Corrected.	B	C	A	N'	Span/ 3	N'corr	Depth of failure	Status
Sh-pillar	35L	35#1	Stope 1	NW-wall	72	3.1	30	0.9		0.9	0.21	6.1	1.0	1.2	3.3	1.2	0	stable
Sh-pillar	35L	35#1	Stope 1	SE-wall	70	3.1	30	1.5	0.5	1.3	0.20	8.0	1.0	2.4	3.3	2.1	0	stable
Sh-pillar	35L	35#1	Stope 1	NE-wall	90	2.4	20	2.0	3	0.8	0.29	8.0	1.0	4.6	2.3	1.9	0	stable
Sh-pillar	35L	35#1	Stope 1	SW-wall	90	2.4	20	2.0	3	0.8	0.29	8.0	1.0	4.6	2.3	1.9	0	stable
Sh-pillar	35L	35#1	Stope 1	SE-wall*	70	3.9	30	1.5		1.5	0.20	8.0	1.0	2.4	3.3	2.4	0	stable
Sh-pillar	35L	35#1	Stope 1	NE-wall*	90	2.9	20	2.0	3	0.8	0.29	8.0	1.0	4.6	2.3	1.9	0	stable
Sh-pillar	35L	35#1	Stope 1	SW-wall*	90	2.9	20	2.0	3	0.8	0.29	8.0	1.0	4.6	2.3	1.9	0	stable
Block 8	30L	29L	Stope1	SW-wall	79	4.2	80	20.0	3.5	5.8	0.22	8.0	1.0	34.9	5.0	10.0	0	stable
Block 8	30L	29L	Stope1	SE-wall	85	2.7	70	8.8		8.8	0.20	7.5	1.0	13.1	3.7	13.1	0	stable
Block 8	30L	29L	Stope1	NW-wall	85	2.7	70	3.5		3.5	0.20	7.5	1.0	5.2	3.7	5.2	0	stable
Block 8	30L	29L	Stope1	crown	0	1.9	80	20.0		20.0	0.20	2.0	1.0	8.0	5.0	8.0	0	stable
Block 8	30L	29L	Stope2	SE-wall	85	5.0	70	8.8	2.5	5.8	0.20	7.5	1.0	13.1	3.0	8.7	0	stable
Block 8	30L	29L	Stope2	NW-wall	85	4.6	70	3.5		3.5	0.20	7.5	1.0	5.2	3.0	5.2	0	stable
Block 8	30L	29L	Stope2	crown	0	3.3	60	15.0	3.5	3.7	0.20	2.0	1.0	6.0	8.3	1.5	0	stable
Block 8	30L	29L	Stope1	NE-wall	74	4.2	80	8.0		8.0	0.22	8.0	1.0	14.0	5.0	14.0	0	stable
Block 2	39L	39#1 S/L	Stope 1	NW-wall	66	4.8	65	1.6		1.6	0.30	5.6	1.0	2.7	5.1	2.7	0	stable
Block 2	39L	39#1 S/L	Stope 1	SE-wall	66	4.8	60	3.0		3.0	0.30	3.8	1.0	3.4	5.1	3.4	0	stable
Block 2	39L	39#1 S/L	Stope 3	NE-wall	90	4.7	40	1.3	3.6	0.9	0.20	8	1.0	2.0	9.4	1.5	0	stable
Block 2	39L	39#1 S/L	Stope 3	SW-wall	90	4.7	40	1.3	3.6	0.9	0.20	8	1.0	2.0	9.4	1.5	0	stable
Block 2	39L	39#1 S/L	Stope 3	SE-wall	54	5.0	60	3.0	2.4	1.9	0.20	3.8	1.0	2.3	5.1	1.4	0	stable
Block 2	39L	39#1 S/L	Stope 3	NW-wall	63	4.9	65	1.6	1.2	1.3	0.29	5.3	1.0	2.5	5.1	2.1	0	stable
Block 2	39L	39#1 S/L	Stope 4	NE-wall	90	4.9	40	1.3		1.3	0.20	8	1.0	2.0	5.2	2.0	0	stable
Block 2	39L	39#1 S/L	Stope 4	SW-wall	90	4.9	40	1.3		1.3	0.20	8	1.0	2.0	5.2	2.0	0	stable
Block 2	39L	39#1 S/L	Stope 4	SE-wall	70	4.8	60	3.0		3.0	0.20	8.2	1.0	4.9	5.1	4.9	0	stable

Block 2	39L	39#1 S/L	Stope 4	NW-wall	60	4.9	65	1.6		1.6	0.29	5	1.0	2.4	5.1	2.4	0	stable
Block 2	39L	39#1 S/L	Stope 5	SW-wall	90	4.2	40	1.3	3.6	0.8	0.20	8	1.0	2.0	5.8	1.3	0	stable
Block 2	39L	39#1 S/L	Stope 5	SE-wall	54	5.0	60	3.0		3.0	0.20	3.8	1.0	2.3	5.1	2.3	0	stable
Block 2	39L	39#1 S/L	Stope 5	NW-wall	63	4.9	65	1.6	3.6	1.0	0.27	5.3	1.0	2.4	5.1	1.4	0	stable
Block 2	39L	39#1 S/L	Pillar 7	NE-wall	90	4.8	40	1.3		1.3	0.20	8.0	1.0	2.0	5.3	2.0	0	stable
Block 2	39L	39#1 S/L	Pillar 7	SW-wall	90	4.8	40	1.3		1.3	0.20	8.0	1.0	2.0	5.3	2.0	0	stable
Block 2	39L	39#1 S/L	Pillar 7	SE-wall	63	4.9	60	3.0		3.0	0.20	3.8	1.0	2.3	5.1	2.3	0	stable
Block 2	39L	39#1 S/L	Pillar 7	NW-wall	72	4.8	65	1.6		1.6	0.20	6.1	1.0	2.0	5.1	2.0	0	stable
Block 2	39L	39#1 S/L	Pillar 7	NE-wall*	90	4.9	40	1.3		1.3	0.20	8	1.0	2.0	5.8	2.0	0	stable
Block 2	39L	39#1 S/L	Pillar 7	SW-wall*	90	4.9	40	1.3		1.3	0.20	8	1.0	2.0	5.8	2.0	0	stable
Block 2	39L	39#1 S/L	Pillar 7	SE-wall*	63	4.8	60	3.0		3.0	0.20	3.8	1.0	2.3	5.1	2.3	0	stable
Block 2	39L	39#1 S/L	Pillar 7	NW-wall*	72	4.8	65	1.6		1.6	0.20	6.1	1.0	2.0	5.1	2.0	0	stable
Block 2	39L	39#1 S/L	Pillar 7	NE-wall**	90	5.0	40	1.3		1.3	0.20	8	1.0	2.0	4.2	2.0	0	stable
Block 2	39L	39#1 S/L	Pillar 7	SW-wall**	90	5.0	40	1.3		1.3	0.20	8	1.0	2.0	4.2	2.0	0	stable
Block 2	39L	39#1 S/L	Pillar 7	SE-wall**	63	5.5	60	3.0		3.0	0.20	3.8	1.0	2.3	5.1	2.3	0	stable
Block 2	39L	39#1 S/L	Pillar 7	NW-wall**	72	5.5	65	1.6		1.6	0.20	6.1	1.0	2.0	5.1	2.0	0	stable
Block 2	39L	39#1 S/L	Pillar 8	NE-wall	90	5.8	40	1.3	2.4	1.0	0.20	8	1.0	2.0	10.7	1.7	0	stable
Block 2	39L	39#1 S/L	Pillar 8	SE-wall	66	4.8	60	3.0		3.0	0.27	3.8	1.0	3.1	5.1	3.1	0	stable
Block 2	39L	39#1 S/L	Pillar 8	NW-wall	71	4.8	65	1.6		1.6	0.29	6.0	1.0	2.8	5.1	2.8	0	stable
Block 2	39L	39#1 S/L	Pillar 8	NE-wall*	90	5.0	40	1.3	2.4	1.0	0.20	8	1.0	2.0	10.7	1.7	0	stable
Block 2	39L	39#1 S/L	Pillar 8	SE-wall*	66	7.8	60	3.0		3.0	0.27	3.8	1.0	3.1	10.0	3.1	0	stable
Block 2	39L	39#1 S/L	Pillar 8	NW-wall*	71	7.7	65	1.6		1.6	0.29	6.0	1.0	2.8	10.0	2.8	0	stable
Block 2	39#1	38#1 S/L	Pillar 7	NE-wall	90	4.8	40	1.3	2.4	0.9	0.20	8	1.0	2.0	6.3	1.5	0	stable

Block 2	39#1	38#1 S/L	Pillar 7	SW-wall	90	4.8	40	1.3		1.3	0.20	8	1.0	2.0	6.3	2.0	0	stable
Block 2	39#1	38#1 S/L	Pillar 7	SE-wall	63	4.9	60	3.0		3.0	0.20	3.8	1.0	2.3	5.1	2.3	0	stable
Block 2	39#1	38#1 S/L	Pillar 7	NW-wall	72	4.8	65	1.6		1.6	0.20	6.1	1.0	2.0	5.1	2.0	0	stable
Block 2	39#1	38#1 S/L	Pillar 7	NE-wall	90	5.9	40	1.3	2.4	0.9	0.20	8	1.0	2.0	6.3	1.5	0	stable
Block 2	39#1	38#1 S/L	Pillar 7	SW-wall	90	5.9	40	1.3	2.4	0.9	0.20	8	1.0	2.0	6.3	1.5	0	stable
Block 2	39#1	38#1 S/L	Pillar 7	SE-wall	63	5.9	60	3.0		3.0	0.20	3.8	1.0	2.3	5.1	2.3	0	stable
Block 2	39#1	38#1 S/L	Pillar 7	NW-wall	72	5.8	65	1.6		1.6	0.20	6.1	1.0	2.0	5.1	2.0	0	stable
Block 7	28L,	27L	Stope 1	NE-wall	90	6.7	40	1.0	3.6	0.7	0.34	8.0	1.0	2.7	6.7	1.9	0	stable
Block 7	28L,	27L	Stope 1	SW-wall	90	6.7	40	1.0	3.6	0.7	0.34	8.0	1.0	2.7	6.7	1.9	0	stable
Block 7	28L,	27L	Stope 1	SE-wall	64	6.5	90	4.5	1.2	3.7	0.20	5.7	1.0	5.1	7.1	4.2	0	stable
Block 7	28L,	27L	Stope 1	NW-wall	73	6.3	60	1.5	2.4	1.1	0.20	6.2	1.0	1.9	7.1	1.4	0	stable
Block 7	28L,	27L	Stope 1	crown	0	5.2	40	1.0	3.6	0.7	0.34	2	1.0	0.7	7.1	0.5	0	stable
Block 7	28L	27L	Stope 2	NE-wall	90	4.7	40	1.0	3.6	0.7	0.34	8	1.0	2.7	3.0	2.0	0	stable
Block 7	28L	27L	Stope 2	SW-wall	90	4.7	40	1.0	3.6	0.7	0.34	8	1.0	2.7	3.0	2.0	0	stable
Block 7	28L	27L	Stope 2	SE-wall	58	5.7	90	4.5	1.2	3.6	0.24	5.7	1.0	6.1	4.5	4.9	0	stable
Block 7	28L	27L	Stope 2	NW-wall	63	5.6	60	1.5	1.2	1.3	0.20	5.3	1.0	1.6	4.5	1.3	0	stable
Block 7	28L	27L	Stope 3	NE-wall	90	4.3	40	1.0	4.8	0.6	0.34	8	1.0	2.7	4.6	1.6	0	stable
Block 7	28L	27L	Stope 3	SW-wall	90	4.3	40	1.0	4.8	0.6	0.34	8	1.0	2.7	4.6	1.6	0	stable
Block 7	28L	27L	Stope 3	SE-wall	54	5.8	70	3.5	1.2	2.8	0.24	5.7	1.0	4.9	5.7	3.8	0	stable
Block 7	28L	27L	Stope 3	NW-wall	60	5.7	60	1.5	3.6	0.9	0.20	5	1.0	1.5	5.7	0.9	0	stable
Block 7	28L	27L	Pillar 3	NE-wall	90	4.4	40	1.0	3.6	0.7	0.34	8	1.0	2.7	4.1	1.8	0	stable
Block 7	28L	27L	Pillar 3	SW-wall	90	4.4	40	1.0	3.6	0.7	0.34	8	1.0	2.7	4.1	1.8	0	stable
Block 7	28L	27L	Pillar 3	SE-wall	56	7.7	75	3.8	1.2	3.0	0.23	5.7	1.0	4.9	9.0	3.9	0	stable
Block 7	28L	27L	Pillar 3	NW-wall	67	7.4	60	1.5	2.4	1.1	0.26	5.7	1.0	2.2	9.0	1.6	0	stable
Block 7	28L	27L	Stope 4	NE-wall	90	4.8	40	1.0	2.4	0.8	0.34	8.0	1.0	2.7	4.1	2.1	0	stable
Block 7	28L	27L	Stope 4	SW-wall	90	4.8	40	1.0	2.4	0.8	0.34	8.0	1.0	2.7	4.1	2.1	0	stable
Block 7	28L	27L	Stope 4	SE-wall	60	7.1	70	3.5	1.2	3.0	0.30	5.7	1.0	6.0	8.1	5.1	0	stable
Block 7	28L	27L	Stope 4	NW-wall	62	7.1	60	1.5	1.2	1.3	0.20	5.2	1.0	1.6	8.1	1.4	0	stable
Block 7	28L	27L	Pillar 4	NE-wall	90	5.0	40	1.0	2.4	0.8	0.34	8	1.0	2.7	4.6	2.1	0	stable
Block 7	28L	27L	Pillar 4	SW-wall	90	5.0	40	1.0	2.4	0.8	0.34	8	1.0	2.7	4.6	2.1	0	stable
Block 7	28L	27L	Pillar 4	SE-wall	66	7.0	70	3.5		3.5	0.26	5.7	1.0	5.2	8.1	5.2	0	stable

Block 7	28L	27L	Pillar 4	NW-wall	70	6.9	60	1.5	2.4	1.2	0.37	5.9	1.0	3.3	8.1	2.6	0	stable
Block 7	28L	27L	Stope 5	NE-wall	90	4.1	40	1.0	3.6	0.6	0.34	8.0	1.0	2.7	2.4	1.7	0	stable
Block 7	28L	27L	Stope 5	SW-wall	90	4.1	40	1.0	3.6	0.6	0.34	8.0	1.0	2.7	2.4	1.7	0	stable
Block 7	28L	27L	Stope 5	SE-wall	61	7.7	70	3.5		3.5	0.21	5.7	1.0	4.2	9.3	4.2	0	stable
Block 7	28L	27L	Stope 5	NW-wall	76	7.3	60	1.5	3.6	1.1	0.44	6.5	1.0	4.3	9.3	3.0	0	stable
Block 7	28L	27L	Pillar 5	NE-wall	90	3.5	40	1.0	2.4	0.7	0.34	8.0	1.0	2.7	2.4	1.9	0	stable
Block 7	28L	27L	Pillar 5	SW-wall	90	3.5	40	1.0	2.4	0.7	0.34	8.0	1.0	2.7	2.4	1.9	0	stable
Block 7	28L	27L	Pillar 5	SE-wall	65	5.1	70	3.5	1.2	3.0	0.20	5.7	1.0	4.0	4.9	3.4	0	stable
Block 7	28L	27L	Pillar 5	NW-wall	76	5.0	60	1.5	1.2	1.3	0.41	6.5	1.0	4.1	4.9	3.6	0	stable
Block 7	28L	27L	Stope 6	NE-wall	90	3.3	40	1.0	2.4	0.6	0.34	8.0	1.0	2.7	3.0	1.7	0	stable
Block 7	28L	27L	Stope 6	SW-wall	90	3.3	40	1.0	2.4	0.6	0.34	8.0	1.0	2.7	3.0	1.7	0	stable
Block 7	28L	27L	Stope 6	SE-wall	66	7.3	70	3.5	1.2	2.8	0.20	5.7	1.0	4.0	8.8	3.1	0	stable
Block 7	28L	27L	Stope 6	NW-wall	68	7.3	60	1.5	1.2	1.3	0.28	5.8	1.0	2.4	8.8	2.0	0	stable
Block 7	28L	27L	Stope 7	NE-wall	90	6.8	40	1.0	3.6	0.8	0.34	8	1.0	2.7	8.3	2.1	0	stable
Block 7	28L	27L	Stope 7	SW-wall	90	6.8	40	1.0	3.6	0.8	0.34	8	1.0	2.7	8.3	2.1	0	stable
Block 7	28L	27L	Stope 7	SE-wall	60	5.2	70	3.5	2.4	2.6	0.20	5.7	1.0	4.0	5.0	3.0	0	stable
Block 7	28L	27L	Stope 7	NW-wall	70	5.1	60	1.5	1.2	1.3	0.28	5.9	1.0	2.5	5.0	2.2	0	stable
Block 7	28L	27L	Stope 8	NE-wall	90	5.0	40	1.0	3.6	0.5	0.34	8.0	1.0	2.7	8.0	1.5	0	stable
Block 7	28L	27L	Stope 8	SW-wall	90	5.0	40	1.0	3.6	0.5	0.34	8.0	1.0	2.7	8.0	1.5	0	stable
Block 7	28L	27L	Stope 8	SE-wall	58	5.3	70	3.5	2.4	2.1	0.21	5.7	1.0	4.1	5.0	2.5	0	stable
Block 7	28L	27L	Stope 8	NW-wall	70	5.1	60	1.5	1.2	1.2	0.27	5.9	1.0	2.4	5.0	2.0	0	stable
Block 7	28L	27L	Stope 3	crown	0	3.8	40	1.0	4.8	0.5	0.20	2	1.0	0.4	4.6	0.2	1.5	unstable ?
Sh-pillar	35L	35#1	Stope 1	crown*	0	2.1	20	2.0	3	0.8	0.40	2.0	1.0	1.6	3.3	0.7	1.5	unstable
Block 7	28L	27L	Stope 2	crown	0	2.7	40	1.0	3.6	0.5	0.20	2	1.0	0.4	3.0	0.2	1.5	unstable
Block 7	28L	27L	Stope 4	crown	0	4.1	40	1.0	2.4	0.7	0.20	2	1.0	0.4	4.1	0.3	1.5	unstable
Block 7	28L	27L	Pillar 4	crown	0	4.4	40	1.0	2.4	0.7	0.20	2.0	1.0	0.4	4.6	0.3	1.5	unstable
Block 7	28L	27L	Stope 5	crown	0	2.9	40	1.0	3.6	0.5	0.20	2.0	1.0	0.4	2.4	0.2	1.5	unstable
Block 7	28L	27L	Pillar 5	crown	0	2.4	40	1.0	2.4	0.6	0.20	2.0	1.0	0.4	2.4	0.2	1.5	unstable
Block 7	28L	27L	Stope 6	crown	0	3.4	40	1.0	2.4	0.6	0.20	2	1.0	0.4	3.0	0.2	1.5	unstable
Block 7	28L	27L	Stope 8	crown	0	4.6	40	1.0	3.6	0.6	0.20	2.0	1.0	0.4	8.0	0.3	1.5	unstable
Sh-pillar	35L	35#1	Stope 1	NW-wall*	72	3.9	30	0.6	2.5	0.4	0.21	6.1	1.0	0.8	3.3	0.5	3.5	caved
Block 8	30L	29L	Stope2	NE-wall	65	6.9	80	8.0	3.5	4.7	0.20	5.5	1.0	8.7	8.3	5.1	5	caved
Block 7	28L	27L	Stope 7	crown	0	4.7	40	1.0	3.6	0.7	0.20	2.0	1.0	0.4	5.0	0.3	5	caved
Block 2	39L	39#1	Stope 5	crown	0	4.0	40	1.3	3.6	0.8	0.20	2.0	1.0	0.5	5.1	0.3	6	caved

Block name	Bottom Level	S/L Top Level	Panel Name	stope surface	Surface Dip	HR (m)	RQD	Q'	Thickness of graphite(m)	Qm' Corrected.	B	C	A	N'	Span/3	N'corr	Depth of failure	Status
Block 2	39L	39#1 S/L	Stope 1	SW-wall	90	4.3	40	1.3		1.3	0.20	8	1.0	2.0	5.6	2.0	6	caved
Block 2	39L	39#1 S/L	Stope 5	NE-wall	90	4.2	40	1.3	3.6	0.8	0.20	8	1.0	2.0	5.8	1.3	6	caved
Block 2	39L	39#1 S/L	Pillar 8	SW-wall*	90	5.0	40	1.3	2.4	1.0	0.20	8	1.0	2.0	10.7	1.7	6	caved
Block 2	39L	39#1 S/L	Stope 3	crown	0	4.9	40	1.3	3.6	0.8	0.20	2	1.0	0.5	5.1	0.3	7	caved
Block 2	39L	39#1 S/L	Stope 1	NE-wall	90	4.3	40	1.3		1.3	0.20	8	1.0	2.0	5.6	2.0	9	caved
Block 2	39L	39#1 S/L	Pillar 8	crown	0	5.2	40	1.3	3.5	0.8	0.20	2	1.0	0.5	5.1	0.3	9	caved
Block 2	39L	39#1 S/L	Stope 4	crown	0	3.8	40	1.3		1.3	0.20	2	1.0	0.5	5.1	0.5	9.5	caved
Block 8	30L	29L	Stope2	SE-wall	79	6.6	80	4.0	3.5	2.5	0.20	6.3	1.0	5.1	8.3	3.2	11	caved
Block 2	39L	39#1 S/L	Pillar 8	SW-wall	90	5.8	40	1.3	2.4	0.9	0.20	8	1.0	2.0	10.7	1.4	11	caved
Block 2	39L	39#1 S/L	Pillar 7	crown	0	3.9	40	1.3		1.3	0.20	2	1.0	0.5	5.1	0.5	12	caved
Block 2	39L	39#1 S/L	Pillar 7	crown*	0	4.1	40	1.3		1.3	0.34	2	1.0	0.9	5.1	0.9	12	caved
Block 2	39#1	38#1 S/L	Pillar 7	crown	0	4.2	40	1.3	2.4	0.9	0.20	2.0	1.0	0.5	5.1	0.4	12	caved
Block 2	39L	39#1 S/L	Pillar 8	crown*	0	7.8	40	1.3	3.5	1.0	0.20	2	1.0	0.5	10.0	0.4	15	caved
Sh-pillar	35L	35#1	Stope 1	crown	0	2.1	20	2.0	2	1.0	0.20	2.0	1.0	0.8	3.3	0.4	20	caved
Block 2	39#1	38#1 S/L	Pillar 7	crown	0	4.2	40	1.3	2.4	0.9	0.20	2	1.0	0.5	5.1	0.4	21	caved
Block 2	39L	39#1 S/L	Stope 1	crown	0	4.0	40	1.3		1.3	0.20	2	1.0	0.5	5.1	0.5	24	caved
Block 2	39L	39#1 S/L	Pillar 7	crown**	0	3.4	40	1.3		1.3	0.20	2	1.0	0.5	5.1	0.5	25.8	caved
Block 7	28L	27L	Pillar 3	crown	0	4.2	40	1.0	3.6	0.6	0.20	2.0	1.0	0.4	9.0	0.2	45	caved

REFERENCES

Agongo, W., Senior Geologist, Kwesi Mensah Shaft, Ashanti Goldfields Company (Gh) Ltd., *Personal Communication.*

Amanor, J.A., and Gyapong, W.A., 1988. The geology of Ashanti Goldfields. *Proc. Int. Conf. Geology of Ghana, Accra*, Ghana, 14 pp.

Amponsah-Mensah, P. Underground Manager, Kwesi Mensah Shaft, Ashanti Goldfields Company (Gh) Ltd., *Personal communication.*

Anderson, E.M., 1942. *The Dynamics of Faulting*. Oliver and Boyd, London, 183 pp.

Anonymous, 1993. Block 2 rockmass characteristics. *Report from Geotechnical Engineering Department*, Ashanti Goldfields Company, (Gh) Ltd.

Archinbault, G., Flamand, R., Rouleau, A., and Daigneault, R., 1992. Mechanics of fault zone development. *Proc. In. Conf. Rock Mechanics*, (ed., Tillerson and Wawersik), Rotterdam: A.A. Balkema, pp. 101-111.

Arjang, B, 1989. Pre-mining stresses at some hard rock mines in Canadian Shield. *Proc. Rock Mech. as a Guide for Efficient Utilization of Natural Resources* (ed. Khair), Rotterdam: A.A. Balkema, pp 545-551.

Barnard, G.A., Jenkins, G.M., and Winsten, C.B., 1962. Likelihood inference and time series. *J.R. Stat. Soc. (A).*

Barton, N., 1976. Recent experiences with Q the Q-system of tunnel support design. *Proc. Symp. Exploration for Rock Engineering, Johannesburg*, A.A. Balkema, Vol. 1, pp. 107-117; session report, Vol. 2, pp. 167-172.

Barton, N., 1988. Rock mass classification and tunnel reinforcement selection using the Q-system. *Rock Classification Systems for Engineering Purposes*, A.S.T.M. STP 984, Louis Kirkaldie (ed.), A.S.T.M., Philadelphia, pp. 59-88.

Barton, N., 1994. A Q-system case record of cavern design in faulted rock. *Proc. Tunnelling in difficult Conditions*, Torino.

Barton, N., Lien, R. and Lunde, J., 1974. Engineering classification of rock masses for the design of tunnel support. *Rock Mechanics*, Vol. 6, pp. 188-236.

Barton, N., Lien, R. and Lunde, J., 1977. Estimation of support requirements for underground excavations. *Proc. 16th U.S. Symp. Rock Mech.*, A.S.C.E., New York, pp. 163-177; discussion on pp. 234-241.

Barton, N.R. 1983. Application of *Q*-system and index tests to estimate shear strength and deformability of rock masses. *Proc. Int. Symp. On Engineering Geology and Underground Construction*, Vol. 2, Lisbon, pp. II.51-70.

Bawden, W.F., 1993. The use of Rock Mechanics principles in Canadian hard rock underground mine design. *Comprehensive Rock Engineering: Principles, Practice and Projects*, (ed. Hudson), Oxford: Pergamon Press, 5, 247-290.

Bawden, W.F., Nantel, J. and Sprott., D., 1989. Practical rock engineering in the optimization of stope dimensions - Application and cost effectiveness. *CIM Bulletin*, 82, (926), pp. 63-70.

Beer, G., and Meek, J.L., 1982. Design curves for roofs and hanging-walls in bedded rock based on 'voussoir' beam and plate solutions. *Trans. Inst. Min. Metall.*, Section A., Vol. 91, pp. A18-A22.

Bernstein, I.H., Garbin, C.P., and Teng, G.K. 1987. *Applied Multivariate Analysis*. Springer-Verlag, Berlin.

Bieniawski, Z.T., 1973. Engineering classification of jointed rockmasses. *Trans. South African Inst. Of civil Engineers*, Vol. 15, pp. 335-344.

Bieniawski, Z.T., 1974. Geomechanics classification of rock masses and its application in tunnelling. *Proc. 3rd Int. Congr. Rock Mech.*, ISRM, Denver, Vol. IIA, pp. 27-32.

Bieniawski, Z.T., 1976. Rock mass classification in rock engineering. *Proc. Symp. Exploration for Rock Engineering*, Johannesburg, A.A. Balkema, Vol. 1., pp. 97-106; session report, Vol. 2, pp. 167-172.

Bieniawski, Z.T., 1978. Determining rock mass deformability: experience from case histories. *Int. J. Rock Mech. and Mining Sci. and Geomech. Abstr.*, Vol. 15, pp. 237-2247.

Bieniawski, Z.T., 1979. The geomechanics classification in rock engineering applications. *Proc. 4th Int. Congr., ISRM*, Montreaux, Vol. 2, pp. 41-48.

Bieniawski, Z.T., 1983. Design procedures for coal mine tunnels. *U.S. Bureau of Mines OFR-85-83*.

Bieniawski, Z.T., 1984. *Rock Mechanics Design in Mining and Tunnelling*, A.A. Balkema, Rotterdam, pp. 97-133.

Bieniawski, Z.T., 1988. The rock mass rating (RMR) system (Geomechanics classification) in engineering practice. *Rock Classification Systems for Engineering Purposes*, A.S.T.M. STP 984, Louise Kirkaldie ed., A.S.T.M., Philadelphia, pp. 17-34.

Bieniawski, Z.T., 1989. *Engineering Rock Mass Classifications*. John Wiley, New York, 251 pp.

Bieniawski, Z.T., 1993. Classification of rock masses for engineering: The RMR system and future trends. *Comprehensive Rock Engineering* (ed. Hudson), Oxford: Pergamon, 3, pp. 553-573.

Bieniawski, Z.T., and Bauer, J. 1982. Discussion. *J. Geotech. Engng. Div., A.S.C.E.*, Vol. 108, pp. 670-672.

Bleeker, W., 1994. *The giant Kidd Creek massive sulphide deposit: a new perspective*. 88 pp.

Boyd, J.M., 1988. Gravity and structurally controlled failures. *Professional Development Seminar on Rock mass Failures in Hard Rock Mines*, Session 1, Sudbury, Ontario, 8 pp.

Brady, B.H.G. and Brown, E.T., 1993. *Rock Mechanics for Underground Mining*. London: Chapman Hall, 527 pp.

Brekke, T.L. and Selmer-Olsen, R, 1966. A survey of main factors influencing the stability of underground constructions in Norway. *Proc. 1st Int. Congr. ISRM*, Lisbon, Rotterdam: A.A. Balkema, pp. 257-260.

Brekke, T.L. and Howard, T., 1972. Stability problems caused by seams and faults. *Proc. First North American Rapid Excavation and Tunnelling Conference*, A.I.M.E., New York, pp. 25-41.

Brisbin, D., Kelly, V., and Cook, R., 1990. Kidd Creek Mine. Geology and Ore Deposits of the Timmins District, (eds. Fyon and Green), *8th IAGOD Symp. Field Trip Guide 6, Geological Survey of Canada, Open File 2161*, pp. 66-76.

Brown, E.T., (ed.) 1981. *Rock Characterization, Testing and Monitoring*, Pergamon, London, 211 pp.

Brummer, R.K, 1990. *Report to Golder Associates*.

Brummer, R.K., and Kaiser, P.K., 1994. Risk-cost-benefit analysis applied to the design of support in burst-prone mines. *Proc. Conf Risk Assessment in the Extractive Industries, IMM*, University of Exeter, March.

Budavari, S. 1983. *Rock Mechanics in Mining Practice*. South Afr. Inst. Min. Metall, 282

Buttler, A.G., 1990. *Classex - An expert system for rock mass classification and tunnel design*. MSc. thesis, University of Waterloo, 116pp.

Carter T.G., and Miller, R.I., Crown pillar assessment-planning aid for cost-effective mine closure remediation. *Trans. Inst. Min. Metall.*, Section A., Vol. 104, pp. A41-A57.

Clark, L., and Pakalnis, R., 1997. An empirical design approach for estimating unplanned dilution for open stope hangingwalls and footwalls. *99th CIM-AGM*, Vancouver, on CD-ROM.

Clark, L.M. and Pakalnis, R.C., 1997. An empirical design approach for estimating unplanned dilution from open stope hangingwalls and footwalls. *CIM-AGM*, Vancouver, on CD-ROM.

Cochrane, L.B, 1988. Control of structural geology on rock mass failures. *Professional Development Seminar on Rock mass Failures in Hard Rock Mines*, Session 4, Sudbury, Ontario, 14 pp.

Cooley, W.W., and Lohnes, P.R., 1985. *Multivariate Data Analysis*. Robert E Krieger Publishing Company, Malabar, Florida.

Craig, H., Technical Services Manager, Kwesi Mensah Shaft, Ashanti Goldfields Company (Gh) Ltd., *Personal Communication*.

Cummins, A.B., and Given, I.A., 1973. *Mining Engineers Handbook*. SME, AIMME, Inc., New York, Vol. 1 & 2.

Cummins, R.A., Kendorski, F.S. and Bieniawski, Z.T., 1982. *Caving Mine Rock Mass Classifications and Support Estimation*. U.S. Bureau of Mines Contract Report #J0100103. Chicago: Engineers International, Inc.

Curran, J H., and Corkum, B.T., 1997. *PHASE^2, 2D finite element program for calculating stresses and estimating support around underground excavations.*

Curran, J H., and Corkum, B.T., 1995. *EXAMINE^{2D} boundary element program for calculating stresses around underground excavations in rock.*

Daemen, J.J.K. 1983. Slip zones for discontinuities parallel to circular tunnels or shafts. *Int. J. Rock Mech. Min. Sci. & Geomech. Abstr.*, Vol. 20, No. 3, pp. 135-148.

Decker, F., Senior Mine Planning Superintendent, George Cappendell Shaft, Ashanti Goldfields Company (Gh) Ltd., *Personal Communication.*

Deere, D.U., 1964. Technical description of rock cores for engineering purposes. *Rock Mechanics and Engineering Geology*, Vol. 1, No. 1, pp. 17-22.

Deere, D.U., 1973. The foliation shear zone - An adverse engineering geologic feature of metamorphic rocks. *ASCE*, Boston Branch, pp. 163-176.

Deere, D.U., 1979. Applied rock Mechanics - The importance of weak geological features. *Proc. 4th Inter. Congr. Rock Mechanics*, ISRM, Montreaux, Rotterdam: A.A. Balkema, Vol. 3, pp. 22-24.

Deere, D.U., and Miller, R. P., 1966. Engineering classification and index properties of intact rock. *Technical Report No. AFNL-TR-65-116*, Air Force Weapons Laboratory, New Mexico.

Diederichs, M.S., and Hoek, E, 1995. *DIPS* version 3.2, Rock Engineering Group, University of Toronto. 43 pp.

Diederichs, M.S. and Kaiser, P.K., 1998. Tensile strength and abutment relaxation as failure control mechanisms in underground excavations. Submitted to *Int. J. Of Rock Mech. And Min. Sci.*

Diederichs, M.S., and Kaiser P.K., 1996. Rock instability and risk in open stope mine design. *Can. Geotech. J.*, Vol. 33, pp. 431-439.

Diering, J.A.C., and Laubscher, D.H., 1987. Practical approach to the numerical stress analysis of mass mining operations. *Trans. Inst. Min. Metall., Section A.*, Vol. 96, pp. A179-A188.

Dune, K., and Pakalnis, R.C., 1996. Dilution aspects of a sublevel retreat stope at Detour Lake Mine. *Proc. 2nd NARMS, Rock Mechanics Symp. On Rock Mechanics Tools and Techniques*, (eds. Aubertin, Hassani and Mitri), Quebec, Rotterdam: A.A. Balkema, Vol. 1, pp.305-313.

Ferguson, G.A., 1993. Caving geomechanics. *Comprehensive Rock engineering, Principles, Practice and Projects*, (ed. Hudson), Vol. 5, pp. 443-453.

Franklin, J.A., 1993. Empirical design and rock mass characterization. *Comprehensive Rock Engineering, Principles, Practice and Projects* (ed. Hudson), Pergamon, pp. 795-806.

Franklin, J.A., and Palasi, M., 1993. Maximum span and stand-time of underground excavations. *Proc. Int. Congr. Innovative Mine Design for the 21st Century*, Kingston, Ontario, (ed., Bawden and Archinbauld), Rotterdam: A.A. Balkema, pp. 443-453.

Fuller, P.G., Barrett, J.R., and Miller, D.R., 1985. Influence of cable support in assessing open stope viability. *Proc. Asian Mining'85*, IMME, pp. 15-26.

Galvin, J.M., Hebblewhite, B.K., and Salamon, M.D.G., 1997. Australian coal pillar performance. *ISRM News Journal*, pp. 33-38.

Germain, P., and Hadjigeorgiou, J., 1998. Influence of stope geometry on mining performance. *Proc. CIM-AGM*, Montreal, on CD-ROM.

Germain, P., Hadjigeorgiou, J. and Lesard, J.F., 1996. On the relationship between stability prediction and observed stope overbreak. *Proc. 2nd NARMS. Rock Mechanics Symp. On Rock Mechanics Tools and Techniques*, (ed. Aubertin, Hassani and Mitri), Quebec, Rotterdam: A.A. Balkema, Vol. 1, pp.277-283.

Golden Software, Inc. 1997. *Surfer for Windows, Contouring and 3D Surface Mapping.*

Goodman, R.E. and Shi, G., 1985. *Block Theory and its Application to Rock Engineering.* Prentice-Hall, Inc., New Jersey, 338 pp.

Goodman, R.E., 1976. *Methods of Geological Engineering.* St. Paul: West Publishing Company, 472 pp.

Goodman, R.E., 1966. On the distribution of stresses around circular tunnels in non-homogeneous rocks. *Proc. 1st Int. Congr. ISRM*, Montreaux, pp.249-255.

Goodman, R.E., and Shi, G., 1985. *Block Theory and its Application to Rock Engineering.* Prentice-Hall International, London.

Greer, 1989. Empirical modelling of open stope stability in a vertical crater retreat application at Inco Thompson's mine. *91st Annual General Meeting of the Canadian Institute of Mining*, Quebec City, Canada, 12 pp.

Grimstat, E., Barton, N. and Loset, F., 1993. N.M.T. Tunnel support design. *World Tunnelling*, pp. 270.

Gyapong, W.A., 1993. *The Geology of Block 2.* Memorandum to Manager, Geology, Ashanti Goldfields (Ghana) Ltd., 3 pp.

Haapamaki, S, 1996. Ground conditions at Kidd Creek Mines. *Deep Mining Forum, Timmins*, 6 pp.

Hadjigeorgiou, J., LeClair, J., and Potvin, Y., 1995. An update of the stability graph method for open stope design. *97th CIM-AGM*, Rock Mechanics and Strata Control Session, Halifax, Nova Scotia.

Hafner, W., 1951. Stress distribution and faulting. *Bulletin of the Geological Society of America*, Vol. 62, pp. 373-398.

Hennings, J.G.. Yu, T.R., and Zou, D.H., 19 Rock mechanics aspects of on sill pillar recovery at Kidd Creek Mine. pp. 93-99.

Hoek E., and Brown, E.T., 1997. Practical estimates of rock mass strength. *Int. J. Rock Mech. and Min. Sci. & Geomech. Abstr.* Vol.34 (8), pp. 1165-1186.

Hoek, E, and Brown, E.T., (1980). Empirical strength criterion for rock masses. *J. Geotech. Engin.* Div., A.S.C.E., Vol. 106, No. GT9, pp. 1013-1035.

Hoek, E. 1983. Strength of jointed rock masses. 23rd Rankine Lecture. *Geotechnique*, 33, (3), 187-223 pp.

Hoek, E. and Brown, E.T., 1980. *Underground Excavations in Rock.* Institution of Mining and Metallurgy, London, 527 pp.

Hoek, E., 1983. Strength of jointed rock masses. Rankine Lecture. *Geotechnique*, Vol. 33 (3), pp. 187-223.

Hoek, E., and Brown, E.T., 1988. The Hoek -Brown failure criterion - a 1988 update. Rock engineering for underground Excavations. *Proc. 15th Canadian Rock Mechanics Symp.*, Toronto, pp. 31-38.

Hoek, E., Kaiser, P.K. and Bawden W.F., 1995. *Support of Underground Excavations in Hard Rock.* Rotterdam: A.A. Balkema, 215 pp.

Hustrulid, W.A., (ed.), 1982. *Underground Mining Methods Handbook*, S.M.E. A.I.M.M.E., Inc., New York.

Jaeger, J.C., 1960. Shear fracture of anisotropic rocks. *Geol. Mag.*, Vol. 97, pp. 65-72.

James, M., 1985. *Classification Algorithms*. John Wiley and Sons, New York, 209 pp.

Johnson, R.A., and Wichern, D.W., 1992. *Applied Multivariate Statistical Analysis*. Prentice Hall, Englewood Cliffs, New Jersey, 3rd Ed., 642 pp.

Kaiser, P.K., Falmagne, V., Suorineni, F.T., Diederichs, M.S., and Tannant, D.D. 1997. Incorporation of rockmass relaxation and degradation into empirical stope design. *CIM-AGM*, Vancouver, 15 pp.

Kastner, H, 1979. Static Des Tunnel -undo Stollenbaues., *2nd edn. Neubearbeitete Auflage*. Springer, Berlin.

Kendorski, F., Cummings, R., Bieniawski, Z.T., and Skinner, E., 1983. Rock mass classification for block caving mine drift support. Proc. *5th Int. Conf. Soc. Rock Mech.*, Melbourne, Rotterdam: A.A. Balkema, pp. B51 - B63.

Kirkaldie, L., 1988. *Rock Classification Systems for Engineering Purposes*, A.S.T.M. STP 984, A.S.T.M., Philadelphia.

Kirsten, H.A.D., 1983. Significance of the probability of failure in slope engineering. *The Civil Engineer in South Africa*, January, pp. 17-27.

Kirsten, H.A.D., 1988. Discussion on Q-system. *Rock Classification Systems for Engineering Purposes*, A.S.T.M. STP 984, Louis Kirkaldie ed., A.S.T.M., Philadelphia, pp. 85-88.

Kirsten, H.A.D., 1988. Discussion on RMR-system. *Rock Classification Systems for Engineering Purposes*, A.S.T.M. STP 984, Louis Kirkaldie ed., A.S.T.M., Philadelphia, pp. 32-33.

Kisrch, G., 1898. Die theorie der elastizitat und die bedurffnisse der festigkeislehre. *Veit Ver. Deut. Ing.*, Vol. 42, pp. 797-807.

Krige, D.G., 1951, 1994. A statistical approach to some mine evaluation problems on the Witwatersrand. *Journal of South African Inst. of Mining and metallurgy*, Vol. 52, (10), pp. 119-139.

Kumar, P., 1997. Slip zones around circular openings in a jointed Hoek-Brown medium. *Int. J. Rock Mech. and Min. Sci. & Geomech. Abstr.* Vol. 34, No. 6, pp. 875-883.

Kumi, R.A.K., Sectional Geologist, ETS shaft, Ashanti Goldfields Company (Gh) Ltd., Personal communication, *Personal Communication*.

Laubscher, D..H. 1993. Planning mass mining operations. *Comprehensive Rock Engineering: Principles, Practice, and Projects*, (ed. Hudson), Oxford: Pergamon Press, 2, pp. 547-583.

Laubscher, D.H. and Taylor, H.W., 1976. The importance of geomechanics classification of jointed rock masses in mining operations. *Exploration for Rock Engineering*, Cape Town: A.A. Balkema, (ed. Bieniawski), 1, pp. 119-128.

Laubscher, D.H., 1977. Geomechanics classification of jointed rock masses - mining applications. *Trans.Inst. Min. Metall.*, Vol. 86, Section A, pp. A1 - A8.

Laubscher, D.H., 1981. Selection of mass underground mining methods. *Proc. Design and Operations of Caving and Subsidence Storing Mines* (ed. Stewart), A.I.M.E., New York, pp. 23-38.

Laubscher, D.H., 1984. Design aspects and effectiveness of support systems in different mining conditions. *Trans. Inst. Min. Metall.*, Vol. 93, A70 - A81.

Laubscher, D.H., 1990. A geomechanics classification system for the rating of rock mass in mine design. *Journal of South African Inst. of Mining and Metallurgy*, Vol. 90, (10), pp. 257-273.

Laubscher, D.H., 1994. Cave mining – the state of the art. *The Journal of the South African Institute of Mining and Metallurgy*, Vol. 90, (10), pp. 279-293.

Lauffer, H. 1958. Gebirgsklassifizierung fur den stollenbau. *Geol. Bauwesen*, 24, (1), pp. 46-51.

Løset, F. 1992. Support needs compared at the Svartisen Road Tunnel. *Tunnels and Tunnelling*, June.

Løset, F., 1990. *Use of the Q-method for securing small weakness zones and temporary support.* NGI internal report no. 548140-1.

Mahtab, M.A., and Dixon, J.D., 1976. Influence of rock fractures and block boundary weakening on cavability. Trans. Vol. 260, *S.M.E.*, A.I.M.E, pp. 6-12.

Martin C.D. and Chandler, N.A., 1994. The progressive fracture of Lac du Bonnet granite. *Int. J. Rock Mech. and Min. Sci. & Geomech. Abstr.* Vol.31 (6), pp. 643-659.

Mathews, K.E., Hoek, E., Wyllie, D.C., and Stewart, S.B.V., 1981. *Prediction of Stable Excavations for Mining at Depth Below 1000 metres in Hard Rock. CANMET Report DSS Serial No. OSQ80-00081, DSS File No. 17SQ.23440-0-9020*, Ottawa: Dept. Energy, Mines and Resources, 39 pp.

McMahon, B.K., and Kedrick, R.F., 1969. Predicting the block caving behaviour of orebodies. *S.M.E.*, A.I.M.E., Preprint No. 69-AU-51, AIME Annual Meeting.

Merrit, A.H., 1972. Geologic prediction for underground excavations. *Proc. Conf. Rapid Excavation and Tunnelling*, New York: AIME, pp. 601-622.

Mikula, P., 1993. The influence of geotechnical monitoring on mine design at Mt Charlotte. *Proc. Conf. On Geotechnical Instrumentation and Monitoring in Open Pit and Underground Mining*, (ed. Szwedzicki), Rotterdam: A.A. Balkema, pp. 375-382.

Miller, F., Potvin, Y., and Jacob, D., 1992. Laser measurement of open stope dilution. *CIM Bulletin*, Vol. 85 (962), pp. 96-102.

Milne, D., and Pakalnis, R., 1997. Theory behind empirical design techniques. *12[e] Colloque en Controle de Terrain de l'Association Minierre du Quebec*, Val d'Or, Quebec, 20 pp.

Milne, D., Pakalnis, R., and Lunder, P., 1996. Approach to the quantification of hanging-wall behaviour. *Trans. Inst. Min. Metall., Section A*, Vol. 105, pp. A69 - A74.

Milne, D., Pakalnis, R.C., and Felderer, M., 1996. Surface geometry assessment for open stope design. *Proc. Rock Mechanics* (eds. Aubertin, Hassani, and Mitri), Rotterdam: A.A. Balkema, pp.315-322.

Mireku-Gyimah, D., and Suglo, R.S., 1993. The state of gold mining in Ghana. *Trans. Inst. Min. Metall., Section A.*, Vol. 102, pp. A59-A67

Nickson, S.D., 1992. *Cable Support Guidelines for Underground Hard Rock Mine Operations*. M.A.Sc. thesis, Dept. Mining and Mineral Engineering, University of British Columbia, 223 pp.

Obert, L, and Duvall, W.I., 1967. *Rock Mechanics and the Design of Structures in Rock*. New York: John Wiley and Sons. 650 pp.

Pakalnis, R. 1986. *Empirical Stope Design at Ruttan Mine*. Ph.D. thesis. University of British Columbia. 276 pp.

Pakalnis, R., and Vongpaisal, S., 1993. Mine design, an empirical approach. *Proc. International Congress on Mine Design*, Kingston, Canada, pp. 455-467.

Pakalnis, R., Nickson, S., Lunder, P., Clark, L., Milne, D., and Mah, P., 1996. Empirical methods for the design of mine structures. *11e Colloque en Controle de Terrain de lAssociation Minierre du Quebec*, Val d'Or, Quebec, 12 pp.

Palmstrom, A., 1995. *RMi-A Rockmass Characterization System for Engineering Purposes*. Ph.D. thesis, NGI, Norway.

Papaliangas, T., Hencher, S.R., Lumsden, A.C., and Manopoulous, S. 1993. The effect of frictional fill thickness on the shear strength of rock discontinuities. *Int. J. Rock Mech. Min. Sci. & Geomech. Abstr.* Vol. 30 No. 2, pp. 81-91.

Pine, R.J., 1992. Risk Analysis design applications in mining geomechanics. *Trans. Inst. Min. Metall., Section A.*, Vol. 101, pp. A149-A157.

Pine, R.J., lay, S., Randall, M.M., Trueman, R., 1992. Rock engineering design developments at South Crofty mine. *Trans. Inst. Min. Metall., Section A.*, Vol. 101, pp. A13-A22.

Potvin, Y. and Milne, D., 1992. Empirical cable bolt support design. *Rock Support*, (eds. Kaiser and McCreath), Rotterdam: A.A. Balkema, pp. 269-275.

Potvin, Y., 1998. Rock mechanics principles for open stope mining at Mount Isa Mines. *CIM-AGM*, Montreal, on CD-ROM.

Potvin., Y., 1988. *Empirical open Stope Design in Canada*. Ph.D. thesis, Dept. Mining and Mineral Processing, University of British Columbia, 343 pp.

Priest, S.D. and Hudson, J.A., 1976. Discontinuity spacings in rock. *Int. J. Rock Mech. Min. Sci. & Geomech. Abstr.*, Vol. 13, pp. 135 - 148.

Priest, S.D., 1993. *Discontinuity Analysis for Rock Engineering*. London: Chapman & Hall, 473 pp.

Priest, S.D., and Hudson, J.A, 1983. Probabilistic stability analysis of variable rock slopes. *Trans. Inst. Min. Metall., Section A*, Vol. 92, pp. A1 - A12.

Quesnel, W.J.F., and Ley, G.M.M., 1991. The development of mine design guidelines for dilution control, Bousque Div., No.1 Shaft, Lac Minerals, Ltd. *93rd CIM-AGM*, Vancouver, British Columbia, 12 pp.

Reschke, A.E, and Romanowski, J., 1993. The success and limitations of Mathews analysis for open stope design at HBMS, Flin Flon operations. *95th CIM-AGM*, Calgary, paper # 136, 13 pp.

Ryder, J.A., 1988. Excess shear stress in the assessment of geologically hazardous situations. *Journal of South African Inst. of Mining and metallurgy*, Vol. 88, (1), pp. 27-39.

Schen, B., and Barton, N., 1997. The disturbed zone around tunnels in jointed rock masses. *Int. J. Rock Mech. and Min. Sci. & Geomech. Abstr.* Vol. 34, No. 1, pp. 117-125.

Scobble, M.J., and Moss, A., 1994. Dilution in underground bulk mining: Implications for production management, mineral resource evaluation II: methods and case histories. *Geological Society Special Publication No. 79*, pp. 95-108.

Sinclair et. al., 1978. *The Geology of Ashanti Goldfields*. Unpublished Geological Report, A.G.C. (Gh) Ltd.

Speight, H.E., 1992. Geomechanical assessment for the stability of bored raises. *Proc. Western Australian Conference on Mining geomechanics*. (eds. Szwedzicki, T., Baird, G.R., and Little, T.N), Kalgoorlie, Western Australia, pp. 105-110.

Stacey, T.R., and Page, C.H., 1986. *Practical Handbook for Underground Rock Mechanics*. Germany, Trans Tech Publications, 144 p.

Stewart, S.B.V., and Forsyth, W.W., 1995. The Mathews method for open stope design. *CIM Bulletin*, Vol. 88 (992), pp. 45-53.

Stini, I., 1950. *Tunnelbaugeologie*; Springer-Verlag, Vienna, 366 pp.

Suorineni, F.T., 1988. Ground control in mineral exploitation in Ghana. *Proc. Int. Conf. Geology of Ghana*, Accra, Ghana, pp. D11-D18

Suorineni, F.T., 1990. Rock property investigation for excavation and performance control. Late paper, *ISRM Int. Symp. On Static and Dynamic Considerations in Rock Engineering*, (ed. Brummer), Swaziland, South Africa.

Suorineni, F.T., and Borsah, J.K., 1993. Typical strength characteristics of some Ghanaian mine rocks. *Proc. National Conf. On Mining*, (ed., Tidzi) Institute of Mining and Mineral Engineering, University of Science and Technology, Kumasi, 9 pp.

Suorineni, F.T., and Tidzi, K.E.N., 1990. Geomechanical characteristics of a pulverized infilling material of a shear zone. *Proc. Int. Conf. On Rock Joints*, Loen, Norway, pp. 317-321.

Suorineni, F.T., Dusseault, M.B., and Brummer, R.K., 1995. Probabilistic risk and reliability evaluation of ground control practices in underground mining: The safety and economic implications. *Proc. 35th U.S. Symp. On Rock Mech.*, (ed. Daemen and Shultz), Reno, Nevada, Rotterdam: A.A. Balkema, pp. 579-584.

Suorineni, F.T., Tannant, D.D., and Kaiser, P.K., 1997. Determination of stope geometry and relative structural orientations for use in the stability graph. *CIM Annual General meeting*, Rock Mechanics and Strata Control Session, Vancouver, published on CD-ROM.

Tannant, D.D., and Diederichs, M.S., 1997. *Cablebolt Optimization in #3 Mine*. Report to Shawn Seldon, Kidd Mines Division, Timmins, Ontario, 65 pp.

Tannant, D.D., Martin, C.D. and Kaiser, P.K., 1997. *Site Characterization of the 6800 to 7800Mining Block.* Report to Kidd Mining Division, 48 pp.

Terzaghi, K., 1946. Rock defects and loads on tunnel supports. *Rock Tunnelling with Steel Supports*, (eds. Proctor and White), Youngstown, OH, Commercial Shearing and Stamping Company, 1, pp. 17-99.

Tinnuci, J., 1995. *Assessment of expected infrastructure conditions in phase two of Kidd Creek #3 Mines.* Report to Falconbridge Lt., Ref. 029-7, 16 pp.

Tyler, D.B., 1991. *Design Guidelines for Open Stopes and Associated Drives in Narrow Vein Metalliferous Deposits.* Ph.D. thesis, Camborne School of Mines.

Tyler, D.B., Trueman, R.T., and Pine, R.J., 1991. Rock bolt support design using probabilistic method of keyblock analysis. *Proc. 32nd U.S. Symp. Rock Mechanics*, Norman, Oklahoma, pp.1037-1047

Tyler, DB., and Trueman, R., 1993. Probabilistic keyblock analysis for support design and effects of mining induced stress keyblock stability – A case study. *Trans. Inst. Min. Metall., Section A.*, Vol. 102, pp. A43-A49.

Udd, J.E., Wang, A., 1985. A comparison of some approaches to the classification of rockmasses for geotechnical purposes. *Proc. 26th U.S. Symp. On Research and Engineering Rock Mechanics*, (ed., Ashworth), Rotterdam: A.A. Balkema, Vol. 1, pp. 69-78

Udo, W., 1996. *Geotechnical investigation reports.* Geotechnical Engineering Department.

Van de Geer, J.P. 1971. *Introduction to Multivariate Analysis for the Social Sciences.* W.H. Freeman and Company, San Fracisco, 293pp.

Wagner, H., and Godfrey, J.B., 1976. Location and support of tunnels in deep level gold mines. *Proc. Tunnelling'76*, (ed. Jones), IMM, pp. 341-347.

White, R.V., 1984. Evaluating calculated risk in geotechnical engineering. *J. Geotech. Engng.*, Vol. 110, No. 2, pp. 145-189.

Whiteway, P., 1996. On the leading edge: Kidd Mine 30th Anniversary. *Supplement to CMJ*, June, pp 16-32.

Wickham, G.E., Tiedmann, H.R., and Skinner, E.H., 1974. Ground support prediction model, RSR concept. *Proc. 2nd RETC*, San Francisco, Vol. 1, pp. 691-707.

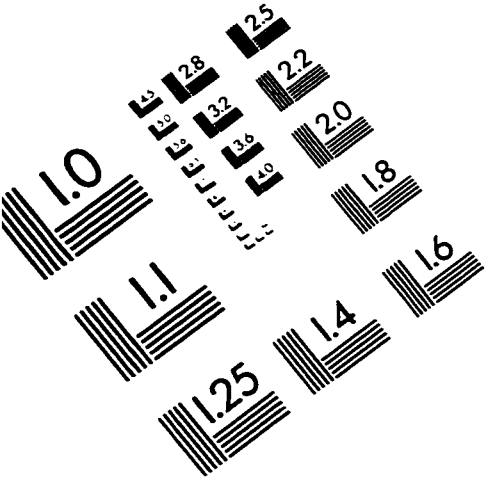
Widerhofer, R. 1970. Die theorie der plastischen zonen in der geomechanik; Ihre anwendung zu einer wirtschaftlichen bemessung einer tunnelauskleidung. *Proc. 2nd ISRM Congr. Beograd*, Vol. 2, pp. 407-418.

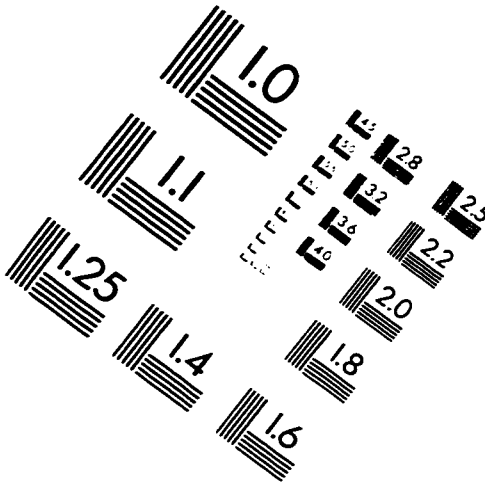
Wiles, T.D., Nicholls, D., 1993. Modelling discontinuous rock masses in three dimensions using Map3D. *1st Canadian Symp. On Numerical Modelling Applications in Mining and Geomechanics*, Montreal, Quebec, pp. 40-49.

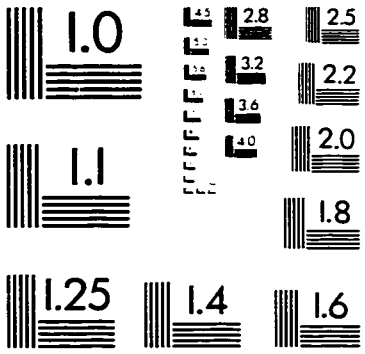
Yu, T.R., and Quesnel, W.J., 1984. Applied rock mechanics for blasthole stoping at Kidd Creek Mines. *Geomechanics Applications in Underground Hard Rock Mining.* SME, pp. 93-108.

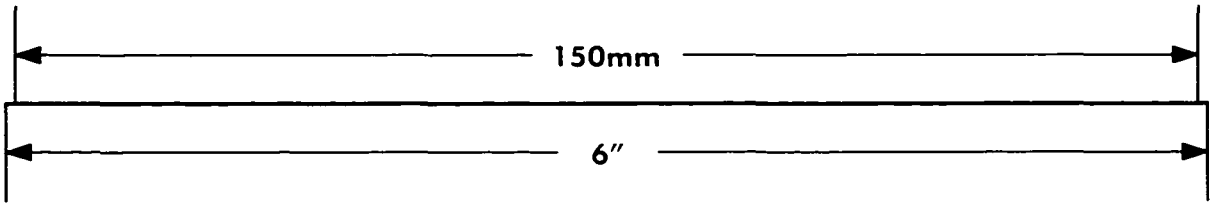
Yu, T.R., and Vongpaisal, S., 1996. New blast damage criteria for underground blasting. *CIM Bulletin*, 89 (998), pp. 139-145.

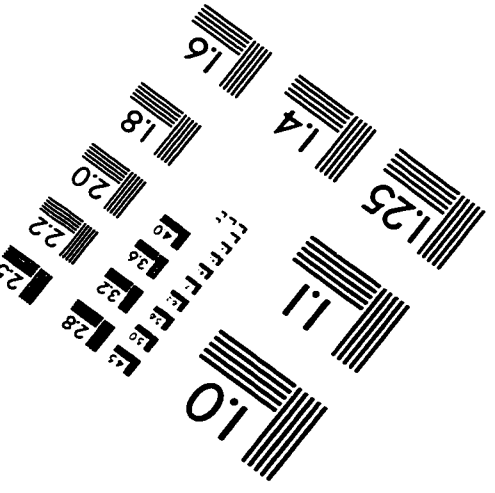
IMAGE EVALUATION
TEST TARGET (QA-3)

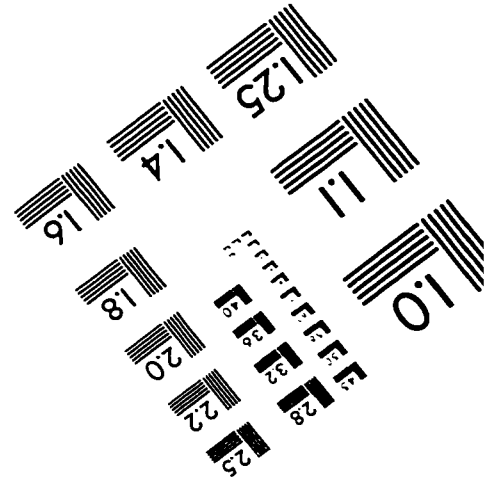












APPLIED IMAGE . Inc
1653 East Main Street
Rochester, NY 14609 USA
Phone: 716/482-0300
Fax: 716/288-5989

© 1993, Applied Image, Inc., All Rights Reserved